TECHNISCHE UNIVERSITÄT MÜNCHEN

TUM School of Engineering and Design

Continuum-based Computational Approaches for Modeling Tumor Growth

Johannes Josef Kremheller

Vollständiger Abdruck der von der TUM School of Engineering and Design der Technischen Universität München zur Erlangung des akademischen Grades eines

Doktors der Ingenieurwissenschaften

genehmigten Dissertation.

Vorsitzende:	Prof. Dr. Petra Mela
Prüfer der Dissertation:	
	1. Prof. Dr.-Ing. Wolfgang A. Wall
	2. Prof. Bernhard Schrefler, Ph.D.

Die Dissertation wurde am 15.04.2021 bei der Technischen Universität München eingereicht und durch die TUM School of Engineering and Design am 31.08.2021 angenommen.

Abstract

Predictive and personalized models of cancer can enhance the understanding of the disease and aid in the development of more effective patient-specific treatment strategies. This thesis deals with computational approaches for such cancer models. Specifically, a group of continuum models for (a-)vascular tumor growth is developed. The models are based on a thermodynamically sound description of tumor tissue as a multiphase porous medium including fluid flow, species transport and solid deformation. One solid phase, the extracellular matrix (ECM), multiple fluid phases, which in the context of this thesis are cells, interstitial fluid (IF) and blood, and various species such as nutrients, growth factors or drugs can be considered. The resulting coupled nonlinear partial differential equations are brought into an arbitrary Lagrangean-Eulerian (ALE) formulation to enable a consistent treatment of large deformations of the solid phase. They are spatially discretized using the finite element method (FEM).

A special focus lies on the vasculature and its interaction with tumor growth. Three different model types are developed, characterized by a homogenized, discrete and hybrid representation of the vascular network, respectively. In the homogenized variant, the vasculature is included as an additional pore space with blood flow and species transport. An evolution equation for the vascular volume fraction governs angiogenesis and blood vessel remodeling. In the discrete variant, the vasculature is embedded as a one-dimensional inclusion into the surrounding tissue. Blood flow and species transport are solved in the 1D domain and coupled with the surrounding tissue via 1D-3D exchange terms. A centerline- and a surface-coupled variant with corresponding line or surface source terms in the governing equations of the 3D domain are discussed, implemented and numerically studied. A major advantage of both schemes is that the 1D and the 3D domain can be meshed independently. The rationale behind the hybrid variant is to resolve larger vessels whose topology and structure can be acquired by non-invasive imaging techniques, and to homogenize smaller vessels which are not accessible in this way. Thus, the heterogeneity of blood flow inside the network can be preserved better than in the homogenized variant, and less anatomic data than in the discrete variant is required. Blood flow and species transport in the two representations of the vasculature are coupled via constraints which are enforced by a mortar-type approach with penalty regularization or a Gauss-point-to-segment scheme.

Partitioned and monolithic algorithms are implemented to resolve the coupling between the single physical fields. Numerical studies reveal that a fully-monolithic scheme is the most efficient and robust one for the tumor growth model over a wide range of parameters.

Several further numerical examples show the validity of the framework and its applicability to tumor growth. Angiogenesis including chemo- and haptotaxis, oxygen transport, necrosis and blood vessel remodeling are among the investigated phenomena. Furthermore, nanoparticle-based drug delivery and hyperthermia treatment are studied as exemplary treatment strategies.

Finally, the hybrid representation of the vasculature is examined in more detail for modeling perfusion through solid tumors. It is validated by a comparison with a corresponding fully-resolved model. Concurrently, its parameters are inversely identified and optimized. All numerical tests are performed on a complex data set of heterogeneous vascular architectures extracted from three different tumors. Excellent agreement in terms of mean representative elementary volume blood and IF pressure is demonstrated. Larger errors are present for flow in the smaller homogenized vessels. A possible strategy to improve the hybrid model by taking the volume fraction of smaller vessels into account is additionally proposed and tested.

Zusammenfassung

Prädiktive und personalisierte Krebsmodelle können das Verständnis der Krankheit verbessern und bei der Entwicklung effektiverer patientenspezifischer Behandlungsstrategien helfen. Die vorliegende Arbeit beschäftigt sich mit numerischen Ansätzen für solche Krebsmodelle. Konkret wird eine Gruppe von Kontinuumsmodellen für (a-)vaskuläres Tumorwachstum entwickelt. Die Modelle basieren auf einer thermodynamisch sauberen Beschreibung des Tumorgewebes als mehrphasiges poröses Medium mit Fluidströmung, Speziestransport und Festkörperdeformation. Es können eine Festkörper-Phase, die extrazelluläre Matrix (ECM), mehrere Fluid-Phasen, im Rahmen dieser Arbeit Zellen, interstitielles Fluid (IF) und Blut, und verschiedene Spezies wie Nährstoffe, Wachstumsfaktoren oder Medikamente berücksichtigt werden. Die resultierenden gekoppelten nichtlinearen partiellen Differentialgleichungen werden in eine *arbitrary Lagrangean-Eulerian* (ALE) Formulierung gebracht, um eine konsistente Behandlung von großen Deformationen der Festkörper-Phase zu ermöglichen. Sie werden mit Hilfe der Finite-Elemente-Methode (FEM) räumlich diskretisiert.

Ein besonderes Augenmerk liegt auf der Vaskulatur und ihrer Interaktion mit dem Tumorwachstum. Es werden drei verschiedene Modelltypen entwickelt, die sich durch eine homogenisierte, diskrete bzw. hybride Darstellung des Gefäßnetzes auszeichnen. In der homogenisierten Variante wird das Gefäßsystem als zusätzlicher Porenraum mit Blutfluss und Speziestransport eingebunden. Eine Evolutionsgleichung für den vaskulären Volumenanteil bestimmt die Angiogenese und das Remodeling der Blutgefäße. In der diskreten Variante wird das Gefäßsystem als eindimensionale Einbettung in das umgebende Gewebe eingebracht. Blutfluss und Speziestransport werden im 1D-Gebiet gelöst und über 1D-3D-Austauschterme mit dem umgebenden Gewebe gekoppelt. Eine linien- und eine oberflächengekoppelte Variante mit entsprechenden Linien- bzw. Oberflächenquelltermen in den vorherrschenden Gleichungen des 3D-Bereichs werden diskutiert, implementiert und numerisch untersucht. Ein großer Vorteil beider Verfahren ist, dass das 1D- und das 3D-Gebiet unabhängig voneinander vernetzt werden können. Der Grundgedanke hinter der hybriden Variante ist die Auflösung größerer Gefäße, deren Topologie und Struktur mit nicht-invasiven bildgebenden Verfahren erfasst werden kann, und die Homogenisierung kleinerer Gefäße, die auf diese Weise nicht zugänglich sind. Dadurch kann die Heterogenität des Blutflusses innerhalb des Netzwerks besser erhalten werden als bei der homogenisierten Variante, und es werden weniger anatomische Daten als bei der diskreten Variante benötigt. Blutfluss und Speziestransport in den beiden Darstellungen des Gefäßsystems sind über Zwangsbedingungen gekoppelt, die durch einen *Mortar*-Ansatz mit *Penalty*-Regularisierung oder ein *Gauss-point-to-segment*-Schema erzwungen werden.

Um die Kopplung zwischen den einzelnen physikalischen Feldern aufzulösen, werden partitionierte und monolithische Algorithmen implementiert. Numerische Untersuchungen zeigen, dass ein vollständig monolithisches Schema das effizienteste und robusteste für das Tumorwachstumsmodell über einen weiten Bereich von Parametern ist.

Mehrere weitere numerische Beispiele zeigen die Gültigkeit des Frameworks und seine Anwendbarkeit auf Tumorwachstum. Angiogenese einschließlich Chemo- und Haptotaxis, Sauerstofftransport, Nekrose und Blutgefäß-Remodeling gehören zu den betrachteten Phänomenen. Des Weiteren werden Nanopartikel-basierte Medikamentenabgabe und Hyperthermie als beispielhafte Behandlungsstrategien untersucht.

Schließlich wird die hybride Darstellung des Gefäßsystems zur Modellierung von Perfusion durch solide Tumoren näher beleuchtet. Sie wird durch einen Vergleich mit einem entsprechenden vollaufgelösten Modell validiert. Gleichzeitig werden die Parameter des hybriden Modells invers identifiziert und optimiert. Alle numerischen Tests werden auf einem komplexen Datensatz von heterogenen Gefäßarchitekturen durchgeführt, die aus drei verschiedenen Tumoren extrahiert wurden. Es wird eine ausgezeichnete Übereinstimmung in Bezug auf den über das repräsentative Elementarvolumen gemittelten Blut- und den IF-Druck gezeigt. Größere Fehler sind für die Strömung in den kleineren homogenisierten Gefäßen vorhanden. Eine mögliche Strategie zur Verbesserung des hybriden Modells durch Berücksichtigung des Volumenanteils der kleineren Gefäße wird zusätzlich vorgeschlagen und getestet.

Danksagung

Die vorliegende Dissertation entstand in der Zeit von 2017 bis 2021 während meiner Tätigkeit als wissenschaftlicher Mitarbeiter am Lehrstuhl für Numerische Mechanik (LNM) der Technischen Universität München (TUM). Während dieser Zeit konnte ich auf die fachliche, moralische und organisatorische Unterstützung von vielen Personen bauen. Diesen möchte ich hier ganz herzlich für ihren Beitrag zum Gelingen dieser Arbeit danken.

Zuallererst danke ich meinem Doktorvater Prof. Dr.-Ing. Wolfgang A. Wall für die Möglichkeit am LNM zu promovieren und für das damit in mich gesetzte Vertrauen. Ich habe die von ihm gewährten Freiräume für meine wissenschaftliche Arbeit stets als Privileg empfunden. Darüber hinaus war er mit seiner Begeisterung für Forschung und Lehre ein Vorbild und Ansporn für mich. Damit und mit seiner menschlichen, humorvollen und offenen Art hat er am Lehrstuhl den Nährboden für exzellente Wissenschaft geschaffen. Weiterhin möchte ich Prof. Bernhard A. Schrefler für die wohlwollende Begleitung meiner Promotion danken. Ohne seinen Anstoß hätte es das Tumor-Projekt am LNM nie gegeben. Unsere Zusammenarbeit war geprägt durch seine Integrität, seine ansteckende Begeisterung für Forschung und seine menschlich sehr angenehme Art. Er persönlich und das von ihm initiierte Projekt haben mir Vieles ermöglicht und einige Türen geöffnet. Für die Übernahme des Vorsitzes meiner Prüfungskommission danke ich Prof. Dr. Petra Mela. Auch Dr.-Ing. Anh-Tu Vuong hat einen großen Anteil am Gelingen dieser Arbeit, wofür ich ihm ganz herzlich danke. Seine wissenschaftlichen Vorarbeiten zu porösen Medien und v.a. der von ihm implementierte Code waren ein enormer Startvorteil für mich. Aber auch unsere fachlichen Diskussionen und so mancher gute Zuspruch waren mir eine große Hilfe.

Ich hatte das gewaltige Glück, am LNM mit talentierten und inspirierenden Kollegen zusammenzuarbeiten. Viele von ihnen sind zu guten Freunden geworden. Allen derzeitigen und ehemaligen Kollegen gebührt mein Dank für fachliche Diskussionen, die Hilfe bei Computer- oder Software-Problemen, gemeinsame Rennrad-Touren und Fußball-Trainings, die morgendliche Kaffee-Runde und das ein oder andere Feierabend-Bier. Insbesondere mein langjähriger Bürokollege Sebastian Fuchs stand mir immer mit Rat/Rad und Tat zur Seite. Außerdem waren er, Jonas Eichinger, Sebastian Brandstäter und Christoph Schmidt eine große moralische Unterstützung in allen Lebenslagen. Barbara Wirthl danke ich für die gute Zusammenarbeit, ihre hervorragenden Abbildungen und das Korrekturlesen. Jonas Nitzler schätze ich für seine fachliche Kompetenz und seine humorvolle Art. Interessante Diskussionen zu Poromechanik in der Lunge durfte ich mit Carolin Geitner führen. Dr.-Ing. Karl-Robert Wichmann danke ich für die Beantwortung all meiner Fragen zu Admin-Angelegenheiten. Schließlich danke ich allen Mitgliedern des Admin-Teams für die gute Zusammenarbeit. Bei allen Studierenden, die ich im Rahmen einer Studienarbeit betreuen durfte, bedanke ich mich für den geleisteten Beitrag.

Zu guter Letzt möchte ich mich bei meiner Familie und bei meinen Freunden bedanken. Ohne ihren Rückhalt und ihre emotionale Unterstützung wäre diese Arbeit undenkbar. Ein ganz besonderes Dankeschön gilt meinen Eltern, die mich immer bestärkt und gefördert haben. Am unmittelbarsten aber hat die letzten viereinhalb Jahre meine Frau Anna mit mir gemeinsam erlebt. Sie war während aller Erfolge und Rückschläge und durch alle Höhen und Tiefen an meiner Seite. Ich danke ihr für ihre guten Ratschläge, ihre bedingungslose Unterstützung, ihren Zuspruch in schwierigen Situationen und ihren Humor.

München, im Oktober 2021 Johannes Kremheller

Contents

Nomenclature

Abbreviations

ALE	Arbitrary Lagrangean-Eulerian
AMF	Alternating magnetic field
AMG	Algebraic multigrid
AUC	Area-under-the-curve
BGS	Block Gauss-Seidel
CEI	Constrained entropy inequality
EC	Endothelial cell
ECM	Extracellular matrix
EPR	Enhanced permeability and retention
FN	Fibronectin
GMRES	Generalized minimal residual method
GPTS	Gauss-point-to-segment
HC	Host/Healthy cell
HV	Homogenized vasculature
IF	Interstitial fluid
LM	Lagrange multiplier
LTC	Living tumor cell
MMP	Matrix metalloproteinase
MP	Mortar Penalty
MTS	Multicellular tumor spheroid
NH	Neo-Hooke
NP	Nanoparticle
NTC	Necrotic tumor cell
OXY	Oxygen
PDE	Partial differential equation
REV	Representative elementary volume
SAR	Specific absorption rate
SEI	Simplified entropy inequality
std. dev.	Standard deviation

SVK	Saint-Venant-Kirchhoff
TAF	Tumor angiogenic factor
TC	Tumor cell
TCAT	Thermodynamically Constrained Averaging Theory
VEGF	Vascular endothelial growth factor

General style for scalars, vectors and tensors

$\mathbf{Q},\ \boldsymbol{\kappa}$	Discrete matrix
$\mathbf{q},\ \boldsymbol{\psi}$	Discrete vector
$\boldsymbol{v}, \boldsymbol{\sigma}$	Style for vectors and tensors
$q,\ Q$	Style for a scalar value

Operators and symbols

$(\bullet)^T$	Transpose of a vector or matrix
$(\bullet)^{-1}$	Inverse of a matrix
$(\bullet)^{-T}$	Inverse of transpose of a matrix
$\mathbf{I},\ \boldsymbol{I}$	Identity matrix
$(\check{\bullet})$	Prescribed quantity at a boundary or at the beginning of a simulation
$\delta\,(\bullet)$	Variation of a quantity
$\boldsymbol{\nabla}\cdot$	Current divergence
$\boldsymbol{\nabla}_0\cdot$	Material divergence
$\frac{\mathrm{d}^\alpha(\bullet)}{\mathrm{d}t}$	Material derivative for phase α
$\boldsymbol{\nabla}$	Current gradient
$\boldsymbol{\nabla}_0$	Material gradient
$\langle\bullet\rangle_+$	Macaulay brackets
$(\bullet,\bullet)_\Omega$	Inner L^2 product
$\det$	Determinant of a matrix
tr	Trace of a matrix
$\mathring{\bullet} = \left.\frac{\partial(\bullet)}{\partial t}\right\vert_{\boldsymbol{X}}$	Time derivative with fixed material skeleton coordinate
$\tilde{H}\,(\bullet)$	Smoothed Heaviside function
$H\,(\bullet)$	Heaviside function

Configurations, domains and boundaries

Γ	Boundary of domain
Λ_0	Material/Reference configuration of 1D vasculature domain
Λ_t	Current/Spatial configuration of 1D vasculature domain

$\mathcal{U}$	Generic domain
Ω_0	Material/Reference configuration of 2D/3D tissue domain
Ω_t	Current/Spatial configuration of 2D/3D tissue domain

TCAT notation

$\boldsymbol{u}^{i\alpha}$	Macroscopic diffusion velocity of species i in phase α
$\boldsymbol{v}^{\alpha}$	Velocity of phase α
$\boldsymbol{v}^{i\alpha}$	Velocity of species i in phase α
$\boldsymbol{g}^{\alpha}$	Body force of phase α
$\mathcal{M}^{\overline{\overline{\alpha}}}$	Macroscale phase mass conservation equation
$\mathcal{M}^{\overline{\overline{i\alpha}}}$	Macroscale species mass conservation equation
$\boldsymbol{\mathcal{P}}^{\overline{\overline{\alpha}}}$	Macroscale phase momentum conservation equation
$\mathfrak{I}_{\mathrm{c}\alpha}$	Index set of entities connected to phase α
$\overset{\kappa\to\alpha}{M}$	Inter-phase mass transfer of from phase κ to phase α
$\overset{i\kappa\to i\alpha}{M}$	Inter-phase mass transfer of species i from phase κ to phase α
$\overset{\kappa\to\alpha}{\mathbf{T}}_0$	Interaction forces between adjacent phases (in current formulation without interfaces)
$\mathfrak{I}_{\mathrm{f}}$	Set of fluid-phase indices
$\mathfrak{I}_p$	Set of phase indices
$\mathfrak{I}_s$	Set of species indices
$\varepsilon^{\alpha} r^{i\alpha}$	Intra-phase production term of species i in phase α
$\omega^{i\,\overline{\alpha}}$	Mass fraction of species i dissolved in phase α
$\sum_{\kappa\in\mathfrak{I}_{c\alpha}}$	Sum over all phases κ connected to phase α

Continuum poro-mechanics

$\boldsymbol{\kappa}$	Conductivity tensor
$\boldsymbol{\sigma}$	Cauchy stress tensor
$\boldsymbol{C}$	Right Cauchy-Green deformation tensor
$\boldsymbol{E}$	Green-Lagrange strain tensor
$\boldsymbol{F}$	Deformation gradient
$\boldsymbol{k}$	Permeability tensor
$\boldsymbol{n}$	Spatial normal vector
$\boldsymbol{P}$	First Piola-Kirchhoff stress tensor
$\boldsymbol{R}$	Rotation tensor
$\hat{\boldsymbol{R}}$	Resistance tensor
$\boldsymbol{S}$	Second Piola-Kirchhoff stress tensor

$\boldsymbol{t}$	Spatial traction vector
$\boldsymbol{U}$	Material stretch tensor
$\boldsymbol{u}$	Displacement
$\boldsymbol{v}$	Spatial stretch tensor
$\boldsymbol{X}$	Material/Reference coordinate
$\boldsymbol{x}$	Spatial/Current coordinate
χ	Mapping between material configuration of solid phase and fluid phase in ALE description
$\varepsilon^\alpha s^\alpha$	Heat source term
λ^s, μ^s	Lamé constants
ν^s	Poisson's ratio
φ	Nonlinear deformation map
ε^α	Volume fraction of phase α
Ψ^s	Strain energy function of solid phase
ρ, ρ_0	Current and reference density
c_p	Specific heat capacity at constant pressure
$\mathrm{d}V$	Infinitesimal volume element
E^s	Young's modulus
J	Determinant of deformation gradient
l_{ma}	Length scale of macroscale
l_{me}	Length scale of megascale
l_{mi}	Length scale of microscale
m	Mass
p	Pressure
T	Temperature
t	Time

Tumor growth model notation

$\boldsymbol{\psi}^{[t,h,l]}$	Vector of generic primary variables of TCs, HCs and IF
$\boldsymbol{j}$	Generic flux term
$\boldsymbol{p}^{[t,h,l]}$	Vector of pressures of TCs, HCs and IF
$\boldsymbol{S}^{[t,h,l]}$	Vector of saturations of TCs, HCs and IF
ε	Volume fraction of pores of the ECM
ψ^f	Generic primary variable of fluid phase $f \in \mathfrak{I}_\varepsilon$ (TCs, HCs and IF)
$\mathfrak{I}_\varepsilon$	Set of tumor cell, host cell and interstitial fluid indices
$C^{n\overline{\alpha}}$	Oxygen concentration in phase $\alpha \in l, v, \hat{v}$
C_{coll}	Law for blood vessel collapse

$P^{\alpha}_{\mathrm{oxy}}$	Partial pressure of oxygen in phase $\alpha \in l, v, \hat{v}$
p^s	Solid pressure
$p^{\alpha\beta}$	Pressure difference between fluid phases $\alpha, \beta \in \mathfrak{I}_\varepsilon$
S^f	Saturation of a fluid phase $f \in \mathfrak{I}_\varepsilon$

Embedded vasculature and 1D-3D coupling

$\boldsymbol{n}$	Normal on lateral surface of 1D inclusion
$\boldsymbol{t}$	Tangent vector of a 1D segment
$\boldsymbol{w}^{(i\,\hat{v})}$	Relative velocity of fluid or species w.r.t. blood vessel velocity in wall normal direction
$\delta_{\Lambda_t}, \delta_{\partial\mathcal{D}_t}$	Dirac measure along centerline of inclusion respectively its lateral surface (in current configuration)
γ	Coordinate along perimeter of inclusion
$\partial\mathcal{D}$	Lateral surface of blood vessel
$\omega^{i\,\hat{v}}$	Mass fraction of species i dissolved in 1D representation of vasculature
φ^l	Fluid or species primary variable in IF
φ^v	Fluid or species primary variable in homogenized vasculature
$\varphi^{\hat{v}}$	Fluid or species primary variable in embedded vasculature
A	Blood vessel area
D	Blood vessel diameter
$f(\bullet)$	Generic function for 1D-3D mass transfer
g	Gap (pressure or mass fraction difference) between 1D and 3D representation of vasculature
L	Length of a 1D segment
$p^{\hat{v}}$	Blood pressure in embedded domain
R	Blood vessel radius
S	Arc-length coordinate of a 1D segment in reference configuration
s	Arc-length coordinate of a 1D segment in current configuration
v^s_t	Projection of solid phase velocity in tangent direction of blood vessel
$v^{\hat{v}}$	Blood velocity in embedded domain

Selected parameters of the tumor growth model

β_T	Heat exchange coefficient to surrounding tissue
χ_0	Chemotactic coefficient
δ	Coefficient in nonlinear law for effective diffusivity (3.43)
(S/V)	Surface-to-volume ratio
μ^α	Viscosity of phase α

$\omega_{\chi_0/2}^{TAF\bar{l}}$	Value of $\omega^{TAF\bar{l}}$ where sensitivity to TAF gradient is half the constant sensitivity χ_0
$\sigma_{\alpha\beta}$	Interfacial tension between fluid phases $\alpha, \beta \in \mathfrak{I}_\varepsilon$
Θ	Haptotactic coefficient
a, b	Model parameters in pressure-saturation laws (3.35) and (3.36)
A_f	Exponent for relative permeability law (3.42) of phase $f \in \mathfrak{I}_\varepsilon$
D^v	Diffusion coefficient of homogenized vasculature
$D_{\text{eff}}^{i\alpha}$	Effective diffusion coefficient of species i in phase α
K	Bulk modulus
k	Intrinsic permeability of ECM
k_{rel}^f	Relative permeability of phase $f \in \mathfrak{I}_\varepsilon$
L_p	Hydraulic conductivity
$T_{1/2}$	Plasma half-life

Time discretization

Δt	Time step size
θ	Parameter of the one-step-θ-scheme
n	Time step
t_0, t_E	Start and end of the simulated time period of interest

Space discretization

$\mathbf{d}^s$	Nodal displacements
$\mathbf{p}^v$	Nodal pressure in homogenized vasculature
$\mathbf{p}^{\hat{v}}$	Nodal blood pressure in 1D domain
$\mathbf{X}$	Discrete nodal points in reference configuration
$\mathbf{x}$	Discrete nodal points in current configuration
$\hat{N}$	Shape function in 1D domain
$\hat{n}_{\text{ele}}$	Number of elements of 1D vasculature domain
$\hat{n}_{\text{nodes}}$	Number of nodes of 1D vasculature domain
$\hat{n}_{\text{spec}}$	Number of species in 1D vasculature domain
$\mathcal{S}$	Primary variable function space
$\mathcal{V}$	Weighting function space
ξ, η	Parameter space coordinates for integration of 1D-3D coupled terms
h	Element size
j	Node index
N	Shape function in 2D/3D domain
n_{ele}	Number of elements of 2D/3D domain

n_{GP}	Number of Gauss points
n_{seg}	Number of segments
n_{dim}	Number of spatial dimensions
n_{nodes}	Number of nodes of 2D/3D domain
n_{spec}	Number of species in 2D/3D domain
$\boldsymbol{\omega}$	Nodal species mass fractions in 2D/3D domain
$\boldsymbol{\varepsilon}^{v}$	Nodal vascular volume fraction
$\boldsymbol{\psi}^{[t,h,l,v]}$	Nodal primary variables of TCs, HCs, IF and HV
$\boldsymbol{\psi}^{[t,h,l]}$	Nodal primary variables of TCs, HCs and IF
$\boldsymbol{\omega}^{i\hat{v}}$	Nodal species mass fractions in 1D domain

Constraint enforcement strategies

$\boldsymbol{\kappa}$	Diagonal scaling matrix for mortar penalty approach
$\boldsymbol{\lambda}$	Discrete nodal Lagrange multiplier vector
$\mathbf{D}$, $\mathbf{M}$	Mortar matrices
$\mathbf{g}$	Weighted nodal pressure gap
ϵ_{GPTS}, ϵ_{MP}	Penalty parameters for GPTS and MP constraint enforcement
κ	Scaling term for mortar penalty approach (corresponds to one entry of diagonal scaling matrix)
λ	Lagrange multiplier
$\mathcal{M}$	Subset of nodes in 3D domain participating in 1D-3D coupling
$\mathcal{S}$	Subset of nodes in 1D domain participating in 1D-3D coupling
Π	Additional penalty or Lagrange multiplier potential

Computational solution approach

$\mathbf{R}$	Discrete nonlinear residual
$\Delta\left(\bullet\right)$	Newton increment of a nodal primary variable
ω_k	Aitken relaxation parameter
$\tilde{(\bullet)}$	Actual solution of Newton scheme employed to construct relaxed solution with Aitken relaxation in equation (4.128)
$\varepsilon_{\mathrm{part}}$	Tolerance for partitioned scheme
$\varepsilon_{\mathrm{sf}}$	Tolerance for single field Newton scheme
i	Newton step
j, k	Partitioned step

Super- and subscripts

$(.)^{\alpha}$	Arbitrary phase

$(.)^{\mathrm{D}}$	Dirichlet
$(.)^{F}$	Fibronectin
$(.)^{f}$	Arbitrary fluid phase
$(.)^{h}$	Host/Healthy cells
$(.)^{\mathsf{h}}$	Discretized in space
$(.)^{i}$	Arbitrary species
$(.)^{ly}$	Lymph system
$(.)^{L}$	Living tumor cells
$(.)^{l}$	Interstitial fluid
$(.)^{N}$	Necrotic tumor cells
$(.)^{n}$	Oxygen
$(.)^{\mathrm{N}}$	Neumann
$(.)^{s}$	Solid phase
$(.)^{TAF}$	Tumor angiogenic factors
$(.)^{\mathrm{tot}}$	Total
$(.)^{t}$	Tumor cells
$(.)^{\hat{v}}$	Discrete, one-dimensional vasculature
$(.)^{v}$	Homogenized vasculature
$(.)_{0}$	Quantity defined in reference configuration
$(.)_{\mathrm{abs}}$	Absolute
$(.)_{\mathrm{adap}}$	Adaptation
$(.)_{\mathrm{app}}$	Apparent
$(.)_{\mathrm{bl}}$	Blood
$(.)_{\mathrm{coll}}$	Collapse
$(.)_{\mathrm{cons}}$	Consumption
$(.)_{\mathrm{crit}}$	Critical
$(.)_{\mathrm{drain}}$	Drainage
$(.)_{\mathrm{eff}}, (.)^{\mathrm{eff}}$	Effective
$(.)_{\mathrm{ele}}$	Element
$(.)_{\mathrm{env}}$	Environmental
$(.)_{\mathrm{ex}}$	Exact
$(.)_{\mathrm{hyp}}$	Hypoxic
$(.)_{\mathrm{inter}}$	Interendothelial
$(.)_{\mathrm{leak}}$	Leakage
$(.)_{\mathrm{lm}}$	Log-mean
$(.)_{\mathrm{osm}}$	Osmotic

$(.)_{\mathrm{oxy}}$	Oxygen
$(.)_{\mathrm{pen}}$	Penalty
$(.)_{\mathrm{prod}}$	Production
$(.)_{\mathrm{rel}}$	Relative
$(.)_{\mathrm{rhs}}$	Right hand side
$(.)_{\mathrm{tc}}$	Transcapillary
$(.)_{\mathrm{thresh}}$	Threshold
$(.)_{\mathrm{trans}}$	Transendothelial
$(.)_{\mathrm{tv}}$	Transvascular
$(.)_t$	Quantity defined in current configuration
$(.)_{\mathrm{up}}$	Uptake

Quantities related to the study of solid tumor perfusion

$(\bullet)\vert_{\mathrm{full}}$	Evaluated in full model
$(\bullet)\vert_{\mathrm{hyb}}$	Evaluated in hybrid model
$(S/V)_{\Lambda_{\mathrm{S}}}$	Surface-to-volume ratio of smaller blood vessels
α	Proportionality constant for linear relationship between permeability and vascular volume fraction (6.39)
Λ_{L}	Subset of large blood vessels
Λ_{S}	Subset of small blood vessels
$\mu(\bullet)$	Mean value
Ω_v	Vascular domain
$\overline{(\bullet)}$	Mean value in a REV
$\overline{E}$	Mean error over all REVs
$\partial\Omega_v$	Boundary of vascular domain
$\varepsilon^v_{\Lambda_{\mathrm{S}}}$	Volume fraction of smaller blood vessels
CV	Coefficient of variation
E	Error
I_{L}	Index set of large blood vessels
I_{S}	Index set of small blood vessels
$n_{\mathrm{nodes},\Lambda}$	Number of nodes in the 1D network
$n_{\mathrm{nodes},\Lambda_{\mathrm{L}}}$	Number of nodes in the 1D network of larger vessels
$n_{\mathrm{nodes},\Omega_v}$	Number of nodes in the 3D vascular domain
$n_{\mathrm{nodes},\Omega}$	Number of nodes in the 3D tissue domain
n_{REV}	Number of REVs
p^l_∞	Far-field IF pressure
Q	Volumetric flow
R^2	Coefficient of determination

1 Introduction

"What does mechanical engineering have to do with cancer research?"

This question had to be answered numerous times by the author over the last years. It expresses the, at first sight, reasonable conjecture that the two distinct disciplines do not have much in common. At second sight, however, multiple points of contact become apparent. (Mechanical) engineers have made substantial contributions to the fight against cancer in aspects as diverse as detection, imaging and treatment. Now, as the physics of cancer and especially the various mechanical interactions of malignant cells with the surrounding tissue and the importance of multiscale mass transport for the success of chemotherapy are unraveled, it is evident that engineers can also improve our general understanding of cancer. A routine task for engineers is to develop, implement and use models of complex physical systems. Analogously, advanced computational models of cancer, as the ones developed in this thesis, can be employed to reduce its complexity to a manageable set of underlying principles and phenomena and to gain insight into processes which are not accessible otherwise. The visionary goals of the present research are an individualized prognosis for disease progression including the outcome of different treatment strategies. This requires mechanistic and predictive mathematical and computational models of cancer, which are the main focus of this thesis. In the long term, they will enable medical practitioners to decide on an optimal course of action for the personalized treatment of patients. Thereby, they can greatly enhance the survival chances of many cancer patients in the future.

This introductory chapter is structured as follows: A concise review of cancer is given in Section 1.1. Then, the potentially huge benefits of mechanistic and personalized models for tumor progression and response to treatment are illustrated, a short overview of cancer modeling in general is given and the unique features of the present model are outlined in Section 1.2. The primary achievements of this thesis are stated in Section 1.3. Finally, a brief outline of the subsequent chapters is given in Section 1.4.

1.1 The Fundamentals of Cancer

The content of the following paragraphs is primarily based on two introductory text books on cancer [106, 274] and common knowledge. References are only given when deemed particularly necessary. A special focus is set on the physical aspects of cancer progression and mass transport through solid tumors as these are the effects for which the current model is developed.

A Very Brief Introduction to Cancer Cancer is characterized by abnormal cell growth. It is not a single disease but a group of diseases with approximately 100 types affecting humans.

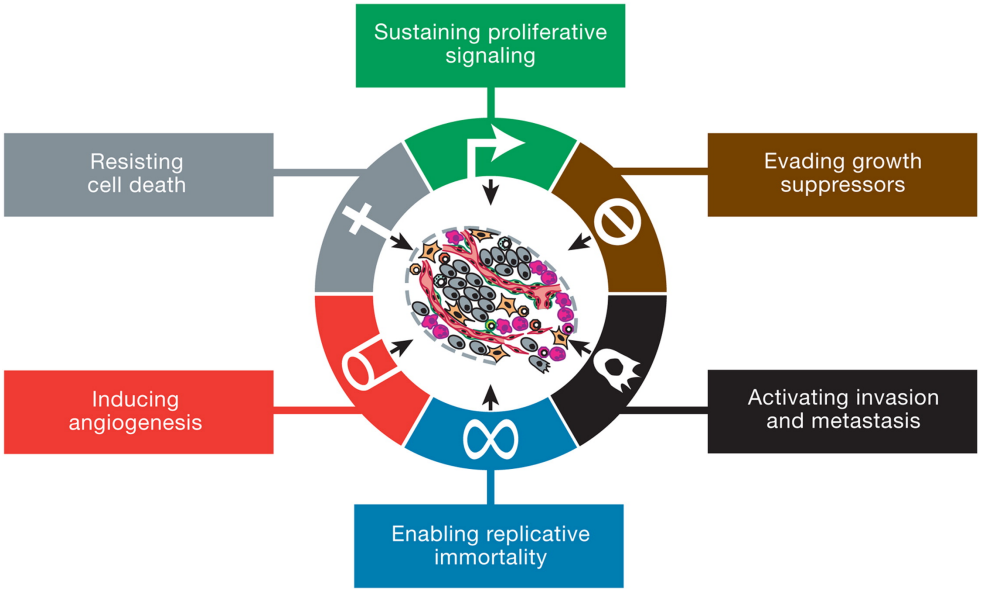

Figure 1.1: The hallmarks of cancer [99, 100] (reprinted from [100] with permission from Elsevier)

Tumors can either be benign or malignant. Malignant tumors can acquire the potential to disperse, that is, to invade healthy areas or to metastasize to distant sites in the body (secondary tumors) from their origin (primary tumor). The majority of tumors in humans or animals are solid tumors occurring in bones, muscles or organs in contrast to blood cancer which does not form tumor masses. Subsequently, only solid tumors will be regarded.

Carcinogenesis, that is, the occurrence of cancer in a specific individual is the result of the cumulative effects of DNA mutations. It is a multistage process which might take years or decades to complete. It is estimated that five to fifteen driver mutations in critical genes, i.e., genes that regulate cell growth and differentiation or DNA repair, are necessary for its development. These genetic alterations may either be inherited ($5-10\,\%$ of cases) or occur randomly due to errors in DNA replication or exposition to carcinogens ($90-95\,\%$ of cases). Factors influencing damage and mutation in DNA are exposure to radiation, diet, smoking and lifestyle. Also infection by viruses, bacteria or other microorganisms may cause cancer. There are potent defense mechanisms in place to detect and repair damaged DNA such that genetic errors are not propagated. However, not all mutations are detected and around one per day is passed on. This is also the reason why the risk of developing cancer significantly increases with age as DNA mutations accumulate.

In an effort to rationalize the description of cancer, Hanahan and Weinberg coined the so-called *hallmarks of cancer*, which are ”distinctive and complementary capabilities that enable tumor growth and metastatic dissemination” [99, 100]. The original six are illustrated in Figure 1.1. Via sustaining proliferative signaling and evading growth suppressors, cancerous cells proliferate at an extremely high rate. They further resist *apoptosis*, i.e., programmed cell death by which the body normally kills defective cells. This enables replicative immortality such that macroscopic clusters of malignant cells, in other words, *tumors* can be formed. These further require access to the vasculature to obtain nutrients from the blood stream and clear waste prod-

ucts. *Angiogenesis*, which is the growth of new vessels induced by the tumor, guarantees the supply of the required nutrients. Finally, invasion and metastasis is the ability to migrate and spread into distant regions in the body. *Invasion* stands for the direct extension and penetration of malignant cells into neighboring tissues, whereas *metastasis* describes the establishment of new cancer colonies in different parts of the body.

Consequently, tumor progression is a process which inherently involves multiple temporal and spatial scales. DNA mutations and metabolism occur at the subcellular scale, cell division and intercellular adhesion on the cellular scale, invasion and angiogenesis on the tissue scale, and finally, metastasis over the whole body. The same applies for time scales during cancer, spanning from fractions of seconds for metabolism to hours for cell division and months or years for invasion and metastasis [155]. Moreover, a precise understanding of cancer is exacerbated by its enormous heterogeneity leading to extensive genetic and phenotypic variations between different tumors but also within the same tumor [33].

Cancer is the second leading cause of death with an estimated 9.6 million deaths, or one in six deaths, globally in 2018. The most common types in men are lung, prostate, colorectal, stomach and liver cancer and in women breast, colorectal, lung, cervical and thyroid cancer [285].

The Phases of Tumor Growth and Their Interaction with the Micro-Environment

Tumor growth can be divided into three phases, namely, the *avascular*, the *vascular* and the *metastatic* phase. The initial avascular phase of cancer progression begins after the occurrence of the previously described DNA mutations. Tumor cells proliferate, interact with and remodel their surrounding *micro-environment* in a dynamic process. Biochemical and mechanical interactions between malignant cells and host cells, the surrounding *extracellular matrix* (ECM), *interstitial fluid* (IF) and blood vessels transform the healthy tissue into a biologically and physically aberrant tumor micro-environment. The ECM is the non-cellular component present within all tissues and organs which provides not only structural support for the cellular constituents via a network of collagen and elastin fibers but is also involved in a large number of biochemical and biomechanical interactions with them [81]. The IF is a body fluid which surrounds the cells, aids in supplying them with nutrients and removes waste products. It seeps out of capillaries at the arteriolar end and is drained at the venular end and by the lymph system. The interplay of tumor cells with their micro-environment and its concurrent manipulation by tumor cells can create a positive tumorigenic feedback loop [47]. It may be involved in tumor initiation, survival, propagation and treatment response [159]. Nowadays, it is well-established that the tumor micro-environment actively influences disease progression and a deeper insight can only be gained by a more comprehensive study of cancers including the environment they themselves shape and reside in. Tumors are not simply masses of cancerous cells but complex ”rogue” organs (or caricatures of organs) [11, 68]. Also therapeutic responses and resistance may be greatly influenced by the tumor micro-environment.

In the early avascular stage of cancer, tumors do not have access to the vascular network. Thus, they rely on diffusion of essential nutrients such as oxygen or glucose and growth factors from surrounding vascularized tissue to continue their growth. In that regard, a major factor is oxygen whose diffusion limit in tissue is $100 - 200\,\mu\mathrm{m}$ [36]. As the tumor grows radially, the outer proliferating cells consume the available oxygen such that the cells in its interior lack oxygen, i.e., they are in a *hypoxic* state and ultimately die. This process is also known as *necrosis*, which

in contrast to normal cell death, is a relatively uncontrolled process. The released chemicals may lead to inflammation. A characteristic shape of such small avascular tumors emerges with an inner necrotic core and an outer viable rim. However, such tumors are confined to sizes of $1-2\,\mathrm{mm}$ as eventually a steady state with a balance between proliferation on the tumor boundary and cell death in its interior is reached.

For further growth, tumors depend on the previously mentioned *angiogenesis* [76, 181]. It is defined as the formation of blood vessels from a pre-existing vasculature [275]. While it also occurs in other growth processes, it is a fundamental process during tumor growth marking the so-called angiogenic switch from an avascular to a much more agressive vascular phenotype with poor prognosis for patients [181]. Angiogenesis is modulated by activator and inhibitor molecules. If the local equilibrium between positive and negative regulators of angiogenesis tips in favor of pro-angiogenic factors, angiogenesis is stimulated. Hypoxic tumors cells may produce these so-called *tumor angiogenic factors* (TAFs), e.g., vascular endothelial growth factors (VEGFs), which diffuse in the IF. Reaching pre-existing blood vessels, TAFs stimulate angiogenesis. Thereby, *endothelial cells*, which line the existing blood vessels, migrate from the pre-existing vasculature towards the tumor [141]. The endothelial cells proliferate, sprout and finally form a new vascular network supplying the tumor with oxygen and other nutrients, the *neovasculature*. As the developed vascular networks are pathological and suffer from several defects as described below, it is a further prime example of the interplay between tumors and their micro-environment. Here, the more direct access to nutrients enables much faster cancer progression. It is well-established that tumor growth is angiogenesis-dependent [76], which underlines that angiogenesis is an essential trait in cancer progression shared by most tumor types as one of the hallmarks of cancer [99].

Metastasis is the third phase of cancer progression and in approximately $90\,\%$ of cases the eventually lethal one. Metastases are new colonies of cancer cells which have left the primary tumor mass, traveled through the blood or lymphatic system and seeded in distant sites throughout the body. In turn, this requires a complex, multi-step process: First, localized invasion of cancerous cells into host tissue must occur. Then, they intravasate into blood or lymphatic vessels and are transported with the general circulation to distant sites. There, they may extravasate into the tissue again and form dormant micrometastases. Finally, these micrometastases may colonize the tissue, in which they have landed, and develop into a secondary tumor, which is the most complex step as the foreign micro-environment they encounter may be quite different to the tumor micro-environment from which they originate. Out of the hundreds to thousands micrometastases found in cancer patients, none might acquire the capability to form a macrometastasis. Overall, the probability for a single cell to successfully complete all these steps is quite low. However, if cancer metastasizes to other tissues or organs, the prognosis for patients decreases dramatically.

Treatment of Cancer The increased understanding of the causes and mechanisms of cancer has only led to relatively minor improvement in treating it. Earlier detection by advanced diagnostic techniques and increased screening may lead to sinking death rates. However, if the tumor is detected in a more advanced stage, only very little progress in terms of treatment success has been made. This might indicate that the potential of traditional cancer therapy strategies has been exhausted and significant improvement can only be expected by novel ones.

The most common cancer treatments are *surgery*, *radiotherapy* and *chemotherapy*. Over decades, these methods have shown that they can extend the survival of cancer patients and even eradicate certain types of tumors. The goal of surgery is to remove the tumor or even its entire host organ via excision. However, this is not always possible, especially if it has metastasized, and it works best if the tumor is contained in one area. Radiotherapy uses ionizing radiation to kill (cancer and host) cells by damaging their DNA and to shrink tumors. It enables a localized treatment of cancerous regions and tries to harm as few normal cells as possible. Chemotherapy refers to chemical treatment of cancer with anti-cancer drugs, so-called chemotherapeutic agents. These drugs are *cytotoxic*, meaning that they kill cells, mostly by affecting cell division. They are usually systemically administered, circulate in the blood stream and can, in principle, affect every cell in the body. Not only the primary tumor but also metastases can be eradicated. However, this may lead to tremendous side effects as drugs are not specific but often target all rapidly proliferating cells, e.g., hair follicles. Fast growing tumors with high proliferation are, in general, more sensitive to chemotherapy. Nowadays, combinations of drugs with distinct and complementary modes of cytotoxicity are used to battle resistance to a single drug.

Subsequently, a short overview of more recent research efforts for cancer treatment is given. The major goal is a more specific targeting of cancer cells best described by Paul Ehrlich's concept of a "magic bullet" which selectively kills cancer cells while leaving surrounding healthy tissue undamaged [69]. Nanoparticle-based treatments could allow for a more targeted drug delivery to cancer cells or for more focused *hyperthermia* treatment, that is, eliminating cancers via heat. For more details see Section 5.3. A treatment strategy which has recently gained more attention is *immunotherapy* with the goal to enhance the immune system's capability to fight cancer. This can be either achieved actively by specifically targeting malignant cells via the immune system or passively by increasing the activity of the immune system. However, also a targeting of the tumor micro-environment and its interactions with cancer may be promising [220]. For instance, *antiangiogenic* cancer therapies are also under research [181, 275] and some have been clinically approved. Their goal is to inhibit angiogenesis and, thus, to cut tumors' supply of nutrients and their ability to metastasize.

The Role of Physics in Cancer Cancer research has recently experienced a paradigm-shift from viewing it as a disease of the cell towards a more holistic description including the micro-environment and especially, the (bio-)physical interactions between its constituents and malignant cells. As the links between cancer biology and physics become more and more apparent, a multidisciplinary approach bringing together biologists, chemicists, physicists and engineers is the only option to make further progress in understanding the disease. The following paragraphs are mainly based on three recent review articles on the role of physics in cancer [168, 171, 180] and introduce only some findings and concepts which are especially relevant for this thesis.

A very prominent and, quite literally, tangible biomechanical trait of cancer is the increased stiffness of tumor tissue. Indeed, *palpation*, that is, feeling for stiffer tissue, is the longest-known way to detect cancer. One cause for this increased stiffness is extracellular matrix deposition and cross linking initiated by *cancer associated fibroblasts*, a cell type abundant in the tumor micro-environment. A further effect is strain-stiffening of collagen, a main fibrous component of the ECM. In turn, increased tissue stiffness can activate signaling pathways which promote tumor progression, invasion and metastasis. It is correlated with more aggressive growth and poor

prognosis in a number of cancer types [47, 81, 144, 191]. A vicious cycle of matrix deposition, stiffening and malignacy may develop [47, 180] such that the tumor micro-environment becomes fibrotic and inflammatory. However, these biophysical interactions may also offer novel targets for therapies.

A further distinct effect are increased solid stresses in tumors. These occur as the added volume of malignant cells stretches and displaces the solid components of tissue. This leads to significant mechanical stresses which may compress or even collapse blood and lymphatic vessels inside tumors. In turn, this influences perfusion and may lead to hypoxia and inefficient delivery of drugs and, therefore, decreased efficacy of treatment.

An additional important physical aspect is that tumor (neo-)vasculature is structurally and functionally abnormal since tumor vessels are tortuous, dilated and have uneven diameter leading to chaotic blood flow inside the tumor [36, 68, 117]. In addition, the vessels have a high permeability. This leakiness has been identified as a reason for elevated IF pressure of tumors because of increased outflow from the vessels [103, 114]. Together with inefficient drainage due to non-functional lymph vessels, this causes an IF pressure increase inside tumors. A typical plateau of IF pressure inside the tumor and a steep decrease across its boundaries induces an outflow of fluid. This physical characteristic might hamper or even inhibit the success of drug delivery [114, 115, 117]. The causes for these structural and functional deficiencies of tumor vasculature are the overexpression of pro-angiogenic molecules leading to chaotic network structures and the continuous remodeling of the vasculature by the growing tumor [68]. The previously mentioned novel nanoparticle-based therapies aim to exploit these properties of the tumor vasculature for a more specific targeting of tumor sites [166].

A different, physics-based perspective on cancer is also proposed by *transport oncophysics*, a term recently coined by Ferrari et al. [74, 183]. Within this framework, the biological hallmarks of cancer are unified to one physical principle, which is the deregulation of mass transport occurring at multiple spatial scales. For instance, tissue invasion is defined as mass transport deregulation at the interface between cells and the micro-environment. Metastasis is a deregulation of cellular transport at the scale of the organism and angiogenesis completely alters mass transport through the tumor micro-environment. Malignant cells have to penetrate across biological barriers that are normally impassable to spread throughout the body. Biological barriers are here defined as the separating elements between different compartments, e.g., between vasculature and surrounding tissue. Drugs follow the inverse pathway from administration, transport through the circulatory system, extravasation and transport through the micro-environment and, hence, encounter similar obstacles. Transport oncophysics aims to identify, describe and overcome these barriers to enable a more rational design of drug delivery systems [27]. Physiological characteristics such as the morphology of tumor vasculature, microvascular flow, the structure of the extracellular matrix or the IF pressure profile may influence the transport of drugs through tumor tissue and ultimately the success of treatment [60]. Frequently, the problem of chemotherapeutic agents is not insufficient toxicity but the fact that cancerous sites are not entirely reached by drug concentrations at adequate levels. A physical description of the multiscale drug transport through the body including the encountered biological barriers can give valuable insight into the causes of this problem and help remedy them by more advanced drugs.

The previously mentioned enormous heterogeneity of cancer is not only caused by genetic variations but is also augmented by physical interactions with the tumor micro-environment. For

instance, different ECM stiffnesses, porosities or vascularization and oxygenation patterns may lead to distinct progressions of growth or responses to therapy.

Unraveling the complexity of cancer requires similar methods as commonly used for other intricate physical phenomena or sophisticated man-made systems such as weather forecasting, particle physics or aircraft design. Physicists or engineers tackle such problems via a tight integration of manipulations, measurements and, in the context of this thesis the most important aspect, computer simulations. Being complementary to theory and experiments, they enable a fast, reproducible, accessible and easily controllable environment to predict the outcome of certain initial states of a system, generate and test hypotheses, elucidate mechanism inaccessible to other methods and aid in making optimal decisions in uncertain scenarios. Integrating quantitative, predictive and physics-based computational models with new theoretical findings and well-designed experiments may be humanity's best hope to further the understanding of cancer and to develop more effective individualized strategies for cure.

1.2 Motivation and Overview of Cancer Modeling

The Need for Mechanistic, Predictive and Personalized Models of Cancer While tremendous progress has been made in the understanding of cancer and the development of more effective cures, the progression and response to therapy of an individual, patient-specific tumor can still not be predicted reliably and reproducibly. This is due to the lack of a validated mathematical theory to describe the spatiotemporal evolution of cancer and its response to treatment [293, 295]. Formulating such a theory which is capable of forecasting cancer progression patient-specifically has been termed the grand challenge of Mathematical Oncology [218]. By contrast, one can argue that "big data" or "machine learning" approaches, where statistical information from a large number of patient cohorts are employed to find statistical patterns indicating optimal treatments, will fail to make dependable predictions for individual patients [293]. The enormous heterogeneity of cancer leads to very different manifestations of the disease based on a unique person's characteristics, which is hidden in population-based data. This limits their applicability for individualized disease management as the intrinsic heterogeneity of cancer is largely ignored. Parametric (computational) models, on the other hand, can be based on patient-specific data and can, thus, predict the occurrence of particular events, such as the outcome of a certain therapy, with a much higher probability for a specific patient [185]. In predictive medicine or oncology, such comprehensive methods would get some initial state of a tumor and the patient's parameters, e.g., from imaging or a biopsy, as an input to forecast the future progression of the disease and its response to therapy by help of biophysical, mathematical and computational models. Even though the goal to find a unifying theory of cancer is extremely complex, mechanistic, predictive and personalized models tailored for certain issues can be developed and validated on the way. These can answer questions for individual patients such diverse as the probable further progression of a grown tumor to determine if a potentially risky surgery is necessary, to find an optimal treatment strategy or to quantify the risk of metastasis. Ultimately, such models could assist oncologists in clinical decision-making by providing accurate personalized predictions of cancer development and treatment response. Hence, they could serve as *digital twins* of an individual patient's tumor for personalized tumor forecasts, *in-silico* testing of different combinations of therapies, dosages or schedules and selection of an optimal treatment strategy.

A Brief Overview of Cancer Models Due to its undeniable potential, mathematical modeling of cancer has been a rich area of research for several decades. Numerous models of varying sophistication have been suggested, see the comprehensive reviews [5, 58, 157, 221, 229] and books [48, 57] for an overview. The review paper by Lowengrub et al. [157] from 2010 alone lists almost 600 references indicating the enormous scientific interest in cancer modeling. Commonly, models are classified into three categories as *discrete*, *continuum* or *hybrid*. Subsequently, a brief introduction into each model category, its use cases and limitations as well as representative examples of each type will be given. Models can also be discerned based on which phase of tumor growth, i.e., avascular, vascular or metastatic, is simulated. For a more in-depth overview, the reader is referred to the previously mentioned reviews.

Discrete models (also called cell-based, agent-based or individual-based models) are valid on the cellular or subcellular scale. Individual cells or subcellular elements are explicitly modeled. Their spatiotemporal evolution is governed by a set of biological or biophysical rules, e.g., for cell-cell or cell-matrix interaction. This enables modeling phenomena occurring at this scale such as carcinogenesis, proliferation, apoptosis, protein production, cellular metabolism, genetic instability and natural selection [58, 155, 157]. Therefore, they offer a high level of detail as biological processes such as mutational events or the cell cycle can be integrated as rules. Nevertheless, they become prohibitively expensive for larger domains at the centimeter scale, which is of interest when studying tumor progression in humans, and often also for the involved temporal scales of days to years. Furthermore, model parameters may be nontrivial to obtain [157] as they have to be measured at the cell scale. The review by Metzcar et al. [167] classifies discrete models into lattice or off-lattice approaches. Representative examples of lattice models are cellular automaton [1, 90, 173] or cellular Potts [253] approaches. In cellular automaton models, each lattice point can only be occupied by one cell. In cellular Potts models, cells may cover several lattice points. A different approach where single cell migration was modeled within a continuum framework was presented by Rauch et al. [212].

Continuum models describe tumor tissue as a continuous medium rather than resolving single cells [58]. Principles from continuum mechanics such as conservation laws are involved to formulate a set of potentially nonlinear partial differential equations (PDEs) describing the evolution and dynamics of the system. Thus, these formulations are (almost always implicitly) valid on the macroscale, meaning that multiple components are superimposed at every point in the domain of interest. Typical model variables and quantities of interest are cell volume fractions and density or nutrient, oxygen, growth factor and drug concentrations. Contributions into the governing equations may often be classified into four categories [155]: *diffusion*, *convection*, *reaction* and *taxis*, which is the directed movement in response to a stimulus. Continuum model parameters are potentially easier to obtain, analyze and control compared to the discrete case and more accessible through experiments [157]. They are typically employed to study overall cancer progression, vascularization, nutrient transport and drug delivery on the scale of entire tumors. Consequently, the modeling of individual cells and discrete events on the cell level is not possible, but often also not necessary for the question at hand. Treatment such as chemo- or radiation therapy may be included. For the latter one, the distribution of a specific drug in the tumor micro-environment can further be studied by additional convection-diffusion-reaction equations. The effect of treatment on the tumor is frequently incorporated by a damage variable, an additional reaction term leading to a decrease of tumor mass and/or a deceleration of tumor growth [50]. A number of different continuum models will be discussed in the next paragraph.

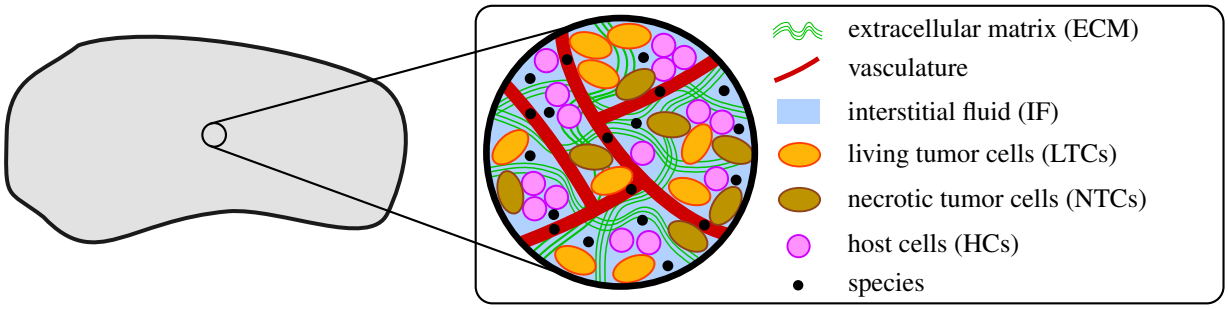

Figure 1.2: Sketch of a typical composition of the tumor micro-environment with ECM, vasculature, IF, (necrotic and living) tumor cells, host cells and numerous species

Hybrid continuum-discrete models combine both modeling strategies to incorporate their respective strengths. Therefore, via a more realistic coupling of biophysical processes across a wide range of length and time scales, they have the potential to connect processes from the micro- or cell-scale to the macro- or tumor-scale [157]. Deisboeck et al. [58] further classify hybrid models into *composite hybrid* and *adaptive hybrid* approaches. In the former ones, cells are treated discretely but interact with chemical or mechanical continuum fields such as a continuous description of nutrient distribution. Also the coupling of continuum tumor growth models with a discrete description of angiogenesis as in [283, 298] is commonly classified in this category. In the latter ones, the models are switched dynamically and adaptively between discrete and hybrid descriptions to achieve higher resolutions when- and whereever necessary but to enable also the study of larger domains. Representative examples of such approaches where the domains for each description are pre-specified are [124, 247] whereas a dynamic switch between the discrete and continuum representation is made in the model of [83].

The Concept behind the Present Model Hereafter, the focus will lie on macroscale continuum models of tumor growth as the here employed and developed group of models is also of this type. More recent continuum models (and the ones employed here) are of *multiphase* type [229]. They accommodate the fact that various distinct phases are present in the tumor micro-environment, such as different cell types, IF, blood and the ECM as sketched in Figure 1.2. Moreover, multiple species which are part of these phases, such as oxygen, nutrients, drugs or growth factors can be included. Thus, these models are very promising as they represent a more general and natural framework to study the biophysics of solid tumor growth with a much higher level of detail. Hence, a multiphase model incorporates at least one solid phase and one liquid phase and can be generalized to incorporate any number of additional phases and species [157].

An extensive review of multiphase models can be found in [229]. For instance, models based on mixture theory have recently become popular. Such approaches can be classified w.r.t. their treatment of the interfaces between specific phases. On the one hand, sharp-interface methods, which have been used in the context of tumor growth modeling by [107, 200, 298], track the interface between different phases and require imposition of boundary conditions at the interface. On the other hand, diffusive-interface or phase-field models do not explicitly track the fronts between phases, but a so-called phase field is introduced which models a smooth transition between different phases via a phase field parameter. A commonly employed phase field description is the Cahn-Hilliard equation which describes the evolution of the phase field pa-

rameter as a fourth-order nonlinear PDE. Representative examples of phase field models may be found in [83, 101, 102, 121, 151–153, 184, 283]. Approaches using isogeometric analysis with smooth C^1-continuous basis functions are also common, see [155, 156, 267, 268, 289, 290] in the context of tumor growth modeling. However, as argued by Sciumè et al. [229], mixture theory lacks a rigorous connection with the microscale, its variables are inadequately defined and implicit approximations concerning system behaviour are introduced. This is due to the fact that conservation equations and closure relations are postulated directly at the macroscale and a consistent averaging of known microscale relations is not performed. Thus, cross-scale consistency is not possible and model errors are difficult to assess and correct.

What is also often overlooked in the formulation of such complex models is the ability to incorporate non-invasively available, quantitative spatiotemporal imaging data [294]. These models are often purely mathematical or phenomenological, for instance, the existence of a generic nutrient species is postulated as in a number of phase-field models [151–153, 156, 289, 290], which governs the availability of nutrients via diffusion-reaction type equations. However, as such a "generic nutrient" is not present *in-vivo*, no data is available for its parameters and its distribution cannot be acquired via imaging for validation. Hence, even though these models claim a high sophistication, they are often purely phenomenological. Furthermore, a sound theoretical basis is frequently lacking as model formulation is performed directly at the macroscale without a clear and firm connection to the microscale in order to guide model closure.

By contrast, recent continuum mechanical tumor growth models have been developed by Schrefler and co-workers [224, 225, 229–233, 235] in the framework of thermodynamically constrained averaging theory (TCAT) [93–95, 97, 169]. This theory allows for formulating consistent macroscale models of cancer based upon first principles, i.e., conservation laws, thermodynamics, and a set of mathematical theorems [170]. While not all these advantageous features of TCAT have been leveraged during derivation of the present model, it offers the possibility to formulate mechanistic, physics-based models of tumor growth with clear, interpretable and measurable parameters. A firm connection between micro- and macroscale is guaranteed which is indispensable when modeling a disease with inherent multiscale characteristics. Additionally, model simplifications and extensions can naturally be integrated.

In essence, a macroscale description of tumor tissue as a porous solid is formulated using TCAT as sketched in Figure 1.2. The tumor micro-environment corresponds to the microscale of the problem where phases and their interfaces are discernible. The governing equations of the model are then obtained at the macroscale by averaging or homogenizing the respective conservation laws from the microscale. The ECM correponds to the sole present solid phase and its voids to a pore space where cells migrate and IF flows. Cells, IF and blood are the considered fluid phases. Even though cells themselves may behave as viscous, elastic or viscoelastic mechanical objects, it is customary to model them as fluids in macroscale tumor growth models [229]. Species, i.e., chemical sub-components, may be present in all fluid and solid phases.

1.3 Research Objective

In line with the visionary goal of this research, namely, a comprehensive patient-specific cancer simulation tool, the short-term goals realized in this thesis and its scientific contributions are listed hereafter. The main research objective of this project is to implement a comprehensive

multi-physics framework to simulate *in-vivo* tumor growth. This involves a consistent incorporation of the vasculature where three distinct variants with designated use-cases are developed. A further objective is a validation of the general applicability of the model to cancer progression and a more specific validation of a hybrid embedded/homogenized approach for solid tumor perfusion which can be applied more directly to modeling mass transport phenomena, e.g., drug delivery.

1.3.1 Specification of Requirements

Subsequently, the key requirements for a comprehensive vascular tumor growth model are listed:

(i) **Sound, Mechanistic and Consistent Description of the Underlying Physical and Biological Phenomena** Insights into the mechanisms underlying cancer progression can only be acquired with models which have a sound theoretical basis and are capable of representing its complexity including the interactions with the micro-environment.

(ii) **Representation of the Interplay between Different Physical and Biological Phenomena** Cancer inherently is a disease occurring across multiple temporal and spatial scales. Additionally, it involves the interplay of multiple physical and biological phenomena such as deformation, fluid flow, species transport phenomena and taxis. A comprehensive model has to take the multi-physics characteristics of tumor growth into account.

(iii) **Physics-Based and Measurable Model Parameters** It is indispensable that model parameters are representative of the involved physical phenomena. These are not always entirely known in a complex system such as cancer and models can actually be applied to elucidate them. In that case, empirical relationships are often inevitable. Their parameters still have to be sensible and measureable.

(iv) **Verifiability** The simulation tool has to deliver physical or biological quantities of interest which are accessible with current state-of-the-art experiments. Only then a validation and further fine-tuning is possible.

(v) **Cutting-Edge Numerical Solvers** Capturing the complexity of cancer with computational models requires advanced numerical algorithms which are robust and accurate over a wide range of potentially unknown parameters.

(vi) **Flexibility and Modularity of the Framework** Both the actual model as well as the code base have to be flexible and modular to incorporate additional physical phenomena and support further extensions.

1.3.2 Contributions of this Work

A combination of theoretical and methodological work with software development for high-performance computing and the actual modeling efforts via well-designed numerical examples is necessary to achieve the research objective and fulfill the requirements outlined above. The following is an overview of the main scientific contributions of this thesis:

Derivation and Implementation of a Group of Models for Vascular Tumor Growth [135, 136] Building on the original avascular tumor growth model of Schrefler and co-workers [224, 225, 229–233, 235] based on TCAT, a group of vascular models, which differ in their representation of the vasculature, is developed. Three different concepts are employed to obtain a *homogenized*, a *discrete* and a *hybrid* variant.

In the homogenized variant, the vasculature is included as an additional porous network with blood flow and species transport resulting in a double-porosity formulation. Angiogenesis and blood vessel remodeling is incorporated via an evolution equation for the vascular volume fraction. This model extension is one of the first vascular tumor growth models to take the dynamic interaction between tumor growth, the vasculature and blood flow and species transport therein into account.

In the discrete variant, the vasculature is embedded as a one-dimensional inclusion into the surrounding tissue. Blood flow and species transport is solved in the 1D representation of the vascular network and coupled with the surrounding tissue via 1D-3D (fluid and species) exchange terms. It is assumed that the embedded blood vessels follow the deformations of the surrounding tissue such that also large deformations of the vessel network as occurring *in-vivo* during tumor growth [236] are considered, which is an additional original contribution of this work.

A further scientific novelty is the hybrid approach, which is a combination of the homogenized and the discrete representation. Its rationale is to resolve the larger vessels, whose topology and structure can be acquired via suitable *in-vivo* imaging techniques, and to homogenize the smaller vessels, which are not accessible non-invasively. This also allows preserving the heterogeneity of blood flow inside the network better than for the homogenized variant and minimizes the required data compared to the discrete one. The two representations of the vascular network are coupled via constraints which are enforced by adaptations of two well-known strategies, a mortar-type approach with penalty regularization or a Gauss-point-to-segment scheme. They are transferred to 1D-3D coupled problems in the author's pioneering work [136]. Under the constraints of the resolution of current state-of-the-art *in-vivo* imaging modalities, the hybrid approach is a very promising alternative to the discrete one.

Setup of a Flexible Finite Element Framework Supporting Further Extensions A holistic computational framework for simulating cancer progression is developed. The governing nonlinear partial differential equations are discretized in time using the one-step-θ-scheme and in space using the finite element method (FEM). An arbitrary number of phases and species can be specified such that further extensions are easily possible. Species transport in all involved solid and fluid phases as well as the embedded vasculature can be considered. In addition, the energy balance equation may be included to simulate hyperthermia treatment. All equations are formulated in an arbitrary Lagrangean-Eulerian description to enable large deformations of the solid phase, i.e., the extracellular matrix, which was not possible in the TCAT tumor growth model before. Deformability can also be neglected, leading to a considerable simplification of the solution process. To the best of the author's knowledge, this is one of the most general and comprehensive frameworks for modeling tumor growth.

Incorporation of Two Different 1D-3D Coupling Concepts for Non-Matching Meshes The complexity of tumor vascular networks can be enormous [59, 252]. The discrete

and the hybrid variant require the resolution of at least the larger vessels of the part of the microcirculation under consideration via a 1D embedded mesh. The coupling concepts developed in this thesis allow for employing a non-matching, e.g., a regular 3D mesh for the encompassing tissue domain. This facilitates the meshing procedure but requires specialized spatial integration schemes to evaluate the 1D-3D mass transfer terms. In addition, two different 1D-3D coupling concepts are implemented and investigated, one with a coupling along the centerline of the 1D embedded vascular domain (and a line source term in the equations of the 3D domain [51–53, 136]) and one with a coupling at its lateral surface (and a corresponding surface source term in the equations of the 3D domain [130]). The involved singularity for the former one is shown to be problematic for cases where the element size of the 3D domain becomes smaller than the diameter of the embedded blood vessels but it is still applicable for practical problems. Previously, such 1D-3D coupled equations were used for simple perfusion and scalar transport problems. In the context of multiphase tumor growth models, the first integration of a consistent 1D-3D coupling between non-matching FEM discretizations is achieved in this work.

Investigation of Different Coupling Algorithms [135] Previously, only a partitioned coupling algorithm could be applied to solve the resulting nonlinear three-field problem of the TCAT tumor growth model. In this thesis, two different partitioned and, for the first time, a hybrid monolithic-partitioned and a monolithic coupling algorithm are implemented and investigated. Numerical experiments reveal the strong coupling between the different fields and especially the strong coupling between fluid phases and solid deformation in the model. For efficient monolithic schemes, the integration of suitable and performant block preconditioners for iterative linear solvers [263] is required. Then, monolithic algorithms are proven to be superior compared to partitioned schemes over a wide range of parameters. The latter ones could still be applied for cases with a weaker coupling though. This significant gain in performance enables the investigation of much more complex scenarios than previously considered.

Validation of the General Applicability of the Framework for (A-)Vascular Tumor Growth and Different Treatment Strategies [135, 136, 282] Several illustrative numerical examples show the applicability of the developed framework for simulating (a-)vascular tumor growth. The examples are designed to showcase its abilities in representing the complexity of *in-vivo* tumor progression. A special focus is set on the interplay between tumor growth and the vasculature by investigating angiogenesis including the effects of chemo- and haptotaxis, oxygen transport, metabolism and delivery, blood vessel compression and regression, and increased leakage of fluid from blood vessels into the IF. Further examples are tailored to examine nanoparticle-based drug delivery and hyperthermia treatment. This represents an original contribution to rationalize drug design based on the transport phenotype of solid tumors which is characterized by well-known dimensionless numbers [282].

Validation and Parameter Optimization of the Hybrid Embedded/Homogenized Representation of the Vasculature for Modeling Solid Tumor Perfusion [137] The approach with a hybrid embedded/homogenized representation of the vasculature is further investigated for modeling solid tumor perfusion. Data sets of vascular networks in three solid tumors with a size of up to $420\,000$ vessel segments and dimensions of up to $6\,\mathrm{mm} \times 8\,\mathrm{mm} \times 11\,\mathrm{mm}$

are employed. The accuracy of the hybrid model w.r.t. a corresponding fully-resolved one is quantified and its parameters are optimized. To date, this is the largest and most challenging data set employed for validating such a hybrid approach. Therefore, this study in itself is one of the prime scientific novelties of this thesis. Excellent agreement in terms of mean representative elementary volume blood and IF pressure is obtained. Further improvements of the hybrid model are discussed and the most promising one is implemented and tested.

As denoted above, parts of this thesis have previously been published in the author's articles (in chronological order):

[135] J. Kremheller, A.-T. Vuong, L. Yoshihara, W. A. Wall, and B. A. Schrefler. A monolithic multiphase porous medium framework for (a-)vascular tumor growth. *Computer Methods in Applied Mechanics and Engineering*, 340:657–683, 2018.

[136] J. Kremheller, A.-T. Vuong, B. A. Schrefler, and W. A. Wall. An approach for vascular tumor growth based on a hybrid embedded/homogenized treatment of the vasculature within a multiphase porous medium model. *International Journal for Numerical Methods in Biomedical Engineering*, 35(11):e3253, 2019.

[282] B. Wirthl[1], J. Kremheller[1], B. A. Schrefler, and W. A. Wall. Extension of a multiphase tumour growth model to study nanoparticle delivery to solid tumours. *PLOS ONE*, 15(2): e0228443, 2020.

[137] J. Kremheller, S. Brandstaeter, B. A. Schrefler, and W. A. Wall. Validation and parameter optimization of a hybrid embedded/homogenized solid tumor perfusion model. *International Journal for Numerical Methods in Biomedical Engineering*, 37(8):e3508, 2021.

These articles constitute a main contribution of this work and previously published text, figures or findings (for which permission to reproduce has been obtained from the respective publishers) are indicated when used. All numerical methods have been implemented in the parallel finite element code BACI [8] which is jointly developed by several reasearch groups across Germany and relies heavily on the Trilinos project [105]. The current framework for cancer modeling builds on a first nested-partitioned implementation of the avascular model variant of Schrefler and co-workers [224, 225, 229–233, 235] by A.-T. Vuong. In Chapter 6, the software framework QUEENS [24], provided by the courtesy of AdCo Engineering^{GW}, is employed and, in particular, the parallelized version of the Levenberg-Marquardt algorithm developed by S. Brandstaeter. Several post-processing routines were added by the author.

1.4 Outline

The remainder of this thesis is organized as follows:

Chapter 2 contains a concise review of continuum mechanics with a special focus on multiphase porous media and a brief introduction into TCAT. The governing equations which serve

[1]This article was co-first-authored with B. Wirthl. Both authors contributed equally to the formal analysis, investigation, methodology, software, visualization and writing of the paper. In this thesis, only some basic ideas and illustrations are re-used from this publication for the nanoparticle transport study in Section 5.3.

as the fundamental building blocks for the group of (a-)vascular tumor growth models are established.

These are then employed to construct the different model types in **Chapter 3**. First, an overview of the distinct variants and their specific use-cases is given. Then, the models of increasing sophistication and complexity are derived.

The computational solution approach for the coupled multi-physics problem is described in **Chapter 4**. Time discretization of the governing equations with the one-step-θ-scheme and space discretization with finite elements is performed after deducing the weak forms of the governing equations. A particular emphasis is put on the numerical evaluation of the 1D-3D coupled terms which require special treatment. Different strategies to solve the resulting strongly coupled nonlinear problem are described.

Numerical examples of the tumor growth framework are presented in **Chapter 5**. These are designed to illustrate its capabilities and to validate its applicability for tumor growth modeling. It is further proven that important physical phenomena and growth patterns occurring during *in-vivo* cancer progression and drug delivery can be reproduced. Several additional academic examples concerning the 1D-3D coupling are presented in **Appendix A**. Further information about the employed mass transfer relationships and parameters may be found in **Appendix B** and **Appendix C**, respectively.

Chapter 6 constitutes a standalone part to this thesis. Based on the concept of a hybrid representation of the vasculature originally incorporated for modeling vascular tumor growth, a hybrid approach for tissue perfusion through solid tumors is proposed. It is further verified and its parameters are optimized by comparing its results to a corresponding fully-resolved model.

Finally, the findings of this thesis are summarized in **Chapter 7**. Additional promising improvements are suggested and a road map towards a validation to enhance the predictive capabilities of the model is laid out.

2 Continuum Mechanics of Multiphase Porous Media

This chapter establishes a macroscale continuum description of multiphase porous media. A brief introduction to porous media with a special focus on TCAT is given in Section 2.1. Basic concepts from nonlinear continuum mechanics as needed in this thesis are recapitulated in Section 2.2. Finally, the governing balance equations, which constitute the building blocks for the homogenized part of the developed group of tumor growth models, are given in Section 2.3. The ones for the 1D resolved vasculature are given directly in Chapter 3.

2.1 A Brief Introduction to Porous Media

Porous media are ubiquitous both in nature and in man-made objects, constructions or materials. They are present over a wide range of length scales ranging from hundreds of kilometers in geotechnical engineering problems to the millimeter scale, for instance, in batteries or biological tissue. Therefore, disciplines concerned with the study of porous media problems are as diverse as geophysics, biomechanics, chemistry, agricultural engineering or materials science with applications such as fuel cells, electrochemical systems, biological tissue and geology [55]. However, the field was initially coined by geotechnical engineers and geologists studying soil mechanics and subsurface flows such as Henri-Philibert Darcy (1803-1858), Karl von Terzaghi (1883-1963) and Maurice Anthony Biot (1905-1985). Many of their fundamental findings and relationships are still in use today and are also partly used within this thesis. Since then, however, their often empirically deduced relations have been supplemented by theoretical derivations which enable modeling of more complex systems. Often, under several simplifying assumptions, the classical results are obtained. The following sections are based on standard text books [15, 46, 95, 146].

2.1.1 Essential Concepts and Definitions

Porous media contain one *solid phase*, often also called the *skeleton* or the *solid matrix* with a connected *pore space* (or *void space*) filled with one or multiple fluid phases. Since it is commonly assumed that the skeleton is always present, *multiphase* porous media problems as treated in this thesis involve two or more immiscible fluid phases. The solid phase can be assumed either rigid or deformable. However, even in the latter case its deformations are small compared to the ones of the fluid phases. Furthermore, depending on the application, temperature changes might play a major role or might be negligible under isothermal conditions. The behaviour of porous medium systems is determined by solving the appropriate (momentum, mass and energy) balance equations. Thus, depending on the problem of interest, the spatial and temporal distribution

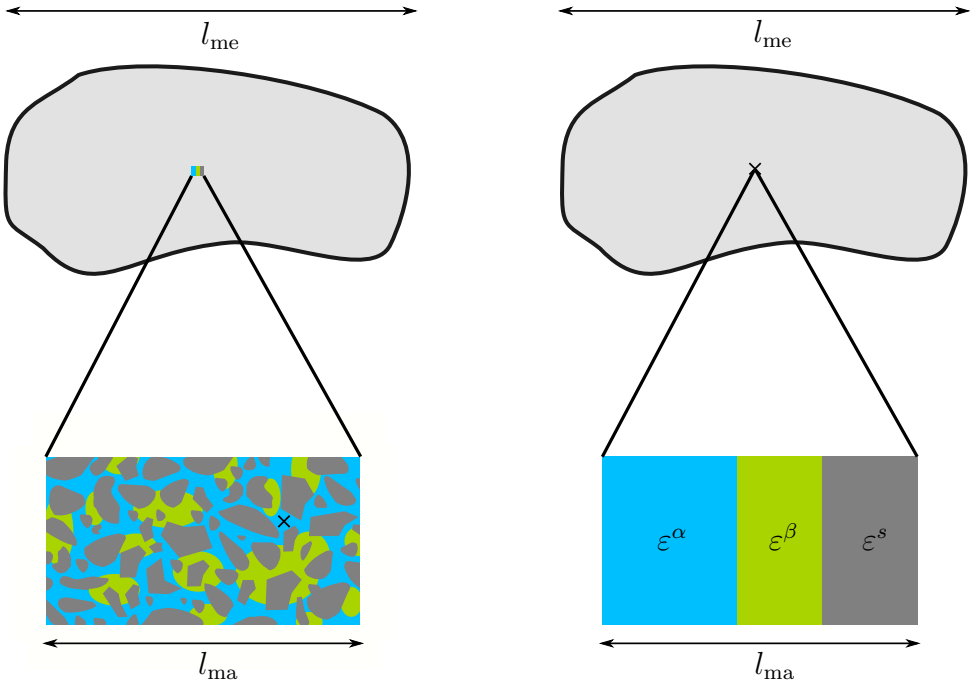

Figure 2.1: Sketch of different length scales (not to scale): On the left side, a small portion of the porous medium is sketched, interfaces between solid phase (grey) and two fluid phases (blue and green) are clearly discernible, cross denotes a point of the microscale which can be assigned to a specific phase and at which continuum assumption with corresponding balance equations holds. On the right side, the homogenized model is depicted, at each point of the macroscale (denoted by a cross), several phases with volume fraction ε are superimposed. Homogenized balance equations are formulated for each macroscopic point to determine the behaviour of the system at the megascale.

of fluid flow, fluid pressure, concentration of a solute, temperature distribution or the stress in the solid skeleton, can be obtained.

In theory, these quantities could be calculated by acquiring the structure and morphology of the porous medium and solving the respective equations including interfacial interactions between the single phases. However, in almost all cases this is impossible since the full topology of the porous medium over the domain of interest is unknown, consider for instance a soil mechanics problem spanning several kilometers. Moreover, such a detailed resolution is also not of interest in most cases. In geotechnical problems, it is not necessary to resolve the fluid flow through large domains on a millimeter level. The average flow over several meters or even kilometers is the quantity of interest. Finally, even if the topology of the porous medium was completely known, it is infeasible to resolve the entire complex physics of these problems involving complicated flow patterns, changing interfaces and multiphysics phenomena. Thus, in porous media mechanics, the so-called *macroscopic* scale, on which balance equations derived from averaging or up-scaling the *microscopic* balance equations hold, is of interest. Averaging the governing equations is a mathematically intricate procedure for which different techniques exist. Here, the thermodynamically constrained averaging theory (TCAT) coined by Gray and

Miller [93–95, 97, 169] is employed, see Section 2.1.2 for a short introduction. For now, the focus is set on defining the length scales of porous media problems. While a more granular definition of scales exists [95], the discussion here will be limited to three distinct length scales, namely the *microscopic*, *macroscopic* and *megascopic* length scale. They are denominated as l_{mi}, l_{ma} and l_{me}, respectively.

At the *microscale*, the continuum assumption holds, that is, each phase behaves as a continuum with the respective balance equations. Thus, at this scale phases and their interfaces are clearly discernible as sketched in the left part of Figure 2.1. Each (mathematical) point can be assigned to one specific phase or an interface between different phases, i.e., a common surface, line or point. A fully-dynamic, microscale continuum formulation with respective governing equations including interface interactions between different phases may be formulated but is impractical as described above. Note that this continuum formulation involves already an averaging of the system behaviour from the molecular scale. As already mentioned in Section 1.2, in the context of this thesis, the tumor micro-environment corresponds to the microscale of the problems where different cell types, the vascular network and the structure of the ECM are discernible.

In a macroscopic or homogenized description, phases and their interfaces are not resolved any more, see Figure 2.1 (right part). The porous medium is modeled as a composition of overlapping or superimposed continua such that multiple phases may be present at every point of the *macroscale*. Each of these continua corresponds to one of the present phases which fill up the entire space and interact with each other. Their behaviour is described via averaged quantities such as their volume fraction ε^{α} at a specific point as depicted in Figure 2.1. These quantities are not present in a microscopic formulation but are obtained when averaging the microscale properties over the macroscale length scale l_{ma}. The up-scaled balance equations are formulated in terms of these macroscale variables and additional closure relations have to be derived. The balance equations on the macroscale correspond to the governing equations of the tumor growth models used in this thesis.

The *megascale* is the length scale of the domain of interest [95]. It comprises the points of the macroscale as depicted in Figure 2.1. The macroscopic balance equations hold over the megascale and boundary conditions for the primary variables of these equations are applied on the boundaries of the megascale domain. Hence, this domain corresponds to the part of the tissue or organ, for which tumor progression is modeled.

Another important aspect is that the length scales representing the aforementioned scales have to be clearly separated which may be stated by the condition

$$l_{\mathrm{mi}} \ll l_{\mathrm{ma}} \ll l_{\mathrm{me}}. \tag{2.1}$$

The macroscopic length scale should be sufficiently larger than the microscopic scale such that it is representative of the average behaviour of the porous medium system. Vice versa, it should be sufficiently smaller than the domain of interest such that gradients of the macroscale variables are present and meaningful. Hence, the macroscopic length scale is equivalent to the notion of a *representative elementary volume* (REV) which should be large enough to filter out small scale spatial resolutions yet small enough to represent larger scale fluctuations in the quantities of interest [56].

This section is concluded by several important definitions based on the book by Gray and Miller [95]. Therein, four types of *entities* are defined: *phases*, *interfaces* (the regions in the

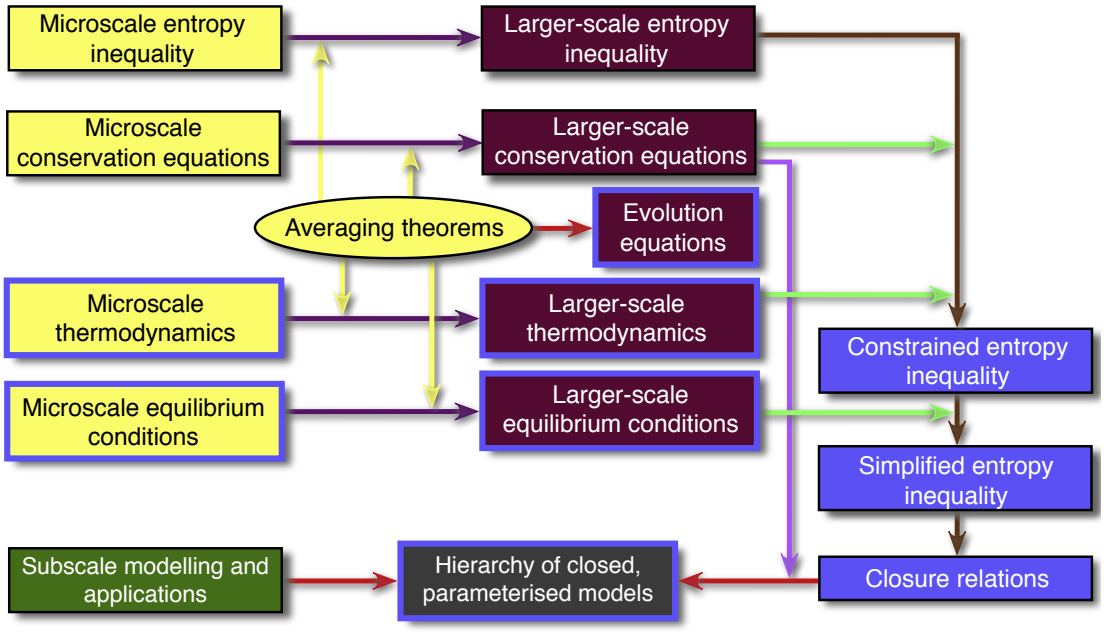

Figure 2.2: Elements of TCAT (reprinted and slightly modified from [97] with permission from Elsevier)

multiphase system at the boundary between two phases), *common curves* (the regions in the multiphase system where three phases meet) and *common points* (the regions in the multiphase system where four phases meet). Conservation equations may be formulated for each of these entities. A *phase* is an entity which is clearly separated from other phases by interphase boundaries. Every phase (or in the more general case, every entity) of a porous medium system may consist of multiple, in some cases even hundreds of *species*, which are chemical subcomponents of this phase. Species-based formulations are useful for two different reasons: First, the spatial or temporal distribution of a species in a phase might be the quantity of interest, for instance, the distribution of a drug inside a tumor. Second, the composition of a phase might influence the physical properties of that phase such as the viscosity of blood which depends on the hematocrit value, i.e., the percentage of red blood cells.

2.1.2 Thermodynamically Constrained Averaging Theory

There exists a large variety of techniques to change the scales of the system, that is, to obtain a macroscopic description from known microscopic balance equations. A comparison of two very commonly applied methods, namely, *volume averaging* and *multiscale asymptotics* can be found in [56]. Ancillary closure relations or constitutive equations have to be formulated at some point during the derivations to obtain a closed, solvable system. The avascular tumor growth model of Schrefler and co-workers [224, 225, 229–233, 235] and its extensions in this thesis is based on a different scale-change method termed thermodynamically constrained averaging theory (TCAT). What makes this approach unique compared to other methods is that thermodynamical relations are included into the modeling formalism. This is an essential component which ensures that macroscale quantities, variables and parameters are well-defined in terms of their microscale

counterparts. Thus, models which are consistent across scales may be derived. The description of this intricate and complex theory is restricted to a conceptual overview here without going into mathematical details which are given in the works of Gray and Miller [93–95, 97, 169]

For this purpose, the elements involved in TCAT and the procedure for deriving a closed model have been sketched in Figure 2.2. The following description of TCAT closely follows the one from the authors of this theory themselves [95, 97]. The yellow boxes on the left side are the starting point of the derivation. They represent the balance equations, thermodynamics and equilibrium conditions at the microscale for all entities. Recall that one prominent feature of TCAT is that entities include not only phases but also interfaces, common lines and points. These lower dimensional entities allow to more accurately resolve underlying physical mechanisms than models based upon phases alone because interfaces and common curves form and evolve in time in multiphase systems. This ability of TCAT makes it especially suited for modeling biological tissue in health and disease since physical interactions of cells with their environment occur at the interfaces of cells with other phases and regulate cell behaviour. Examples of these important mechanisms are the previously mentioned ECM remodeling, cell migration and cell adhesion. Such effects cannot consistently be included in models based on mixture theory [101, 102, 151–153, 184, 185] which do not provide a consistent definition of interfaces, a sound connection between micro- and macroscale and the thermodynamic coherency of the TCAT.

Using suitable averaging theorems, one obtains five types of larger scale equations denoted by the purple boxes, which are the larger scale entropy inequality, conservation equations, thermodynamics and equilibrium conditions. In addition, evolution equations for geometric densities such as the volume fraction of a phase or the interfacial area per volume of a phase are developed. These are averaged measures of geometric quantities at the microscale. The evolution equations are not conservation equations but rather describe the change of the geometrical configuration of the system over time and space by employing suitable macroscale measures. Another unique feature of TCAT is that the averaging theorems are also applied to microscale thermodynamics and microscale equilibrium conditions to obtain their large scale counterparts. This strategy guarantees consistency of the quantities in the resulting equations. At this point, all necessary pieces have been gathered but the system is still unclosed, i.e., there are more unknowns than equations which have to be eliminated by suitable constitutive relationships. The steps necessary for closure are denoted by blue colour in Figure 2.2. First, a constrained entropy inequality (CEI) is derived. Through additional assumptions and manipulations this more general form is transformed into the so-called simplified entropy inequality (SEI) given in force-flux form which finally allows closing the system based on thermodynamical constraints and the known equilibrium conditions, e.g., by postulating a linear relation between heat flux and temperature gradient. It is important to emphasize that the path from the constrained inequality to the final closed system is not unique. After deriving a SEI from a CEI, a whole hierarchy of closed, parameterized models with different sophistication can be obtained based on the assumptions made in closing the system. If additional experimental data becomes available or if the porous medium model does not give suitable accuracy since some physical effects which are not represented are more dominant than expected, one can go back to the SEI and enhance the model with different closure terms. In summary, this approach enables a flexible switching between models with different accuracy depending on the requirements and the present physical effects.

However, it is important to emphasize that not all these eminent and universally applicable features of TCAT have been leveraged to derive and close the present tumor growth models.

The reason for that is the involved mathematical complexity of the approach. Even for more than two fluid phases, which are routinely needed for modeling tumor growth, no simplified entropy inequality has been derived by experts in TCAT so far. While some equations have been closed via fulfilling a suitable entropy inequality, only empirical relationships have been postulated for several other quantities, such as effective diffusivities and mass balance equations [224, 225, 229–233, 235]. In addition, interfacial effects are not represented via a sound derivation employing TCAT but closure is achieved by constitutive equations on the macroscale. First theoretical derivations for two types of models involving two phases (one solid, one fluid) and three phases (one solid, two fluid) including the interfaces and common curves have been performed by Miller et al. [170]. However, these are much simpler systems than the ones considered throughout this thesis, where up to four interacting fluid phases (plus one fluid phase, which is not explicitly modeled, the lymphatic system), several species including drugs, spatially varying temperature distributions due to hyperthermia treatment and a deformable solid phase are incorporated. Also, a computational solution procedure of the related, more complex TCAT model derived by Miller et al. [170] is still pending. Nonetheless, the present modeling and computational framework has been set up in such a flexible way that these supplemental results can easily be integrated.

2.2 Review of Nonlinear Continuum Mechanics

Before delving into the depths of poromechanics, a few basic concepts from nonlinear continuum mechanics are repeated. This section is by no means an exhaustive review of this broad topic but rather a concise introduction of the most important aspects for later re-use throughout this thesis. For a more in-depth coverage, the reader is referred to the vast literature in this field, e.g. [28, 110, 163, 186, 286].

2.2.1 Kinematics

Figure 2.3 shows the two commonly distinguished configurations in nonlinear continuum mechanics, namely, the *material* or *reference configuration* $\Omega_0 \subset \mathbb{R}^{n_{\text{dim}}}$ and the *spatial* or *current configuration* $\Omega_t \subset \mathbb{R}^{n_{\text{dim}}}$ with $n_{\text{dim}} \in \{2, 3\}$. One global Cartesian coordinate system $\{\boldsymbol{e}_1, \boldsymbol{e}_2, \boldsymbol{e}_3\}$ is employed for both configurations. The material configuration is the domain occupied by material points $\boldsymbol{X}$ at time $t = 0$. As the continuum deforms, the smooth, nonlinear *deformation map*

$$\varphi : \begin{cases} \Omega_0 \to \Omega_t, \quad \boldsymbol{X} \to \boldsymbol{x} \\ \varphi(\boldsymbol{X}, t) = \boldsymbol{x}(\boldsymbol{X}, t) \end{cases} \tag{2.2}$$

assigns a point $\boldsymbol{X}$ of the material configuration to a spatial point $\boldsymbol{x}$ in the current configuration Ω_t at time t. This map has to be bijective such that a physically reasonable deformation without gaps or penetrations is obtained, i.e., the inverse map $\boldsymbol{X}(\boldsymbol{x}, t) = \varphi^{-1}(\boldsymbol{x}, t)$ has to exist. The current configuration Ω_t is defined as the domain occupied by the continuum at time t.

Two different observer positions can hence be distinguished. The first one is the *Lagrangean* observer which follows the material particles during their movement. This viewpoint is usually applied in nonlinear solid mechanics while following the deformation of a fixed set of material

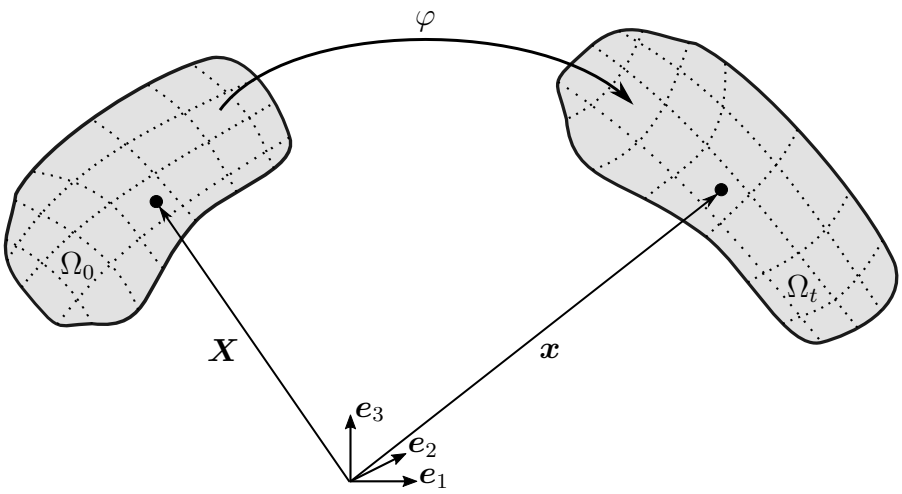

Figure 2.3: Cartesian coordinate system, reference configuration Ω_0, current configuration Ω_t and the mapping between the configurations φ (sketch after [197, 272])

particles. The second one is the *Eulerian* observer which remains at a fixed spatial position $\boldsymbol{x}$ as different material particles $\boldsymbol{X}$ occupy this position over time during the deformation of the body. This formulation is commonly applied in fluid mechanics. For fluid-structure interaction problems and, in a certain sense, also poromechanical problems another description is useful, the so-called *arbitrary Lagrangean-Eulerian* (ALE) approach, where an additional independently moving reference configuration is introduced [66, 269, 270]. This special setting in the context of poromechanics where the Lagrangean observer follows the solid phase and, thus, represents an independently moving observer for the fluid phases will be introduced in Section 2.3.4.

Essentially, solving a solid mechanics problem involves calculating the time-dependent deformation map $\varphi(\boldsymbol{X}, t)$ describing the motion of a continuum composed of a rigid body movement and a change in shape, that is, a deformation. More commonly, however, the *displacement* vector field $\boldsymbol{u}(\boldsymbol{X}, t)$ is chosen as the unknown of the problem. It is defined as the difference between the position vectors of current and reference configuration as

$$\boldsymbol{u}(\boldsymbol{X}, t) = \boldsymbol{x}(\boldsymbol{X}, t) - \boldsymbol{X}. \tag{2.3}$$

The elementary measure of local deformation is the *deformation gradient*

$$\boldsymbol{F} = \frac{\partial \boldsymbol{x}(\boldsymbol{X}, t)}{\partial \boldsymbol{X}} = \boldsymbol{I} + \frac{\partial \boldsymbol{u}(\boldsymbol{X}, t)}{\partial \boldsymbol{X}} \tag{2.4}$$

relating infinitesimal line elements $\mathrm{d}\boldsymbol{X}$ in reference configuration with infinitesimal line elements $\mathrm{d}\boldsymbol{x}$ in current configuration via

$$\mathrm{d}\boldsymbol{x} = \boldsymbol{F} \cdot \mathrm{d}\boldsymbol{X}. \tag{2.5}$$

Vice versa, its inverse can be employed to map infinitesimal line elements $\mathrm{d}\boldsymbol{x}$ in current configuration to their counterparts in material configuration as $\mathrm{d}\boldsymbol{X} = \boldsymbol{F}^{-1} \cdot \mathrm{d}\boldsymbol{x}$. Infinitesimal volume elements $\mathrm{d}V_0$ in the material configuration can be transformed into volume elements $\mathrm{d}V$ in spatial configuration with the help of the Jacobian determinant of the deformation gradient

$$J = \det \boldsymbol{F} \tag{2.6}$$

as

$$\mathrm{d}V = J \cdot \mathrm{d}V_0. \tag{2.7}$$

Since a physically reasonable deformation map has to be smooth and bijective, the determinant has to be positive, that is, $J > 0$. Finally, the deformation gradient can be decomposed into a rigid motion component and a stretch component using polar decomposition

$$\boldsymbol{F} = \boldsymbol{R} \cdot \boldsymbol{U} = \boldsymbol{v} \cdot \boldsymbol{R} \tag{2.8}$$

where $\boldsymbol{R}$ is a volume-preserving orthogonal rotation tensor and $\boldsymbol{U}$ and $\boldsymbol{v}$ are volume-changing stretch tensors, the *material stretch tensor* respectively the *spatial stretch tensor*. They play an important role in defining objective strain measures which do not depend on the observer and, thus, do not change when a subsequent rigid body motion is imposed on an already deformed body. The *Green-Lagrange strain tensor* defined as

$$\boldsymbol{E} = \frac{1}{2}\left(\boldsymbol{C} - \boldsymbol{I}\right) = \frac{1}{2}\left(\boldsymbol{F}^T \cdot \boldsymbol{F} - \boldsymbol{I}\right) \tag{2.9}$$

with the *right Cauchy-Green tensor*

$$\boldsymbol{C} = \boldsymbol{F}^T \cdot \boldsymbol{F} = \boldsymbol{U}^T \cdot \boldsymbol{R}^T \cdot \boldsymbol{R} \cdot \boldsymbol{U} = \boldsymbol{U}^T \cdot \boldsymbol{U} \tag{2.10}$$

is such an objective strain tensor and is the only strain definition employed here. For alternative strain measures, the reader is referred to the aforementioned literature on continuum mechanics.

2.2.2 The Concept of Stresses

The concept of stresses is best introduced by defining a conceived surface of size Δa with (spatial) normal vector $\boldsymbol{n}$ cutting through the body in its current configuration. The resulting force on this internal plane surface is denoted as $\Delta \boldsymbol{f}$. Taking the limit

$$\boldsymbol{t}\left(\boldsymbol{n}, \boldsymbol{x}, t\right) = \lim_{\Delta a \to 0} \frac{\Delta \boldsymbol{f}}{\Delta a} \tag{2.11}$$

defines a spatial *traction vector* $\boldsymbol{t}$, that is, a force measured per unit surface area in current configuration. Cauchy's stress theorem states that there exists a unique spatial tensor field defined as

$$\boldsymbol{t} = \boldsymbol{\sigma} \cdot \boldsymbol{n}. \tag{2.12}$$

Therein, the symmetric second order *Cauchy stress tensor* $\boldsymbol{\sigma}$ has been introduced. It is the stress measure with the clearest interpretation in nonlinear solid mechanics representing the internal stress state in the deformed continuum with diagonal components accounting for normal stresses and off-diagonal components for shear stresses. However, since the deformed configuration is not known a-priori it is often more practical to work with stresses defined in the reference configuration. The *first Piola Kirchhoff stress tensor* is defined as

$$\boldsymbol{P} = J\boldsymbol{\sigma} \cdot \boldsymbol{F}^{-T} \tag{2.13}$$

via the *pull-back* of the Cauchy stress tensor. Like the deformation gradient, it is a so-called two point tensor with one basis vector in current and one in material configuration and is unsymmetric. By contrast, the *second Piola Kirchhoff stress tensor* or *material* stress tensor is defined completely in the reference configuration and given by

$$\boldsymbol{S} = \boldsymbol{F}^{-1} \cdot \boldsymbol{P} = J\boldsymbol{F}^{-1} \cdot \boldsymbol{\sigma} \cdot \boldsymbol{F}^{-T}. \tag{2.14}$$

Note that the previously mentioned symmetry of the Cauchy and the second Piola-Kirchhoff stress tensor

$$\boldsymbol{\sigma}^T = \boldsymbol{\sigma} \quad \text{and} \quad \boldsymbol{S}^T = \boldsymbol{S} \tag{2.15}$$

can be derived from the local balance of angular momentum. Thus, this balance equation is typically not solved but the symmetry of the stress tensors is enforced via suitable constitutive laws.

2.3 Governing Macroscale Equations of Multiphase Poro-elasticity

In this section a set of macroscale conservation and balance equations for species in a phase or the phase as a whole is introduced based on the textbook on TCAT by Gray and Miller [95, Section 6.5]. Lower dimensional entities such as interfaces, common curves and common points are not included in the derivation. Interfacial effects are accounted for by suitable constitutive equations in Chapter 3. The phase and species balance equations represent the building blocks for the homogenized tumor growth models developed in Chapter 3. They are the conservation of mass, see Section 2.3.1, the conservation of linear momentum, see Section 2.3.2, and the conservation of energy, see Section 2.3.3. All these are extensive quantities which are known to be conserved in physical systems. The balance equations are then brought into the ALE description which is particularly suited for large deformation poro-elasticity in Section 2.3.4.

Remark 2.1. *The entropy balance equation is an additional governing equation of the system. In the TCAT formalism this is incorporated via the SEI at the macroscale providing closure relations for the system. As stated previously, a complete SEI for the present multiphase tumor growth model has not yet been derived, only certain aspects in closing the avascular precursor model have been addressed [230] and for the remaining model phenomenological constitutive relations have been employed. For a more consistent derivation in terms of TCAT, the reader is referred to the theoretical paper on the TCAT tumor growth model [170].*

Remark 2.2. *To be able to precisely define quantities at both macro- and microscale including mathematical operations on both scales and between scales, TCAT involves a lot of subtle notation. Since no averaging or derivations, for which this notation is important, is performed in this thesis, a simplified notation employed for the tumor growth model [135, 136, 224, 225, 229–233, 235, 282] is preferred. Throughout this thesis, only macroscale quantities are considered and denoted by superscripts and all equations are posed on the macroscale.*

2.3.1 Conservation of Mass

The macroscale mass conservation equation of a generic species i in a phase α, which in TCAT notation is denoted by $\mathcal{M}^{\overline{\overline{i\alpha}}}$, may be written as

$$\mathcal{M}^{\overline{\overline{i\alpha}}} := \left.\frac{\partial(\varepsilon^\alpha \rho^\alpha \omega^{i\,\overline{\alpha}})}{\partial t}\right|_{\boldsymbol{x}} + \boldsymbol{\nabla}\cdot\left(\varepsilon^\alpha \rho^\alpha \omega^{i\,\overline{\alpha}} \boldsymbol{v}^{i\alpha}\right) - \sum_{\kappa\in\mathfrak{I}_{c\alpha}} \overset{i\kappa\to i\alpha}{M} - \varepsilon^\alpha r^{i\alpha} = 0 \tag{2.16}$$

with the mass density ρ^α and volume fraction ε^α of the phase α and the mass fraction $\omega^{i\,\overline{\alpha}}$ of the species i in the generic phase α and its velocity $\boldsymbol{v}^{i\alpha}$. Here, the equation is given in spatial or Eulerian formulation denoted by the spatial coordinate $\boldsymbol{x}$ and derivative at fixed spatial coordinate $\left.\frac{\partial(\bullet)}{\partial t}\right|_{\boldsymbol{x}}$. Furthermore, the mass transfer of species i between phase α and κ is denoted as

$$\overset{i\kappa\to i\alpha}{M} = -\overset{i\alpha\to i\kappa}{M}. \tag{2.17}$$

The preceded sum in (2.16) implies a summation of mass transfer terms between all species i in generic phases κ with the given species i in phase α. Actually, in the TCAT formalism $\mathfrak{I}_{c\alpha}$ denotes all interfaces which separate the α phase from adjacent phases. Since the interface is treated as massless in the present formulation, it is equivalent to a sum over all involved phases. The last term on the left hand side in (2.16) is the intra-phase production term $\varepsilon^\alpha r^{i\alpha}$ of species i in phase α, that is, a source term of the considered species.

By contrast to species, phases are characterized by their volume fraction ε^α at each macroscale point. Naturally, the volume fractions have to satisfy the relation

$$\sum_{\alpha\in\mathfrak{I}_p} \varepsilon^\alpha = 1, \tag{2.18}$$

i.e., all present phases collected in the phase set $\mathfrak{I}_p$ have to sum up to one. The macroscale mass balance equation $\mathcal{M}^{\overline{\alpha}}$ of a phase α can either be obtained by averaging its microscale counterpart or by summation of the mass balances of all species i in the species set $\mathfrak{I}_s$ as

$$\sum_{i\in\mathfrak{I}_s} \mathcal{M}^{\overline{\overline{i\alpha}}} = \mathcal{M}^{\overline{\alpha}} := \left.\frac{\partial(\varepsilon^\alpha \rho^\alpha)}{\partial t}\right|_{\boldsymbol{x}} + \boldsymbol{\nabla}\cdot\left(\varepsilon^\alpha \rho^\alpha \boldsymbol{v}^\alpha\right) - \sum_{\kappa\in\mathfrak{I}_{c\alpha}} \overset{\kappa\to\alpha}{M} = 0. \tag{2.19}$$

Therein, the velocity $\boldsymbol{v}^\alpha$ of the α phase has been defined as

$$\boldsymbol{v}^\alpha = \sum_{i\in\mathfrak{I}_s} \omega^{i\,\overline{\alpha}} \boldsymbol{v}^{i\alpha} \tag{2.20}$$

as the sum of all species velocities $\boldsymbol{v}^{i\alpha}$ weighted with their mass fraction $\omega^{i\,\overline{\alpha}}$ and a generic mass transfer term from phase α to another phase κ as

$$\overset{\kappa\to\alpha}{M} = \sum_{i\in\mathfrak{I}_s} \overset{i\kappa\to i\alpha}{M} = -\overset{\alpha\to\kappa}{M}. \tag{2.21}$$

Hence, the sum of all species mass transfer terms between phases α and κ must correspond to the overall mass transfer between the phases. In (2.19) the single mass transfer terms are

again summed up for all involved mass transfers between different phases κ. Furthermore, the following relations can be deduced:

$$\sum_{i\in\mathfrak{I}_s} \omega^{i\,\overline{\alpha}} = 1 \tag{2.22}$$

and

$$\sum_{i\in\mathfrak{I}_s} r^{i\alpha} = 0, \tag{2.23}$$

i.e., mass fractions of all species in a specific phase α have to sum up to one and no species mass can be generated in a phase without simultaneous loss of another species. In summary, equations (2.16) and (2.19) govern the mass balance of a phase and its composition in terms of all the species which constitute the phase. For the problems considered in this thesis, it is convenient to employ a slightly different formulation of the species mass balance (2.16) in terms of the macroscopic diffusion velocity $\boldsymbol{u}^{i\alpha}$, which is the relative velocity of the species w.r.t. the velocity of the phase defined as

$$\boldsymbol{u}^{i\alpha} = \boldsymbol{v}^{i\alpha} - \boldsymbol{v}^{\alpha}. \tag{2.24}$$

Inserting this definition in the species mass balance (2.16) yields an alternative but equivalent formulation for the mass balance of a species i in phase α:

$$\overline{\overline{\mathcal{M}}}^{i\alpha} = \frac{\partial(\varepsilon^{\alpha}\rho^{\alpha}\omega^{i\,\overline{\alpha}})}{\partial t}\bigg|_{\boldsymbol{x}} + \boldsymbol{\nabla}\cdot\left(\varepsilon^{\alpha}\rho^{\alpha}\omega^{i\,\overline{\alpha}}\boldsymbol{v}^{\alpha}\right) + \boldsymbol{\nabla}\cdot\left(\varepsilon^{\alpha}\rho^{\alpha}\omega^{i\,\overline{\alpha}}\boldsymbol{u}^{i\alpha}\right) - \sum_{\kappa\in\mathfrak{I}_{c\alpha}} \overset{i\kappa\to i\alpha}{M} - \varepsilon^{\alpha} r^{i\alpha} = 0. \tag{2.25}$$

Combining the definition of the diffusion velocity (2.24) with the phase velocity (2.20) and the constraint on species mass fraction (2.22) results in an additional constraint

$$\sum_{i\in\mathfrak{I}_s} \omega^{i\,\overline{\alpha}}\boldsymbol{u}^{i\alpha} = 0 \tag{2.26}$$

for the diffusion velocities of all considered species. Therefore, in a phase composed of N species only $N-1$ are independent. The last mass fraction and velocity can be obtained from (2.22) and (2.26), respectively.

In the context of tumor growth modeling, it is not possible to resolve the entire composition of a phase and also not of interest. For instance, the interstitial fluid or cell phases may consist of numerous species, such as nutrients, macromolecules or chemical signals where only a subpart is relevant for the model or the question at hand. Moreover, the phases usually consist of a dominant water species in biological tissue. Typically, the balance of mass of all phases will be solved in combination with the balance of mass of the species of interest which are only a subpart of all present species.

The final species mass balance equation equation can be obtained when applying the product rule to the temporal derivative in (2.25) which results in

$$\begin{aligned}\overline{\overline{\mathcal{M}}}^{i\alpha} = {} & \varepsilon^{\alpha}\rho^{\alpha}\,\frac{\partial\omega^{i\,\overline{\alpha}}}{\partial t}\bigg|_{\boldsymbol{x}} + \varepsilon^{\alpha}\rho^{\alpha}\boldsymbol{v}^{\alpha}\cdot\boldsymbol{\nabla}\omega^{i\,\overline{\alpha}} + \boldsymbol{\nabla}\cdot\left(\varepsilon^{\alpha}\rho^{\alpha}\boldsymbol{D}^{i\alpha}_{\text{eff}}\boldsymbol{\nabla}\omega^{i\,\overline{\alpha}}\right) \\ & - \sum_{\kappa\in\mathfrak{I}_{c\alpha}} \overset{i\kappa\to i\alpha}{M} - \varepsilon^{\alpha} r^{i\alpha} + \omega^{i\,\overline{\alpha}} \underbrace{\left[\frac{\partial}{\partial t}\left(\varepsilon^{\alpha}\rho^{\alpha}\right)\bigg|_{\boldsymbol{x}} + \boldsymbol{\nabla}\cdot\left(\varepsilon^{\alpha}\rho^{\alpha}\boldsymbol{v}^{\alpha}\right)\right]}_{\overset{(2.19)}{=}\sum_{\kappa\in\mathfrak{I}_{c\alpha}} \overset{\kappa\to\alpha}{M}} = 0\end{aligned} \tag{2.27}$$

where the balance of mass of the α phase (2.19) has been exploited. Furthermore, the diffusive flux has been approximated with a Fickian diffusion law as

$$\omega^{i\overline{\alpha}}\boldsymbol{u}^{i\alpha} = \boldsymbol{D}_{\text{eff}}^{i\alpha}\boldsymbol{\nabla}\omega^{i\overline{\alpha}} \tag{2.28}$$

with the effective diffusion tensor $\boldsymbol{D}_{\text{eff}}^{i\alpha}$ of species i in the α phase.

2.3.2 Conservation of Momentum

The momentum balance equation can also be formulated for a species in a phase or the phase as a whole. However, the momentum balance of species is not explicitly considered since the diffusion velocity of a specific species $\boldsymbol{u}^{i\alpha}$ and, therefore, also its velocity $\boldsymbol{v}^{i\alpha}$ is determined by the diffusion law (2.28). Thus, only the momentum balance of the entire phase $\boldsymbol{\mathcal{P}}^{\overline{\overline{\alpha}}}$ in spatial formulation according to Sciumè et al. [230]

$$\begin{aligned}\boldsymbol{\mathcal{P}}^{\overline{\overline{\alpha}}} := \left.\frac{\partial(\varepsilon^\alpha\rho^\alpha\boldsymbol{v}^\alpha)}{\partial t}\right|_{\boldsymbol{x}} &+ \boldsymbol{\nabla}\cdot(\varepsilon^\alpha\rho^\alpha\boldsymbol{v}^\alpha\boldsymbol{v}^\alpha) - \boldsymbol{\nabla}\cdot(\varepsilon^\alpha\boldsymbol{\sigma}^\alpha)\\ &- \varepsilon^\alpha\rho^\alpha\boldsymbol{g}^\alpha - \sum_{\kappa\in\mathfrak{I}_{c\alpha}}\left(\sum_{i\in\mathfrak{I}_s}\overset{i\kappa\to i\alpha}{M}\boldsymbol{v}^\alpha + \overset{\kappa\to\alpha}{\mathbf{T}_0}\right) = \mathbf{0}\end{aligned} \tag{2.29}$$

is considered hereafter. Therein, $\boldsymbol{g}^\alpha$ is a body force, $\overset{i\kappa\to i\alpha}{M}\boldsymbol{v}^\alpha$ the exchange of momentum between phases α and κ due to species mass exchange and $\overset{\kappa\to\alpha}{\mathbf{T}_0} = -\overset{\alpha\to\kappa}{\mathbf{T}_0}$ represents the interaction forces between adjacent phases since interfaces are not explicitly considered [230]. Furthermore, $\boldsymbol{\sigma}^\alpha$ denotes the spatial or Cauchy stress tensor of the α phase at the macroscale. The above equation can further be simplified by neglecting the inertia terms, that is, the first two terms in the previous equation, which is justified considering the slow dynamics of tumor growth. In addition, the domain sizes employed in this thesis are so small that gravitational effects by a body force do not have to be taken into account. Finally, also the forces occuring as a byproduct of mass transfer are dropped since they are of the same order of magnitude as the inertial terms [230]. Thus, only the divergence of the stress tensor and the interaction forces with other phases remain in the final form

$$\boldsymbol{\mathcal{P}}^{\overline{\overline{\alpha}}} = -\boldsymbol{\nabla}\cdot(\varepsilon^\alpha\boldsymbol{\sigma}^\alpha) - \sum_{\kappa\in\mathfrak{I}_{c\alpha}}\overset{\kappa\to\alpha}{\mathbf{T}_0} = \mathbf{0}. \tag{2.30}$$

This momentum balance in spatial formulation applies to the solid phase and all involved fluid phases. However, different closure relations are required which will be given in Section 2.3.2.1 and 2.3.2.2, respectively.

2.3.2.1 Formulation and Closure Relations for Fluid Phases

Closure for the momentum balance equations of a generic fluid phase has been demonstrated by Sciumè et al. [230, Appendix A] based on TCAT which is why the derivation is not repeated here. It follows that the macroscale stress tensor of a fluid phase $f \in \mathfrak{I}_{\text{f}}$ is given by the fluid pressure p^f as

$$\boldsymbol{\sigma}^f = -p^f\boldsymbol{I} \tag{2.31}$$

when neglecting also the viscous contribution to the stress tensor on the macroscale. The final momentum balance equation emerges as

$$\varepsilon^f \boldsymbol{\nabla} p^f = -\hat{\boldsymbol{R}}^f \cdot \left(\boldsymbol{v}^f - \boldsymbol{v}^s\right) \tag{2.32}$$

with a second order resistance tensor $\hat{\boldsymbol{R}}$. Setting $\boldsymbol{k}^f/\mu^f = \left(\varepsilon^f\right)^2 \cdot \left(\hat{\boldsymbol{R}}^f\right)^{-1}$, one obtains the well-known Darcy-equation for flow through porous media

$$-\frac{\boldsymbol{k}^f}{\mu^f}\boldsymbol{\nabla} p^f = \varepsilon^f \cdot \left(\boldsymbol{v}^f - \boldsymbol{v}^s\right) \tag{2.33}$$

with permeability tensor $\boldsymbol{k}^f$ and viscosity μ^f which is the governing momentum balance equation for a generic fluid phase f in the present model. Note that this does not imply that the fluid is inviscid but that the resistance acting on the flow is dominated by adhesion to the skeleton. If the viscous forces of the fluid on the macroscale cannot be neglected, the Darcy-Brinkman equation is obtained, see [269, 272].

Remark 2.3. *The momentum balance equation for a generic solid or fluid phase (2.30) actually contains a sum over all involved interactions between the different phases, however, in the Darcy equation only one pair of interactions is considered, namely, between the respective fluid phase f and the solid phase s. This is due to the fact that interaction forces between different fluid phases are not taken directly into account but via a constitutive law for the relative permeability of the fluid phases as proposed by Sciumè et al. [230, 232], see also Section 3.2.4.*

2.3.2.2 Formulation and Closure Relations for Solid Phase

The momentum balance equation of the solid phase is given by

$$\boldsymbol{\mathcal{P}}^{\bar{\bar{s}}} = \boldsymbol{\nabla} \cdot \left(\varepsilon^s \boldsymbol{\sigma}^s\right) + \sum_{f \in \mathfrak{I}_\mathrm{f}} \boldsymbol{\nabla} \cdot \left(\varepsilon^f \boldsymbol{\sigma}^f\right) = \boldsymbol{0}. \tag{2.34}$$

Here, the momentum balance equations of all present fluid phases have been inserted into (2.30) to eliminate the interaction force terms. Another way to obtain the previous equation is to sum the momentum balance equations of all present phases $\alpha \in \mathfrak{I}_p$ such that the interaction forces between adjacent phases cancel out. Thus, the previous equation can also be interpreted as the momentum balance equation of the porous medium system as a whole [95]. This is even more evident when defining the total stress as the weighted sum of the stress tensors of all entities as

$$\boldsymbol{\sigma}^{\mathrm{tot}} = \sum_{\alpha \in \mathfrak{I}_p} \varepsilon^\alpha \boldsymbol{\sigma}^\alpha. \tag{2.35}$$

The momentum balance equation (2.34) may then be rewritten as

$$\boldsymbol{\mathcal{P}}^{\bar{\bar{s}}} = \boldsymbol{\nabla} \cdot \boldsymbol{\sigma}^{\mathrm{tot}} = \boldsymbol{0}. \tag{2.36}$$

While the fluid phase stress tensors have already been defined in equation (2.31), the solid phase stress tensor is yet to be specified. This is achieved via a suitable constitutive law for the elastic behaviour of the solid phase. For that, the solid phase stress tensor is re-written as

$$\varepsilon^s \boldsymbol{\sigma}^s = -\varepsilon^s p^s \boldsymbol{I} + \varepsilon^s \boldsymbol{\tau}^s = -\varepsilon^s p^s \boldsymbol{I} + \boldsymbol{\sigma}^{\mathrm{eff}} \tag{2.37}$$

where p^s accounts for the solid phase pressure exerted by the pore fluids on the skeleton. For now, it will be disregarded and reconsidered in Sections 3.2.2 and 3.3.2 and the second term, the so-called *effective stress tensor* $\boldsymbol{\sigma}^{\text{eff}}$, will be investigated in more detail. This quantity accounts for stresses due to changes in porosity, spatial variation of porosity, and the deformation of the solid matrix [86]. Its pull-back in the material configuration is given as

$$\boldsymbol{S}^{\text{eff}} = J\boldsymbol{F}^{-1} \cdot \boldsymbol{\sigma}^{\text{eff}} \cdot \boldsymbol{F}^{-T}. \tag{2.38}$$

Under the assumption of constant skeleton density ρ^s, it follows from the dissipation inequality for the solid phase (see [272] and [46, Section 3.4.1]) that the second Piola-Kirchhoff effective stress tensor can be obtained as the derivative of a *strain energy function* Ψ^s as postulated in solid mechanics for *hyperelastic* materials. For this class of material laws it is assumed that the strain energy function depends only on the current deformation state of the solid as $\Psi^s(\boldsymbol{F})$ and not on the history of the deformation. Objectivity dictates that the strain energy function depends on the stretch component $\boldsymbol{U}$ of the deformation gradient and not on the rotational part $\boldsymbol{R}$ from its polar decomposition (2.8). In practice, strain energy functions are often given in terms of the Green-Lagrange strain tensor as $\Psi^s(\boldsymbol{E})$ such that the effective stress may be obtained as

$$\boldsymbol{S}^{\text{eff}} = \frac{\partial \Psi^s}{\partial \boldsymbol{E}}, \tag{2.39}$$

that is, as the derivative of the strain energy function w.r.t. the Green-Lagrange strain tensor.

Throughout this thesis, only two simple isotropic constitutive laws for the solid phase are regarded. The first one is the *Saint-Venant-Kirchhoff* material with the strain energy function

$$\Psi^s_{\text{SVK}} = \frac{\lambda^s}{2} \left(\text{tr}\left(\boldsymbol{E}\right)\right)^2 + \mu^s \boldsymbol{E} : \boldsymbol{E}. \tag{2.40}$$

This material law comprises two parameters, the so-called Lamé constants

$$\lambda^s = \frac{E^s \nu^s}{(1+\nu^s)(1-2\nu^s)} \quad \text{and} \quad \mu^s = \frac{E^s}{2(1+\nu^s)} \tag{2.41}$$

which can be calculated from the well-known *Young's modulus* E^s and *Poisson's ratio* ν^s of the solid phase. The Saint-Venant-Kirchhoff material law describes a linear relationship between second Piola-Kirchhoff stress tensor and Green-Lagrange strain tensor. The second constitutive law is the *Neo-Hooke* model whose strain energy function reads as

$$\Psi^s_{\text{NH}} = \frac{\mu^s}{2} \left(\text{tr}\left(\boldsymbol{C}\right) - 3\right)^2 - \mu^s \ln(J) + \frac{\lambda^s}{2} \left(\ln(J)\right)^2, \tag{2.42}$$

thereby postulating a nonlinear stress-strain relationship.

Remark 2.4. *In general, any hyperelastic material law can be applied for the ECM. Numerous more sophisticated constitutive laws can be found in the textbooks [28, 110, 163, 186]. However, the main focus of this thesis does not lie on modeling the ECM behaviour. A more realistic description of the ECM can, for example, be achieved via homogenized fiber material models [87]. Also ECM remodeling by the growing tumor via ECM dissolution, deposition and increased cross-linking can have a major impact on its constitutive behaviour [47].*

2.3.3 Conservation of Energy

In this thesis, the energy balance equation is only considered in the context of hyperthermia. Considering its relevant time scales of of 60 minutes or longer [259], a macroscale local equilibrium assumption for the temperature can be made [95, Chapter 10.8] meaning that temperature gradients exist within the system but the macroscale temperature T is independent of the entity, i.e., equal for all present phases and species such that

$$T^\alpha = T, \quad \text{for } \alpha \in \mathfrak{I}. \tag{2.43}$$

Furthermore, as described by Pesavento et al. [194], viscous dissipation, mechanical work, density variation and the kinetic energy are negligible in the current case such that an enthalpy balance for each phase $\alpha \in \mathfrak{I}_p$ emerges as

$$c_p^\alpha \left.\frac{\partial(\rho^\alpha \varepsilon^\alpha T)}{\partial t}\right|_{\boldsymbol{x}} + c_p^\alpha \boldsymbol{\nabla} \cdot (\rho^\alpha \varepsilon^\alpha T \boldsymbol{v}^\alpha) - \boldsymbol{\nabla} \cdot (\varepsilon^\alpha \boldsymbol{\kappa}^\alpha \boldsymbol{\nabla} T) - \varepsilon^\alpha s^\alpha = 0, \tag{2.44}$$

where c_p^α is the specific heat capacity of the α phase at constant pressure, $\boldsymbol{\kappa}^\alpha$ its conductivity tensor and $\varepsilon^\alpha s^\alpha$ a heat source term. As in (2.27), the product rule can be applied to the temporal derivative in (2.44) yielding

$$c_p^\alpha \rho^\alpha \varepsilon^\alpha \left.\frac{\partial T}{\partial t}\right|_{\boldsymbol{x}} + c_p^\alpha \rho^\alpha \varepsilon^\alpha \boldsymbol{v}^\alpha \cdot \boldsymbol{\nabla} T - \boldsymbol{\nabla} \cdot (\varepsilon^\alpha \boldsymbol{\kappa}^\alpha \boldsymbol{\nabla} T) - \varepsilon^\alpha s^\alpha + c_p^\alpha T \sum_{\kappa \in \mathfrak{I}_{c\alpha}} \overset{\kappa\to\alpha}{M} = 0. \tag{2.45}$$

Summing this equation over all present phases $\alpha \in \mathfrak{I}_p$ yields the energy balance of the entire porous medium system

$$\begin{aligned}(c_p\rho)_{\text{eff}} \left.\frac{\partial T}{\partial t}\right|_{\boldsymbol{x}} + \sum_{\alpha\in\mathfrak{I}_p} c_p^\alpha \rho^\alpha \varepsilon^\alpha \boldsymbol{v}^\alpha \cdot \boldsymbol{\nabla} T - \boldsymbol{\nabla} \cdot (\boldsymbol{\kappa}_{\text{eff}} \boldsymbol{\nabla} T) \\ - \sum_{\alpha\in\mathfrak{I}_p} \varepsilon^\alpha s^\alpha + \sum_{\alpha\in\mathfrak{I}_p} \left(c_p^\alpha T \sum_{\kappa\in\mathfrak{I}_{c\alpha}} \overset{\kappa\to\alpha}{M} \right) = 0.\end{aligned} \tag{2.46}$$

with effective heat capacity

$$(c_p\rho)_{\text{eff}} = \sum_{\alpha\in\mathfrak{I}_p} \rho^\alpha \varepsilon^\alpha c_p^\alpha \tag{2.47}$$

and effective isotropic conductivity tensor

$$\boldsymbol{\kappa}_{\text{eff}} = \sum_{\alpha\in\mathfrak{I}_p} \varepsilon^\alpha \boldsymbol{\kappa}^\alpha = \sum_{\alpha\in\mathfrak{I}_p} \varepsilon^\alpha \kappa^\alpha \boldsymbol{I}. \tag{2.48}$$

In the last term of (2.46), each phase mass transfer term is present once positive and once negative due to (2.21) and the sum over all phases. Therefore, this term can be canceled if the heat capacities of all phases are equal.

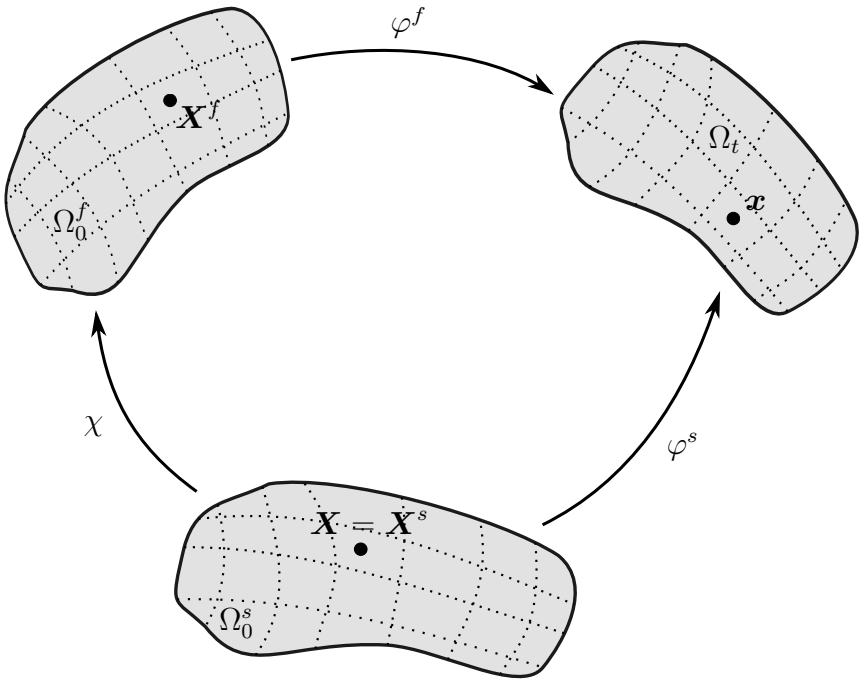

Figure 2.4: Sketch of configurations and corresponding mappings (after [66, 272])

2.3.4 Final Set of Governing Equations in Arbitrary Lagrangean-Eulerian Description

In the previous sections, all equations have been written with respect to the spatial configuration $\boldsymbol{x}$. As all phases can deform independently of each other, each phase α has distinct kinematics with its own material configuration $\boldsymbol{X}^\alpha$. In other words, macroscopic material particles of different phases which occupy the same spatial configuration $\boldsymbol{x}$ at a specific time t have not necessarily been at the same material configuration at time $t = 0$. The material point of each phase α has been at the material configuration $\boldsymbol{X}^\alpha$ of that phase, see also Figure 2.4. Thus, in situations where solid deformations are significant but still small compared to the deformation of the fluid phases, it is important to distinguish between the different configurations such that a precise definition of material time derivatives with respect to the single phases is possible. This approach was introduced by [269, 272] for single fluid phase flow through a porous medium and is here transferred to the case when multiple fluid phases are present. In the previous publications on the tumor growth model [224, 225, 229–233, 235] this distinction has not been made but was only introduced in the author's publication [135]. The following section is a recapitulation of the derivations and explanations in the papers of Donea et al. [66] and Vuong et al. [269] and the thesis of Vuong [272]. Then, the governing equations for mass transport in the fluid phase, mass transport in the solid phase and the balance of energy in ALE form are detailed, which are the essential components of the developed tumor growth models.

2.3.4.1 Recapitulation of Employed Arbitrary Lagrangean-Eulerian Formulation

The different configurations and mappings are sketched in Figure 2.4 for the solid phase s and a single fluid phase f. The case with multiple fluid phases follows analogously. Here, Ω_t denotes

the current configuration and Ω_0^s and Ω_0^f the material configuration of the solid and the fluid phase, respectively. Three distinct bijective mappings have been defined, namely,

$$\varphi^f : \begin{cases} \Omega_0^f \to \Omega_t, \quad \boldsymbol{X}^f \to \boldsymbol{x} \\ \varphi^f\left(\boldsymbol{X}^f, t\right) = \boldsymbol{x}\left(\boldsymbol{X}^f, t\right) \end{cases} \tag{2.49}$$

which maps a material point of a fluid phase $\boldsymbol{X}^f$ on a spatial point $\boldsymbol{x}$ and

$$\varphi^s : \begin{cases} \Omega_0^s \to \Omega_t, \quad \boldsymbol{X} \to \boldsymbol{x} \\ \varphi^s\left(\boldsymbol{X}, t\right) = \boldsymbol{x}\left(\boldsymbol{X}, t\right) \end{cases} \tag{2.50}$$

which maps a material point of the solid phase $\boldsymbol{X}^s = \boldsymbol{X}$ on a spatial point $\boldsymbol{x}$ and

$$\chi = \left(\varphi^f\right)^{-1} \circ \varphi^s : \begin{cases} \Omega_0^s \to \Omega_0^f, \quad \boldsymbol{X} \to \boldsymbol{X}^f \\ \chi\left(\boldsymbol{X}, t\right) = \boldsymbol{X}^f\left(\boldsymbol{X}, t\right) \end{cases} \tag{2.51}$$

which defines a mapping between the two different material configuration. By that, a material point of the solid phase $\boldsymbol{X}$ is mapped on a material point of the fluid phase $\boldsymbol{X}^f$.

Material time derivatives describe the change in time of the physical properties of a physical particle or material element, for instance, the change in temperature of a particle as it is transported through a certain domain with spatially and temporally varying temperature field. This is equivalent to the Lagrangean observer following the path of a material element. Since multiple phases with different material configurations and, hence, different Lagrangean observers are present, one has to distinguish also between multiple material time derivatives. The material time derivative of a generic quantity $(\bullet)$ is defined as

$$\frac{\mathrm{d}^\alpha\left(\bullet\right)}{\mathrm{d}t} = \left.\frac{\partial\left(\bullet\right)}{\partial t}\right|_{\boldsymbol{X}^\alpha}, \tag{2.52}$$

for a specific phase α, that is, the temporal derivative of this quantity while keeping the α phase's material particle $\boldsymbol{X}^\alpha$ fixed, i.e., following the material particle of this phase. The material time derivative with respect to the skeleton phase of a *material quantity* $(\bullet)\left(\boldsymbol{X}, t\right)$ is then simply given by

$$\frac{\mathrm{d}^s\left(\bullet\right)\left(\boldsymbol{X}, t\right)}{\mathrm{d}t} = \left.\frac{\partial(\bullet)\left(\boldsymbol{X}, t\right)}{\partial t}\right|_{\boldsymbol{X}}. \tag{2.53}$$

The velocity of the skeleton phase follows as

$$\boldsymbol{v}^s = \frac{\mathrm{d}^s\boldsymbol{x}}{\mathrm{d}t} = \left.\frac{\partial\boldsymbol{x}}{\partial t}\right|_{\boldsymbol{X}} \tag{2.54}$$

and the total time derivative of a *spatial quantity* $(\bullet)\left(\boldsymbol{x}, t\right)$ as

$$\frac{\mathrm{d}^s\left(\bullet\right)\left(\boldsymbol{x}\left(\boldsymbol{X}, t\right)\right)}{\mathrm{d}t} = \left.\frac{\partial(\bullet)\left(\boldsymbol{x}, t\right)}{\partial t}\right|_{\boldsymbol{X}} + \frac{\partial\left(\bullet\right)}{\partial\boldsymbol{x}} \cdot \left.\frac{\partial\boldsymbol{x}}{\partial t}\right|_{\boldsymbol{X}} = \left.\frac{\partial(\bullet)\left(\boldsymbol{x}, t\right)}{\partial t}\right|_{\boldsymbol{X}} + \boldsymbol{\nabla}\left(\bullet\right) \cdot \boldsymbol{v}^s \tag{2.55}$$

where the definition of the solid phase velocity (2.54) has been employed. Therein, the second part is the typical convective derivative of a spatial quantity which additionally accounts for

the movement of the material particle. Both derivatives are equivalent to classical continuum mechanics descriptions with a Lagrangean observer following the skeleton.

The material coordinates of the solid phase $\boldsymbol{X}$ move independently of the fluid phase and can, therefore, be interpreted as an independently moving reference configuration with respect to the fluid phase similar to an ALE approach [66]. The solid and fluid material reference configurations are related via the respective mappings, i.e., a material point $\boldsymbol{X}$ of the solid phase can be mapped on the spatial configuration $\boldsymbol{x}\left(\boldsymbol{X},t\right)$ either by application of the solid deformation map φ^s or by first mapping it on the fluid reference configuration with the mapping χ and then on the spatial configuration with the fluid deformation map φ^f as $\boldsymbol{x}\left(\boldsymbol{X}^f\left(\boldsymbol{X},t\right),t\right)$. We can exploit this dependency $\boldsymbol{X}^f\left(\boldsymbol{X},t\right)$ to reformulate material time derivatives of a generic *spatial quantity* $(\bullet)\left(\boldsymbol{x},t\right)$ with respect to the fluid phase in derivatives with respect to the skeleton phase as

$$\begin{aligned}\frac{\mathrm{d}^f\left(\bullet\right)\left(\boldsymbol{x}\left(\boldsymbol{X},t\right)\right)}{\mathrm{d}t} &= \left.\frac{\partial(\bullet)\left(\boldsymbol{x}\left(\boldsymbol{X},t\right),t\right)}{\partial t}\right|_{\boldsymbol{X}} + \left.\frac{\partial\left(\bullet\right)\left(\boldsymbol{x}\left(\boldsymbol{X},t\right),t\right)}{\partial\boldsymbol{x}}\cdot\frac{\partial\boldsymbol{x}}{\partial t}\right|_{\boldsymbol{X}^f} \\ &= \left.\frac{\partial(\bullet)}{\partial t}\right|_{\boldsymbol{X}} + \left.\frac{\partial\left(\bullet\right)}{\partial\boldsymbol{x}}\cdot\frac{\partial\boldsymbol{x}}{\partial\boldsymbol{X}}\cdot\frac{\partial\boldsymbol{x}}{\partial t}\right|_{\boldsymbol{X}^f}.\end{aligned} \tag{2.56}$$

From that, the velocity of the fluid phase can be calculated as

$$\boldsymbol{v}^f = \frac{\mathrm{d}^f\boldsymbol{x}}{\mathrm{d}t} = \left.\frac{\partial\boldsymbol{x}\left(\boldsymbol{X},t\right)}{\partial t}\right|_{\boldsymbol{X}} + \left.\frac{\partial\boldsymbol{x}}{\partial\boldsymbol{X}}\cdot\frac{\partial\boldsymbol{x}}{\partial t}\right|_{\boldsymbol{X}^f}. \tag{2.57}$$

Solving the previous equation for the second summand and re-inserting it into (2.56) yields

$$\frac{\mathrm{d}^f\left(\bullet\right)\left(\boldsymbol{x}\left(\boldsymbol{X},t\right)\right)}{\mathrm{d}t} = \left.\frac{\partial(\bullet)}{\partial t}\right|_{\boldsymbol{X}} + \left(\boldsymbol{v}^f-\boldsymbol{v}^s\right)\cdot\boldsymbol{\nabla}\left(\bullet\right) \tag{2.58}$$

with the skeleton velocity (2.54). This equation establishes a relation for the material time derivative of the fluid phase as the local time derivative with fixed solid material particle plus an additional convective term depending on the relative velocity of the fluid with respect to the solid $\boldsymbol{v}^f-\boldsymbol{v}^s$. This equation is equivalent to the fundamental ALE equation [66] with the solid phase as an independently moving reference configuration and its velocity $\boldsymbol{v}^s$ as the grid velocity. Two special cases are contained in this formulation: if the solid does not deform $(\boldsymbol{v}^s=\boldsymbol{0})$, this is equivalent to a Eulerian description with fixed observer. If the solid velocity is equal to the fluid velocity $(\boldsymbol{v}^s=\boldsymbol{v}^f)$, the convective term cancels and a Lagrangean point of view is obtained where the observer follows the movement of a fluid particle. The equation allows reformulating material time derivatives of the fluid phase in an ALE type formulation with the solid phase as the reference configuration. Equivalently, local derivatives at fixed spatial position $\boldsymbol{x}$ may be rewritten as

$$\left.\frac{\partial(\bullet)\left(\boldsymbol{x}\left(\boldsymbol{X},t\right)\right)}{\partial t}\right|_{\boldsymbol{x}} = \left.\frac{\partial(\bullet)\left(\boldsymbol{x}\left(\boldsymbol{X},t\right)\right)}{\partial t}\right|_{\boldsymbol{X}} - \boldsymbol{v}^s\cdot\boldsymbol{\nabla}\left(\bullet\right), \tag{2.59}$$

where the relation between local and total time derivative

$$\frac{\mathrm{d}^f\left(\bullet\right)\left(\boldsymbol{x}\left(\boldsymbol{X},t\right)\right)}{\mathrm{d}t} = \left.\frac{\partial(\bullet)\left(\boldsymbol{x}\left(\boldsymbol{X},t\right)\right)}{\partial t}\right|_{\boldsymbol{x}} + \boldsymbol{v}^f\cdot\boldsymbol{\nabla}\left(\bullet\right) \tag{2.60}$$

has been employed together with (2.58). In the following sections, this equation will be utilized to transform the balance equations of the model, which were written in spatial formulation in Sections 2.3.1, 2.3.2 and 2.3.3, into the ALE description.

2.3.4.2 Fluid Phases

The balance of mass (2.19) of a generic fluid phase $f \in \mathfrak{I}_\mathrm{f}$ can be re-cast via the fundamental ALE equation (2.59) as

$$\left.\frac{\partial\left(\varepsilon^f\rho^f\right)}{\partial t}\right|_{\boldsymbol{X}} + \underbrace{\varepsilon^f\rho^f\boldsymbol{\nabla}\cdot\boldsymbol{v}^s + \boldsymbol{\nabla}\cdot\left(\varepsilon^f\rho^f\left(\boldsymbol{v}^f-\boldsymbol{v}^s\right)\right)}_{-\boldsymbol{v}^s\cdot\boldsymbol{\nabla}\left(\varepsilon^f\rho^f\right)+\boldsymbol{\nabla}\cdot\left(\varepsilon^f\rho^f\boldsymbol{v}^f\right)} = \sum_{\kappa\in\mathfrak{I}_{cf}} \overset{\kappa\to f}{M}\,. \tag{2.61}$$

Here, the Darcy equation (2.33) can be inserted resulting in

$$\left.\frac{\partial\left(\varepsilon^f\rho^f\right)}{\partial t}\right|_{\boldsymbol{X}} + \varepsilon^f\rho^f\boldsymbol{\nabla}\cdot\boldsymbol{v}^s - \boldsymbol{\nabla}\cdot\left(\rho^f\frac{\boldsymbol{k}^f}{\mu^f}\boldsymbol{\nabla}p^f\right) = \sum_{\kappa\in\mathfrak{I}_{cf}} \overset{\kappa\to f}{M} \qquad \text{in } \Omega_t\times[t_0,t_e]\,. \tag{2.62}$$

This is the final form governing the balance of mass of a generic fluid phase in ALE form. It is valid in the current domain Ω_t and in the considered time interval $[t_0,t_e]$ and constitutes an essential building block for the different continuum models for (a-)vascular tumor growth derived in Chapter 3. Note, however, that this equation is not closed since either a relationship between the volume fraction ε^f (or rather saturation S^f) and the pressure p^f or an additional evolution equation for one of the variables has to be specified, conf. Section 3.2.4 and Section 3.3.1.1. The species balance of mass (2.27) can equivalently be reformulated with the fundamental ALE equation (2.59) resulting in

$$\begin{aligned}\varepsilon^f\rho^f\left.\frac{\partial\omega^{i\overline{f}}}{\partial t}\right|_{\boldsymbol{X}} + \varepsilon^f\rho^f\left(\boldsymbol{v}^f-\boldsymbol{v}^s\right)\cdot\boldsymbol{\nabla}\omega^{i\overline{f}} + \boldsymbol{\nabla}\cdot\left(\varepsilon^f\rho^f\boldsymbol{D}^{if}_{\mathrm{eff}}\boldsymbol{\nabla}\omega^{i\overline{f}}\right)&\\ = \sum_{\kappa\in\mathfrak{I}_{cf}} \overset{i\kappa\to if}{M} + \varepsilon^f r^{if} - \omega^{i\overline{f}}\sum_{\kappa\in\mathfrak{I}_{cf}} \overset{\kappa\to f}{M}&\end{aligned} \tag{2.63}$$

for a fluid phase $f\in\mathfrak{I}_\mathrm{f}$. Again, the convective term can be replaced by the Darcy equation (2.33) yielding

$$\begin{aligned}\varepsilon^f\left.\frac{\partial\omega^{i\overline{f}}}{\partial t}\right|_{\boldsymbol{X}} - \frac{\boldsymbol{k}^f}{\mu^f}\boldsymbol{\nabla}p^f\cdot\boldsymbol{\nabla}\omega^{i\overline{f}} + \boldsymbol{\nabla}\cdot\left(\varepsilon^f\boldsymbol{D}^{if}_{\mathrm{eff}}\boldsymbol{\nabla}\omega^{i\overline{f}}\right)&\\ = \frac{1}{\rho^f}\left(\sum_{\kappa\in\mathfrak{I}_{cf}} \overset{i\kappa\to if}{M} + \varepsilon^f r^{if} - \omega^{i\overline{f}}\sum_{\kappa\in\mathfrak{I}_{cf}} \overset{\kappa\to f}{M}\right) \qquad \text{in } \Omega_t\times[t_0,t_e]\,,&\end{aligned} \tag{2.64}$$

where fluid density gradients have been neglected to bring ρ^f to the right hand side. This equation governing the mass balance of a generic species i in a fluid phase f is another building block of the different tumor growth models.

2.3.4.3 Solid Phase

As in the previous section, the balance of mass of the solid phase s can be obtained when applying the ALE equation (2.59), which for the solid phase is actually only the definition of the

material time derivative, to the generic mass balance (2.19) resulting in

$$\left.\frac{\partial(\varepsilon^s\rho^s)}{\partial t}\right|_{\boldsymbol{X}} + \varepsilon^s\rho^s\boldsymbol{\nabla}\cdot\boldsymbol{v}^s = \sum_{\kappa\in\mathfrak{I}_{cs}} \overset{\kappa\to s}{M} \qquad \text{in } \Omega_t\times[t_0,t_e]\,. \tag{2.65}$$

Note that unlike in the mass balance of a fluid phase (2.61) no convective term is present which is typical for the employed formulation with Lagrangean (skeleton) observer. The balance of mass of a species in the solid phase with mass fraction $\omega^{i\,\bar{s}}$ may be written as

$$\varepsilon^s\left.\frac{\partial\omega^{i\,\bar{s}}}{\partial t}\right|_{\boldsymbol{X}} + \boldsymbol{\nabla}\cdot\left(\varepsilon^s\boldsymbol{D}^{is}_{\text{eff}}\boldsymbol{\nabla}\omega^{i\,\bar{s}}\right) = \frac{1}{\rho^s}\left(\sum_{\kappa\in\mathfrak{I}_{cs}} \overset{i\kappa\to is}{M} + \varepsilon^s r^{is} - \omega^{i\,\bar{s}}\sum_{\kappa\in\mathfrak{I}_{cs}} \overset{\kappa\to s}{M}\right) \qquad \text{in } \Omega_t\times[t_0,t_e] \tag{2.66}$$

where again equation (2.61) has been applied to the generic species mass balance (2.27). Once more, the convective term cancels.

The balance of momentum of the solid phase was given in spatial form in (2.36). In material form, it emerges as

$$\boldsymbol{\nabla}_0\cdot\left(\boldsymbol{F}\cdot\boldsymbol{S}^{\text{tot}}\right) = \boldsymbol{0} \qquad \text{in } \Omega_0\times[t_0,t_e] \tag{2.67}$$

with divergence operator in reference configuration $\boldsymbol{\nabla}_0\cdot$, deformation gradient $\boldsymbol{F}$ and the second Piola-Kirchhoff stress tensor $\boldsymbol{S}^{\text{tot}}$ representing the pull-back of the spatial total stress tensor $\boldsymbol{\sigma}^{\text{tot}}$.

2.3.4.4 Energy Balance

Finally, also the energy or rather enthalpy balance equation (2.46) is brought in the employed ALE formulation by applying the fundamental ALE relation (2.59):

$$\begin{aligned}(c_p\rho)_{\text{eff}}\left.\frac{\partial T}{\partial t}\right|_{\boldsymbol{X}} + \sum_{f\in\mathfrak{I}_{\text{f}}} c_p^f\rho^f\varepsilon^f\left(\boldsymbol{v}^f-\boldsymbol{v}^s\right)\cdot\boldsymbol{\nabla}T - \boldsymbol{\nabla}\cdot\left(\boldsymbol{\kappa}_{\text{eff}}\boldsymbol{\nabla}T\right)&\\ - \sum_{\alpha\in\mathfrak{I}_p}\varepsilon^\alpha s^\alpha + \sum_{\alpha\in\mathfrak{I}_p}\left(c_p^\alpha T\sum_{\kappa\in\mathfrak{I}_{c\alpha}}\overset{\kappa\to\alpha}{M}\right) = 0.&\end{aligned} \tag{2.68}$$

Convective terms are only present for all fluid phases f and not the skeleton. These can again be replaced by the Darcy equation (2.33) resulting in

$$\begin{aligned}(c_p\rho)_{\text{eff}}\left.\frac{\partial T}{\partial t}\right|_{\boldsymbol{X}} - \sum_{f\in\mathfrak{I}_{\text{f}}} c_p^f\rho^f\frac{\boldsymbol{k}^f}{\mu^f}\cdot\boldsymbol{\nabla}T - \boldsymbol{\nabla}\cdot\left(\boldsymbol{\kappa}_{\text{eff}}\boldsymbol{\nabla}T\right)&\\ - \sum_{\alpha\in\mathfrak{I}_p}\varepsilon^\alpha s^\alpha + \sum_{\alpha\in\mathfrak{I}_p}\left(c_p^\alpha T\sum_{\kappa\in\mathfrak{I}_{c\alpha}}\overset{\kappa\to\alpha}{M}\right) = 0 \qquad \text{in } \Omega_t\times[t_0,t_e]\,.&\end{aligned} \tag{2.69}$$

This is the utilized energy balance equation in ALE form.

3 A Group of Continuum Models for (A-)vascular Tumor Growth

This chapter contains the derivation of the group of continuum models for (a-)vascular tumor growth based on the governing equations of multiphase porous media introduced in the previous chapter and topological model reduction of the vasculature to a 1D network of embedded blood vessels. A short overview of the different model types is given in Section 3.1. Then, the models of increasing sophistication are developed in Sections 3.2-3.5. Finally, a brief summary collecting the governing equations of all model types can be found in Section 3.6.

3.1 Overview

Figure 3.1 depicts an overview of the four model types developed in the following sections. The avascular model variant based on Schrefler and co-workers [224, 225, 229–233, 235] is introduced in Section 3.2. The remaining three model variants are of vascular type but differ in their incorporation of the vasculature into the tumor growth framework. First, a homogenized variant is introduced in Section 3.3. Therein, the blood vessels are homogenized and enter the model as an additional pore space in the ECM, in which blood flow and species transport takes place. Thus, it combines the original avascular variant with a homogenized representation of the vasculature. By contrast, in the second variant, the vascular network is resolved and embedded as a discrete, one-dimensional inclusion into the surrounding tissue. In this 1D representation, blood flow and species transport are accounted for by 1D PDEs. Transvascular species or fluid mass exchange is incorporated via a 1D-3D coupling of the distinct domains. Hence, this variant corresponds to a combination of the original avascular model with a discrete embedded representation of the vasculature. The third model variant merges the discrete embedded and the homogenized continuum representation of the vasculature into a hybrid approach for modeling the vascular network. Only the larger vessels are explicitly resolved and embedded as the previously mentioned 1D inclusion. The smaller vessels are again homogenized as a porous network. Blood flow and species transport in both domains is coupled via suitable constraints. The model with homogenized representation of the vasculature was introduced in the author's first article [135] while the discrete and hybrid variant were introduced in the author's second article [136].

3.2 The Avascular Tumor Growth Model

The avascular tumor growth model is the simplest model considered throughout this thesis. It is based on the avascular multiphase model of Sciumè et al. [230] with the extensions to three-phase flow [232] and a deformable ECM [233]. However, in these papers the equations were

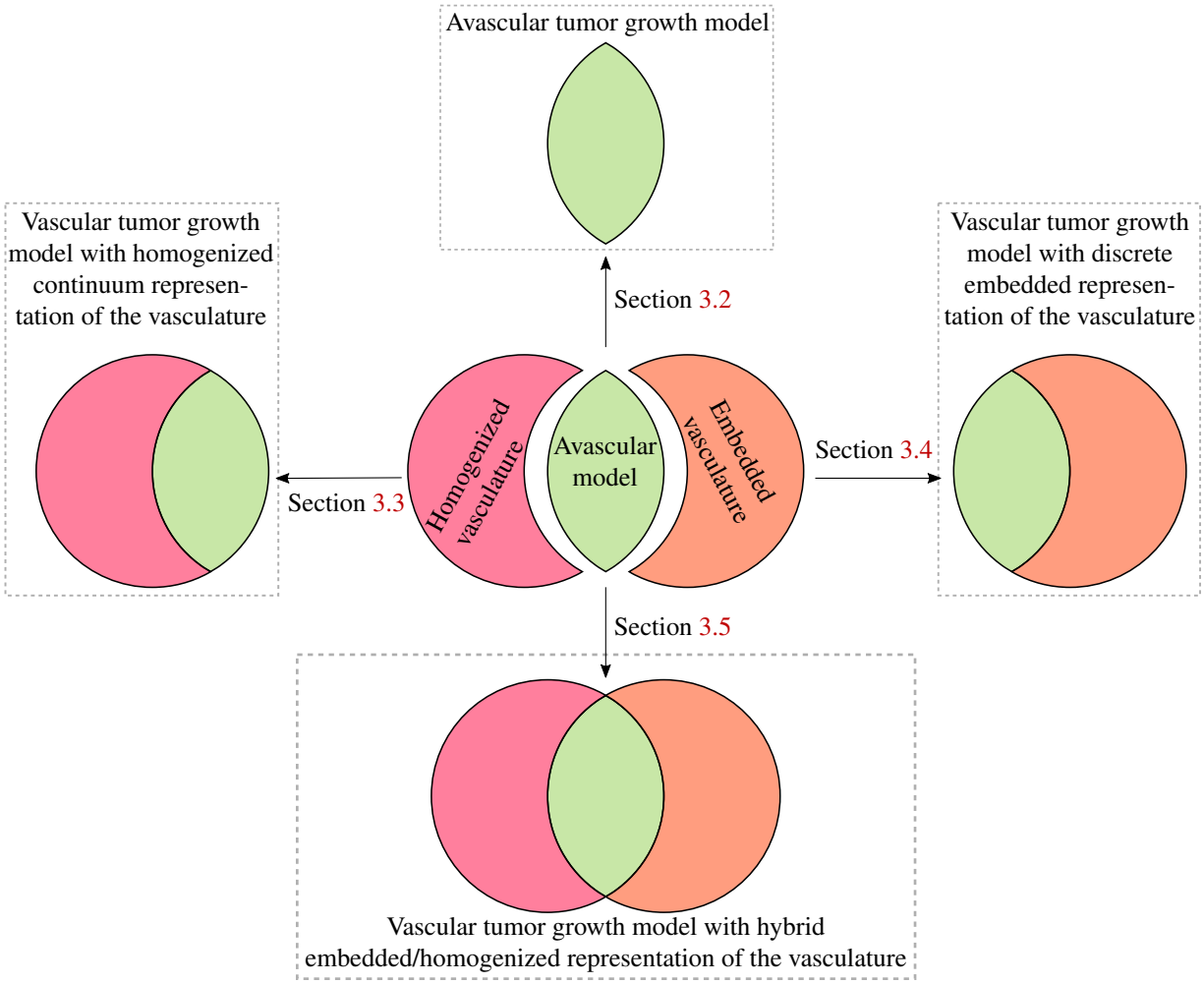

Figure 3.1: Schematic overview of the different model types with separate building blocks

not brought to the ALE formulation as in Kremheller et al. [135], which allows for a more consistent treatment of large solid deformations. The following derivations are based on the original avascular tumor growth model of Sciumè et al. [233] with the additional improvements in the author's publication [135] especially concerning the choice of arbitrary primary variables for the fluid phases.

Four phases as collected in the set of all phases

$$\mathfrak{I}_p = \{s, t, h, l\} \tag{3.1}$$

are considered in the avascular model. These are the ECM as the sole present solid phase, that is, the skeleton (indicated as s) and three distinct fluid phases filling the pores of the ECM, tumor cells (TCs), host cells (HCs) and the interstitial fluid (IF). These are denoted by t, h and l, respectively. They are assembled in the set

$$\mathfrak{I}_\varepsilon = \mathfrak{I}_\mathrm{f} = \{t, h, l\}, \tag{3.2}$$

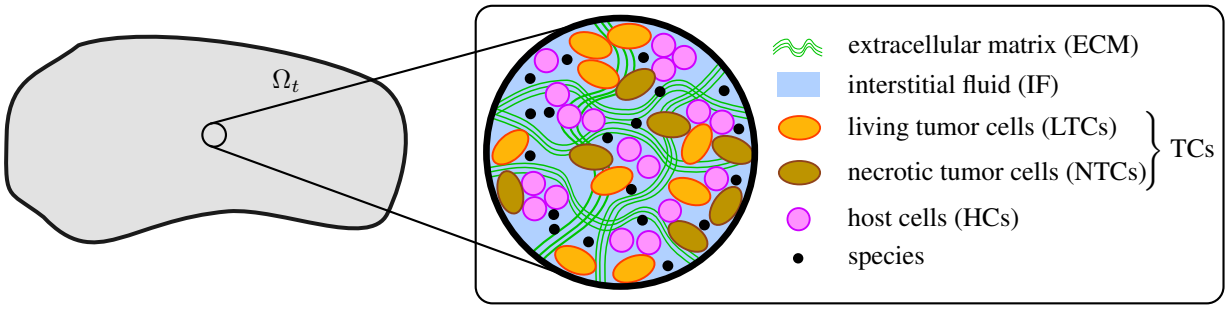

Figure 3.2: Sketch of avascular tumor growth model – solid phase (ECM), three fluid phases (TCs, HCs, IF), NTCs (species of TCs) and generic species

which for the avascular case is equal to the set of fluid phases $\mathfrak{I}_\mathrm{f}$. Summing up the volume fractions of the single fluid phases yields the *porosity* ε of the ECM as

$$\varepsilon = \varepsilon^l + \varepsilon^h + \varepsilon^t. \tag{3.3}$$

This allows us to get the volume fraction of the ECM from the constraint on volume fractions (2.18) as

$$\varepsilon^s = 1 - \varepsilon. \tag{3.4}$$

A typical composition of the tumor micro-environment as considered by the avascular model at the microscale is sketched in Figure 3.2. Note that in this and all other variants it is assumed that TCs partition into two dominant species, which are living tumor cells (LTCs) and necrotic tumor cells (NTCs). This implies that only one species mass balance equation has to be solved to obtain the composition of this phase. As in previous publications [224, 225, 229–233, 235], the balance of mass of NTCs with species mass fraction $\omega^{N\bar{t}}$ is chosen. The mass fraction of LTCs follows from the constraint on mass fractions (2.22) as $\omega^{L\bar{t}} = 1 - \omega^{N\bar{t}}$.

Having established these principal definitions, the governing equations for the fluid phases, the solid phase and species transport will be developed in Sections 3.2.1, 3.2.2 and 3.2.3, respectively. The building blocks for these equations are the balance of (phase and species) mass and momentum in ALE description as given in Section 2.3.4.

3.2.1 Governing Equations for the Fluid Phases

Saturations of TCs, HCs and IF are defined as

$$S^f = \frac{\varepsilon^f}{\varepsilon}, \quad \text{or} \quad \varepsilon^f = \varepsilon S^f, \quad f \in \mathfrak{I}_\varepsilon, \tag{3.5}$$

which have to follow the relation

$$\sum_{f \in \mathfrak{I}_\varepsilon} S^f = 1. \tag{3.6}$$

This constraint on the saturations can be obtained from the definition of the ECM porosity (3.3). Inserting their definition into the mass balance of a generic fluid phase (2.62) yields

$$\left.\frac{\partial\left(\varepsilon S^f \rho^f\right)}{\partial t}\right|_{\boldsymbol{X}} + \varepsilon S^f \rho^f \boldsymbol{\nabla} \cdot \boldsymbol{v}^s - \boldsymbol{\nabla} \cdot \left(\rho^f \frac{\boldsymbol{k}^f}{\mu^f} \boldsymbol{\nabla} p^f\right) = \sum_{\kappa \in \mathfrak{I}_{cf}} \overset{\kappa \to f}{M}. \tag{3.7}$$

Next, the product rule can be applied to the temporal derivative, which results in

$$\frac{\varepsilon S^f}{\rho^f}\left.\frac{\partial \rho^f}{\partial t}\right|_{\boldsymbol{X}} + S^f \left.\frac{\partial \varepsilon}{\partial t}\right|_{\boldsymbol{X}} + \varepsilon \left.\frac{\partial S^f}{\partial t}\right|_{\boldsymbol{X}} + \varepsilon S^f \boldsymbol{\nabla}\cdot\boldsymbol{v}^s - \boldsymbol{\nabla}\cdot\left(\frac{\boldsymbol{k}^f}{\mu^f}\boldsymbol{\nabla} p^f\right) = \frac{1}{\rho^f}\sum_{\kappa\in\mathfrak{I}_{cf}} \overset{\kappa\to f}{M}. \tag{3.8}$$

This equation has additionally been scaled with the inverse of the fluid phase density ρ^f. Density gradients have been neglected to pull the density also out of the last term on the left hand side, i.e., the Darcy equation. Subsequently, we want to substitute the temporal derivative of the ECM porosity. For that, we reformulate the balance of mass of the solid phase (2.65) by inserting the definition of the solid volume fraction (3.4). Again applying the product rule to the temporal derivative and dividing through the solid phase density ρ^s gives a relation for the temporal derivative of the ECM porosity

$$\left.\frac{\partial \varepsilon}{\partial t}\right|_{\boldsymbol{X}} = \frac{1-\varepsilon}{\rho^s}\left.\frac{\partial \rho^s}{\partial t}\right|_{\boldsymbol{X}} + (1-\varepsilon)\,\boldsymbol{\nabla}\cdot\boldsymbol{v}^s - \frac{\sum_{\kappa\in\mathfrak{I}_{cs}} \overset{\kappa\to s}{M}}{\rho^s} \tag{3.9}$$

which is inserted into (3.8) to obtain

$$\begin{aligned}\frac{\varepsilon S^f}{\rho^f}\left.\frac{\partial \rho^f}{\partial t}\right|_{\boldsymbol{X}} + \frac{S^f(1-\varepsilon)}{\rho^s}\left.\frac{\partial \rho^s}{\partial t}\right|_{\boldsymbol{X}} + \varepsilon \left.\frac{\partial S^f}{\partial t}\right|_{\boldsymbol{X}} + S^f \boldsymbol{\nabla}\cdot\boldsymbol{v}^s - \boldsymbol{\nabla}\cdot\left(\frac{\boldsymbol{k}^f}{\mu^f}\boldsymbol{\nabla} p^f\right) \\ = \frac{\sum_{\kappa\in\mathfrak{I}_{cf}} \overset{\kappa\to f}{M}}{\rho^f} + S^f\frac{\sum_{\kappa\in\mathfrak{I}_{cs}} \overset{\kappa\to s}{M}}{\rho^s}.\end{aligned} \tag{3.10}$$

Remark 3.1. *In all presented numerical examples of this thesis, the phases are assumed to be incompressible with*

$$\rho^\alpha = \rho_0^\alpha = \text{const}, \quad \alpha \in \mathfrak{I}_p. \tag{3.11}$$

For cells and IF, this is a reasonable assumption as they consist to a large extent of water. Concerning the ECM, it implies that the Biot coefficient tends to one, see also Remark 3.3. In principle, the computational framework is capable of including compressibility via simple equations of state in which the density depends solely on the pressure [233]. These are

$$\frac{1}{\rho^f}\frac{\partial \rho^f}{\partial p^f} = \frac{1}{K_f} \quad \textit{and} \quad \left.\frac{1}{\rho^f}\frac{\partial \rho^f}{\partial t}\right|_{\boldsymbol{X}} = \frac{1}{K_f}\left.\frac{\partial p^f}{\partial t}\right|_{\boldsymbol{X}} \tag{3.12}$$

for the fluid phases and equivalently for the solid

$$\frac{1}{\rho^s}\frac{\partial \rho^s}{\partial p^s} = \frac{1}{K_s} \quad \textit{and} \quad \left.\frac{1}{\rho^s}\frac{\partial \rho^s}{\partial t}\right|_{\boldsymbol{X}} = \frac{1}{K_s}\left.\frac{\partial p^s}{\partial t}\right|_{\boldsymbol{X}}, \tag{3.13}$$

where K_f is the bulk modulus of a generic fluid phase f and K_s the bulk modulus of the ECM. Using the previous equations, one could define a relationship between the density of a phase and its pressure as

$$\rho^\alpha = \rho_0^\alpha e^{\frac{p^\alpha - p_0^\alpha}{K_\alpha}}, \quad \alpha \in \mathfrak{I}_p \tag{3.14}$$

with reference density of the α phase ρ_0^α at reference pressure p_0^α which can be deduced by solving the ODEs (3.12) and (3.13). This has so far not yet been realized in the computational framework

to calculate the fluid and solid phase densities which appear in the right hand side of (3.10). In this section, the more general form of the governing equations with compressible phases will be employed. The incompressible case follows for $K_\alpha \to \infty$. For the sake of simplicity, the governing equations of the vascular model types in the subsequent sections will be written for the incompressible case.

Inserting the relations for the time derivatives of the densities gives

$$\frac{\varepsilon S^f}{K_f}\left.\frac{\partial p^f}{\partial t}\right|_{\boldsymbol{X}} + \frac{S^f(1-\varepsilon)}{K_s}\left.\frac{\partial p^s}{\partial t}\right|_{\boldsymbol{X}} + \varepsilon\left.\frac{\partial S^f}{\partial t}\right|_{\boldsymbol{X}} + S^f \boldsymbol{\nabla}\cdot\boldsymbol{v}^s - \boldsymbol{\nabla}\cdot\left(\frac{\boldsymbol{k}^f}{\mu^f}\boldsymbol{\nabla}p^f\right) = \frac{\sum_{\kappa\in\mathfrak{I}_{cf}}\overset{\kappa\to f}{M}}{\rho^f} + S^f\frac{\sum_{\kappa\in\mathfrak{I}_{cs}}\overset{\kappa\to s}{M}}{\rho^s}. \tag{3.15}$$

In the last two equations the previously mentioned solid pressure p^s has been employed. For now, it can be assumed that it is a macroscale measure of the normal force exerted on the solid surface by the surrounding fluids [194] and that it depends on the saturations and pressures of the fluid phases as $p^s\left(S^f, p^f\right),\ f \in \mathfrak{I}_\varepsilon$.

A crucial step for the tumor growth model is the choice of primary variables for TCs, HCs and the IF, i.e., for the three present fluid phases in the pores of the ECM. Going back to (3.15), it is clear that this equation is not closed since a relationship between fluid pressure and fluid saturation is not stated. Closure is achieved via pressure-saturation relationships based on the work of Schrefler and co-workers [232, 233, 235], see also Section 3.2.4. However, even if these relationships have been specified, there is still some flexibility in the choice of the primary variables. In principle, they can be either fluid phase saturations S^f, fluid phase pressures p^f or pressures differences between two fluid phases defined as $p^{\alpha\beta} = p^\alpha - p^\beta,\ \alpha,\beta \in \mathfrak{I}_\varepsilon$. In the earlier publications on the avascular model [230, 232, 233], the equations were written in terms of a pre-chosen set of primary variables ($\left[S^t, S^h, p^l\right]$ in [230, 232] and $\left[p^l, p^{hl}, p^{th}\right]$ in [233]). In Kremheller et al. [135], a more flexible approach was followed formulating the equations in terms of generic primary variables

$$\boldsymbol{\psi}^{[t,h,l]} = \begin{bmatrix}\psi^t\\ \psi^h\\ \psi^l\end{bmatrix}. \tag{3.16}$$

Remark 3.2. *The primary variables have to be independent of each other. For instance, a choice $\boldsymbol{\psi}^{[t,h,l]} = \left[S^t, S^h, S^l\right]^T$ is not possible since saturations are not independent due to the constraint (3.6). Also $\boldsymbol{\psi}^{[t,h,l]} = \left[p^t, p^h, p^{th}\right]^T$ is no valid choice because the third primary variable (pressure difference between tumor and host cell phase) is a linear combination of the first two. In all numerical examples presented in this thesis the primary variables are $\boldsymbol{\psi}^{[t,h,l]} = \left[p^{th}, p^{hl}, p^l\right]^T$. This is a convenient choice since the pressure-saturation relationships are also formulated in terms of the two differential pressures p^{th} and p^{hl}, see Section 3.2.4.*

Without going into the details of the employed pressure-saturation relationships it is only assumed that a correct choice of primary variables delivers functional dependencies of the fluid saturation

$$S^f\left(\psi^t, \psi^h, \psi^l\right),\ f \in \mathfrak{I}_\varepsilon \tag{3.17}$$

and fluid pressure

$$p^f\left(\psi^t, \psi^h, \psi^l\right), \ f \in \mathfrak{I}_\varepsilon \tag{3.18}$$

and, thus, also for the solid pressure $p^s\left(\psi^t, \psi^h, \psi^l\right)$ on the primary variables, see also Remark 3.5. These relations can be used to transform the time derivatives of saturations, fluid pressures and the solid pressure as well as the spatial fluid pressure gradient in time derivatives and spatial gradients of the generic primary variables by means of the chain rule

$$\frac{\partial\left((\bullet)\left(\psi^t, \psi^h, \psi^l\right)\right)}{\partial a} = \sum_{\beta\in\mathfrak{I}_\varepsilon} \frac{\partial\left(\bullet\right)}{\partial\psi^\beta}\frac{\partial\psi^\beta}{\partial a}. \tag{3.19}$$

By inserting it into the fluid mass balance (3.15) the balance of mass of a fluid phase $f \in \mathfrak{I}_\varepsilon$ in terms of the generic fluid phase primary variables emerges:

$$\begin{aligned}\frac{\varepsilon S^f}{K_f}\sum_{\beta\in\mathfrak{I}_\varepsilon}\frac{\partial p^f}{\partial\psi^\beta}\left.\frac{\partial\psi^\beta}{\partial t}\right|_{\boldsymbol{X}} + \frac{S^f(1-\varepsilon)}{K_s}\sum_{\beta\in\mathfrak{I}_\varepsilon}\frac{\partial p^s}{\partial\psi^\beta}\left.\frac{\partial\psi^\beta}{\partial t}\right|_{\boldsymbol{X}} + \varepsilon\sum_{\beta\in\mathfrak{I}_\varepsilon}\frac{\partial S^f}{\partial\psi^\beta}\left.\frac{\partial\psi^\beta}{\partial t}\right|_{\boldsymbol{X}} + S^f\boldsymbol{\nabla}\cdot\boldsymbol{v}^s \\ -\boldsymbol{\nabla}\cdot\left(\frac{\boldsymbol{k}^f}{\mu^f}\sum_{\beta\in\mathfrak{I}_\varepsilon}\frac{\partial p^f}{\partial\psi^\beta}\boldsymbol{\nabla}\psi^\beta\right) = \frac{\sum_{\kappa\in\mathfrak{I}_{cf}}\overset{\kappa\to f}{M}}{\rho^f} + S^f\frac{\sum_{\kappa\in\mathfrak{I}_{cs}}\overset{\kappa\to s}{M}}{\rho^s} \qquad \text{in } \ \Omega_t\times[t_0,t_e]\,.\end{aligned} \tag{3.20}$$

The previous equation is employed as the governing equation for the TC and HC phase in the considered time interval $[t_0, t_e]$. The equation for remaining fluid phase, i.e., the IF is treated in a slightly different way to cancel out several terms. Summing the mass balance equation (3.15) over all involved fluid phases $\gamma \in \mathfrak{I}_\varepsilon$ yields

$$\begin{aligned}\sum_{\gamma\in\mathfrak{I}_\varepsilon}\left(\frac{\varepsilon S^\gamma}{K_\gamma}\left.\frac{\partial p^\gamma}{\partial t}\right|_{\boldsymbol{X}}\right) + \sum_{\gamma\in\mathfrak{I}_\varepsilon}\left(\frac{S^\gamma(1-\varepsilon)}{K_s}\left.\frac{\partial p^s}{\partial t}\right|_{\boldsymbol{X}}\right) + \sum_{\gamma\in\mathfrak{I}_\varepsilon}\left(\varepsilon\left.\frac{\partial S^\gamma}{\partial t}\right|_{\boldsymbol{X}}\right) + \sum_{\gamma\in\mathfrak{I}_\varepsilon}S^\gamma\boldsymbol{\nabla}\cdot\boldsymbol{v}^s \\ -\sum_{\gamma\in\mathfrak{I}_\varepsilon}\left(\boldsymbol{\nabla}\cdot\left(\frac{\boldsymbol{k}^\gamma}{\mu^\gamma}\boldsymbol{\nabla}p^\gamma\right)\right) = \sum_{\gamma\in\mathfrak{I}_\varepsilon}\left(\frac{\sum_{\kappa\in\mathfrak{I}_{c\gamma}}\overset{\kappa\to\gamma}{M}}{\rho^\gamma}\right) + \sum_{\gamma\in\mathfrak{I}_\varepsilon}\left(S^\gamma\frac{\sum_{\kappa\in\mathfrak{I}_{cs}}\overset{\kappa\to s}{M}}{\rho^s}\right).\end{aligned} \tag{3.21}$$

Now, the constraint for the sum of saturations (3.6) can be invoked. Thus, the third term on the left hand side drops out completely. Additionally, the sum of the saturations occurs also in the second and fourth term on the left hand side and in the last term on the right hand side. The previous equation can hence be simplified to

$$\begin{aligned}\sum_{\gamma\in\mathfrak{I}_\varepsilon}\left(\frac{\varepsilon S^\gamma}{K_\gamma}\left.\frac{\partial p^\gamma}{\partial t}\right|_{\boldsymbol{X}}\right) + \frac{(1-\varepsilon)}{K_s}\left.\frac{\partial p^s}{\partial t}\right|_{\boldsymbol{X}} + \boldsymbol{\nabla}\cdot\boldsymbol{v}^s - \sum_{\gamma\in\mathfrak{I}_\varepsilon}\left(\boldsymbol{\nabla}\cdot\left(\frac{\boldsymbol{k}^\gamma}{\mu^\gamma}\boldsymbol{\nabla}p^\gamma\right)\right) \\ = \sum_{\gamma\in\mathfrak{I}_\varepsilon}\left(\frac{\sum_{\kappa\in\mathfrak{I}_{c\gamma}}\overset{\kappa\to\gamma}{M}}{\rho^\gamma}\right) + \frac{\sum_{\kappa\in\mathfrak{I}_{cs}}\overset{\kappa\to s}{M}}{\rho^s}.\end{aligned} \tag{3.22}$$

Note also that the sum of the mass transfer terms involving the fluid phases, i.e., the first term on the right hand side could possibly cancel if the densities of two involved fluid phases are equal

as each mass transfer term appears once positive and once negative due to the involved sum over all fluid phases. The summed-up equation is again formulated in terms of fluid pressures and saturations. Inserting the partial derivatives for the generic primary variables (3.19) for the temporal derivatives and the gradient results in

$$\sum_{\gamma\in\mathcal{I}_\varepsilon}\left(\frac{\varepsilon S^\gamma}{K_\gamma}\sum_{\beta\in\mathcal{I}_\varepsilon}\frac{\partial p^\gamma}{\partial\psi^\beta}\left.\frac{\partial\psi^\beta}{\partial t}\right|_{\boldsymbol{X}}\right)+\frac{(1-\varepsilon)}{K_s}\sum_{\beta\in\mathcal{I}_\varepsilon}\frac{\partial p^s}{\partial\psi^\beta}\left.\frac{\partial\psi^\beta}{\partial t}\right|_{\boldsymbol{X}}+\boldsymbol{\nabla}\cdot\boldsymbol{v}^s$$
$$-\sum_{\gamma\in\mathcal{I}_\varepsilon}\left(\boldsymbol{\nabla}\cdot\left(\frac{\boldsymbol{k}^\gamma}{\mu^\gamma}\sum_{\beta\in\mathcal{I}_\varepsilon}\frac{\partial p^\gamma}{\partial\psi^\beta}\boldsymbol{\nabla}\psi^\beta\right)\right)=\sum_{\gamma\in\mathcal{I}_\varepsilon}\left(\frac{\sum_{\kappa\in\mathcal{I}_{c\gamma}}\overset{\kappa\to\gamma}{M}}{\rho^\gamma}\right)+\frac{\sum_{\kappa\in\mathcal{I}_{cs}}\overset{\kappa\to s}{M}}{\rho^s}\quad\text{in}\quad\Omega_t\times[t_0,t_e]\,. \tag{3.23}$$

This is the final governing equation for the IF. Together with (3.20) evaluated with $f=t,h$, three equations govern the flow of the three present fluid phases in the pores of the ECM. Additionally required constitutive relations and mass transfer terms will be defined in Section 3.2.4 and Appendix B.

3.2.2 Governing Equations for the Solid Phase

The governing equations for the solid phase are its balance of mass (2.65) and momentum (2.67). However, in all model types, the former one enters the formulation in integral form to obtain its volume fraction respectively the porosity of the ECM, see equations (3.30)-(3.34).

The remaining equation is the balance of momentum in reference configuration (2.67). This is a quasi-static formulation since inertia terms have been neglected due to the large time scales of tumor growth. Subsequently, the solid phase stress tensor has been split into a solid pressure part and an effective stress part in equation (2.37) where the effective stress part is modeled as the derivative of a strain energy function as in classical solid mechanics problems. It remains to specify the solid pressure p^s and to combine it with the balance of momentum of the solid phase. There exist various definitions and interpretations of this quantity as described by Gray et al. [86, 96]. It can be understood as a macroscale measure of the pressure acting on the solid phase. For the avascular model, the definition of Lewis and Schrefler [146, 147] as the weighted sum of the present fluid phases

$$p^s=\sum_{f\in\mathcal{I}_\varepsilon}S^f p^f=S^t p^t+S^h p^h+S^l p^l \tag{3.24}$$

is employed. This definition is equivalent to the one of Bishop [26] if the solid surface fraction in contact with a fluid phase is assumed to be equal to the saturation of this fluid phase. Inserting it into the definition of the total stress tensor in spatial description (2.35) yields

$$\boldsymbol{\sigma}^{\text{tot}}=(1-\varepsilon)\left(-p^s\boldsymbol{I}\right)+\boldsymbol{\sigma}^{\text{eff}}+\sum_{f\in\mathcal{I}_\varepsilon}-\varepsilon S^f p^f\boldsymbol{I}=\boldsymbol{\sigma}^{\text{eff}}-p^s\boldsymbol{I} \tag{3.25}$$

when invoking the definition of the fluid phase stress tensors (2.31). The pull-back into the material configuration may then be obtained as

$$\boldsymbol{S}^{\text{tot}}=\boldsymbol{S}^{\text{eff}}-p^s J\boldsymbol{C}^{-1} \tag{3.26}$$

where the first term represents the effective stress tensor in material configuration and the second term the pull-back of the solid pressure contribution with the inverse of the right Cauchy-Green tensor $\boldsymbol{C}$. This final form of the total stress tensor in material configuration can now be inserted into the balance of momentum of the solid phase (2.67) yielding

$$\boldsymbol{\nabla}_0 \cdot \left(\boldsymbol{F} \cdot \left(\boldsymbol{S}^{\text{eff}} - p^s J \boldsymbol{C}^{-1} \right) \right) = \boldsymbol{0} \qquad \text{in } \Omega_0 \times [t_0, t_e] \,. \tag{3.27}$$

The balance of momentum may then be closed with the material laws for the solid phase introduced in Section 2.3.2.2.

Remark 3.3. *The definition of the solid pressure (3.24) is closely related to the traditional engineering approach in soil mechanics with a single fluid phase, that is, Terzaghi's principle of effective stress and its extension by Biot. If multiple fluid phases are present, there exist several derivations and definitions. In the papers analysing the solid pressure based on TCAT [86, 96] and the corresponding textbook [95, Section 9.7.1], a close evaluation is performed including interfacial effects and the compressibility of the solid matrix. Thus, the assumptions which have implicitly been made here are obtained explicitly. For the sake of completeness, it is stated here again that the assumptions for the form of the pressure in equation (3.24) are that interfacial effects can be neglected, the Bishop parameter (the solid surface fraction in contact with the respective fluid phase) of each phase is equal to its own saturation and the Biot coefficient is equal to one. The latter quantity relates the compressibility of the solid material with the compressibility of the solid structure including the pore space. If the compressibility of the solid matrix compared to the bulk structure with pores is negligible, which it is here as we assume an incompressible matrix, see also Remark 3.1, the Biot coefficient is equal to one.*

3.2.3 Governing Equations for Species Transport

The governing equation for a generic species i in a fluid phase f has been defined in equation (2.64) with primary variable $\omega^{i\overline{f}}$, that is, the mass fraction of species i in fluid phase f. Here, we only need to insert the definition of saturations (3.5) to obtain

$$\begin{aligned} \varepsilon S^f \left. \frac{\partial \omega^{i\overline{f}}}{\partial t} \right|_{\boldsymbol{x}} - \frac{\boldsymbol{k}^f}{\mu^f} \boldsymbol{\nabla} p^f \cdot \boldsymbol{\nabla} \omega^{i\overline{f}} + \boldsymbol{\nabla} \cdot \left(\varepsilon S^f \boldsymbol{D}^{if}_{\text{eff}} \boldsymbol{\nabla} \omega^{i\overline{f}} \right) \\ = \frac{1}{\rho^f} \left(\sum_{\kappa \in \mathfrak{I}_{cf}} {}^{i\kappa \to if}_{} M + \varepsilon^f r^{if} - \omega^{i\overline{f}} \sum_{\kappa \in \mathfrak{I}_{cf}} {}^{\kappa \to f}_{} M \right) \qquad \text{in } \Omega_t \times [t_0, t_e] \,. \end{aligned} \tag{3.28}$$

The previous equation is again written in terms of fluid saturations and fluid pressure gradients. Inserting the functional dependencies (3.17) and (3.18) yields an equation for the species mass balance in terms of its mass fraction $\omega^{i\overline{f}}$ and the generic fluid primary variables. The mass balance for a species in the solid phase is given by (2.66). However, no species transport in the solid phase is considered in the avascular model in this thesis.

3.2.4 Closure Relations and Constitutive Equations

Calculation of Porosity For calculating the porosity, the conservation of mass of the solid phase is considered under the assumption of a vanishing mass transfer term between the solid phase and all other phases, that is,

$$\overset{\kappa \to s}{M} = 0, \ \kappa \in \mathfrak{I}_p. \tag{3.29}$$

A material domain $\mathcal{U}_0 \subseteq \Omega_0$ is deformed via the solid phase deformation map (2.50) on a spatial domain $\mathcal{U}_t \subseteq \Omega_t = \varphi^s(\mathcal{U}_0, t)$. If no mass transfer from the solid phase to other phases occurs, the solid phase mass has to be conserved, that is, the initial mass of the material domain $m_0^s(\mathcal{U}_0)$ must correspond to the mass of the spatial domain $m^s(\mathcal{U}_t, t)$:

$$m_0^s(\mathcal{U}_0) = m^s(\mathcal{U}_t, t). \tag{3.30}$$

Inserting the definition of the solid phase mass as the integral of the volume fraction of the solid times its density in the respective domain yields

$$\int_{\mathcal{U}_0} \rho_0^s (1 - \varepsilon_0) \, \mathrm{d}V_0 = \int_{\mathcal{U}_t} \rho^s (1 - \varepsilon) \, \mathrm{d}V = \int_{\mathcal{U}_0} \rho^s (1 - \varepsilon) \, J \mathrm{d}V_0. \tag{3.31}$$

In the last step, the integral over the spatial domain $\mathcal{U}_t$ has been transformed in an integral over the material domain $\mathcal{U}_0$ by means of the determinant of the solid phase deformation gradient as specified in (2.6). Since the equality has to hold for volumes of arbitrary size, it can be pulled out of the integral yielding a point-wise relationship between current solid phase density ρ_s, porosity ε, Jacobian determinant J, reference solid phase density ρ_0^s and reference ECM porosity ε_0:

$$J \cdot \rho^s (1 - \varepsilon) = \rho_0^s (1 - \varepsilon_0). \tag{3.32}$$

Solving for the porosity results in

$$\varepsilon = 1 - \frac{1 - \varepsilon_0}{J} e^{-\frac{p^s - p_0^s}{K_s}} \tag{3.33}$$

where the relationship between reference and current density (3.14) has been employed. In case of an incompressible solid phase, the previous equation simplifies to

$$\varepsilon = 1 - \frac{1 - \varepsilon_0}{J}. \tag{3.34}$$

A dilation of the domain $(J > 1)$ leads to an increase of the ECM porosity while a compression $(J < 1)$ decreases the available pore space. In case of an undeformable ECM, the porosity does not change and remains fixed to the initial value of ε_0. Note that the balance of mass of the solid phase (2.65) can actually be derived from (3.31) by taking the total derivative of the mass in the current configuration [272, eqn. 3.6].

Remark 3.4. *As described in Section 1.1, the interaction of the ECM with growing tumors is an emerging physical trait of cancer. On the one hand, ECM can be deposited leading to a stiffer, more dense structural phase. On the other hand, ECM degradation and remodeling by*

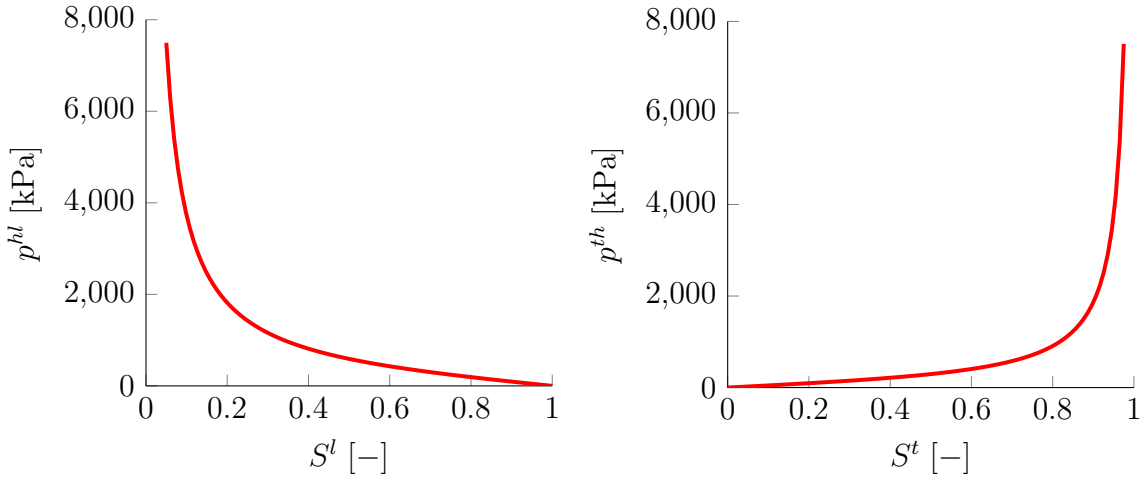

Figure 3.3: Pressure-saturation relationships (typical values for the coefficients have been inserted)

matrix metalloproteinases (MMPs) plays an important role during angiogenesis and metastasis [11, 220]. Both processes would enter the model as mass transfer terms in the ECM mass balance. For instance, ECM deposition was considered by Santagiuliana et al. [224] via a mass transfer term $\overset{l\to s}{M}$ *and the porosity was updated over time using explicit time integration. A more consistent approach using a varying reference porosity similar to a damage parameter was proposed in [271, 272].*

Pressure-Saturation Relationships The pressure-saturation relationships are an important ingredient of all considered tumor growth models since they provide the missing link between fluid pressures and fluid saturations to close the fluid mass balance equation (3.15). Since a full SEI for three-phase flow has not been achieved with the TCAT formalism, Sciumè et al. [232, 235] have proposed two pressure-saturation relationships for three phase flow, one where tumor and host cell populations have an equal pressure and one where a pressure difference between the two cell phases is present. Here, only the more general latter case will be considered.

These relationships have been derived starting from the Young-Laplace equation at the microscale which relates interfacial tension, pressure difference and interfacial curvature at phase interfaces. After up-scaling this equation to the macroscale, a macroscopic surrogate for the pressure difference between fluid phases is typically defined via a function of the fluid saturations in geo-mechanics. Note that these pressure differences do not indicate that the system is not in equilibrium but are only a statement that pressures in adjacent phases can be different [235]. For the tumor growth model the derivations can be found in [232, 235] and are not repeated here. The healthy system $(h-l)$ is defined as the reference and two pressure-saturation relationships similar to previous heuristic models [189, 190] are postulated as

$$p^{hl}\left(S^l\right) = p^h - p^l = a \cdot \tan\left[\frac{\pi}{2}\left(1-S^l\right)^b\right] \tag{3.35}$$

and

$$p^{th}\left(S^t\right) = p^t - p^h = a\frac{\sigma_{th}}{\sigma_{hl}} \cdot \tan\left[\frac{\pi}{2}\left(S^t\right)^b\right] \tag{3.36}$$

relating the HC-IF pressure difference p^{hl} with the IF saturation S^l and the TC-HC pressure difference p^{th} with the TC saturation S^t. Herein, a and b are model constants and $\sigma_{\alpha\beta}$ the interfacial tension between fluids α and β. Subsequently, b will be set to one. The TC-IF pressure difference follows as

$$p^{tl}\left(S^t, S^l\right) = p^t - p^l = p^{th}\left(S^t\right) - p^{hl}\left(S^l\right). \tag{3.37}$$

Thus, only two of the three pressure differences are independent (and consequently only two of the three can be chosen as primary variables). The functional dependencies are depicted in Figure 3.3. IF is present in the entire domain, otherwise p^{hl} would go to infinity. Vice versa, large values of the TC saturation lead to very high TC pressures. The functions have been designed such that they are invertible and the saturations can be obtained via the inverses $S^l\left(p^{hl}\right)$ and $S^t\left(p^{th}\right)$. The relation for HCs can be derived as

$$S^h\left(p^{th}, p^{hl}\right) = 1 - S^l\left(p^{hl}\right) - S^t\left(p^{th}\right) \tag{3.38}$$

from the constraint on saturations (3.6). This provides the closure relationships between saturations, fluid pressures and primary variables needed for the fluid mass balance (3.15).

Remark 3.5. *The common choice of primary variables* $\boldsymbol{\psi}^{[t,h,l]} = \left[\psi^t, \psi^h, \psi^l\right]^T = \left[p^{th}, p^{hl}, p^l\right]^T$ *is further investigated here to enhance the understanding of the model. For solving the fluid mass balances* (3.20) *and* (3.23)*, the dependency of fluid pressures and fluid saturations on the generic primary variables* $\boldsymbol{\psi}$ *including partial derivatives is required. The dependency of the fluid pressure on the primary variables* (3.18) *is given by*

$$\boldsymbol{p}^{[t,h,l]}\left(\boldsymbol{\psi}^{[t,h,l]}\right) = \begin{bmatrix} p^t \\ p^h \\ p^l \end{bmatrix} = \begin{bmatrix} 1 & 1 & 1 \\ 0 & 1 & 1 \\ 0 & 0 & 1 \end{bmatrix} \begin{bmatrix} \psi^t \\ \psi^h \\ \psi^l \end{bmatrix} \tag{3.39}$$

from which also partial derivatives of the fluid pressures w.r.t. the generic primary variables needed in (3.20) *and* (3.23) *can be calculated straightforwardly. The dependency of the fluid saturation* (3.17) *on the primary variables is given by*

$$\boldsymbol{S}^{[t,h,l]}\left(\boldsymbol{\psi}^{[t,h,l]}\right) = \begin{bmatrix} S^t \\ S^h \\ S^l \end{bmatrix} = \begin{bmatrix} S^t\left(\psi^t\right) \\ 1 - S^t\left(\psi^t\right) - S^l\left(\psi^h\right) \\ S^l\left(\psi^h\right) \end{bmatrix} \tag{3.40}$$

when employing the inverses of the pressure-saturation relationships (3.35) *and* (3.36) *together with* (3.38)*. From that, the derivatives of the saturations w.r.t. the generic primary variables can be computed and inserted into* (3.20) *and* (3.23)*. Also second derivatives of the saturations w.r.t. the primary variables which are required for linearizing the mass balances* (3.20) *and* (3.23) *can be acquired easily. An important aspect is the definition of Dirichlet boundary or initial conditions. It is convenient to specify those in terms of saturations of the phases. The chosen primary variables* p^{hl}*,* p^{th} *and* p^l *offer the flexibility to specify the two saturations* S^t *and* S^l *(the third one follows from the constraint on saturations in* (3.40)*). The values for the primary variables for the*

desired saturations can then be obtained from (3.35) *and* (3.36)*. Furthermore, the IF pressure* p^l *can be specified as a boundary or initial condition. However, other choices are possible (which satisfy the independence of primary variables as described in Remark 3.2): If a saturation is chosen as primary variable, its dependency on the primary variable is straightforward. For the dependency of pressure on the saturation, the pressure-saturation relationships* (3.35) *and* (3.36) *have to be invoked.*

Permeability Tensor and Viscosity Following Sciumè et al. [230, 232] the permeability tensor of each fluid phase $f \in \mathfrak{I}_\varepsilon$ occurring in the Darcy equation (2.33) is modeled as isotropic with the relationship

$$\boldsymbol{k}^f = k^f_{\text{rel}} \cdot \boldsymbol{k} = k^f_{\text{rel}} \cdot k \cdot \boldsymbol{I}, \tag{3.41}$$

where $\boldsymbol{k}$ is the intrinsic permeability tensor of the ECM with scalar intrinsic ECM permeability k. The relative permeability of each fluid phase $f \in \mathfrak{I}_\varepsilon$ is defined depending on its saturation as

$$k^f_{\text{rel}} = \left(S^f\right)^{A_f} \tag{3.42}$$

where A_f is a model coefficient with $A_f > 1$. This ensures that the relative permeability of each phase and also the sum of the relative permeabilities of all phases is smaller than one. If only one phase is present, $S^f = 1$ and the permeability of the phase is equal to the intrinsic permeability. However, the presence of different fluid phases interferes with the flow due to viscous forces at the interfaces between phases (at the microscale) which makes the domain less permeable for the considered phase. Thus, this relationship also accounts for the interactions between other fluid phases, that is, the macroscale interaction forces $\overset{\kappa\to\alpha}{\mathbf{T}}_0$ between different fluid phases which were neglected in the derivation of the Darcy equation (2.33) as stated in Remark 2.3. According to Sciumè et al. [232] this relationship gives realistic agreement with classical porous medium models [260]. However, such an ad-hoc closure formulation at the macroscale is not consistent with TCAT. Therefore, this constitutive relationship should be replaced by a more theoretically sound TCAT formulation considering also interfaces [170].

The viscosities μ^f of the fluid phases are assumed constant but different for each phase throughout this thesis. In [232] an additional constitutive relationship for the viscosities of the cell phases has been proposed relating it to the pressure gradient in the fluid to model cell adherence. If a certain pressure gradient is exceeded, the cells start to move which is similar to the stick-slip behaviour in contact mechanics. This formulation has been implemented in the employed computational framework [8] by the author but is not considered in the numerical examples.

Diffusivity Tensor The diffusivity tensor in the species mass balance equation (2.64) and (2.66) is also isotropic with

$$\boldsymbol{D}^{i\alpha}_{\text{eff}} = D^{i\alpha}_{\text{eff}} \cdot \boldsymbol{I} = D^{i\alpha}_0 \cdot \left(\varepsilon^\alpha\right)^\delta \cdot \boldsymbol{I}. \tag{3.43}$$

This relationship was used in the previous publications on the avascular model [224, 225, 229–233, 235]. The rationale behind this definition is to model a nonlinear dependency of the macroscopic effective diffusivity on the volume fraction ε^α of the α phase in which the species i

diffuses. The parameter δ may then be interpreted as a measure of the tortuosity of the porous network. The higher its value, the more tortuous the network resulting in a hindered diffusion of the species under consideration and, therefore, a smaller effective diffusion coefficient. If δ is set to zero, the influence of the tortuosity may be neglected and the effective diffusivity is equal to the free diffusivity of the species $D_0^{i\alpha}$ in the phase α.

Remark 3.6. *Structural anisotropy of the ECM has been integrated into the model in the term paper by Bui [32] under the author's supervision. Therein, the permeability tensor and the diffusivity tensor was modeled as transversely isotropic, i.e., as rotationally symmetric to the main ECM fiber direction with higher permeabilites along the fibers. The anisotropy of the permeability tensor led to increased growth along the ECM fibers in comparison with the orthogonal direction. Thus, it was possible to reproduce experimental results of [208, 209, 215] which showed that the alignment of collagen fibers facilitates invasion by which cells migrate along these fibers into healthy tissue. Considering the diffusivity tensor, an anisotropic definition only makes sense for species whose particle radius is comparable to the fiber radius since only then diffusion is influenced by the arrangement of the fibers [248].*

3.2.5 Summary and Variants of the Model

In summary, the governing equations of the avascular tumor growth model are the mass balances of TCs ((3.20) with $f = t$) and HCs ((3.20) with $f = h$), the sum of the mass balances of TCs, HCs and IF (3.23), the balance of momentum of the solid phase (3.27) and the balance of species mass for all involved species (3.28).

The introduction of the avascular model will be concluded by illustrating two different possible variants of the avascular model. The first one corresponds to the case where no HCs and ECM are present, that is, only two fluid phases which are TCs and the IF. This case corresponds to an *in-vitro* situation of TCs growing avascularly in a quiescent, cell culture medium resulting in a so-called multicellular tumor spheroid (MTS). The growth of MTSs has been studied by Sciumè et al. [230, 233] to validate the avascular model. A second variant emerges under the assumption of an undeformable ECM. In that case, the balance of momentum of the solid phase (3.27) does not have to be solved. Consequently, solid phase displacements and velocities are equal to zero. This considerably simplifies the entire model: First, the porosity of the ECM remains constant (equation (3.34) with $J = 1$). Second, the divergence of the solid phase velocity from the governing equations (3.20) and (3.23) is equal to zero. Third, it is not necessary to apply the ALE formulation which is a significant reduction in complexity. A Eulerian description with fixed mesh emerges for fluid flow and species transport. As will be shown later, the coupling between fluid phases and deformable solid phase constitutes a significant cost factor of the entire computational algorithm. Yet another slightly different variant is possible under the assumption of small deformations. Then, a linear solid mechanics problem may be formulated whose deformations and velocities do not necessitate an ALE description. Hence, this would result in a one-way coupled problem where only fluid flow influences the solid phase and not vice versa. However, this variant is not considered hereafter.

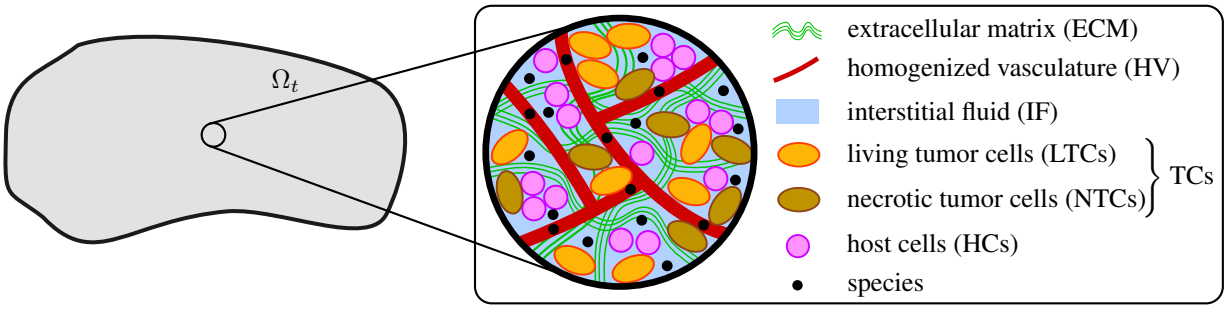

Figure 3.4: Sketch of vascular tumor growth model with homogenized representation of vasculature – solid phase (ECM), additional porous network (HV), three fluid phases (TCs, HCs, IF) in the pores of the ECM, NTCs (species of TCs) and generic species (both in HV and other phases)

3.3 The Vascular Tumor Growth Model with a Homogenized Continuum Representation of the Vasculature

The model introduced in the previous section allows to study avascular tumor growth and, hence, excludes a crucial phase in the progression of tumors, namely the vascular stage. The vasculature is of preeminent importance for cancer progression: As described in Chapter 1, without their own vascular network, tumors are usually confined to a certain size beyond which they cannot grow any further and will become necrotic [36, 76, 181]. This can be attributed to insufficient supply with oxygen or other nutrients which cannot diffuse from the tumor boundary into its center. However, if tumors have access to nutrients via their own vascular network induced by angiogenesis, tumor growth can proceed much more rapidly. In summary, modeling the vascular stage including angiogenesis is crucial since together with metastatic tumor growth it is the clinically relevant stage in tumor progression, which actually causes the patient to die [221]. The abnormality of tumor vasculature, which ultimately leads to increased IF pressure due to the interplay of leaky vessels and impaired lymphatic drainage is a further physical phenomenon which influences therapeutic resistance. It can be studied with the vascular variant which may be classified as a dynamic vascular tumor growth model in the sense that tumor growth is dynamically two-way coupled with the vascular network [157]. On the one hand, tumor growth can influence the vasculature via angiogenesis and blood vessel remodeling. On the other hand, the vasculature and the nutrients therein modulate tumor growth.

In the vascular tumor growth model with continuum representation of the vasculature, the vasculature is represented as an additional porous network in the ECM in which blood flows. This enhancement of the avascular tumor growth model was proposed in the author's publication [135] where blood pressure was set constant and, thus, blood flow was neglected as well as species transport in the vasculature. Subsequently, in Kremheller et al. [136] blood flow and species transport in the homogenized vasculature was introduced. Effectively, this formulation is a double-porosity model with two separate porous networks, the first one is the pore space between the ECM fibers (as in the avascular model) and the second one the vasculature as sketched

in Figure 3.4. Thus, the set of all phases may be defined as

$$\mathfrak{I}_p = \{s, t, h, l, v\} \tag{3.44}$$

comprising the ECM (solid phase), TCs, HCs, the IF and an additional fluid phase denoted by v which is either referred to as the vasculature or blood. Now, four fluid phases are present, which are collected in the set of fluid phases

$$\mathfrak{I}_\mathrm{f} = \{t, h, l, v\}. \tag{3.45}$$

The original three fluid phases of the avascular model are again assembled in the set

$$\mathfrak{I}_\varepsilon = \{t, h, l\} \tag{3.46}$$

indicating that they occupy the pores of the ECM with porosity ε. The derivation of the model equations in the subsequent sections closely follows the author's publications [135, 136]. Some minor improvements are included, namely a simple model for blood vessel remodeling as introduced by Wirthl et al. [282] (co-first authored) and haptotaxis which was included in the Master's thesis of Wirthl [281] under close guidance by the author.

3.3.1 Governing Equations for the Fluid Phases

In this section the governing equations of all present fluid phases of the vascular tumor growth model are detailed. This includes, first, blood flow in the homogenized vasculature and an evolution equation for the vasculature volume fraction in Section 3.3.1.1 and, second, the flow of the original three fluid phases of the avascular model in the pores of the ECM in Section 3.3.1.2. Due to the presence of the additional porous network, these equations have to be slightly adapted [135, 136].

3.3.1.1 Homogenized Vasculature

Blood flow in the homogenized vasculature is governed by the mass balance equation for a generic fluid phase (2.62), which can be detailed for the vasculature as

$$\left.\frac{\partial \varepsilon^v}{\partial t}\right|_{\boldsymbol{X}} + \varepsilon^v \boldsymbol{\nabla} \cdot \boldsymbol{v}^s - \boldsymbol{\nabla} \cdot \left(\frac{\boldsymbol{k}^v}{\mu^v} \boldsymbol{\nabla} p^v \right) = \frac{\sum_{\kappa \in \mathfrak{I}_{cv}} \overset{\kappa \to v}{M}}{\rho^v} \qquad \text{in } \Omega_t \times [t_0, t_e] \tag{3.47}$$

when assuming constant blood density ρ^v. Blood pressure p^v is one primary variable of the homogenized vascular network. The right hand side term represents a possible mass exchange with other phases. Typically, this is an outflow of fluid from the vasculature into the IF due to the increased leakiness of tumor blood vessels.

So far, the volume fraction of the homogenized vasculature ε^v has not yet been specified. It represents another independent primary variable of the porous medium system which will be modeled with an additional evolution equation. It is important to emphasize in this regard that endothelial cells (ECs) are not directly modeled as a phase or species of the system but rather the vasculature as a whole as represented by its volume fraction at a specific macroscale point. This

results in the aforementioned double-porosity formulation. The influence of angiogenesis including EC migration on the vascular volume fraction is then incorporated by additional flux terms. Furthermore, in some of the numerical examples of Chapter 5, the homogenized vasculature may specifically be interpreted as the neo-vasculature formed by angiogenesis and originating from pre-existing vessels while in others it is a homogenized representation of the (pre-existing and neo-) vasculature as an additional porous network.

Remark 3.7. *The balance of mass of blood* (3.47) *has been derived from the balance of mass of a generic fluid phase by assuming the Darcy equation* (2.33) *for blood flow in the homogenized vasculature. Thus,* $\boldsymbol{v}^v$ *is the blood velocity within the vasculature. In Kremheller et al. [135], the notation was different since blood flow was not considered but only constant pressure. Therein, the HV velocity was also denoted by* $\boldsymbol{v}^v$*. This might be confusing to the reader which is why the derivation and also notation of the evolution equation is adapted compared to [135]. Instead of defining a velocity, this term is now denoted as generic flux term* $\boldsymbol{j}^v$*.*

The following evolution equation is postulated for the vasculature volume fraction:

$$\left.\frac{\partial \varepsilon^v}{\partial t}\right|_{\boldsymbol{x}} + \boldsymbol{\nabla} \cdot \boldsymbol{j}^v = -C_{\text{coll}}. \tag{3.48}$$

Therein, $\boldsymbol{j}^v$ denotes a flux term which is employed to model angiogenesis and C_{coll} a simple model for blood vessel collapse. The latter term was introduced by Wirthl et al. [282, S1 Appendix] and denoted as M_{coll} there. Here it is rather written as C to prevent confusion with a mass transfer term. It accounts for regression, compression and collapse of blood vessels induced by growing tumors. Its exact expression along with further details will follow in Section 3.3.4. Applying the fundamental ALE equation (2.59) results in

$$\left.\frac{\partial \varepsilon^v}{\partial t}\right|_{\boldsymbol{X}} + \varepsilon^v \boldsymbol{\nabla} \cdot \boldsymbol{v}^s + \boldsymbol{\nabla} \cdot (\boldsymbol{j}^v - \varepsilon^v \cdot \boldsymbol{v}^s) = -C_{\text{coll}}. \tag{3.49}$$

The flux term is approximated as

$$\boldsymbol{j}^v - \varepsilon^v \boldsymbol{v}^s \approx \underbrace{-D^v \boldsymbol{\nabla} \varepsilon^v}_{\substack{\text{random} \\ \text{motility}}} + \underbrace{\varepsilon^v \varepsilon^l S^l \chi\left(\omega^{TAF\bar{l}}\right) \boldsymbol{\nabla} \omega^{TAF\bar{l}}}_{\text{chemotaxis}} + \underbrace{\varepsilon^v \varepsilon^s \Theta \boldsymbol{\nabla} \omega^{F\bar{s}}}_{\text{haptotaxis}} \tag{3.50}$$

which results in a standard formulation governing angiogenesis similarly also applied in [6, 225].

Herein, the first term on the right hand side represents *random motion* of ECs at sprout tips modeled as a diffusion process with diffusivity D^v acting on the vascular volume fraction gradient.

The second term accounts for *chemotaxis*. In general, this refers to the response of cells to a gradient of a soluble substance often manifesting itself in directional migration towards this chemical gradient [141]. Here, it reflects the response of ECs on TAFs produced by hypoxic TCs. The varying chemotactic coefficient $\chi\left(\omega^{TAF\bar{l}}\right)$ as in [6] depends on the TAF level. Its exact form is detailed in Section 3.3.4. Dozens of factors such as the aforementioned VEGFs are involved in triggering EC migration [141] and maturation and stabilization of the emerging new vascular network [181]. This complex interplay of different bio-chemical signals is represented

as an ancillary TAF species within the IF which represents the excess of pro-angiogenic regulators compared to inhibitory factors [6, 83]. The chemical gradient of the TAF species in the IF $\boldsymbol{\nabla}\omega^{TAF\,\bar{l}}$ triggers EC migration towards the tumor following the TAF gradient as described by the second term in equation (3.50).

The last term is the influence of *haptotaxis*. This describes the directional migration towards a gradient of a bound substance, typically an immobilized ECM component [141] which regulates the adhesion of migrating cells to the ECM. A common example is fibronectin (FN), which mediates cellular interactions such as migration and adhesion with the ECM [188]. According to experimental studies [243, 244], haptotactic endothelial cell migration is guided and regulated by the FN gradient in the ECM $\boldsymbol{\nabla}\omega^{F\,\bar{s}}$. Thus, haptotaxis is included with a similar additional haptotactic flux in response to FN gradients [6] with constant haptotactic coefficient Θ. FN itself is modeled as an additional chemical species bound to the ECM which does not diffuse. Like the TAF species, it can be understood as a surrogate of several chemical substances bound to the ECM and mediating EC migration [141].

The final evolution equation of the homogenized vascular volume fraction emerges as

$$\left.\frac{\partial \varepsilon^v}{\partial t}\right|_{\boldsymbol{X}} + \varepsilon^v \boldsymbol{\nabla}\cdot\boldsymbol{v}^s - \boldsymbol{\nabla}\cdot\left(D^v\boldsymbol{\nabla}\varepsilon^v\right) + \boldsymbol{\nabla}\cdot\left(\varepsilon^v\varepsilon S^l \chi\left(\omega^{TAF\,\bar{l}}\right)\boldsymbol{\nabla}\omega^{TAF\,\bar{l}}\right) + \boldsymbol{\nabla}\cdot\left(\varepsilon^v\varepsilon^s\Theta\boldsymbol{\nabla}\omega^{F\,\bar{s}}\right) = -C_{\text{coll}} \quad \text{in } \Omega_t\times[t_0,t_e]\,. \tag{3.51}$$

In conclusion, the porous medium model for the vasculature comprises the two equations (3.47) and (3.51): the first one governs blood flow in the vasculature and the second one governs the evolution of the vascular volume fraction depending on angiogenic stimuli and blood vessel collapse due to excessive tumor growth.

3.3.1.2 Tumor Cells, Host Cells and Interstitial Fluid

Incorporating a fifth phase into the model as described above requires several modifications of the equations of the avascular model. The volume fraction of the ECM is now given as

$$\varepsilon^s = 1 - \varepsilon - \varepsilon^v \tag{3.52}$$

from the sum of all present volume fractions (2.18) and the definition of the porosity of the ECM as the sum of the volume fractions of TCs, HCs and the IF (3.3). Inserting the solid phase volume fraction (3.52) into the solid phase balance of mass (2.65) yields

$$\left.\frac{\partial \varepsilon}{\partial t}\right|_{\boldsymbol{X}} = \frac{1-\varepsilon-\varepsilon^v}{\rho^s}\left.\frac{\partial \rho^s}{\partial t}\right|_{\boldsymbol{X}} + \left(1-\varepsilon-\varepsilon^v\right)\boldsymbol{\nabla}\cdot\boldsymbol{v}^s - \left.\frac{\partial \varepsilon^v}{\partial t}\right|_{\boldsymbol{X}} \tag{3.53}$$

where the mass transfer term between the solid phase and other phases has been set to zero in accordance with (3.29) and Remark 3.4. Furthermore, the product rule has been applied to the temporal derivative as in (3.9) to obtain the temporal derivative of the porosity of the ECM. Compared to this expression for the avascular case, ancillary terms depending on the volume fraction ε^v may be identified which account for the presence of the additional porous network. These are the additional time derivative of the vasculature volume fraction and the time derivative of the solid phase density and the divergence of the solid phase velocity scaled with the negative

vascular volume fraction $-\varepsilon^v$. The time derivative of the ECM porosity may then be inserted into the mass balance of TCs, HCs and IF which are given by equation (3.8). This results in an intermediate mass balance equation

$$\frac{\varepsilon S^f}{\rho^f}\left.\frac{\partial \rho^f}{\partial t}\right|_{\boldsymbol{X}} + \frac{S^f(1-\varepsilon-\varepsilon^v)}{\rho^s}\left.\frac{\partial \rho^s}{\partial t}\right|_{\boldsymbol{X}} + \varepsilon\left.\frac{\partial S^f}{\partial t}\right|_{\boldsymbol{X}} - S^f\left.\frac{\partial \varepsilon^v}{\partial t}\right|_{\boldsymbol{X}} + S^f\left(1-\varepsilon^v\right)\boldsymbol{\nabla}\cdot\boldsymbol{v}^s - \boldsymbol{\nabla}\cdot\left(\frac{\boldsymbol{k}^f}{\mu^f}\boldsymbol{\nabla}p^f\right) = \frac{\sum_{\kappa\in\mathfrak{I}_{cf}}\overset{\kappa\to f}{M}}{\rho^f} \tag{3.54}$$

which under the assumption of incompressible solid and fluid phases can be simplified to

$$\varepsilon\sum_{\beta\in\mathfrak{I}_\varepsilon}\frac{\partial S^f}{\partial\psi^\beta}\left.\frac{\partial\psi^\beta}{\partial t}\right|_{\boldsymbol{X}} - S^f\left.\frac{\partial\varepsilon^v}{\partial t}\right|_{\boldsymbol{X}} + S^f(1-\varepsilon^v)\boldsymbol{\nabla}\cdot\boldsymbol{v}^s - \boldsymbol{\nabla}\cdot\left(\frac{\boldsymbol{k}^f}{\mu^f}\sum_{\beta\in\mathfrak{I}_\varepsilon}\frac{\partial p^f}{\partial\psi^\beta}\boldsymbol{\nabla}\psi^\beta\right) = \frac{\sum_{\kappa\in\mathfrak{I}_{cf}}\overset{\kappa\to f}{M}}{\rho^f} \quad \text{in } \Omega_t\times[t_0,t_e]\,. \tag{3.55}$$

This is the governing equation for the balance of mass of TCs, HCs and IF, i.e., for $f\in\mathfrak{I}_\varepsilon$, in the vascular tumor growth model with homogenized vasculature. The generic primary variables $\boldsymbol{\psi}^{[t,h,l]}$ of these phases as defined in Section 3.2 have been inserted. Compared to the avascular model (3.20), two additional terms are present: The time derivative of the volume fraction of the vasculature scaled with the saturation and the additional divergence of the grid velocity scaled with the negative volume fraction of the vasculature $-\varepsilon^v$. These terms have been introduced since the modified balance of mass of the solid phase (3.53) incorporates the temporally varying vascular volume fraction. Obviously, if no vasculature is present ($\varepsilon^v=0$) the original avascular model (equation (3.20) with incompressible solid and fluid phases) is recovered. The third governing equation, the mass balance of the IF, may again be obtained by summing the balance of mass (3.55) over the TC, HC and IF phase as

$$-\left.\frac{\partial\varepsilon^v}{\partial t}\right|_{\boldsymbol{X}} + (1-\varepsilon^v)\boldsymbol{\nabla}\cdot\boldsymbol{v}^s - \sum_{\gamma\in\mathfrak{I}_\varepsilon}\left(\boldsymbol{\nabla}\cdot\left(\frac{\boldsymbol{k}^\gamma}{\mu^\gamma}\sum_{\beta\in\mathfrak{I}_\varepsilon}\frac{\partial p^\gamma}{\partial\psi^\beta}\boldsymbol{\nabla}\psi^\beta\right)\right) = \sum_{\gamma\in\mathfrak{I}_\varepsilon}\left(\frac{\sum_{\kappa\in\mathfrak{I}_{c\gamma}}\overset{\kappa\to\gamma}{M}}{\rho^\gamma}\right) \quad \text{in } \Omega_t\times[t_0,t_e]\,. \tag{3.56}$$

Comparing it to its avascular counterpart (equation (3.23) with incompressible solid and fluid phases) the additional terms are again the time derivative of the vascular volume fraction and the additional divergence of the grid velocity scaled with the negative volume fraction of the vasculature $-\varepsilon^v$.

In summary, the fluid part of the porous medium model now accounts for two independent porous networks. The first one are the pores of the ECM which are filled by three interacting fluid phases, namely, TCs, HCs and the IF. The second one is the vasculature, which is here considered in a homogenized way in which one additional fluid phase, blood, flows. This results in two additional primary variables, the blood pressure p^v and the blood vessel volume fraction ε^v on top of the three generic primary variables of the avascular system $\boldsymbol{\psi}^{[t,h,l]}$. Moreover, several variants of the model are possible, either with static vasculature or without blood flow depending on the phenomena which are included into the model, see Section 3.3.5

3.3.2 Governing Equations for the Solid Phase

The presence of an additional fluid phase, namely, blood flowing in the homogenized vasculature necessitates also a re-definition of the solid pressure accounting for the interaction of all fluid phases with the solid skeleton. A suitable definition is

$$p^s = \frac{\varepsilon}{\varepsilon + \varepsilon^v} \sum_{f \in \mathfrak{I}_\varepsilon} S^f p^f + \frac{\varepsilon^v}{\varepsilon + \varepsilon^v} p^v = \frac{\varepsilon}{\varepsilon + \varepsilon^v} \left(S^t p^t + S^h p^h + S^l p^l \right) + \frac{\varepsilon^v}{\varepsilon + \varepsilon^v} p^v, \tag{3.57}$$

which may be inserted into the definition of the total stress tensor (2.35) resulting in

$$\boldsymbol{\sigma}^{\mathrm{tot}} = \underbrace{(1 - \varepsilon - \varepsilon^v)}_{=\varepsilon^s} (-p^s \boldsymbol{I}) + \boldsymbol{\sigma}^{\mathrm{eff}} + \sum_{f \in \mathfrak{I}_\varepsilon} -\varepsilon S^f p^f \boldsymbol{I} - \varepsilon^v p^v \boldsymbol{I} = \boldsymbol{\sigma}^{\mathrm{eff}} - p^s \boldsymbol{I} \tag{3.58}$$

together with the definition (2.31) of the stress tensors of the present fluid phases and the split into effective stress and solid pressure part (2.37). In equation (3.57), the original definition of the solid pressure in the avascular model (3.24) as the weighted sum of saturations and pressures is scaled with the ratio of the ECM porosity ε to the total volume fraction of both porous networks $\varepsilon + \varepsilon^v$. The same applies for the homogenized blood pressure, which is scaled with the ratio of the blood vessel volume fraction ε^v to the total volume fraction of both porous networks $\varepsilon + \varepsilon^v$. Thus, a classical model of the total stress tensor as effective stress in the solid matrix $\boldsymbol{\sigma}^{\mathrm{eff}}$ plus the combined effect of all fluid phases on the solid matrix collected in the solid pressure is derived. Furthermore, this definition recovers the solid pressure in the case where no vasculature is present ($\varepsilon^v = 0$) as well as the classical Terzaghi effective stress tensor for $\varepsilon = 0$, that is, if only the vascular network with one single fluid phase, namely blood, is present. The pull-back of the total stress tensor may again be written as

$$\boldsymbol{S}^{\mathrm{tot}} = \boldsymbol{S}^{\mathrm{eff}} - p^s J \boldsymbol{C}^{-1} \tag{3.59}$$

and inserted into the balance of linear momentum of the solid phase (2.67) which yields

$$\boldsymbol{\nabla}_0 \cdot \left(\boldsymbol{F} \cdot \left(\boldsymbol{S}^{\mathrm{eff}} - p^s J \boldsymbol{C}^{-1} \right) \right) = \boldsymbol{0} \qquad \text{in } \Omega_0 \times [t_0, t_e] \,. \tag{3.60}$$

Evidently, the balance of momentum is equivalent to the one of the vascular model given by (3.27). The only modification is the different definition of the solid pressure from (3.57) such that the avascular model is conveniently contained within the vascular one for the case $\varepsilon^v = 0$. Again, the Saint-Venant-Kirchhoff or the Neo-Hooke material law from Section 2.3.2.2 are required to close the equation through a suitable constitutive model for the effective stress tensor.

The balance of mass of the solid phase again enters the model in integral form via the calculation of the ECM porosity, which also has to be slightly adapted for the vascular case, see Section 3.3.4.

Remark 3.8. *In a related publication on a similar vascular tumor growth model with homogenized representation of the vasculature [234] based on the original works of Sciumè et al. [229, 230, 231, 232, 233, 235], a slightly different hierarchy of the two porous networks was assumed. Instead of defining the vascular network as an additional pore space inside the ECM (alongside the pores of the ECM), a nested arrangement with the vascular component inside the*

pores of the ECM was derived. Together with the definition of the solid pressure in the avascular model (3.24) the total stress tensor in the notation of the present thesis was given as

$$\boldsymbol{\sigma}^{\mathrm{tot}} = \boldsymbol{\sigma}^{\mathrm{eff}} - p^s \boldsymbol{I} + \varepsilon^v \left(p^s - p^v\right) \boldsymbol{I}. \tag{3.61}$$

It is not entirely clear if the nested or the juxtaposed model resembles the in-vivo arrangement of the networks more closely.

3.3.3 Governing Equations for Species Transport

Compared to the avascular model, species transport in the homogenized vasculature can now also be considered. The governing equation is the species mass balance equation in a generic fluid phase (2.64) for each species i dissolved in a fluid phase $f \in \mathfrak{I}_{\mathrm{f}}$ with mass fraction $\omega^{i\,\overline{f}}$. The respective volume fraction required in this equation is simply the vascular volume fraction

$$\varepsilon^f = \varepsilon^v. \tag{3.62}$$

The pressure gradient $\boldsymbol{\nabla} p^f$ is the blood pressure gradient $\boldsymbol{\nabla} p^v$, i.e., the gradient of the second primary variable of the homogenized vascular network and the permeability tensor is the one of the homogenized vasculature $\boldsymbol{k}^v$. Hence, the balance of mass of a species dispersed in the HV is given by

$$\begin{aligned} \varepsilon^v \left.\frac{\partial \omega^{i\,\overline{v}}}{\partial t}\right|_{\boldsymbol{X}} - \frac{\boldsymbol{k}^v}{\mu^v} \boldsymbol{\nabla} p^v \cdot \boldsymbol{\nabla} \omega^{i\,\overline{v}} + \boldsymbol{\nabla} \cdot \left(\varepsilon^v \boldsymbol{D}^{iv}_{\mathrm{eff}} \boldsymbol{\nabla} \omega^{i\,\overline{v}}\right) \\ = \frac{1}{\rho^v} \left(\sum_{\kappa \in \mathfrak{I}_{cf}} \overset{i\kappa \to iv}{M} + \varepsilon^v r^{iv} - \omega^{i\,\overline{v}} \sum_{\kappa \in \mathfrak{I}_{cv}} \overset{\kappa \to v}{M} \right) \qquad \text{in } \Omega_t \times [t_0, t_e]\,. \end{aligned} \tag{3.63}$$

As before, species transport in TCs, HCs and the IF is considered by (3.28), that is, the mass balance equation for a species in a generic fluid phase (2.64) with

$$\varepsilon^f = \varepsilon S^f, \quad f \in \mathfrak{I}_{\varepsilon} \tag{3.64}$$

and the respective pressure gradients and permeability tensors as detailed in Section 3.2.

Species transport in the solid phase, e.g., for fibronectin is governed by the mass balance of a species in the solid phase (2.66).

3.3.4 Closure Relations and Constitutive Equations

Unchanged Closure Relations and Constitutive Equations for TCs, HCs and IF
Pressure-saturation relationships, permeability tensors, viscosities and diffusivity tensors for TCs, HCs and IF and the species therein are adopted from the avascular model, see Section 3.2.4.

Calculation of ECM Porosity The calculation of the ECM porosity is equivalent to the avascular model in Section 3.2.4, where the conservation of mass of the solid phase was considered under the assumption of zero mass transfer between the solid phase and all other phases. With the presence of the vascular volume fraction in the definition of the volume fraction of the ECM (3.52), equation (3.31) may be rewritten as

$$\int_{\mathcal{U}_0} \rho_0^s \left(1 - \varepsilon_0 - \varepsilon_0^v\right) \mathrm{d}V_0 = \int_{\mathcal{U}_t} \rho^s \left(1 - \varepsilon - \varepsilon^v\right) \mathrm{d}V = \int_{\mathcal{U}_0} \rho^s \left(1 - \varepsilon - \varepsilon^v\right) J \mathrm{d}V_0 \tag{3.65}$$

where the left hand side is the solid mass of an arbitrary volume $\mathcal{U}_0$ in reference configuration which has to be equal to the solid mass of its spatial counterpart $\mathcal{U}_t = \varphi^s\left(\mathcal{U}_0, t\right)$. The quantities in the previous equation are again the current solid phase density ρ^s, ECM porosity ε, Jacobian determinant of the solid phase J, reference solid phase density ρ_0^s, reference ECM porosity ε_0 and, additionally, the vascular volume fraction ε^v and the vascular volume fraction in reference configuration ε_0^v. To satisfy mass conservation, the integrands have to be point-wise equal which gives a relation for the ECM porosity

$$\varepsilon = 1 - \varepsilon^v - \frac{1 - \varepsilon_0 - \varepsilon_0^v}{J} \tag{3.66}$$

under the assumption of an incompressible solid phase ($\rho_0^s = \rho^s$). This result is equivalent to the result of the avascular model (3.34) with additional terms due to the presence of the homogenized vasculature. Now, two mechanisms influencing the ECM porosity are present: First, deformation with non-constant Jacobian determinant J may de- or increase the ECM porosity. Second, an increased vascularization decreases the ECM porosity and, vice versa.

Chemotactic Coefficient For the functional dependency of the chemotactic coefficient χ on the TAF mass fraction of equation (3.50) and (3.51) the same receptor-kinetic law as in Anderson [6] is employed, namely

$$\chi\left(\omega^{TAF\bar{l}}\right) = \chi_0 \frac{\omega_{\chi_0/2}^{TAF\bar{l}}}{\omega_{\chi_0/2}^{TAF\bar{l}} + \omega^{TAF\bar{l}}}. \tag{3.67}$$

The above equation incorporates a decreasing sensitivity of endothelial cells, or in the present case, of the homogenized representation of the vasculature to the TAF gradients if the TAF mass fraction increases. At a mass fraction of $\omega_{\chi_0/2}^{TAF\bar{l}}$, the sensitivity is exactly half the value of the constant sensitivity χ_0. This relationship is more realistic than the constant chemotactic coefficient of other models [225] where the same response regardless of stimulus or TAF concentration is assumed [6].

Haptotactic Coefficient The haptotactic coefficient Θ is assumed constant as suggested by Anderson [6].

Blood Vessel Compression, Regression and Collapse As described in more detail in Section 3.4.5, angiogenesis is not the only way how tumors modify and interact with the vasculature. Additional relevant effects include blood vessel compression, regression and collapse

induced by the growing tumor all leading to a decrease of the vascular volume fraction. In the present model this is incorporated via the right hand side term

$$C_{\text{coll}} = \gamma^v_{\text{coll}} \cdot \tilde{H}\left(p^t - p^t_{\text{coll},v}\right) \cdot \tilde{H}\left(\varepsilon^v\right) \tag{3.68}$$

in the evolution equation of the vascular volume fraction (3.51). $\tilde{H}(\bullet)$ is a smoothed approximation of the Heaviside function which is beneficial for the convergence behaviour of the numerical methods as compared to employing the discontinuous Heaviside function. This term is equivalent to the formulation employed by Wirthl et al. [282, Supporting Information] apart from the additional smoothing of the Heaviside function for the vascular volume fraction. It incorporates a reduction of the vascular volume fraction based solely on the TC pressure. If it is larger than a certain threshold $p^t_{\text{coll},v}$, it decreases with a rate of γ^v_{coll}. The second factor with the Heaviside function ensures that the vascular volume fraction does not drop below zero.

Permeability Tensor, Viscosity and Diffusivity Tensor of Homogenized Vasculature Permeability and diffusivity tensors of the homogenized vasculature are set constant and isotropic as

$$\boldsymbol{k}^v = k^v \cdot \boldsymbol{I} \tag{3.69}$$

and

$$\boldsymbol{D}^{iv}_{\text{eff}} = D^{iv}_0 \cdot \boldsymbol{I} \tag{3.70}$$

with scalar permeability k^v and diffusivity D^{iv}_0. In addition, blood viscosity μ^v is assumed constant. In reality, however, blood behaves as a non-Newtonian fluid due to the presence of red blood cells. Therefore, the viscosity depends on blood vessel radius R and hematocrit, i.e., the volume fraction of red blood cells. This is incorporated in the discrete, one-dimensional representation of the vasculature in Sections 3.4 and 3.5 via a diameter-dependent viscosity. However, the information about the morphology including blood vessel diameters is not available in the homogenized representation which is why a constant blood viscosity is assumed. Averaging the blood vessel diameter distribution with corresponding viscosities could yield a more physically reasonable description.

Remark 3.9. *Anisotropy of the vascular network was incorporated into the model under the author's supervision in the term paper by Bui [32] with transversely isotropic permeability and diffusivity tensors similar to the structural anisotropy of the ECM as described in Remark 3.6. A special focus was set on the angiogenesis-induced growth of the vasculature. As stated above, the neovasculature is much more tortuous than a healthy vasculature but still has a preferential direction following the trigger for growth, namely, the TAF gradient. Thus, the principal direction of the transversely isotropic tensors was set to be aligned with the TAF gradient* $\boldsymbol{\nabla}\omega^{TAF\,\bar{l}}$. *In discrete models such as [6, 42, 83, 158, 185, 287–289, 298], which completely resolve the neovasculature formed during angiogenesis, this is inherently included since the full topology of the blood vessels and specifically their primary direction towards the TAF gradient is resolved. Using the present homogenized treatment of the vasculature, the anisotropic tensors offer an alternative to include this behaviour. In [32] the anisotropy was additionally controlled via the dispersion of the blood vessels around the preferential direction similar to corresponding structural material models [87]. This could be a convenient measure of the influence of the TAF gradient on the structure of the resulting blood vessel network. A small dispersion indicates a more directed growth of the neovasculature and a larger dispersion a more tortuous result.*

3.3.5 Summary and Variants of the Model

In summary, the governing equations of the tumor growth model with homogenized representation of the vasculature are the balance of mass of blood (3.47), the evolution equation of the vascular volume fraction (3.51), the mass balances of TCs ((3.55) with $f = t$) and HCs ((3.55) with $f = h$), the sum of the mass balances of TCs, HCs and IF (3.56), the balance of momentum of the solid phase (3.60) and the balance of species mass for species in TCs, HCs and IF (3.28), in the solid phase (2.66) and in the HV (3.63).

The description of the vascular model is completed by illustrating several possible variants of the model. As for the avascular model, a considerable reduction in computational complexity may be achieved when neglecting the deformability of the solid phase. In that case, a Eulerian problem description emerges and the solid phase momentum equation (3.60) does not have to be solved.

In addition, two different variants concerning the homogenized vasculature are conceivable and will actually be used. First, blood flow and possibly also species transport in the vasculature can be neglected. This is equivalent to the model used in the author's publication [135] where blood pressure and species mass fractions in the homogenized vasculature were set constant. Hence, only one governing equation is evaluated for the homogenized vasculature, that is, the evolution equation for the vascular volume fraction (3.51) whereas the balance of mass (3.47) yielding the blood pressure distribution is not solved. The second possibility is the variant with a static vasculature with constant vascular volume fraction $\varepsilon^v = \varepsilon_0^v$. Consequently, the evolution equation for the vascular volume fraction (3.51) is not included but only the balance of mass of blood (3.47) and possibly species transport therein. Such a model can be employed if the influence of angiogenesis and blood vessel collapse are negligible such that the vascular volume fraction does not change. In that case, the porosity of the ECM (3.66) is only influenced by the deformation of the domain.

3.4 The Vascular Tumor Growth Model with a Discrete Embedded Representation of the Vasculature

In the previous section, the vascular network including flow and species transport therein was introduced in a homogenized way into the tumor growth model. Here, a second variant, which is termed discrete embedded approach hereafter, is presented. This was incorporated in the author's publication [136], from which major parts of the following sections have been taken. Some improvements have been made to the original paper, which is highlighted whenever necessary. The employed approach follows a common strategy to model flow, species transport and transvascular exchange in the microcirculation via topological model reduction. Thereby, the vascular domain is shrinked to its centerline resulting in a network of one-dimensional blood vessel segments which are embedded into the encompassing three-dimensional porous domain. The model reduction yields one-dimensional PDEs describing blood flow and species transport inside this 1D domain Λ. The surrounding tissue is represented by the avascular four-phase tumor growth model and both domains are coupled via transvascular exchange terms of fluid or species from the embedded vasculature into the IF. The general concept is sketched in Figure 3.5, where a one-dimensional blood vessel network $\Lambda_t \subset \Omega_t$ is embedded into the 3D tissue domain Ω_t. At each

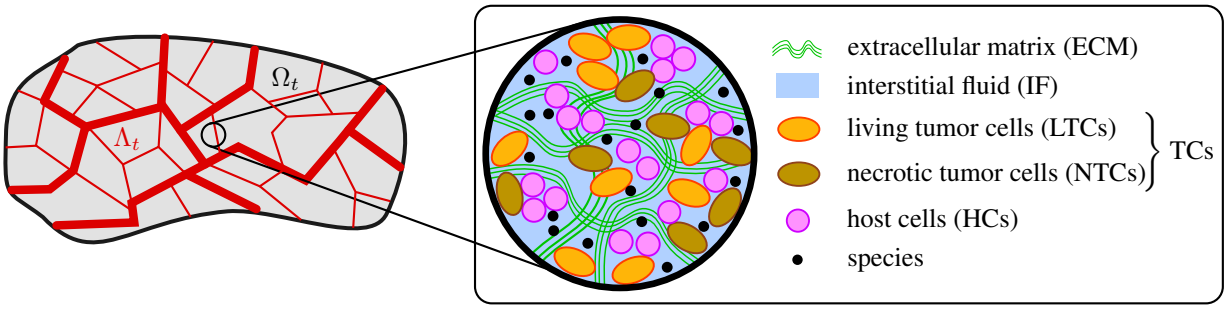

Figure 3.5: Sketch of vascular tumor growth model with discrete embedded representation of vasculature – embedded 1D vasculature $\Lambda_t \subset \Omega_t$ is sketched on the left and components of the avascular 3D multiphase model on the right with solid phase (ECM), three fluid phases (TCs, HCs, IF), NTCs (species of TCs) and generic species.

macroscale point of the 3D domain, the avascular multiphase tumor growth model holds. Additional source terms in the mass balance of fluid and species in the IF account for transvascular fluid and species mass flux at the position of the embedded vessels.

First contributions to study such 1D-3D coupled transport problems were made by Secomb et al. [237, 241]. They used Green's functions which limits the applicability of the method as nonlinear or transient problems. Arbitrary boundary conditions and domain shapes and heterogeneous material parameters cannot be considered [125]. In the context of finite elements, the papers and the thesis of D'Angelo [51–53] introduce an approach termed "embedded multiscale method" where such 1D-3D coupled problems are derived, mathematically investigated and numerically solved. Further applications have been realized such as drug delivery to tumors [38, 39] and nanoparticle-mediated hyperthermia cancer treatment [177, 178]. The intricacy of this formulation is that the employed 1D line source terms lead to a singularity in the governing equations of the 3D domain. Thus, two different variants will be employed in this thesis, one where the source terms are concentrated on the centerline leading to the aforementioned singularity, and one where they are evaluated on the lateral surface of the 1D inclusions, thus, lifting the regularity of the solution as proposed by Köppl et al. [130, 131]. An advantageous feature of all implemented approaches is that they allow for non-matching 1D and 3D discretizations, i.e., the 1D and 3D domain can be meshed independently of each other. Considering the complexity of *in-vivo* blood vessel networks, it is very challenging or even unfeasible to perform a discretization with matching 1D and 3D grids. To the best of the author's knowledge, this thesis and the associated publication [136] constitute the first contributions incorporating a consistent 1D-3D coupling between non-matching FEM discretization in the context of tumor growth modeling. In the following, the terms discrete and fully-resolving will be utilized synonymously to refer to approaches which aim for a full resolution of the vascular network by contrast to the other two vascular model variants, where at least a part of the vasculature is homogenized.

Numerous such models with a discrete representation of the vasculature have been proposed as summarized in a number of reviews [58, 157, 160, 185, 216, 245, 267]. Angiogenesis is incorporated into these frameworks based on the discrete variant of Anderson and Chaplain [6, 42] or similar approaches where leading tip endothelial cells guide the formation of vascular networks sprouting from pre-existing vessels and migrating towards a TAF gradient. This inevitably involves a certain stochasticity, e.g., via a random-walk model of the network tips. Further rela-

tionships respectively decisions are involved if and when tips sprout, branch or form loops. Such a discrete angiogenesis model has not yet been incorporated into the present framework but a homogenized adaptation can be considered with the hybrid version from Section 3.5. Furthermore, a detailed comparison of the multitude of numerical approaches is beyond the scope of this thesis and the reader is referred to the aforementioned review papers. Representative models with discrete representation of the vasculature include the works of [83, 158, 287–289, 298]. A drawback is that they do not explicitly consider blood flow and species transport in the 1D embedded domain and, thus, no two-way coupling between tumor growth and the availability of nutrients. More recent state-of-the-art fully-resolved blood vessel network models [276–279, 287] are based on an integrative framework for vascular remodeling [216] including angiogenesis as well as vessel regression, dilation and collapse during tumor progression. Thereby, the initial arterio-venous vasculature in host tissue develops into a tumor specific vessel network. However, this approach does only allow for matching 1D and 3D hexagonal grids together with a finite difference discretization of the governing equations.

In the following, the vascular variant with discrete embedded representation of the vasculature will be introduced with a special focus on the terms arising due to 1D-3D coupling for which the two aforementioned concepts are considered. The governing equations for blood flow and species transport in the embedded domain are introduced and the adaptation of the avascular model to take 1D-3D mass exchange into account are outlined. A further novelty of this thesis, which was not included in the previous publications of the author, is the incorporation of an empirical relationship for blood vessel network remodeling via blood vessel diameter adaptation.

3.4.1 Problem Setting and Notation

As described above, the computational effort for solving blood flow and species transport in the vasculature domain can be significantly diminished by a topological model reduction to a one-dimensional blood vessel network $\Lambda \subset \Omega$ embedded in the 3D tissue domain Ω. Under several assumptions based on the flow physics in the microcirculation, this can be further simplified to a model of 1D Poiseuille flow in cylinders. Recent experimental data by Seano et al. [236] suggests that the deformation of blood vessel networks in the brain subject to mechanical stress exerted by growing tumors may be significant. Therefore, a large deformation approach of the embedded network inside the tissue, i.e., the extracellular matrix (ECM) is adopted. In the following, the main assumptions and simplifications and their impact on the model formulation in an ALE setting are discussed. These are:

(i) **Hagen-Poiseuille flow is assumed in the 1D vasculature.** In the microcirculation, the Reynolds and the Womersley numbers (relating the frequency of a pulse and the viscosity of a fluid to each other) are very low [Table 1.7][77]. Thus, inertia terms and the pulsatility of blood flow are neglible. Body forces such as gravity can also be disregarded [131]. Then, the Hagen-Poiseuille equation can be derived from the Navier-Stokes equations assuming a stationary and laminar flow through cylindrical cross-sections. However, in the current formulation transcapillary respectively radial flow is present such that the assumptions of Poiseuille are not rigorously satisfied. Nevertheless, if radial flow is small compared to axial flow, this is still an acceptable assumption [178].

(ii) **The deformation of the 1D embedded blood vessel network is completely described through the deformation of the underlying porous medium domain.** Only smaller blood vessels such as arterioles, venules and capillaries are considered here. Then, the surrounding ECM acts as a scaffold which provides mechanical integrity to the enclosed blood vessel [214]. If the scaffolding material deforms, the blood vessel deforms equally.

(iii) **Blood vessel segments have negligible stiffness compared to the ECM.** Any contribution of these small blood vessels to the stiffness of the surrounding ECM is neglected since their wall does not consist of smooth muscle cells but only a thin basement membrane which provides structural integrity [161].

(iv) **The change in area of the blood vessel segments is described via an algebraic relationship for blood vessel diameter adaptation.** This implies that lateral deformation of blood vessels induced through the deformation of the ECM is neglected. Only the deformation of the centerline following the ECM deformation is regarded. For example, axial elongation of a blood vessel does not evoke any radial constriction and vice versa. This effect is insignificant compared to the much more substantial influence of blood vessel adaptation due to other stimuli such as wall shear stess or constriction and collapse during tumor growth. This can be included through suitable constitutive laws for the blood vessel diameter as in [261, 287]. The employed algebraic relationships are introduced in Section 3.4.5.

(v) **Time scales of blood vessel area change are large.** Neglecting the pulsatility of blood flow, the only mechanism of blood vessel diameter change is the interaction with the tumor growth model via blood vessel remodeling as described above. The time scales of this adaptation process are very large (in the order of days) compared to the time scales of blood flow and species transport such that the temporal derivatives of the cross-sectional area can safely be neglected.

(vi) **The non-Newtonian behaviour of blood is represented by an algebraic relationship for its viscosity.** The viscosity of blood is either set constant or represented by a constitutive relationship [201], see also Section 3.4.5.

One could also extend the proposed approach to remove one or all of the above assumptions but as they appear reasonable for the problems of interest in this thesis, they are introduced to not artificially complicate the method. For instance, the stiffness of the blood vessel network could be included by modeling them as one-dimensional beams. On the one hand, this would result in a 1D-3D beam-to-solid meshtying problem as in Steinbrecher et al. [246] under the assumption that they move with the surrounding ECM. On the other hand, their deformation could also be decoupled from the movement of the ECM such that they can move independently.

The notation of the problem is depicted in Figure 3.6. The one-dimensional vasculature and the 3D tissue domain in reference configuration are denoted as Λ_0 and Ω_0, respectively. Their counterparts in spatial configuration are Λ_t and Ω_t. Assumption (ii) from above holds if a point $\boldsymbol{X}^\Lambda \in \Lambda_0$ on the one-dimensional vasculature reference configuration and a reference point $\boldsymbol{X}^\Omega \in \Omega_0$ of the three-dimensional domain, which are at the same location in reference configuration, share a common point $\boldsymbol{x}^\Lambda\left(\boldsymbol{X}^\Lambda\right) = \boldsymbol{x}^\Omega\left(\boldsymbol{X}^\Omega\right)$ also in spatial configuration $\boldsymbol{x}^\Lambda \in \Lambda_t$

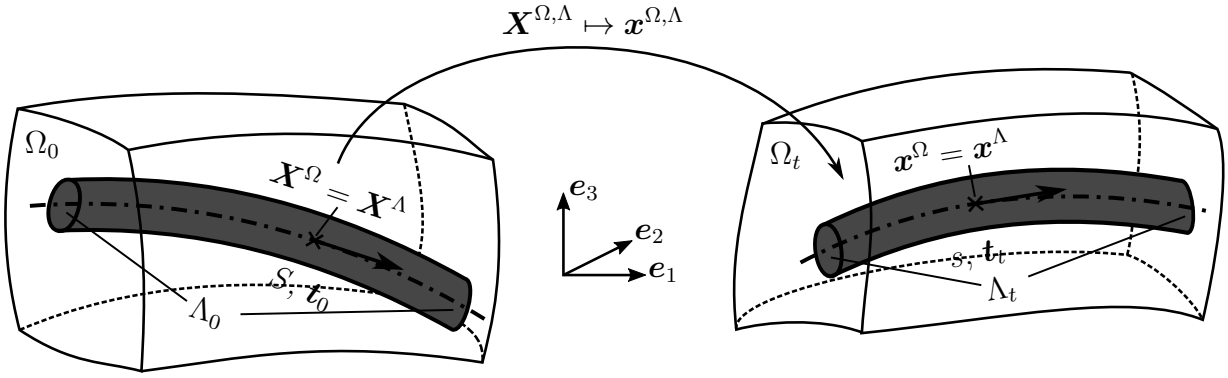

Figure 3.6: Notation for 1D-3D coupling. Figure taken from the author's publication [136].

respectively $\boldsymbol{x}^{\Omega} \in \Omega_t$ throughout the deformation. Hence, the superscripts for the distinct domains can be dropped. In addition, a single blood vessel segment will be considered hereafter, the case with multiple segments follows via the assembly of these segments in the FEM formulation. The arc-length coordinate of each vessel segment in reference configuration is referred to as $S \in [0, L_0]$ and in spatial configuration as $s \in [0, L_t]$ with the respective lengths L_0 and L_t. The coordinates are related through the deformation of the domain via

$$s(S) = \int_0^S \|\boldsymbol{F}\left(\boldsymbol{x}\left(\boldsymbol{X}\left(S'\right)\right)\right) \cdot \boldsymbol{t}_0(S')\| dS' \tag{3.71}$$

with unit tangent vector in reference configuration $\boldsymbol{t}_0$ and deformation gradient $\boldsymbol{F}$. The corresponding unit tangent vector in spatial configuration follows as

$$\boldsymbol{t}_t = \frac{\boldsymbol{F} \cdot \boldsymbol{t}_0}{\|\boldsymbol{F} \cdot \boldsymbol{t}_0\|}. \tag{3.72}$$

The lateral surface of a blood vessel segment is given by $\partial\mathcal{D}_t$ in spatial configuration and by $\partial\mathcal{D}_0$ in reference configuration. It is further assumed that the vessel cross-section is circular and perpendicular to the centerline of the 1D domain and remains so during the deformation. Its diameter is D_0 respectively D_t. In the following, quantities such as pressures or velocities defined in the vasculature domain will be identified by superscript $(.)^{\hat{v}}$. Due to the topological model order reduction to a one-dimensional network Λ_t these values are area-averaged. Thus, they are constant over the cross-section of the 1D domain and depend only on the respective position along the centerline s.

3.4.2 Governing Equations in 1D Vasculature Domain

3.4.2.1 Governing Equations for Blood Flow in 1D Vasculature Domain

According to Peiró and Veneziani [192] the mass conservation equation for an incompressible fluid in the vasculature domain may be written as

$$\left.\frac{\partial A}{\partial t}\right|_{\boldsymbol{x}} + \frac{\partial\left(A v^{\hat{v}}\right)}{\partial s} = -\frac{\overset{\hat{v}\to l}{M}}{\rho^{\hat{v}}} \qquad \text{on } \Lambda_t \tag{3.73}$$

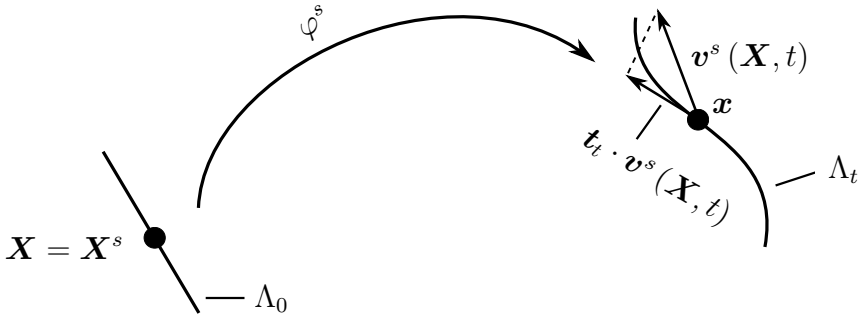

Figure 3.7: Sketch of 1D ALE description – the Lagrangean observer of the solid phase $\boldsymbol{X}$ moves with a velocity of $v_t^s = \boldsymbol{t}_t \cdot \boldsymbol{v}^s$ in tangential direction to the 1D domain Λ_t w.r.t. the Eulerian observer at fixed spatial position $\boldsymbol{x}$.

with blood vessel area A and area-averaged fluid velocity $v^{\hat{v}}$ in axial direction. The right hand side is an outflow of fluid per unit length and unit time across the permeable blood vessel wall. This mass transfer is denoted as

$$\overset{\hat{v}\to l}{M} = \int_{\partial\mathcal{D}_t(s)} \rho \cdot \boldsymbol{w} \cdot \boldsymbol{n} \, \mathrm{d}\gamma \tag{3.74}$$

following TCAT notation. Fluid with density ρ, which is not necessarily equal to blood density $\rho^{\hat{v}}$, leaves the 1D blood vessel with a relative velocity $\boldsymbol{w}$ w.r.t. to the movement of the vessel wall in normal direction $\boldsymbol{n}$ and passes into the IF. This mass transfer term is evaluated as a closed line integral along the perimeter of the blood vessel $\partial\mathcal{D}_t(s)$ at coordinate s. Further details on the definition and evaluation of such a 1D-3D mass transfer terms will follow in Section 3.4.3.

As stated above, in the employed ALE formulation, the observer of the 1D vasculature domain is the Lagrangean observer of the deforming solid phase. Thus, a one-dimensional adaptation of the fundamental ALE equation (2.59) may be devised as

$$\left.\frac{\partial(\bullet)}{\partial t}\right|_{\boldsymbol{x}} = \left.\frac{\partial(\bullet)}{\partial t}\right|_{\boldsymbol{X}} - v_t^s \cdot \frac{\partial(\bullet)}{\partial s} \qquad \text{on } \Lambda_t \tag{3.75}$$

with the projection of the solid phase velocity $\boldsymbol{v}^s$ in the tangential direction $\boldsymbol{t}_t$ of the blood vessel segment

$$v_t^s = \boldsymbol{t}_t \cdot \frac{1}{A} \int_A \boldsymbol{v}^s \, \mathrm{d}A \approx \boldsymbol{t}_t \cdot \boldsymbol{v}^s. \tag{3.76}$$

Here, the area-average over the blood vessel cross-section of the solid phase velocity has been neglected. This allows rewriting equation (3.73) in ALE form as

$$\left.\frac{\partial A}{\partial t}\right|_{\boldsymbol{X}} + A\frac{\partial(v_t^s)}{\partial s} + \frac{\partial\left(A\left(v^{\hat{v}} - v_t^s\right)\right)}{\partial s} = -\frac{\overset{\hat{v}\to l}{M}}{\rho^{\hat{v}}} \qquad \text{on } \Lambda_t. \tag{3.77}$$

For illustrative purposes, the employed 1D ALE formulation with the observer of the 1D vasculature moving tangentially to the current 1D domain Λ_t is sketched in Figure 3.7.

By assuming cylindrical blood vessels with radius R_t in spatial configuration and the Poiseuille relation

$$v^{\hat{v}} - v_t^s = -\frac{R_t^2}{8\mu^{\hat{v}}}\frac{\partial p^{\hat{v}}}{\partial s} \qquad s \in \Lambda_t, \tag{3.78}$$

the balance of mass can be rewritten as

$$\pi R_t^2 \frac{\partial v_t^s}{\partial s} - \frac{\partial}{\partial s}\frac{\pi R_t^4}{8\mu^{\hat{v}}}\frac{\partial p^{\hat{v}}}{\partial s} = -\frac{\overset{\hat{v}\to l}{M}}{\rho^{\hat{v}}} \qquad \text{on } \Lambda_t \times [t_0, t_e]\,, \tag{3.79}$$

where also the temporal derivative of the blood vessel cross-sectional area has been neglected (Assumption (v)). The Poiseuille equation (3.78) represents the balance of momentum of blood in the 1D representation of the vasculature. The projection of the skeleton velocity in current tangential segment direction v_t^s has been included to account for the underlying solid phase movement. Hence, this term is similar to the Darcy equation (2.33) in a porous medium. The pressure gradient in the capillaries induces a flow relative to the solid phase movement in axial vessel direction. Blood viscosity is denoted as $\mu^{\hat{v}}$ and either assumed constant or modeled with a suitable algebraic relationship accounting for the non-Newtonian behaviour of blood (Assumption (vi)), see Section 3.4.5.

Remark 3.10. *The employed ALE formulation can alternatively also be derived from the Reynolds transport theorem applied to a tube whose outer boundaries in longitudinal direction move with the solid phase and whose outer boundaries in radial direction move with boundaries of the tube as its radius changes. The derivation is analogous to the one given in Peiró and Veneziani [192] with the additional longitudinal movement.*

3.4.2.2 Governing Equations for Species Transport in 1D Vasculature Domain

Blood flow in the one-dimensional embedded vasculature can also transport several species such as oxygen, anticancer drugs or nanoparticles. These are advected by the flow and may cross the vessel walls into the IF. The mass balance of a species i dispersed in the blood vessel network with (area-averaged) mass fraction $\omega^{i\,\hat{v}}$ may be written as

$$A\,\frac{\partial \omega^{i\,\hat{v}}}{\partial t}\bigg|_{\boldsymbol{x}} + \frac{\partial}{\partial s}\left(A \cdot v^{\hat{v}} \cdot \omega^{i\,\hat{v}} - A \cdot D^{i\hat{v}}\frac{\partial \omega^{i\,\hat{v}}}{\partial s}\right) = -\frac{\overset{i\hat{v}\to il}{M}}{\rho^{\hat{v}}} \qquad \text{on } \Lambda_t \tag{3.80}$$

when neglecting the temporal derivative of the blood vessel area (Assumption (v)). Such one-dimensional diffusion-advection-reaction equations with diffusivity $D^{i\hat{v}}$ have been used previously in related 1D-3D coupling formulations [38, 52, 131, 177, 178]. However, here the primary variable is chosen as a mass fraction $\omega^{i\,\hat{v}}$ rather than a (mass) concentration which makes it easier to couple it to the multiphase tumor growth model where species are generally identified by mass fractions. The right hand side represents a 1D-3D species mass transfer term from species i in the embedded vasculature to the considered species i in the IF. Again, species mass is transferred from the embedded vasculature into the IF with a relative species velocity $\boldsymbol{w}^{i\,\hat{v}}$ across the blood vessel wall along the perimeter of the embedded 1D vasculature

$$\overset{i\hat{v}\to il}{M} = \int_{\partial\mathcal{D}_t(s)} \rho \cdot \boldsymbol{w}^{i\,\hat{v}} \cdot \boldsymbol{n}\,\mathrm{d}\gamma \tag{3.81}$$

equivalent to the mass transfer term for blood flow (3.85). Typically, the term depends on the mass fractions of the species in the vasculature and in the 3D domain as outlined in Section 3.4.3.

Furthermore, intra-phase reaction terms have been omitted as those are not present in the current model. Applying the product rule for the convective term yields

$$A\left.\frac{\partial \omega^{i\hat{v}}}{\partial t}\right|_{\boldsymbol{x}} + A\cdot v^{\hat{v}}\cdot\frac{\partial \omega^{i\hat{v}}}{\partial s} - \frac{\partial}{\partial s}\left(A\cdot D^{i\hat{v}}\frac{\partial \omega^{i\hat{v}}}{\partial s}\right) = -\frac{\overset{i\hat{v}\to il}{M}}{\rho^{\hat{v}}} + \underbrace{\omega^{i\hat{v}}\frac{\overset{\hat{v}\to l}{M}}{\rho^{\hat{v}}}}_{=-\omega^{i\hat{v}}\cdot\frac{\partial\left(Av^{\hat{v}}\right)}{\partial s}} \qquad \text{on } \Lambda_t. \tag{3.82}$$

Here, the 1D balance of mass of blood (3.73) has additionally been inserted. Next, the fundamental ALE equation (3.75) may be invoked to transform the temporal derivative on the 1D domain to a derivative w.r.t. the reference configuration. Inserting into (3.80) results in

$$\pi R_t^2\left.\frac{\partial \omega^{i\hat{v}}}{\partial t}\right|_{\boldsymbol{X}} - \pi R_t^2 v_t^s\cdot\frac{\partial \omega^{i\hat{v}}}{\partial s} + \pi R_t^2 v^{\hat{v}}\cdot\frac{\partial \omega^{i\hat{v}}}{\partial s} - \frac{\partial}{\partial s}\left(\pi R_t^2 D^{i\hat{v}}\frac{\partial \omega^{i\hat{v}}}{\partial s}\right) = \frac{1}{\rho^{\hat{v}}}\left(-\overset{i\hat{v}\to il}{M} + \omega^{i\hat{v}}\overset{\hat{v}\to l}{M}\right) \qquad \text{on } \Lambda_t. \tag{3.83}$$

The convective term in ALE form can then be replaced by the Poiseuille law (3.78), which yields the final mass balance equation for species i

$$\pi R_t^2\left.\frac{\partial \omega^{i\hat{v}}}{\partial t}\right|_{\boldsymbol{X}} - \frac{\pi R_t^4}{8\mu^{\hat{v}}}\frac{\partial p^{\hat{v}}}{\partial s}\cdot\frac{\partial \omega^{i\hat{v}}}{\partial s} - \frac{\partial}{\partial s}\left(\pi R_t^2 D^{i\hat{v}}\frac{\partial \omega^{i\hat{v}}}{\partial s}\right) = \frac{1}{\rho^{\hat{v}}}\left(-\overset{i\hat{v}\to il}{M} + \omega^{i\hat{v}}\overset{\hat{v}\to l}{M}\right) \qquad \text{on } \Lambda_t\times[t_0,t_e]\,. \tag{3.84}$$

In summary, equations (3.79) and (3.84) are the governing equations for fluid flow and species transport in the embedded 1D vascular network. They are coupled in three ways to the multiphase tumor growth model for the surrounding three-dimensional tissue. First, in a one-way coupling, the deformation of the ECM induces also deformation of the embedded blood vessels. Second, the growing tumor remodels the vascular network which is represented by an adaptation of its diameter. Third, fluid flow and species transport in the pre-existing vasculature and in the surrounding IF are coupled via transvascular exchange over the blood vessel wall. The formulation of these mass transfer terms will be detailed in the next section.

3.4.3 Two Different Variants for 1D-3D Coupling – Lateral Surface or Centerline Coupling

In this thesis, two different variants for 1D-3D coupling will be employed. A detailed derivation of the second one termed lateral surface coupling including the topological model order reduction to a 1D vascular network may be found in [40, 130, 131], which is why it is only outlined here. The derivation is based on defining a "full model" of two distinct domains, one corresponding to the vascular network and the second one to the surrounding tissue. An interface, i.e., the vessel wall which allows fluid or species mass flux from vasculature into IF separates these two domains. From that, a "reduced model", where the vasculature is shrinked to a 1D inclusion and the porous domain is enlarged such that it encompasses the entire domain, is deduced. The main

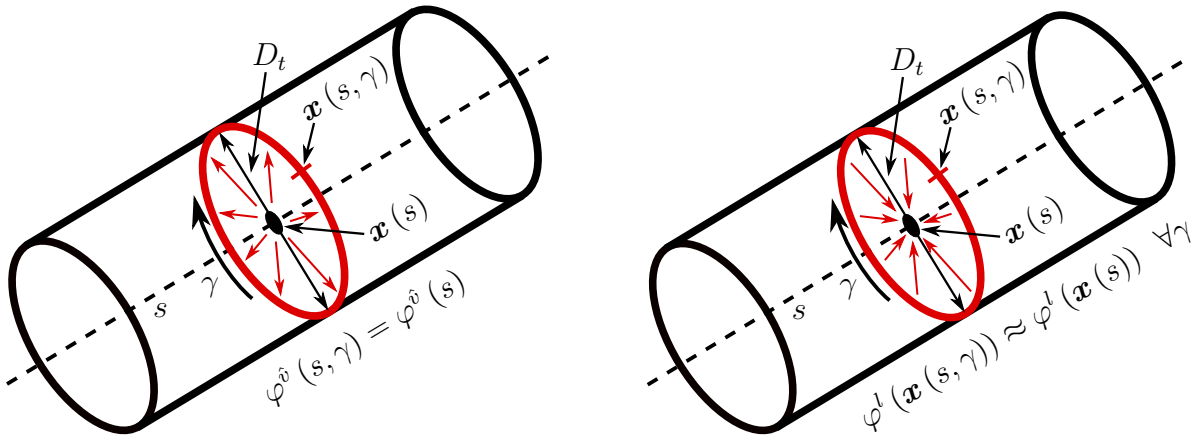

(a) Lateral surface coupling

(b) Centerline coupling

Figure 3.8: Comparison between lateral surface and centerline coupling – for lateral surface coupling (left) the values from the 1D embedded blood vessel are projected on the lateral surface, for centerline coupling (right) the values of the 3D domain are projected on the centerline of the blood vessel (Figure after [131]).

assumption is that the radius of the vascular network is small compared to the dimensions of the 3D domain. Thus, a 1D description of blood flow and species transport with uniform, area-averaged quantities depending only on the position along the centerline s as already presented in the previous section is possible. Lastly, again under the assumption of small inclusions, the porous medium domain is identified with the entire 3D domain including the space occupied by the vascular network such that its equations and primary variables are defined on the entire 3D domain. This allows embedding the vessels into arbitrary 3D discretizations which do not have to be fitted to the outer surface of the network. Subsequently, the evaluation of generic 1D-3D mass transfer terms, for example, an outflow of fluid from the embedded vasculature into the IF or, for species transport, oxygen exchange or drug release from the embedded vasculature into the IF, is introduced for the two different coupling concepts.

Hereafter, it will be assumed that the (fluid or species) mass transfer terms are given as a possibly nonlinear algebraic relationship of the form

$$\rho \cdot \boldsymbol{w}^{(i\,\hat{v})} \cdot \boldsymbol{n} = f\left(\varphi^{\hat{v}}, \varphi^{l}\right), \tag{3.85}$$

that is, the mass transfer depends on species or blood primary variables $\varphi^{\hat{v}}$ on the 1D domain and species or IF primary variables φ^{l} in the 3D domain according to a generic function $f(\bullet)$. For instance, a common formulation for outflow of blood plasma from the vasculature into the IF would read as

$$f\left(p^{\hat{v}}, p^{l}\right) = \rho^{l} \cdot \kappa\left(p^{\hat{v}} - p^{l}\right) \tag{3.86}$$

depending on the blood vessel wall permeability κ and the pressure difference between the two domains. If an additional osmotic term is added, the well-known Starling equation (B.15) is obtained. Inserting the algebraic relationship (3.85) back into the right hand side term of equa-

tion (3.73) respectively (3.80) yields

$$\begin{aligned}\int_{\partial\mathcal{D}_t(s)} \rho \cdot \boldsymbol{w}^{(i\,\hat{v})} \cdot \boldsymbol{n}\,\mathrm{d}\gamma &= \int_0^{\pi D_t(s)} f\left(\varphi^{\hat{v}}\left(s,\gamma\right),\varphi^{l}\left(\boldsymbol{x}\left(s,\gamma\right)\right)\right)\,\mathrm{d}\gamma \\ &= \int_0^{\pi D_t(s)} f\left(\varphi^{\hat{v}}\left(s\right),\varphi^{l}\left(\boldsymbol{x}\left(s,\gamma\right)\right)\right)\,\mathrm{d}\gamma, \end{aligned} \tag{3.87}$$

where the area-averaged quantities defined in the embedded vasculature are constant along the integral and do not depend on their position at the perimeter as sketched in Figure 3.8a. As an integral over the lateral surface of the entire vascular network has to be evaluated in this case, it is termed lateral surface coupling hereafter.

The fluid or species mass flux across the vessel surface goes from the vascular network into the IF. Consequently, this term is represented as a source term concentrated at the lateral surface of the embedded vasculature in the balance of fluid or species mass in the IF. For that, it is scaled with the Dirac measure $\delta_{\partial\mathcal{D}_t}$ which is equal to one on the lateral surface of the 1D vasculature and zero everywhere else. The resulting term which is added as a right hand side contribution into the corresponding equations reads as

$$\delta_{\partial\mathcal{D}_t}\rho \cdot \boldsymbol{w}^{(i\,\hat{v})} \cdot \boldsymbol{n} = \delta_{\partial\mathcal{D}_t} \cdot f\left(\varphi^{\hat{v}}\left(s,\gamma\right),\varphi^{l}\left(\boldsymbol{x}\left(s,\gamma\right)\right)\right) = \delta_{\partial\mathcal{D}_t} \cdot f\left(\varphi^{\hat{v}}\left(s\right),\varphi^{l}\left(\boldsymbol{x}\left(s,\gamma\right)\right)\right) \tag{3.88}$$

with the aforementioned Dirac measure accounting for the 1D-3D transvascular fluid or species exchange over the blood vessel wall. The Dirac term satisfies

$$\int_{\Omega_t} \delta_{\partial\mathcal{D}_t} \cdot f\left(\boldsymbol{x}\right)\mathrm{d}\Omega_t = \int_0^{L_t}\int_0^{\pi D_t(s)} f\left(\boldsymbol{x}\left(s,\gamma\right)\right)\,\mathrm{d}\gamma\,\mathrm{d}s \tag{3.89}$$

for any function $f\left(\boldsymbol{x}\right)$ defined in Ω_t. In summary, blood flow and species transport in the 1D vasculature is coupled with the balance of fluid and species mass of the IF in the 3D porous medium domain via transvascular exchange. Fluid or species leaving the 1D vasculature enter the IF at the lateral surface of the 1D vasculature via a surface source term in its governing equations.

In the previous publication of the author [136], an alternative coupling along the centerline was performed. As this corresponds to a projection of the values from the 3D domain onto the centerline of the one-dimensional embedded vasculature as sketched in Figure 3.8b, this variant is subsequently termed centerline coupling. It is identical to the lumped approximation of D'Angelo [52]. However, the mass transfer term into the IF is concentrated as a line source leading to a singularity of the 3D primary variables along the embedded 1D manifold [130, 131]. Reconstructing the pressure or mass fraction values of the 3D domain via a simple evaluation at the centerline is, thus, not mathematically sound. Convergence cannot be achieved if the element size of the 3D domain becomes smaller than the diameter of the 1D domain [52], see also Appendix A.1, where different variants are compared and discussed in more detail. In practical problems, this is usually not the case and the method can be applied for cases with $h > D$. Recently, alternative approaches to approximate the Dirac measure by smearing it over a finite length using kernel functions have also been proposed [125–127].

Under the assumption that the diameter of the blood vessel is very small or in the context of an FE approximation sufficiently smaller than the characteristic mesh size of the 3D domain, the

values at the lateral surface of the 1D vasculature may be approximated as

$$\varphi^l\left(\boldsymbol{x}\left(s,\gamma\right)\right) \approx \varphi^l\left(\boldsymbol{x}\left(s\right)\right) \quad \forall\gamma \tag{3.90}$$

i.e., as constant along the perimeter. Thus, the 1D-3D mass transfer term (3.87) simplifies to

$$\int_{\partial\mathcal{D}_t(s)} \rho \cdot \boldsymbol{w}^{(i\,\hat{v})} \cdot \boldsymbol{n}\,\mathrm{d}\gamma \approx \pi D_t \cdot f\left(\varphi^{\hat{v}}\left(s\right), \varphi^l\left(\boldsymbol{x}\left(s\right)\right)\right) \tag{3.91}$$

such that the actual perimeter integral does not have to be evaluated. Hence, also the counterpart of the mass transfer term appearing as a source term in the governing (fluid or species) mass balance equation of the IF, i.e. equation (3.88), may be approximated as

$$\delta_{\partial\mathcal{D}_t} \cdot f\left(\varphi^{\hat{v}}\left(s\right), \varphi^l\left(\boldsymbol{x}\left(s,\gamma\right)\right)\right) \approx \delta_{\partial\mathcal{D}_t} \cdot f\left(\varphi^{\hat{v}}\left(s\right), \varphi^l\left(\boldsymbol{x}\left(s\right)\right)\right) = \delta_{\Lambda_t} \cdot \pi D_t(s) \cdot f\left(\varphi^{\hat{v}}\left(s\right), \varphi^l\left(\boldsymbol{x}\left(s\right)\right)\right) \tag{3.92}$$

where a further Dirac measure δ_{Λ_t} has been introduced. It is equal to one along the 1D centerline of the embedded domain and zero elsewhere. Analogously to the measure defined on the lateral surface the following property can be deduced:

$$\int_{\Omega_t} \delta_{\Lambda_t} \cdot f\left(\boldsymbol{x}\right) \mathrm{d}\Omega_t = \int_0^{L_t} f\left(\boldsymbol{x}\left(s\right)\right)\,\mathrm{d}s. \tag{3.93}$$

Furthermore, if the approximation (3.90) holds, the two Dirac terms are related via

$$\begin{aligned}\int_{\Omega_t} \delta_{\partial\mathcal{D}_t} \cdot f\left(\varphi^{\hat{v}}\left(s\right), \varphi^l\left(\boldsymbol{x}\left(s\right)\right)\right)\,\mathrm{d}\Omega_t &= \int_0^{L_t}\int_0^{\pi D_t(s)} f\left(\varphi^{\hat{v}}\left(s\right), \varphi^l\left(\boldsymbol{x}\left(s\right)\right)\right)\,\mathrm{d}\gamma\,\mathrm{d}s \\ = \int_0^{L_t} \pi D_t(s) \cdot f\left(\varphi^{\hat{v}}\left(s\right), \varphi^l\left(\boldsymbol{x}\left(s\right)\right)\right)\,\mathrm{d}s &= \int_{\Omega_t} \delta_{\Lambda_t} \cdot \pi D_t(s) \cdot f\left(\varphi^{\hat{v}}\left(s\right), \varphi^l\left(\boldsymbol{x}\left(s\right)\right)\right)\,\mathrm{d}\Omega_t,\end{aligned} \tag{3.94}$$

which has been exploited in the last step of the reformulation in (3.92). The Dirac distribution now correponds to a line source term in the mass balance of the 3D domain leading to the aforementioned singularity.

In the following, the general notation

$$\delta_{\Lambda_t/\partial\mathcal{D}_t}\,{}^{(i)\hat{v}\to(i)l}M \tag{3.95}$$

will be employed to refer to the 1D-3D mass transfer terms in the IF balance of (fluid or species) mass. Depending on which variant for 1D-3D coupling is applied, it refers either to lateral surface coupling according to (3.88) or centerline coupling with the approximation (3.92). In Appendix A.1, both variants are further compared for an academic example and classified w.r.t. previous approaches.

3.4.4 Governing Equations in 3D Porous Medium Domain

The surrounding three-dimensional tissue into which the vasculature is embedded is still modeled with the avascular multiphase tumor growth model of Section 3.2. The only required modifications are the transcapillary exchange terms of fluid and species mass which represent a mass

transfer from the 1D embedded vasculature into the 3D tissue domain or, more precisely, into the IF as described in Section 3.4.3. These adaptations are presented in this section.

As for the avascular model, the set of phases

$$\mathfrak{I}_p = \{s, t, h, l\} \tag{3.96}$$

comprises four different phases. These are the ECM (indicated as s) and the three fluid phases in its pores, namely, TCs t, HCs h and the IF l. They form the set

$$\mathfrak{I}_\varepsilon = \mathfrak{I}_\mathrm{f} = \{t, h, l\}, \tag{3.97}$$

which for this case is again equal to the set of fluid phases $\mathfrak{I}_\mathrm{f}$ in the multiphase porous medium.

3.4.4.1 Governing Equations for the Fluid Phases

For tumor and host cells, the equations are adopted unchanged from the avascular model of Section 3.2. Hence, the mass balance equation (3.20) with incompressible fluid and solid phases for $f = t, h$ is the governing equation for each of these phases. For the IF, the major modification due to the coupling with the one-dimensional blood flow model is the additional transvascular mass exchange $\delta_{\Lambda_t/\partial\mathcal{D}_t}\overset{\hat{v}\to l}{M}$ from (3.95). As discussed in Section 3.4.3, for the two different coupling concepts it is scaled with the Dirac measure on the centerline of the embedded vasculature or on its lateral surface. Thus, the balance of mass of the IF is given by

$$\varepsilon \sum_{\beta\in\mathfrak{I}_\varepsilon} \frac{\partial S^l}{\partial \psi^\beta} \left.\frac{\partial \psi^\beta}{\partial t}\right|_{\boldsymbol{X}} + S^l \boldsymbol{\nabla}\cdot\boldsymbol{v}^s - \boldsymbol{\nabla}\cdot\left(\frac{\boldsymbol{k}^l}{\mu^l}\sum_{\beta\in\mathfrak{I}_\varepsilon}\frac{\partial p^l}{\partial\psi^\beta}\boldsymbol{\nabla}\psi^\beta\right) = \frac{\sum_{\kappa\in\mathfrak{I}_{cl}}\overset{\kappa\to l}{M}}{\rho^l} + \delta_{\Lambda_t/\partial\mathcal{D}_t}\frac{\overset{\hat{v}\to l}{M}}{\rho^l} \quad \text{in } \Omega_t \tag{3.98}$$

where the additional source term (3.95) due to an outflow of fluid from the vascular network into the IF has been added to the right hand side. Apart from that, it is identical to equation (3.20) for a generic fluid phase $f \in \mathfrak{I}_\varepsilon$ with primary variable ψ^f under the assumption of incompressible solid and fluid phases and without mass transfer to the solid phase. As for the avascular model, the governing equation for the IF is obtained by summing up the balance of mass of all involved fluid phases $f \in \mathfrak{I}_\varepsilon$ which results in

$$\boldsymbol{\nabla}\cdot\boldsymbol{v}^s - \sum_{\gamma\in\mathfrak{I}_\varepsilon}\left(\boldsymbol{\nabla}\cdot\left(\frac{\boldsymbol{k}^\gamma}{\mu_\gamma}\sum_{\beta\in\mathfrak{I}_\varepsilon}\frac{\partial p^\gamma}{\partial\psi^\beta}\boldsymbol{\nabla}\psi^\beta\right)\right) = \sum_{\gamma\in\mathfrak{I}_\varepsilon}\left(\frac{\sum_{\kappa\in\mathfrak{I}_{c\gamma}}\overset{\kappa\to\gamma}{M}}{\rho^\gamma}\right) + \delta_{\Lambda_t/\partial\mathcal{D}_t}\frac{\overset{\hat{v}\to l}{M}}{\rho^l} \quad \text{in } \Omega_t\times[t_0, t_e]\,. \tag{3.99}$$

This equation is again equivalent to the one of the avascular model (3.23) without mass transfer to the solid phase and incompressible solid and fluid phases. Only the 1D-3D mass transfer term is additionally present as a (line or surface) source term.

Remark 3.11. *Theoretically, one could also consider mass exchange from the 1D embedded vasculature to all involved fluid phases and not only to the IF. The right hand side of the 1D blood flow equation* (3.79) *would then contain the sum over all phases exchanging mass with the 1D vasculature instead of only mass exchange with the IF. The counterpart in the right hand*

side of a generic fluid phase $f \in \mathfrak{I}_\mathrm{f}$ would comprise an additional term $\delta_{\Lambda_t/\partial\mathcal{D}_t} \frac{1}{\rho^f} \overset{\hat{v}\to f}{M}$ as in the mass balance of the IF (3.98) and the summed-up equation (3.99) would also contain the sum of the 1D-3D exchange terms $\delta_{\Lambda_t/\partial\mathcal{D}_t} \sum_{\gamma\in\mathfrak{I}_\varepsilon} \left(\frac{1}{\rho^\gamma} \overset{\hat{v}\to\gamma}{M} \right)$. The actual implementation of the 1D-3D coupled model is capable of such exchange terms to all fluid phases but they are not considered here since they are not present and also not biophysically relevant.

3.4.4.2 Governing Equations for the Solid Phase

The governing equation for the solid phase is adopted from the avascular model as it is assumed that the presence of the embedded vascular network does not influence the deformation of the ECM. Consequently, it is given by the balance of momentum of the solid phase (3.27) with the definition of the solid pressure (3.24) of the avascular model. Furthermore, the Saint-Venant-Kirchhoff material law or the Neo-Hooke material law as given in Section 2.3.2.2 are applied as material models.

3.4.4.3 Governing Equations for Species Transport

The governing equation for species transport of a generic species i in a fluid phase $f \in \mathfrak{I}_\varepsilon$ has been defined in Section 3.2.3 by equation (3.28). For species in tumor and host cells, for which no transvascular exchange is present, this balance of species mass still holds. As elaborated in Section 3.4.3, species in the 1D vasculature, such as drugs or oxygen, can pass through the blood vessel wall from the embedded manifold Λ_t into the IF. This enters the species mass balance as an additional species mass transfer term scaled with Dirac measure $\delta_{\Lambda_t/\partial\mathcal{D}_t}$ on the 1D manifold Λ_t or on its lateral surface $\partial\mathcal{D}_t$:

$$\begin{aligned} &\varepsilon S^l \left.\frac{\partial \omega^{i\bar{l}}}{\partial t}\right|_{\boldsymbol{X}} - \frac{\boldsymbol{k}^l}{\mu^l} \boldsymbol{\nabla} p^l \cdot \boldsymbol{\nabla} \omega^{i\bar{l}} - \boldsymbol{\nabla} \cdot \left(\varepsilon S^l \boldsymbol{D}^{il}_{\mathrm{eff}} \boldsymbol{\nabla} \omega^{i\bar{l}} \right) = \\ &\quad \frac{1}{\rho^l} \left(\sum_{\kappa\in\mathfrak{I}_{\mathrm{cl}}} \overset{i\kappa\to il}{M} + \varepsilon^l r^{il} - \omega^{i\bar{l}} \sum_{\kappa\in\mathfrak{I}_{\mathrm{cl}}} \overset{\kappa\to l}{M} + \delta_{\Lambda_t/\partial\mathcal{D}_t} \cdot \left(\overset{i\hat{v}\to il}{M} - \omega^{i\bar{l}} \overset{\hat{v}\to l}{M} \right) \right) \qquad \text{in } \Omega_t \times [t_0, t_e]\,. \end{aligned} \tag{3.100}$$

Therein, the term $\delta_{\Lambda_t/\partial\mathcal{D}_t} \overset{i\hat{v}\to il}{M}$ is the aforementioned transvascular species exchange which is the counterpart of the right-hand side term in the 1D species mass balance equation (3.80). The second term scaled with the Dirac measure arises when applying the product rule on the temporal derivative of species mass as in (2.27). Then, the balance of mass of the IF, which now additionally contains the 1D-3D mass transfer term, can again be identified and brought to the right hand side.

Remark 3.12. *In principle, the computational framework is also capable of 1D-3D mass exchange to species in all other phases and not only species in the IF. The respective 1D-3D mass transfer terms can simply be added to the balance of mass of these species.*

3.4.5 Closure Relations and Constitutive Equations

Unchanged Closure Relations and Constitutive Equations for the 3D Multiphase Porous Medium System Pressure-saturation relationships, permeability tensors, viscosities and diffusivity tensors for TCs, HCs and IF as well as the calculation of the ECM porosity are adopted from the avascular model, see Section 3.2.4.

Vascular Network Remodeling via a Blood Vessel Diameter Adaptation and Collapse Model As described above, tumors are greatly influenced by the vasculature which provides them with nutrients and offers a pathway for metastasis. Vice versa, the vascular network is dynamically remodeled by the growing tumor by means of multiple mechanical and chemical stimuli. In the present model, this is included via a constitutive model for blood vessel diameter adaptation which will be introduced after a short recapitulation of the mechanisms involved in tumor vasculature remodeling. The current methodology for blood vessel diameter adaptation is partly based on preliminary work in the Master's thesis of Plöckl [195].

The most prominent example of vasculature remodeling by the growing tumor is angiogenesis as described in Section 3.3. However, this is not included in the framework for blood vessel adaptation employed hereafter as the neovasculature formed by this process is always treated in a homogenized way either in the variant with homogenized vasculature from Section 3.3 or in the variant with hybrid representation of the vasculature from Section 3.5. Here, other equally important physical phenomena affecting the blood vessel diameter by remodeling of the vascular network are addressed. For a more detailed review of blood vessel remodeling during tumor growth, the reader is referred to the abundant literature on this topic, e.g. [132, 154, 205, 216].

The concrete consequences of this remodeling are vessel *dilation* (circumferential growth), *regression*, *pruning* and *collapse* affecting the morphological and hydrodynamic properties of the initial network and transforming it into a tumor-specific vasculature [276] with the aforementioned irregularities. Via spatio-temporal changes of blood flow parameters, oxygen/nutrient supply and growth factor concentration fields an interdependence of tumor growth and vascular remodeling emerges.

As mentioned above, several growth factors are involved in angiogenesis leading not only to sprouting angiogenesis but also dilation [70] especially towards the interior of the tumor resulting in thicker vascular branches there [64]. A further important aspect in the structural adaptation of the micro-vasculature is the response to blood flow and the generated wall shear stress inside the vessels [204]. Endothelial cells lining the blood vessels may sense the mechanical stresses [10] and enlarge the vessel diameter if blood flow increases and, vice versa, decrease the diameter if blood flow reduces to obtain optimal flow conditions [205]. A further important remodeling process is blood vessel regression. It may occur during co-opting tumor growth patterns where an initial tumor grows along pre-existing vessels. Via molecular signaling these vessels are destabilized and regress [291, 296]. "Trimming" respectively regression of entire vascular branches is termed pruning [132, 205]. This can again depend on hemodynamic forces induced by blood flow evoking regression of the least blood flow-carrying vessels. However, also too high oxygenation by a too dense vascular network might lead to a removal of redundant sub-networks. A further factor influencing the blood vessel diameter is tumor growth-induced solid stress which compresses or even collapses the blood vessels embedded in tumors [236, 249]. As argued by Padera et al. [187], this *blood vessel compression* is not due to the elevated IF pressure inside

tumors, which is lower or at most equal to blood pressure, but due to compressive forces exerted by the growing tumor, which may reach much higher values [249]. All these effects are interrelated and their study in tumors is further complicated by their abnormal structure and blood flow patterns. For instance, it is conceivable that a specific vascular segment is collapsed by the growing tumor or starts to regress. Hence, blood flow is decreased or even completely inhibited leading to further regression and pruning of neighbouring blood vessels.

Two comprehensive reviews of the numerous mathematical models for vascular remodeling were performed by Rieger and Welter [216] and Scianna et al. [227]. Here, a few important contributions are further singled out. Pries et al. [204] considered remodeling based on wall shear stress induced by flow inside the network and transmural pressure and included further stimuli based on the local metabolic conditions in [206]. Similarly, vessel remodeling depending on wall shear stress, intravascular pressure, hematocrit and hydrostatic-induced vessel collapse was included by Wu et al. [287, 288]. Remodeling of capillary radius, wall thickness and pore size was incorporated by Vavourakis et al. [261, 262]. In addition, blood vessel collapse above a certain pressure threshold was considered. A model with vessel remodeling based on VEGF concentration and collapse according to a pressure threshold value was designed by Cai et al. [34]. An integrative framework for vascular remodeling including angiogenesis as well as vessel regression, dilation, and collapse during tumor progression was developed in the works of [82, 216, 217, 276–279].

In this thesis, an empirical model combining the separate influences into a single equation is employed. Vessel growth is neglected and only radial constriction is allowed. Thereby, the blood vessel diameter at a time step $n+1$ is calculated according to

$$D_{t,n+1} = D_0 \cdot \tilde{H}\left(S^t_{\text{crit}}\left(D_0\right) - S^t\right) + f_{\text{coll}} \cdot D_{t,n} \cdot \tilde{H}\left(S^t - S^t_{\text{crit}}\left(D_0\right)\right) \tag{3.101}$$

from the initial blood vessel diameter D_0 at the start of the simulation and the blood vessel diameter from the previous time step $D_{t,n}$. $\tilde{H}(\bullet)$ again denotes a smoothed approximation of the Heaviside function. If the TC saturation at the location of the blood vessel, i.e., at a specific point at its centerline is below a critical saturation S^t_{crit}, the diameter remains unaffected and equal to the initial blood vessel diameter. If, however, the saturation is higher than the critical saturation, the second summand becomes active and the diameter is decreased by a factor of $f_{\text{coll}} < 1$ from the diameter of the previous time step $D_{t,n}$. The critical saturation depends on the initial diameter of the blood vessel via

$$S^t_{\text{crit}}\left(D_0\right) = \frac{S^t_{\text{max}} - S^t_{\text{min}}}{D_{\text{max}} - D_{\text{min}}} \cdot \left(D_0 - D_{\text{min}}\right) + S^t_{\text{min}} \tag{3.102}$$

with the four parameters D_{min}, D_{max}, S^t_{min} and S^t_{max}. Thus, initially thicker vascular branches can sustain higher TC saturations before they are affected by the growing tumor since the critical saturation, above which collapse sets in, increases linearly. Finally, it is assumed that blood vessels whose diameter falls below a certain threshold $D_{\text{coll-thresh}}$ are entirely collapsed:

$$D_{t,n+1} < D_{\text{coll-thresh}} \longrightarrow \text{collapsed} \tag{3.103}$$

In Section 4.3.3.3, more details on the actual realization of this approach in the numerical framework will be given. Note that it has so far only been included for the centerline-coupled variant. In summary, the proposed relationship leads to blood vessel diameter decrease depending solely

on the TC saturation and the initial diameter. Thus, the single effects described above are not treated separately as in the more complex models listed above. As will be demonstrated in Section 5.5, this rather simple approach already allows a physiologically sensible behaviour leading to blood vessel regression and pruning as the tumor grows.

Remark 3.13. *The implementation of the blood vessel adaptation model is more flexible than described in the preceding paragraphs. Actually, the dependency of the diameter can be provided as a generic functional relationship of the form*

$$D_{t,n+1} = f_{\text{adap}}\left(D_0, D_{t,n}, \boldsymbol{p}^{[t,h,l]}, \boldsymbol{S}^{[t,h,l]}, \varepsilon, p^{\hat{v}}\right) \tag{3.104}$$

depending on phase pressures and saturations, the ECM porosity and blood pressure inside the embedded vasculature [195]. Thus, more complex realizations of blood vessel diameter adaptation, for instance, depending on the wall shear stress or the pressure difference between blood and tumor pressure as in the models cited above are easily possible to refine the approach.

Blood Viscosity Due to the presence of red blood cells, non-continuum phenomena occur in blood flow. The tendency of red blood cells to migrate away from the vessel walls towards the center causes the *Fahraeus-Lindqvist effect* leading to a decline of the apparent viscosity of blood in smaller vessels [240]. Thus, the apparent blood viscosity $\mu^{\hat{v}}$ in general depends on hematocrit (the volume percentage of red blood cells in blood) and the blood vessel diameter.

A number of empirical relationships depending on these two parameters was derived from experiments, see e.g. [201, 203]. Here, the one by developed by Pries and Secomb [201] is reused. Another important aspect is red blood cell flux partitioning [240]: At diverging bifurcations this leads to higher hematocrit values in the branches with higher flow. Recently, it was also studied via a numerical model that the abnormal morphology of tumor vasculature with many bifurcations leads to disruption of red blood cell flux which further causes heterogeneous oxygen distributions in tumors [20]. However, such insight can only be obtained by resolving the red blood cells as particles transported with the flow. This is impractical at the temporal and spatial scale of interest in this thesis. Thus, the hematocrit distribution is not explicitly modeled but it is set to a fixed value of 0.45 as in [252] such that blood viscosity depends on the blood vessel diameter alone. Alternatively, blood viscosity can be assumed constant in the current framework.

3.4.6 Summary and Variants of the Model

In summary, the governing equations of the tumor growth model with discrete representation of the vasculature are the balance of mass of blood in the 1D embedded vasculature (3.79), the mass balances of TCs ((3.20) with $f = t$) and HCs ((3.20) with $f = h$), the sum of the mass balances of TCs, HCs and IF (3.99), the balance of momentum of the solid phase (3.27) and the balance of species mass for species in TCs, HCs (3.28), IF (3.100), and in the embedded vasculature (3.84).

As for the previously presented models, a variant of the vascular model with discrete vasculature emerges when the balance of momentum of the solid phase is disregarded. This again leads to a significant simplification of the model. As described in Section 3.2.5, the ALE formulation for the 3D tissue domain becomes obsolete. For the 1D-3D coupling introduced in this section further simplifications arise: Also the ALE formulation of the 1D domain becomes a Eulerian

one with fixed 1D domain Λ_0. The velocity divergence term in the 1D balance of mass (3.79) cancels as well. Finally, the 1D-3D exchange terms can be evaluated with Dirac measure $\delta_{\Lambda_0/\partial\mathcal{D}_0}$ defined on the 1D reference configuration respectively its lateral surface.

3.5 The Vascular Tumor Growth Model with a Hybrid Embedded/Homogenized Representation of the Vasculature

In the previous sections, two different concepts for incorporating the vasculature into the present tumor growth model were discussed, namely, a homogenized and a discrete embedded approach. In this section, a third variant, with a hybrid embedded/homogenized representation of the vasculature is introduced. This approach was coined in the author's publications [136, 137], from which major parts of the following sections have been taken.

The rationale behind such hybrid models of the vasculature, which have concurrently also been developed by Kojic et al. [128], Köppl et al. [130] and Shipley et al. [242] for less complex tissue perfusion problems, is that only the larger blood vessels have to be explicitly resolved while the smaller scales of the vasculature are homogenized. Compared to pure homogenized formulations, their advantage is that the structure of the larger vessels is retained. Therefore, the heterogeneity of blood flow and pressure in the major vessel branches is better represented. Moreover, compared to discrete models, less anatomic data is needed since the morphology of the smallest vessels is not required. This could also have the additional advantage of a smaller computational cost and make them applicable to larger domains. Also quantities typically needed for validation such as tissue perfusion, blood flow or pressures at the resolution of current imaging techniques can equally be acquired from hybrid models. In Chapter 6, the developed hybrid approach will be used to study tissue perfusion through solid tumors. Additional details are presented there. Here, the focus lies on the incorporation of this approach into the entire tumor growth framework. The general concept is sketched in Figure 3.9. Compared to the fully-resolved variant of Figure 3.5, now only the larger vessels are resolved and embedded as 1D inclusions into the porous medium domain. The smaller vessels are homogenized and represented as an additional porous network in the ECM as in the variant with homogenized representation of the vasculature from Figure 3.4. Thus, the hybrid variant may be understood as a combination of these two approaches as already preempted in the overview of the different models of Figure 3.1.

In the context of tumor growth modeling, one possible application is to study angiogenesis originating from pre-existing vessels. For that case, the resolved, larger 1D vessels correspond to the pre-existing vessel network and the homogenized vasculature to the neovasculature formed by angiogenesis. The reason why such a combined approach may be favourable over a full resolution of pre-existing and neovasculature is the abnormal structure and mechanics of tumor neovasculature. It is well-established that tumor-induced angiogenesis results in a tortuous, dilated blood vessel network with variable vessel lengths and diameters and without the usual vascular hierarchy of arterioles, capillaries and venules [12, 36]. This causes highly heterogeneous blood flow [116]. While, at first sight, discrete models such as the ones introduced in the previous section [58, 157, 160, 185, 216, 245, 267, 276–279, 287] seem to offer more insight into the formation of the specific network and its structure, this can and should also be challenged. It ap-

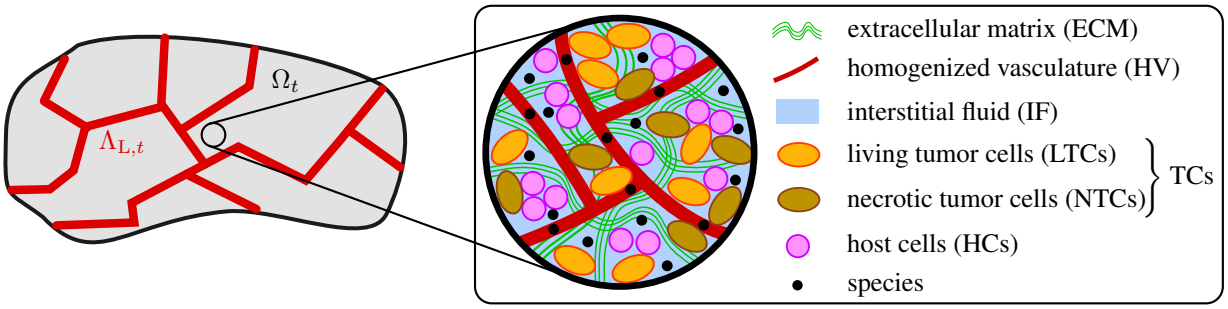

Figure 3.9: Sketch of vascular tumor growth model with hybrid embedded/homogenized representation of vasculature – embedded 1D vasculature $\Lambda_{\mathrm{L},t} \subset \Omega_t$ (corresponding to larger vessels) is sketched on the left and components of the vascular 3D multiphase model on the right with solid phase (ECM), additional porous network (HV, corresponding to smaller vessels), three fluid phases (TCs, HCs, IF) in the pores of the ECM, NTCs (species of TCs) and generic species (both in HV and other phases).

pears virtually impossible to resolve the complex morphology of the network and the full spatial and temporal heterogeneity of blood flow inside tumors where almost no relationship between vessel diameter and flow velocity is present [60, 61]. Furthermore, it is more than questionable if a fully-resolved blood vessel network offers more information on the actual quantities of interest especially when considering the inherently stochastic nature of angiogenesis and tumor vasculature remodeling which precludes predicting the specific *in-vivo* network topology. Relevant quantities which could be obtained from *in-silico* models and can actually be acquired through imaging are microvascular densities, hotspots of vascularization or very badly vascularized regions inside the tumor and averaged transport properties to detect hypoxic and drug resistant areas [207, 299]. To obtain this information from resolved models averaging over several different simulations is necessary [277]. Therefore, a hybrid approach integrating a homogenized or smeared representation of the neovasculature and a full resolution of the larger vessels, for which information about structure and blood flow might be available, is a very promising alternative, which combines the advantages of both methods.

In the subsequent sections, the governing equations of the hybrid variant will be introduced based on the previously developed models. For the discrete part of the vascular network, the 1D governing equations are re-used and for the surrounding 3D tissue domain including the smaller, homogenized vessels, the ones of the variant with porous medium representation of the vasculature. A special focus lies on the coupling between 1D embedded and 3D homogenized representation of the vasculature. In Section 3.5.3, a constraint of matching blood pressure respectively mass fraction is formulated to couple both domains along the centerline of the inclusion or on its lateral surface, again, enabling non-matching 1D and 3D grids.

3.5.1 Governing Equations for Blood Flow and Species Transport in 1D Vasculature Domain

The governing equations in the one-dimensional embedded vasculature domain which now corresponds to the resolved portion of the vasculature, i.e., the larger vessels, remain unchanged

w.r.t. the discrete model introduced in Section 3.4.2. Thus, blood flow in the 1D domain is still governed by equation (3.79) and species transport in the 1D domain by (3.84). Also the respective mass transfer terms into the IF are inherited. The 1D-3D coupling with the porous medium representation of the vasculature is achieved via a pressure or species mass fraction constraint as detailed in Section 3.5.3. Enforcing this constraint by suitable coupling methods leads to a further 1D-3D (species or fluid) mass transfer term between the two representations of the vascular network, see Sections 4.3.1.3 and 4.3.3.2.

3.5.2 Governing Equations in 3D Porous Medium Domain

The three-dimensional domain in the hybrid model corresponds to the vascular model including the homogenized representation of the vasculature forming an additional porous network as presented in Section 3.3. The only difference is that the HV now represents only the smaller vessels and not the entire vasculature, of which a part, namely, the larger vessels, is resolved. Consequently, the set of all phases is again given by

$$\mathfrak{I}_p = \{s, t, h, l, v\} \tag{3.105}$$

with the ECM (solid phase), TCs, HCs, the IF and the homogenized part of the vasculature (respectively blood therein). Four fluid phases

$$\mathfrak{I}_\mathrm{f} = \{t, h, l, v\}. \tag{3.106}$$

are defined. TCs, HCs and IF are present in the pores of the ECM and collected in the phase set

$$\mathfrak{I}_\varepsilon = \{t, h, l\}. \tag{3.107}$$

In the following, the modifications of the governing equations of the vascular tumor growth model with homogenized representation of the vasculature due to the hybrid modeling approach with the presence of an embedded one-dimensional vascular network are described.

3.5.2.1 Governing Equations for the Fluid Phases

Homogenized Vasculature The governing equations for the smaller, homogenized vessels are the balance of mass of blood (3.47) and the evolution equation (3.51) of the vascular model from Section 3.3. Hence, the primary variables are again the vascular volume fraction ε^v (now only representing the smaller vessels) and the blood pressure p^v therein. The coupling with the resolved embedded part of the vasculature is formulated as a constraint between blood pressure p^v in the 3D homogenized compartment and blood pressure $p^{\hat{v}}$ in the 1D resolved compartment in Section 3.5.3. As will be shown in Sections 4.3.1.3 and 4.3.3.2 this enters the balance of mass of blood (3.47) as a 1D-3D mass transfer term between the discrete embedded part of the vasculature and the homogenized part of the vasculature. Apart from that, the equations and specifically the evolution equation (3.51) are not affected.

Tumor Cells, Host Cells and Interstitial Fluid The governing equations for tumor and host cells are also taken from the homogenized vascular model of Section 3.3. Therefore, they are the fluid mass balance equations (3.55) evaluated for $f = t, h$. However, due to the presence of the 1D embedded blood vessel network with the corresponding 1D-3D exchange, the balance of mass of the IF has to be adapted. Its governing equation is given by

$$\varepsilon \sum_{\beta \in \mathfrak{I}_\varepsilon} \frac{\partial S^l}{\partial \psi^\beta} \left. \frac{\partial \psi^\beta}{\partial t} \right|_{\boldsymbol{X}} - S^l \left. \frac{\partial \varepsilon^v}{\partial t} \right|_{\boldsymbol{X}} + S^l (1 - \varepsilon^v) \boldsymbol{\nabla} \cdot \boldsymbol{v}^s - \boldsymbol{\nabla} \cdot \left(\frac{\boldsymbol{k}^l}{\mu^l} \sum_{\beta \in \mathfrak{I}_\varepsilon} \frac{\partial p^l}{\partial \psi^\beta} \boldsymbol{\nabla} \psi^\beta \right) = \frac{\sum_{\kappa \in \mathfrak{I}_{cl}} \overset{\kappa \to l}{M}}{\rho^l} + \delta_{\Lambda_t / \partial \mathcal{D}_t} \frac{\overset{\hat{v} \to l}{M}}{\rho^l} \quad \text{in } \Omega_t \times [t_0, t_e] \tag{3.108}$$

under the assumption of incompressible solid and fluid phases. This is simply the balance of fluid mass (3.55) of the vascular model with homogenized vasculature plus the 1D-3D mass transfer term from embedded vasculature into IF scaled with the Dirac delta measure $\delta_{\Lambda_t / \partial \mathcal{D}_t}$. Alternatively, it may be interpreted as the balance of mass of the IF of the vascular model with discrete vasculature as derived in (3.98) with additional terms due to the presence of the homogenized vasculature. These terms are introduced via the time derivative of the ECM porosity (3.53). This equation nicely illustrates how the hybrid model can be understood as a combination of the avascular model with both discrete and homogenized vasculature as sketched in Figure 3.1. Once more, the balance of mass of the IF enters the system of equations via the sum of the balances of mass of TCs, HCs and IF, which is

$$- \left. \frac{\partial \varepsilon^v}{\partial t} \right|_{\boldsymbol{X}} + (1 - \varepsilon^v) \boldsymbol{\nabla} \cdot \boldsymbol{v}^s - \sum_{\gamma \in \mathfrak{I}_\varepsilon} \left(\boldsymbol{\nabla} \cdot \left(\frac{\boldsymbol{k}^\gamma}{\mu_\gamma} \sum_{\beta \in \mathfrak{I}_\varepsilon} \frac{\partial p^\gamma}{\partial \psi^\beta} \boldsymbol{\nabla} \psi^\beta \right) \right) = \sum_{\gamma \in \mathfrak{I}_\varepsilon} \left(\frac{\sum_{\kappa \in \mathfrak{I}_{c\gamma}} \overset{\kappa \to \gamma}{M}}{\rho^\gamma} \right) + \delta_{\Lambda_t / \partial \mathcal{D}_t} \frac{\overset{\hat{v} \to l}{M}}{\rho^l} \quad \text{in } \Omega_t \times [t_0, t_e]\,. \tag{3.109}$$

In summary, the governing equations for TCs, HCs and IF in the hybrid model are equation (3.108) evaluated for TCs and HCs and the summed-up mass balance (3.109).

3.5.2.2 Governing Equations for the Solid Phase

The governing equation for the solid phase is adopted from the vascular model with homogenized representation of the vasculature. Consequently, it is given by the balance of momentum of the solid phase (3.60) with the definition of the solid pressure (3.57) of the vascular model. The Saint-Venant-Kirchhoff or the Neo-Hooke material law as given in Section 2.3.2.2 are applied for the ECM.

3.5.2.3 Governing Equations for Species Transport

The governing equations for the balance of species mass in the fluid phases of the 3D porous medium system may again be derived from the generic species mass balance (2.64). For TCs

and HCs the respective equations follow by setting $\varepsilon^f = \varepsilon S^f, \ f = t, h$, i.e., they are equivalent to (3.28). For the IF, the balance of species mass is identical to the one of the model with discrete embedded vasculature, that is, equation (3.100) including the additional 1D-3D exchange terms. For species transport in the homogenized part of the vasculature, the governing equation is the same as the one of the vascular model with homogenized vasculature from Section 3.3.3, i.e., equation (3.63). The only adaptation is the coupling to the 1D embedded blood vessel network which will be realized via a constraint of matching species mass fractions in Section 3.5.3. Similar to the coupling of blood flow between the two domains, this will result in an additional 1D-3D species mass transfer term between resolved and homogenized vasculature as will be shown in Sections 4.3.1.3 and 4.3.3.2.

3.5.3 Coupling between 1D Embedded and 3D Homogenized Representation of the Vasculature

The main novelty of the vascular model with hybrid representation of the vasculature is the partitioning of the vasculature into a part which is resolved via a 1D embedded discretization as in the discrete model from Section 3.4 and a part which is homogenized and represented as an additional porous network in the ECM as in the continuum model from Section 3.3. The remaining question is how to couple blood flow and species transport between these two descriptions of the vasculature. In analogy to mesh tying in solid mechanics, a non-conforming coupling between blood flow and species transport in embedded and homogenized vasculature was proposed by Kremheller et al. [136]. This approach aims to reproduce the fact that the pressure or mass fraction in a smaller vessel branching from a larger vessel at a specific location is equal to the pressure or mass fraction in the larger vessel at this location. In the hybrid model, such smaller vessels are homogenized and, thus, removed from the 1D representation. However, blood pressure and species mass fraction in both representations of the vasculature still have to be equal along the 1D vessel domain. Therefore, the constraint to interconnect the two domains may be formulated as

$$g = \varphi^{\hat{v}}\left(s,t\right) - \varphi^{v}\left(\boldsymbol{x}\left(s\right),t\right) = 0 \qquad \text{on} \ \ \Lambda_t \tag{3.110}$$

with

$$\varphi^{\hat{v}} = p^{\hat{v}} \ \ \text{and} \ \ \varphi^{v} = p^{v} \tag{3.111}$$

for coupling of blood flow or

$$\varphi^{\hat{v}} = \omega^{i\,\hat{v}} \ \ \text{and} \ \ \varphi^{v} = \omega^{i\,\overline{v}} \tag{3.112}$$

for coupling of species transport. Herein, a "gap" g between blood pressures or species mass fractions of species i in blood in the 1D domain w.r.t. the 3D domain has been introduced. This pressure or species mass fraction difference has to vanish in order to couple blood flow and species transport in the embedded blood vessels with the porous medium representation of the vasculature. Note that the primary variable for blood flow or species transport of the 3D domain in the definition of the gap has been projected on the centerline of the embedded vasculature via the approximation (3.90). Hence, this formulation is identical to the coupling variant termed centerline coupling from Section 3.4.3. Alternatively, it is possible to define the constraint on the lateral surface of the embedded vasculature as

$$g = \varphi^{\hat{v}}\left(s,t\right) - \varphi^{v}\left(\boldsymbol{x}\left(s,\gamma\right),t\right) = 0 \qquad \text{on} \ \ \partial\mathcal{D}_t. \tag{3.113}$$

It couples blood pressure or species mass fractions in the 1D domain, which are constant across the diameter, with blood pressure and species mass fraction in the homogenized vasculature evaluated on the lateral surface of the inclusion. This variant is analogous to lateral surface coupling. Blood flow in the vasculature on Λ_t is governed by equation (3.79), while the corresponding equation for the homogenized vasculature in Ω_t is equation (3.47). The two domains are coupled via the constraint (3.110) respectively (3.113). The same holds for species transport in the pre-existing vasculature (3.84) and in the homogenized vasculature, which is equation (3.63). In Section 4.3.1.3 it will be elaborated how to enforce this coupling between the two distinct domains with two penalty-based methods, a Gauss-point-to-segment (GPTS) or a mortar penalty (MP) approach. Effectively, both approaches result in additional (species or fluid) mass transfer terms between the 1D embedded representation of the vasculature and the 3D homogenized representation of the vasculature.

Remark 3.14. *The non-conforming coupling between the embedded 1D and the homogenized 3D representation of the vasculature* (3.110) *respectively* (3.113) *is enforced along the entire network of 1D embedded vessels. If only the pre-existing vasculature is resolved and the neovasculature formed by angiogenesis is homogenized, this allows modeling of angiogenesis. This process is initiated laterally from a pre-existing blood vessel through angiogenic sprouting followed by growth radially away from the pre-existing vessel and subsequent network formation [19]. In Section 5.6 it will be demonstrated how angiogenesis can be triggered from the pre-existing vessel with the proposed method. In alternative hybrid approaches [128, 130, 242], the coupling between resolved and homogenized vasculature was realized at the free ends of the larger vessels, i.e., as an outflow at the tips of the 1D discretization into the homogenized 3D vasculature domain. This was also due to the fact that the employed data sets had a clear vascular architecture of larger arterioles and venules and smaller capillaries such that the split into larger and smaller vessels was performed with a radius-based criterion. Such an approach is unfeasible due to the irregular, chaotic and heterogeneous distribution of the radii in tumor vascular networks and as a clear connectivity between larger and smaller vessels at specific points is lacking from corresponding imaging data [150]. Thus, a coupling along the entire resolved blood vessel network is advantageous as further elaborated in Chapter 6 where this hybrid variant is employed to study tissue perfusion through solid tumors.*

3.5.4 Closure Relations and Constitutive Equations

Unchanged Closure Relations for the Embedded Vasculature The blood vessel diameter adaptation and collapse model defined by (3.101)-(3.103) and the empirical blood viscosity relationship may be applied for the part of the vascular network which is resolved and embedded as a 1D network.

Unchanged Closure Relations and Constitutive Equations for the 3D Multiphase Porous Medium System Including Homogenized Vasculature Pressure-saturation relationships, permeability tensors, viscosities and diffusivity tensors for TCs, HCs and IF are adopted from the avascular model, see Section 3.2.4. The calculation of the ECM porosity is equivalent to the homogenized vascular model from Section 3.3.4. Also the closure relations for

	Solid[a]	Fluid					Species in				
model type		TCs	HCs	IF	HV	1D	Solid[b]	TCs, HCs	IF	HV	1D
Avascular	(3.27)	(3.20)	(3.20)	(3.23)	–	–	(2.66)	(3.28)	(3.28)	–	–
Homogenized	(3.60)	(3.55)	(3.55)	(3.56)	(3.47),(3.51)	–	(2.66)	(3.28)	(3.28)	(3.63)	–
Discrete	(3.27)	(3.20)	(3.20)	(3.99)	–	(3.79)	(2.66)	(3.28)	(3.100)	–	(3.84)
Hybrid	(3.60)	(3.55)	(3.55)	(3.109)	(3.47)[c],(3.51)	(3.79)[c]	(2.66)	(3.28)	(3.100)	(3.63)[d]	(3.84)[d]

[a] Actually, these equations are identical but differ in the definition of the solid pressure for the avascular variant and the variant with homogenized vasculature, (3.24) and (3.57), respectively.

[b] Species transport in the solid phase is so far only considered for fibronectin in combination with the model with homogenized vasculature. However, in principle, it is also possible for all other versions.

[c] Blood flow in embedded and homogenized vasculature is additionally coupled via the constraint of matching blood pressure (3.110) respectively (3.113) with (3.111).

[d] Species transport in embedded and homogenized vasculature is additionally coupled via the constraint of matching mass fractions (3.110) respectively (3.113) with (3.112).

Table 3.1: Summary and overview of the governing equations of the different model variants

the homogenized part of the vasculature, the functional dependency of the chemotactic coefficient, the constant, isotropic permeability and diffusivity tensor and the model for blood vessel compression and collapse are applied.

3.5.5 Summary and Variants of the Model

In summary, the governing equations of the tumor growth model with hybrid representation of the vasculature are the balance of mass of blood in the 1D resolved portion of the vasculature (3.79), the balance of mass of blood in the homogenized part of the vasculature (3.47), the evolution equation of the vascular volume fraction (3.51), the mass balances of TCs ((3.55) with $f = t$) and HCs ((3.55) with $f = h$), the sum of the mass balances of TCs, HCs and IF (3.109), the balance of momentum of the solid phase (3.60) and the balance of species mass for species in TCs, HCs (3.28), IF (3.100), HV (3.63) and in the embedded vasculature (3.84). In addition the constraint of matching pressure or species mass fractions (3.110) respectively (3.113) couples blood flow and species mass transport in resolved and homogenized vasculature.

Finally, different variants are also possible for the vascular model with hybrid representation of the vasculature. Again, the most straightforward one is to neglect the deformability of the ECM, which simplifies the governing equations to a Eulerian description including the 1D-3D coupling terms for mass transfer and coupling of pressures and species mass fractions between resolved and homogenized part of the vasculature. Additionally, the versions for the homogenized vasculature described in Section 3.3.5 are possible, especially the model with static vasculature and constant vascular volume fraction may be applied.

3.6 Summary of Equations of All Model Types

The different variants of all models described in Sections 3.2.5, 3.3.5, 3.4.6 and 3.5.5 illustrate again that the framework does not comprise only the four different models with the distinct representations of the vasculature and the original avascular model but a whole group of (a-)vascular models with different use-cases depending on the phenomena which have to be included and modeled, for instance, a deformable ECM, a dynamic vasculature with varying vascular volume fractions and/or blood flow and species transport in the homogenized vasculature. Together with

the possibility to specify an arbitrary number of species in all involved phases, this gives an extremely flexible computational framework for modeling (a-)vascular tumor growth.

For easier reference, the governing equations, that is, the balance of momentum of the solid phase, the mass balances of the single fluid phases and the species mass balances of all model variants have been summarized in Table 3.1. If hyperthermia treatment is considered, the energy balance (2.68) is a further governing equation. However, it can currently only be combined with the avascular model and the vascular model with homogenized representation of the vasculature. An integration into a model with discrete vasculature can be found in [177, 178]. As also illustrated via the interrelation of the single models from Figure 3.1, the model with hybrid embedded/homogenized vasculature is the most complex one involving both representations of the vascular network. All other model variants are contained in its governing equations.

4 Computational Solution Approach

This chapter illustrates the numerical and computational approach to solve the coupled system of nonlinear PDEs constituting the tumor growth framework. Time discretization as well as initial and boundary conditions are presented in Sections 4.1 and 4.2. The weak forms of the governing equations of the variant with hybrid embedded/homogenized representation of the vasculature are derived in Section 4.3. This variant is chosen as it is the most general of the group of models introduced in the previous chapter containing both a homogenized and a 1D embedded vasculature. The governing equations of the other variants may be interpreted as special cases of the hybrid one and can be obtained from it. A particular focus is set on the spatial discretization and numerical evaluation of 1D-3D coupling as the arising terms are non-standard and require special integration techniques. Finally, four different algorithms to resolve the coupling between the three present physical fields are proposed in Section 4.4.

4.1 Time Discretization

There exist numerous methods for the time discretization of differential equations, conf. the text book by Quarteroni et al. [210] for a first introduction. Throughout this thesis, the time period of interest $[t_0, t_e]$ is divided into equidistant steps of length Δt. For each time step $n+1$, its discrete time level is then obtained as $t_{n+1} = t_n + \Delta t$ from the time level t_n of the previous time step n. Any present temporal derivatives are approximated by finite difference quotients. In a one-step time integration method, the generic state $y_{n+1} = y(t_{n+1})$ depends only on the value from the previous time step $y_n = y(t_n)$ and not on earlier time instances. Furthermore, *explicit* methods allow for a direct computation of the state at time t_{n+1} from the state of the previous time steps while *implicit* methods require a possibly nonlinear solution step to obtain the new state y_{n+1}. Since implicit time integration methods can be shown to be unconditionally stable and, thus, generally enable relatively large time steps, they are the method of choice here.

4.1.1 One-step-θ-scheme

The sole implicit time integration scheme employed hereafter is the *one-step-θ-scheme*, which is sometimes also referred to as the *generalized trapezoidal rule*. This scheme involves one single scalar parameter $\theta \in [0, 1]$ which determines an intermediate time instant $t_{n+\theta} = (1-\theta)t_n + \theta t_{n+1}$ at which the equations are evaluated. Since inertia terms were neglected due to the long time scales during tumor growth, a first derivative is the highest occurring temporal derivative in all model equations. A general first-order differential equation

$$\dot{y}(t) = f(y(t), t), \tag{4.1}$$

where the common notation of the temporal derivative with a dot has been employed, is discretized as

$$\dot{y}_{n+\theta} = f_{n+\theta}. \tag{4.2}$$

The quantities evaluated at the intermediate time step are given by

$$\dot{y}_{n+\theta} = (1-\theta)\dot{y}_n + \theta\dot{y}_{n+1} \approx \frac{y_{n+1} - y_n}{\Delta t} \tag{4.3}$$

and

$$f_{n+\theta} = (1-\theta)f(y_n, t_n) + \theta f(y_{n+1}, t_{n+1}). \tag{4.4}$$

The temporal derivative has been approximated with a finite difference quotient. Directly solving for the time level $n+1$ yields the more familiar form of the one-step-θ-scheme:

$$y_{n+1} = y_n + (1-\theta)\Delta t \underbrace{f(y_n, t_n)}_{\dot{y}_n} + \theta\Delta t f(y_{n+1}, t_{n+1}). \tag{4.5}$$

Here and in equation (4.4), the right hand side was interpolated at the intermediate time $t_{n+\theta}$. Alternatively, one could also employ the interpolation of the state $y_{n+\theta} = (1-\theta)y_n + \theta y_{n+1}$ to obtain $f_{n+\theta} = f(y_{n+\theta}, t_{n+\theta})$ which would yield a slightly different expression for a nonlinear right hand side. In general, the one-step-θ-scheme is an implicit time integration scheme as the right hand side in equation (4.2) depends on the state at t_{n+1} itself. Only the choice $\theta = 0$ would yield the explicit forward Euler scheme. The implicit backward Euler scheme is obtained for $\theta = 1$. For the choice $\theta = 0.5$ (also termed *Crank-Nicolson scheme* or *trapezoidal rule*), second-order accuracy in time is achieved whereas all other values of θ yield a first-order scheme. Finally, unconditional stability is guaranteed in the range $\theta \in [0.5, 1]$. Consequently, in all numerical examples, θ is chosen from this range.

The governing equations of the tumor growth model are given in ALE formulation. The difficulty which arises in this case is to evaluate time derivatives over moving and temporally changing domains. Robust and accurate time integration schemes for ALE formulations are discussed in [78, 79] with the following requirements to fulfill the so-called *geometric conservation law*:

(i) All spatial integrals have to be evaluated at the same time level.

(ii) The time level to integrate is the one at which the new solution is sought, that is, t_{n+1} for the one-step-θ-scheme.

To obtain the same level of temporal accuracy for the moving mesh scheme as for the non-moving scheme a further condition arises for the grid velocity:

(iii) The temporal discretization of the mesh motion has to have the same temporal order of accuracy as the overall algorithm.

Following this approach, all spatial integrals of the ALE formulation are evaluated at time level t_{n+1} over the domain $\Omega_{t_{n+1}}$ respectively $\Lambda_{t_{n+1}}$. Furthermore, the solid phase velocity which is equivalent to the grid velocity for the porous medium equations in ALE formulation is calculated as

$$\boldsymbol{v}^s_{n+1} = \frac{\boldsymbol{d}^s_{n+1} - \boldsymbol{d}^s_n}{\theta\Delta t} - \frac{1-\theta}{\theta}\boldsymbol{v}^s_n \tag{4.6}$$

at time step t_{n+1} with the solid phase displacements at time t_n and t_{n+1} and the velocity of the previous time step n. This relationship may be obtained from the one-step-θ-scheme (4.3). Thus, second order accuracy can be achieved for the time integration with the choice $\theta = 0.5$.

4.1.2 Time-discrete Form

Based on the considerations from the previous section, the time-discrete form of the governing equations is introduced next. For that, the model with a hybrid embedded/homogenized representation of the vasculature is exemplarily regarded since it is the most general of the group of tumor growth models introduced in Chapter 3. Subsequently, the notation

$$\mathring{\bullet} = \left.\frac{\partial(\bullet)}{\partial t}\right|_{\boldsymbol{X}} \tag{4.7}$$

is applied for time derivatives evaluated for the observer moving with the solid phase.

Tumor Cells, Host Cells and Interstitial Fluid The first governing equation is the balance of mass of tumor and host cells (3.55). For $f = t, h$, the time-discrete form of this equation with primary variable ψ^f is given by

$$\psi^f_{n+1} - \psi^f_n + \Delta t f^f_{n+\theta} = 0 \;\text{ in }\; \Omega_t \tag{4.8}$$

with

$$f^f_{n+\theta} = -(1-\theta)\mathring{\psi}^f_n + \theta f^f_{n+1} \tag{4.9}$$

and

$$f^f_{n+1} = \left[\left(\varepsilon \frac{\partial S^f}{\partial \psi^f}\right)^{-1} \left(\varepsilon \sum_{\beta \in \mathcal{I}_\varepsilon, \beta \neq f} \frac{\partial S^f}{\partial \psi^\beta} \mathring{\psi}^\beta - S^f \mathring{\varepsilon}^v + S^f (1-\varepsilon^v) \boldsymbol{\nabla} \cdot \boldsymbol{v}^s \right.\right.$$
$$\left.\left. - \boldsymbol{\nabla} \cdot \left(\frac{\boldsymbol{k}^f}{\mu^f} \sum_{\beta \in \mathcal{I}_\varepsilon} \frac{\partial p^f}{\partial \psi^\beta} \boldsymbol{\nabla} \psi^\beta \right) - \frac{\sum_{\kappa \in \mathcal{I}_{cf}} \overset{\kappa \to f}{M}}{\rho^f} \right) \right]_{n+1} . \tag{4.10}$$

Note that the previous equation contains the solid phase velocity and temporal derivatives of generic primary variables and vascular volume fraction evaluated at time step $n+1$. The latter ones can be evaluated as in equation (4.6) using the employed time discretization scheme.

The governing equation for the IF is the sum of the mass balance equation given by (3.109). Since this equation is stationary in terms of the primary variable of the IF ψ^l it can simply be evaluated at time step $n+1$ as

$$f^l_{n+1} = \left[-\mathring{\varepsilon}^v + (1-\varepsilon^v) \boldsymbol{\nabla} \cdot \boldsymbol{v}^s - \sum_{\gamma \in \mathcal{I}_\varepsilon} \left(\boldsymbol{\nabla} \cdot \left(\frac{\boldsymbol{k}^\gamma}{\mu_\gamma} \sum_{\beta \in \mathcal{I}_\varepsilon} \frac{\partial p^\gamma}{\partial \psi^\beta} \boldsymbol{\nabla} \psi^\beta \right) \right) - M^l_{\text{rhs}} \right]_{n+1} = 0 \;\text{ in }\; \Omega_t . \tag{4.11}$$

Therein, the different mass transfer terms have been denoted as M^l_{rhs} to achieve a more compact notation.

Homogenized Vasculature The governing equation for blood flow in the homogenized vasculature is the balance of mass of blood (3.47) where no temporal derivative of its primary variable, namely, the homogenized blood pressure p^v occurs. Thus, the time discrete form at time step $n+1$ emerges as

$$f^{p^v}_{n+1} = \left[\mathring{\varepsilon}^v + \varepsilon^v \boldsymbol{\nabla} \cdot \boldsymbol{v}^s - \boldsymbol{\nabla} \cdot \left(\frac{\boldsymbol{k}^v}{\mu^v} \boldsymbol{\nabla} p^v \right) - \frac{\sum_{\kappa \in \mathfrak{I}_{cv}} \overset{\kappa \to v}{M}}{\rho^v} \right]_{n+1} = 0 \ \text{ in } \ \Omega_t \tag{4.12}$$

Remark 4.1. *The time-discrete forms for the IF (4.11) and blood flow in the homogenized vasculature (4.12) are stationary in terms of the primary variable of the respective equation but a temporal derivative of the homogenized vascular volume fraction ε^v is present in both equations. It has to be evaluated at time t_{n+1} which can be done analogously to equation (4.6). After inserting this definition into (4.11) and (4.12), it can alternatively be interpreted as a one-step-θ-scheme similar to (4.8) for ε^v. Hence, only for the avascular model respectively the vascular model with static vasculature, i.e., constant vascular volume fraction, these equations do not contain any temporal contributions.*

The second governing equation of the homogenized vasculature is the evolution equation (3.51) for its volume fraction ε^v. Temporal discretization yields

$$\varepsilon^v_{n+1} - \varepsilon^v_n + \Delta t f^{\varepsilon^v}_{n+\theta} = 0 \ \text{ in } \ \Omega_t \tag{4.13}$$

with

$$f^{\varepsilon^v}_{n+\theta} = -(1-\theta)\mathring{\varepsilon}^v_n + \theta f^{\varepsilon^v}_{n+1} \tag{4.14}$$

and

$$f^{\varepsilon^v}_{n+1} = \Big[\varepsilon^v \boldsymbol{\nabla} \cdot \boldsymbol{v}^s - \boldsymbol{\nabla} \cdot (D^v \boldsymbol{\nabla} \varepsilon^v) + \boldsymbol{\nabla} \cdot \left(\varepsilon^v \varepsilon S^l \chi \left(\omega^{TAF\bar{l}} \right) \boldsymbol{\nabla} \omega^{TAF\bar{l}} \right) + \boldsymbol{\nabla} \cdot \left(\varepsilon^v \varepsilon^s \Theta \boldsymbol{\nabla} \omega^{F\bar{s}} \right) + C_{\text{coll}} \Big]_{n+1}. \tag{4.15}$$

Solid Phase A quasi-static solid phase is assumed in all cases because inertia effects are negligible. Thus, the time-discrete form of the balance of momentum of the solid phase, that is, either equation (3.27) or (3.60) with the respective definitions of the solid pressure (3.24) and (3.57) is simply given by

$$\boldsymbol{f}^s_{n+1} = \left[\boldsymbol{\nabla}_0 \cdot \left(\boldsymbol{F} \cdot \left(\boldsymbol{S}^{\text{eff}} - p^s J \boldsymbol{C}^{-1} \right) \right) \right]_{n+1} = \boldsymbol{0} \ \text{ in } \ \Omega_0 \tag{4.16}$$

at time step t_{n+1}.

Species Transport in Tissue Domain and Energy Balance Species transport may be relevant in all present phases of the model. However, the temporal discretization is only shown generically for a species in a fluid phase $f \in \mathfrak{I}_{\text{f}}$ whose governing equation is (2.64). Temporal discretization yields

$$\omega^{i\bar{f}}_{n+1} - \omega^{i\bar{f}}_n + \Delta t f^{if}_{n+\theta} = 0 \ \text{ in } \ \Omega_t \tag{4.17}$$

with

$$f_{n+\theta}^{if} = -(1-\theta)\mathring{\omega}_n^{i\,\overline{f}} + \theta f_{n+1}^{if} \tag{4.18}$$

and

$$f_{n+1}^{if} = \left[\left(\varepsilon^f\right)^{-1} \left(-\frac{\boldsymbol{k}^f}{\mu^f} \boldsymbol{\nabla} p^f \cdot \boldsymbol{\nabla} \omega^{i\,\overline{f}} - \boldsymbol{\nabla} \cdot \left(\varepsilon^f \boldsymbol{D}_{\text{eff}}^{if} \boldsymbol{\nabla} \omega^{i\,\overline{f}} \right) - M_{\text{rhs}}^{if} \right) \right]_{n+1} . \tag{4.19}$$

The term M_{rhs}^{if} is a compact notation of the mass transfer terms on the right hand side from (2.64). If species transport in the IF including 1D-3D mass transfer is regarded, it comprises additionally the respective terms from equation (3.100). Species transport in the solid phase is governed by equation (2.66). Its temporal derivation follows equivalently as in (4.17)-(4.19) without a convective term. Finally, the time discretization of the enthalpy balance equation in ALE description (2.69) is also straightforward and, therefore, not performed here in detail.

Blood Flow in Embedded Vasculature The governing equation for blood flow in the one-dimensional representation of the vasculature is the stationary Hagen-Poiseuille equation (3.79). Thus, it can be evaluated at time step $n+1$ as

$$f_{n+1}^{\hat{v}} = \left[\pi R_t^2 \frac{\partial v_t^s}{\partial s} - \frac{\partial}{\partial s} \frac{\pi R_t^4}{8\mu^{\hat{v}}} \frac{\partial p^{\hat{v}}}{\partial s} + \frac{\overset{\hat{v}\to l}{M}}{\rho^{\hat{v}}} \right]_{n+1} = 0 \qquad \text{on } \Lambda_t. \tag{4.20}$$

Species Transport in Embedded Vasculature Species transport in the 1D vasculature is governed by (3.84). Temporal discretization of this equation is achieved via

$$\omega_{n+1}^{i\,\hat{v}} - \omega_n^{i\,\hat{v}} + \Delta t f_{n+\theta}^{i\hat{v}} = 0 \quad \text{on } \Lambda_t \tag{4.21}$$

with

$$f_{n+\theta}^{i\hat{v}} = -(1-\theta)\mathring{\omega}_n^{i\,\hat{v}} + \theta f_{n+1}^{i\hat{v}} \tag{4.22}$$

and

$$f_{n+1}^{i\hat{v}} = \left[\left(\pi R_t^2\right)^{-1} \left(-\frac{\pi R_t^4}{8\mu^{\hat{v}}} \frac{\partial p^{\hat{v}}}{\partial s} \cdot \frac{\partial \omega^{i\,\hat{v}}}{\partial s} - \frac{\partial}{\partial s} \left(\pi R_t^2 D^{i\hat{v}} \frac{\partial \omega^{i\,\hat{v}}}{\partial s} \right) + \frac{1}{\rho^{\hat{v}}} \left(\overset{i\hat{v}\to il}{M} - \omega^{i\,\hat{v}} \overset{\hat{v}\to l}{M} \right) \right) \right]_{n+1} . \tag{4.23}$$

Coupling between 1D and 3D Representation of the Vasculature The coupling between the resolved one-dimensional and the homogenized three-dimensional representation of the vasculature in the hybrid model has been formulated as a constraint in Section 3.5.3. This constraint of equal pressures or species mass fractions given by (3.110) for centerline coupling at time t_{n+1} reads as

$$g_{n+1} = \varphi_{n+1}^{\hat{v}}(s) - \varphi_{n+1}^{v}(\boldsymbol{x}(s)) = 0 \qquad \text{on } \Lambda_t. \tag{4.24}$$

For lateral surface coupling, the corresponding time-discrete version of (3.113) is given by

$$g_{n+1} = \varphi_{n+1}^{\hat{v}}(s) - \varphi_{n+1}^{v}(\boldsymbol{x}(s,\gamma)) = 0 \qquad \text{on } \partial\mathcal{D}_t. \tag{4.25}$$

Therein, $\varphi_{n+1}^{\hat{v}}$ and φ_{n+1}^{v} denote blood pressures and species mass fractions at time t_{n+1} as in (3.111) and (3.112), respectively. The previous two equations represent the time-discrete coupling conditions between the two representations of the vascular network.

Summary of Time-Discrete Form In summary, the time-discrete form of the governing equations of the hybrid model is given by equations (4.8), (4.11), (4.12), (4.13), (4.16), (4.20) and (4.21) together with the coupling constraints (4.24) or (4.25). In case that species in the solid phase are relevant and/or the temperature distribution, the respective time-discrete form of these equations, which have not been given here explicitly, additionally enter the coupled system of nonlinear equations. Finally, if the deformation of the domain is neglected, a standard one-step-θ-scheme of a Eulerian description on fixed domains Ω_0 respectively Λ_0 emerges.

4.2 Initial and Boundary Conditions

In order to complete the description of the employed tumor growth model, appropriate initial and boundary conditions have to be specified. Initial conditions are applied at the beginning of the time period of interest t_0. Boundary conditions are applied on the boundary of the domains Λ or Ω, which are denoted as Γ_Λ respectively Γ_Ω. The boundary of each domain is further partitioned into two disjoint subsets as

$$\Gamma = \Gamma^{\mathrm{D}} \cup \Gamma^{\mathrm{N}} \quad \text{with} \quad \Gamma^{\mathrm{D}} \cap \Gamma^{\mathrm{N}} = \emptyset, \tag{4.26}$$

that is, into a *Dirichlet* and a *Neumann* part of the boundary where the respective conditions are applied. In the following, the possible boundary conditions on all compartments are presented.

Tumor Cells, Host Cells and Interstitial Fluid TCs, HCs and the IF allow for prescribing the initial and Dirichlet values of the corresponding primary variables as

$$\psi^f = \check{\psi}_0^f \qquad \text{in } \Omega_t \times \{t_0\} \text{ for } f \in \mathfrak{I}_\varepsilon \tag{4.27}$$

$$\psi^f = \check{\psi}^f \qquad \text{on } \Gamma_{\Omega_t}^{\mathrm{D},f} \times [t_0, t_E] \text{ for } f \in \mathfrak{I}_\varepsilon. \tag{4.28}$$

For further information on the choice of primary variables and how to prescribe pressures and saturations, consider Remark 3.5. In addition, Neumann boundary conditions may be applied as

$$\frac{\boldsymbol{k}^f}{\mu^f} \boldsymbol{\nabla} p^f \cdot \boldsymbol{n} = \check{h}^f \qquad \text{on } \Gamma_{\Omega_t}^{\mathrm{N},f} \times [t_0, t_E] \text{ for } f = t, h \tag{4.29}$$

and

$$\sum_{\gamma \in \mathfrak{I}_\varepsilon} \left(\frac{\boldsymbol{k}^\gamma}{\mu^\gamma} \boldsymbol{\nabla} p^\gamma \right) \cdot \boldsymbol{n} = \check{h}^l \qquad \text{on } \Gamma_{\Omega_t}^{\mathrm{N},l} \times [t_0, t_E]. \tag{4.30}$$

The latter equation with the sum over TC, HC and IF pressure gradient arises due to the special treatment of the third mass balance equation as the sum over the single mass balance equations. Thus, the normal phase velocities scaled with their respective volume fractions can be set with the help of the Neumann conditions (4.29), (4.30) and Darcy's law (2.33) for non-moving boundaries. If, however, the boundary moves, the Neumann boundary condition represents the relative normal velocity scaled with the respective volume fraction.

Homogenized Vasculature Initial and boundary conditions for the pressure in the HV may be applied as

$$p^v = \check{p}_0^v \qquad \text{in } \Omega_t \times \{t_0\} \tag{4.31}$$

$$p^v = \check{p}^v \qquad \text{on } \Gamma_{\Omega_t}^{\mathrm{D},p^v} \times [t_0, t_E] \tag{4.32}$$

$$\frac{\boldsymbol{k}^v}{\mu^v} \boldsymbol{\nabla} p^v \cdot \boldsymbol{n} = \check{h}^v \qquad \text{on } \Gamma_{\Omega_t}^{\mathrm{N},p^v} \times [t_0, t_E] \tag{4.33}$$

and for the volume fraction of the HV as

$$\varepsilon^v = \check{\varepsilon}_0^v \qquad \text{in } \Omega_t \times \{t_0\} \tag{4.34}$$

$$\varepsilon^v = \check{\varepsilon}^v \qquad \text{on } \Gamma_{\Omega_t}^{\mathrm{D},\varepsilon^v} \times [t_0, t_E] \tag{4.35}$$

$$\left(D^v \boldsymbol{\nabla} \varepsilon^v - \varepsilon^v \varepsilon S^l \chi \left(\omega^{TAF\,\bar{l}} \right) \boldsymbol{\nabla} \omega^{TAF\,\bar{l}} - \varepsilon^v \varepsilon^s \Theta \boldsymbol{\nabla} \omega^{F\,\bar{s}} \right) \cdot \boldsymbol{n} = \check{j}^v \qquad \text{on } \Gamma_{\Omega_t}^{\mathrm{N},\varepsilon^v} \times [t_0, t_E]. \tag{4.36}$$

The latter condition enables specifying the normal part of the total flux term (3.50).

Solid Phase For the solid phase, the initial displacement and velocity can be specified as

$$\boldsymbol{d}^s = \check{\boldsymbol{d}}_0^s \qquad \text{in } \Omega_0 \times \{t_0\} \tag{4.37}$$

$$\boldsymbol{v}^s = \check{\boldsymbol{v}}_0^s \qquad \text{in } \Omega_0 \times \{t_0\}. \tag{4.38}$$

However, in all numerical examples considered in this thesis both will be set to zero. Besides, Dirichlet and Neumann boundary conditions may be assigned to domain boundaries as

$$\boldsymbol{d}^s = \check{\boldsymbol{d}}^s \qquad \text{on } \Gamma_{\Omega_0}^{\mathrm{D},s} \times [t_0, t_E] \tag{4.39}$$

$$\left(\boldsymbol{F} \cdot \boldsymbol{S}^{\mathrm{tot}} \right) \cdot \boldsymbol{N} = \check{\boldsymbol{t}}_0^{\mathrm{tot}} \qquad \text{on } \Gamma_{\Omega_0}^{\mathrm{N},s} \times [t_0, t_E]. \tag{4.40}$$

Therein, the Neumann boundary condition represents a traction on the entire porous medium system.

Species Transport in Tissue Domain and Energy Balance For a generic species in a solid or fluid phase, the initial and Dirichlet boundary conditions may be set as

$$\omega^{i\,\bar{\alpha}} = \check{\omega}_0^{i\,\bar{\alpha}} \qquad \text{in } \Omega_t \times \{t_0\} \tag{4.41}$$

$$\omega^{i\,\bar{\alpha}} = \check{\omega}^{i\,\bar{\alpha}} \qquad \text{on } \Gamma_{\Omega_t}^{\mathrm{D},i\,\bar{\alpha}} \times [t_0, t_E]. \tag{4.42}$$

Furthermore, the diffusive normal flux may be defined as

$$\varepsilon^\alpha \boldsymbol{D}_{\mathrm{eff}}^{i\alpha} \boldsymbol{\nabla} \omega^{i\,\bar{\alpha}} \cdot \boldsymbol{n} = \check{h}^{i\,\bar{\alpha}} \qquad \text{on } \Gamma_{\Omega_t}^{\mathrm{N},i\,\bar{\alpha}} \times [t_0, t_E] \tag{4.43}$$

on the Neumann boundary of the domain. Similarly, initial and Dirichlet boundary conditions for the temperature are

$$T = \check{T}_0 \qquad \text{in } \Omega_t \times \{t_0\} \tag{4.44}$$

$$T = \check{T} \qquad \text{on } \Gamma_{\Omega_t}^{\mathrm{D},T} \times [t_0, t_E] \tag{4.45}$$

with a corresponding Neumann boundary condition

$$\boldsymbol{\kappa}_{\text{eff}} \boldsymbol{\nabla} T \cdot \boldsymbol{n} = \check{h}^T \qquad \text{on } \Gamma_{\Omega_t}^{\text{N},T} \times [t_0, t_E] \tag{4.46}$$

involving the diffusive temperature flux with effective conductivity tensor (2.48).

Remark 4.2. *An important aspect regarding the equations for blood flow (3.47) and species transport in the HV (3.63) is the treatment of certain areas where no HV is present. This can occur due to blood vessel compression and regression if an initially vascularized area becomes avascular or during angiogenesis as the neovasculature grows into a previously avascular region. Naturally, the two aforementioned equations are not valid here but only in the part of the domain with $\varepsilon^v > 0$. In the current implementation using finite elements, the corresponding equations are only solved if the HV volume fraction inside a specific element from the last time step ε_n^v is bigger than a threshold value of $\varepsilon_{\text{thresh}}^v = 0.01$. Only in these elements the aforementioned equations are solved while in the rest of the domain they are not evaluated. This is equivalent to a no-flux boundary condition at the interface between regions in which HV is present and avascular areas. Considering the underlying physical problem this assumption states that there is no flux of species or fluid across the sprout tips during angiogenesis or into collapsed regions with collapsed vasculature, which seems reasonable. The element-wise treatment is only a very crude approximation of the actual interface but showed to be sufficient here.*

Blood Flow in Embedded Vasculature The employed initial and boundary conditions for blood flow in the 1D vasculature read as

$$p^{\hat{v}} = \check{p}_0^{\hat{v}} \qquad \text{on } \Lambda_t \times \{t_0\} \tag{4.47}$$

$$p^{\hat{v}} = \check{p}^{\hat{v}} \qquad \text{on } \Gamma_{\Lambda_t}^{\text{D},\hat{v}} \times [t_0, t_E] \tag{4.48}$$

$$\frac{\pi R_t^4}{8\mu^{\hat{v}}} \frac{\partial p^{\hat{v}}}{\partial s} - \pi R_t^2 v_t^s = \check{h}^{\hat{v}} \qquad \text{on } \Gamma_{\Lambda_t}^{\text{N},\hat{v}} \times [t_0, t_E]. \tag{4.49}$$

Here, the boundary of the 1D domain are simply its free ends. Moreover, the Neumann boundary condition (4.49) allows specifying the blood velocity defined by the Poiseuille relation (3.78) or, as the equation is scaled with the blood vessel area, rather the volumetric blood flow at the possibly moving tips of the 1D domain.

Species Transport in Embedded Vasculature Finally, for species transport in the 1D representation of the vasculature, the following initial and boundary conditions in the domain respectively on its tips can be applied:

$$\omega^{i\,\hat{v}} = \check{\omega}_0^{i\,\hat{v}} \qquad \text{on } \Lambda_t \times \{t_0\} \tag{4.50}$$

$$\omega^{i\,\hat{v}} = \check{\omega}^{i\,\hat{v}} \qquad \text{on } \Gamma_{\Lambda_t}^{\text{D},i\hat{v}} \times [t_0, t_E] \tag{4.51}$$

$$\pi R_t^2 D^{i\hat{v}} \frac{\partial \omega^{i\,\hat{v}}}{\partial s} = \check{h}^{i\hat{v}} \qquad \text{on } \Gamma_{\Lambda_t}^{\text{N},i\hat{v}} \times [t_0, t_E]. \tag{4.52}$$

The last equation represents the diffusive species flux at the free ends of the domain.

4.3 Finite Element Formulation

Using the finite element method (FEM), the spatial discretization of the time-discrete form of the governing equations derived in the previous section are introduced in the following. Basic knowledge of the main concepts of the FEM as described in the text books [18, 286, 300–302] is presumed. For FEM formulations in the context of poro-mechanics, the reader is referred to [148, 265, 269, 270, 272]. It has to be noted, though, that the present approach uses only the pressure as the primary variable for fluid flow as the Darcy equation has been directly inserted into the fluid mass balance to eliminate the fluid phase velocity, refer to Section 2.3.4.2. Such a formulation lacks accuracy in terms of mass conservation and reconstruction of the velocities of the fluid phases. This can be remedied by mixed formulations [31] with fluid velocities and pressures as primary variables including suitable stabilization terms [9, 272] or special exactly divergence-free finite element spaces [213].

4.3.1 Weak Forms of the Governing Equations

The FEM requires transforming the strong form of the governing equations into a so-called *weak* or *variational formulation*. This is achieved by multiplying the strong forms with suitable *weighting* or *test function* and integrating over the respective domain. Finally, Gauss' theorem is applied to terms containing a second spatial derivative to decrease the differentiability requirements of the solution function space. In the following, the common notation

$$(\bullet, \bullet)_\Omega = \int (\bullet) \cdot (\bullet) \, \mathrm{d}\Omega \tag{4.53}$$

will be employed to refer to the inner L^2 product. Furthermore, function spaces for primary variables are denoted by $\mathcal{S}$ and the respective test or weighting function spaces by $\mathcal{V}$.

Once more, the hybrid model variant will be regarded as it is the most general one. In that case, fulfilling the constraint of matching pressure between resolved and homogenized representation of the vasculature leads to a 1D-3D mass transfer term which will be detailed in Section 4.3.1.3.

4.3.1.1 Porous Medium Domain

Tumor Cells, Host Cells and Interstitial Fluid The solution and test function spaces for TCs, HCs and IF, that is, for $f \in \mathfrak{I}_\varepsilon$ are given by

$$\mathcal{S}_f = \left\{ \psi^f \in H^1(\Omega_t) \,\middle|\, \psi^f = \check{\psi}^f \text{ on } \Gamma_{\Omega_t}^{\mathrm{D},f} \right\} \quad \text{and} \tag{4.54}$$

$$\mathcal{V}_f = \left\{ \delta\psi^f \in H^1(\Omega_t) \,\middle|\, \delta\psi^f = 0 \text{ on } \Gamma_{\Omega_t}^{\mathrm{D},f} \right\}. \tag{4.55}$$

Typically, the solution function space must satisfy the Dirichlet boundary conditions defined on $\Gamma_{\Omega_t}^{\mathrm{D},f}$ while the corresponding weighting function is zero there. Furthermore, H^1 is the Sobolev space of functions with square integrable values and square integrable first derivatives. Thus, the

weak form of the time-discrete governing equation (4.8) for TCs and HCs is given by

$$\begin{aligned}
&\left(\delta\psi^f, \sum_{\beta\in\mathcal{I}_\varepsilon}\left(\left(\varepsilon\frac{\partial S^f}{\partial\psi^\beta}\right)_{n+1}\left(\psi^\beta_{n+1}-\psi^\beta_n-(1-\theta)\,\Delta t\cdot\mathring{\psi}^\beta_n\right)\right)\right)_{\Omega_{t_{n+1}}}\\
&-\theta\Delta t\left(\delta\psi^f,\left(S^f\mathring{\varepsilon}^v\right)_{n+1}\right)_{\Omega_{t_{n+1}}}+\theta\Delta t\left(\delta\psi^f,\left(S^f\left(1-\varepsilon^v\right)\boldsymbol{\nabla}\cdot\boldsymbol{v}^s\right)_{n+1}\right)_{\Omega_{t_{n+1}}}\\
&+\theta\Delta t\left(\boldsymbol{\nabla}\delta\psi^f,\left(\frac{\boldsymbol{k}^f}{\mu^f}\sum_{\beta\in\mathcal{I}_\varepsilon}\frac{\partial p^f}{\partial\psi^\beta}\boldsymbol{\nabla}\psi^\beta\right)_{n+1}\right)_{\Omega_{t_{n+1}}}-\theta\Delta t\left(\delta\psi^f,\left(\frac{\sum_{\kappa\in\mathcal{I}_{cf}}\overset{\kappa\to f}{M}}{\rho^f}\right)_{n+1}\right)_{\Omega_{t_{n+1}}}\\
&-\theta\Delta t\left(\delta\psi^f,\check{h}^f\right)_{\Gamma^{\mathrm{N},f}_{\Omega_{t_{n+1}}}}=0
\end{aligned}\tag{4.56}$$

for $f = t, h$. Note that partial integration has been performed on the Darcy term such that the Neumann boundary condition (4.29) naturally arises and is also fulfilled in a weak sense. Additionally, the inverse pre-factor of (4.10) has been multiplied and terms related to the time discretization of the TC, HC and IF phase have been grouped in the first term. Actually, this term collects the definition of the temporal derivative of the saturation evaluated at t_{n+1}. The weak form of the time-discrete summed up equation (4.11) emerges as

$$\begin{aligned}
&-\left(\delta\psi^l,\mathring{\varepsilon}^v_{n+1}\right)_{\Omega_{t_{n+1}}}+\left(\delta\psi^l,\left(\left(1-\varepsilon^v\right)\boldsymbol{\nabla}\cdot\boldsymbol{v}^s\right)_{n+1}\right)_{\Omega_{t_{n+1}}}\\
&+\left(\boldsymbol{\nabla}\delta\psi^l,\sum_{\gamma\in\mathcal{I}_\varepsilon}\left(\frac{\boldsymbol{k}^\gamma}{\mu_\gamma}\sum_{\beta\in\mathcal{I}_\varepsilon}\frac{\partial p^\gamma}{\partial\psi^\beta}\boldsymbol{\nabla}\psi^\beta\right)_{n+1}\right)_{\Omega_{t_{n+1}}}-\left(\delta\psi^l,M^l_{\mathrm{rhs},n+1}\right)_{\Omega_{t_{n+1}}}-\left(\delta\psi^l,\check{h}^l\right)_{\Gamma^{\mathrm{N},l}_{\Omega_{t_{n+1}}}}=0
\end{aligned}\tag{4.57}$$

when applying the same procedure. Again, the Neumann boundary condition (4.30) is fulfilled in a weak sense.

The mass transfer term $M^l_{\mathrm{rhs},n+1}$ may contain 1D-3D coupling terms which require special attention due to the scaling with the Dirac measure as introduced in Section 3.4.3. The respective contribution of a generic 1D-3D mass transfer term with arbitrary function $f(\bullet)$ has been introduced in equation (3.88). The weak formulation of such a term reads as

$$-\left(\delta\psi^l,\delta_{\partial\mathcal{D}_t}\cdot f\left(\varphi^{\hat{v}}(s),\varphi^l\left(\boldsymbol{x}(s,\gamma)\right)\right)\right)_{\Omega_{t_{n+1}}}=-\left(\delta\psi^l,f\left(\varphi^{\hat{v}}(s),\varphi^l\left(\boldsymbol{x}(s,\gamma)\right)\right)\right)_{\partial\mathcal{D}_{t_{n+1}}}\tag{4.58}$$

where the integral over the domain has been re-written as an integral over the lateral surface of the embedded network. For that, the property of the Dirac function defined on the lateral surface as given by (3.89) has been invoked. By contrast, for centerline coupling the values of the 3D porous domain are projected on the centerline of the 1D vasculature by the approximation (3.90) and not evaluated on the lateral surface. The contribution by mass transfer to the weak form (4.57) for this coupling variant emerges as

$$\begin{aligned}
&-\left(\delta\psi^l,\delta_{\Lambda_t}\cdot\pi D_t(s)\cdot f\left(\varphi^{\hat{v}}(s),\varphi^l\left(\boldsymbol{x}(s)\right)\right)\right)_{\Omega_{t_{n+1}}}\\
&=-\left(\delta\psi^l,\pi D_t(s)\cdot f\left(\varphi^{\hat{v}}(s),\varphi^l\left(\boldsymbol{x}(s)\right)\right)\right)_{\Lambda_{t_{n+1}}}.
\end{aligned}\tag{4.59}$$

Here, the property of the Dirac distribution defined along the 1D centerline (3.93) has been exploited. Thus, compared to equation (4.58), the two-dimensional integration over the lateral surface of the embedded domain is replaced by a one-dimensional integration along the centerline of the domain. Spatially discretizing and linearizing these two terms requires 2D Gauss integration of products of shape functions over the lateral surface respectively 1D Gauss integration of products of shape functions along the centerline of the inclusion. Details will follow in Section 4.3.3.

Homogenized Vasculature Solution and test function spaces for the pressure in the homogenized vasculature are defined by

$$\mathcal{S}_{p^v} = \left\{ p^v \in H^1(\Omega_t) \,\middle|\, p^v = \check{p}^v \text{ on } \Gamma_{\Omega_t}^{\mathrm{D},p^v} \right\} \quad \text{and} \tag{4.60}$$

$$\mathcal{V}_{p^v} = \left\{ \delta p^v \in H^1(\Omega_t) \,\middle|\, \delta p^v = 0 \text{ on } \Gamma_{\Omega_t}^{\mathrm{D},p^v} \right\} \tag{4.61}$$

with the corresponding weak form

$$\begin{aligned} &\left(\delta p^v, \mathring{\varepsilon}_{n+1}^v\right)_{\Omega_{t_{n+1}}} + \left(\delta p^v, \left(\varepsilon^v \boldsymbol{\nabla} \cdot \boldsymbol{v}^s\right)_{n+1}\right)_{\Omega_{t_{n+1}}} + \left(\boldsymbol{\nabla}\delta p^v, \left(\frac{\boldsymbol{k}^v}{\mu^v}\boldsymbol{\nabla} p^v\right)_{n+1}\right)_{\Omega_{t_{n+1}}} \\ &\quad - \left(\delta p^v, \left(\frac{\sum_{\kappa\in\mathcal{I}_{cv}} \overset{\kappa\to v}{M}}{\rho^v}\right)_{n+1}\right)_{\Omega_{t_{n+1}}} - \left(\delta p^v, \check{h}^v\right)_{\Gamma_{\Omega_{t_{n+1}}}^{\mathrm{N},p^v}} = 0 \end{aligned} \tag{4.62}$$

derived from its strong time-discrete counterpart (4.12).

Equivalently, the evolution equation for the vascular volume fraction (4.15) may be transformed into a weak formulation with the following function spaces

$$\mathcal{S}_{\varepsilon^v} = \left\{ \varepsilon^v \in H^1(\Omega_t) \,\middle|\, \varepsilon^v = \check{\varepsilon}^v \text{ on } \Gamma_{\Omega_t}^{\mathrm{D},\varepsilon^v} \right\} \tag{4.63}$$

$$\mathcal{V}_{\varepsilon^v} = \left\{ \delta\varepsilon^v \in H^1(\Omega_t) \,\middle|\, \delta\varepsilon^v = 0 \text{ on } \Gamma_{\Omega_t}^{\mathrm{D},\varepsilon^v} \right\} \tag{4.64}$$

resulting in

$$\begin{aligned} &\left(\delta\varepsilon^v, \varepsilon_{n+1}^v - \varepsilon_n^v - (1-\theta)\,\Delta t \cdot \mathring{\varepsilon}_n^v\right)_{\Omega_{t_{n+1}}} + \theta\Delta t \left(\delta\varepsilon^v, \left(\varepsilon^v \boldsymbol{\nabla}\cdot\boldsymbol{v}^s\right)_{n+1}\right)_{\Omega_{t_{n+1}}} \\ &+\theta\Delta t \left(\boldsymbol{\nabla}\delta\varepsilon^v, \left(D^v\boldsymbol{\nabla}\varepsilon^v - \varepsilon^v\varepsilon S^l \chi\left(\omega^{TAF\bar{l}}\right)\boldsymbol{\nabla}\omega^{TAF\bar{l}} - \varepsilon^v\varepsilon^s\Theta\boldsymbol{\nabla}\omega^{F\bar{s}}\right)_{n+1}\right)_{\Omega_{t_{n+1}}} \\ &+\theta\Delta t \left(\delta\varepsilon^v, C_{\mathrm{coll},n+1}\right)_{\Omega_{t_{n+1}}} - \theta\Delta t \left(\delta\varepsilon^v, \check{j}^v\right)_{\Gamma_{\Omega_{t_{n+1}}}^{\mathrm{N},\varepsilon^v}} = 0. \end{aligned} \tag{4.65}$$

Here, integration by parts is performed on the entire flux term governing angiogenesis. Once more, the Neumann boundary condition (4.36) for this term arises naturally.

Solid Phase The solution and test function spaces for the displacement field are defined as

$$\mathcal{S}_s = \left\{ \boldsymbol{d}^s \in \left[H^1(\Omega_0)\right]^{n_{\mathrm{dim}}} \,\middle|\, \boldsymbol{d}^s = \check{\boldsymbol{d}}^s \text{ on } \Gamma_{\Omega_0}^{\mathrm{D},s} \right\} \quad \text{and} \tag{4.66}$$

$$\mathcal{V}_s = \left\{ \delta\boldsymbol{d}^s \in \left[H^1(\Omega_0)\right]^{n_{\mathrm{dim}}} \,\middle|\, \delta\boldsymbol{d}^s = \boldsymbol{0} \text{ on } \Gamma_{\Omega_0}^{\mathrm{D},s} \right\}. \tag{4.67}$$

Thereby, the weak form of the momentum balance (4.16)

$$\left(\delta \boldsymbol{E}, \left(\boldsymbol{S}^{\mathrm{eff}} - p^s J \boldsymbol{C}^{-1}\right)_{n+1}\right)_{\Omega_0} - \left(\delta \boldsymbol{d}^s, \check{\boldsymbol{t}}_0^{\mathrm{tot}}\right)_{\Gamma_{\Omega_0}^{\mathrm{N},s}} = 0 \tag{4.68}$$

may be obtained. Here, $\delta \boldsymbol{E}$ is the variation of the Green-Lagrange strain tensor which may be expressed in terms of the deformation gradient and the gradient of the variation of the displacements, see e.g. [286].

Species Transport in Tissue Domain and Energy Balance Again, species transport in a generic fluid phase $f \in \mathfrak{I}_{\mathrm{f}}$ serves as a surrogate for the similar equations of species transport in the solid phase and the energy balance. The weak forms of the latter two equations can be deduced equivalently. The weak form for species transport in a fluid phase is obtained by means of the usual function spaces

$$\mathcal{S}_{i\overline{f}} = \left\{ \omega^{i\,\overline{f}} \in H^1\left(\Omega_t\right) \,\middle|\, \omega^{i\,\overline{f}} = \check{\omega}^{i\,\overline{f}} \text{ on } \Gamma_{\Omega_t}^{\mathrm{D},i\,\overline{f}} \right\} \quad \text{and} \tag{4.69}$$

$$\mathcal{V}_{i\overline{f}} = \left\{ \delta\omega^{i\,\overline{f}} \in H^1\left(\Omega_t\right) \,\middle|\, \delta\omega^{i\,\overline{f}} = 0 \text{ on } \Gamma_{\Omega_t}^{\mathrm{D},i\,\overline{f}} \right\} \tag{4.70}$$

as

$$\begin{aligned} &\left(\delta\omega^{i\,\overline{f}}, \varepsilon_{n+1}^f \left(\omega_{n+1}^{i\,\overline{f}} - \omega_n^{i\,\overline{f}} - (1-\theta)\,\Delta t \cdot \mathring{\omega}_n^{i\,\overline{f}}\right)\right)_{\Omega_{t_{n+1}}} \\ &+\theta\Delta t \left(\delta\omega^{i\,\overline{f}}, \left(-\frac{\boldsymbol{k}^f}{\mu^f} \boldsymbol{\nabla} p^f \cdot \boldsymbol{\nabla} \omega^{i\,\overline{f}}\right)_{n+1}\right)_{\Omega_{t_{n+1}}} + \theta\Delta t \left(\boldsymbol{\nabla}\delta\omega^{i\,\overline{f}}, \left(\varepsilon^f \boldsymbol{D}_{\mathrm{eff}}^{if} \boldsymbol{\nabla}\omega^{i\,\overline{f}}\right)_{n+1}\right)_{\Omega_{t_{n+1}}} \\ &-\theta\Delta t \left(\delta\omega^{i\,\overline{f}}, M_{\mathrm{rhs},n+1}^{if}\right)_{\Omega_{t_{n+1}}} - \theta\Delta t \left(\delta\omega^{i\,\overline{f}}, \check{h}^{i\,\overline{f}}\right)_{\Gamma_{\Omega_{t_{n+1}}}^{\mathrm{N},i\,\overline{f}}} = 0 \end{aligned} \tag{4.71}$$

This equation corresponds to the time-discrete balance of species mass (4.17). The volume fraction ε_{n+1}^f has been brought to the left hand side and the diffusive term has been integrated by parts.

For the case $f = l$, the mass transfer term M_{rhs}^{if} may again contain 1D-3D species mass exchange from the embedded blood vessel network into the IF. The weak form of these terms which are scaled with the Dirac delta distribution is obtained just like (4.58) as

$$-\theta\Delta t \left(\delta\omega^{i\,\bar{l}}, f\left(\varphi^{\hat{v}}\left(s\right), \varphi^l\left(\boldsymbol{x}\left(s,\gamma\right)\right)\right)\right)_{\partial\mathcal{D}_{t_{n+1}}} \tag{4.72}$$

for a generic mass transfer term with function $f(\bullet)$. Again, the integral over the domain of a term scaled with the Dirac measure has been re-written as an integral over the lateral surface of the embedded network. The weak form for centerline coupling follows in the same way as

$$-\theta\Delta t \left(\delta\omega^{i\,\bar{l}}, \pi D_t(s) \cdot f\left(\varphi^{\hat{v}}\left(s\right), \varphi^l\left(\boldsymbol{x}\left(s\right)\right)\right)\right)_{\Lambda_{t_{n+1}}}. \tag{4.73}$$

4.3.1.2 Embedded One-Dimensional Vasculature Domain

Blood Flow in Embedded Vasculature To obtain the weak form of equation (4.20) governing blood flow in the embedded vasculature, the typical function spaces

$$\mathcal{S}_{\hat{v}} = \left\{ p^{\hat{v}} \in H^1(\Lambda_t) \,\middle|\, p^{\hat{v}} = \breve{p}^{\hat{v}} \text{ on } \Gamma^{\mathrm{D},\hat{v}}_{\Lambda_t} \right\} \quad \text{and} \tag{4.74}$$

$$\mathcal{V}_{\hat{v}} = \left\{ \delta p^{\hat{v}} \in H^1(\Lambda_t) \,\middle|\, \delta p^{\hat{v}} = 0 \text{ on } \Gamma^{\mathrm{D},\hat{v}}_{\Lambda_t} \right\} \tag{4.75}$$

are defined, this time as the Sobolev space $H^1(\Lambda_t)$ on the 1D embedded vasculature. Then, the weak formulation is obtained as

$$\left(\frac{\partial \delta p^{\hat{v}}}{\partial s}, \left(\frac{\pi R_t^4}{8\mu^{\hat{v}}} \frac{\partial p^{\hat{v}}}{\partial s} - \pi R_t^2 v_t^s \right)_{n+1} \right)_{\Lambda_{t_{n+1}}} + \left(\delta p^{\hat{v}}, \left(\frac{M^{\hat{v}\to l}}{\rho^{\hat{v}}} \right)_{n+1} \right)_{\Lambda_{t_{n+1}}} - \left(\delta p^{\hat{v}}, \breve{h}^{\hat{v}} \right)_{\Gamma^{\mathrm{N},\hat{v}}_{\Lambda_{t_{n+1}}}} = 0. \tag{4.76}$$

Partial integration has here also been performed on the term containing the spatial derivative of the solid phase velocity projected on the tangential blood vessel segment direction v_t^s. Thus, the spatial derivative is transferred to the test function which makes the evaluation of this term after performing spatial discretization easier. However, an additional boundary term $\left(\delta p^{\hat{v}}, \pi R_t^2 v_t^s\right)_{\Gamma^{\hat{v}}_{\Lambda_t}}$ arises. It is combined in the Neumann boundary term $\breve{h}^{\hat{v}}$ from (4.49) together with the pressure gradient, which also stems from partial integration of the Hagen-Poiseuille term. No actual integration of the Neumann boundary conditions has to be performed since the boundary of the 1D domain are simply discrete points at which the respective conditions have to be evaluated.

The transvascular fluid exchange term once more requires the evaluation of 1D-3D coupled terms with the contribution

$$\left(\delta p^{\hat{v}}, \int_0^{\pi D_t(s)} f\left(\varphi^{\hat{v}}(s), \varphi^l(\boldsymbol{x}(s,\gamma))\right) \mathrm{d}\gamma \right)_{\Lambda_{t_{n+1}}} = \left(\delta p^{\hat{v}}, f\left(\varphi^{\hat{v}}(s), \varphi^l(\boldsymbol{x}(s,\gamma))\right) \right)_{\partial \mathcal{D}_{t_{n+1}}} \tag{4.77}$$

of the generic mass transfer term (3.87) to the weak form. In turn, an integral over the lateral surface of the embedded vasculature has to be evaluated as the variation of the 1D pressure defined on the centerline of the inclusion can be pulled into the perimeter integral. By contrast, for centerline coupling the corresponding integral can be simplified to a simple multiplication of the mass transfer term with the arbitrary function, see (3.91), resulting in the following 1D integral along the centerline:

$$\left(\delta p^{\hat{v}}, \pi D_t \cdot f\left(\varphi^{\hat{v}}(s), \varphi^l(\boldsymbol{x}(s))\right) \right)_{\Lambda_{t_{n+1}}}. \tag{4.78}$$

These contributions have their counterparts, that is the weak terms (4.58) and (4.59), in the mass balance of the IF.

Species Transport in Embedded Vasculature Species transport in the one-dimensional representation of the vascular network is governed by the time-discrete equation (4.21). Defining

the function spaces

$$\mathcal{S}_{i\hat{v}} = \left\{ \omega^{i\,\hat{v}} \in H^1\left(\Lambda_t\right) \,\middle|\, \omega^{i\,\hat{v}} = \breve{\omega}^{i\,\hat{v}} \text{ on } \Gamma_{\Lambda_t}^{\mathrm{D},i\hat{v}} \right\} \quad \text{and} \tag{4.79}$$

$$\mathcal{V}_{i\hat{v}} = \left\{ \delta\omega^{i\,\hat{v}} \in H^1\left(\Lambda_t\right) \,\middle|\, \delta\omega^{i\,\hat{v}} = 0 \text{ on } \Gamma_{\Lambda_t}^{\mathrm{D},i\hat{v}} \right\} \tag{4.80}$$

and integrating the product of the test functions with the strong form over the 1D embedded domain Λ_t yields the weak formulation

$$\begin{aligned} &\left(\delta\omega^{i\,\hat{v}}, \pi R_{t,n+1}^2 \left(\omega_{n+1}^{i\,\hat{v}} - \omega_n^{i\,\hat{v}} - (1-\theta)\,\Delta t \cdot \mathring{\omega}_n^{i\,\hat{v}}\right)\right)_{\Lambda_{t_{n+1}}} \\ &+\theta\Delta t \left(\delta\omega^{i\,\hat{v}}, \left(-\frac{\pi R_t^4}{8\mu^{\hat{v}}} \frac{\partial p^{\hat{v}}}{\partial s} \cdot \frac{\partial \omega^{i\,\hat{v}}}{\partial s}\right)_{n+1}\right)_{\Lambda_{t_{n+1}}} + \theta\Delta t \left(\frac{\partial \delta\omega^{i\,\hat{v}}}{\partial s}, \left(\pi R_t^2 D^{i\hat{v}} \frac{\partial \omega^{i\,\hat{v}}}{\partial s}\right)_{n+1}\right)_{\Lambda_{t_{n+1}}} \\ &+\theta\Delta t \left(\delta\omega^{i\,\hat{v}}, \left(\frac{1}{\rho^{\hat{v}}} \left(\overset{i\hat{v}\to il}{M} - \omega^{i\,\hat{v}} \overset{\hat{v}\to l}{M}\right)\right)_{n+1}\right)_{\Lambda_{t_{n+1}}} - \theta\Delta t \left(\delta\omega^{i\,\hat{v}}, \check{h}^{i\hat{v}}\right)_{\Gamma_{\Lambda_{t_{n+1}}}^{\mathrm{N},i\hat{v}}} = 0. \end{aligned} \tag{4.81}$$

Therein, transvascular species mass transfer terms may again be identified. As the 1D-3D coupling terms for fluid mass transfer, they may be brought into the form

$$\begin{aligned} &\theta\Delta t \left(\delta\omega^{i\,\hat{v}}, \int_0^{\pi D_t(s)} f\left(\varphi^{\hat{v}}\left(s\right), \varphi^{l}\left(\boldsymbol{x}\left(s,\gamma\right)\right)\right) \,\mathrm{d}\gamma\right)_{\Lambda_{t_{n+1}}} = \\ &\qquad \theta\Delta t \left(\delta\omega^{i\,\hat{v}}, f\left(\varphi^{\hat{v}}\left(s\right), \varphi^{l}\left(\boldsymbol{x}\left(s,\gamma\right)\right)\right)\right)_{\partial\mathcal{D}_{t_{n+1}}} \end{aligned} \tag{4.82}$$

for lateral surface coupling and

$$\theta\Delta t \left(\delta\omega^{i\,\hat{v}}, \pi D_t \cdot f\left(\varphi^{\hat{v}}\left(s\right), \varphi^{l}\left(\boldsymbol{x}\left(s\right)\right)\right)\right)_{\Lambda_{t_{n+1}}} \tag{4.83}$$

for centerline coupling with the previously mentioned integrals.

Remark 4.3. *The convection-diffusion-reaction equations for species transport* (4.71) *and* (4.81) *may require additional stabilization terms if convection dominates. In principle, different stabilization formulations are available in the computational framework [8], however, they have not been used here as spurious oscillations of species transport were not observed with the employed mesh sizes. By contrast, minor oscillations were present during growth in the primary variables of the TC phase at the tumor front. This can be explained by the dominating reactive term and the quite low relative permeability calculated according to* (3.42) *at the edge of the growing tumor. Further mathematical analysis might be necessary to investigate the cause of these oscillations and devise a strategy for stabilization.*

4.3.1.3 Constraint Enforcement Strategies

In the following, it will be demonstrated how the constraints (3.110) and (3.113) for coupling blood flow and species transport between embedded and homogenized vasculature can be fulfilled through two different constraint enforcement strategies, a Gauss-point-to-segment (GPTS)

scheme or a penalized mortar-type method, which have been adapted from mesh tying and contact formulations in solid mechanics. These two methods perfectly fit into the finite element discretization of the transcapillary mass transfer terms as described above. The following section was previously published in the author's article [136]. However, there only the centerline variant was treated. Here, an adaptation for the surface-coupled variant is additionally presented.

Gauss-point-to-segment approach The first choice to fulfill the centerline constraint (3.110) of equal pressures or species mass fractions is through a Gauss-point-to-segment approach. For that, a penalty potential may be defined as

$$\Pi_{\text{pen}} = \frac{1}{2}\epsilon_{\text{GPTS}} \cdot \int_{\Lambda_t} g^2 \, \mathrm{d}s \qquad \text{on } \Lambda_t. \tag{4.84}$$

The weak formulation of (4.84) follows as

$$\begin{aligned} \delta\Pi_{\text{pen}} &= \epsilon_{\text{GPTS}} \left(\delta\varphi^{\hat{v}}, \varphi^{\hat{v}} - \varphi^{v}\right)_{\Lambda_t} - \epsilon_{\text{GPTS}} \left(\delta\varphi^{v}, \delta_{\Lambda_t} \cdot \left(\varphi^{\hat{v}} - \varphi^{v}\right)\right)_{\Omega_t} \\ &= \epsilon_{\text{GPTS}} \left(\delta\varphi^{\hat{v}}, \varphi^{\hat{v}} - \varphi^{v}\right)_{\Lambda_t} - \epsilon_{\text{GPTS}} \left(\delta\varphi^{v}, \varphi^{\hat{v}} - \varphi^{v}\right)_{\Lambda_t} \end{aligned} \tag{4.85}$$

with corresponding test functions $\delta\varphi^{\hat{v}}$ and $\delta\varphi^{v}$ as above. The major benefit of this GPTS approach is that it can easily be combined with the non-conforming 1D-3D coupling for mass exchange between embedded vasculature and IF. Indeed, the coupling term may be interpreted as a 1D-3D mass exchange term between embedded and homogenized vasculature of the form

$$\overset{(i)\hat{v}\to(i)v}{M} = f\left(\varphi^{\hat{v}}, \varphi^{v}\right) = \epsilon_{\text{GPTS}} \left(\varphi^{\hat{v}} - \varphi^{v}\right) \tag{4.86}$$

with very large permeability ϵ_{GPTS} such that pressures and species in the two domains immediately equalize. So, the first term involving the variation of the 1D primary variable from (4.85) simply has to be evaluated at time t_{n+1} and added to the weak form of the 1D blood flow (4.76) respectively 1D species transport (4.81). In the latter case, it has to be additionally scaled with the time factor $\theta\Delta t$. This guarantees a correct evaluation of the mass transfer term (4.86) at the intermediate time instant $t_{n+\theta}$ together with the other right hand side term (4.83). Note that the evaluation at time t_n and the corresponding scaling with the time factor $(1-\theta)\Delta t$ is done by evaluating the time derivative of the primary variable at time t_n in (4.81). Correspondingly, the second term involving the variation of the 3D primary variable from (4.85) can be added to the weak form of the 3D blood flow (4.62) respectively 3D species transport (4.71) (with $\varepsilon^{\alpha} = \varepsilon^{v}$) and again scaled with the time factor $\theta\Delta t$ in the latter case.

For lateral surface coupling, the constraint is defined on the lateral surface of the embedded vasculature via (3.113). Consequently, the penalty potential is modified to

$$\Pi_{\text{pen}} = \frac{1}{2}\epsilon_{\text{GPTS}} \cdot \int_{\partial\mathcal{D}_t} g^2 \, \mathrm{d}\gamma\mathrm{d}s \qquad \text{on } \partial\mathcal{D}_t \tag{4.87}$$

with the corresponding variation

$$\begin{aligned} \delta\Pi_{\text{pen}} &= \epsilon_{\text{GPTS}} \left(\delta\varphi^{\hat{v}}, \varphi^{\hat{v}} - \varphi^{v}\right)_{\partial\mathcal{D}_t} - \epsilon_{\text{GPTS}} \left(\delta\varphi^{v}, \delta_{\partial\mathcal{D}_t} \cdot \left(\varphi^{\hat{v}} - \varphi^{v}\right)\right)_{\Omega_t} \\ &= \epsilon_{\text{GPTS}} \left(\delta\varphi^{\hat{v}}, \varphi^{\hat{v}} - \varphi^{v}\right)_{\partial\mathcal{D}_t} - \epsilon_{\text{GPTS}} \left(\delta\varphi^{v}, \varphi^{\hat{v}} - \varphi^{v}\right)_{\partial\mathcal{D}_t}. \end{aligned} \tag{4.88}$$

Once more, these terms represent 1D-3D mass transfer terms between embedded and homogenized vasculature with permeability ϵ_{GPTS} between the two domains. After evaluation at t_{n+1} and scaling them with the appropriate time factor as described above, they can be added to the respective equations. Now, they are equivalent to the contributions with the lateral surface coupling variant, that is, equations (4.58) and (4.72) respectively equations (4.77) and (4.82).

The approach has been termed Gauss-point-to-segment approach here since evaluating (4.85) and (4.88) in their discretized forms will ultimately require Gauss integration of the terms along the vessel centerline respectively over the lateral surface of Λ_t, see also Section 4.3.3. The drawback of such GPTS methods is the penalty parameter ϵ_{GPTS}. If its value is chosen too low, the constraint is nut fulfilled with sufficient accuracy. If it is chosen too high, the problem is overconstrained, see also Section A.2.

Mortar approach with penalty regularization An alternative constraint enforcement scheme, which does not suffer from the aforementioned shortcomings, is the Lagrange multiplier (LM) method whose contribution to the weak form can be written as

$$\delta\Pi_{\mathrm{LM}} = \left(\lambda, \delta\varphi^{\hat{v}} - \delta\varphi^{v}\right)_{\Lambda_t} \tag{4.89}$$

for the centerline coupling variant. Again, this allows interpreting the (scalar-valued) Lagrange multiplier λ defined on the embedded domain Λ_t as a mass exchange term between embedded vasculature and neovasculature, i.e.,

$$\lambda = {}^{(i)\hat{v}\to(i)v}M \quad . \tag{4.90}$$

Typically, the variational form of the constraint (3.110), which is not given here, additionally enters the weak formulation of the system, for more details see also Section 6.2.3. Consequently, the LM formulation transforms the resulting system of equations into a saddle point problem meaning that its solution will be a maximum with respect to the Lagrange multipliers and a minimum with respect to the primary variables. In the context of solid mechanics mesh tying and contact algorithms such a formulation with a discretization of the Lagrange multiplier field is usually termed mortar method [17]. The nodal Lagrange multipliers enter the system of equations as additional unknowns or are condensed out via a dual approach [198, 199]. However, in the following, a different strategy with a penalty regularization of the Lagrange multiplier method similar to Yang et al. [292] will be pursued to eliminate the Lagrange multipliers. This formulation has two major advantages: First, it is formulated in terms of the primary unknowns of the problem without the additional Lagrange multipliers and, therefore, the original size of the system is not changed. Second, the resulting system of equations is not of saddle point structure any more such that standard iterative linear solvers and preconditioners can be applied.

For the lateral surface variant of 1D-3D coupling, one possible weak form of the Lagrange multiplier method may be written as follows:

$$\delta\Pi_{\mathrm{LM}} = \left(\lambda, \delta\varphi^{\hat{v}} - \delta\varphi^{v}\right)_{\partial\mathcal{D}_t} = \left(\lambda, \int_0^{\pi D_t(s)} \delta\varphi^{\hat{v}} - \delta\varphi^{v}\,\mathrm{d}\gamma\right)_{\Lambda_t} . \tag{4.91}$$

Therein, λ is again the Lagrange multiplier defined on the centerline of the embedded 1D domain Λ_t. Thus, it does not depend on the position on the lateral surface and can be pulled out of

the perimeter integral. However, this has one major implication: The formulation given in (4.91) does not enforce the constraint of equal pressure respectively mass fractions at all points on the lateral surface as dictated by (3.110) but a weaker constraint given by

$$g = \int_0^{\pi D_t} \varphi^{\hat{v}}(s,t) - \varphi^{v}(\boldsymbol{x}(s,\gamma),t)\,\mathrm{d}\gamma = 0 \qquad \text{on } \Lambda_t. \tag{4.92}$$

This requires only that the value of the 3D primary variable integrated along the perimeter of the inclusion is equal to the respective integrated primary variable of the 1D domain at each point on the centerline of the embedded domain. Correspondingly, the Lagrange multiplier acts as a yet to be specified mass transfer term to enforce this constraint.

The employed one-step-θ-scheme again dictates that the mass transfer term originating from the Lagrange multiplier (4.90) has to be evaluated at the correct time instant, i.e., at t_{n+1} and scaled with the appropriate time factor before adding them to the respective weak forms just as described above for the GPTS scheme.

4.3.2 Spatial Discretization

For spatial discretization, the two- or three-dimensional tissue domain of interest is approximated by partitioning it into n_{ele} non-overlapping subdomains, the so-called elements, as

$$\Omega \approx \Omega^{\mathsf{h}} = \bigcup_{e=1}^{n_{\text{ele}}} \Omega_e \quad \text{with} \quad \Omega_e \cap \Omega_f = \emptyset,\ e \neq f. \tag{4.93}$$

Here and in the following, a spatially discretized quantity is denoted by the superscript $(.)^{\mathsf{h}}$ and Ω_e denotes the element domain. The same procedure is applied for the one-dimensional embedded domain whose spatial discretization Λ^{h} is given by

$$\Lambda \approx \Lambda^{\mathsf{h}} = \bigcup_{e=1}^{\hat{n}_{\text{ele}}} \Lambda_e \quad \text{with} \quad \Lambda_e \cap \Lambda_f = \emptyset,\ e \neq f \tag{4.94}$$

with $\hat{n}_{\text{ele}}$ one-dimensional elements Λ_e. The primary unknowns are then interpolated by defining shape functions at the n_{nodes} nodes of the 2D/3D domain Ω^{h} as

$$\boldsymbol{d}^{s} \approx \boldsymbol{d}^{s,\mathsf{h}} = \sum_{j=1}^{n_{\text{nodes}}} N_j \cdot \mathbf{d}_j \tag{4.95}$$

$$\boldsymbol{\psi}^{[t,h,l]} \approx \boldsymbol{\psi}^{[t,h,l],\mathsf{h}} = \sum_{j=1}^{n_{\text{nodes}}} N_j \cdot \boldsymbol{\psi}_j^{[t,h,l]} \tag{4.96}$$

$$\varepsilon^{v} \approx \varepsilon^{v,\mathsf{h}} = \sum_{j=1}^{n_{\text{nodes}}} N_j \cdot \varepsilon_j^{v} \tag{4.97}$$

$$p^{v} \approx p^{v,\mathsf{h}} = \sum_{j=1}^{n_{\text{nodes}}} N_j \cdot \mathsf{p}_j^{v} \tag{4.98}$$

$$\boldsymbol{\omega} \approx \boldsymbol{\omega}^{\mathsf{h}} = \sum_{j=1}^{n_{\text{nodes}}} N_j \cdot \boldsymbol{\omega}_j. \tag{4.99}$$

Therein, the shape function at a specific node j is denoted by N_j. Identical spatial discretizations for all unknown fields are used within the present computational approach. Only bi- respectively trilinear Lagrange polynomials are employed. Note that it has been assumed that n_{spec} species are present in the multiphase model (both in fluid phases and solid phase) which have been collected in the vector of species mass fractions $\boldsymbol{\omega} \in \mathbb{R}^{n_{\text{spec}}}$. The discrete nodal values of the respective primary variables of all fields are defined by

$$\mathbf{d}^s \in \mathbb{R}^{n_{\text{nodes}} \cdot n_{\text{dim}}},\ \boldsymbol{\psi}^{[t,h,l]} \in \mathbb{R}^{n_{\text{nodes}} \cdot 3},\ \boldsymbol{\varepsilon}^v \in \mathbb{R}^{n_{\text{nodes}}},\ \mathbf{p}^v \in \mathbb{R}^{n_{\text{nodes}}},\ \boldsymbol{\omega} \in \mathbb{R}^{n_{\text{nodes}} \cdot n_{\text{spec}}} \tag{4.100}$$

as nodal displacements, nodal generic primary variables of TCs, HCs and the IF, nodal HV volume fraction, nodal HV pressure and nodal species mass fractions. The respective scalar- or vector-valued nodal value at node j is employed for the interpolation in equations (4.95)-(4.99).

The spatial discretization of the 1D embedded vasculature is performed using $\hat{n}_{\text{ele}}$ elements and $\hat{n}_{\text{nodes}}$ nodes. Thus, the primary unknowns are approximated as

$$p^{\hat{v}} \approx p^{\hat{v},\mathsf{h}} = \sum_{j=1}^{\hat{n}_{\text{nodes}}} \hat{N}_j \cdot \mathsf{p}_j^{\hat{v}} \tag{4.101}$$

$$\boldsymbol{\omega}^{i\hat{v}} \approx \boldsymbol{\omega}^{i\hat{v},\mathsf{h}} = \sum_{j=1}^{\hat{n}_{\text{nodes}}} \hat{N}_j \cdot \boldsymbol{\omega}_j^{i\hat{v}} \tag{4.102}$$

with shape functions on the 1D domain $\hat{N}_j$. Linear Lagrange polynomials are used and the nodal primary variables of the 1D embedded domain are

$$\mathbf{p}^{\hat{v}} \in \mathbb{R}^{\hat{n}_{\text{nodes}}} \quad \text{and} \quad \boldsymbol{\omega}^{i\hat{v}} \in \mathbb{R}^{\hat{n}_{\text{nodes}} \cdot \hat{n}_{\text{spec}}}, \tag{4.103}$$

that is, nodal pressures and nodal species mass fractions. Here, it has been assumed that an arbitrary number of species $\hat{n}_{\text{spec}}$ are transported in the 1D domain. Following a Bubnov-Galerkin approach, the weighting functions are interpolated using the same shape functions as

$$\delta\boldsymbol{d}^s \approx \delta\boldsymbol{d}^{s,\mathsf{h}} = \sum_{j=1}^{n_{\text{nodes}}} N_j \cdot \delta\mathbf{d}_j \tag{4.104}$$

$$\delta\boldsymbol{\psi}^{[t,h,l]} \approx \delta\boldsymbol{\psi}^{[t,h,l],\mathsf{h}} = \sum_{j=1}^{n_{\text{nodes}}} N_j \cdot \delta\boldsymbol{\psi}_j^{[t,h,l]} \tag{4.105}$$

$$\delta\varepsilon^v \approx \delta\varepsilon^{v,\mathsf{h}} = \sum_{j=1}^{n_{\text{nodes}}} N_j \cdot \delta\varepsilon_j^v \tag{4.106}$$

$$\delta p^v \approx \delta p^{v,\mathsf{h}} = \sum_{j=1}^{n_{\text{nodes}}} N_j \cdot \delta\mathsf{p}_j \tag{4.107}$$

$$\delta\boldsymbol{\omega} \approx \delta\boldsymbol{\omega}^{\mathsf{h}} = \sum_{j=1}^{n_{\text{nodes}}} N_j \cdot \delta\boldsymbol{\omega}_j \tag{4.108}$$

in the porous medium domain and as

$$\delta p^{\hat{v}} \approx \delta p^{\hat{v},\mathsf{h}} = \sum_{j=1}^{\hat{n}_{\text{nodes}}} \hat{N}_j \cdot \delta \mathsf{p}_j^{\hat{v}} \tag{4.109}$$

$$\delta \boldsymbol{\omega}^{i\hat{v}} \approx \delta \boldsymbol{\omega}^{i\hat{v},\mathsf{h}} = \sum_{j=1}^{\hat{n}_{\text{nodes}}} \hat{N}_j \cdot \delta \boldsymbol{\omega}_j^{i\hat{v}} \tag{4.110}$$

in the embedded vasculature domain. The corresponding discrete nodal variations have identical dimensions as the primary variables defined by (4.100) respectively (4.103). Finally, the isoparametric concept is applied, thereby approximating material and current coordinates of the 3D domain with the same shape functions as the displacements

$$\boldsymbol{X} \approx \boldsymbol{X}^{\mathsf{h}} = \sum_{j=1}^{n_{\text{nodes}}} N_j \cdot \mathbf{X}_j \tag{4.111}$$

$$\boldsymbol{x} \approx \boldsymbol{x}^{\mathsf{h}} = \sum_{j=1}^{n_{\text{nodes}}} N_j \cdot \mathbf{x}_j \tag{4.112}$$

where $\mathbf{X}$ and $\mathbf{x}$ are nodal coordinates in reference and current configuration, respectively.

Remark 4.4. *Due to the similarity of the energy balance equation (2.69) to species transport, it is evaluated together with all involved species. Thus, if the temperature field is relevant, it is a part of the discrete nodal vector of species primary variables $\boldsymbol{\omega}$ in the 3D domain. The corresponding discrete nodal temperature vector $\mathbf{T} \in \mathbb{R}^{n_{\text{nodes}}}$ and its variation is interpolated like all other primary variables. Since this is straightforward, it is not shown here in detail. If species transport is referred to in the following, it may always implicitly contain the energy balance equation.*

4.3.3 Spatial Discretization and Numerical Evaluation of 1D-3D Coupling

In this section, the spatial discretization of the different contributions to 1D-3D coupling, that is, transvascular exchange terms, the constraint enforcement between embedded and homogenized vasculature and the blood vessel diameter adaptation and collapse model is illustrated. An advantageous feature of the developed methods is that they allow for non-matching meshes in 1D and 3D domain such that the respective discretizations are completely independent. Constructing a 3D mesh which conforms with the embedded 1D mesh may become very expensive or even infeasible considering the complexity of blood vessel networks. By contrast, a regular grid may be employed here for the 3D tissue domain. It does not have to follow the embedded vasculature, see also Figure 4.1. However, this complicates the evaluation of the 1D-3D coupled terms which is why a special focus lies on their numerical spatial integration in the following sections. Note that the centerline coupling variant can also be applied for problems with a two-dimensional tissue domain resulting in a 1D-2D coupled problem.

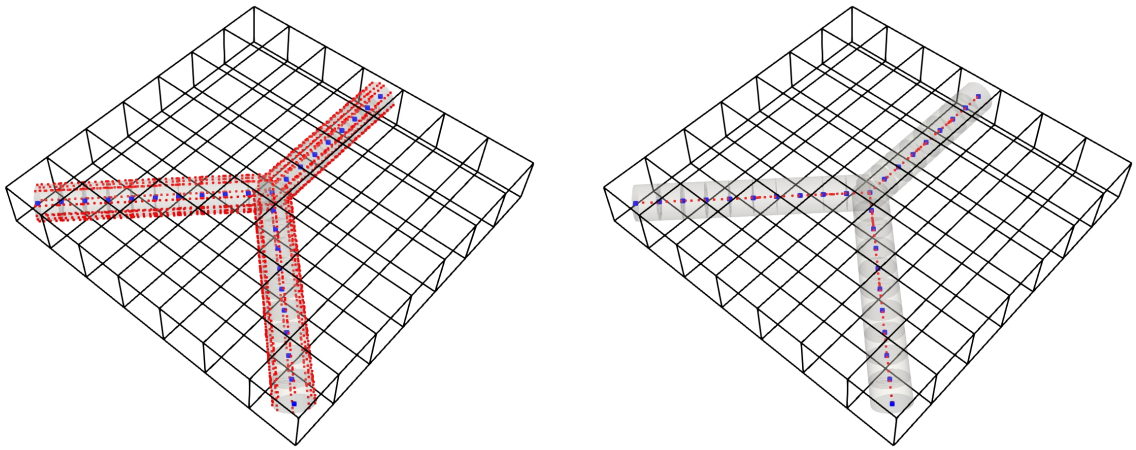

(a) Gauss points for lateral surface coupling

(b) Gauss points for centerline coupling

Figure 4.1: Comparison of Gauss points for lateral surface and centerline coupling – Gauss points are plotted in red, nodes of 1D embedded vasculature in blue.

4.3.3.1 Transvascular Exchange Terms

The generic transvascular exchange terms require either a two-dimensional integration of these terms across the lateral surface of the 1D embedded domain, see Figure 4.1a, or a one-dimensional integration along its centerline, see Figure 4.1b. Similar integrals of non-matching discretizations have to be evaluated in the context of contact or mesh-tying in solid mechanics. Commonly, two different approaches are discerned, namely, element-based integration or segment-based integration, conf. Farah et al. [73] for an extensive review and investigation. In the following, both variants are transferred to 1D-3D coupled problems and applied where appropriate.

Remark 4.5. *Movement of the embedded one-dimensional domain with the ALE formulation as well as blood vessel compression and collapse is currently only realized for the centerline coupling variant. Hence, in the following paragraphs the explanations will be given for the non-moving case, i.e., in terms of* $\boldsymbol{X}$*,* S *and* D_0*, which are the three-dimensional reference configuration, the arc-length coordinate of the 1D discretization in reference configuration and the constant reference element diameter* D_0*. The case of large deformations of the embedded vasculature domain is considered in more detail in Section A.3.*

Two-dimensional Element-based Integration for Lateral Surface Coupling The lateral surface coupling variant requires the integration of terms given by the contributions to the weak forms (4.58), (4.72), (4.77) and (4.82). These terms comprise the product of shape functions either defined on the 1D domain or on the 3D domain multiplied with a generic mass transfer term $f\left(\varphi^{\hat{v}}\left(S\right), \varphi^{l}\left(\boldsymbol{X}\left(S,\gamma\right)\right)\right)$. All terms have to be integrated across the lateral surface of the embedded domain to evaluate the potentially nonlinear mass transfer depending on the respective primary variables. Their linearization then involves products of the corresponding shape functions.

The strategy to evaluate these terms with an element-based approach is sketched in Figure 4.2. For every 1D element, Gauss quadrature is employed with a linear mapping of Gauss points

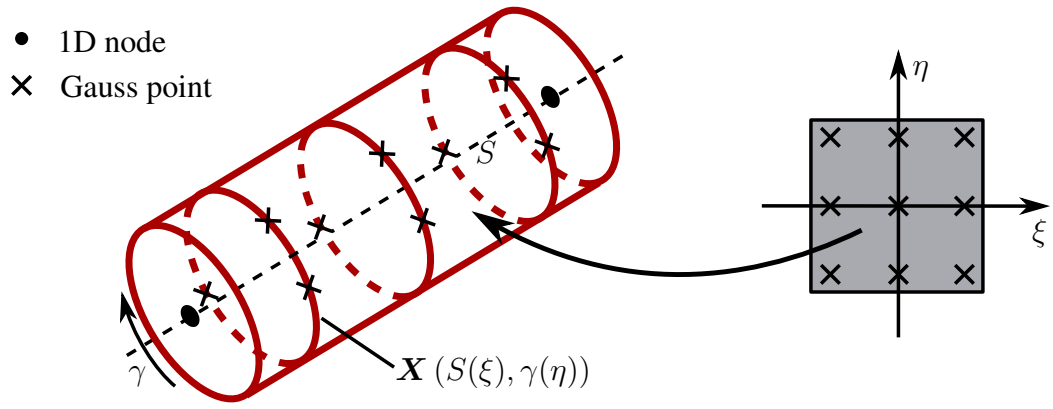

Figure 4.2: Sketch of two-dimensional element-based integration for lateral surface coupling – exemplarily, 3×3 Gauss points are defined in the typical two-dimensional parameter space and mapped onto lateral surface where integration is performed.

(GPs) from the typical parameter space $(\xi, \eta) \in [-1.0, 1.0] \times [-1.0, 1.0]$ onto the lateral surface of the considered 1D element defined by axial and circumferential coordinate S respectively γ. This yields the 1D primary variable at the axial coordinate $\varphi^{\hat{v}}\left(S\left(\xi\right)\right)$ (recall that 1D primary variables do not depend on the position at the circumference) and the reference coordinate $\boldsymbol{X}\left(S\left(\xi\right), \gamma\left(\eta\right)\right)$ of the respective GP. The 3D primary variable of the IF or a species in the IF $\varphi^{l}\left(\boldsymbol{X}\left(S\left(\xi\right), \gamma\left(\eta\right)\right)\right)$ at this point is required to evaluate the transvascular exchange. It is simply obtained via FE interpolation as the product of the three-dimensional shape functions inside the element, in which the coordinate is located, with the corresponding nodal values. Hence, the 3D element, in which a specific coordinate $\boldsymbol{X}\left(S\left(\xi\right), \gamma\left(\eta\right)\right)$ lies, has to be identified along with the values of the 3D shape functions at this coordinate. The described Gauss quadrature is applied for each 1D element. The single contributions to the 1D and 3D governing equations are then assembled using the standard FEM procedure to evaluate transvascular exchange over the entire discretized 1D domain. As a single 1D element may potentially interact with multiple 3D elements due to the non-matching discretizations, the mass transfer of a single 1D element is assembled into the DOFs of multiple 3D elements.

The proposed element-based scheme suffers from the shortcoming that integration over weak discontinuities, that is, kinks of 3D primary variables and shape functions employed to interpolate these primary variables is performed. This occurs as GPs are simply defined on the lateral surface of the 1D element without accounting for different 3D elements with which it may interact. Correspondingly, integration is performed across boundaries of 3D elements where kinks of shape functions are present. However, the numerical error introduced by this method can usually be minimized by employing a higher number of GPs [73]. This will also be done here as a segmentation, that is, a generation of integration patches, where all 3D shape functions are continuous, is quite intricate. For strong discontinuities (jumps), however, which would correspond to a 1D element sticking out of the 3D domain in the present case, the error is much higher and cannot be remedied by employing more GPs [73]. Therefore, these cases are not possible with the current implementation. An additional inaccuracy is introduced by the overlap of 1D elements at junctions. Consider for instance the situation depicted in Figure 4.1a: At the junction in the middle of the domain the surfaces overlap and protrude into each other which is due

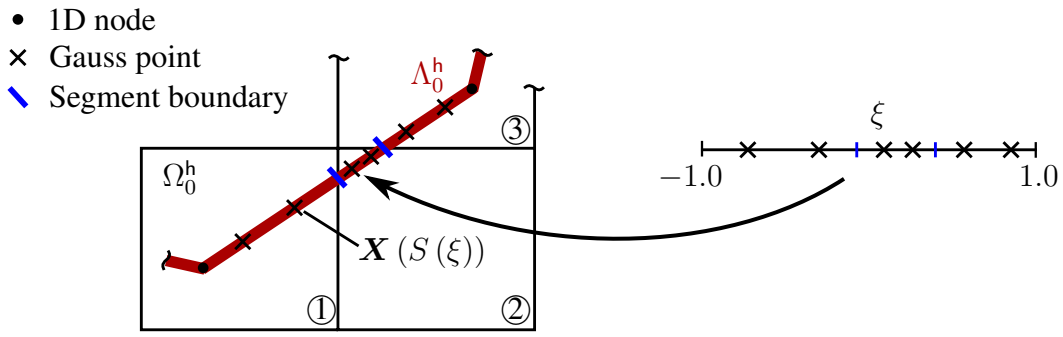

Figure 4.3: Sketch of one-dimensional segment-based integration for centerline coupling (in 2D) – exemplarily two Gauss points per segment are defined in the one-dimensional parameter space and mapped onto the centerline where integration is performed. The 1D element here interacts with three 2D elements which defines three integration segments. Figure taken from the author's article [137].

to the approximation of the embedded domain by straight cylinders. Similarly, this occurs at nodes, where only two non-parallel elements meet with an overlap on one side and a gap on the other side of the node. A better representation of the lateral surface of the vascular network via a smooth approximation with GPs defined there could help to prevent this error. In any case, it can be expected to be much lower than the modeling error.

One-dimensional Segment-based Integration for Centerline Coupling The centerline coupling variant requires the integration of similar terms which are given by the contributions to the weak forms (4.59), (4.73), (4.78) and (4.83). Again, these terms comprise the product of shape functions either defined on the 1D domain or on the 3D domain multiplied with a generic mass transfer term $\pi D_0(S) \cdot f\left(\varphi^{\hat{v}}(S), \varphi^{l}(\boldsymbol{X}(S))\right)$. The major difference is that these terms now have to be integrated along the centerline of the embedded domain and not across the lateral surface and correspondingly depend only on the axial coordinate S. In turn, the linearization of the potentially nonlinear mass transfer then involves products of the appropriate shape functions.

A one-dimensional segment-based integration has been implemented for this variant. The following explanation of this procedure is taken from the author's publication [137]. As sketched in Figure 4.3, the 1D integrals are again evaluated with Gauss quadrature. However, at first each 1D element is segmented by finding the intersections with its 2D or 3D interaction partners. This yields 1D pieces interacting with a single 2D/3D element on which also the shape functions of the respective 2D/3D element are continuous. Then, GPs are defined in the single segments, mapped from the element parameter space on the 1D centerline and the 1D primary variable at the axial coordinate $\varphi^{\hat{v}}(S(\xi))$ can again be obtained. In addition, the spatial coordinate $\boldsymbol{X}(S(\xi))$ of the respective GP, which is now defined on the 1D centerline and not on the lateral surface of the inclusion, is required to obtain the 2D/3D primary variable projected on the centerline as $\varphi^{l}(\boldsymbol{X}(S(\xi)))$. Once more, this requires obtaining the shape function values of the respective 2D/3D element at this coordinate. The integral for a specific 1D element then emerges as the sum over the integrals of all its segments and the respective contributions are assembled into the DOFs of the 1D and the interacting 2D/3D elements.

The employed segmentation algorithm can also deal with 1D elements protruding out of the 2D or 3D domain. In that case, the protruding part, that is, the protruding segment of this element is simply not evaluated for transvascular exchange. Such cases could be of interest if blood flow or species transport in a larger part of the circulatory system is studied, but transvascular exchange should only be included for a specific sub-part, possibly an organ where the 3D distribution of a chemical species is required.

4.3.3.2 Constraint Terms

The second type of interaction between the 1D embedded domain and the multiphase porous medium system are the coupling terms between resolved and homogenized representation of the vasculature. They occur only for the hybrid model variant. In Section 4.3.1.3, two different approaches were introduced, a Gauss-point-to-segment and a mortar-type approach. It was further shown that the Gauss-point-to-segment scheme simply represents an additional mass transfer term between resolved and homogenized vasculature. Therefore, this term is treated as the exchange terms between embedded vasculature and IF and is evaluated either via the 2D element-based integration for lateral surface coupling or the 1D segment-based integration for centerline coupling. Hence, only the discretization of the mortar-type approach and the employed penalty regularization will be illustrated in the following. The following section was previously published in the author's article [136], where only the centerline variant was treated. Here, an adaptation for the surface-coupled variant is additionally presented.

Subsequently, the LM field λ is expressed explicitly in terms of the primary variables of homogenized and embedded vasculature. This can be achieved by a penalty regularization of the constraint of matching pressures and mass fractions. Consequently, the nodal LMs do not enter the problem formulation as additional DOFs.

The spatially discretized form of the LM potential (4.89) respectively (4.91) is given by

$$\delta\Pi^{\mathsf{h}}_{\mathrm{LM}} = \sum_{j\in\mathcal{S}}\sum_{k\in\mathcal{S}} \lambda_j D_{jk} \delta\varphi^{\hat{v}}_k - \sum_{j\in\mathcal{S}}\sum_{l\in\mathcal{M}} \lambda_j M_{jl} \delta\varphi^{v}_l \tag{4.113}$$

with the well-known mortar matrices

$$\mathbf{D}\,[j,k] = D_{jk} = \int_{\Lambda^{\mathsf{h}}_t} \hat{\Phi}_j \hat{N}_k \,\mathrm{d}s, \qquad \mathbf{M}\,[j,l] = M_{jl} = \int_{\Lambda^{\mathsf{h}}_t} \hat{\Phi}_j N_l \,\mathrm{d}s \tag{4.114}$$

for centerline coupling and

$$\mathbf{D}\,[j,k] = D_{jk} = \int_{\Lambda^{\mathsf{h}}_0} \pi D_0(S) \hat{\Phi}_j \hat{N}_k \,\mathrm{d}S, \qquad \mathbf{M}\,[j,l] = M_{jl} = \int_{\Lambda^{\mathsf{h}}_0} \hat{\Phi}_j \int_0^{\pi D_0(S)} N_l \,\mathrm{d}\gamma \mathrm{d}S \tag{4.115}$$

for lateral surface coupling. The latter one is evaluated in reference configuration since a moving embedded domain has not yet been realized for this variant. In the spatially discretized form of (4.113) a nodal Lagrange multiplier λ_j, as well as nodal variations of the primary variables $\delta\varphi^{\hat{v}}_k$ on the discretized 1D domain Λ^{h} and nodal variations of the primary variables $\delta\varphi^{v}_l$ in the discretized 3D domain Ω^{h} were introduced. The indices j and k identify nodes on the discretized 1D domain, while l is employed for nodes in the 3D domain. $\mathcal{S}$ and $\mathcal{M}$ denote the subsets of

nodes on the 1D domain respectively in the 3D domain which actually form the discrete interface. Shape functions in those domains are denoted with $\hat{N}_k$ and N_l, respectively. Furthermore, the Lagrange multiplier shape function at a node belonging to the 1D discretization is $\hat{\Phi}_j$. It is assumed that every node of the 1D domain carries a nodal Lagrange multiplier with corresponding shape function, which has to be chosen from a suitable function space to ensure inf-sup stability [17]. In the following, only linear shape functions for both primary variables and Lagrange multiplier interpolation on the 1D domain will be applied, that is, $\hat{\Phi}_j = \hat{N}_j$. These shape functions of the 1D domain do also not depend on the position at the lateral surface which is why they can be pulled out of the circumferential integral in (4.115).

For the penalty regularization of the constraint, the discretized weighted pressure or species "gap" at node j of the discretized one-dimensional domain is defined as

$$g_j := \frac{1}{\kappa_j} \left(\sum_k D_{jk} \varphi_k^{\hat{v}} - \sum_l M_{jl} \varphi_l^{v} \right) \tag{4.116}$$

with

$$\kappa_j = \int_{\Lambda_t^h} \hat{\Phi}_j \, \mathrm{d}s \tag{4.117}$$

and

$$\kappa_j = \int_{\Lambda_0^h} \pi D_0(S) \hat{\Phi}_j \, \mathrm{d}S \tag{4.118}$$

for the two different variants. As in [292], the scaling with the inverse of (4.117) respectively (4.118) guarantees consistent units of the weighted "gap" g_j. It can be employed for a penalty regularization of the nodal Lagrange multiplier λ_j as

$$\lambda_j = \epsilon_{\mathrm{MP}} \cdot g_j \tag{4.119}$$

with (mortar) penalty parameter ϵ_{MP}. This definition is then inserted into (4.113) to eliminate the Lagrange multipliers from the global problem. Hence, after scaling with the appropriate time factor as described above, the discretized weak form (4.113) can be assembled into the appropriate global DOFs. More details on the exact form of the arising entries in matrix-vector notation are also given in Section 6.2.3. Again, the penalty parameter determines how accurately the constraint will be fulfilled. However, as will be shown in Section A.2, the MP method is not prone to overconstrainment as opposed to the GPTS scheme.

Remark 4.6. *It has to be emphasized that the dimensions of the mass transfer equations defined on the embedded domain and the surrounding tissue are different. The balance of mass of blood* (3.79) *and species* (3.84) *are written in terms of* $[\mathrm{length}]^2/[\mathrm{time}]$ *while the ones of the 3D tissue domain, e.g.,* (3.99) *or* (3.100) *are formulated in terms of* $1/[\mathrm{time}]$. *The coupling between the equations is achieved via the Dirac terms* δ_{Λ_t} *or* $\delta_{\mathcal{D}_t}$ *whose dimensions are actually* $1/[\mathrm{length}]^2$ *and* $1/[\mathrm{length}]$ *according to their definitions* (3.93) *respectively* (3.89). *Hence, the units of the penalty parameters* ϵ_{GPTS} *and* ϵ_{MP} *are* $[\mathrm{length}]^2/[\mathrm{time} \cdot \mathrm{pressure}]$ *for the coupling of pressures and* $[\mathrm{length}]^2/[\mathrm{time}]$ *for the coupling of species in the centerline variant. In the lateral surface variant their units are* $[\mathrm{length}]/[\mathrm{time} \cdot \mathrm{pressure}]$ *and* $[\mathrm{length}]/[\mathrm{time}]$, *respectively,*

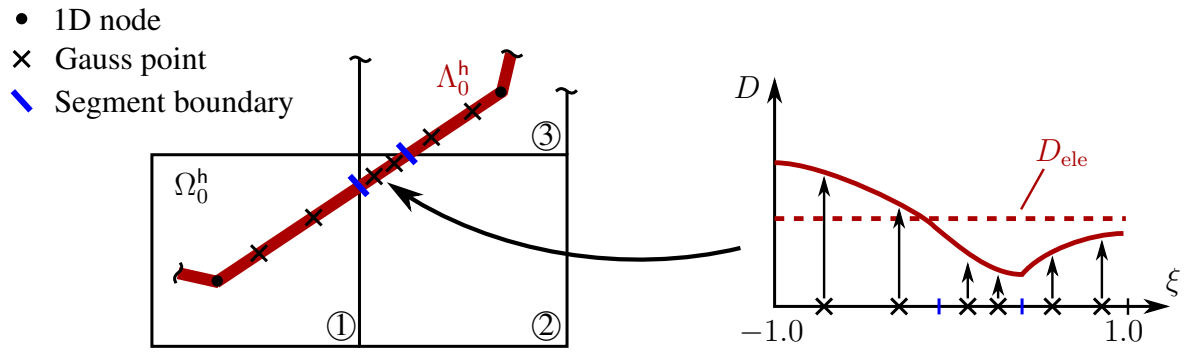

Figure 4.4: Sketch of evaluation of diameter for blood vessel diameter adaptation and collapse (in 2D) – diameter may possibly vary along the element, element diameter D_{ele} is evaluated via segment-based Gaussian quadrature.

since the terms are additionally integrated across the diameter. Both definitions make the interpretation of the penalty parameters as permeabilities straightforward. From a modeling point of view, such finite permeabilities might even be advantageous. For instance, they could be employed to account for the partition of red blood cell flux between pre-existing and homogenized vasculature. Red blood cells might preferentially follow the higher blood flow in the pre-existing, developed vasculature such that hematocrit and correspondingly the oxygen mass fraction in the homogenized vasculature is lower [240].

4.3.3.3 Blood Vessel Diameter Adaptation and Collapse

The third contribution to 1D-3D interaction is via the blood vessel diameter adaptation and collapse model introduced in Section 3.4.5. Using the current formulation, the diameter of the embedded vasculature is shrinked according to the influence of the growing tumor. Thus, the diameter depends on the primary variables of the surrounding porous medium domain. This nonlinear dependency has to be evaluated for each embedded 1D element and also linearized to solve the coupled system of equation with a Newton-Raphson scheme. Preliminary work on this topic was done under close guidance by the author in a Master's thesis [195]. Due to the non-conforming 1D and 3D mesh, also for this type of coupling, which has currently only been realized for the centerline coupling variant, several interesting aspects arise. Figure 4.4 depicts that, if the diameter along the 1D element is calculated with the functional dependency (3.101) or in the more general case with (3.104), it may possibly vary because the primary variables in the 2D/3D domain change along its length. The average element diameter may be computed via a segment-based Gauss quadrature along the considered 1D element of length L_{ele}

$$D_{ele} = \frac{1}{L_{ele}} \sum_{i=1}^{n_{seg}} \sum_{g=1}^{n_{GP}} w_g \cdot D\left(\xi_g\right) J\left(\xi_g\right), \tag{4.120}$$

with Gauss points ξ_g, weights w_g and Jacobian J. This element-wise constant diameter is employed for all but the 1D-3D exchange terms, i.e., for the first and last term in the weak form of blood flow (4.76) and all terms except for the exchange terms in the weak form of 1D species transport (4.81). For evaluating the exchange terms (equations (4.59), (4.78), (4.73), (4.83)),

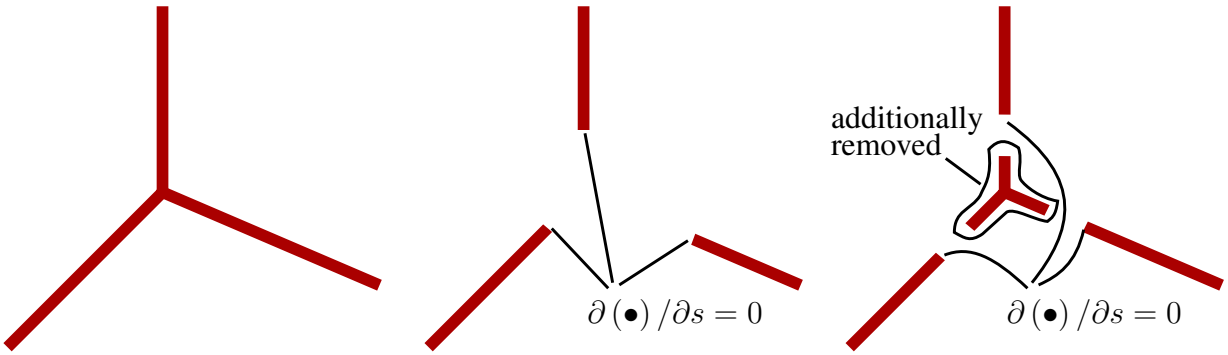

(a) Initial network (b) Collapse with open ends (c) Collapse with free-hanging part

Figure 4.5: Different cases occurring during blood vessel collapse

which are scaled with the diameter for centerline coupling, the diameter at the GPs $D(\xi_g)$ is employed. This procedure was proposed in the Master's thesis by Plöckl [195]. As described in more detail there, on the one hand, the advantage of this formulation is that velocity and flow inside a specific 1D element are still constant despite the varying diameter (as for the case where the diameter is constant inside each element). It can be calculated with the Poiseulle relation (3.78) by employing the average element diameter D_{ele}. Otherwise, the flow would continuously change inside each 1D element according to the varying diameter. On the other hand, employing the GP diameter for the 1D-3D exchange terms does not require the calculation of additional linearizations from different segments of the same 1D element [195] which would be a considerable computational effort.

Finally, the treatment of the collapse of 1D elements requires special attention. According to (3.103), elements collapse entirely if their average element diameter D_{ele} drops below the diameter threshold $D_{\text{coll-thresh}}$. For the sake of simplicity, these elements are removed and it is further assumed that they remain collapsed over the subsequent course of the simulation. The implications for the 1D embedded domain are sketched in Figure 4.5. Starting from the initial topology of Figure 4.5a, two different cases are illustrated. Let us assume that the inner part of the network has fallen below the diameter threshold in Figure 4.5b. The corresponding elements are taken out and, automatically, a no-flux boundary condition is set for blood flow and species transport in the embedded domain at the newly formed tips. Also from a physiological stand point, this seems reasonable as vessel occlusion is occupied with flow stasis [132, Figure 2]. A second case is sketched in Figure 4.5c. Here, connecting elements have collapsed such that a free-hanging network part, that is, a part which is not connected to boundary conditions on the initial network tips emerges. Numerically, 1D pressure and species mass fraction are not defined in this part. Hence, these elements are additionally removed from the 1D blood vessel network. This approach can also be motivated physiologically: Since this sub-part is not connected to the rest of the network any more, flow and wall shear stress inside it is zero. Therefore, it will regress quickly once endothelial cells sense the absence of flow [62]. In the actual implementation, the removal of these small unconnected sub-parts is realized by sorting the graph associated with the vessel network into connected sub-components. Separate parts which are not connected to any in- or outlet are deleted.

Remark 4.7. *In the preceding paragraphs it was assumed that the interaction partners of 1D and 3D discretization, i.e., the respective elements are known such that the coupling terms can simply be evaluated by numerical integration and assembled into the respective DOFs. However, in the actual parallel implementation of the computational framework [8] this is far from trivial. The following strategy has been devised: Possible interaction partners, i.e., intersecting 1D and 3D elements are determined via a spatial search using an octree. If a 1D and a 3D element interacting with each other do not lie on the same processor, the 1D element is additionally "ghosted" on the owning processor of the 3D element. This extended ghosting assures that the respective 1D-3D contributions can be evaluated and assembled.*

4.3.4 Final Discrete System

The final discrete system of equations is obtained with the standard assembly procedure of the finite element method. A coupled system of discrete nonlinear residuals $\mathbf{R}$ at time step $n+1$ emerges as

$$\mathbf{R}^{s}_{n+1}\left(\underline{\mathbf{d}^{s}_{n+1}}, \boldsymbol{\psi}^{[t,h,l]}_{n+1}, \boldsymbol{\varepsilon}^{v}_{n+1}, \mathbf{p}^{v}_{n+1}\right) = \mathbf{0} \quad \text{with} \quad \mathbf{R}^{s}_{n+1} \in \mathbb{R}^{n_{\text{nodes}} \cdot n_{\text{dim}}} \tag{4.121}$$

$$\mathbf{R}^{[t,h,l,v]}_{n+1}\left(\mathbf{d}^{s}_{n+1}, \underline{\boldsymbol{\psi}^{[t,h,l]}_{n+1}}, \underline{\boldsymbol{\varepsilon}^{v}_{n+1}}, \underline{\mathbf{p}^{v}_{n+1}}, \boldsymbol{\omega}_{n+1}, \mathbf{p}^{\hat{v}}_{n+1}\right) = \mathbf{0} \quad \text{with} \quad \mathbf{R}^{[t,h,l,v]}_{n+1} \in \mathbb{R}^{n_{\text{nodes}} \cdot 5} \tag{4.122}$$

$$\mathbf{R}^{\text{spec}}_{n+1}\left(\mathbf{d}^{s}_{n+1}, \boldsymbol{\psi}^{[t,h,l]}_{n+1}, \boldsymbol{\varepsilon}^{v}_{n+1}, \mathbf{p}^{v}_{n+1}, \underline{\boldsymbol{\omega}_{n+1}}, \boldsymbol{\omega}^{i\hat{v}}_{n+1}\right) = \mathbf{0} \quad \text{with} \quad \mathbf{R}^{\text{spec}}_{n+1} \in \mathbb{R}^{n_{\text{nodes}} \cdot n_{\text{spec}}} \tag{4.123}$$

$$\hat{\mathbf{R}}^{\hat{v}}_{n+1}\left(\mathbf{d}^{s}_{n+1}, \boldsymbol{\psi}^{[t,h,l]}_{n+1}, \mathbf{p}^{v}_{n+1}, \underline{\mathbf{p}^{\hat{v}}_{n+1}}\right) = \mathbf{0} \quad \text{with} \quad \hat{\mathbf{R}}^{\hat{v}}_{n+1} \in \mathbb{R}^{\hat{n}_{\text{nodes}}} \tag{4.124}$$

$$\hat{\mathbf{R}}^{\text{spec}}_{n+1}\left(\mathbf{d}^{s}_{n+1}, \boldsymbol{\psi}^{[t,h,l]}_{n+1}, \boldsymbol{\varepsilon}^{v}_{n+1}, \mathbf{p}^{v}_{n+1}, \boldsymbol{\omega}_{n+1}, \mathbf{p}^{\hat{v}}_{n+1}, \underline{\boldsymbol{\omega}^{i\hat{v}}_{n+1}}\right) = \mathbf{0} \quad \text{with} \quad \hat{\mathbf{R}}^{\text{spec}}_{n+1} \in \mathbb{R}^{\hat{n}_{\text{nodes}} \cdot \hat{n}_{\text{spec}}} \tag{4.125}$$

where the primary variable of each equation has been underlined. The weak form of the balance of linear momentum (4.68) is entering the system through the discrete residual (4.121). The multiphase system with the weak forms of the evolution equation for the vascular volume fraction (4.65), the balance of mass of blood in the homogenized vasculature (4.62) and the balance of mass of TCs, HCs and the IF (4.56)-(4.57) is represented by (4.122). Species transport in the multiphase system with the respective weak form (4.71) is described through (4.123). Equation (4.124) corresponds to the Hagen-Poiseuille equation for blood flow in the 1D embedded vasculature (4.76) while (4.125) constitutes the discretized form of species transport in the 1D embedded vasculature (4.81).

The nonlinear system of equations (4.121)-(4.125) represents the most general situation if the hybrid model type is employed. All other variants are included in this formulation, for instance, the one with homogenized representation of the vasculature corresponds to the first three discrete nonlinear residuals. In the following, the strategy to solve this coupled system of nonlinear equations in the employed computational framework is presented. For the solution of the single field nonlinear residuals in partitioned schemes or the combined solution with monolithic schemes, the Newton-Raphson algorithm is employed which requires a linearization of the respective nonlinear equations at every Newton step. A detailed description of the necessary linearizations is omitted here.

4.4 Coupling Schemes

There exist different solution schemes for nonlinear systems of equations such as (4.121)-(4.125) originating from a FEM formulation of coupled physical problems. Generally, they can be classified into partitioned and monolithic schemes. The latter ones solve the entire set of nonlinear equations simultaneously within one nonlinear solution procedure, commonly a Newton-Raphson scheme, per time step. For strongly coupled problems with bi-directional dependencies, they have been proven to be the most efficient and robust schemes, see e.g. [88, 138] in the context of fluid-structure interaction problems and [54] in the context of thermo-structure interaction problems.

Their counterparts are partitioned schemes where the nonlinear sub-problems are solved consecutively (with fixed contributions from the other fields). The major advantage of partitioned solution procedures is their flexibility since different methods or existing solvers for the single fields, e.g., commercial software codes can be coupled and re-used [263], and their straighforward implementation compared to monolithic algorithms. They can be further sub-divided into loosely coupled or staggered schemes and strongly coupled or iteratively staggered schemes [54]. Loosely coupled schemes involve only one nonlinear solution algorithm per field per time step, i.e., the fields are solved sequentially without any additional iterations between the fields. They are the method of choice for uni-directional or weak couplings between the fields. By contrast, strongly coupled schemes involve iterations between the fields until a certain pre-defined convergence criterion is met, see also Figures 4.6, 4.7 and 4.8. For each nonlinear solution procedure of a single field, the last obtained values from the other fields are applied and this single field is solved with these fixed contributions for its primary variable. Subsequently, this new solution is applied to the next field, which is in turn solved with fixed values from all other fields. This algorithm is continued until convergence is achieved, that is, until all fields are in equilibrium.

Due to the strong bi-directional relations in the five-field problem (4.121)-(4.125), especially the strong coupling present in large deformation porous medium problems [269, 270, 272], only strongly coupled schemes are sensible, that is, either monolithic schemes or partitioned schemes with iterations between the fields. Furthermore, while the residuals are written down as a five-field problem, from a physical point of view only three fields are present, namely, solid deformation, fluid flow and species transport: Hence, the first field is the structural deformation of the ECM described by (4.121). The second one is the tumor growth model with interacting phases in the 3D domain (4.122) coupled with the 1D embedded vasculature with blood flow (4.124). The third one is species transport in the porous medium system (4.123) coupled with species transport in the 1D embedded vasculature (4.125). Hence, even in the partitioned schemes presented here the 1D-3D coupled (flow and species transport) subproblems are solved simultaneously as in other related publications [38, 51, 53, 130, 131, 177, 178].

In the following sections, several coupling schemes will be introduced: two partitioned ones in Sections 4.4.1 and 4.4.2 with slightly different strategies, one hybrid monolithic-partitioned scheme in Section 4.4.3 where the porous medium part including skeleton deformation of the problem is resolved monolithically while the coupling with species transport is treated iteratively and, finally, the fully-monolithic scheme where the global problem is solved within on global solution procedure per time step. Except for the nested-partitioned scheme from Section 4.4.2, the following sections were previously published in the author's article [135] for the model variant with homogenized vasculature. Here, the algorithms are extended for the most general

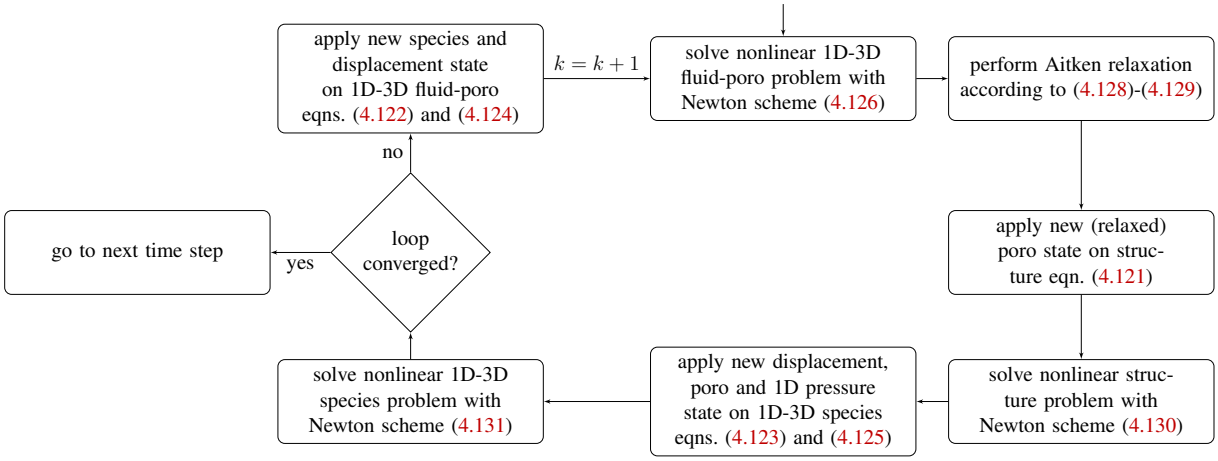

Figure 4.6: Algorithm for one time step of sequential-partitioned scheme (adapted from the author's publication [135])

case of the hybrid model including also a 1D representation of the vasculature with the respective additional nonlinear residuals (4.124) and (4.125). As before, the other model variants can be obtained by only solving a subset of its governing equations respectively nonlinear residuals.

4.4.1 Sequential-Partitioned Scheme

The first coupling algorithm is termed sequential-partitioned scheme. Each of the three single blocks (4.121), (4.122) together with (4.124), and (4.123) together with (4.125) is solved individually for its 1D and 3D primary variables. Then, the coupling variables are transferred between the fields. Figure 4.6 depicts the algorithm for the three-field coupled partitioned scheme. First, the nonlinear problems of the tumor growth model including the homogenized vasculature (4.122) coupled with blood flow in the 1D inclusion (4.124) at the partitioned step k are solved with a Newton scheme

$$\begin{bmatrix} \frac{\partial \mathbf{R}^{[t,h,l,v]}}{\partial \boldsymbol{\psi}^{[t,h,l,v]}} & \frac{\partial \mathbf{R}^{[t,h,l,v]}}{\partial \mathbf{p}^{\hat{v}}} \\ \frac{\partial \hat{\mathbf{R}}^{\hat{v}}}{\partial \boldsymbol{\psi}^{[t,h,l,v]}} & \frac{\partial \hat{\mathbf{R}}^{\hat{v}}}{\partial \mathbf{p}^{\hat{v}}} \end{bmatrix}^{i}_{n+1,k} \begin{bmatrix} \Delta\boldsymbol{\psi}^{[t,h,l,v]} \\ \Delta \mathbf{p}^{\hat{v}} \end{bmatrix}^{i+1}_{n+1,k} = - \begin{bmatrix} \mathbf{R}^{[t,h,l,v]} \\ \hat{\mathbf{R}}^{\hat{v}} \end{bmatrix}^{i}_{n+1,k},$$
$$\begin{bmatrix} \tilde{\boldsymbol{\psi}}^{[t,h,l,v]} \\ \mathbf{p}^{\hat{v}} \end{bmatrix}^{i+1}_{n+1,k} = \begin{bmatrix} \tilde{\boldsymbol{\psi}}^{[t,h,l,v]} \\ \mathbf{p}^{\hat{v}} \end{bmatrix}^{i}_{n+1,k} + \begin{bmatrix} \Delta\boldsymbol{\psi}^{[t,h,l,v]} \\ \Delta \mathbf{p}^{\hat{v}} \end{bmatrix}^{i+1}_{n+1,k} \tag{4.126}$$

for each Newton iteration $i \to i+1$. Note the block matrix structure of the linearized system of equations where the main-diagonal terms correspond to linearizations of the respective residual with respect to its governing primary variable as underlined in (4.121)-(4.125). The off-diagonal coupling terms here represent the 1D-3D coupled terms, i.e., the mass transfer and constraint enforcement terms between embedded 1D vasculature and 3D porous tissue. Furthermore, a nodal primary variable vector $\boldsymbol{\psi}^{[t,h,l,v]}$, which comprises both the generic nodal fluid primary variables $\boldsymbol{\psi}^{[t,h,l]}$ of TCs, HCs and the IF as well as the nodal homogenized vasculature primary variables, that is, the nodal volume fraction $\boldsymbol{\varepsilon}^v$ and nodal homogenized blood pressure $\mathbf{p}^v$, has

been defined as

$$\boldsymbol{\psi}^{[t,h,l,v]} = \begin{bmatrix} \boldsymbol{\psi}^{[t,h,l]} \\ \boldsymbol{\varepsilon}^{v} \\ \mathbf{p}^{v} \end{bmatrix}. \tag{4.127}$$

Note that the structure equation does not directly depend on the 1D blood pressure $\mathbf{p}^{\hat{v}}$. Therefore, only the solution of the homogenized compartment is then transferred to the structure equation after performing relaxation with Aitken's Δ^2 method [139, 140].

Aitken relaxation is a simple, flexible and easy to implement method which can significantly improve the convergence behaviour and stability of generic partitioned schemes. The basic idea behind this scheme is to employ the secant method with the solutions of the last two partitioned steps to accelerate the convergence of the partitioned loop. An extensive discussion of the method for interface-coupled fluid-structure interaction can be found in the thesis of Küttler [138]. With this approach, not the actual solution $\tilde{\boldsymbol{\psi}}_{n+1,k}^{[t,h,l,v]}$ of the Newton scheme (4.126) is transferred to the structural field, but a relaxed state defined as

$$\boldsymbol{\psi}_{n+1,k}^{[t,h,l,v]} = \boldsymbol{\psi}_{n+1,k-1}^{[t,h,l,v]} + \omega_k \left(\tilde{\boldsymbol{\psi}}_{n+1,k}^{[t,h,l,v]} - \boldsymbol{\psi}_{n+1,k-1}^{[t,h,l,v]} \right) \tag{4.128}$$

with Aitken relaxation parameter ω_k and the relaxed solution $\boldsymbol{\psi}_{n+1,k-1}^{[t,h,l,v]}$ of the previous partitioned step $k-1$. The relaxation parameter is dynamically adapted. It is defined recursively as

$$\omega_k = -\omega_{k-1} \frac{\left(\tilde{\boldsymbol{\psi}}_{n+1,k}^{[t,h,l,v]} - \boldsymbol{\psi}_{n+1,k-1}^{[t,h,l,v]} \right)^T \cdot \left(\left(\tilde{\boldsymbol{\psi}}_{n+1,k}^{[t,h,l,v]} - \boldsymbol{\psi}_{n+1,k-1}^{[t,h,l,v]} \right) - \left(\tilde{\boldsymbol{\psi}}_{n+1,k-1}^{[t,h,l,v]} - \boldsymbol{\psi}_{n+1,k-2}^{[t,h,l,v]} \right) \right)}{\left\| \left(\tilde{\boldsymbol{\psi}}_{n+1,k}^{[t,h,l,v]} - \boldsymbol{\psi}_{n+1,k-1}^{[t,h,l,v]} \right) - \left(\tilde{\boldsymbol{\psi}}_{n+1,k-1}^{[t,h,l,v]} - \boldsymbol{\psi}_{n+1,k-2}^{[t,h,l,v]} \right) \right\|^2} \tag{4.129}$$

for each partitioned step k from the two previous solutions of the partitioned loop. The new relaxed state $\boldsymbol{\psi}_{n+1,k}^{[t,h,l,v]}$ is transferred to the structure equation (4.121), which is evaluated for this state and can in turn be solved with a Newton scheme

$$\left[\frac{\partial \mathbf{R}^s}{\partial \mathbf{d}^s} \right]_{n+1,k}^{i} \Delta \mathbf{d}_{n+1,k}^{s,i+1} = -\mathbf{R}_{n+1,k}^{s,i}, \qquad \mathbf{d}_{n+1,k}^{s,i+1} = \mathbf{d}_{n+1,k}^{s,i} + \Delta \mathbf{d}_{n+1,k}^{s,i+1} \tag{4.130}$$

for the displacements. Finally, the current solution of the partitioned iteration at step k, i.e., displacements $\mathbf{d}_{n+1,k}^{s}$, 1D pressures $\mathbf{p}_{n+1,k}^{\hat{v}}$ as well as (relaxed) fluid primary variables $\boldsymbol{\psi}_{n+1,k}^{v}$ are applied to the 1D-3D coupled species problem (4.123) and (4.125). Again, this nonlinear equation is solved with a Newton scheme

$$\begin{bmatrix} \frac{\partial \mathbf{R}^{\mathrm{spec}}}{\partial \boldsymbol{\omega}} & \frac{\partial \mathbf{R}^{\mathrm{spec}}}{\partial \boldsymbol{\omega}^{i\hat{v}}} \\ \frac{\partial \hat{\mathbf{R}}^{\mathrm{spec}}}{\partial \boldsymbol{\omega}} & \frac{\partial \hat{\mathbf{R}}^{\mathrm{spec}}}{\partial \boldsymbol{\omega}^{i\hat{v}}} \end{bmatrix}_{n+1,k}^{i} \begin{bmatrix} \Delta \boldsymbol{\omega} \\ \Delta \boldsymbol{\omega}^{i\hat{v}} \end{bmatrix}_{n+1,k}^{i+1} = - \begin{bmatrix} \mathbf{R}^{\mathrm{spec}} \\ \hat{\mathbf{R}}^{\mathrm{spec}} \end{bmatrix}_{n+1,k}^{i},$$
$$\begin{bmatrix} \boldsymbol{\omega} \\ \boldsymbol{\omega}^{i\hat{v}} \end{bmatrix}_{n+1,k}^{i+1} = \begin{bmatrix} \boldsymbol{\omega} \\ \boldsymbol{\omega}^{i\hat{v}} \end{bmatrix}_{n+1,k}^{i} + \begin{bmatrix} \Delta \boldsymbol{\omega} \\ \Delta \boldsymbol{\omega}^{i\hat{v}} \end{bmatrix}_{n+1,k}^{i+1} \tag{4.131}$$

for the n_{spec} present species in the homogenized domain and the $\hat{n}_{\mathrm{spec}}$ species in the resolved 1D domain, i.e., equations (4.123) and (4.125) are solved simultaneously for all considered species.

Coupling terms between different species arise due to (1D-3D or 3D-3D) mass transfer terms and the coupling between resolved and homogenized vasculature.

Lastly, only the new 3D species states $\boldsymbol{\omega}_{n+1,k}$ and the new displacement state $\mathbf{d}^s_{n+1,k}$ is fed back to the 1D-3D fluid poro sub-problem (4.122) and (4.124) since there is no direct dependency of this problem on the 1D species state $\boldsymbol{\omega}^{i\hat{v}}$. This loop is repeated until convergence has been achieved. Subsequently, the algorithm progresses to the next time step. The convergence criterion is the relative change in the solution primary variables from one partitioned iteration step to the next which has to be smaller than a pre-defined tolerance ϵ_{part}, i.e.,

$$\begin{aligned}
&\frac{\left\|\tilde{\boldsymbol{\psi}}^{[t,h,l,v]}_{n+1,k} - \tilde{\boldsymbol{\psi}}^{[t,h,l,v]}_{n+1,k-1}\right\|}{\left\|\tilde{\boldsymbol{\psi}}^{[t,h,l,v]}_{n+1,k}\right\|} < \epsilon_{\text{part}} \quad \text{and} \quad \frac{\left\|\mathbf{d}^s_{n+1,k} - \mathbf{d}^s_{n+1,k-1}\right\|}{\left\|\mathbf{d}^s_{n+1,k}\right\|} < \epsilon_{\text{part}} \quad \text{and} \\
&\frac{\left\|\boldsymbol{\omega}_{n+1,k} - \boldsymbol{\omega}_{n+1,k-1}\right\|}{\left\|\boldsymbol{\omega}_{n+1,k}\right\|} < \epsilon_{\text{part}} \quad \text{and} \quad \frac{\left\|\mathbf{p}^{\hat{v}}_{n+1,k} - \mathbf{p}^{\hat{v}}_{n+1,k-1}\right\|}{\left\|\mathbf{p}^{\hat{v}}_{n+1,k}\right\|} < \epsilon_{\text{part}} \quad \text{and} \\
&\frac{\left\|\boldsymbol{\omega}^{i\hat{v}}_{n+1,k} - \boldsymbol{\omega}^{i\hat{v}}_{n+1,k-1}\right\|}{\left\|\boldsymbol{\omega}^{i\hat{v}}_{n+1,k}\right\|} < \epsilon_{\text{part}}.
\end{aligned} \tag{4.132}$$

Also the single field Newton schemes need a suitable convergence criterion. Naturally, it has to be defined stricter than the partitioned convergence criterion of (4.132) such that the error in the single field solvers does not influence the convergence of the partitioned loop. Again, relative increments from one Newton step to the next with a single field tolerance of

$$\epsilon_{\text{sf}} = 0.01\epsilon_{\text{part}} \tag{4.133}$$

are evaluated. In addition, a further check

$$\begin{aligned}
&\frac{\left\|\mathbf{R}^{[t,h,l,v]}_{n+1,k}\right\|}{\sqrt{n_{\text{nodes}} \cdot 5}} < \epsilon_{\text{sf}} \quad \text{and} \quad \frac{\left\|\mathbf{R}^{s}_{n+1,k}\right\|}{\sqrt{n_{\text{nodes}} \cdot n_{\text{dim}}}} < \epsilon_{\text{sf}} \quad \text{and} \quad \frac{\left\|\mathbf{R}^{\text{spec}}_{n+1,k}\right\|}{\sqrt{n_{\text{nodes}} \cdot n_{\text{spec}}}} < \epsilon_{\text{sf}} \quad \text{and} \\
&\frac{\left\|\hat{\mathbf{R}}^{\hat{v}}_{n+1,k}\right\|}{\sqrt{\hat{n}_{\text{nodes}}}} < \epsilon_{\text{sf}} \quad \text{and} \quad \frac{\left\|\hat{\mathbf{R}}^{\text{spec}}_{n+1,k}\right\|}{\sqrt{\hat{n}_{\text{nodes}} \cdot \hat{n}_{\text{spec}}}} < \epsilon_{\text{sf}}
\end{aligned} \tag{4.134}$$

guarantees that also the residuals of the single fields have reached convergence within their Newton loop. Here, the RMS norm is employed to have a mesh-independent quantity.

Remark 4.8. *In almost all practical cases investigated for the tumor growth model, convergence without relaxation was impossible to obtain. A relaxation with constant parameter* $0 < \omega_k < 1$ *was also implemented and tested. Preliminary simulations revealed an improved robustness, see Section 5.1, but the dynamic relaxation using Aitken's method was by far more stable and more efficient.*

4.4.2 Nested-Partitioned Scheme

A similar partitioned algorithm is depicted in Figure 4.7. Instead of a sequential solution of all three fields, an alternative nested solution strategy is performed. The experience of similar

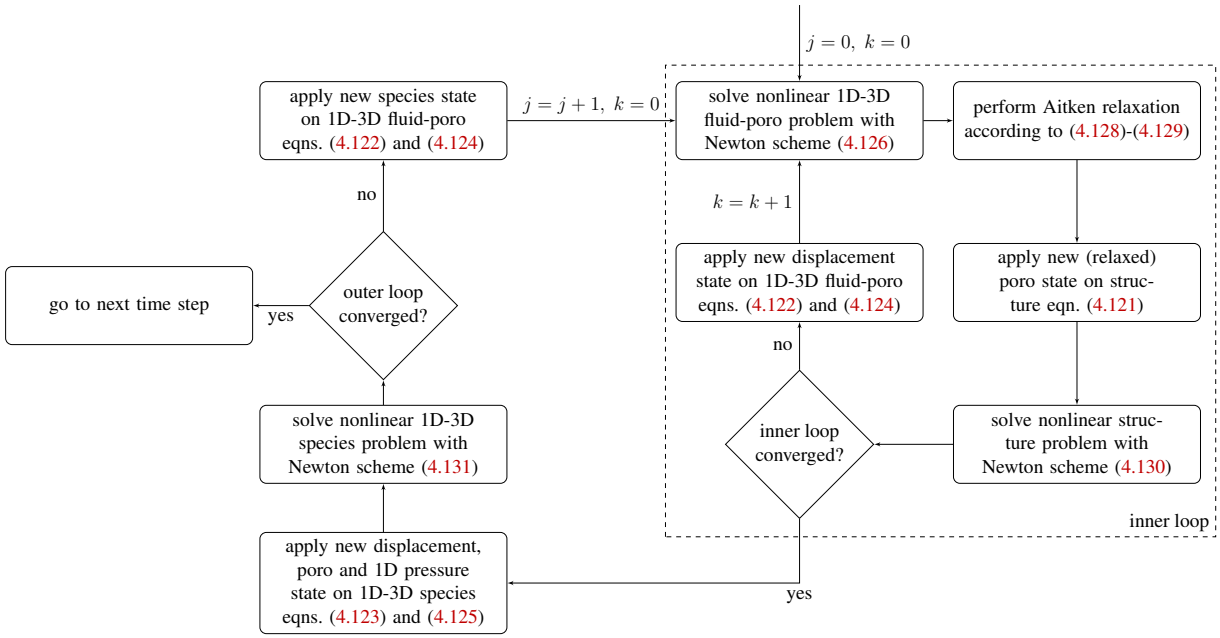

Figure 4.7: Algorithm for one time step of nested-partitioned scheme

porous medium systems [269, 270] including species transport [212, 271, 272] shows that the coupling between fluid flow and large structural deformation is much stronger than the coupling with species transport. Hence, the rationale behind this approach is to first resolve the strongest coupling between structural deformation and flow in the porous medium, and then to resolve the coupling between the deformable porous medium problem and species transport therein.

The 1D-3D coupled poro-fluid and structure problem are solved in an inner partitioned loop with the respective Newton schemes (4.126) and (4.130) in combination with Aitken relaxation until convergence between the two fields is reached, while the species solution is kept fixed. The obtained equilibrium configuration, that is, converged solid displacements $\mathbf{d}^{s}_{n+1,j}$, tumor growth model variables $\boldsymbol{\psi}^{[t,h,l,v]}_{n+1,j}$ and 1D blood pressures $\mathbf{p}^{\hat{v}}_{n+1,j}$ of the nested loop, is then applied on the nonlinear 1D-3D coupled species transport problem, which is in turn solved with the Newton scheme (4.131). Next, the coupled porous medium problem including structural deformation is again iteratively solved with the newly obtained species solution. This is repeated until convergence in the outer loop is achieved and the algorithm progresses to the next time step. Convergence checks of partitioned loops and single field solvers are performed as described in the previous section.

Remark 4.9. *The nested partitioned scheme would offer the possibility to add another relaxation scheme for the outer loop with a respective Aitken scheme by relaxing displacement, multiphase and 1D pressure state before applying them on the nonlinear 1D-3D species problem* (4.131)*. However, this approach was not further investigated as the studies from Section 5.1 showed that convergence in the outer loop was achieved rapidly while the inner loop needed much more iterations due to the strong coupling between ECM deformation and tumor growth.*

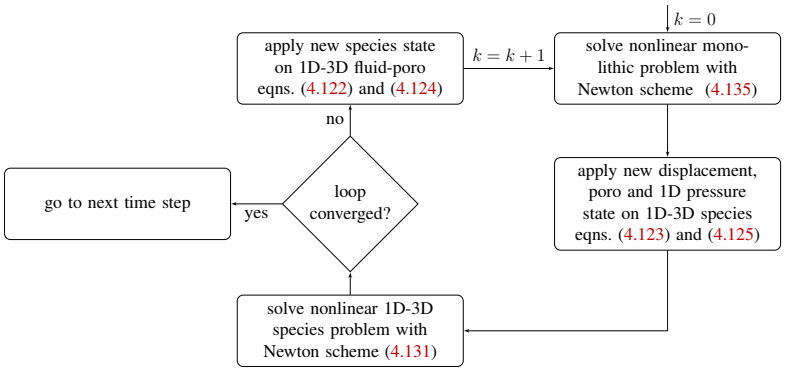

Figure 4.8: Algorithm for one time step of monolithic-partitioned scheme (adapted from the author's publication [135])

4.4.3 Monolithic-Partitioned Scheme

As a first improvement to the partitioned algorithms, a hybrid monolithic-partitioned scheme similar to [212, 271, 272] can be devised. As mentioned above, the strongest coupling is present for the poro-elasticity sub-problem. Thus, most of the computational time is spent in resolving the coupling between the structural deformation and the cell respectively fluid flow. Hence, in a first step, the nonlinear coupling between these two fields (4.121) and (4.122) (plus the 1D problem (4.124)) can be resolved monolithically, while a partitioned scheme is employed for the coupling with species transport. The corresponding algorithm is depicted in Figure 4.8. Compared to the nested-partitioned scheme of Figure 4.7, the inner loop between fluid flow and structural deformation has been replaced by a monolithic coupling. Now, a Newton scheme

$$\begin{bmatrix} \frac{\partial \mathbf{R}^s}{\partial \mathbf{d}^s} & \frac{\partial \mathbf{R}^s}{\partial \boldsymbol{\psi}^{[t,h,l,v]}} & \mathbf{0} \\ \frac{\partial \mathbf{R}^{[t,h,l,v]}}{\partial \mathbf{d}^s} & \frac{\partial \mathbf{R}^{[t,h,l,v]}}{\partial \boldsymbol{\psi}^{[t,h,l,v]}} & \frac{\partial \mathbf{R}^{[t,h,l,v]}}{\partial \mathbf{p}^{\hat{v}}} \\ \frac{\partial \hat{\mathbf{R}}^{\hat{v}}}{\partial \mathbf{d}^s} & \frac{\partial \hat{\mathbf{R}}^{\hat{v}}}{\partial \boldsymbol{\psi}^{[t,h,l,v]}} & \frac{\partial \hat{\mathbf{R}}^{\hat{v}}}{\partial \mathbf{p}^{\hat{v}}} \end{bmatrix}^{i}_{n+1,k} \begin{bmatrix} \Delta \mathbf{d}^s \\ \Delta \boldsymbol{\psi}^{[t,h,l,v]} \\ \Delta \mathbf{p}^{\hat{v}} \end{bmatrix}^{i+1}_{n+1,k} = - \begin{bmatrix} \mathbf{R}^s \\ \mathbf{R}^{[t,h,l,v]} \\ \hat{\mathbf{R}}^{\hat{v}} \end{bmatrix}^{i}_{n+1,k},$$

$$\begin{bmatrix} \mathbf{d}^s \\ \boldsymbol{\psi}^{[t,h,l,v]} \\ \mathbf{p}^{\hat{v}} \end{bmatrix}^{i+1}_{n+1,k} = \begin{bmatrix} \mathbf{d}^s \\ \boldsymbol{\psi}^{[t,h,l,v]} \\ \mathbf{p}^{\hat{v}} \end{bmatrix}^{i}_{n+1,k} + \begin{bmatrix} \Delta \mathbf{d}^s \\ \Delta \boldsymbol{\psi}^{[t,h,l,v]} \\ \Delta \mathbf{p}^{\hat{v}} \end{bmatrix}^{i+1}_{n+1,k} \tag{4.135}$$

is applied to simultaneously solve for the unknown nodal displacements $\mathbf{d}^s_{n+1,k}$, homogenized fluid primary variables $\boldsymbol{\psi}^{[t,h,l,v]}_{n+1,k}$ and 1D nodal pressures $\mathbf{p}^{\hat{v}}_{n+1,k}$. Hence, the single-field Newton schemes (4.126) and (4.130) are replaced by a monolithic approach. Due to the linearization of the sub-problems with respect to the primary variables of the other field, additional off-diagonal blocks in the monolithic system matrix on the left hand side of (4.135) are present, for instance, the derivative of the solid residual $\mathbf{R}^s$ w.r.t. the primary variables $\boldsymbol{\psi}^{[t,h,l,v]}$ of the homogenized porous medium system and vice versa. As the residual of the structure does not directly depend on the 1D pressure, the corresponding off-diagonal coupling block is empty. The monolithic system is solved with a Newton-Raphson algorithm until convergence is achieved and its solution is then applied to the 1D-3D species transport problem (4.123) and (4.125), which is again

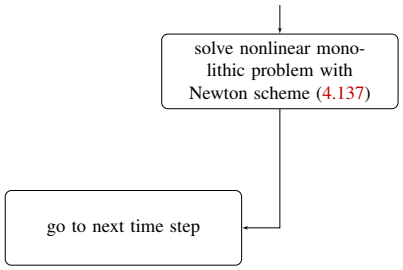

Figure 4.9: Algorithm for one time step of fully-monolithic scheme (adapted from the author's publication [135])

solved by its Newton scheme (4.131). The calculated species solution is transferred to the poro-elasticity problem and the iteration is continued until convergence. The convergence check for the partitioned scheme is given by (4.132) as before. Relative increments and the residual criterion defined in (4.134) are employed to assess convergence of the species field and the monolithic Newton scheme (4.135) with tolerance ϵ_{sf} defined by (4.133).

Remark 4.10. *Via the deformation of the surrounding tissue, the residual of blood flow in the embedded vasculature* $\mathbf{R}^{\hat{v}}$ *depends on the ECM deformation* $\mathbf{d}^s$*. So far, this contribution is not consistently linearized w.r.t. the deformations. The corresponding submatrix in* (4.135) *is instead set to zero:*

$$\frac{\partial \hat{\mathbf{R}}^{\hat{v}}}{\partial \mathbf{d}^s} = \mathbf{0} \tag{4.136}$$

Neglecting this term did not show any significant influence on the convergence of the Newton scheme for typical deformations occuring during tumor growth.

4.4.4 Monolithic Scheme

Finally, the coupled nonlinear system (4.121)-(4.125) can be solved with a fully-monolithic algorithm resulting in the following Newton scheme

$$\begin{bmatrix} \frac{\partial \mathbf{R}^s}{\partial \mathbf{d}^s} & \frac{\partial \mathbf{R}^s}{\partial \boldsymbol{\psi}^{[t,h,l,v]}} & \mathbf{0} & \mathbf{0} & \mathbf{0} \\ \frac{\partial \mathbf{R}^{[t,h,l,v]}}{\partial \mathbf{d}^s} & \frac{\partial \mathbf{R}^{[t,h,l,v]}}{\partial \boldsymbol{\psi}^{[t,h,l,v]}} & \frac{\partial \mathbf{R}^{[t,h,l,v]}}{\partial \boldsymbol{\omega}} & \frac{\partial \mathbf{R}^{[t,h,l,v]}}{\partial \mathbf{p}^{\hat{v}}} & \mathbf{0} \\ \frac{\partial \mathbf{R}^{\text{spec}}}{\partial \mathbf{d}^s} & \frac{\partial \mathbf{R}^{\text{spec}}}{\partial \boldsymbol{\psi}^{[t,h,l,v]}} & \frac{\partial \mathbf{R}^{\text{spec}}}{\partial \boldsymbol{\omega}} & \frac{\partial \mathbf{R}^{\text{spec}}}{\partial \mathbf{p}^{\hat{v}}} & \frac{\partial \mathbf{R}^{\text{spec}}}{\partial \boldsymbol{\omega}^{i\hat{v}}} \\ \frac{\partial \hat{\mathbf{R}}^{\hat{v}}}{\partial \mathbf{d}^s} & \frac{\partial \hat{\mathbf{R}}^{\hat{v}}}{\partial \boldsymbol{\psi}^{[t,h,l,v]}} & \mathbf{0} & \frac{\partial \hat{\mathbf{R}}^{\hat{v}}}{\partial \mathbf{p}^{\hat{v}}} & \mathbf{0} \\ \frac{\partial \hat{\mathbf{R}}^{\text{spec}}}{\partial \mathbf{d}^s} & \frac{\partial \hat{\mathbf{R}}^{\text{spec}}}{\partial \boldsymbol{\psi}^{[t,h,l,v]}} & \frac{\partial \hat{\mathbf{R}}^{\text{spec}}}{\partial \boldsymbol{\omega}} & \frac{\partial \hat{\mathbf{R}}^{\text{spec}}}{\partial \mathbf{p}^{\hat{v}}} & \frac{\partial \hat{\mathbf{R}}^{\text{spec}}}{\partial \boldsymbol{\omega}^{i\hat{v}}} \end{bmatrix}^{i}_{n+1} \begin{bmatrix} \Delta \mathbf{d}^s \\ \Delta \boldsymbol{\psi}^{[t,h,l,v]} \\ \Delta \boldsymbol{\omega} \\ \Delta \mathbf{p}^{\hat{v}} \\ \Delta \boldsymbol{\omega}^{i\hat{v}} \end{bmatrix}^{i+1}_{n+1} = - \begin{bmatrix} \mathbf{R}^s \\ \mathbf{R}^{[t,h,l,v]} \\ \mathbf{R}^{\text{spec}} \\ \hat{\mathbf{R}}^{\hat{v}} \\ \hat{\mathbf{R}}^{\text{spec}} \end{bmatrix}^{i}_{n+1},$$

$$\begin{bmatrix} \mathbf{d}^s \\ \boldsymbol{\psi}^{[t,h,l,v]} \\ \boldsymbol{\omega} \\ \mathbf{p}^{\hat{v}} \\ \boldsymbol{\omega}^{i\hat{v}} \end{bmatrix}^{i+1}_{n+1} = \begin{bmatrix} \mathbf{d}^s \\ \boldsymbol{\psi}^{[t,h,l,v]} \\ \boldsymbol{\omega} \\ \mathbf{p}^{\hat{v}} \\ \boldsymbol{\omega}^{i\hat{v}} \end{bmatrix}^{i}_{n+1} + \begin{bmatrix} \Delta \mathbf{d}^s \\ \Delta \boldsymbol{\psi}^{[t,h,l,v]} \\ \Delta \boldsymbol{\omega} \\ \Delta \mathbf{p}^{\hat{v}} \\ \Delta \boldsymbol{\omega}^{i\hat{v}} \end{bmatrix}^{i+1}_{n+1} \tag{4.137}$$

with a corresponding 5×5 block structure of the monolithic tangent matrix. Compared to the monolithic porous medium system (4.135), additional off-diagonal matrices have been added as well as the main-diagonal tangent matrices of the 1D-3D coupled species problem. Note also that several zero off-diagonal block matrices reflect the fact that no coupling terms are present between different fields, e.g., structural deformation is not directly coupled to 1D and 3D species transport and the same applies to blood flow in the 1D discretization. The fully-monolithic algorithm of Figure 4.9 requires a solution of the monolithic Newton scheme (4.137) for each time step until the desired tolerance is met. For that, residuals in RMS norm (4.134) as well as relative increments (4.133) are employed with the Newton loop.

Remark 4.11. *Again, the linearization of the blood flow equation on the embedded 1D domain and, additionally, species transport on the 1D domain w.r.t. the displacements is not consistently done and the respective contributions in* (4.137) *are set to zero:*

$$\frac{\partial \hat{\mathbf{R}}^{\hat{v}}}{\partial \mathbf{d}^s} = \mathbf{0} \quad \text{and} \quad \frac{\partial \hat{\mathbf{R}}^{\text{spec}}}{\partial \mathbf{d}^s} = \mathbf{0}. \tag{4.138}$$

Neglecting these terms did not show any significant influence on the convergence of the Newton scheme for typical deformations occuring during tumor growth. In addition, the weak form of species transport in the embedded vasculature (4.81) *including the exchange term* (4.83) *and its counterpart* (4.73) *acting on species transport in the tissue domain depend on the radius of the embedded domain. If blood vessel diameter adaptation in the form of* (3.101) *or the more general form of* (3.104) *is considered, the diameter depends directly on blood pressure or fluid primary variables of the surrounding tissue domain. The respective linearizations of the residuals* $\hat{\mathbf{R}}^{\text{spec}}$ *and* $\mathbf{R}^{\text{spec}}$ *w.r.t. the discrete 1D pressure* $\mathbf{p}^{\hat{v}}$ *and the 3D primary variables* $\boldsymbol{\psi}^{[t,h,l,v]}$ *are also neglected. In preliminary runs, a minor deterioration of the convergence behaviour of the Newton scheme was observed.*

4.4.5 Efficient Solvers for Large Linear Systems of Equations with Block Matrix Structure

For each Newton step of the monolithic algorithm illustrated in Figure 4.9, a linear system of equations with 5×5 block pattern shown in Figure 4.10 has to be solved. However, also the partitioned schemes require the solution of block matrix-type systems due to the present 1D-3D coupling. For instance, the 1D-3D coupled porous medium system is contained in the system of Figure 4.10 (with main-diagonal blocks $[2,2]$ and $[4,4]$ and off-diagonal coupling blocks $[2,4]$ and $[4,2]$) as well as the 1D-3D coupled species transport system (with main-diagonal blocks $[3,3]$ and $[5,5]$ and off-diagonal coupling blocks $[3,5]$ and $[5,3]$). The same applies to the monolithic-partitioned scheme with corresponding 3×3 sub-system. The sparsity pattern depicted in Figure 4.10 is representative of the studied 1D-3D problems where the one-dimensional discretization usually has considerably less nodes than the 3D mesh. Only partitioned algorithms for the avascular tumor growth model and the vascular tumor growth model with homogenized representation of the vasculature do not require the solution of these block matrix systems but of the single block matrices $[1,1]$, $[2,2]$ and $[3,3]$ from Figure 4.10. For all other model types and algorithms, at least one such block matrix system has to be repeatedly solved in a corresponding

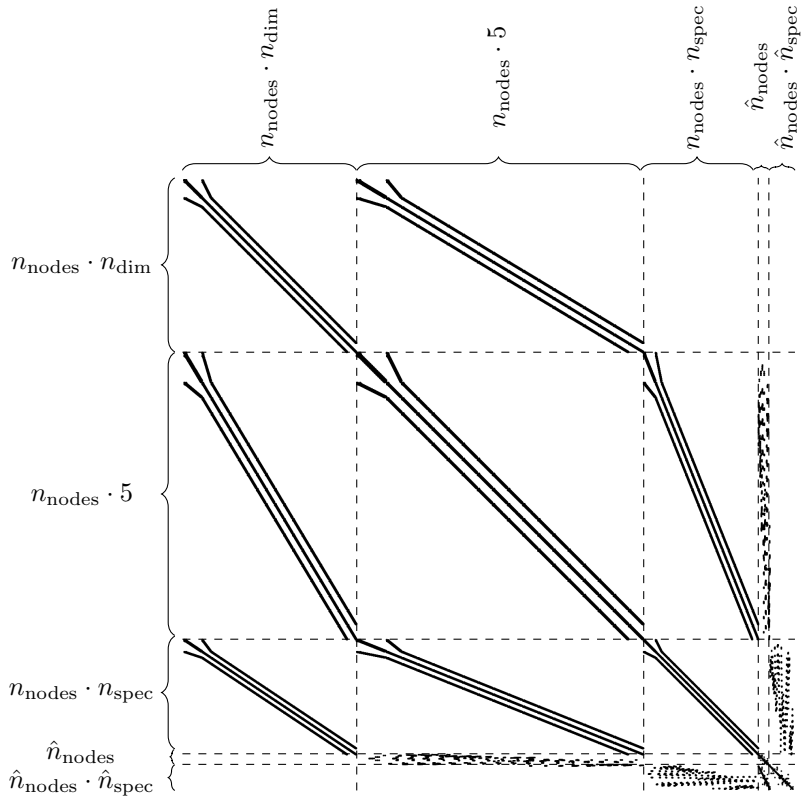

Figure 4.10: Typical sparsity pattern of monolithic system (4.137). Submatrices from (4.138) are set to zero due to missing linearizations.

Newton loop. Efficient solvers for these types of linear equations are vital for the performance of the tumor growth models since the linear solver time usually constitutes a considerable amount of the total computational time.

The distinct fields represented by their respective sparse main- and off-diagonal blocks introduce their different physical characteristics and parameters into the system often leading to a bad conditioning of the global system matrices. Hence, standard iterative linear solvers for sparse matrices such as the generalized minimal residual method (GMRES) cannot be applied without sophisticated, problem-specific preconditioners. Powerful preconditioners are a major factor for improving the performance of the presented algorithms. The preconditioners employed in this thesis are based on the work of Verdugo and Wall [263], where an efficient solution framework for an arbitrary number of fields has been developed and applied to thermo- and fluid-structure interaction. This implementation has been re-used here. Recently, it has also been applied to a coupled model of the human lung [264] and to three-dimensional, coupled finite element models of lithium-ion cells [72].

A detailed description of these preconditioning techniques can be found in [72, 263, 264]. Here, only the general idea behind them is outlined briefly. Basically, they consist of a block Gauss-Seidel (BGS) method combined with an algebraic multigrid (AMG) method. Two variants were presented by Verdugo and Wall [263]: The first variant is termed BGS(AMG) method and consists of an outer BGS loop to uncouple the respective subsystems, in the most general

case the five fields of (4.137) and Figure 4.10. Then, each of the individual fields is separately preconditioned using the AMG method with corresponding V-cycle. However, the coupling between the physical fields is only enforced on the finest AMG level through the outer block iteration and not on its coarser representations of the AMG hierarchies which are independent of each other. Therefore, Verdugo and Wall [263] developed a second variant termed AMG(BGS) preconditioner based on earlier work of Gee et al. [88]. This method can be interpreted as the reversed version of the BGS(AMG) scheme. First, an outer AMG hierarchy for the entire system is constructed and on each of the AMG levels a BGS iteration is performed. Thus, all AMG levels are inherently coupled in contrast to the BGS(AMG) method where only the finest level is.

Both methods have different advantages and use-cases as summarized by Fang et al. [72]: The BGS(AMG) method is comparably easy to implement in contrast to the more intricate AMG(BGS) preconditioner. Nevertheless, due to its intrinsic coupling also on coarser levels, the latter one usually performs better for strongly coupled problems. Vice versa, for weakly coupled problems its overall larger computational effort may lead to a reduced efficiency. In these cases, the BGS(AMG) scheme might already be sufficient. Furthermore, it offers a more flexible environment for fine-tuning the method because the single AMG solvers can be tailored to the specific field and each field can have a different number of levels, which is not possible with the AMG(BGS) variant. In summary, both methods offer a versatile and robust tool to solve large block matrix-type systems of equations. Both variants have successfully been employed for the tumor growth model in combination with the GMRES iterative solver but a detailed performance comparison of the preconditioners is not the main focus of this thesis.

5 Numerical Examples

This chapter contains several numerical examples of increasing complexity to showcase the capabilities of the developed tumor growth framework. All model variants are employed to illustrate their different use cases. The presentation of the single examples mirrors the development of the distinct models in Chapter 3: The performance of the different coupling schemes is investigated with an avascular example in Section 5.1. Then, two cases with homogenized representation of the vasculature follow. One is employed to illustrate the interplay between angiogenesis and tumor growth in Section 5.2 and the second one to study nanoparticle-based drug delivery and hyperthermia in Section 5.3. The model variant with discrete vasculature is used in Sections 5.4 and 5.5. In the latter one, a special focus lies on the developed methodology for blood vessel compression, collapse and regression. Finally, the hybrid version and its capability to induce angiogenesis from a pre-existing blood vessel network is studied in more detail in Section 5.6.

However, these examples do not represent a validation of the group of models with clinically relevant data. Rather, they should be understood as a validation of the models themselves in the sense that they are capable of all the features introduced in the previous chapters. A further validation to bring them towards clinical applicability was beyond the scope of this thesis which mainly focuses on their derivation and computational implementation. Nevertheless, it has to be emphasized that the avascular variant was partly validated and its parameters were fit with experimental data on multi-cellular tumor spheroids (MTSs) by Sciumè et al. [230, 233]. Moreover, the following cases have been designed to replicate physiological phenomena occurring during tumor growth and parameter values, for which data is available, are based on literature. Whenever possible, the results are verified with known empirical quantities and relationships such as the IF pressure range, oxygen and drug distributions, the time scales of angiogenesis or specific tumor growth patterns. An extensive comment on the necessary next steps for a validation of the model with *in-vitro* or *in-vivo* studies is given in Chapter 7. To enhance the readability of this chapter without too many technical explanations, the empirical mass transfer relationships and the model parameters are summarized in Appendix B and C.

5.1 Performance Comparison between Different Monolithic and Partitioned Coupling Schemes

In this section a concise evaluation of the different coupling schemes introduced in Section 4.4 is performed. It has previously been published in the author's article [135]. Here, the nested-partitioned coupling scheme, which was not considered in the original publication, is additionally investigated. For that, all calculations have been repeated with a more recent version of the computational framework.

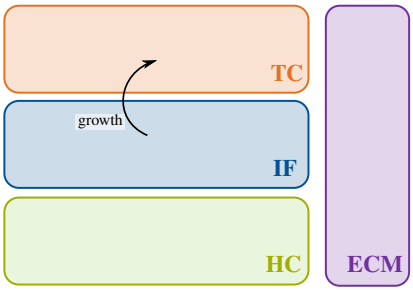

Phase	Mass transfer terms
ECM	0
HC	0
TC	$\overset{l\to t}{M}_{\text{growth}}$
IF	$-\overset{l\to t}{M}_{\text{growth}}$

(a) Phases with respective mass transfer relations

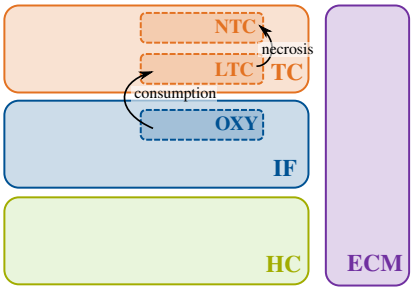

Species	Mass transfer terms
NTC	$\varepsilon^t r^{Nt} - \omega^{N\,\bar{t}}\,\overset{l\to t}{M}_{\text{growth}}$
OXY	$-\overset{nl\to t}{M}_{\text{cons}} - \omega^{n\,\bar{l}}\left(-\overset{l\to t}{M}_{\text{growth}}\right)$

(b) Species with respective mass transfer relations

Figure 5.1: Schematic overview of avascular model and mass transfer relations

The radial growth of a micro-metastasis over 120 hours in host tissue within a deformable ECM is chosen as a simple yet representative benchmark. Similar cases have been studied by Sciumè et al. [232, 233] and the computational setup and model variant is based on these contributions. Micro-metastases are often compared to the common experimental *in-vitro* model of MTSs to study cancer progression and response to therapy even though several conceptual differences exist, e.g., the lack of an initial ECM and other stroma components [176]. After being seeded in a petri dish, cells form spherical clusters, the so-called MTSs. As observed during the initial avascular growth of a micro-metastasis and in intercapillary tumor microregions, a proliferative outer rim emerges and necrosis may occur towards their center due to a lack of nutrients. As no vascular network is present after seeding of the micro-metastasis and in corresponding MTS experiments, the avascular model according to the overview in Figure 5.1 is used. Three phases (TCs, HCs, IF) are present in the pores of the ECM. In addition, two species are considered, namely oxygen in the IF and NTCs as part of the TCs. Their respective mass fractions are denoted as $\omega^{n\,\bar{l}}$ and $\omega^{N\,\bar{t}}$. Here and in the following, it is assumed that TCs partition into two dominating species, namely, NTCs and LTCs. Then, the LTC mass fraction does not have to be explicitly solved for as it is simply given by $\omega^{L\,\bar{t}} = 1 - \omega^{N\,\bar{t}}$ from the sum of species mass fractions (2.22). Without loss of generality, oxygen is the sole nutrient considered in all model types whose local level regulates tumor growth, hypoxia and necrosis. Further nutrients can simply be added as additional species in the IF. One phase mass transfer relationship corresponding to the growth of the TC phase is present. Two more species mass transfer relationships, one accounting for consumption of oxygen by LTCs and one accounting for necrosis, are considered. The exact expressions are given in Appendix B along with further explanations.

Figure 5.2 depicts geometry, initial and boundary conditions of the benchmark example used throughout this section. For symmetry reasons only a $9° \times 9°$ segment of the spherical 3D geom-

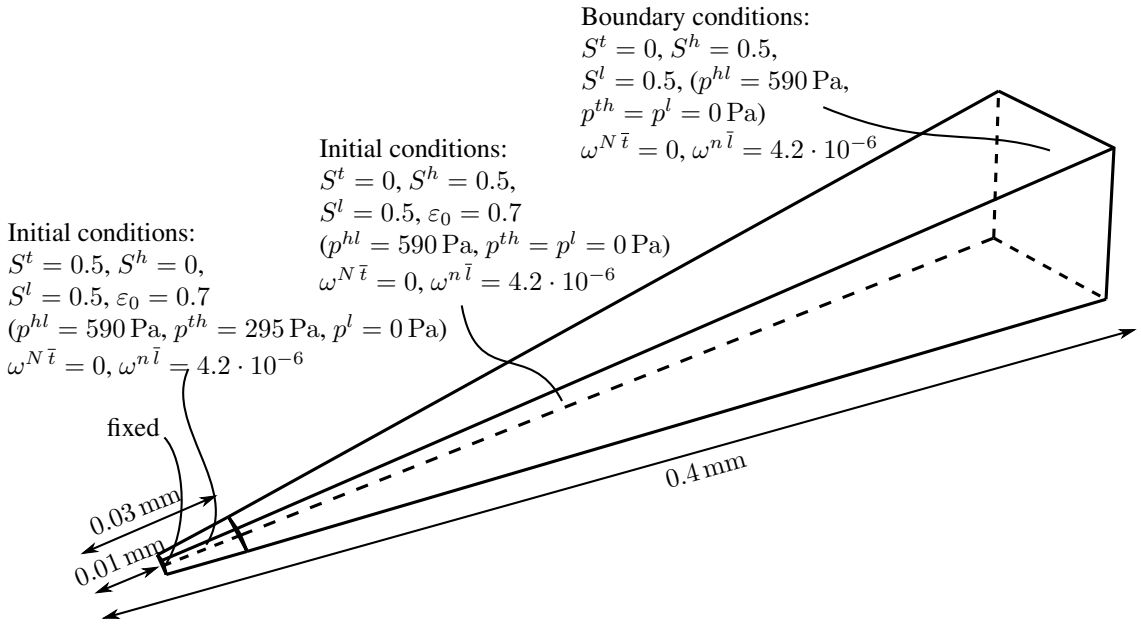

Figure 5.2: Geometry, initial and boundary conditions of the 3D benchmark problem (not to scale). Figure taken from the author's article [135].

etry with radius $0.4\,\mathrm{mm}$ is considered with appropriate boundary conditions on its side faces. If a boundary condition for a primary variable is not explicitly specified, a zero Neumann boundary condition is automatically assumed here and in the following examples. There is an inner region with radius $r = 0.03\,\mathrm{mm}$ with an initial TC saturation of $S^t = 0.5$ and a larger outer region where it is zero. 250 trilinear 3D elements are employed in radial direction resulting in a system consisting of in total 9632 degrees of freedom (structure, fluid and species). Before the actual simulation with 720 time steps is started, pressures are linearly increased from $p^l, p^t, p^h = 0$ in 10 steps until the desired saturations in the sub-domains as shown in Figure 5.2 are reached. This is necessary since otherwise the solid pressure p^s would act immediately at $t = 0$. This caused an unstable behaviour at the beginning of the simulation such that without this initialization procedure sometimes no convergence was achieved in the first time step. During the initialization, the structure deforms slightly such that also the porosity increases from the initial value ε_0 to a value of $\varepsilon \approx 0.8$ depending on the material parameters.

The Saint Venant-Kirchhoff material model is employed for the ECM. The parameters of the benchmark problem have been taken from [233, Table 3, 4, 5] and are here collected in Tables C.1, C.2, C.4 and C.5. A backward Euler scheme, that is, $\theta = 1$, is employed for time discretization with 720 steps of $\Delta t = 600\,\mathrm{s}$. The BGS(AMG) method is applied for preconditioning the monolithic systems (4.135) and (4.137) (without contributions from homogenized and discrete vasculature as the avascular model is studied) in combination with a GMRES iterative linear solver. For solving the linear systems of equations of the single fields in the partitioned schemes, also the GMRES method with AMG preconditioners is used. A strict outer convergence criterion for the monolithic and partitioned schemes of 1×10^{-6} is employed, which implies that the single field tolerances for convergence according to (4.133) are $\epsilon_{\mathrm{sf}} = 1 \times 10^{-8}$. For the nested-partitioned scheme depicted in Figure 4.7, the convergence criterion for the inner loop is chosen as 1×10^{-7} such that it is one order of magnitude smaller than the one of the outer loop. For

performance comparison all simulations were run in parallel on two cores of an Intel Xeon E5-2690 v4 dual socket system which was specially configured to allow reliable time measurements (cluster-on-die mode and forced C0 state).

The primary interest of this section is to assess the efficiency of the proposed algorithms, which is why only results concerning the performance of the schemes are shown. Figure 5.3 depicts the number of coupling iterations, i.e., the number of Newton steps for the monolithic scheme and the number of (outer) partitioned iterations for the partitioned algorithms, respectively. The monolithic, monolithic-partitioned and nested-partitioned scheme exhibit a very similar convergence behaviour with three coupling iterations on average compared to the sequential-partitioned one, which needs a mean of twelve partitioned steps per time step to converge. Around time step 300 a necrotic core starts to develop, which means that an additional species, namely, necrotic cells are present. Therefore, the coupling between the fluid phases and the species becomes stronger, such that more partitioned iterations are necessary, which is why the partitioned schemes show a peak for their respective number of coupling iterations. Still, the fully-monolithic scheme converges within three Newton iterations throughout the simulation except for some time steps at the beginning of the simulation. The number of coupling iterations is closely coupled to the CPU time per time step for monolithic, monolithic-partitioned and nested-partitioned scheme as shown in Figure 5.3. Evidently, the fully-monolithic scheme is the most efficient one followed by the monolithic-partitioned solution procedure, the sequential-partitioned scheme and, the least performant one, the nested-partitioned scheme.

The monolithic-partitioned variant is less efficient in terms of computational time than the fully-monolithic one even if the same number of coupling iterations is required since more linear solver calls and element evaluations are needed in total. The small amplitudes in computational time are related to how often the monolithic fluid-structure system (4.135) has to be evaluated for each time step, which differs slightly for some steps.

Concerning the two partitioned schemes, the sequential-partitioned one is faster by a factor of approximately 1.8 for the investigated case. This is due to the large number of inner fluid-structure iteration steps (approximately 10) per outer partitioned iteration step for the nested-partitioned coupling. Thus, this algorithm requires on average 3×10 nonlinear solver calls for both the fluid and the solid field per time step and three nonlinear solver calls for species transport per time step. Thus, on average 63 single-field nonlinear solver calls per time step are made. By contrast, the sequential-partitioned scheme requires only a total of 36 nonlinear solver calls (12 per time step for all three present fields) and, therefore, out-performs the other variant since the nonlinear solver time of the different fields is almost equal in the considered numerical example.

Still, both schemes which resolve the fluid-structure coupling monolithically are far superior than the partitioned ones with an average computational time per time step of $1.3\,\mathrm{s}$ and $2.0\,\mathrm{s}$ compared to $6.0\,\mathrm{s}$ and $10.9\,\mathrm{s}$, respectively. Clearly, this is due to the strong coupling between fluid flow and structural deformation which is much stronger than the coupling with species transport. This is also evident from the corresponding number of required partitioned steps (three outer steps vs. $10 - 12$ inner steps or sequential outer steps). It was also tried to induce a small compressibility of the fluid and solid phases of approximately 10% by reducing their bulk moduli to $10\,000\,\mathrm{Pa}$ to test if a slight compressibility was beneficial to the convergence of the partitioned schemes but only an insignificant gain in performance could be achieved. Only for even smaller, yet unrealistic bulk moduli, a substantial effect was present.

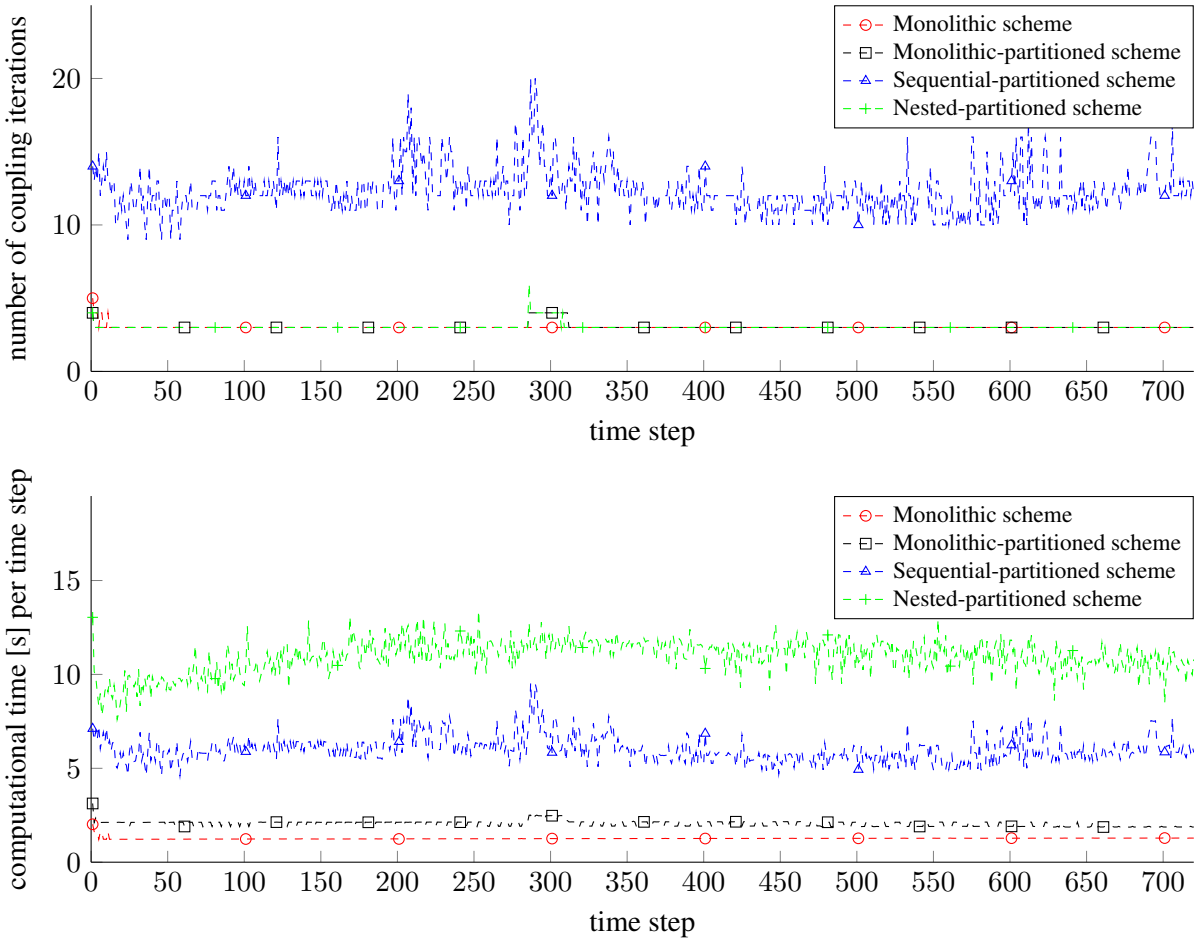

Figure 5.3: Number of coupling iterations and calculation time per time step. Figure based on the author's article [135], results for nested-partitioned scheme are additionally shown.

For a rigid ECM, i.e., a non-moving mesh (not shown here), the performance of a monolithic algorithm for fluid-species coupling was also compared to a corresponding partitioned algorithm. For that, the inner loop of the nested-partitioned scheme from Figure 4.7 respectively the solution of the solid field for the sequential partitioned scheme from Figure 4.6 may be omitted. In that case, the monolithic algorithm was still faster, albeit only by a factor of 1.7, which once more proves that resolving the coupling between solid and fluid phases is the most challenging part. Hence, this factor seems to be the additional performance gain for resolving the fluid-species coupling with a monolithic scheme. Actually, it is also almost identical to the difference in performance between the fully-monolithic scheme and the monolithic-partitioned scheme from above for a deformable ECM.

To further evaluate the efficiency of the distinct approaches, studies on three key parameters were conducted. The results are given in Figure 5.4, where on the left side the respective mean number of coupling iterations per time step and on the right side the mean computational time per time step is depicted. The first investigated parameter is the Young's modulus of the ECM which is varied while all other parameters are fixed to the values of Tables C.1, C.2, C.4 and C.5. The performances of the different schemes are shown in Figure 5.4a. A softer ECM effects a stronger

coupling between the fluid and solid phases. Consequently, the performance of the sequential- and nested-partitioned scheme deteriorates considerably as shown by the average number of coupling iterations and the average CPU time per time step in Figure 5.4a. While the number of outer coupling iterations for the latter one does not change, the number of inner fluid-structure interactions rises substantially, which explains the worse performance in terms of computational time. Increasing the stiffness of the ECM has an opposing effect leading to smaller deformations and, hence, a weaker coupling, which can more easily be resolved by the partitioned algorithms. By contrast, the performance of the monolithic and monolithic-partitioned algorithm is unaffected by the choice of the Young's modulus.

Interestingly, the number of monolithic Newton steps decreases even marginally for a softer ECM. This hides the effect that the GMRES iterative linear solver with BGS(AMG) preconditioner needs more iterations and more computational time to resolve the stronger coupling between fluid and structure phases when the ECM is less stiff. In that regard, it is important to emphasize that for systems of larger size than considered here a suboptimal scaling of the employed preconditioner could slightly deteriorate the performance of the monolithic schemes. Even under these circumstances the partitioned algorithms with their large number of coupling iterations can certainly not compete with the monolithic ones.

A further study was conducted on the intrinsic permeability of the ECM. Results are depicted in Figure 5.4b. Again, all other parameters are equivalent to Tables C.1, C.2, C.4 and C.5 and the Young's modulus is re-set to $E^s = 400\,\mathrm{Pa}$. A similar picture as in Figure 5.4a emerges. Lower permeabilities lead to a stronger coupling between fluid phases and the solid phase since larger pressures and pressure gradients develop in the computational domain. The lower the permeability of the ECM, the less efficient the partitioned schemes while both monolithic schemes do not show any change in performance. As before, three coupling iterations are needed on average per time step for a wide range of permeabilities while the computational time for the iterative linear solver increases minimally due to the stronger coupling for lower permeabilities. The computational time of both partitioned algorithms decreases for higher permeabilities, however, the monolithic schemes are still faster by at least a factor of 2.6 and 1.8 compared to the sequential-partitioned scheme, respectively.

Finally, the influence of the time step size Δt was investigated. This is due to the fact that Turska and Schrefler [258] found a lower limit for the ratio of time step size and element length $\Delta t/h^2$ to guarantee convergence of a partitioned solution scheme for a consolidation problem of similar type. The existence of this lower limit for a given set of material parameters implies that the time step size cannot be reduced arbitrarily if the mesh is not refined at the same time [233]. With the aim of triggering this instability, a study on the time step size was performed while leaving the material parameters and the mesh unchanged. The results are depicted in Figure 5.4c. The behaviour predicted by Turska and Schrefler [258] can be reproduced in this case. Below a time step size of $\Delta t = 600\,\mathrm{s}$ the number of coupling iterations for the sequential-partitioned scheme and the number of inner coupling iterations for the nested-partitioned scheme starts to increase. This indicates that the partitioned schemes become unstable for the given material parameters and discretization. Still, convergence could be achieved even for the smallest time step size considered in Figure 5.4c, which is probably due to the employed Aitken relaxation. Both monolithic algorithms exhibit a completely different behaviour. If the time step size is decreased, the Newton algorithm converges in less iterations and vice versa, just as expected. As also a larger number of outer coupling iterations is needed for the nested-partitioned scheme, the same effect

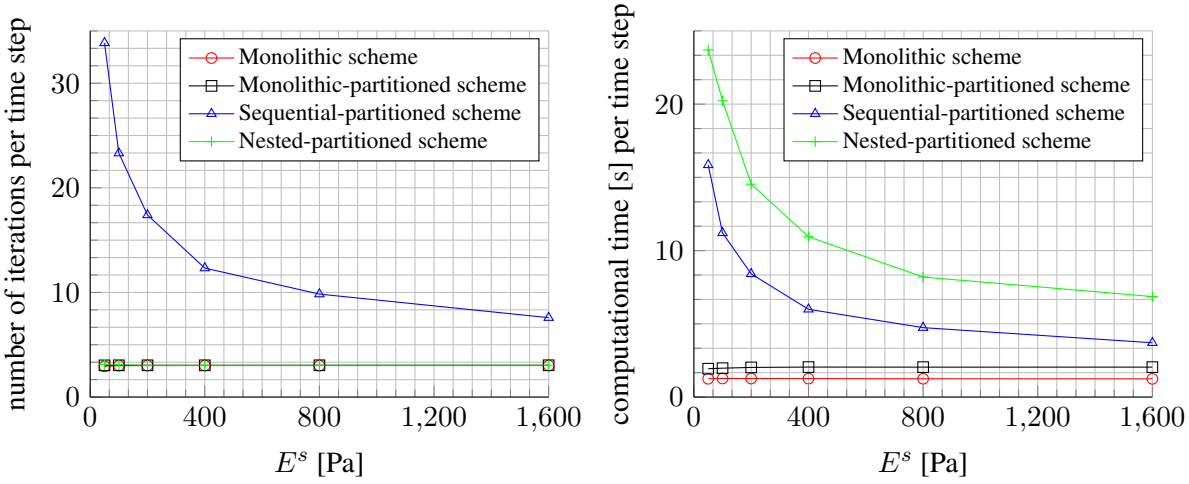

(a) Performance of coupling schemes depending on Young's modulus

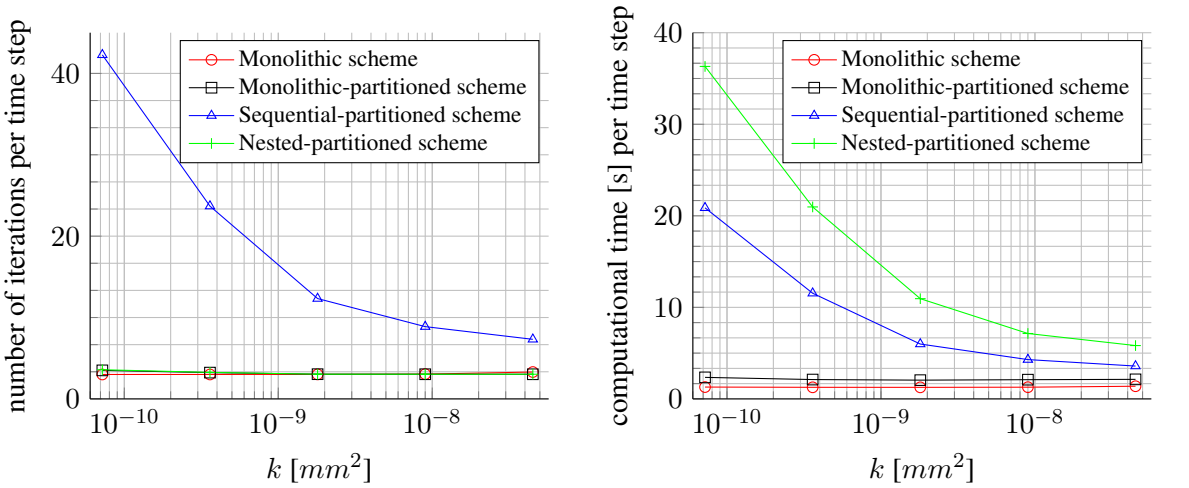

(b) Performance of coupling schemes depending on ECM permeability

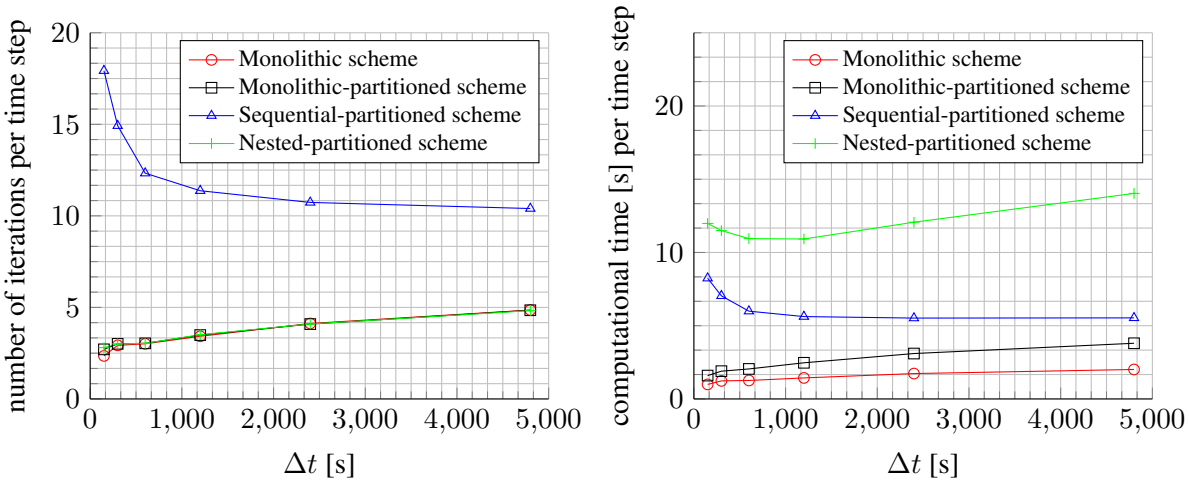

(c) Performance of coupling schemes depending on time step size

Figure 5.4: Performance of coupling schemes depending on different parameters. Figure based on the author's article [135], nested-partitioned scheme is additionally investigated.

can be observed. It is not present for the sequential-partitioned scheme because the number of coupling iterations is dominated by resolving the fluid-structure coupling. Nevertheless, even for the largest time step of $\Delta t = 4800\,\mathrm{s}$, it cannot compete with the monolithic algorithms.

In summary, the fully-monolithic coupling is the most efficient scheme for a wide range of parameter sets. For both monolithic schemes the computational cost is nearly independent of material and simulation parameters. In the context of tumor growth, where many parameters might be unknown or uncertain, such an efficient algorithm is especially advantageous. However, only a relatively small numerical example with a comparatively low number of degrees of freedoms was studied. Nevertheless, it is still of high relevance as it can be employed to perform sensitivity analysis of the model, see the Master's thesis of Rodenberg [219] for preliminary investigations, or as a low-fidelity approximation of a more advanced model variant for efficient uncertainty quantification [22]. Both cases require the repeated evaluation of such a smaller numerical model. Thus, the overall performance of the algorithms can make a considerable difference here. For larger examples, the scalability of the monolithic algorithms depends strongly on efficient preconditioners, whose performance has been evaluated in [72, 263, 264]. The excellent scalability of both variants was also observed in the larger and more complex examples investigated in the following sections. There, also the AMG(BGS) preconditioner which performs better than the BGS(AMG) variant for strongly coupled problem is employed.

Despite the fact that the computational effort of the nested- and sequential-partitioned solution procedures might become prohibitively large for certain parameter combinations, they have proven to be remarkably stable in combination with Aitken relaxation. In further studies it was found that no convergence was possible without any relaxation. If a constant relaxation parameter of $\omega_k = 0.1$ was chosen in every partitioned step k instead of the recursive definition with Aitken relaxation from (4.129), on average three times more partitioned steps were needed to converge. For larger constant relaxation parameters, no convergence was possible. This underlines the importance of the applied procedure with a dynamic adaptation of the relaxation parameter. Obviously, the inferior performance of the partitioned algorithms can be attributed to the strong coupling between incompressible fluid and solid phases. The performance of the sequential-partitioned algorithm was better than the nested-partitioned one in all examples considered here. However, the latter one might still have a specific use case if the solution time of the (non-)linear solver for species transport dominates the overall solution time, for instance, if a system consisting of a very large number of species is analysed. This could easily be the case as numerous bio-chemical species are present and relevant during tumor growth. In that situation, the lower number of evaluations of the species transport subproblem due to the lower number of (outer) partitioned steps compared to the sequential-partitioned variant could make the nested-partitioned algorithm competitive.

If a rigid ECM is considered, the partitioned algorithm is still slower than the fully-monolithic one but might be worth considering for a fast implementation of the model. It has to be noted, though, that the comparison was restricted to a relatively simple example without considering the vascular system. In more complex scenarios the partitioned algorithms are likely to perform even worse especially when considering angiogenesis, which represents an additional coupling between species transport and the vascular volume fraction through chemo- and haptotaxis. Finally, the monolithic-partitioned algorithm could be a sensible compromise between computational efficiency and implementational effort for moving meshes. Still, the fully-monolithic

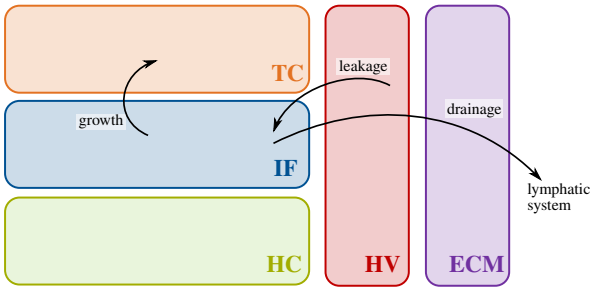

Phase	Mass transfer terms
ECM	0
HC	0
TC	$\overset{l\to t}{M}_{\text{growth}}$
IF	$\overset{v\to l}{M}_{\text{leak}} - \overset{l\to ly}{M}_{\text{drain}} - \overset{l\to t}{M}_{\text{growth}}$
HV	$-\overset{v\to l}{M}_{\text{leak}}$

(a) Phases with respective mass transfer relations

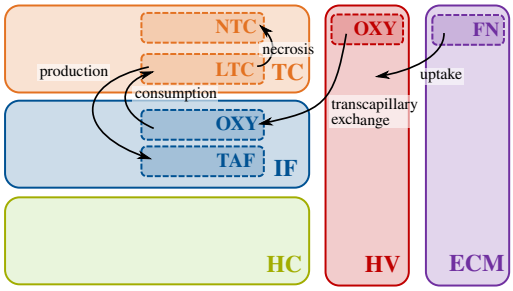

Species	Mass transfer terms
NTC	$\varepsilon^t r^{Nt} - \omega^{N\,\bar{t}}\,\overset{l\to t}{M}_{\text{growth}}$
OXY/IF	$-\overset{nl\to t}{M}_{\text{cons}} + \overset{nv\to nl}{M}_{\text{tv,s}} - \omega^{n\,\bar{l}}\left(\overset{v\to l}{M}_{\text{leak}} - \overset{l\to t}{M}_{\text{growth}}\right)$
TAF	$\overset{TAFt\to TAFl}{M}_{\text{prod}} - \omega^{TAF\,\bar{l}}\left(\overset{v\to l}{M}_{\text{leak}} - \overset{l\to t}{M}_{\text{growth}}\right)$
FN	$-\overset{Fs\to Fv}{M}_{\text{up}}$

(b) Species with respective mass transfer relations

Figure 5.5: Schematic overview of vascular model with homogenized representation of the vasculature and mass transfer relations

algorithm is the most efficient one which is why it will be employed in all subsequent numerical examples.

5.2 Two-dimensional Growth of a Vascular Tumor Including Angiogenesis

In this section the growth of a vascular tumor including angiogenesis will be studied by means of a simplified two-dimensional numerical example. It has been designed to elucidate the interplay between tumor growth and angiogenesis in the vascular model with homogenized representation of the vasculature. In that context, the homogenized vasculature may be understood as the neo-vasculature (NV) formed through the process of angiogenesis. The example was published previously in the author's publication [135]. The subsequent description of its setup and the investigation in Section 5.2.1 is taken from the aforementioned paper. Then, two further effects are included which were not considered in [135], namely haptotaxis in Section 5.2.2 and blood vessel compression by the growing tumor in Section 5.2.3.

Since the focus lies on modeling angiogenesis in combination with tumor growth, blood flow and oxygen transport in the homogenized vasculature is not considered. Rather, blood pressure and oxygen mass fraction in the homogenized vasculature are set constant. This still implies that the interrelation between angiogenesis and tumor growth, namely, the more efficient supply with nutrients, and leakage of fluid from the vasculature into the IF leading to increased interstitial pressure, may be examined. Only transport and flow in the vasculature is not taken into account. In summary, the employed model type in this section is the vascular tumor growth model with

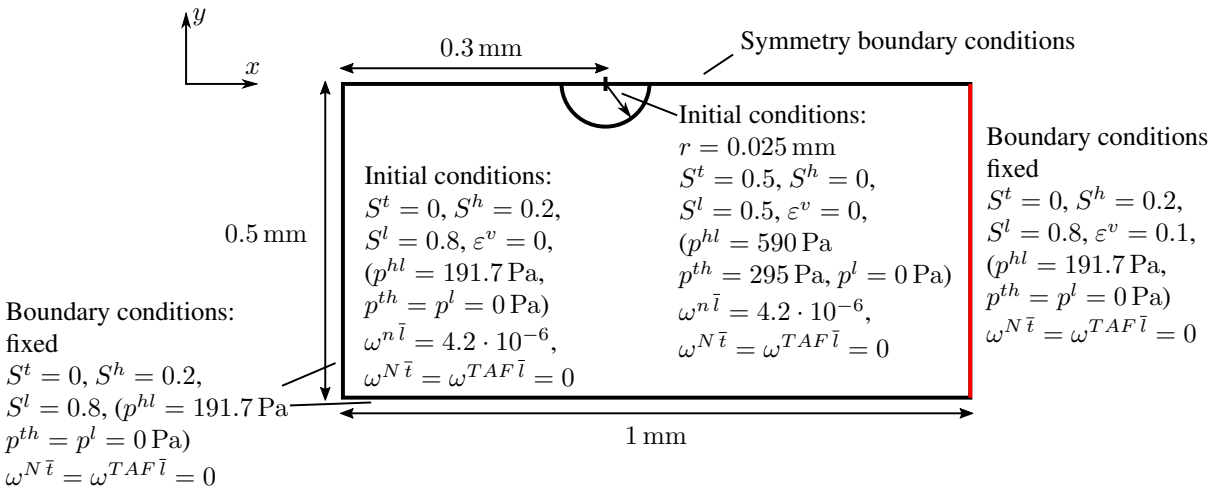

Figure 5.6: Geometry, initial and boundary conditions of the 2D angiogenesis example (not to scale). Figure taken from the author's article [135].

homogenized representation of the vasculature from Section 3.3 without blood flow, that is, without equation (3.47).

A schematic overview with the respective phases and species is given in Figure 5.5. Now, the homogenized neovasculature is present as an additional porous network inside the ECM. In addition to the term accounting for tumor growth, two supplementary phase mass transfer relationships act on the IF. These are the leakage of fluid from the neovasculature due to abnormal vessel characteristics given by (B.2) and the uptake of IF by the lymph system given by (B.4). Functioning lymph vessels remove excessive liquid as well as waste products. However, in many tumors this mechanism is impaired since the proliferating cancer cells compress or even collapse the lymph vessels [36, 103, 115]. Combined with the increased outflow due to the irregular and leaky blood vessels this plays a major role for interstitial hypertension in tumors [36, 103, 115]. Until now, the lymph system is not explicitly present in the model as a proper phase but it is assumed that it continuously drains excessive liquid from the IF throughout the domain with the exception of the tumor region. A straightforward extension (and one which is actually possible with the current version of the computational framework) would be to employ a lymphatic density or volume fraction analogous to [287]. It might then also be possible to model the evolution of the lymph vessel system with a similar equation as (3.51) to take also lymphangiogenesis [4] into account.

Three species are present, namely oxygen in the IF (and in the HV where its mass fraction is set to a constant value), TAF in the IF and NTCs as part of the TCs. In Section 5.2.2 a further species, fibronectin (FN), which is modeled as a macromolecule of the solid phase, is added. The transvascular exchange of oxygen from the HV into the IF is modeled with the simplified transvascular oxygen exchange term (B.12). TAFs are produced by the LTCs if the nutrient mass fraction falls below the hypoxic limit, see (B.13). Currently, the uptake of TAFs through endothelial cells [225] has not been included, however, the extension is straightforward if the results indicate that this term is necessary. The previously introduced terms for oxygen con-

sumption by LTCs and necrosis are re-used. As a simplification of the mass transfer relations for species, it is assumed that fluid drainage through the lymph system does not influence the mass balance of the species dispersed in the IF, i.e., oxygen and TAF, which implies

$$\overset{il\to ily}{M} - \omega^{i\bar{l}} \cdot \left(\overset{l\to ly}{-M_{\text{drain}}} \right) = 0. \tag{5.1}$$

If interstitial liquid is drained, the corresponding species is taken up in equal measure by the lymph system.

A Neo-Hookean material law whose material parameters are given in Table C.1 is employed for the ECM. The additional parameters for the other phases and species are given in Tables C.2, C.3, C.4, C.5 and C.7 together with further explanations.

The geometry of the example including initial and boundary conditions is sketched in Figure 5.6. A circular tumor with initial radius $r = 0.025\,\text{mm}$ is growing in healthy tissue. Similar cases have been studied by Macklin et al. [158] and Santagiuliana et al. [225] for their models with homogenized and discrete vascular network, respectively. It is assumed that angiogenesis occurs from a pre-existing vessel (which is not explicitly modeled) on the right side of the domain. Here, a Dirichlet boundary condition for the homogenized vasculature volume fraction of $\varepsilon^v = 0.1$ has been set to trigger angiogenesis from the position of the assumed blood vessel. The left, bottom and right boundary of the domain are fixed and appropriate boundary conditions are applied to make use of the symmetry of the problem. Note that the oxygen mass fraction in IF is not prescribed on any boundary of the domain but it is assumed that it is solely provided by the developing neovasculature via transcapillary exchange. The oxygen mass fraction in the NV and the blood pressure therein are fixed to $\omega^{n\bar{v}} = 4.2 \times 10^{-6}$ (corresponding to fully oxygen-saturated blood plasma) and $p^v = 3000\,\text{Pa}$, respectively. The setup is designed in this way as it allows to illustrate the capabilities of the model with homogenized vasculature including angiogenesis. In more biologically realistic scenarios such a large initially non-vascularized domain would not occur.

The domain is discretized with 240×120 bilinear elements in space. The time step size is $\Delta t = 1800\,\text{s}$ for the one-step-theta scheme with $\theta = 0.52$ over 1152 time steps, i.e., the total simulated time is 24 days.

5.2.1 Investigation of the Interplay between Tumor Growth and Angiogenesis

For this example, the chemotactic coefficient χ_0, which governs the migration of ECs towards the tumor and, thus, the formation of the NV, and the transcapillary diffusion coefficient over the vessel wall thickness D_{tc}/t, which governs the availability of oxygen, are the key parameters. Three different combinations of these parameters as given in Table 5.1 are studied to exemplify their effect on the model. In this section, haptotaxis and blood vessel compression and regression are not considered to investigate only the dynamic interrelation between chemotaxis-driven angiogenesis and tumor growth.

The evolution of the living tumor cell volume fraction $\varepsilon_{\text{LTC}} = \varepsilon S^t \left(1 - \omega^{N\bar{t}}\right)$ for case 2 is depicted in Figure 5.7, where also the vascular volume fraction ε^v is shown via contour lines. After six days a round tumor emerges while the neovasculature starts to grow slightly into the

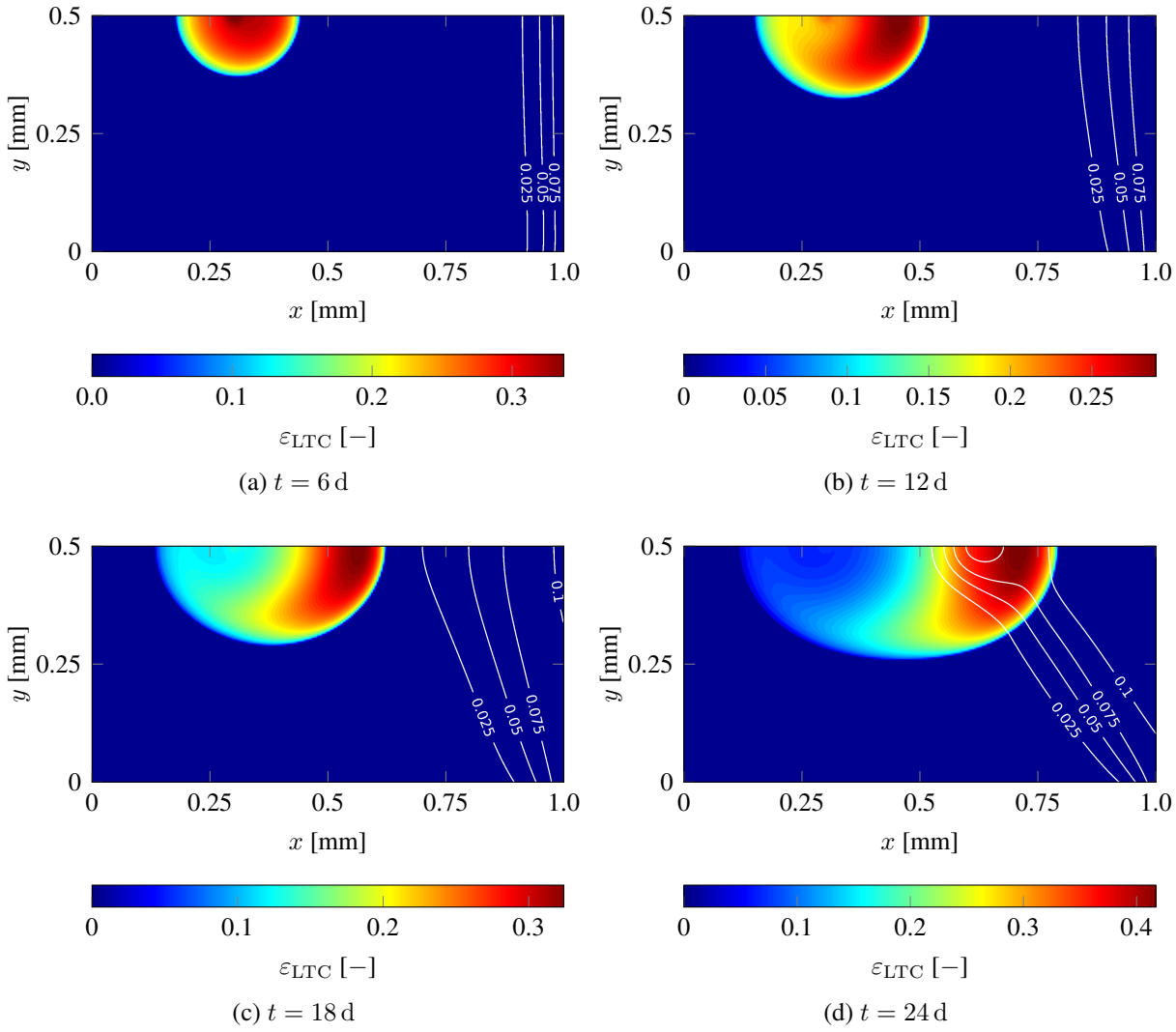

Figure 5.7: Evolution of living tumor cells and neovasculature (contour lines) for case 2. Figure taken from the author's article [135].

Quantity	Symbol	Value	Unit
Chemotactic coefficient	χ_0	case 1: 5×10^{-3}	$\mathrm{m^2\,s^{-1}}$
		case 2: 1×10^{-2}	$\mathrm{m^2\,s^{-1}}$
		case 3: 2×10^{-2}	$\mathrm{m^2\,s^{-1}}$
Transcapillary diffusion coefficient over wall thickness	D_{tc}/t	case 1: 2×10^{-5}	$\mathrm{m\,s^{-1}}$
		case 2: 1×10^{-5}	$\mathrm{m\,s^{-1}}$
		case 3: 5×10^{-6}	$\mathrm{m\,s^{-1}}$

Table 5.1: Parameters for angiogenesis and transvascular oxygen exchange for the three investigated cases. Table taken from the author's article [135].

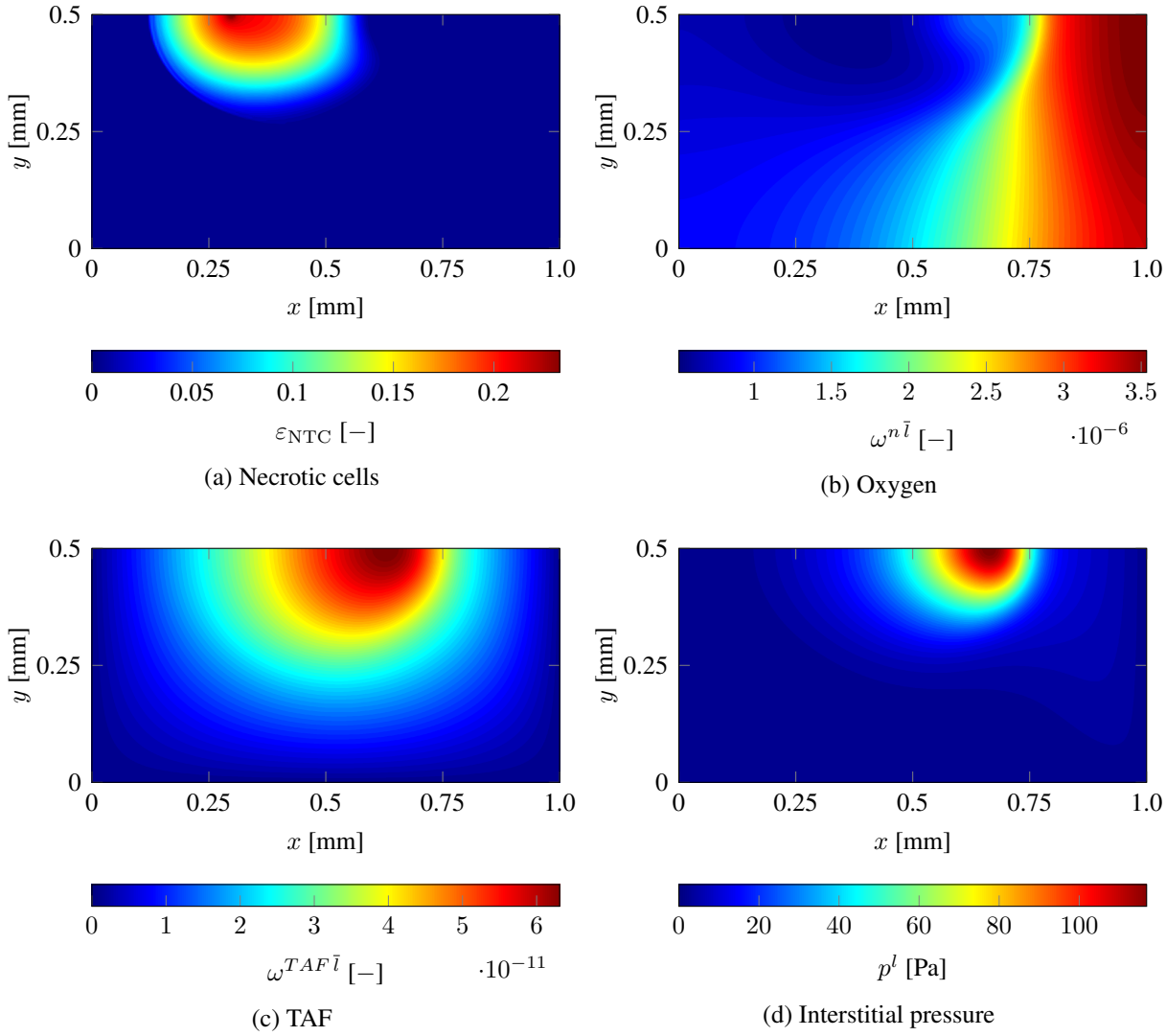

(a) Necrotic cells

(b) Oxygen

(c) TAF

(d) Interstitial pressure

Figure 5.8: Results of necrotic cells, oxygen in IF, TAF and interstitial pressure for case 2 at $t = 24d$. Figure taken from the author's article [135].

domain and provides oxygen on its right side. This actuates the tumor to evolve unsymmetrically towards the source of oxygen to the right after twelve days, see Figure 5.7b. A half-moon shape of LTCs emerges since in the region further away from the blood vessel, necrosis sets in, see also Figure 5.8a. The tumor continues to progress towards the neovasculature over the course of the simulation, see Figures 5.7c-5.7d. TAFs are constantly produced by the hypoxic TCs. After twelve days the chemotactic response of endothelial cells to TAF starts to dominate the growth of the neovasculature towards the tumor, which results in the shape shown in Figures 5.7c-5.7d. Most of the oxygen is needed by proliferating TCs at the symmetry axis of the domain, hence, here most of the TAFs are produced, see Figure 5.8c, which explains that the neovasculature grows faster in the region close to the symmetry axis. Finally, after 24 days a hot spot of vascularization with a large number of LTCs emerges. This is consistent with experimental findings

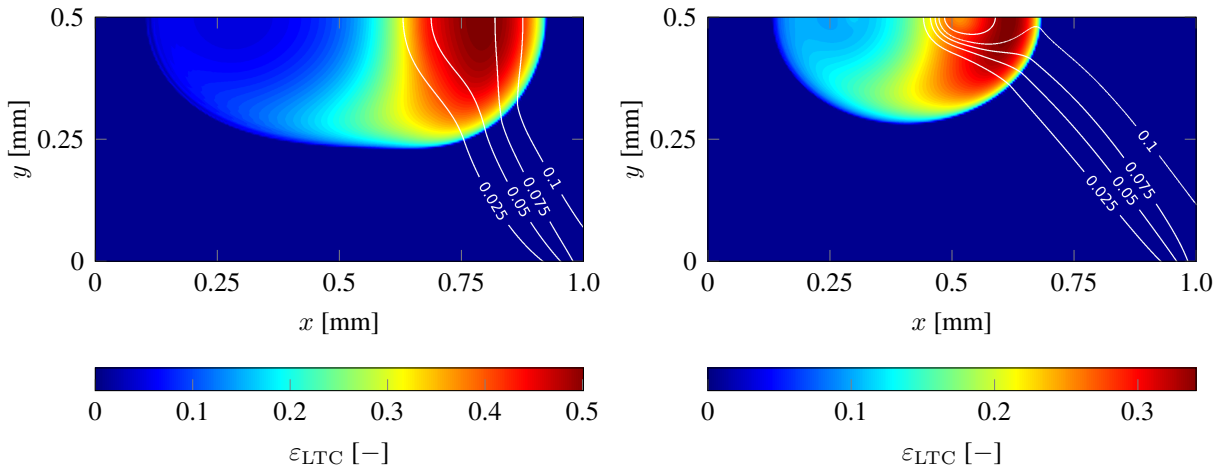

(a) case 1, $t = 24d$ (b) case 3, $t = 24d$

Figure 5.9: Evolution of living tumor cells and neovasculature (contour lines) for cases 1 and 3. Figure taken from the author's article [135].

which indicate that angiogenesis takes approximately 20 days [36]. Qualitatively, these results are also in good agreement with the similar angiogenesis example of Macklin et al. [158].

In addition, the necrotic cell volume (or mass) fraction after 24 days $\varepsilon_{\mathrm{NTC}} = \varepsilon S^t \omega^{N\bar{t}}$ is depicted in Figure 5.8a. As already mentioned before, the necrotic region develops on the left in the zone further away from the emerging vasculature. The oxygen mass fraction in the IF $\omega^{n\bar{l}}$ is plotted in Figure 5.8b. A large area with a very low oxygen concentration exists in the left part of the domain. During growth the tumor consumes almost all the oxygen there while diffusion of oxygen generated by the pre-existing blood vessel and beginning angiogenesis is not enough to sustain its rapid growth. This causes the development of the aforementioned necrotic region. On the right side of the domain an oxygen-rich region is present due to transcapillary exchange of oxygen. Finally, the interstitial pressure is shown in Figure 5.8d. An increased pressure can be observed in the vascular tumor region. This is due to the leakage of fluid from the irregular neovasculature into the domain. Outside of the tumor region the lymphatic system drains this excessive fluid via (B.4). However, TCs compress the lymph vessels limiting or completely inhibiting drainage. Therefore, IF accumulates with the corresponding pressure increase. This means that there is a net outflow of IF from the vascular tumor region. The increase of interstitial pressure has been physiologically observed and identified as critical to drug delivery to the tumor [103, 114, 115]. The vascular model with the inclusion of angiogenesis and appropriate inter-phase exchange terms enable the simulation of this phenomenon. These improvements will be employed in Section 5.3 to study nanoparticle transport and hyperthermia treatment in the tumor micro-environment by means of the homogenized vascular tumor growth model similar to [281, 282].

So far, only the parameter set of case 2 has been examined. Now, results of all cases are compared. For case 1 and 3, they are given after 24 days in Figures 5.9a and 5.9b, respectively. The parameter sets from Table 5.1 were chosen such that two distinct scenarios evolve. In the first case more oxygen is provided by the vasculature while the sensitivity of endothelial cells to TAFs

is decreased. This results in faster tumor growth compared to case 2 and 3 since more oxygen is available. At the same time angiogenesis occurs much slower due to the lower chemotactic coefficient and the overall higher oxygen concentration with less hypoxic cells producing TAFs. For case 3 the exact opposite behaviour can be observed. Less oxygen is present which slows down tumor growth. Vice versa, in combination with the higher chemotactic coefficient, this leads to faster angiogenesis than in case 1 and 2.

For a quantitative comparison of the three cases, the present volume fractions have been evaluated at the horizontal symmetry axis. Volume fractions of extracellular matrix (ECM), interstitial fluid (IF), healthy cells (HC), living tumor cells (LTC), necrotic tumor cells (NTC) and neovasculature (NV) are shown in Figure 5.10. As already evident from the two-dimensional plots from above, tumor growth progresses fastest for case 1 while the best and quickest vascularization is observed for case 3 due to the chosen parameters as explained before. However, also the largest necrotic zone develops for case 1 since the larger tumor consumes more oxygen which is insufficiently provided in the area further away from the tumor. In the early stages of growth blood vessels start to grow into the domain and displace HCs, IF and to a certain extent also ECM. This is due to the appearance of the blood pressure p^v in the definition of the solid pressure (3.57). As the domain is stretched ($J > 1$) in this region, the ECM volume fraction decreases according to (3.65) and (3.66). If a rigid ECM had been assumed, the volume fraction of the ECM would have been unaffected by angiogenesis. The inclusion of the homogenized vasculature as an additional pore space allows to model the interaction between porosity, ECM and NV volume fraction. Later, excessive tumor and IF pressure increase the porosity ε of the ECM in the proliferating zone. This is also due to the fact that an important aspect of tumor growth, namely, ECM remodeling and deposition [47, 81, 144] has not yet been included. This leads to a stiffer and denser ECM which enhances cell growth and migration [144] and limits penetration of macromolecules [149]. One further effect of the increased rigidity of the solid phase would be a decrease in stretch in the tumor area and, thus, a higher ECM volume fraction. First simple inclusions of these phenomena in mathematical models can be found in [224, 257].

In the region with especially high tumor and IF pressure, for example around $x = 0.2$ in Figure 5.10k, also the neovasculature volume fraction ε^v decreases slightly which is the effect of the grid velocity divergence term from (3.51) which is positive in this area. In reality, the instable blood vessels of the neovasculature are likely to be compressed by the tumor in this region and to regress from the proliferating cells. This effect will be included in Section 5.2.3.

5.2.2 Investigation of the Influence of Haptotaxis

Now, the influence of haptotaxis is investigated by adding the fibronectin species in the ECM. Thus, the governing equation for a species in the solid phase, that is, equation (2.66) is solved to obtain the mass fraction of fibronectin throughout the domain. The diffusion coefficient of fibronectin in the ECM is set to zero as proposed by Anderson [6] based on earlier findings summarized by [25, 111] who state that fibronecin is bound to the ECM. As described in Section 3.3.1.1, haptotaxis in response to fibronectin gradients is incorporated as a haptotactic flux in (3.50) with constant haptotactic coefficient Θ which enters the evolution equation of the vascular volume fraction (3.51). Furthermore, the uptake and binding of fibronectin by migrating endothelial cells [111] is included by a simple uptake term as given in Figure 5.5b. The uptake term is similar to the formulation of Anderson [6] and stated in (B.14) along with further expla-

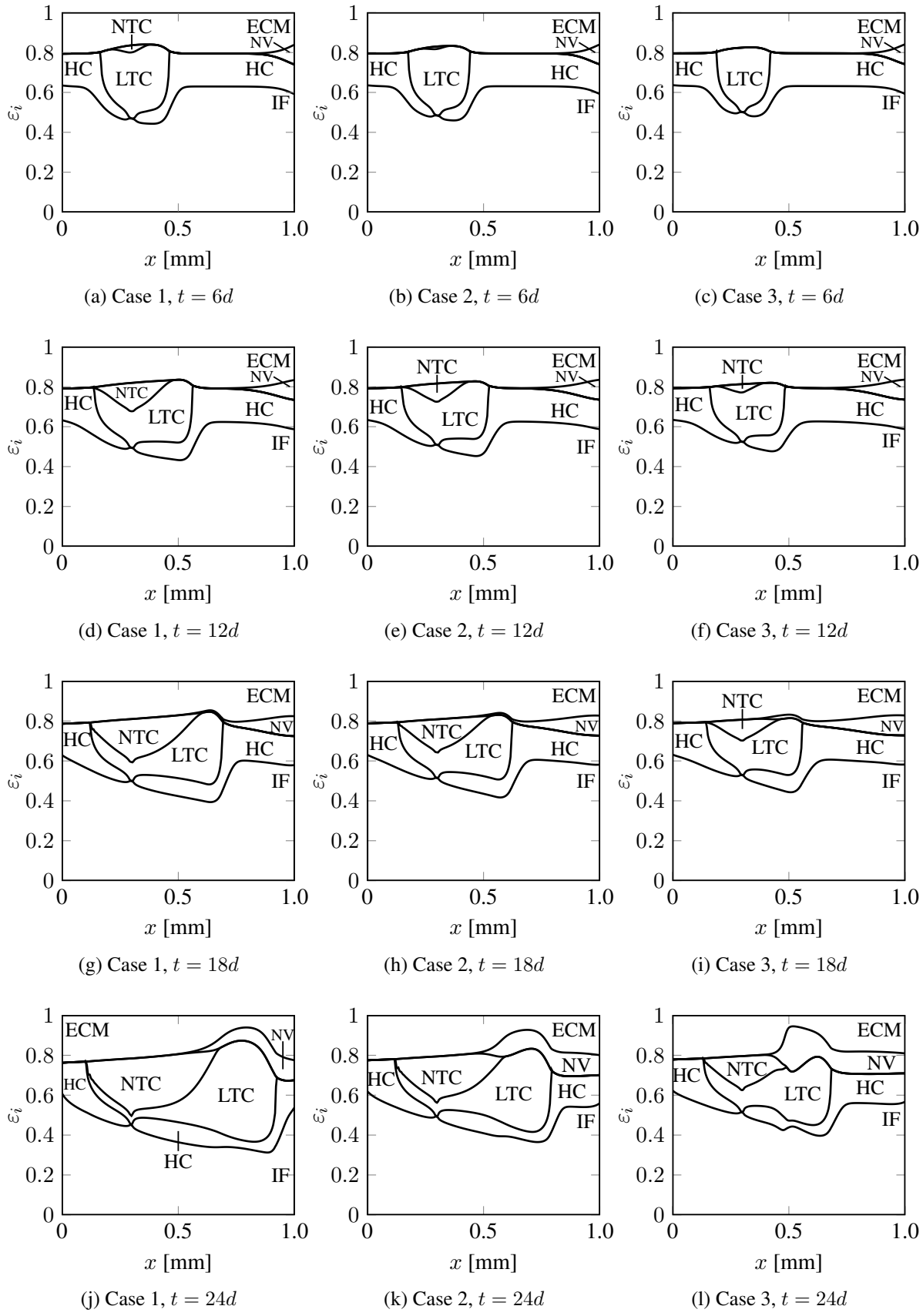

(a) Case 1, $t = 6d$ (b) Case 2, $t = 6d$ (c) Case 3, $t = 6d$

(d) Case 1, $t = 12d$ (e) Case 2, $t = 12d$ (f) Case 3, $t = 12d$

(g) Case 1, $t = 18d$ (h) Case 2, $t = 18d$ (i) Case 3, $t = 18d$

(j) Case 1, $t = 24d$ (k) Case 2, $t = 24d$ (l) Case 3, $t = 24d$

Figure 5.10: Volume fractions at symmetry axis (taken from the author's article [135])

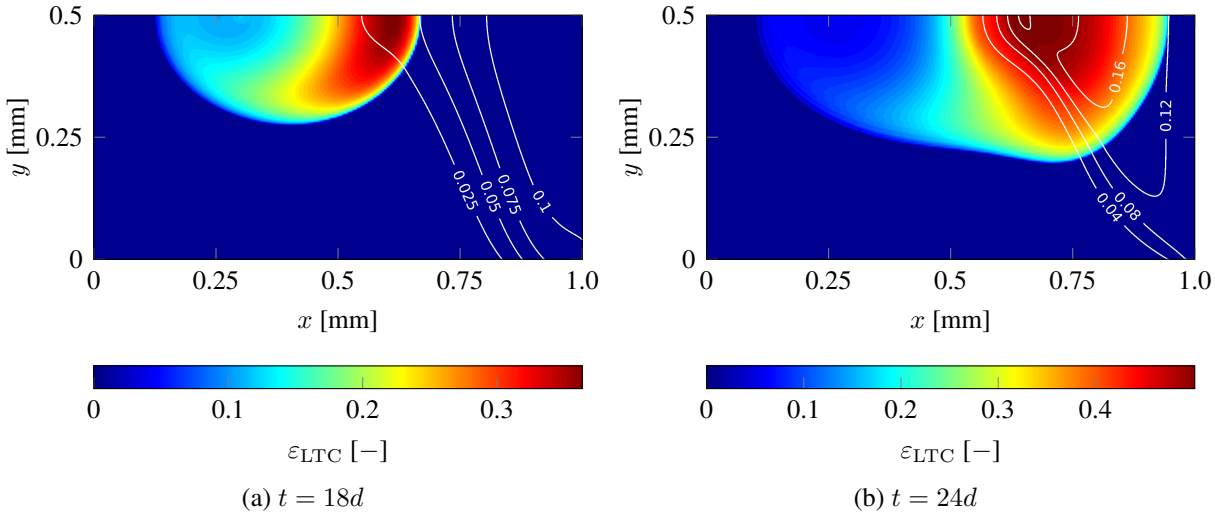

(a) $t = 18d$ (b) $t = 24d$

Figure 5.11: Evolution of living tumor cells and neovasculature (contour lines) for case 2 including haptotaxis

nations. The two additional parameters for the fibronectin species are given in Table C.8 and the employed haptotactic coefficient in Table C.3. The initial mass fraction of fibronectin is set to $\omega_0^{F\,\bar{s}} = 1 \times 10^{-10}$ and no-flux boundary conditions are assigned on all boundaries of the domain.

Results for the parameter set of case 2 including haptotaxis are shown in Figure 5.11 after 18 and 24 days. Comparing them to the same simulation without haptotaxis (Figure 5.7c and 5.7d), angiogenesis occurs much faster and the new vascular network migrates further to the left. In turn, the tumor grows more rapidly due to the increased access to oxygen which accompanies the better vascularization. Therefore, a much larger area of proliferating cells including not only the outer rim but also a substantial amount of LTCs further away from the right side emerges after 24 days. Also the values for the vascular volume fraction are approximately 1.5 times higher than without haptotaxis.

The reason for the more sustained angiogenesis lies in the haptotactic response following the fibronectin gradient. This is visualized in Figure 5.12 via the mass fraction of fibronectin in the ECM. The uptake by the growing neovasculature causes the shown distribution with lower values in areas with a high vascular volume fraction. This induces a fibronectin gradient which, in turn, leads to increased haptotaxis-driven angiogenesis.

The volume fractions of the present phases as well as living and necrotic tumor cells at the horizontal symmetry axis are given in Figure 5.11. As stated above, compared to the case without haptotaxis (Figures 5.10e, 5.10h and 5.10k), a much higher volume fraction of LTCs is present. In addition, the tumor grows much further to the right as a better vascularization is reached already after 12 and 18 days and, in general, higher values of the vascular volume fraction are achieved. The combination of these phenomena leads to a higher solid pressure and increased deformation of the ECM which can be seen from the low solid phase volume fraction ε^s as the ECM is stretched in the tumor area.

This numerical example demonstrates the general influence of haptotaxis leading to increased endothelial cell migration and, therefore, better vascularization, which in turn facilitates tumor

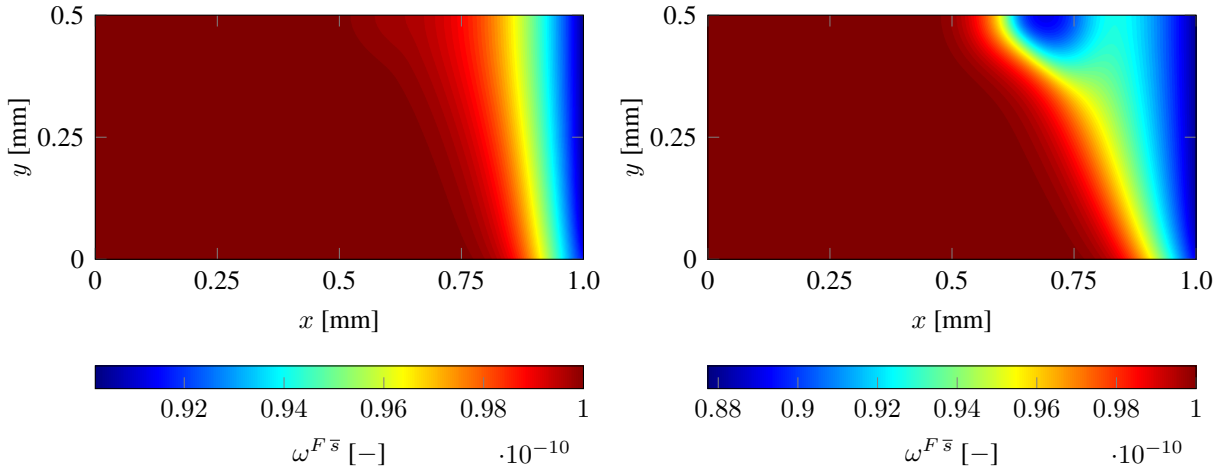

(a) $t = 18d$ (b) $t = 24d$

Figure 5.12: Mass fraction of fibronectin in the ECM for case 2 including haptotaxis

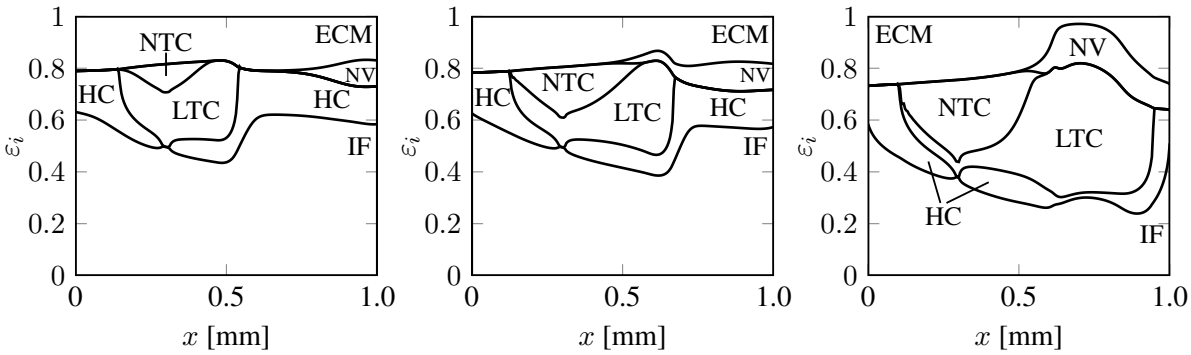

(a) $t = 12d$ (b) $t = 18d$ (c) $t = 24d$

Figure 5.13: Volume fractions of components at symmetry axis for case 2 including haptotaxis

growth. Here, this is solely due to the fibronectin gradient induced by uptake of ECs. It is well-known that further ECM components play an important role for haptotaxis [141]. Their influence could be included in further studies for a more realistic model of angiogenesis.

5.2.3 Investigation of the Influence of Blood Vessel Compression and Regression

Finally, the influence of blood vessel compression and regression on this numerical example is studied. For that, haptotaxis is switched off again while the empirical collapsing and regression model (3.68) is now present. This term appears negatively in the right hand side of the evolution equation for the vascular volume fraction (3.51). The two additional parameters of the blood vessel compression equation are γ^v_{coll} and $p^t_{\text{coll},v}$. Both are given in Table C.3. The blood vessel collapse threshold is set slightly higher than the lymph vessel collapse threshold as it is assumed

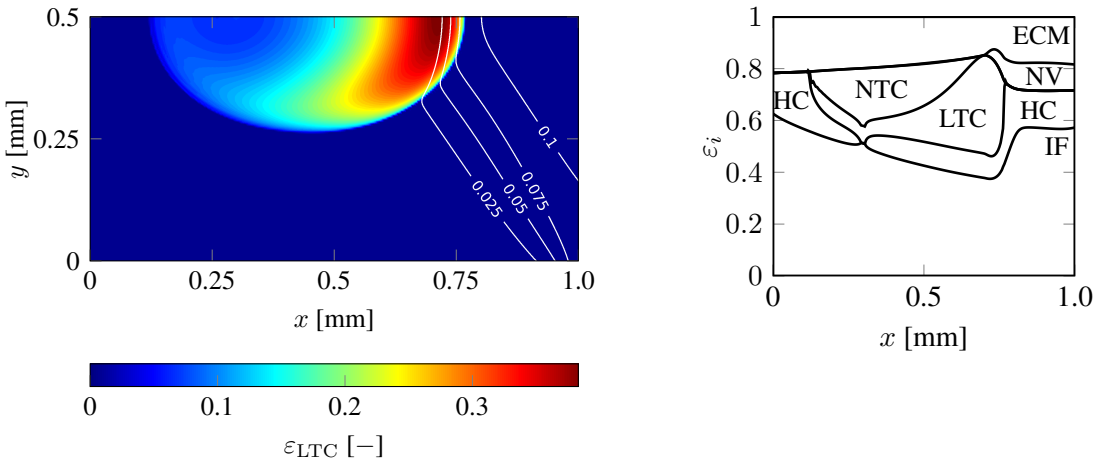

Figure 5.14: Results for case 2 with blood vessel compression after 24 days

that blood vessels can withstand the compression by the growing tumor for a longer period than the lymphatic vessels. The rate of blood vessel collapse is estimated.

Again, the angiogenesis and blood vessel parameters of case 2 from Table 5.1 are applied to investigate the influence of blood vessel compression. Until 18 days, tumor growth and angiogenesis progresses identically as for case 2 in Figures 5.7a-5.7c. Only as the growing tumor front and the edge of the neovasculature come into contact, the phenomenologically motivated blood vessel compression and regression term (3.68) becomes active leading to a decrease of the vascular volume fraction ε^v. This is also obvious from the results after 24 days shown in Figure 5.14: With the present parameter set, the decrease of the vascular volume dominates over the angiogenic response of the vasculature leading to a very distinct result compared to Figure 5.7d. Only the very edge of the growing tumor is well-vascularized whereas blood vessels further inside regress from the growing tumor mass. Conversely, less oxygen is available leading to a larger necrotic zone shown on the right in Figure 5.14 in comparison to the case without blood vessel compression and regression (Figure 5.10k). Additionally, the ECM is not deformed as strongly as the TC saturation and, hence, also the TC pressure is lower leading to less stretch in the ECM and higher solid phase volume fractions.

In summary, the combined effects of angiogenesis and the interaction with the growing tumor mass generate a very-well vascularized outer rim of the tumor whereas its inner core becomes necrotic. Compared to the examples from the previous sections, the vasculature cannot penetrate as deeply into the tumor. Nevertheless, as the tumor's outer rim is still well-vascularized, growth can proceed rapidly while co-opting, that is, growing along the vascular network [291]. However, it is obvious that the homogenized variant cannot provide results of this growth pattern with the same fidelity as a corresponding discrete approach, see Section 5.5 where a similar example with a discrete treatment of the vasculature with the corresponding framework for blood vessel compression and regression is studied.

5.3 Nanoparticle Delivery to a Vascular Tumor and Hyperthermia Treatment

In this section, the capabilities of the vascular model to study drug delivery and hyperthermia treatment are demonstrated. A numerical example which is designed similar to the author's co-first authored publication [282] is employed for that. Specifically, nanoparticle (NP) delivery to a solid vascular tumor with subsequent hyperthermia treatment is considered. Here, the tumor growth model is first employed to achieve a grown tumor state with a physiologically reasonable transport phenotype before drug delivery is studied. In future work, this first step could be skipped and imaging data to obtain the transport properties inside a specific tumor could be employed to directly study the accumulation of drugs. Computational studies on drug delivery and the success of specific treatment strategies could have a major and direct impact for many patients and the transition to clinical practice could be achieved much more rapidly than for the entire growth model.

Background Regardless of the effectiveness of a specific therapeutic agent, chemotherapy relies on the fact that a large fraction of cancerous cells is actually reached by the administered drug [60]. Vice versa, its tremendous toxic side effects could be reduced if only tumor cells were reached and killed and healthy tissue was left intact. However, conventional small molecule therapeutics are usually distributed non-selectively throughout tissue and target all rapidly proliferating cells. Nanomedicine has a strong potential to overcome this shortcoming and enhance local drug concentrations at sites of disease while reducing systemic toxicity [142, 149]. This can be achieved by fine-tuning the properties of nanoparticles, which are solid particles whose diameter lies in a range of 1 to $100\,\mathrm{nm}$. Advances in material science have made the manufacturing of nanoparticle-based drug delivery systems of various sizes, shapes and surface chemistry possible to optimize their pharmacokinetics, tumor accumulation and elimination. These nanocarriers can then be employed to encapsulate a chemotherapeutic substance, to image the extent of a tumor or for hyperthermia treatment. The selective accumulation of NPs in diseased tissue can be influenced by active targeting, that is, by decorating their surface such that they specifically adhere to tumor regions. By contrast, passive targeting relies on the so-called *enhanced permeability and retention* (EPR) effect exploiting the increased leakage and reduced lymphatic drainage inside tumors. Unlike smaller molecules which are rapidly cleared via the lymphatic system, NPs then preferentially accumulate in tumors [166].

Despite these attractive features, a recent meta study suggests that only $0.7\,\%$ of the administered NPs actually reach the tumor site [280]. This is due to several physiological and technical obstacles occurring *in-vivo* during the delivery process. Especially transport barriers encountered by all NPs are a major bottleneck limiting their efficacy. These include vascular barriers reducing the extravasation of NPs and micro-environment barriers such as denser ECM structures impeding the movement of NPs within the tumor and the elevated IF pressure inside solid tumors reducing particle penetration into the tumor center [117, 149]. The goal of transport oncophysics, which views cancer as a physical mass transport phenomenon, is to overcome these barriers by rational drug design [27, 74]. To that end, tumors are characterized based on their transport phenotype, i.e., their transport properties for a better understanding of the limitations of current NP-based delivery systems [183]. It lies at hand to use computational tools to aid in the design

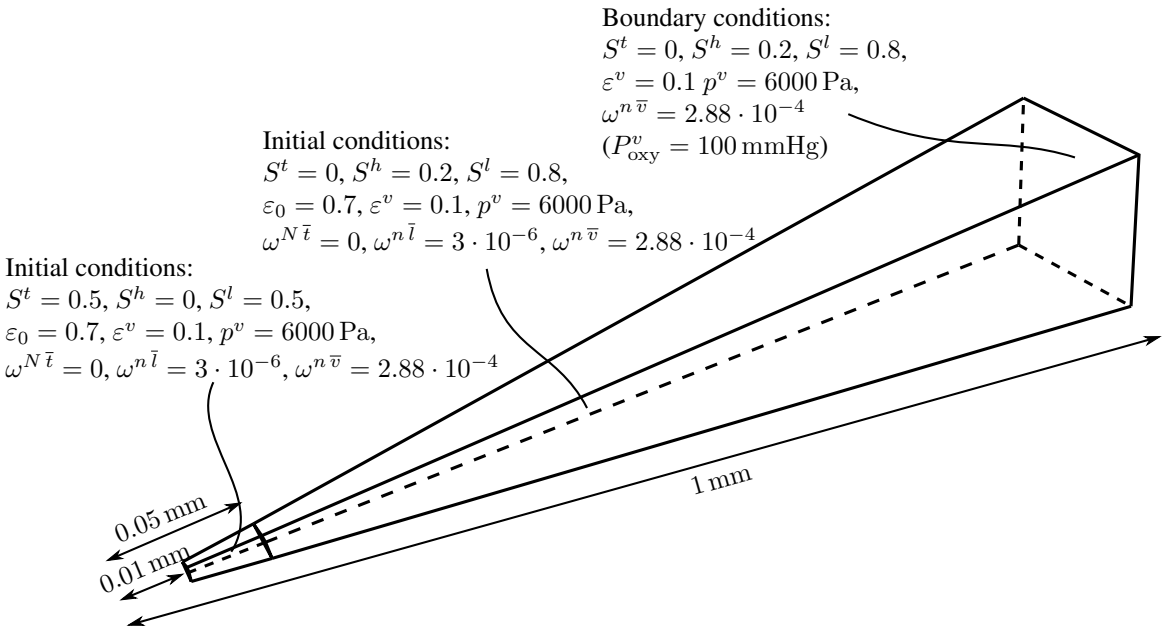

Figure 5.15: Geometry, initial and boundary conditions of the example for nanoparticle transport (not to scale)

of drugs whose transport properties are optimized for the tumor micro-environment. Two recent review papers [63, 164] summarize mathematical models for NP-based drug delivery. Representative examples of continuum approaches similar to the one employed here are [50, 84, 288]. They aim to predict drug or NP accumulation inside solid tumors.

An alternative cancer treatment is *hyperthermia*, that is, heating the tumor. The interplay between heat and tumor regression has been known for centuries and has recently gained renewed attention. According to van der Zee [259] several treatment modalities are possible. With local hyperthermia induced by external or internal energy sources the goal is to increase mainly the tumor temperature. Regional hyperthermia is applied by perfusion of organs, limbs or body cavities with heated fluids. Whole body hyperthermia involves heating the entire body and is, therefore, limited to temperatures of at most $42\,^{\circ}\mathrm{C}$. Higher local temperatures can be achieved with local hyperthermia. Temperatures above $50\,^{\circ}\mathrm{C}$ are referred to as *thermal ablation* leading to cell death [123]. By contrast, hyperthermia is associated with elevated temperatures in the range of 40 to $45\,^{\circ}\mathrm{C}$ [43] which is less damaging to the surrounding tissue. In addition, already these smaller rises may lead to tumor regression as the abnormal tumor micro-environment makes them more sensitive to heat. Finally, the combination of hyperthermia with traditional therapies such as chemo- and radiation therapy might be promising due to complementary effects and enhanced cytotoxicity of chemotherapeutic agents under higher temperatures [43].

Hereafter, only local, nanoparticle-mediated hyperthermia is considered. This can be achieved using gold or superparamagnetic iron oxide NPs which are administered by direct intratumoral or intravenous injection. Either via photothermal activation or an alternating magnetic field (AMF), heat is generated by these types of NPs [43, 123] and rapidly released to the surrounding tissue. The effect that NPs accumulate preferentially inside tumors and not in healthy tissue is also beneficial for hyperthermia as it allows a localization of the temperature increase in the tumor. Hence, also "inside-out" hyperthermia where the deeper regions in which the tumor is located are

heated more than the body surface is possible. This cannot be achieved with conventional methods involving heating from outside the body with a heat source [43]. Hence, it is clear that the biodistribution of NPs in the tumor is also of paramount importance for hyperthermia. Accumulation in tumor tissue enables a more concentrated tumor targeting whereas insufficient delivery might endanger the success of treatment if the generated temperatures are too low. This offers another appealing usage of the present model. First, NP transport may be investigated. Then, the effect of hyperthermia with the obtained NP distribution my be studied. Various approaches for computational modeling of hyperthermia are summarized in the review papers [7, 120].

Setup The setup and geometry of this numerical example follows common experiments for NP transport studies in mice models, see e.g. [67, 299]: TCs are injected and seed in a specific organ. Subsequently, multiple metastases form and continue growing. After $7 - 14$ days, macromolecular drug carriers are injected and their transport in the tumor micro-environment is imaged. To replicate this, the variant with homogenized vasculature is first employed to study the growth of a metastasis in vascularized tissue. Thereafter, the transport and accumulation of several common NPs of different size is investigated followed by a hypothetical hyperthermia treatment.

The computational domain including initial and boundary conditions for the primary growth phase is sketched in Figure 5.15. As in Section 5.1 a radially symmetric spherical tumor is considered. Making use of the symmetry of the problem, only the depicted segment is studied. Over the entire domain an initial vascular volume fraction of $\varepsilon_0^v = 0.1$ and a blood pressure of $p^v = 6000\,\mathrm{Pa} \approx 45\,\mathrm{mmHg}$ is set. These values are additionally assigned as boundary conditions on the outer surface of the domain. They lie in the range of the volume fraction inside solid tumors [252, 299], respectively, blood pressure inside arterioles [77]. A single metastasis originates in the center of the domain as indicated by the initial TC saturation there. In the rest of the domain and on its boundaries, the values for healthy tissue from the previous section are re-used including the IF pressure which is set to zero at the domain boundary. Since the deformation of the domain can be expected to have only a neglible influence on NP transport if no remodeling with associated decreased penetrability of NPs is included, the ECM is considered as undeformable. Therefore, the balance of momentum (3.60) is not solved resulting in a standard Eulerian formulation on a non-moving mesh. As in Wirthl et al. [282], angiogenesis is not considered as the domain will remain vascularized in this example and its influence is insignificant for the considered time span. However, blood vessel compression by the growing tumor via (3.68) is included.

An overview of the employed model variant with homogenized vasculature is given in Figure 5.16. Phase mass transfer terms are equivalent to the previous section. However, now blood flow in the HV via is explicitly modeled by (3.47). Two species are present in the preliminary growth phase, which are NTCs as a part of TCs, and oxygen (in HV and IF). The value for oxygen in blood corresponding to full saturation with $P_{\mathrm{oxy}}^v = 100\,\mathrm{mmHg}$ is applied on the outer surface of the domain. Compared to the previous section, also the advection-diffusion-reaction equation (3.63) of oxygen in the HV is now solved. For transvascular oxygen exchange across the blood vessel wall into the IF, (B.11) is employed. As before, oxygen is further transported in the IF via convection and diffusion and metabolized by the growing tumor. TAFs are not present

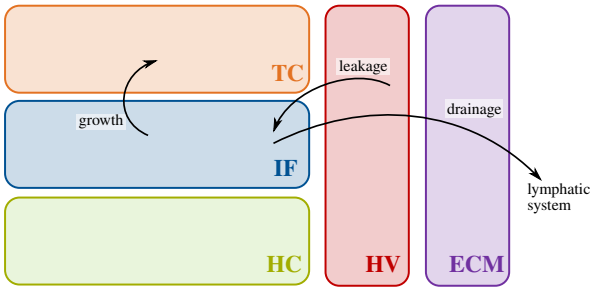

Phase	Mass transfer terms
ECM	0
HC	0
TC	$= \overset{l\to t}{M}_{\text{growth}}$
IF	$= \overset{v\to l}{M}_{\text{leak}} - \overset{l\to ly}{M}_{\text{drain}} - \overset{l\to t}{M}_{\text{growth}}$
HV	$= - \overset{v\to l}{M}_{\text{leak}}$

(a) Phases with respective mass transfer relations

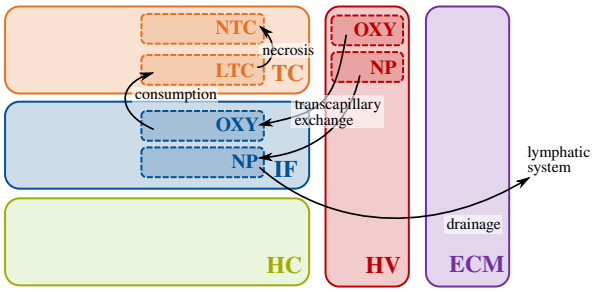

Species	Mass transfer terms
NTC	$\varepsilon^t r^{Nt} - \omega^{N\,\bar{t}} \overset{l\to t}{M}_{\text{growth}}$
OXY/IF	$- \overset{nl\to t}{M}_{\text{cons}} + \overset{nv\to nl}{M}_{\text{tv}} - \omega^{n\,\bar{l}} \left(- \overset{l\to t}{M}_{\text{growth}} \right)$
OXY/HV	$- \overset{nv\to nl}{M}_{\text{tv}}$
NP/IF	$\overset{NPv\to NPl}{M}_{\text{tv}} - \overset{NPl\to NPly}{M}_{\text{drain}} - \omega^{NP\,\bar{l}} \left(- \overset{l\to ly}{M}_{\text{drain}} \right)$

(b) Species with respective mass transfer relations

Figure 5.16: Schematic overview of vascular model with homogenized representation of the vasculature and mass transfer relations (including nanoparticles)

as angiogenesis is not regarded. The mass transfer relationships for NP transport will be given in more detail later.

Parameters are again listed in Tables C.2, C.3, C.4, C.5 and C.6. However, in preliminary simulations it was observed that the TC pressure is much higher for this example than in the previous examples. Thus, the empirical collapsing thresholds for vasculature and lymph system are increased to $p^t_{\text{coll},ly} = 1000\,\text{Pa}$ and $p^t_{\text{coll},v} = 2000\,\text{Pa}$, respectively. Also the conductivity for transvascular flow and lymphatic drainage are slightly adapted to $L_{p,v} = 4.2 \times 10^{-11}\,\text{m}\,\text{Pa}^{-1}\,\text{s}^{-1}$ and $\left(L_p \frac{S}{V}\right)_{ly} = 2.08 \times 10^{-6}\,\text{Pa}^{-1}\,\text{s}^{-1}$, which are double the values proposed by Baxter and Jain [13, 14] but still lie within a reasonable range [282].

The domain is meshed with 1000 trilinear elements in radial direction. Tumor growth is simulated over 12.5 days. This matches the time range for corresponding experiments [67, 299]. A step size of $\Delta t = 1800\,\text{s}$ and $\theta = 0.5$ are chosen for time discretization.

Vascular Tumor Growth The growth of the considered vascular tumor is visualized in Figure 5.17 with the volume fractions of the respective components along the radius of the spherical domain. First, note that the volume fraction of the ECM remains constant unlike in the examples from the previous section. This is due to the assumption of an undeformable ECM such that the Jacobian J is equal to one and the ECM volume fraction does not change in compliance with (3.66). Once more, a necrotic core emerges due to insufficient oxygen supply in its center. By contrast, most of the proliferating TCs are located on the tumor periphery. Due to the compression by the growing tumor and further blood vessel regression, the vascular volume fraction in the center of the domain has dropped to 0.05, which is half the initial value. After 12.5 days, the tumor has reached a radius of $0.7\,\text{mm}$.

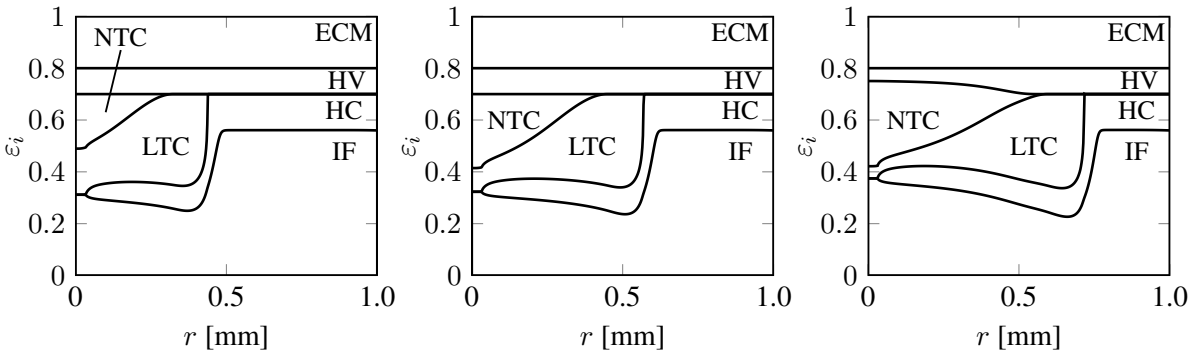

(a) $t = 7.5d$ (b) $t = 10d$ (c) $t = 12.5d$

Figure 5.17: Volume fractions of components along radius

Figure 5.18 additionally illustrates pressure and oxygen distribution in vasculature and IF. Blood pressure drops from the outer rim of the tumor towards its center due to leakage of fluid from vasculature into IF. Vice versa, the IF pressure ascends. As described previously, the elevated IF pressure in the tumor center is due to impaired lymphatic drainage as the growing tumor compresses the lymph vessels. Thus, fluid, which would normally be drained via the lymphatic system, accumulates in the tumor's interior. This is further exacerbated by the increased leakiness of tumor vasculature. Outside of the tumor, the lymph system still functions and drains the excessive fluid which results in the typical plateau of the IF pressure in the central region [103, 118] as observed in *in-vivo* experiments by Boucher et al. [30]. A maximum IF pressure of $p^l_{\max} \approx 1100\,\mathrm{Pa} \approx 8.25\,\mathrm{mmHg}$ emerges in the center of the domain. It lies within the range of $5 - 10\,\mathrm{mmHg}$ stated by Dewhirst and Secomb [60]. Nevertheless, according to other studies, the increased IF pressure can reach values as high as $37\,\mathrm{mmHg}$ [180] or even $60\,\mathrm{mmHg}$ [103]. At the tumor periphery, a steep IF pressure gradient emerges as the pressure drops towards the normal value. This yields an outflow of IF from the tumor which is a major factor contributing to the insufficient penetration of drugs into tumors [297]. In addition, the oxygen partial pressure in the IF and the vasculature are plotted in Figure 5.18b. Inside the tumor, both drop significantly due to the immense oxygen demand of the growing tumor, thus, leading to a hypoxic and even necrotic inner core. In summary, after 12.5 days of growth, a badly-perfused necrotic core with increased IF pressure emerges.

Nanoparticle Transport Study NPs are intravenously injected and subsequently transported by the vasculature. However, while the computational framework is capable of explicitly modeling transport in the vasculature, this is not considered hereafter but the NP mass fraction in the vasculature is prescribed via the relationship

$$\omega^{NP\,\overline{v}} = \omega_0^{NP\,\overline{v}} \cdot 0.5^{\frac{t}{T_{1/2}}} \tag{5.2}$$

with $\omega_0^{NP\,\overline{v}} = 2.0 \times 10^{-3}$. This models the decay of NPs in blood over time. The parameter $T_{1/2}$ is the plasma-half life which is the time where the mass fraction of the NPs in blood is equal to half the maximum mass fraction $\omega_0^{NP\,\overline{v}}$ according to experimental data [67].

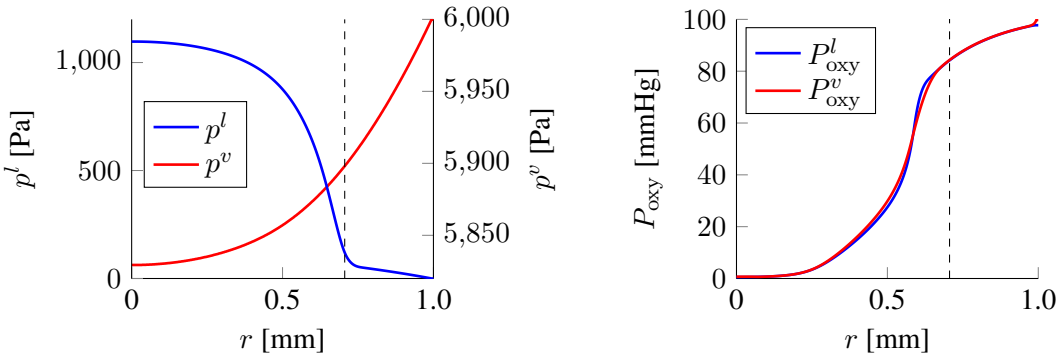

(a) Blood and IF pressure

(b) Blood and IF oxygen partial pressure

Figure 5.18: Blood and IF pressure and oxygen partial pressure along radius (Dashed line indicates edge of tumor with $S^t = 0.05$)

NPs may extravasate through the semipermeable capillary walls [145] and are subsequently transported in the IF via convection and diffusion. Two different pathways are possible for the extravasation of NPs into the IF: the transendothelial and the interendothelial pathway [172, 280]. Thus, the mass transfer from the vasculature to the IF is commonly modeled via the Staverman-Kedem-Katchalsky equation as

$$\begin{aligned} \overset{NPv\to NPl}{M_{\text{tv}}} &= \overset{NPv\to NPl}{M_{\text{inter}}} + \overset{NPv\to NPl}{M_{\text{trans}}} \\ &= \underbrace{\rho^v \cdot \left(L_p \frac{S}{V}\right)_v \left[p^v - p^l - \omega_{\text{osm}}\left(\pi^v - \pi^l\right)\right] \Delta\omega_{\text{lm}}^{\text{NP}} \cdot \varepsilon^v}_{\substack{\text{Interendothelial} \\ \text{pathway}}} + \underbrace{\rho^v \cdot P_v \cdot \frac{S}{V} \left\langle \omega^{NP\,\overline{v}} - \omega^{NP\,\bar{l}} \right\rangle_+ \cdot \varepsilon^v}_{\substack{\text{Transendothelial} \\ \text{pathway}}}. \end{aligned} \tag{5.3}$$

As sketched in Figure 5.19, the first term describes transport through the interendothelial pathway which is a convective process as NPs are dragged by the transvascular fluid flow [113]. In fact, this term corresponds to the leakage of fluid from vasculature into IF, that is the Starling equation (B.2), scaled with the log-mean concentration within the pore $\Delta\omega_{\text{lm}}^{\text{NP}}$. Therein, L_p is the hydraulic conductivity and S/V the surface-to-volume ratio for transcapillary flow [115, 287]. Furthermore, $\omega_{\text{osm}}(\pi^v - \pi^l)$ is the osmotic pressure difference as described in Section B.1. In healthy vasculature, endothelial cells around capillary vessels are tightly lined such that larger molecules are not able to pass through the space between cells. However, in tumor vasculature endothelial cells are poorly aligned [117] resulting in larger gaps between adjacent cells of $100 - 500\,\text{nm}$ in size [280]. The resulting increased fluid extravasation through the leaky and hyperpermeable vessel walls passively transports NPs from the vasculature through pores or fenestrations into the IF [172].

The second term in (5.3) corresponds to the transendothelial pathway which is the second transport mechanism across vessel walls and also depicted in Figure 5.19. It represents the diffusive flux of NPs through the capillary vessel wall, e.g. through interconnected cytoplasmic vesicles and vacuoles [280]. The flux is proportional to the vascular permeability P^v and the

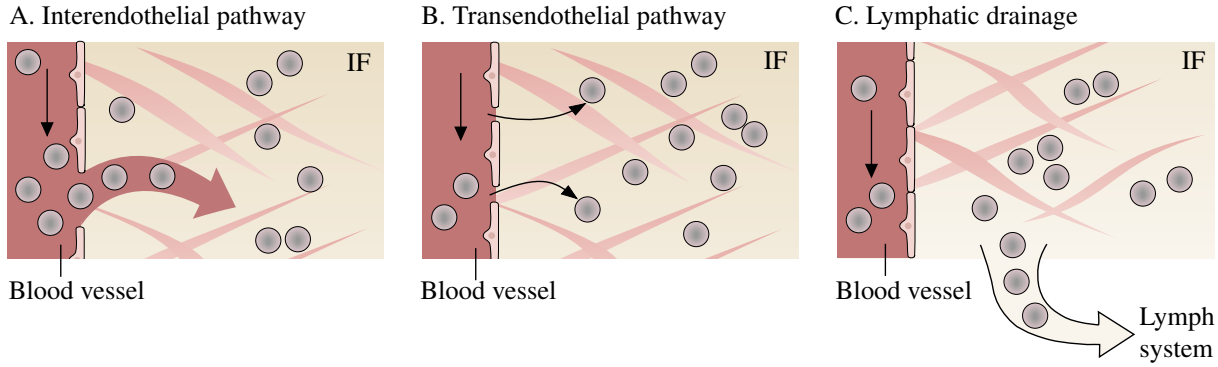

Figure 5.19: Mechanisms for nanoparticle transport to and from the interstitial fluid (IF). Transcapillary exchange of nanoparticles from the vasculature to the IF consisting of (A) the interendothelial and (B) the transendothelial pathway; (C) Lymphatic drainage for transport from the IF to the lymph system. Figure taken from the author's co-authored article [282].

mass fraction difference of NPs across the vessel wall $\omega^{NP\bar{v}} - \omega^{NP\bar{l}}$. Macaulay brackets $\langle \bullet \rangle_+$ allow only mass transfer from the vasculature into the IF and not vice versa.

This formulation for NP extravasation was employed by Wirthl et al. [282]. However, here a slightly different mass transfer exchange is preferred. This is due to the fact that in experiments the direction and magnitude of convection across the blood vessel is often not accessible [67]. Only the apparent vascular permeability $P_{v,\mathrm{app}}$ which contains both the influence of the transendothelial and the unknown influence of the interendothelial pathway can be measured from concentration differences across the vessel wall. Thus, following Dreher et al. [67], NP extravasation is re-written as

$$\overset{NPv\rightarrow NPl}{M_{\mathrm{tv}}} \approx \rho^v \cdot P_{v,\mathrm{app}} \cdot \frac{S}{V} \left\langle \omega^{NP\bar{v}} - \omega^{NP\bar{l}} \right\rangle_+ \cdot \varepsilon^v. \tag{5.4}$$

The apparent vascular permeability $P_{v,\mathrm{app}}$ now contains both diffusive and convective flux.

The third mass transfer contribution for NPs illustrated in Figure 5.19 is drainage via the lymphatic system. As described above, the lymph vessels absorb extravasated fluid as well as molecules from the IF. For that, the relationship

$$\overset{NPl\rightarrow NPly}{M_{\mathrm{drain}}} = \rho^l \cdot \left(\left(L_p \frac{S}{V} \right)_{ly} \cdot \left\langle p^l - p^{ly} \right\rangle_+ \cdot \omega^{NP\bar{l}} + \left(P \cdot \frac{S}{V} \right)_{\mathrm{ly}} \left\langle \omega^{NP\bar{l}} \right\rangle_+ \right) \cdot \left\langle 1 - \frac{p^t}{p^t_{\mathrm{coll},ly}} \right\rangle_+ \tag{5.5}$$

is employed. Again, the first term represents drainage of NPs via convective flux with the term for fluid drainage (B.4) and the second term via diffusion into the lymph vessels. As described in Appendix B.1 it is assumed that the lymphatic pressure is small with $p^{ly} \approx 0$ and that drainage is impaired by the growing tumor, which is modeled via the last term with a linear decrease until the collapse threshold $p^t_{\mathrm{coll},ly}$ above which no drainage is possible any more.

The interplay of excessive leakage, including macromolecules and NPs, into the interstitium and impaired lymphatic drainage inside the tumor results in the accumulation of NPs in the tumor. This phenomenon was first described by Matsumura and Maeda [166] in 1986 and termed

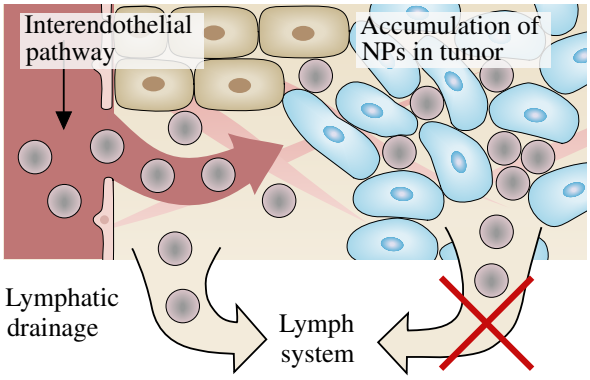

Figure 5.20: EPR effect. Nanoparticles leak from the vasculature to the IF. In the tumor region, the lymphatic drainage is impaired and hence the particles are not removed by the lymph system. This results in a passive accumulation of NPs in the tumor. This phenomenon is called the EPR (enhanced permeability and retention) effect [166]. Figure taken from author's co-authored article [282].

EPR effect. As depicted in Figure 5.20, it leads to a passive retention of NPs in the tumor as lymphatic clearance is inhibited there. Over recent years, it has become a gold standard for the design of anti-cancer agents based on macromolecules and NPs since it is possible to achieve very high local concentrations inside the tumor ($10-50$-fold higher than in normal tissue) [112]. Thus, tumor sites can be selectively targeted while the damage induced by the anti-cancer drug to surrounding tissue is minimized.

Hereafter, the distribution of NPs is studied following common experiments [67, 299] where dextrans of various, clinically relevant molecular weights have been considered. For that, the grown state after 12.5 days of vascular tumor growth depicted in Figures 5.17c and 5.18 is employed as a starting point. NP transport in the IF governed by (3.28) is solved for an additional period of 500 minutes with time steps of $\Delta t = 20\,\mathrm{s}$. The respective mass transfer relationships accounting for transvascular exchange into and lymphatic drainage from the IF are once more given in Figure 5.16. The entire tumor growth model is still computed but the quantities such as saturations and pressures can be considered stationary in the comparably short period in which NP transport is investigated.

Additional parameters governing NP transport are given in Table C.9 and the parameters depending on the molecular weight of dextran ranging from $3.3\,\mathrm{kDa} - 2\,\mathrm{MDa}$ are collected in Table 5.2. In general, larger molecules have smaller diffusivities and vascular permeabilities but longer half-lives in blood plasma as smaller molecules can extravasate more easily but can also be cleared more rapidly. As stated above, the NP mass fraction in the vasculature is specified with the relationship (5.2) depending on the plasma half life $T_{1/2}$. A no-flux boundary condition for NPs in the IF is applied on the outer surface of the domain in addition to the no-flux boundary conditions for symmetry reasons on all other surfaces.

Results for all four studied particle types are shown in Figure 5.21. Therein, the temporal evolution of the NP distribution in the IF along the tumor radius is displayed. The EPR effect is evident for all cases as the particles accumulate only in the tumor region. Outside of the tumor they are drained by the still-functioning lymphatic system. Note the different scale for each sub-

Molecular Weight [kDa]	D_0^{NPl} [$\mathrm{m^2\,s^{-1}}$][a]	$P_{v,\mathrm{app}}$ [$\mathrm{m\,s^{-1}}$][b]	$T_{1/2}$ [s][b]	Pe [−][c]
3.3	30.83×10^{-12}	1.54×10^{-7}	240	12
10	17.28×10^{-12}	3.2×10^{-8}	360	22
70	3.01×10^{-12}	9.8×10^{-9}	1260	124
$2000 = 2\,\mathrm{MDa}$	0.26×10^{-12}	1.7×10^{-9}	1800	1434

[a] Values from Chou et al. [45].

[b] Values from Dreher et al. [67]. There, the plasma half-life is related to vascular fluorescence intensity. Here, it has been assumed that the vascular mass fraction is proportional to the vascular fluorescence intensity such that the same half-lives can be employed.

[c] Calculated as

$$\mathrm{Pe} = \frac{\overline{S^l}^{A_l - 1} \cdot k \cdot \Delta p^l}{\bar{\varepsilon} \cdot \mu_l} \tag{5.6}$$

from (3.28) with mean saturation $\overline{S^l}$ and porosity $\bar{\varepsilon}$ over the entire domain computed as in (5.7). Δp^l is pressure difference between center of domain and outer radius such that length scale chosen as the radius cancels out.

Table 5.2: Properties of dextran at various molecular weights for diffusivity in IF D_0^{NPl}, apparent vascular permeability $P_{v,\mathrm{app}}$, plasma half-life $T_{1/2}$ and Péclet number in IF

figure: By far the highest mass fraction is present for the smallest NP. This is effected by its high apparent vascular permeability. The larger the NP, the lower the values in the domain due to decreased extravasation. However, the smaller NPs with weights of $3.3\,\mathrm{kDa}$ and $10\,\mathrm{kDa}$ are also eliminated from the domain much faster than the larger ones. This has two causes: First, their mass fraction in the vasculature drops rapidly due to their lower plasma half-life such that the actual time period in which they may enter from the vasculature into the IF is much shorter ($12\,\mathrm{min}$ and $26\,\mathrm{min}$ vs. $92\,\mathrm{min}$ and $193\,\mathrm{min}$). Second, their diffusivity is higher. Hence, they diffuse much faster through the entire domain and, crucially, also out of the tumor where the lymph system is functional such that they are removed from the domain.

Initially, all particles accumulate at the periphery of the tumor which is the influence of the higher vascular volume fraction which due to blood vessel compression and regression is approximately twice as high as in the center of the domain, compare Figure 5.17c. However, the larger diffusivity of the smaller particles enables also a much more rapid penetration against the acting pressure gradient towards the center of the domain resulting in a much more uniform profile over the radius. By contrast, the larger particles remain concentrated at the tumor edge and can only very slowly reach also the tumor center in higher quantities. The Péclet numbers for all cases relating the influence of convection and diffusion are given in Table 5.2. Notably, all cases are convection-dominated due to the high IF pressure gradient. In [282] far less of the heavier NPs reached the tumor core compared to the results here because an inner area without any vasculature appeared due to blood vessel compression and regression. Thus, in contrast to the smaller particles, the larger particles were not able to diffuse into the tumor center. In the present case, the tumor is still vascularized in its interior, albeit worse than on its outer rim. Nevertheless, this vascularization in the tumor core also makes extravasation of NPs directly into the core possible, thus leading to a considerable mass fraction there. Via diffusion, the heavier NPs cannot reach or can only very slowly reach the tumor center.

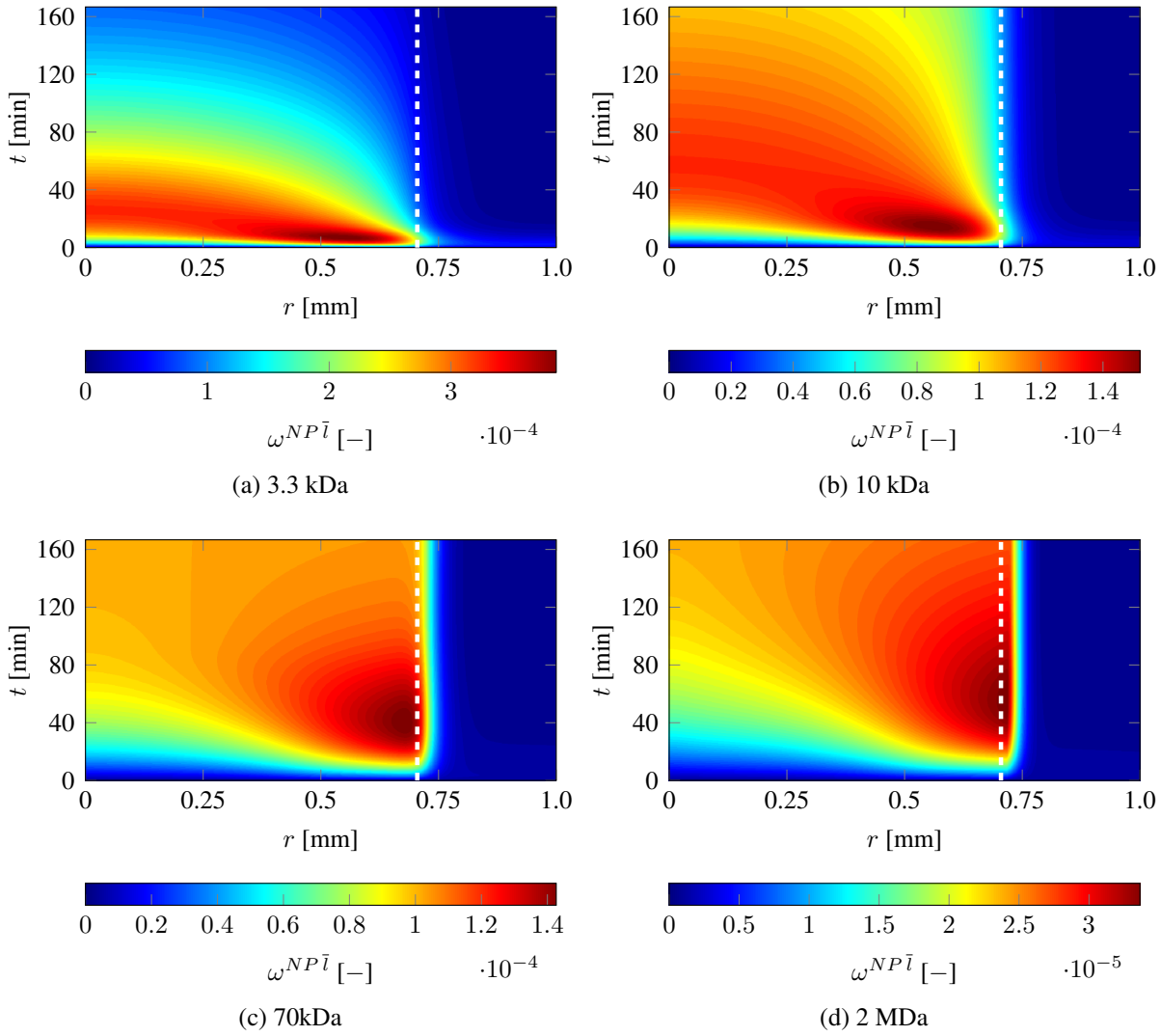

(a) 3.3 kDa (b) 10 kDa

(c) 70kDa (d) 2 MDa

Figure 5.21: Distribution of nanoparticles in IF over radius and time (Dashed white line indicates edge of tumor with $S^t = 0.05$)

The temporal evolution of the mean NP mass fraction in the IF

$$\overline{\omega^{NP\bar{l}}} = \frac{1}{V} \int \omega^{NP\bar{l}} \, \mathrm{d}\Omega \tag{5.7}$$

is further investigated in Figure 5.22. Qualitatively, these results are in very good accordance with experimental data by Dreher et al. [67, Fig. 4 and Fig. 5]. The smaller molecules extravasate very quickly into the IF but are also drained much faster. By contrast, the heavier particles persist much longer and their mass fraction remains almost constant after $200\,\mathrm{min}$. This is not supported by the experimental data where also these particles are being drained after $40 - 100\,\mathrm{min}$. Additionally, it seems that the model with the present parameters over-estimates the initial peak of 3.3 kDa dextran. Potentially, both phenomena are due to an inaccurate model for lymphatic drainage. If drainage of NPs was present to some extent also in the tumor region where it is

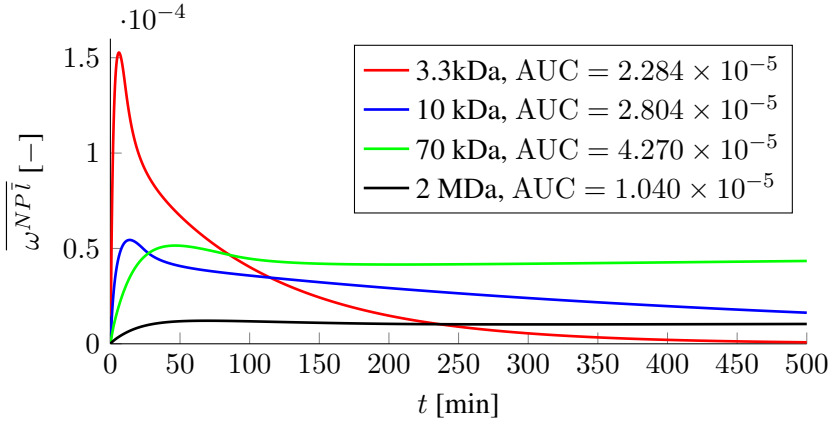

Figure 5.22: Mean mass fraction of nanoparticles in IF over time

currently completely switched off via (5.5), the initial peak would be not as high and the larger particles accumulating primarily in the tumor region would be drained more rapidly. All in all, clearance is much slower than in the experiments of [67]. Thus, while the overall agreement is very good, proper calibration of the lymphatic drainage of NPs could improve the predictive capabilities of the model in this respect.

A very common method to measure the exposure of cancer cells to a specific drug is to determine its so-called area-under-the-curve (AUC) value [67, 280]. It can be obtained by temporal integration over the curves from Figure 5.22 as

$$\mathrm{AUC} = \frac{1}{t_E - t_0} \int_{t_0}^{t_E} \overline{\omega^{NPl}} \, \mathrm{d}t \tag{5.8}$$

where $[t_0, t_E]$ is the considered time interval of NP treatment ($500\,\mathrm{min}$ in this case). Hence, the cumulative exposure of cancer cells to the toxic drug in the extravascular compartment is calculated. Assuming that the number of cells killed is proportional to the concentration of a specific drug, it may quantify the success of drug delivery. The AUC values are computed by trapezoidal integration of the curves from Figure 5.22 and are given there. Hypothetically, 70 kDa dextran would have the best drug delivery efficiency for this example followed by 10 kDa, 3.3 kDa and 2 MDa dextran. This is again supported by the experimental data of [67] where the AUC was also calculated. Nevertheless, it is highly likely that all values for the AUC are overestimated due to the decreased lymphatic drainage as described above since either the initial value is too high or clearance is not as fast as in the experiments.

A straightforward extension is to include the cytotoxicity of a chemotherapeutic substance which could either be encapsulated by the NPs or attached to their surface. For high drug concentrations, this could be realized by a killing term acting on TCs and for lower concentrations by a deceleration of tumor growth as proposed by Curtis et al. [50]. Also additional factors leading to therapeutic resistance such as a denser, remodeled ECM in the tumor region could be incorporated. Computational modeling of ”smart” NPs which alter their size and, thus, their transport properties during different delivery stages [142, 149] to optimize their *in-vivo* performance could be an invaluable tool for the design of next-generation NPs. For instance, the break-up of larger NPs into smaller drugs at the tumor site and their subsequent distribution can be included in the current framework as additional species transport convection-diffusion-reaction equations.

Hyperthermia Treatment Finally, the temperature increase during a hypothetical nanoparticle-mediated hyperthermia treatment is investigated. This is partly based on preliminary work in the Master's thesis of B. Wirthl [281]. 70kDa dextran is employed as it has a hydrodynamic radius of $5-7\,\mathrm{nm}$ [44, 256]. The hydrodynamic radius of common superparamagnetic iron oxide NPs, for which experimental data about their hyperthermic performance is available [41], lies also in this range. Thus, the transport properties of these NPs, i.e., their blood half-life, diffusivity and vascular permeability are identical to 70 kDa dextran, and it can be expected that their distribution in the domain over time is equivalent to the results for 70 kDa dextran presented in the previous paragraphs. 150 minutes after the NP injection, the mass fraction of 70 kDa in the IF is almost stationary, see Figure 5.22. Thus, this time instant is taken as the starting point for simulating hyperthermia treatment for an additional 100 time steps of $\Delta t = 20\,\mathrm{s}$. For that, the source term in the enthalpy balance (2.68) representing the heating induced by the AMF is set to

$$\sum_{\alpha\in\mathfrak{I}_p} \varepsilon^\alpha s^\alpha = \rho^l \cdot \mathrm{SAR} \cdot \omega^{NP\bar{l}} \tag{5.9}$$

depending on the density of the IF, the specific absorption rate of the NPs $\mathrm{SAR}\,[\mathrm{W\,kg^{-1}}]$ and their mass fraction in the IF. Note that 150 minutes after injection, the mass fraction of NPs in the vasculature is negligible, otherwise one would also have to take them into account in the temperature source term as for example done by Wirthl [281]. A heat sink term as proposed in the Pennes' bioheat equation [193] is not included due to the controversy associated with this formulation [281]. Nakayama and Kuwahara [179] compared different bioheat formulations for the case of a single fluid phase, i.e., blood. Under the assumption of thermal equilibrium with equal temperatures in blood and tissue, they arrived at an equivalent formulation as the here employed enthalpy balance (2.46). If thermal non-equilibrium between blood and the other phases should be considered, a strict derivation with TCAT [95] is warranted. The heat source term from (5.9) is equivalent to the term employed by Cervadoro et al. [41] such that their experimental data for the SAR, which is the amount of heat generated by applying the electromagnetic field, can be used. The average mass fraction of NPs in the domain for 70 kDa dextran remains constant with a value of approximately 5×10^{-5} after 150 minutes, see Figure 5.22, and maximum values inside the tumor of 1×10^{-4}, see Figure 5.21c. Together with the IF density this corresponds to a NP concentration in the IF of $0.05\,\mathrm{mg\,ml^{-1}}$ respectively $0.1\,\mathrm{mg\,ml^{-1}}$. The SAR for heating with a high-frequency field ($30\,\mathrm{MHz}$) for these NP concentrations lies in a range of $0.5 \times 10^7 - 3 \times 10^7\,\mathrm{W\,kg^{-1}}$ [41, Figure 2D].

A Robin boundary condition

$$\boldsymbol{\kappa}_{\mathrm{eff}} \boldsymbol{\nabla} T \cdot \boldsymbol{n} = -\beta_T \cdot (T - T_{\mathrm{bl}}) \tag{5.10}$$

is applied on the outer radial surface of the domain similar to [177, 178]. This term accounts for the heat transfer with heat exchange coefficient β_T to the surrounding tissue whose temperature is equal to the blood temperature $T_{\mathrm{bl}} = 37\,^\circ\mathrm{C}$. All required additional parameters are based on previous hyperthermia studies [41, 177, 178] and are given in Table C.11. As the heat capacity of all phases is equal, the last term of the energy balance (2.68) cancels in combination with (2.21). During the simulation of hyperthermia treatment for an additional time period of $2000\,\mathrm{s}$ starting 150 minutes after NP injection, the entire tumor growth model including NP transport is still solved but the values remain almost stationary. The initial temperature in the domain is set to $37\,^\circ\mathrm{C}$.

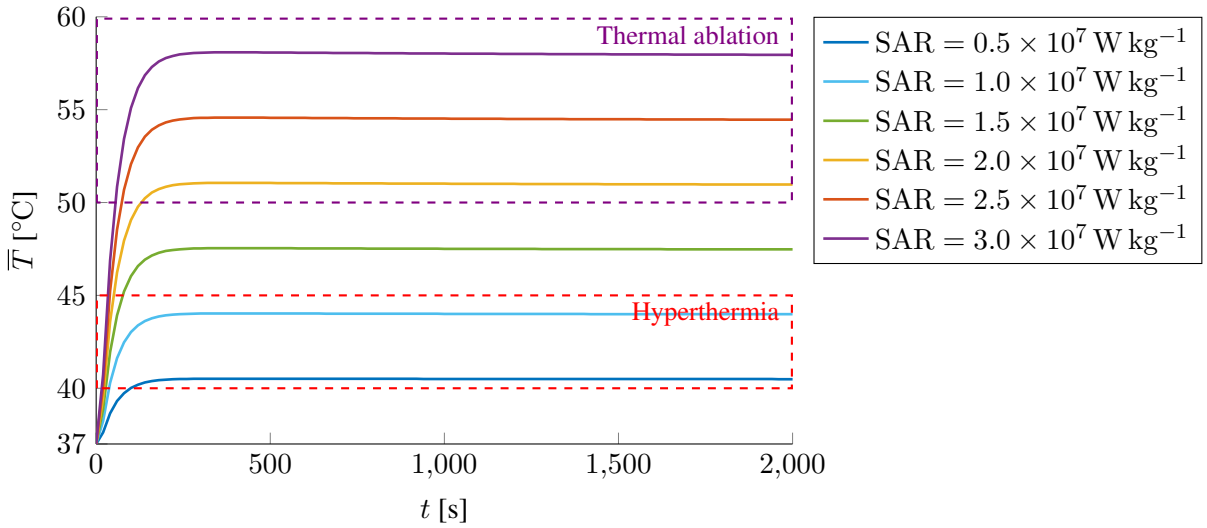

Figure 5.23: Mean temperature over time during hyperthermia treatment

Due to the small domain size and the high diffusivity, the temperature in the domain is almost uniform with slightly higher values in the center. The maximum temperature difference between center and outer surface amounts to $0.8\,°\mathrm{C}$. The mean temperature in the domain over time for the different SAR values is shown in Figure 5.23. Starting from $37\,°\mathrm{C}$, the domain heats up over $200\,\mathrm{s}$. Afterwards, the temperature remains stationary at values ranging from $40.5 - 58\,°\mathrm{C}$. Naturally, higher SARs lead to higher obtained temperature values. In addition, the temperature ranges for hyperthermia ($40 - 45\,°\mathrm{C}$ [43]) and thermal ablation ($\geq 50\,°\mathrm{C}$ [123]) are designated illustrating that, depending on the SAR, both ranges can be reached with the present numerical model for nanoparticle-mediated hyperthermia. Thereby, the principal applicability of the model to simulate hyperthermia treatment is proven. Further validation is necessary to tune it for clinically more relevant cases. Nevertheless, its promising and unique potential by combining initial tumor growth with subsequent drug delivery, here exemplarily studied for NPs, and hyperthermia into one single framework has been showcased.

Remark 5.1. *As elaborated by Cervadoro et al. [41], the SAR values may also contain the influence of non-specific heating of salts through the high-frequency field. For lower electromagnetic frequencies, this effect is not present and the SAR lies in a range of* $4000 - 20\,000\,\mathrm{W\,kg^{-1}}$ *for NP concentrations of* $1 - 3\,\mathrm{mg\,ml^{-1}}$. *As Nabil et al. [177, 178] also used a very high value of* $1 \times 10^6\,\mathrm{W\,kg^{-1}}$ *and as the heat exchange coefficent* β_T *is based on their papers, the specified SAR range is preferred here in line with the goal of this example to illustrate that the model is generally capable of describing hyperthermia.*

5.4 Three-dimensional Growth of a Tumor inside a Network of Pre-existing Blood Vessel

Subsequently, the growth of a tumor inside a three-dimensional pre-existing blood vessel network is studied. This numerical example was previously published in the author's article [136]

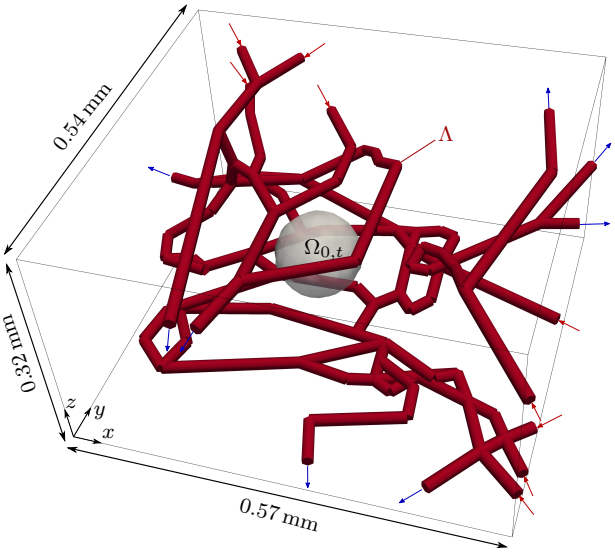

Initial conditions	
$\Omega_{0,t}$	$S_t = 0.5$, $S_h = 0$, $S_l = 0.5$
	$(p_{hl} = 590\,\text{Pa}, p_{th} = 295\,\text{Pa}, p_l = 0\,\text{Pa})$
	$\varepsilon_0 = 0.8$, $\omega^{n\,\bar{l}} = 2.0 \cdot 10^{-6}$, $\omega^{N\,\bar{t}} = 0$
$\Omega_{0,h}$	$S_t = 0$, $S_h = 0.2$, $S_l = 0.8$
	$(p_{hl} = 191.7\,\text{Pa}, p_{th} = p_l = 0\,\text{Pa})$
	$\varepsilon_0 = 0.8$, $\omega^{n\,\bar{l}} = 2.0 \cdot 10^{-6}$, $\omega^{N\,\bar{t}} = 0$
Λ_0	$p^{\hat{v}} = 3000\,\text{Pa}$
	$\omega^{n\,\hat{v}} = 2.88 \cdot 10^{-4}$ $(P^{\hat{v}}_{\text{oxy}} \approx 100\,\text{mmHg})$
Boundary conditions	
Γ_Ω	$S_t = 0$, $S_h = 0.2$, $S_l = 0.8$
	$(p_{hl} = 191.7\,\text{Pa}, p_{th} = p_l = 0\,\text{Pa})$
	$\omega^{N\,\bar{t}} = 0$
$\Gamma_{\Lambda,i}$	$p^{\hat{v}} = 3000\,\text{Pa}$, $\omega^{n\,\hat{v}} = 2.88 \cdot 10^{-4}$
$\Gamma_{\Lambda,o}$	$p^{\hat{v}} = 2833\,\text{Pa}$

Figure 5.24: Geometry, initial and boundary conditions of the example for three-dimensional vascular tumor growth. Figure taken from the author's article [136].

and was re-computed here using the lateral surface variant for 1D-3D coupling. Nevertheless, major parts of the following text are taken from [136] since almost identical results are obtained with both variants. In Sections 5.2 and 5.6, cases inspired by the classical model of angiogenesis where the tumor first grows avascularly and then angiogenesis occurs from nearby vessels are studied. However, a different mechanism of growth is possible for certain tumor types such as astrocytomas [19, 108, 109]. They can first acquire access to blood circulation by co-opting pre-existing blood vessels and growing along them which makes them a non-angiogenic but nevertheless well-vascularized tumor. Subsequently, the pre-existing vasculature regresses such that a necrotic core inside the tumor evolves due to a lack of nutrients. Only then angiogenesis at the tumor boundary is initiated to enable further tumor growth [109]. The goal of the numerical example presented in this section is to illustrate how the model with discrete embedded representation of the vasculature can capture this co-opting growth pattern.

In Kremheller et al. [136], the centerline variant for 1D-3D coupling was employed to investigate this numerical example. In this thesis, the surface-coupled formulation is employed for comparison. The computational domain of Figure 5.24 is considered. Note that the original volume used in [136] is slightly enlarged such that it encompasses the entire network including its surface on the tips which would otherwise protrude. Apart from that, the setup is identical to [136] with the computational domain of Figure 5.24. The depicted blood vessel network has been obtained from R3230AC mammary carcinoma in rat dorsal skin flap preparation by Secomb et al. [238] and has been employed in several other publications to study oxygen transport [241], drug delivery [38, 39] and hyperthermia treatment [177, 178]. The network topology is publicly available [239]. The enclosing 3D tissue domain has been enlarged by $0.01\,\text{mm}$ in positive and negative x- and y-direction and by $0.066\,\text{mm}$ in positive and negative z-direction as compared to the dimensions $0.55\,\text{mm} \times 0.52\,\text{mm} \times 0.188\,\text{mm}$ of the network geometry. The three-dimensional domain is discretized uniformly in space with $114 \times 108 \times 64$ trilinear elements and the one-dimensional network with 8298 linear elements. Hence, the 3D mesh with

uniform mesh size $h = 5\,\mu\text{m}$ is finer by a factor of two compared to [136]. The meshes of both domains are completely independent which is the main advantage of the non-conforming 1D-3D coupling employed throughout this thesis. The 1D network is discretized rather finely compared to the 3D domain to avoid instabilities due to convection-dominated oxygen transport in this example. Following Nabil et al. [177, 178] a uniform radius of $R = 7.64\,\mu\text{m}$ is assumed in the entire network. Consequently, the diameter of the embedded inclusion is three times larger than the element size in the 3D domain which necessitates the usage of the surface-coupled version. Tumor growth is simulated for a time period of $360\,\text{h}$. Time discretization parameters are set to $\theta = 0.5$ and $\Delta t = 1800\,\text{s}$.

In this example, angiogenesis is not present because the goal is to simulate the first growth stage along the blood vessel network as described above. Furthermore, deformations of the surrounding ECM and, hence, also of the embedded blood vessels are neglected. In essence, the model with discrete vasculature introduced in Section 3.4 without the balance of momentum of the solid phase, that is, without equation (3.27) is considered here. A schematic overview of the present phases and species is given in Figure 5.25. The original avascular model with three fluid phases (TCs, HCs, IF) is solved for the tissue domain and blood flow in the 1D embedded domain. The Starling equation (B.15) respectively (B.17) accounts for the 1D-3D leakage of fluid into the IF. Furthermore, two species are present, namely, NTCs and oxygen (in 1D embedded vasculature and IF). Oxygen is provided via transvascular exchange from the vasculature into the IF via the 1D-3D mass transfer relations (B.19) and (B.22). Note that oxygen consumption by the HCs is now also included via (B.7).

Initially, a spherical tumor with radius $r_0 = 0.03\,\text{mm}$ around the point $[0.25, 0.25, 0.11]$ is present inside the domain. Primary variables for TC, HC, the IF and for NTCs are fixed on the entire boundary of the cuboid Γ_Ω. Nine open ends of the network are identified as inflows $\Gamma_{\Lambda,i}$ (denoted by red arrows) where pressure and mass fraction of oxygen in the 1D network are fixed. The remaining eight open ends are outflows $\Gamma_{\Lambda,o}$ (denoted by blue arrows) with fixed pressure. This approach has been proposed to prescribe the pressure drop along the network such that a physiologically reasonable blood velocity is obtained [38, 39, 177].

The parameters employed in this example are the same as given in Tables C.2, C.4, C.5, C.6 and C.10 apart from the coefficients for oxygen consumption. The oxygen consumption rate is elevated w.r.t. the examples from the previous section under the assumption that the tissue considered here is well-vascularized which implies a heavy oxygen or nutrient demand. Therefore, the consumption by TCs is increased to $\gamma^{nt}_{\text{growth}} = 9.6 \times 10^{-4}\,\text{kg}\,\text{m}^{-3}\,\text{s}^{-1}$ and $\gamma^{nt}_0 = 2.4 \times 10^{-3}\,\text{kg}\,\text{m}^{-3}\,\text{s}^{-1}$ and for HCs to $\gamma^{nh}_0 = 1 \times 10^{-3}\,\text{kg}\,\text{m}^{-3}\,\text{s}^{-1}$ compared to the values of Table C.5. Note that all the values applied for oxygen consumption lie in the physiological range of oxygen consumption rates of $0.01 - 0.3\,\text{min}^{-1}$ (in terms of oxygen concentration [205]).

The results for tumor growth over the considered time span are visualized in Figure 5.26. Initially, the tumor grows radially. As more and more oxygen is consumed, tumor growth continues along the vasculature by co-option of the blood vessels because this is the region with the highest oxygen concentration in the IF which is provided by the vasculature through transcapillary 1D-3D exchange. This behaviour is further visualized in Figure 5.27 where the oxygen distribution in the IF throughout the computational domain is shown after 90 and 270 hours. The oxygen mass fraction decreases in radial direction from the embedded blood vessels due to the consumption by HCs and TCs. In this example, blood vessel remodeling via the blood vessel

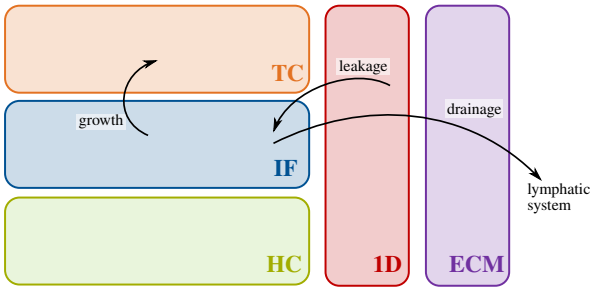

Phase	Mass transfer terms
ECM	0
HC	0
TC	$\overset{l\to t}{M}_{\text{growth}}$
IF	$\delta_{\partial\mathcal{D}_t} \cdot \overset{\hat{v}\to l}{M}_{\text{leak}} - \overset{l\to ly}{M}_{\text{drain}} - \overset{l\to t}{M}_{\text{growth}}$
1D	$-\overset{\hat{v}\to l}{M}_{\text{leak}}$

(a) Phases with respective mass transfer relations

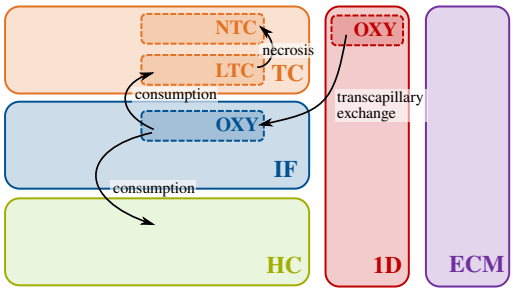

Species	Mass transfer terms
NTC	$\varepsilon^t r^{Nt} - \omega^{N\,\bar{t}} \overset{l\to t}{M}_{\text{growth}}$
OXY/IF	$-\overset{nl\to t}{M}_{\text{cons}} - \overset{nl\to h}{M}_{\text{cons}} + \delta_{\partial\mathcal{D}_t} \cdot \overset{n\hat{v}\to nl}{M}_{\text{tv}} - \omega^{n\,\bar{l}} \left(- \overset{l\to t}{M}_{\text{growth}} \right)$
OXY/1D	$= - \overset{n\hat{v}\to nl}{M}_{\text{tv}}$

(b) Species with respective mass transfer relations

Figure 5.25: Schematic overview of vascular model with discrete representation of the vasculature and mass transfer relations

diameter adaptation model introduced in Section 3.4.5 is not included. Nevertheless, the influence of blood vessel collapse and regression on the growth of the tumor can be imitated if the exchange terms between pre-existing vasculature and IF, that is, the mass transfer terms for leakage and oxygen exchange are switched off once the tumor has reached a specific embedded 1D element. This approach is applied here. After 180 hours, a necrotic core starts to appear due to a lack of oxygen in its interior since nutrient diffusion from the outside to the inside of the tumor is a limiting factor. This effect is also evident from Figure 5.27b: The region around the inlets is still well oxygenated. However, the interior region of the domain is hypoxic as oxygen diffusion alone cannot sustain the vast consumption due to rapid tumor growth. Finally, TCs become necrotic and the aforementioned necrotic core starts to develop while the outer, proliferating cells of the tumor continue co-opting the vasculature.

These results are almost identical to Kremheller et al. [136, Figure 13] where the centerline-based 1D-3D coupling variant was employed. This shows that both variants can be applied if the blood vessel diameter is in the range of the 3D element mesh size. The centerline coupling variant was also tested for the twice as fine mesh employed here and results were again qualitatively similar. However, the surface-coupled variant proved to be more robust and required less Newton iterations per time step with the employed monolithic scheme and showed a more stable and uniform convergence behaviour. For the centerline variant, convergence could not be achieved in some Newton steps. This may be due to the fact that the involved singularity may lead to high oxygen mass fractions in the IF at the position of the embedded vessels. A comparison of both variants with an academic example is performed in Appendix A.1.

The goal of this example is to highlight the capabilities of the non-conforming coupling to represent the complexity of *in vivo* vessel networks and their interaction with the TCAT multi-

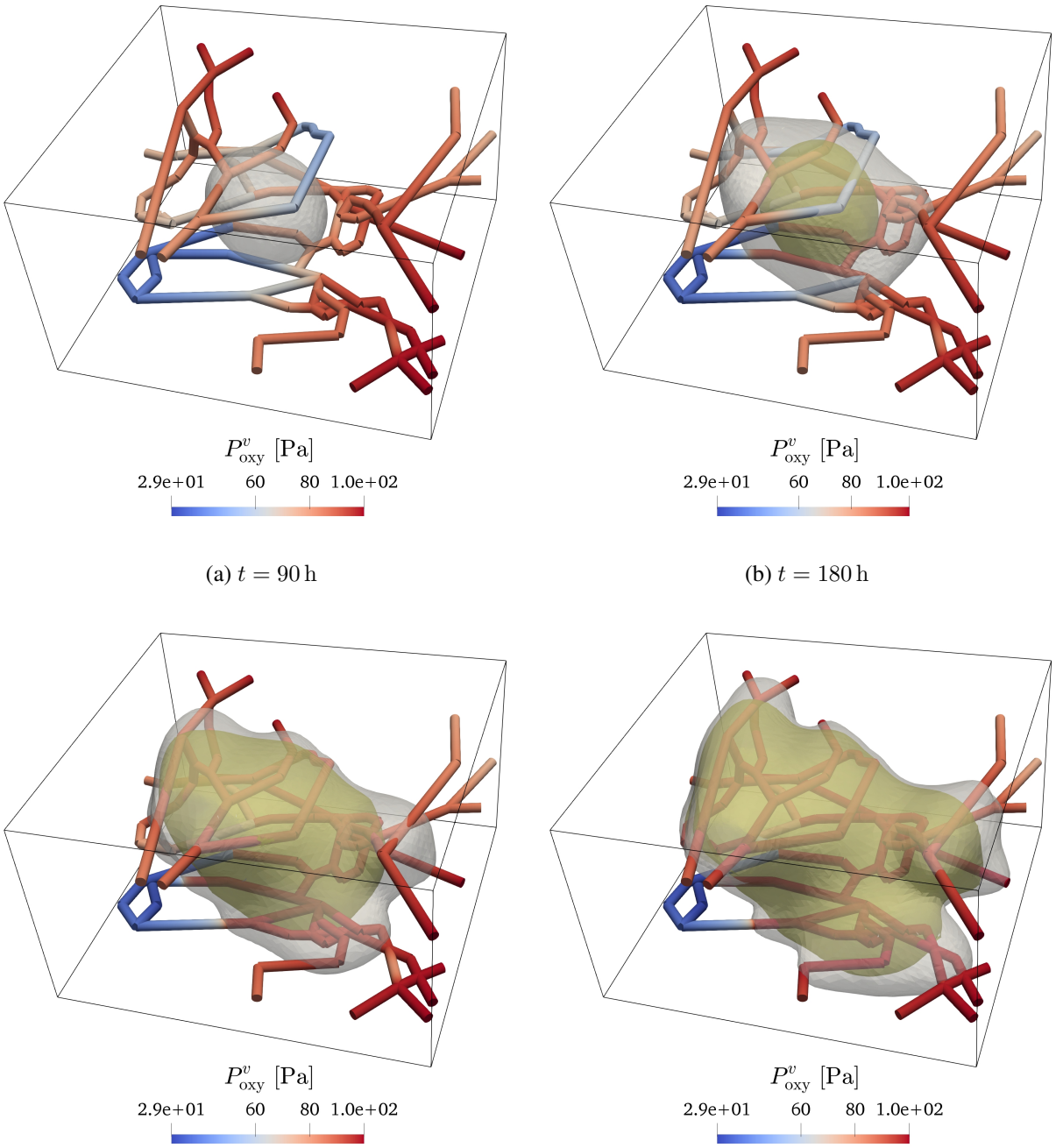

(a) $t = 90\,\text{h}$ (b) $t = 180\,\text{h}$

(c) $t = 270\,\text{h}$ (d) $t = 360\,\text{h}$

Figure 5.26: Three-dimensional growth of a tumor along a pre-existing blood vessel network (outline of tumor is visualized in grey with isosurface $S_t = 0.05$, outline of necrotic core is visualized in olive green with isosurface $\omega^{N\,\bar{t}} = 0.05$). Figure based on the author's article [136] but the respective numerical example has been re-calculated with lateral surface 1D-3D coupling.

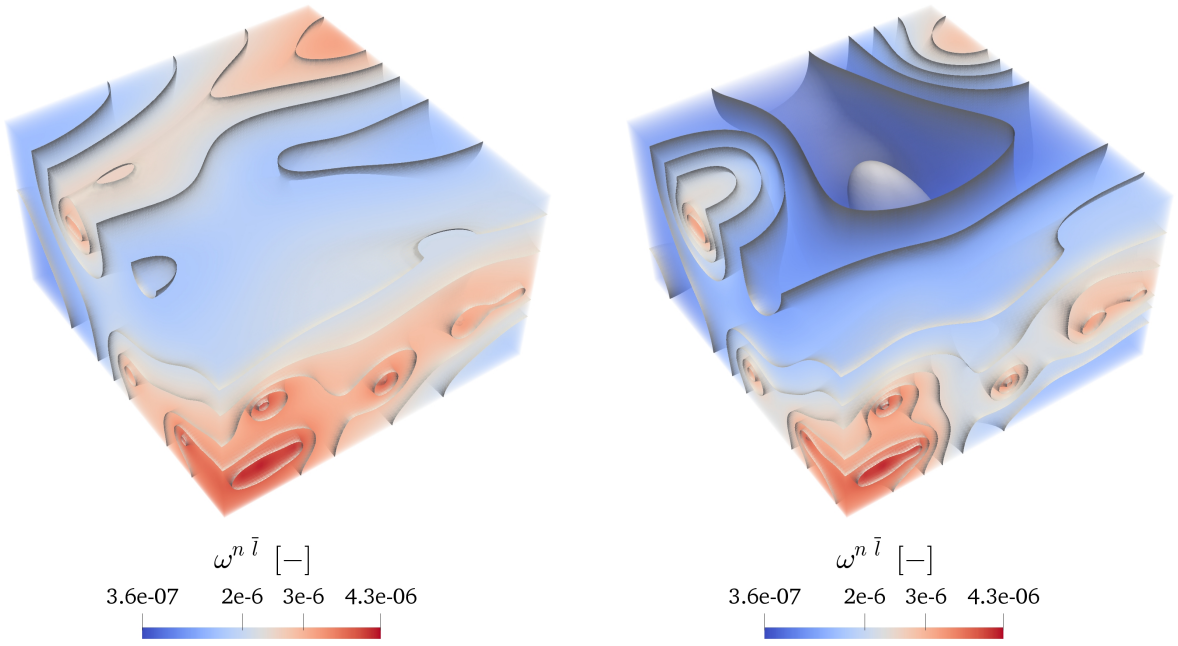

(a) $t = 90\,\mathrm{h}$ (b) $t = 270\,\mathrm{h}$

Figure 5.27: Oxygen distribution in IF – planes denote isosurfaces with constant oxygen level

phase tumor growth model. Here, the major advantage of non-matching meshes for the 1D and the 3D domain becomes evident as a regular mesh can be employed for the 3D domain while the 1D mesh follows the structure of the embedded vasculature. Therefore, the proposed methodology for embedding arbitrary blood vessel networks into surrounding tissue can be applied as a tumor growth model with discrete representation and full resolution of the vasculature. However, one has to be aware that this example is only the first step towards a more realistic description of *in-vivo* tumor growth. For instance, the second stage of angiogenesis on the tumor boundary occurring after blood vessel regression has not been included. In addition, blood vessel regression, compression by TCs and adaptation is not modeled satisfactorily in this example but will be studied in the next section.

5.5 Two-dimensional Growth of a Tumor Including Blood Vessel Compression

Whereas blood vessel compression was only imitated in the previous section via switching off exchange terms in the tumor region, it is incorporated in a more consistent way into the model variant with discrete representation of the vasculature in this section. For that, the empirical relationships (3.101)-(3.103) of the blood vessel diameter adaptation and collapse model together with the developed algorithms described in Section 4.3.3.3 is employed. The additionally required parameters are summarized in Table C.12. These parameters have been estimated to obtain a physiologically reasonable behaviour. The other parameters are again collected in Ta-

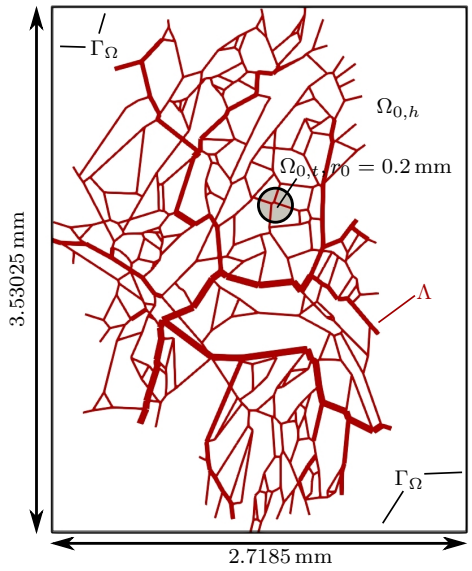

Initial conditions	
$\Omega_{0,t}$	$S_t = 0.2$, $S_h = 0$, $S_l = 0.8$
	$(p_{hl} = 191.7\,\mathrm{Pa}, p_{th} = 95.9\,\mathrm{Pa}, p_l = 0\,\mathrm{Pa})$
	$\varepsilon_0 = 0.8$, $\omega^{n\,\bar{l}} = 2.0 \cdot 10^{-6}$, $\omega^{N\,\bar{t}} = 0$
$\Omega_{0,h}$	$S_t = 0$, $S_h = 0.2$, $S_l = 0.8$
	$(p_{hl} = 191.7\,\mathrm{Pa}, p_{th} = p_l = 0\,\mathrm{Pa})$
	$\varepsilon_0 = 0.8$, $\omega^{n\,\bar{l}} = 2.0 \cdot 10^{-6}$, $\omega^{N\,\bar{t}} = 0$
Λ_0	$p^{\hat{v}} = 3000\,\mathrm{Pa}$
	$\omega^{n\,\hat{v}} = 2.88 \cdot 10^{-4}$ $(P^{\hat{v}}_{\mathrm{oxy}} \approx 100\,\mathrm{mmHg})$
Boundary conditions	
Γ_Ω	$S_t = 0$, $S_h = 0.2$, $S_l = 0.8$
	$(p_{hl} = 191.7\,\mathrm{Pa}, p_{th} = p_l = 0\,\mathrm{Pa})$
Γ_Λ	$p^{\hat{v}}$ estimated with algorithm of Fry et al. [85]
Λ	$\omega^{n\,\hat{v}} = 2.88 \cdot 10^{-4}$ $(P^{\hat{v}}_{\mathrm{oxy}} \approx 100\,\mathrm{mmHg})$

Figure 5.28: Geometry, initial and boundary conditions of the example for two-dimensional vascular tumor growth including blood vessel compression (radius of embedded vasculature not to scale)

bles C.2, C.4, C.5, C.6 and C.10. As in the previous section, two species (NTCs and oxygen) are present. Oxygen is transported in the 1D embedded vasculature and may pass the blood vessel wall into the IF. The same mass transfer terms as given in Figure 5.25 are employed. However, here the centerline variant is used for 1D-3D coupling between embedded vasculature and surrounding tissue since a two-dimensional example is investigated.

The computational domain as well as the embedded vascular network is depicted in Figure 5.28. The network topology was obtained from the rat mesentery by Pries et al. [202] and subsequently used for a number of numerical studies [85, 201, 242]. It is available from [273] and consists of 546 blood vessel segments which connect 388 unique nodes. The radius of the blood vessel segments varies from $1.6\,\mu\mathrm{m}$ to $30\,\mu\mathrm{m}$ with a mean radius of $6.98\,\mu\mathrm{m}$. Several thicker branches can be identified with smaller connections between them. The original network covers a domain of $4.563\,\mathrm{mm} \times 7.060\,\mathrm{mm}$. For this example, the entire domain is scaled by a factor of 1/2 to obtain a denser vascular network than present in the original data set. The radius is not adapted but the original radius is kept. In addition, the scaled domain is enlarged by $0.5\,\mathrm{mm}$ in x-direction as shown in Figure 5.28. It is assumed that an initial tumor of radius $0.2\,\mathrm{mm}$ is present around the point $[1.5\,\mathrm{mm}, 2.2\,\mathrm{mm}]$ measured from the bottom left of the domain. Initial and boundary conditions are listed in Figure 5.28. For the sake of simplicity, the oxygen partial pressure in the entire embedded blood vessel network is set to $100\,\mathrm{mmHg}$. Boundary conditions for the pressure on the tips of the vascular network are estimated with the algorithm of Fry et al. [85] which is publicly available via [251]. This scheme addresses the problem that it is impossible to measure all or even a significant portion of the blood pressure values on the boundaries of large vascular networks. Thus, a constrained optimization problem is solved for the incomplete pressure boundary data by minimizing the error of pressures and wall shear stress w.r.t. pre-defined target values.

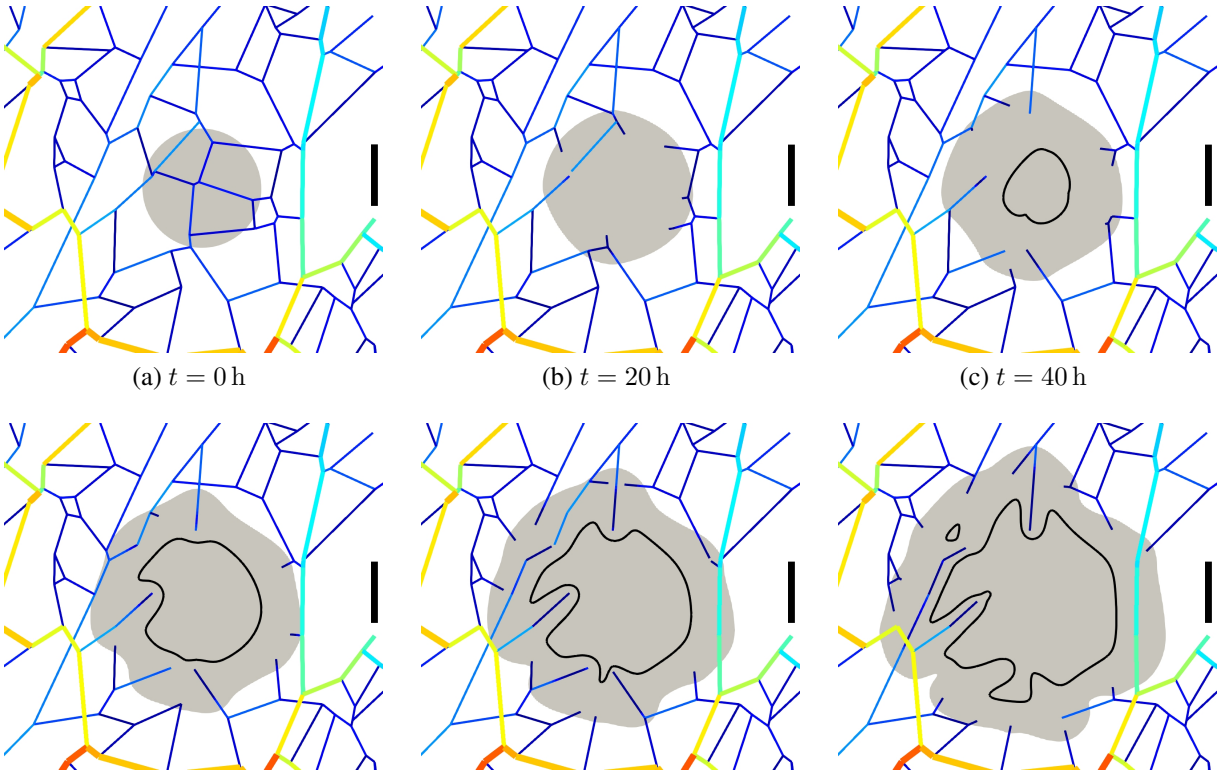

(a) $t = 0\,\mathrm{h}$ (b) $t = 20\,\mathrm{h}$ (c) $t = 40\,\mathrm{h}$

(d) $t = 60\,\mathrm{h}$ (e) $t = 80\,\mathrm{h}$ (f) $t = 100\,\mathrm{h}$

Figure 5.29: Detail view of growth during first 100 hours (black bar denotes $200\,\mu\mathrm{m}$, tumor domain in grey, outline of necrotic zones in black, radius of embedded vasculature not to scale, color scale for element radius as in Figure 5.30)

The 2D domain is discretized with a regular grid of 556×706 quadrilateral (bilinear) elements with an approximate element size of $h = 5\,\mu\mathrm{m}$. The mesh of the embedded domain is completely independent and consists of 6676 linear elements with an approximate element size of $h = 0.01\,\mathrm{mm}$. The time step size is set to $\Delta t = 1800\,\mathrm{s}$ and the time integration parameter θ to 0.5. Tumor growth is studied for a period of $360\,\mathrm{h}$, i.e., 720 time steps.

Results for the first 100 hours of growth are shown in Figure 5.29. The tumor is placed in a sub-network of smaller blood vessels. After 20 hours, it has grown radially outwards. At the same time, it compresses the embedded blood vessels such that the network in its center collapses. This leads to the occurence of a necrotic core after 40 to 60 hours since it is depleted of oxygen. Only the tumor's outer rim is still well-vascularized and contains a considerable amount of oxygen, see also Figure 5.31a. The distance between necrotic zones and the tumor front lies between 100 and $200\,\mu\mathrm{m}$ which is in good agreement with the diffusion limit of oxygen [36]. The tumor continues to grow and to collapse the smaller vessels. Consequently, the network regresses from the tumor center. Some larger vessels are able to withstand the compression by the tumor longer. Cuffs of LTCs form around these branches and grow along them whereas necrotic areas are present in the gaps between the vessels.

Tumor growth until 360 hours is further visualized in Figure 5.30. After 100 hours, also parts of the thicker branches are reached by the growing tumor. With the chosen parameters they

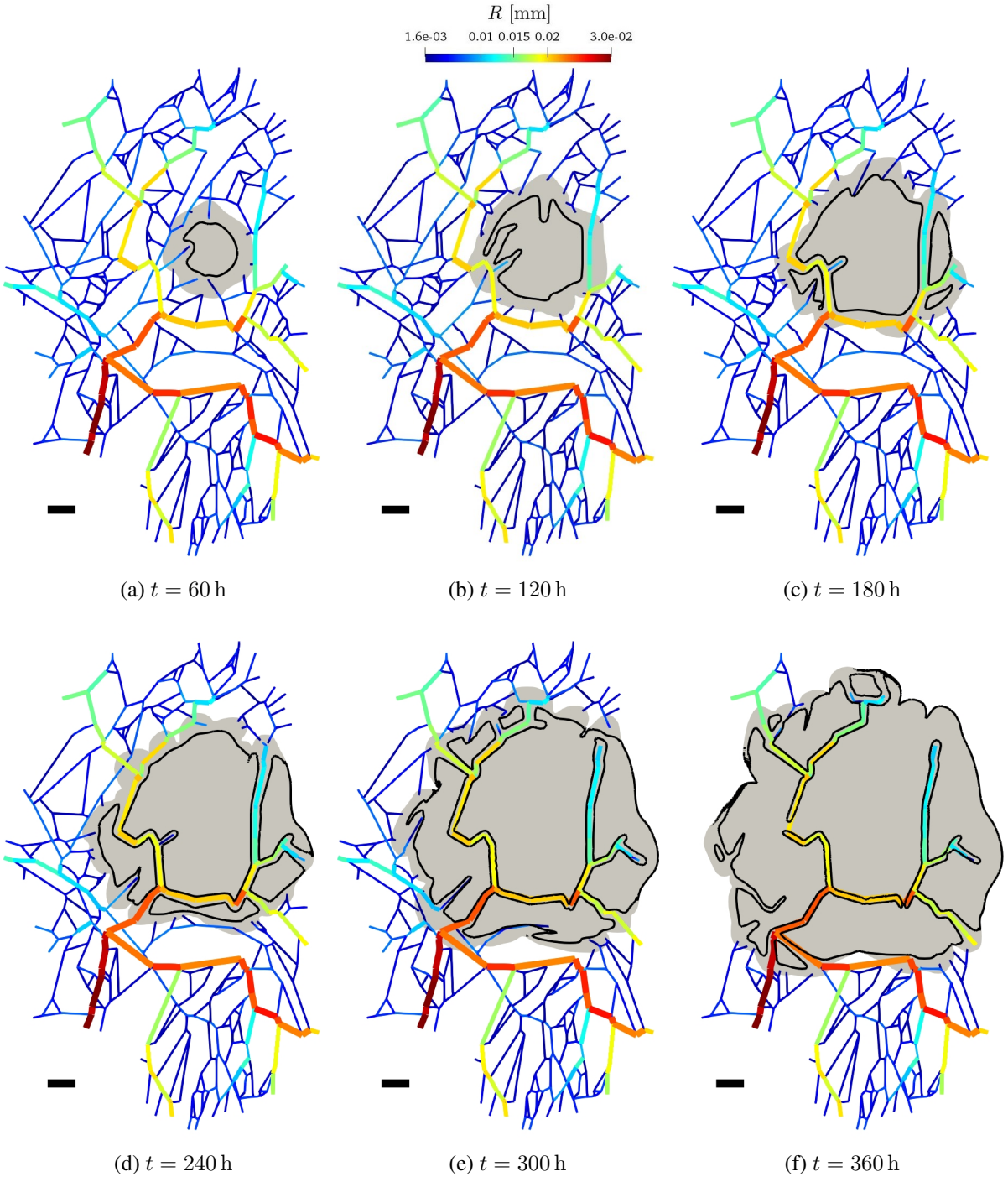

(a) $t = 60\,\mathrm{h}$ (b) $t = 120\,\mathrm{h}$ (c) $t = 180\,\mathrm{h}$

(d) $t = 240\,\mathrm{h}$ (e) $t = 300\,\mathrm{h}$ (f) $t = 360\,\mathrm{h}$

Figure 5.30: Two-dimensional growth of a tumor including blood vessel compression (black bar denotes $200\,\mu\mathrm{m}$, tumor domain in grey, outline of necrotic zones in black, radius of embedded vasculature not to scale)

are unaffected by the proliferating TCs such that their diameter remains constant. Thus, the viable regions continue to grow along the thicker branches while further away and between them necrotic areas form. Simultaneously, the tumor also grows along thinner vascular branches with small fingers forming its edge. However, these thinner vessels are gradually collapsed such that the necrotic area increases and consistently follows the tumor front at a distance of 100 to $200\,\mu\mathrm{m}$. At the right side of the domain, where no blood vessels are located, tumor growth comes to an end and this entire region becomes necrotic. Finally, after 300 to 360 hours almost all smaller vessels are collapsed. Necrosis has occurred throughout the tumor. Only the area around the larger branches is free of NTCs.

Oxygen transport is the main driver for this behaviour as it regulates tumor growth and necrosis. Therefore, the oxygen distribution in the IF is exemplarily given for $t = 60\,\mathrm{h}$ and $t = 240\,\mathrm{h}$ in Figure 5.31. In both pictures, the region without TCs is well-oxygenated. There, the oxygen distribution closely follows the structure of the embedded vascular network with the highest oxygen concentration along its branches which provide a source term for oxygen in the IF. Further away from the 1D network, it drops to lower values as the oxygen diffuses in the IF and is consumed by HCs. By contrast, the tumor area is almost entirely devoid of oxygen due to the vast oxygen consumption of TCs. After 60 hours, only some smaller regions corresponding to the remaining smaller vascular branches extending into the tumor domain from Figure 5.29d are well oxygenated. This leads to the emergence of the previously mentioned necrotic zones further away from these blood vessels. After 240 hours, only the thicker branches remain intact with the corresponding oxygen distribution around these branches.

Qualitatively, the results for tumor growth and the remaining vasculature in the domain are again in good agreement with tumor growth patterns and vascular structures observed *in-vivo* [64, 65, 108, 109]: There exists a large necrotic area in which only a few larger internal vessels remain. Around these vessels, cuffs of viable tumor cells form whereas the rest of the domain becomes necrotic. Exactly this behaviour is reproduced by the model. By contrast, the tumor's outer rim is still well-vascularized with smaller vessels. Also this pattern is present in vascular tumors [109]. However, angiogenesis, which was excluded here, is a major factor for this phenomenon leading to neo-vascularization with very high vascular densities at the tumor periphery. Robust angiogenesis is necessary for further tumor growth after the initial host vessel co-option and regression phase [291]. Here, the better vascularization at the tumor boundary is solely due to the pre-existing vascular network which is slowly compressed during growth. A further challenge for the model and a promising extension would be how to include these effects. Basically, two different approaches seem possible: First, one could also include the influence of angiogenesis into the model variant with discrete representation of the vasculature similar to the discrete variant of Anderson [6] and other tumor growth models [83, 158, 185, 287–289, 298]. Second, one could employ the hybrid model to trigger angiogenesis from the grown state with the remaining vessels after 360 hours as will be illustrated in Section 5.6.

Finally, only the simple empirical relationships (3.101)-(3.103) for blood vessel compression, collapse and regression have been employed in a first step. As demonstrated, already this simple approach allows to simulate blood vessel compression, pruning and regression. As stated in Remark 3.13, the much more complex real-life behaviour of vascular remodeling [204–206] and the transformation of the pre-existing vasculature into a tumor-specific vasculature [216, 217, 276–279, 287] can theoretically be incorporated in the current framework. Despite these shortcomings, the principal applicability of the extension for blood vessel compression, regression and

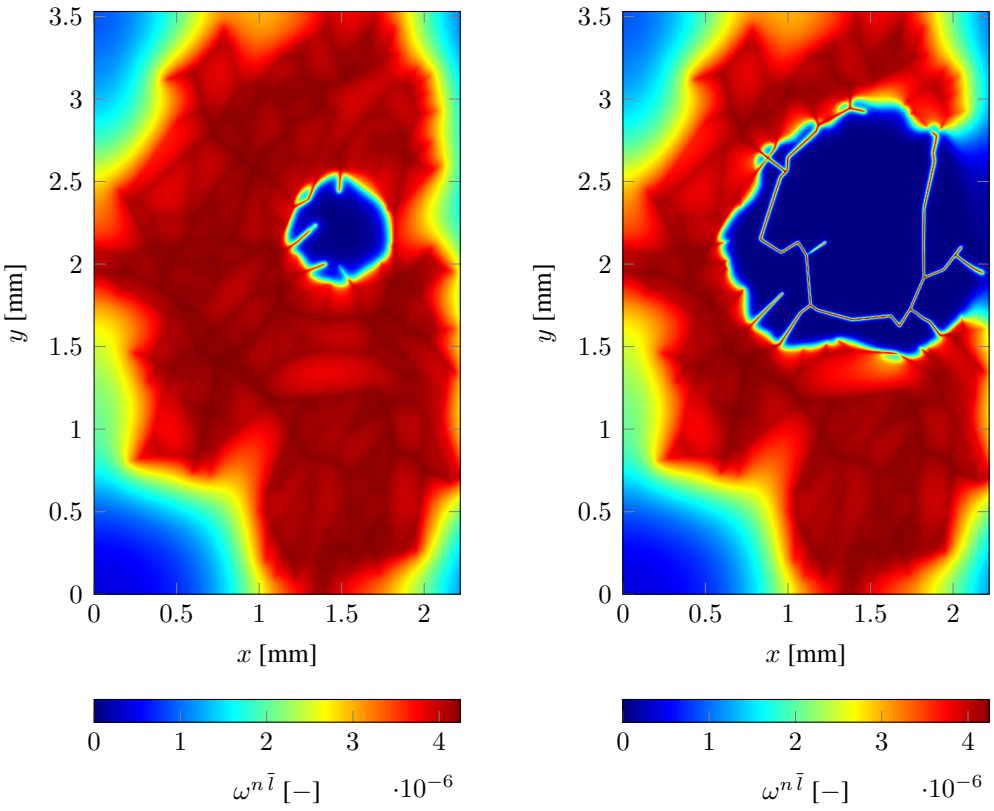

(a) $t = 60\,\mathrm{h}$ (b) $t = 240\,\mathrm{h}$

Figure 5.31: Oxygen distribution in IF

collapse has been proven. The open issues summarized above remain to be addressed and might constitute a promising future research direction in combination with a strict validation of the vascular variant of the model.

5.6 Two-dimensional Growth of a Tumor close to a Pre-existing Blood Vessel

This section and the associated numerical example was previously published in the author's article [136]. The variant with hybrid embedded/homogenized vasculature is employed to study the growth of an initially avascular tumor which is located close to a pre-existing blood vessel. By means of this case the coupling between the discrete embedded vasculature and the homogenized vasculature is exemplified. The centerline coupling variant is used for evaluating the 1D-3D coupled terms (or rather 1D-2D coupled as a 2D example is studied). As in Section 5.2, the HV may be understood as the neovasculature formed through angiogenesis originating from a pre-existing blood vessel. The 1D resolved part of the vascular network corresponds to the pre-existing blood vessels from which angiogenesis can occur. The two-dimensional domain with the embedded simple blood vessel network is depicted in Figure 5.32 where also initial and boundary

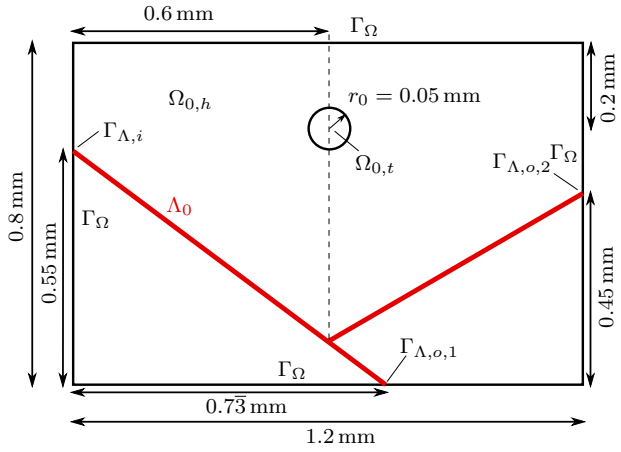

Initial conditions	
$\Omega_{0,t}$	$S_t = 0.5, S_h = 0, S_l = 0.5$
	$(p_{hl} = 590\,\text{Pa}, p_{th} = 295\,\text{Pa}, p_l = 0\,\text{Pa})$
	$\varepsilon^v = 0, \varepsilon_0 = 0.8, \omega^{n\,\bar{l}} = 1.0 \cdot 10^{-6},$
	$\omega^{N\,\bar{t}} = \omega^{TAF\,\bar{l}} = \omega^{n\,\bar{v}} = 0$
$\Omega_{0,h}$	$S_t = 0, S_h = 0.2, S_l = 0.8$
	$(p_{hl} = 191.7\,\text{Pa}, p_{th} = p_l = 0\,\text{Pa})$
	$\varepsilon^v = 0, \varepsilon_0 = 0.8, \omega^{n\,\bar{l}} = 1.0 \cdot 10^{-6},$
	$\omega^{N\,\bar{t}} = \omega^{TAF\,\bar{l}} = \omega^{n\,\bar{v}} = 0$
Λ_0	$S_t = 0, S_h = 0.2, S_l = 0.8$
	$(p_{hl} = 191.7\,\text{Pa}, p_{th} = p_l = 0\,\text{Pa})$
	$\varepsilon^v = 0.1, \varepsilon_0 = 0.7, \omega^{n\,\bar{l}} = 3.0 \cdot 10^{-6},$
	$\omega^{N\,\bar{t}} = \omega^{TAF\,\bar{l}} = 0, p^{\hat{v}} = p^v = 3000\,\text{Pa}$
	$\omega^{n\,\hat{v}} = \omega^{n\,\bar{v}} = 2.88 \cdot 10^{-4}$ $(P^{\hat{v}}_{\text{oxy}} \approx 100\,\text{mmHg})$

Boundary conditions	
Γ_Ω	$\mathbf{d}_s = \mathbf{0}, S_t = 0, S_h = 0.2, S_l = 0.8$
	$(p_{hl} = 191.7\,\text{Pa}, p_{th} = p_l = 0\,\text{Pa})$
	$\omega^{N\,\bar{t}} = \omega^{TAF\,\bar{l}} = 0$
$\Gamma_{\Lambda,i}$	$p^{\hat{v}} = 3000\,\text{Pa}, \omega^{n\,\hat{v}} = 2.88 \cdot 10^{-4}$
$\Gamma_{\Lambda,o,1}$	$p^{\hat{v}} = 2600\,\text{Pa}$
$\Gamma_{\Lambda,o,2}$	$p^{\hat{v}} = 2400\,\text{Pa}$
Λ_0	$\varepsilon^v = 0.1$

Figure 5.32: Geometry, initial and boundary conditions for tumor growing close to a pre-existing blood vessel (red). Figure taken from the author's article [136].

conditions are listed. This setup may either correspond to a vessel-ingrowth scenario where the whole tumor vasculature grows from outside into the tumor [216] or a case where blood vessels have regressed after initial tumor growth with only the depicted larger vessels remaining. While this situation with a distance of the initial tumor spheroid of $0.4\,\text{mm}$ to the nearest blood vessel might be considered non-physiological, the numerical example which has been designed similar to corresponding discrete models [6, 158, 289] enables the methodological investigation of the proposed hybrid embedded/homogenized approach described in Section 3.5.

A schematic overview of the hybrid vascular variant and the respective mass transfer relations is given in Figure 5.33. Now, the vasculature is split into large vessels, represented as 1D inclusions, and small vessels, which for this case correspond to the homogenized neovasculature. Leakage of fluid occurs from both representations of the vascular network, either via the 1D-3D mass transfer term (B.16) respectively (B.18) or the previously employed leakage from HV into IF, i.e., equation (B.2). The mass transfer terms for tumor growth with three fluid phases (TCs, HCs, IF) and one solid phase (ECM) are the same as before. In addition, three species are present, namely, oxygen (in the IF, the pre-existing and the homogenized vasculature), TAFs in the IF and NTCs as a part of TCs. Oxygen is transported in both representations of the vasculature and transvascular exchange into the IF occurs either between HV and IF via (B.11) or via the 1D-3D exchange term (B.20) respectively (B.23). The consumption of oxygen by LTCs and HCs, the production of TAFs by hypoxic LTCs and the necrosis term are equivalent to the previous examples.

At the beginning of the simulation, the tumor covers a circular area with radius $0.05\,\text{mm}$ as sketched in Figure 5.32. The outline of the 2D domain is fixed but the tissue inside is assumed to be deformable. At the inflow on the left end of the 1D inclusion a Dirichlet boundary condition for the pressure in the 1D embedded vasculature $p^{\hat{v}}$ and the oxygen mass fraction $\omega^{n\,\hat{v}}$ therein is set. At the two outflows of the vessel domain the pressure is also fixed. Angiogenesis occurs

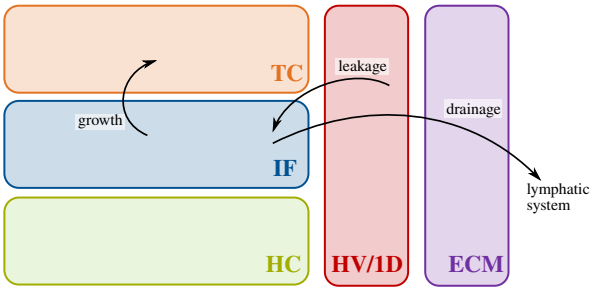

Phase	Mass transfer terms
ECM	0
HC	0
TC	$\overset{l\to t}{M}_{\text{growth}}$
IF	$\delta_{\Lambda_t} \cdot \overset{\hat{v}\to l}{M}_{\text{leak}} + \overset{v\to l}{M}_{\text{leak}} - \overset{l\to ly}{M}_{\text{drain}} - \overset{l\to t}{M}_{\text{growth}}$
HV	$-\overset{v\to l}{M}_{\text{leak}}$
1D	$-\overset{\hat{v}\to l}{M}_{\text{leak}}$

(a) Phases with respective mass transfer relations

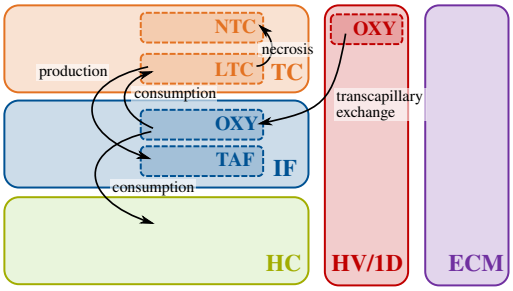

Species	Mass transfer terms
NTC	$\varepsilon^t r^{Nt} - \omega^{N\,\bar{t}} \overset{l\to t}{M}_{\text{growth}}$
OXY/IF	$-\overset{nl\to t}{M}_{\text{cons}} - \overset{nl\to h}{M}_{\text{cons}} + \delta_{\Lambda_t} \cdot \overset{n\hat{v}\to nl}{M}_{\text{tv}} + \overset{nv\to nl}{M}_{\text{tv}} - \omega^{n\,\bar{l}} \left(- \overset{l\to t}{M}_{\text{growth}} \right)$
OXY/HV	$-\overset{nv\to nl}{M}_{\text{tv}}$
TAF	$\overset{TAFt\to TAFl}{M}_{\text{prod}}$
OXY/1D	$-\overset{n\hat{v}\to nl}{M}_{\text{tv}}$

(b) Species with respective mass transfer relations

Figure 5.33: Schematic overview of vascular model with hybrid representation of the vasculature and mass transfer relations

from the pre-existing blood vessel network which has a constant radius of $R = 0.015\,\text{mm}$. For that, a boundary condition of $\varepsilon^v = 0.1$ is assumed along the 1D network. To trigger angiogenesis from the location of the pre-existing blood vessel, this value is applied on all 2D elements which are "cut" by the blood vessels. Along the 1D inclusion, the pressure in the HV p^v as well as the oxygen mass fraction in the HV $\omega^{n\,\overline{v}}$ are coupled with the values in the 1D domain $p^{\hat{v}}$ respectively $\omega^{n\,\hat{v}}$ with the mortar penalty approach developed in Section 4.3.3.2. At this line, from which the neovasculature originates, the constraint of equal blood pressures and oxygen mass fractions in the two representations of the vascular network is enforced with penalty parameters of $\epsilon_{\text{MP}} = 1 \times 10^{-10}\,\text{m}^2\,\text{Pa}^{-1}\,\text{s}^{-1}$ for the coupling of pressures and $\epsilon_{\text{MP}} = 1 \times 10^{-5}\,\text{m}^2\,\text{s}^{-1}$ for the coupling of species.

The employed model parameters are once more given in Tables C.1-C.7. In addition, the parameters for the 1D resolved part of the vasculature may be found in Table C.10. Blood vessel compression and regression (both for homogenized and embedded vasculature) are not considered and the Neo-Hookean material law is employed for the ECM.

Both domains are discretized in space completely independent from each other. The two-dimensional domain is meshed with a regular grid of 210×140 bilinear elements. The 1D vasculature is represented by 805 linear elements. The growth of the tumor is studied over 24 days. For time integration, the one-step-θ scheme with $\theta = 0.5$ and a time step size of $\Delta t = 900\,\text{s}$ is applied.

The example of this section is designed to imitate the classical model of the angiogenic switch [19]. If angiogenesis did not occur from the pre-existing blood vessel, the initial tumor of this example would not grow any further since a steady state of proliferation and TC death due to the hypoxic conditions would be reached. By contrast, in the case studied here the

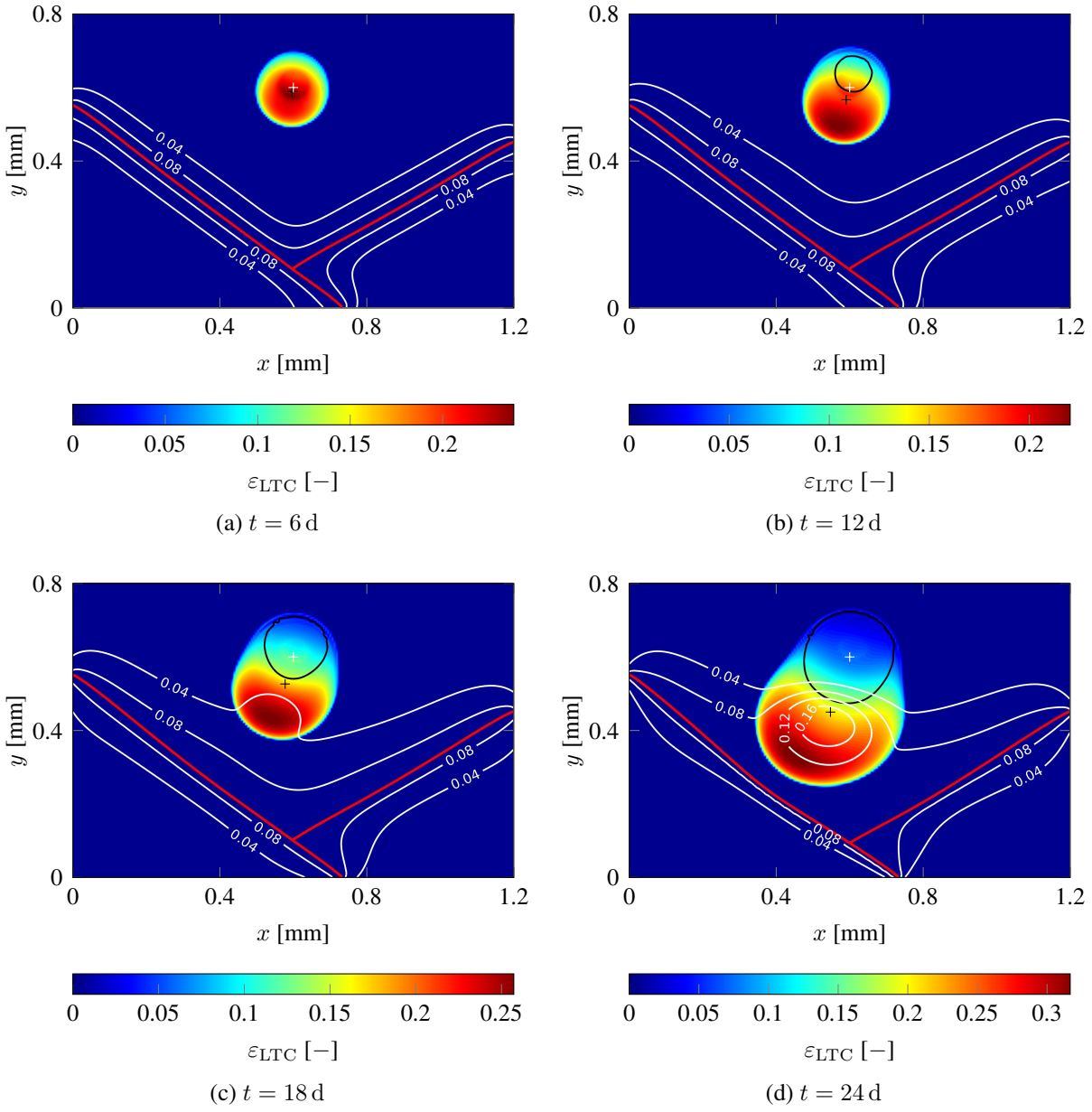

(a) $t = 6\,\mathrm{d}$ (b) $t = 12\,\mathrm{d}$

(c) $t = 18\,\mathrm{d}$ (d) $t = 24\,\mathrm{d}$

Figure 5.34: Evolution of living tumor cells (in colour), neovasculature (white contour lines) and necrotic region (inside black contour line with value $\varepsilon_{\mathrm{NTC}} = \varepsilon S^t \omega^{N\,\bar{t}} = 0.05$), tumor's initial center of mass is denoted by white cross, current center of mass by black cross. Figure taken from the author's article [136].

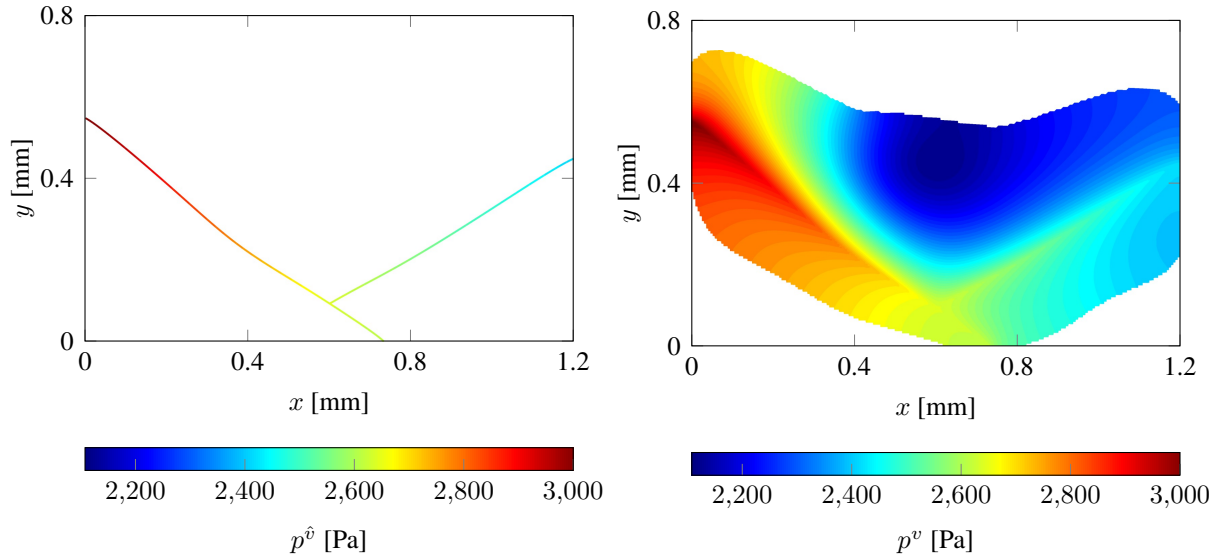

Figure 5.35: Pressure in pre-existing (left) and neovasculature (right) after 24 days. Figure taken from the author's article [136].

onset of angiogenesis enables rapid tumor growth. The evolution of the LTC volume fraction $\varepsilon_{\mathrm{LTC}} = \varepsilon S^t \left(1 - \omega^{N\bar{t}}\right)$ is shown in Figure 5.34 as well as the neovasculature volume fraction ε^v which is visualized with white contour lines. The pre-existing blood vessels are plotted in red. The behaviour is similar to the case studied in Section 5.2. After six to twelve days a slightly unsymmetrical growth towards the pre-existing blood vessels can be observed. Oxygen is provided by the pre-existing network and diffuses in the IF which is why the tumor grows towards the blood vessel with higher nutrient availability. A necrotic region develops in the part of the tumor further away from the vessels. Its outline is shown in Figure 5.34 by the black contour line. Concurrently, the hypoxic TCs constantly produce TAFs which triggers endothelial cell migration towards the tumor from the pre-existing vasculature where the boundary condition on the neovasculature volume fraction is set. A small vascular volume fraction is also present below the pre-existing blood vessel due to the diffusive term in the formulation for angiogenesis (3.51). After 18 days both angiogenesis and tumor growth have continued such that the neovasculature has reached the region with a high proliferation of TCs. A characteristic bulge of the vascular volume fraction towards the tumor starts to develop since the TAF concentration is highest there. Hence, the time period over which angiogenesis occurs is again in good agreement with literature data [36]. The higher availability of oxygen enables rapid tumor progression in the interval between 18 and 24 days. After 24 days the tumor has grown in a similar half-moon shape as observed in Section 5.2 towards the pre-existing blood vessels. This is further visualized by the motion of its center of mass. In the period from 18 to 24 days it moves with an average velocity of $0.013\,\mathrm{mm/d}$ in direction of the vessel. At the same time the increased TC and IF pressure in the LTC region leads to a deformation of the ECM. Under the assumption that the blood vessel network completely follows the movement of the underlying ECM, this induces also a slight deformation of the initially straight blood vessels which are, in this case, slightly pushed away from the tumor.

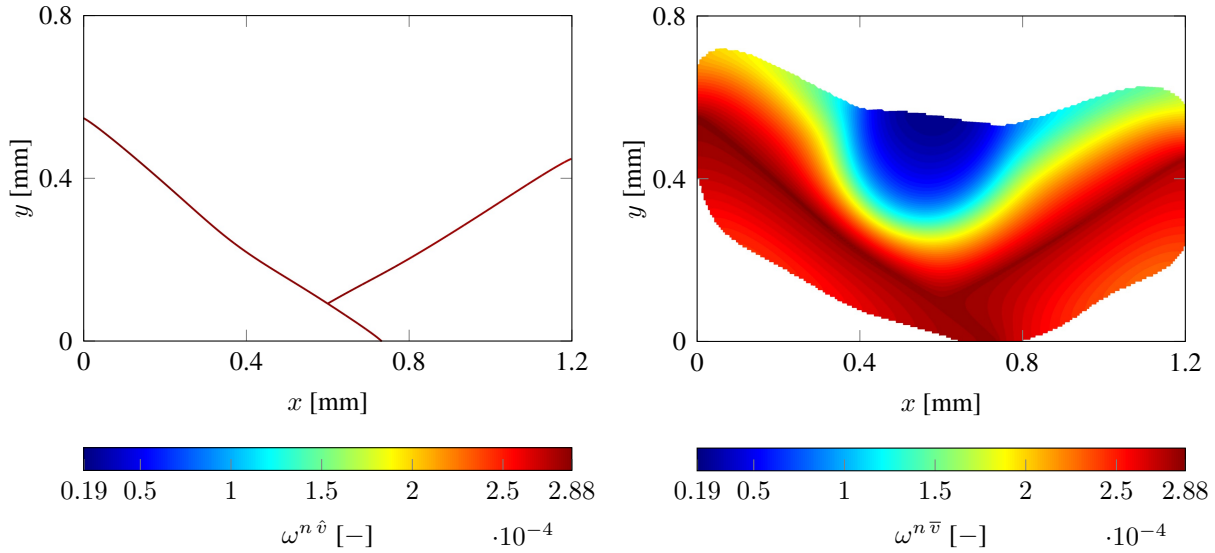

Figure 5.36: Mass fraction of oxygen in pre-existing (left) and neovasculature (right) after 24 days. Figure taken from the author's article [136].

To elucidate the coupling between 1D embedded and homogenized vasculature, pressures in the pre-existing vasculature $p^{\hat{v}}$ and in the neovasculature p^{v} after 24 days are depicted in Figure 5.35. Clearly, the constraint of equal pressures on the embedded domain Λ_t^{h} is fulfilled such that flow in pre-existing and neovasculature are coupled. As stated in Remark 4.2 the balance of mass of blood in the neovasculature (3.47) is only valid in the area the neovasculature has already reached, which explains the shape of the pressure distribution p^{v} in Figure 5.35 including the area below the blood vessel. Only those elements where the aforementioned equation can actually be solved are depicted. In the rest of the domain the equation is not evaluated which is equivalent to a no-flux boundary condition at the edge of the neovasculature. A considerable pressure drop from the pre-existing vasculature towards the edge of the neovasculature can be observed, which is due to the large leakage of fluid from the abnormal neovasculature into the IF.

Also species transport of oxygen in the 1D embedded and the homogenized vasculature are coupled via the MP approach. The corresponding distributions are shown in Figure 5.36. Again, species transport of oxygen in the neovasculature can only be solved in the portion of the domain where it is present greater than a threshold value of, in this case, $\varepsilon^{v}_{\text{thresh}} = 0.01$. As for blood pressure, this results in a no-flux boundary condition across the edge of the neovasculature in the species transport equation (3.63). The proposed approach works well in capturing the shape of the neovasculature domain in this case but for different scenarios the threshold value could be defined as a certain percentage of the degree of vascularization over the whole domain. Transcapillary exchange of oxygen from the pre-existing and the neovasculature into the IF cause the depicted oxygen distributions. In the tumor area a lot of oxygen is required due to the vast oxygen consumption by proliferating TCs. At the beginning of tumor progression oxygen is provided from the pre-existing vasculature into the IF through transcapillary exchange. Diffusion in the IF is necessary to reach the tumor. During angiogenesis the developing neovasculature enables a more efficient transport of oxygen. Oxygen can now also be transported from the

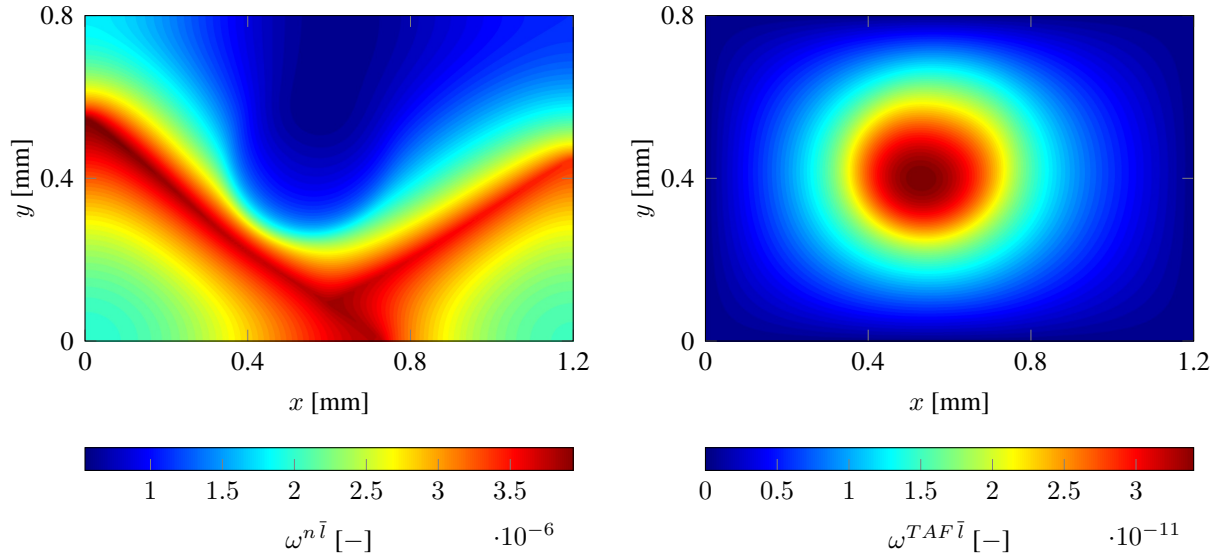

Figure 5.37: Mass fraction of oxygen in IF (left) and TAF in IF (right) after 24 days. Figure taken from the author's article [136].

pre-existing into the neovasculature due to the coupling of species transport and then from the neovasculature into the IF much closer to the site of the tumor. This behaviour is augmented by the pressure drop in the HV, which develops due to the large leakage of fluid, such that oxygen is advected from the inflow through the vasculature. Still, the high oxygen demand leads to very low oxygen mass fractions in both the HV and the IF, see also Figure 5.37 (left). Also in the IF most of the oxygen is present close to the pre-existing vasculature while a hypoxic region emerges inside the tumor. In the right part of Figure 5.37 the TAF mass fraction in the IF which is produced during hypoxia by LTCs and triggers angiogenesis is additionally shown.

The goal of this numerical example is to demonstrate that the treatment of angiogenesis with a homogenized representation of the neovasculature and a discrete representation of the pre-existing vasculature is able to produce biologically and physically reasonable results. The information about the structure of the pre-existing vasculature can be preserved while not every single capillary segment of the neovasculature has to be resolved as in most other vascular tumor growth models. At least qualitatively the results are in good agreement with ingrowth simulations using discrete vasculature models [158, 289]. It becomes evident how angiogenesis completely shifts the supply of the tumor with nutrients from diffusion in the IF to the more efficient transport in the (neo-)vasculature. One drawback of the model is the difficulty to initiate sprouts from the pre-existing vasculature. For now, a Dirichlet boundary condition has been set on the pre-existing vasculature to trigger angiogenesis.

Compared to the experimental results shown for brain tissue by Seano et al. [236], the deformation of the pre-existing vasculature during tumor growth is actually quite small due to the chosen material parameters and boundary conditions. Hence, it might be justified to neglect the deformability of blood vessels in this case and simply evaluate the respective terms in reference configuration. Especially the solid velocity term in (3.79) is insignificant since time scales during tumor growth are quite large. In Appendix A.3 a further example is presented which illustrates

the capabilities of the framework to include also larger deformations of the embedded vascular network.

Pre-existing and neovasculature are of comparable scale in this example. Hence, the motivation for representing one as a 1D inclusion and the other in a homogenized way is not scale separation but rather the previously described abnormal structure/morphology and function of tumor neovasculature. Due to these complexities and the associated heterogeneity, the homogenized approach for modeling the neovasculature with a blood vessel density rather than single blood vessel segments is more suitable than a resolved approach. Naturally, quantities of interest such as microvascular density or average blood flow and species transport are available. Another possible application of the hybrid formulation apart from angiogenesis is the modeling of larger tissue domains at the scale of a whole tumors or even organs. Here, it is also possible to model only the larger vessels patient-specifically as 1D inclusions and treat the smaller blood vessels, i.e., the capillary bed in a homogenized sense with a hybrid model [128, 242, 266]. This approach is followed in Chapter 6 to validate the hybrid approach for modeling perfusion through entire solid tumors.

6 Validation and Parameter Optimization of the Hybrid Embedded/Homogenized Representation of the Vasculature with a Study of Solid Tumor Perfusion

This chapter is concerned with investigating the validity of the previously developed hybrid embedded/homogenized representation of the vasculature. Here, this idea is transferred for modeling perfusion through solid tumors where hybrid models relying only on non-invasively available imaging data can have a major impact for understanding the involved transport mechanisms and for designing novel therapies. Hence, the employed model is only a part of the entire tumor growth framework presented in the preceding chapters. The approach is validated and its parameters are inversely identified by comparing its results to a corresponding fully-resolved model with discrete representation of the vascular network based on several suitable metrics. A complex data set of three different tumor types with heterogeneous vascular architectures serves as a basis to perform these numerical tests. The content of this chapter was previously published in the author's article [137].

The subsequent sections are structured as follows: First, a short introduction of the main goals of this investigation is given in Section 6.1. Then, both model types are introduced in Section 6.2. The employed tumor vasculature data sets as well as the setup of the models including the assignment of boundary conditions and the extraction of the hybrid model from the fully-resolved one are described in Section 6.3. Numerical experiments to compare the accuracy of the hybrid model w.r.t. the full model and to evaluate its main errors are conducted in Section 6.4. Several possible improvements of the hybrid model are illustrated in Section 6.5 before the findings are summarized in Section 6.6.

6.1 Introduction

A validation with experimental data or even a transfer to clinical practice is extremely complex for the sophisticated tumor growth models developed in the previous chapters due to the lack of well-suited experimental data and the involved uncertainties with the thousands of parameters influencing tumor growth *in-vivo*. While a comprehensive cancer simulation tool is still desirable, a high benefit can also be expected from less complex models. For instance, to evaluate the

transport phenotype of a grown tumor in a specific patient and to optimize drug delivery based on this phenotype, it is not necessary to first replicate cancer progression with a suitable tumor growth framework. A mathematical model of blood flow and mass transport through the tumor domain suffices to answer highly relevant biomedical questions such as the transport of nutrients, oxygen or drugs across the vascular system and inside the tissue micro-environment. These methods can ultimately lead to a new rationale for developing and non-invasive testing of novel therapies [60]. Overcoming the barriers currently encountered by drug delivery systems requires an integration of such *in-silico* models with corresponding experiments to aid in cheaper, faster and more targeted drug design [74, 183].

Therefore, this chapter is concerned with the simulation of blood flow and tissue perfusion through solid tumors. This includes, first, the vasculature, which is embedded in the encompassing tissue, second, passage across the blood vessel walls into the surrounding extravascular space and, third, flow of the fluid filling this space, namely the interstitial fluid (IF). For that, the distinct modeling strategies introduced in Chapter 3 for these transport processes, namely with continuum, discrete or hybrid description of the vasculature are applicable. These approaches have been extracted from the entire tumor growth framework to build a computational model for solid tumor perfusion.

As already discussed in Chapter 3, the distinct representations of the blood vessels have different use cases: Discrete models can and should be applied when the entire structure of the vasculature including the smallest scales, i.e., the capillaries, is known and its resolution is needed for the question at hand. This is usually restricted to small domain sizes of an order of several mm^3. By contrast, continuum models are used to simulate mass transport at larger scales, e.g., through whole organs. Both approaches have advantages and disadvantages: On the one hand, the computational cost of continuum models is usually smaller than for discrete ones which makes the application to larger domains possible in the first place. On the other hand, the information about the exact morphology of the vascular network is lost such that blood flow can only be described in an averaged sense. Discrete models, however, are computationally more expensive. Furthermore, they require the full structure of the part of the vasculature under consideration. This is usually realized via a graph whose edges are assigned the radius of the blood vessel segments between nodes. Such high-resolution data including blood vessel radii, connectivity and positions can at present only be acquired through *ex-vivo* imaging [242]. In addition, the acquisition of high-quality data is still challenging and error-prone especially on the finest scales [131]. By contrast, *in-vivo* imaging is currently only possible for larger vessels and flow therein [150, 242]. Therefore, discrete models rely on data which is not available via non-invasive imaging. An additional difficulty is the assignment of blood pressure or flow boundary conditions which can only be estimated for large networks [85, 252]. In any case, validation of these models is usually only performed on macroscopic quantities such as tissue perfusion [59] since measuring flow or pressures inside single micro-vessels is not possible [252].

By contrast, the developed hybrid approach is especially suited for cases where the full vascular morphology is unknown or too large to be modeled with a discrete approach. As in other hybrid approaches [128, 130, 242], this is achieved by resolving only the larger vessels through a discrete model while the smaller ones are homogenized. This enables a better representation of the heterogeneity of blood flow and pressure in the major vessel branches which is lost in purely homogenized approaches. Moreover, compared to discrete models the morphology of the smallest vessels which is not available via non-invasive *in-vivo* imaging is not required. Nevertheless,

validation is equally possible with quantities such as tissue perfusion, blood flow or pressures at the resolution of current imaging techniques. A related approach, where no homogenization of the capillaries is needed, is to generate a discrete surrogate network of the smaller scales based on the oxygen demand of the tissue [131].

This chapter focuses on the validation of the hybrid embedded/homogenized scheme with three complex tumor-specific vascular networks based on large tissue samples containing more than $100\,000$ blood vessels [59, 252]. A special emphasis is put on the extraction of the larger vessels from the fully-resolved network data such that it qualitatively matches the topology and distribution of larger vascular structures inside tumors available via *in-vivo* imaging. Thus, it is assured that the hybrid approach is investigated for cases which closely resemble real-life scenarios where the structure of the considered part of the microcirculation is not entirely known. Here, the entire topology of the vasculature in the given tissue domain is known which allows to generate reference solutions with a fully-resolved model and to quantify the error introduced by the homogenization in the hybrid model. This error is evaluated by means of several well-defined metrics involving the agreement of pressures and flow between the two models. Concurrently, the parameters of the hybrid model are identified such that the correspondence of the models is maximized. Evaluating the model discrepancy of the hybrid model in comparison to a fully-resolved one is a first and indispensable step towards realistic hybrid models of tumor perfusion relying only on non-invasively available physiological data. For a full validation and parameter optimization, similar methods as applied herein need to be combined with advanced *in-vivo* imaging techniques. The comparison of two purely numerical approaches enables investigating the hybrid model in a controlled environment unaffected by any further influences such as uncertainties in experimental or clinical data.

6.2 Employed Model Types and Numerical Methods

In this section, the employed model types to solve the interaction between microcirculation and interstitial tissue perfusion including their main simplifications are described. The fully-resolved and the hybrid approach and their discretization by means of the FEM are introduced. The centerline variant for 1D-3D coupling is employed since the diameter of the 1D embedded blood vessels is sufficiently larger than the element size in the 3D domain in all considered cases, see also Table 6.1.

6.2.1 Problem Setting

As before, topology and structure of the microcirculation is described by a graph with straight edges, i.e., blood vessel segments. The segments connect the nodes of the network. A radius R_k is assigned to each segment Λ_k. Available experimental data including the one employed here is also commonly provided in this format. This 1D embedded blood vessel network is again denoted with Λ. Note that a distinction between reference and current domains as introduced in the previous chapters is not necessary here as only perfusion through the system is considered and no deformation. Similar to Vidotto et al. [266], the vascular domain is further divided into two subsets Λ_{L} and Λ_{S} which correspond to the larger and smaller vessels in the network such

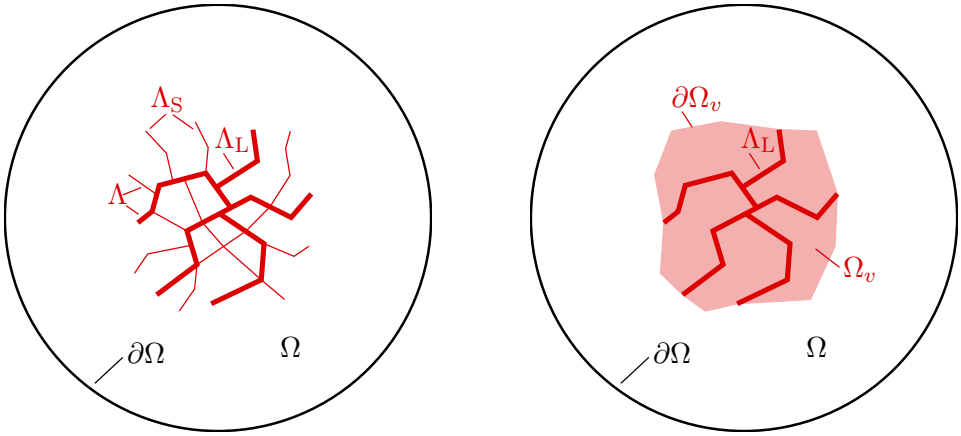

(a) Fully-resolved (b) Hybrid

Figure 6.1: Notation for domains and boundaries. Figure taken from the author's article [137].

that

$$\Lambda_{\mathrm{L}} := \bigcup_{k \in I_{\mathrm{L}}} \Lambda_k, \quad \Lambda_{\mathrm{S}} := \bigcup_{k \in I_{\mathrm{S}}} \Lambda_k \quad \text{and} \quad \Lambda = \Lambda_{\mathrm{L}} \cup \Lambda_{\mathrm{S}} \tag{6.1}$$

with the index sets of large and small blood vessel segments I_{L} and I_{S}, respectively. This partition will be detailed in Section 6.3.3. Whereas the larger vessels are kept in the hybrid model, the smaller scale vessels are replaced by an appropriate homogenized representation as a porous network occupying the domain $\Omega_v \subset \Omega$, conf. Figure 6.1b.

6.2.2 Fully-resolved 1D-3D Model

Based on the same assumptions as introduced in Section 3.4.1, blood flow in the 1D vasculature domain is given by

$$-\frac{\partial}{\partial s}\left(\frac{\pi R^4}{8\mu^{\hat{v}}}\frac{\partial p^{\hat{v}}}{\partial s}\right) = -\frac{\overset{\hat{v}\to l}{M}_{\mathrm{leak}}}{\rho^{\hat{v}}} \qquad \text{on } \Lambda, \tag{6.2}$$

with the Hagen-Poiseuille law, constant blood density $\rho^{\hat{v}}$, blood vessel radius R, the pressure inside the vasculature $p^{\hat{v}}$ and blood viscosity $\mu^{\hat{v}}$. Again, s is the arc length coordinate along the 1D blood vessel segment. Throughout this chapter, the algebraic relationship for the non-Newtonian behaviour of blood developed by Pries and Secomb [201] is applied. As in [252], hematocrit is fixed to 0.45, thus, the blood viscosity $\mu^{\hat{v}}$ in each individual blood vessel segment depends only on its diameter. Finally, the right-hand-side term

$$\overset{\hat{v}\to l}{M}_{\mathrm{leak}} = \rho^l \cdot 2\pi R \cdot L_{p,\hat{v}} \cdot \left(p^{\hat{v}} - p^l - \sigma\left(\pi^b - \pi^l\right)\right) \tag{6.3}$$

is employed to model leakage of fluid across the blood vessel wall into the interstitium. This term is equivalent to (B.16), that is, the centerline variant for 1D-3D coupling with Starling's law accounting for transvascular flux with hydraulic conductance $L_{p,\hat{v}}$, density of blood plasma ρ^l, oncotic reflection coefficient σ and the oncotic pressures of blood π^b and the interstitial fluid (IF) π^l. In summary, the mass transfer from the vascular network into the IF is proportional to the

pressure difference between vasculature and IF whose pressure in (6.3) is denoted as p^l. Note that the investigated data sets are whole-tumor blood vessel networks where also larger vessels are leaky [59, 252] which is why the transvascular exchange term (6.3) is applied also on the subset of larger vessels Λ_{L}. As explained before, the associated increased interstitial fluid pressure may lead to resistance to efficient drug delivery [13, 103, 114].

The tissue domain Ω is again modeled as a porous medium. However, in contrast to the entire tumor growth model, now only a single fluid phase, namely the IF, is considered to account for flow through the pores of the ECM in the 3D tissue domain. Fluid flow therein is governed by the following Darcy equation

$$-\boldsymbol{\nabla} \cdot \left(\frac{\boldsymbol{k}^l}{\mu^l} \boldsymbol{\nabla} p^l \right) = \delta_\Lambda \cdot \frac{\overset{\hat{v} \to l}{M}_{\text{leak}}}{\rho^l} \qquad \text{in } \Omega \tag{6.4}$$

with (isotropic) permeability $\boldsymbol{k}^l = k^l \cdot \boldsymbol{I}$ and IF viscosity μ^l. Hence, the primary variable for fluid flow through the tissue is the IF pressure p^l. The right hand side represents outflow from the embedded vessels into the IF scaled with the Dirac term along the centerline of the inclusion. The weak form of the employed 1D-3D coupled problem may then be written as

$$\left(\frac{\partial \delta p^{\hat{v}}}{\partial s}, \frac{\pi R^4}{8 \mu^{\hat{v}}} \frac{\partial p^{\hat{v}}}{\partial s} \right)_\Lambda + \left(\delta p^{\hat{v}}, \frac{\overset{\hat{v} \to l}{M}_{\text{leak}}}{\rho^{\hat{v}}} \right)_\Lambda = 0 \tag{6.5a}$$

$$\left(\boldsymbol{\nabla} \delta p^l, \frac{\boldsymbol{k}^l}{\mu^l} \boldsymbol{\nabla} p^l \right)_\Omega - \left(\delta p^l, \frac{\overset{\hat{v} \to l}{M}_{\text{leak}}}{\rho^l} \right)_\Lambda = 0 \tag{6.5b}$$

with test functions $\delta p^{\hat{v}}$ defined on the 1D domain and δp^l defined on the 3D domain. The integration of the mass transfer terms along the centerline is once more performed with the segment-based approach as detailed in Section 4.3.3.1. After space discretization, the nodal primary variables of both domains are

$$\mathbf{p}^{\hat{v}} \in \mathbb{R}^{n_{\text{nodes},\Lambda}} \quad \text{and} \quad \mathbf{p}^l \in \mathbb{R}^{n_{\text{nodes},\Omega}}, \tag{6.6}$$

that is, the nodal blood pressure in the discretized 1D domain and the nodal IF pressure in the discretized 3D domain, which consist of $n_{\text{nodes},\Lambda}$ and $n_{\text{nodes},\Omega}$, respectively. Details on the employed boundary conditions are given in Section 6.3.2.1.

Finally, a global system of linear equations arises, which may be written as a 2×2 block matrix

$$\begin{bmatrix} \mathbf{K}^{\hat{v}\hat{v}} & \mathbf{G}^{\hat{v}l} \\ \mathbf{H}^{l\hat{v}} & \mathbf{K}^{ll} \end{bmatrix} \begin{bmatrix} \mathbf{p}^{\hat{v}} \\ \mathbf{p}^l \end{bmatrix} = \begin{bmatrix} \mathbf{F}^{\hat{v}} \\ \mathbf{F}^l \end{bmatrix}. \tag{6.7}$$

Herein, the main diagonal blocks $\mathbf{K}^{ii}$ comprise contributions from the diffusive term and the exchange term in (6.5a) and (6.5b) while the off-diagonal submatrices $\mathbf{G}^{\hat{v}l}$ and $\mathbf{H}^{l\hat{v}}$ contain the "mixed" contributions from the exchange term. The right hand side terms $\mathbf{F}^i$ represent the constant contribution to the exchange term stemming from the oncotic pressures in (6.3). To solve the coupled linear system (6.7) the AMG(BGS) block preconditioner presented of Verdugo and Wall [263] with a GMRES iterative solver is once more employed.

6.2.3 Hybrid 1D-3D Model

The main idea behind the proposed hybrid 1D-3D model is the same as in the context of the tumor growth model with hybrid representation of the vasculature: The full resolution of the larger vessels Λ_L is kept, i.e., these are still modeled as a 1D embedded vasculature. Consequently, the hierarchy, topology and vascular properties such as individual blood vessel radii and viscosities of each segment are retained, see also Figure 6.1b. The smaller vessels Λ_S, for which this high-resolution data might either not be available through non-invasive imaging techniques or susceptible to errors, are instead represented as an additional porous network. This results in a double-porosity formulation where the first porous network is, as before, the interstitial space and the second one the smaller vessels occupying the domain Ω_v. In the following, the governing equations and the spatial discretization of this formulation is presented.

As stated above, the model for the larger vessels does not change. Therefore, the mass balance equation inside the large vessels is given by

$$-\frac{\partial}{\partial s}\left(\frac{\pi R^4}{8\mu^{\hat{v}}}\frac{\partial p^{\hat{v}}}{\partial s}\right) = -\frac{\overset{\hat{v}\to l}{M}_\mathrm{leak}}{\rho^{\hat{v}}} \qquad \text{on } \Lambda_\mathrm{L} \tag{6.8}$$

with the only difference to (6.2) being that it holds only on the subset $\Lambda_\mathrm{L} \subset \Lambda$ of bigger vessels. The mass balance equation for the smaller vessels Λ_S is replaced by a homogenized Darcy equation in the vascular domain Ω_v formulated as

$$-\boldsymbol{\nabla}\cdot\left(\frac{\boldsymbol{k}^v}{\mu^v}\boldsymbol{\nabla}p^v\right) = -\frac{\overset{v\to l}{M}_\mathrm{leak}}{\rho^v} \qquad \text{in } \Omega_v. \tag{6.9}$$

The unknown in this equation is the blood pressure p^v in the homogenized part of the vasculature which is now defined in the entire 3D domain Ω_v, thereby replacing the blood pressure of the smaller vessels in the 1D domain Λ_S as the variable governing flow inside the smaller vessels. For simplicity, only an isotropic permeability tensor $\boldsymbol{k}^v = k^v \cdot \boldsymbol{I}$ is considered for the additional porous network. This permeability and the averaged blood viscosity μ^v are the two model parameters governing this equation together with the right hand side term

$$\overset{v\to l}{M}_\mathrm{leak} = \begin{cases} \rho^l \cdot L_{p,v}(S/V)_{\Lambda_\mathrm{S}} \cdot \left(p^v - p^l - \sigma\left(\pi^b - \pi^l\right)\right) & \text{in } \Omega_v \\ 0 & \text{in } \Omega\backslash\Omega_v \end{cases}. \tag{6.10}$$

This term replaces the outflow of fluid from the smaller vessels into the IF by a homogenized representation of the Starling equation (6.3) involving the surface-to-volume ratio of the smaller blood vessels $(S/V)_{\Lambda_\mathrm{S}}$ as an additional parameter. The mass balance equation of the IF for the fully-resolved model (6.4) is adapted as

$$-\boldsymbol{\nabla}\cdot\left(\frac{\boldsymbol{k}^l}{\mu^l}\boldsymbol{\nabla}p^l\right) = \frac{1}{\rho^l}\left(\delta_{\Lambda_\mathrm{L}}\cdot\overset{\hat{v}\to l}{M}_\mathrm{leak} + \overset{v\to l}{M}_\mathrm{leak}\right) \qquad \text{in } \Omega \tag{6.11}$$

in the homogenized formulation. Comparing the two equations, it is obvious that leakage from the large vessels is still treated equivalently, i.e., the large vessels are still embedded as 1D inclusions in the tissue with a Dirac measure (now defined only on $\Lambda_\mathrm{L} \subset \Lambda$ employing the

centerline-coupled variant). By contrast, leakage from the smaller blood vessels is replaced by the homogenized mass transfer term (6.10) from the vascular domain Ω_v into the interstitium, i.e., from (6.9) into (6.11).

So far, this procedure is analogous to other hybrid approaches [242, 266]. The main difference to the hybrid embedded/homogenized methodology followed in this thesis lies in the coupling between the larger vessels Λ_L and the homogenized vasculature Ω_v. In the aforementioned publications, this was realized at the free ends of the larger vessels, i.e., as an outflow at the tips of the 1D discretization into the homogenized 3D vasculature domain. This was possible since the employed data sets had a clear vascular hierarchy with larger arterioles and venules connected to smaller capillaries. The here employed vascular networks, which will be described in detail in Section 6.3.1, have been segmented from solid tumors and, therefore, have a much more complex, disorganized structure including variable vessel lengths and diameters as well as dead ends. All this is typical for tumor-specific vasculature [12, 36]. As shown in detail in Section 6.3.3, for this data and the employed methodology to distinguish between large, flow-carrying vessels and smaller ones, another approach is more sensible, namely, to enforce the coupling between larger vessels and the homogenized vasculature along the entire 1D representation of larger vessels Λ_L with a line-based coupling instead of a point-based coupling at the tips of the larger vessels flowing into the capillary bed. Compared to these hybrid approaches, the proposed method also has the advantage that no additional parameter – apart from the penalty parameter – is involved for the coupling of the two representations.

So, a line-based constraint of equal pressures in Λ_L and Ω_v is formulated equivalent to (3.110) as

$$g = p^{\hat{v}} - p^{v} = 0 \qquad \text{on} \;\; \Lambda_\mathrm{L}, \tag{6.12}$$

which enforces a coupling between pressures $p^{\hat{v}}$ in the one-dimensional, large vessel domain Λ_L and homogenized pressures p^v in the 3D domain Ω_v. This aims to reproduce that the pressure in a smaller vessel branching from a larger vessel at a specific node is equal to the pressure at the same node. If this smaller vessel is homogenized and, thus, removed from the 1D representation, these equal pressures should be enforced between the resolved part and the homogenized part of the vasculature along the 1D vessel domain Λ_L. Here, only the mortar scheme with penalty regularization is employed as the Gauss-point-to-segment scheme could suffer from over-constraining of the system for large penalty parameters see Section A.2 and [134, 136, 246]. In Section 6.3.3, it will be justified why this constraint is formulated along the entire 1D domain Λ_L considering the connectivity between larger and smaller vessels in the studied cases. Thus, the same strategy as in the hybrid variant of the vascular multiphase model, see Sections 3.5 and 4.3.1.3, and the related solid mechanics problem of beam-to-solid mesh tying [134, 246] is employed and the constraint is incorporated with an additional Lagrange multiplier (LM) field into the weak form of the hybrid model, which reads as

$$\left(\frac{\partial \delta p^{\hat{v}}}{\partial s}, \frac{\pi R^4}{8\mu^{\hat{v}}} \frac{\partial p^{\hat{v}}}{\partial s}\right)_{\Lambda_\mathrm{L}} + \left(\delta p^{\hat{v}}, \frac{\overset{\hat{v}\to l}{M}_\mathrm{leak}}{\rho^{\hat{v}}}\right)_{\Lambda_\mathrm{L}} + \left(\delta p^{\hat{v}}, \lambda\right)_{\Lambda_\mathrm{L}} = 0 \tag{6.13a}$$

$$\left(\boldsymbol{\nabla} \delta p^{v}, \frac{\boldsymbol{k}^{v}}{\mu^{v}} \boldsymbol{\nabla} p^{v}\right)_{\Omega_v} + \left(\delta p^{v}, \frac{\overset{v\to l}{M}_\mathrm{leak}}{\rho^{v}}\right)_{\Omega_v} - \left(\delta p^{v}, \lambda\right)_{\Lambda_\mathrm{L}} = 0 \tag{6.13b}$$

$$\left(\boldsymbol{\nabla}\delta p^l, \frac{\boldsymbol{k}^l}{\mu^l}\boldsymbol{\nabla}p^l\right)_\Omega - \left(\delta p^l, \frac{\overset{\hat{v}\to l}{M}_{\text{leak}}}{\rho^l}\right)_{\Lambda_\text{L}} - \left(\delta p^l, \frac{\overset{v\to l}{M}_{\text{leak}}}{\rho^l}\right)_{\Omega_v} = 0 \tag{6.13c}$$

$$\left(\delta\lambda, \left(p^{\hat{v}} - p^v\right)\right)_{\Lambda_\text{L}} = 0 \tag{6.13d}$$

Therein, the first line is the weak form of flow in the larger vessels (6.8) which is coupled to the weak form of flow in the homogenized vasculature domain, i.e., the second line (6.13b) with a continuous LM field λ defined along the blood vessel center line. The third line is the weak form of flow in the IF. Compared to the fully-resolved model, conf. equation (6.5b), the additional mass transfer term arises due to leakage from the homogenized part of the vasculature into the IF. The fourth line represents the variational form of the coupling constraint (6.12). The LM field employed to enforce this constraint can then again be interpreted as a mass transfer term from the 1D resolved bigger vessels into the 3D homogenized vasculature, i.e., $\lambda = \overset{\hat{v}\to v}{M}$.

For the sake of completeness, the spatial discretization of the weak form including a penalty regularization of a mortar-type method, which was outlined for the hybrid variant of the vascular tumor growth model in Section 4.3.1.3, is repeated here. The weak form (6.13a)-(6.13d) leads to a saddle-point problem with nodal primary variables

$$\mathbf{p}^{\hat{v}} \in \mathbb{R}^{n_{\text{nodes},\Lambda_\text{L}}}, \boldsymbol{\lambda} \in \mathbb{R}^{n_{\text{nodes},\Lambda_\text{L}}}, \mathbf{p}^l \in \mathbb{R}^{n_{\text{nodes},\Omega}} \text{ and } \mathbf{p}^v \in \mathbb{R}^{n_{\text{nodes},\Omega_v}}, \tag{6.14}$$

that is, nodal pressures and nodal LMs in $\Lambda_\text{L}^\text{h}$, nodal IF pressures in Ω^h and nodal blood pressures of the homogenized vasculature in Ω_v^h. In the following, the focus lies on the discretization of the terms arising due to the LM method. Approximating those contributions with a finite element interpolation yields a mortar-type formulation where the nodal LMs are additional degrees of freedom or condensed out with a dual approach [199, 284]. Alternatively, a penalty regularization of the mortar method can be employed to remove the additional degrees of freedom and the saddle-point structure [292] which is the chosen method here as in previous work on 1D-3D couplings [134, 246]. The contributions to the weak form of the mass balance equations, i.e., the two last terms in (6.13a) and (6.13b) can be written as

$$\delta\Pi_{\text{LM}}^\text{h} = \sum_{j=1}^{n_{\text{nodes},\Lambda_\text{L}}} \sum_{k=1}^{n_{\text{nodes},\Lambda_\text{L}}} \lambda_j D_{jk} \delta p_k^{\hat{v}} - \sum_{j=1}^{n_{\text{nodes},\Lambda_\text{L}}} \sum_{l=1}^{n_{\text{nodes},\Omega_v}} \lambda_j M_{jl} \delta p_l^v \tag{6.15}$$

with the previously defined mortar matrices of the centerline-based coupling variant

$$\mathbf{D}\,[j,k] = D_{jk} = \int_{\Lambda_\text{L}^\text{h}} \hat{\Phi}_j \hat{N}_k \, ds \tag{6.16}$$

and

$$\mathbf{M}\,[j,l] = M_{jl} = \int_{\Lambda_\text{L}^\text{h}} \hat{\Phi}_j N_l \, ds. \tag{6.17}$$

The integrals of products of LM shape functions $\hat{\Phi}_j$ defined on the discretized 1D domain $\Lambda_\text{L}^\text{h}$ with 1D shape functions $\hat{N}_k$ and with trilinear shape functions N_l defined in the 3D domain Ω_v^h

are again evaluated using a segment-based approach as detailed in Section 4.3.3.1. Linear shape functions are chosen for both primary variables and the LM interpolation, i.e., $\hat{\Phi}_j = \hat{N}_j$. The weak form of the constraint (6.13d) can for this case be written in discretized form as

$$\delta\Pi_\lambda^{\mathrm{h}} = \delta\boldsymbol{\lambda}^T \left(\mathbf{D}\mathbf{p}^{\hat{v}} - \mathbf{M}\mathbf{p}^{v}\right) =: \delta\boldsymbol{\lambda}^T \mathbf{g}\left(\mathbf{p}^{\hat{v}}, \mathbf{p}^{v}\right), \tag{6.18}$$

with the weighted pressure gap $\mathbf{g}$ at each node in $\Lambda_{\mathrm{L}}^{\mathrm{h}}$. As before, this gap is then further used for the penalty regularization of the mortar method to explicitly define the nodal LMs in terms of 1D and 3D nodal blood pressures as

$$\boldsymbol{\lambda} = \epsilon\boldsymbol{\kappa}^{-1}\mathbf{g}\left(\mathbf{p}^{\hat{v}}, \mathbf{p}^{v}\right). \tag{6.19}$$

Hence, the LMs are no longer independent variables in the system but depend on the primary variables $\mathbf{p}^{\hat{v}}$ and $\mathbf{p}^{v}$. This overcomes the two major drawbacks of the LM method, namely, the increased system size and its saddle-point structure. Depending on the penalty parameter $\epsilon > 0$, the constraint $\mathbf{g} = \mathbf{0}$ is relaxed and the exact solution is only recovered for $\epsilon \to \infty$. Additionally, the nodal LM in (6.19) is scaled with the inverse of the diagonal matrix

$$\boldsymbol{\kappa}[j,j] = \int_{\Lambda_{\mathrm{L}}^{\mathrm{h}}} \hat{\Phi}_j \, ds. \tag{6.20}$$

As proposed by Yang et al. [292] this removes the dependency of the nodal LM on its "gap", i.e., in the present case it makes its entries independent of the element lengths associated with its corresponding node. This can now be used to replace the LM vector such that the matrix-vector form of the hybrid model emerges as

$$\begin{bmatrix} \mathbf{K}^{\hat{v}\hat{v}} + \epsilon\mathbf{D}^T\boldsymbol{\kappa}^{-1}\mathbf{D} & \mathbf{G}^{\hat{v}l} & -\epsilon\mathbf{D}^T\boldsymbol{\kappa}^{-1}\mathbf{M} \\ \mathbf{H}^{l\hat{v}} & \mathbf{K}^{ll} & \mathbf{J}^{lv} \\ -\epsilon\mathbf{M}^T\boldsymbol{\kappa}^{-1}\mathbf{D} & \mathbf{L}^{vl} & \mathbf{K}^{vv} + \epsilon\mathbf{M}^T\boldsymbol{\kappa}^{-1}\mathbf{M} \end{bmatrix} \begin{bmatrix} \mathbf{p}^{\hat{v}} \\ \mathbf{p}^{l} \\ \mathbf{p}^{v} \end{bmatrix} = \begin{bmatrix} \mathbf{F}^{\hat{v}} \\ \mathbf{F}^{l} \\ \mathbf{F}^{v} \end{bmatrix}. \tag{6.21}$$

As in the fully-resolved model (6.7), main diagonal blocks are denoted as $\mathbf{K}^{ii}$ and the coupling blocks $\mathbf{G}^{\hat{v}l}$ and $\mathbf{H}^{l\hat{v}}$ stem again from the transvascular 1D-3D exchange term. Additionally, the coupling blocks $\mathbf{J}^{lv}$ and $\mathbf{L}^{vl}$ account for exchange between homogenized vasculature and IF. The terms involving the mortar matrices $\mathbf{D}$, $\mathbf{M}$ and $\boldsymbol{\kappa}$ couple blood flow in the larger vessels with the homogenized vasculature using the mortar penalty approach. Obviously, the LMs are no longer part of the system which is, consequently, not of saddle-point type anymore. The drawback, however, is that the choice of the penalty parameter influences the accuracy with which the constraint is fulfilled. Large penalty parameters yield better accuracy in terms of constraint fulfillment but can lead to an ill-conditioning of the system matrix. A comment on the choice of the penalty parameter is made in Remark 6.4.

Remark 6.1. *The concrete implementation of the hybrid model is slightly different than described here for illustrative purposes. The equations for IF flow and blood flow are evaluated simultaneously on the 3D domain and not assembled into two separate block matrices as written in* (6.21)*. This corresponds to the residuum of the vascular multiphase tumor growth model where primary variables of TCs, HCs and IF are always evaluated together with HV volume fractions and pressures, see* (4.122)*. Hence, the degrees of freedom are actually re-ordered in a*

	LS174T	GL261	SW1222	Unit
No. of segments (elements) of 1D network	186 092	120 340	419 198	–
No. of nodes of 1D network	178 592	110 062	385 218	–
Tumor volume	190.5	24.6	235.5	mm^3
Tumor dimensions	$4.5 \times 7.6 \times 10.9$	$2.4 \times 4.6 \times 5.3$	$6.4 \times 8.1 \times 11.1$	$\mathrm{mm} \times \mathrm{mm} \times \mathrm{mm}$
Blood vessel volume fraction	1.13	4.01	14.90	%
Blood vessel surface-to-volume ratio	1.85×10^{-3}	6.93×10^{-3}	7.43×10^{-3}	$\mu\mathrm{m}^{-1}$
Mean blood vessel diameter $\pm$ std. dev.	22.0 ± 7.2	17.6 ± 10.0	44.6 ± 39.2	µm
Mean blood vessel segment length $\pm$ std. dev.	27.2 ± 6.8	25.4 ± 7.7	28.7 ± 9.2	µm
No. of boundary nodes of 1D network on tumor hull	1559	2419	1933	–
No. of boundary nodes of 1D network inside domain	1855	6599	13 772	–
No. of elements of 3D domain	15 955 142	15 141 173	13 231 813	–
No. of nodes of 3D domain	2 660 273	2 524 666	2 207 655	–
Mean element size in Ω_v	76.4	39.7	78.1	µm
Edge length of REV	1250	750	1500	µm

Table 6.1: Details on tumor vasculature data sets and discretization

node-wise manner compared to (6.21) *such that one row corresponding to the nodal IF pressure at a node j is followed by a row corresponding to the homogenized blood pressure at this node j. Therefore, a system which is blocked with 2×2 submatrices analogous to* (4.126) *is solved, where the upper part corresponds to the resolved part of the vasculature and the lower part to the IF and the homogenized vasculature. For solving this system, the AMG(BGS) preconditioner [263] combined with the GMRES iterative solver is once more used.*

6.3 Setup of Computational Models

This section describes the setup of the fully-resolved and hybrid model. First, the real-world tumor data sets which will be employed for all numerical tests are analysed. Subsequently, the assignment of boundary conditions in both models is described. Then, the creation of the hybrid model with homogenized vasculature starting from the full topology of the vascular networks is illustrated. Finally, the definition of representative elementary volumes for homogenization is introduced.

6.3.1 Analysis of Real-world Tumor Data Sets

For this study, three different vasculature data sets from REANIMATE [59, 252], which is a framework combining mathematical modeling with high-resolution imaging data to predict transport through tumors, are examined. More details about the framework and the experimental procedure are given in the two aforementioned papers. Two different colorectal cell lines, namely SW1222, LS174T, and one glioma cell line, GL261, were grown subcutaneously for 10 to 14 days in mice, resected and optically cleared, and finally imaged using optical projection tomography. The data was then segmented to obtain the complete blood vessel networks inside the tumors in the graph format as discussed before.

The topologies and blood vessel radii of the three distinct cases are illustrated in Figure 6.2 together with representative results of blood vessel and IF pressure of the fully-resolved model.

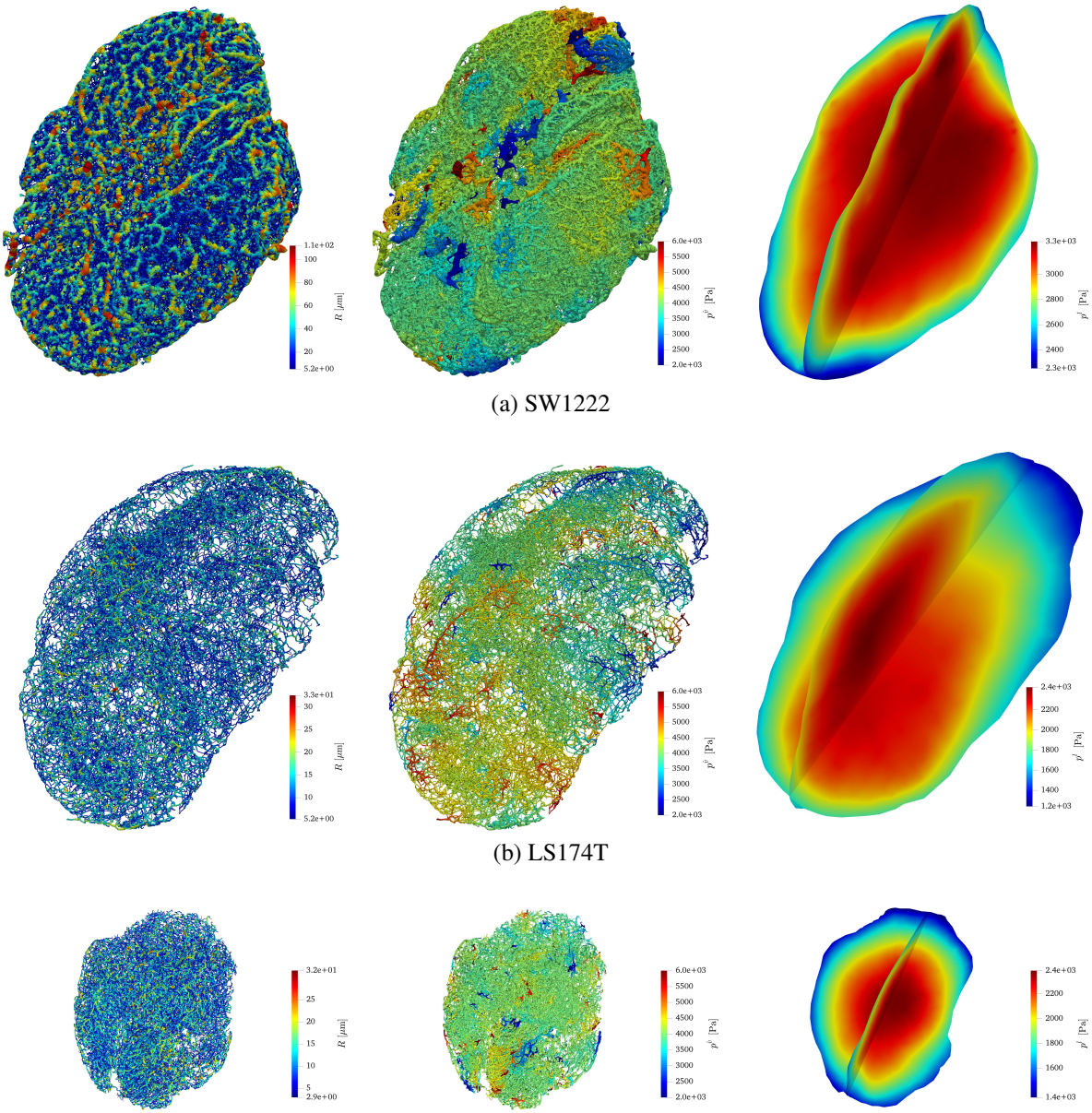

(a) SW1222

(b) LS174T

(c) GL261

Figure 6.2: Full topology and structure of the vascular networks (left, colour-coded by the respective radii), representative results for simulated blood pressures (middle) and IF pressures (right) in the fully-resolved model (Same spatial scale is used for all three cases). Figure taken from the author's article [137].

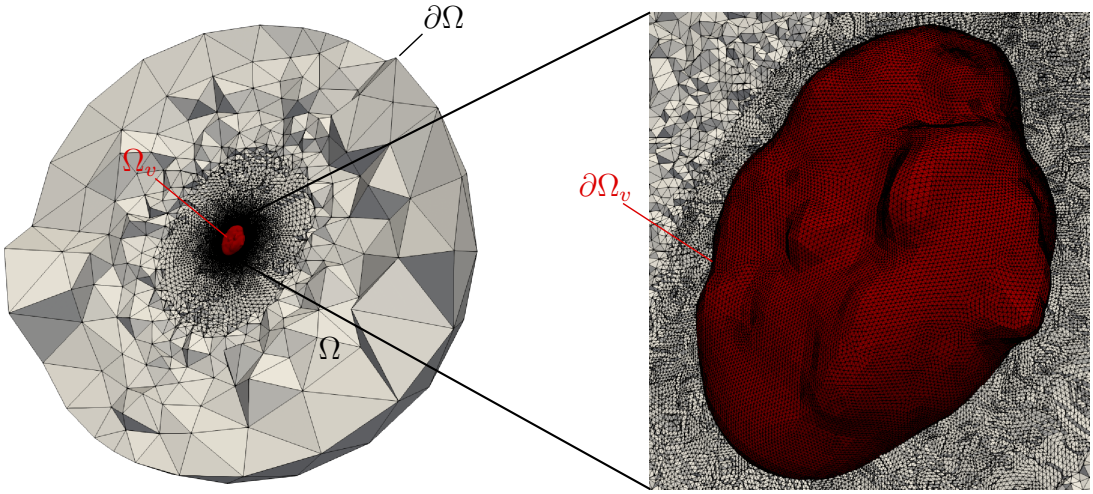

Figure 6.3: Mesh of three-dimensional domain for SW1222 tumor. Tumor domain (equivalent to the domain Ω_v on which the additional porous network of smaller vessels is present in the hybrid model) is depicted in red and has been obtained as the alpha shape of nodes of the vascular network. Figure taken from the author's article [137].

Further network data is collected in Table 6.1: All three networks contain more than 100 000 blood vessel segments and nodes. The SW1222 case is the biggest tumor both in network size and tissue volume. The latter has been calculated by approximating the hull of the tumor using the `alphaShape` function of Matlab [165]. The hull is then smoothed, remeshed using Gmsh (version 4.4.1, [89]) and slightly enlarged to encompass all vasculature nodes. Its enclosed region is integrated to give the tumor volume, see also Figure 6.3 for the SW1222 tumor. Note that this tumor domain corresponds to the domain Ω_v on which the additional porous network of smaller vessels is present in the hybrid model and where its additional governing equation (6.9) is defined and solved. Furthermore, all topologies are rotated such that their principal axes align with the coordinate axes. The three different cases show distinct vascular architectures, for instance, the SW1222 network is much denser with a higher blood vessel volume fraction and blood vessel surface-to-volume ratio than the two other types. In addition, its blood vessel diameters are generally larger and have a much higher variability. All topologies have a comparable number of boundary nodes lying on the aforementioned enclosing alpha shape whereas the GL261 and SW1222 tumors have a much higher number of tips inside the domain than the LS174T tumor.

6.3.2 Assignment of Boundary Conditions

The assignment of physiologically reasonable boundary conditions on large vascular networks is quite challenging since flows or pressures cannot be measured on the level of individual microvessels. Sweeney et al. [252] developed an algorithm [251] to apply boundary conditions which match *in-vivo* measurements of perfusion for the present data set. This framework is re-used here to generate the boundary conditions for the fully-resolved case and briefly described in Section 6.3.2.1. Boundary conditions for the hybrid model are detailed in Section 6.3.2.2.

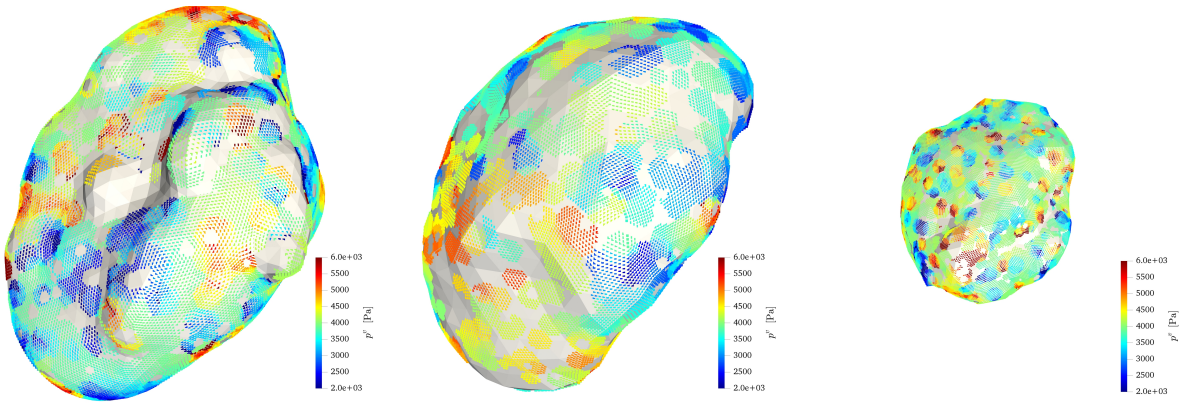

(a) SW1222 (b) LS174T (c) GL261

Figure 6.4: Exemplary distributions of boundary conditions for homogenized pressure p^v on boundary of vascular domain $\partial\Omega_v$ in the hybrid model variant for all three cases. Figure taken from the author's article [137].

6.3.2.1 Fully-resolved Model

For the fully-resolved model, boundary conditions for the blood pressure $p^{\hat{v}}$ in the 1D network and the IF pressure p^l need to be assigned. For the blood vessel pressure, the approach of Sweeney et al., which has been made publicly available [251] and is based on earlier work by Fry et al. [85], is re-used. Thereby, boundary conditions are assigned on the tips of the network, more precisely, on the boundary nodes of the 1D representation of the vasculature both on the tumor hull and inside the tumor as given in Table 6.1. The following algorithm is applied: First, a high or low pressure of $5999.4\,\mathrm{Pa}$ or $1999.8\,\mathrm{Pa}$ (corresponding to $45\,\mathrm{mmHg}$ or $15\,\mathrm{mmHg}$) is randomly applied to the boundary points on the tumor hull until $5\,\%$ of *all* end points of the 1D network have been assigned such a high/low pressure. Additionally, the method prevents that points which are in close proximity to each other are assigned the far apart pressure values which would produce unphysiologically large flows. Second, a no-flux boundary condition is randomly assigned to the interior boundary nodes until $33\,\%$ of *all* boundary nodes have this condition. This value is consistent with the fraction of dead ends in tumor vasculature estimated from experimental studies [174]. Third, the remaining $62\,\%$ of boundary nodes remain as unknowns in the flow optimization scheme of Fry et al. [85]. This scheme, which was previously employed in Section 5.5 to assign pressure boundary conditions, aims at solving a constrained optimization problem for incomplete pressure boundary data by minimizing the error of pressures and wall shear stress w.r.t. pre-defined target values. D'Esposito et al. [59] and Sweeney et al. [252] have shown that this procedure for assignment of boundary conditions ensures that tumor perfusion is in good agreement with experimental data. Note that the entire algorithm is not deterministic due to the random selection of nodes for high/low boundary conditions on the external surface of the tumor and of nodes for no-flux boundary condition in its interior. Therefore, the analyses in the following sections will be performed on five different sets of pressure boundary conditions on the 1D network per tumor case.

Concerning the IF pressure, the far-field pressure for the IF is prescribed as $p^l_\infty = 0\,\mathrm{Pa}$ following Sweeney et al. [252]. In order to achieve this within the employed finite element approach,

the domain Ω is radially enlarged to a sphere of radius $80\,\mathrm{mm}$ as shown in Figure 6.3 for the SW1222 case. This allows setting a Dirichlet boundary condition of $p^l = 0\,\mathrm{Pa}$ on its boundary $\partial\Omega$ and, thereby, to mock the far-field pressure. This approach has been validated in the following way for all three vascular networks: The fully-resolved model was solved (for one specific set of pressure boundary conditions on the 1D network) and the IF pressure solution compared with a case where the domain was only enlarged to a sphere with radius $40\,\mathrm{mm}$ (with corresponding zero IF pressure Dirichlet boundary condition on its outer surface). No visible differences in the IF pressure distribution in the domain of interest inside and around the tumor domain could be detected. This indicates that the enlargement is big enough insofar as the solution in the domain of interest is not influenced by the size of the enlargement any more. The mesh can also be gradually coarsened when moving away further from the vascular domain as depicted in Figure 6.3 since the IF pressure gradient flattens and tends to zero further away from the center of the domain. This enables using a sufficiently fine mesh for the region surrounding the embedded vascular network while the computational cost for extending the domain is not too high.

6.3.2.2 Hybrid Model

In addition to boundary conditions for the IF pressure p^l and the blood pressure $p^{\hat{v}}$, the hybrid model requires boundary conditions for the pressure in the homogenized vasculature p^v. The IF pressure is treated as in the fully-resolved model and set to zero at the boundary of the domain $\partial\Omega$. In the following, the accuracy of the hybrid variant will always be compared w.r.t. the fully-resolved one for one specific set of pressure boundary conditions on the 1D network obtained with the procedure described in the previous section. To perform this comparison, the pressure boundary conditions on the 1D network are transferred from the fully-resolved model to the hybrid model in the following manner: The boundary conditions of blood pressure $p^{\hat{v}}$ on the larger vessels Λ_L can directly be taken from the boundary conditions of the fully-resolved model. If a node with a Dirichlet boundary condition in the fully-resolved vasculature Λ is part of the larger vessels Λ_L, this boundary condition on the 1D discretization is kept also in the hybrid model. Dirichlet boundary conditions on the smaller vessels Λ_S cannot be assigned on the 1D discretization since smaller vessels are homogenized. However, they can be employed to assign boundary conditions for p^v on the boundary of the domain of homogenized vessels $\partial\Omega_v$ as depicted in Figures 6.1b and 6.3. Similar to Vidotto et al. [266], these values are smoothed to account for the homogenization of the smaller vessels: Each condition belonging to a node of the smaller vessels Λ_S at the tumor surface is assigned to all 3D nodes lying on the surface $\partial\Omega_v$ within a distance of less than $400\,\mu\mathrm{m}$ for the SW1222 and the LS174T tumor and less than $200\,\mu\mathrm{m}$ for the GL261 tumor. Nodes of the 3D mesh which lie within this distance of multiple boundary nodes on Λ_S are assigned the mean pressure value of all these boundary nodes. On the rest of the surface $\partial\Omega_v$ a no-flux boundary condition is set. Nodes of the 3D mesh in close proximity to end nodes of the 1D network are excluded since this would mean setting different boundary conditions on nodes whose pressures should be coupled due to the constraint on pressures $p^{\hat{v}}$ and p^v and, thus, would lead to an overconstrainment of the system. The resulting distribution of boundary conditions p^v over $\partial\Omega_v$ is illustrated in Figure 6.4 for three exemplary cases.

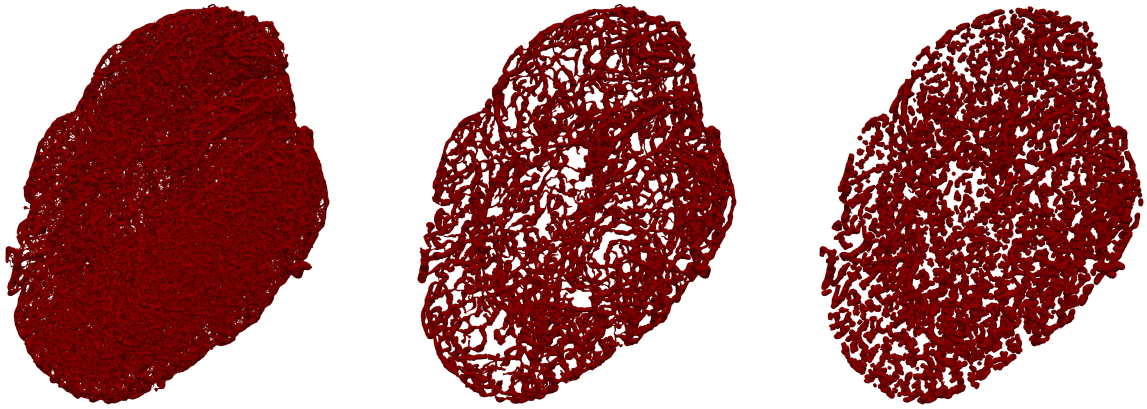

(a) full topology (b) 10 % with highest flow (c) 10 % with largest radius

Figure 6.5: Extraction of large vessels Λ_{L} from the entire network Λ – Comparison between flow-based criterion (and sorting out of small connected components) and radius-based criterion. Figure taken from the author's article [137].

6.3.3 Distinction between Fully-resolved and Hybrid Model

As previously stated, the hybrid model could be applied in cases where the full structure of the vascular network is unknown such that only the topology of the larger vessels can be acquired via non-invasive imaging. However, in the employed data sets the full structure is available. In line with the main goals of this chapter, namely, to validate the hybrid approach, to quantify the error with respect to the fully-resolved case and to determine its optimal parameters for perfusion through solid tumors, the hybrid model is artificially created from the fully-resolved one. In other hybrid approaches [242, 266] this was realized by a radius-based criterion. Their employed data sets had a clear hierarchy typical for the microcirculation with larger arterioles branching into smaller capillaries which in turn connect and form larger venules. Thus, it was possible to exploit the hierarchical structure of the vasculature by keeping only the larger vessels in the set I_{L}.

For the tumor vasculature data sets of REANIMATE this is not as straightforward. While there are some thicker vascular branches, especially in the SW1222 case, no clear hierarchical vascular architecture can be extracted from the topologies in Figure 6.2 with a radius-based criterion. To illustrate the challenge, the full architecture of the SW1222 network is compared with a network where only the top 10 % of vessels with the largest radius are kept in Figures 6.5a and 6.5c. Many small unconnected clusters of several blood vessel segments appear due to the heterogeneous, extremely variable distribution of the radius and lack of vascular hierarchy. Branches connecting these clusters which have a smaller radius are removed. Applying the present or any hybrid model on this topology would not be possible as hybrid approaches also rely on a "sensible" topology for Λ_{L} which preserves the structure of the entire network via one or several connected subgraphs of larger vessels which feed respectively drain the smaller, homogenized vessels. Only then, the 1D blood flow model and corresponding boundary conditions can reasonably be applied on Λ_{L} together with suitable exchange terms into the smaller vessels. Thus, smaller and larger vessels are distinguished based on the flow within the vessels. This yields a better preservation of the network architecture for the hybrid case, see Figures 6.5a and 6.5b. Now,

	case 5 %		case 10 %		case 15 %		case 20 %	
mean diameter [µm]	D_{Λ_L}	D_{Λ_S}	D_{Λ_L}	D_{Λ_S}	D_{Λ_L}	D_{Λ_S}	D_{Λ_L}	D_{Λ_S}
SW1222	104.7	41.4	95.7	38.9	88.4	36.9	81.5	35.4
LS174T	28.7	21.7	27.6	21.5	27.0	21.2	26.5	21.0
GL261	28.6	17.1	27.4	16.6	26.5	16.1	25.7	15.7

Table 6.2: Comparison of mean blood vessel radius in larger vessels Λ_L and smaller vessels Λ_S (all values indicate the mean taken over five different sets of pressure boundary conditions on the 1D network produced by the methodology described in Section 6.3.2.1, "case X %" denotes the case where X % of the 1D blood vessels are retained in the hybrid approach). Table taken from the author's article [137].

connected subgraphs of larger vessels Λ_L emerge which connect in- and outlets of the main flow-carrying vessels with the smaller vessels.

Hence, the employed strategy to obtain Λ_L is as follows: First, the fully-resolved model is solved (using the boundary conditions described in Section 6.3.2.1). Then, all elements except the ones with the highest flow are deleted from the vascular graph, e.g., the top $10\,\%$ with the highest flow are kept. However, some very small clusters consisting of only a few segments remain in the graph. Connected components in the graph whose overall length is smaller than $250\,\mu\mathrm{m}$, i.e., sub-components which are smaller than ten segments with the average segment lengths given in Table 6.1, are additionally deleted. This amounts to removing an additional $0.1-0.8\,\%$ of segments which are part of these smaller sub-components. This methodology gives the set I_L of larger vascular branches which are kept in the hybrid approach as exemplarily shown in Figure 6.5b. Here, only the SW1222 case is depicted but equivalent results hold for the other two network topologies. In the following, cases where the top X % of elements with highest flow are kept and the small connected components are removed according to the procedure described above are denoted as "case X %".

Recall that the assignment of pressure boundary conditions on the fully-resolved vascular network is not deterministic. Moreover, different boundary conditions produce distinct flow patterns in the vasculature and, hence, also different sets of large and small vessels and a different topology for Λ_L. Therefore, the following analysis will always be performed for five sets of pressure boundary conditions on the 1D network with corresponding distinct sets of large and small vessels I_L and I_S.

In Table 6.2 the mean diameters D_{Λ_L} and D_{Λ_S} of larger and smaller vessels are compared. It is obvious that the diameters in the set of small vessels I_S which are removed from the hybrid model are considerably smaller than the diameters of the large vessels. This behaviour is most pronounced for the SW1222 topology where for the case $5\,\%$ the mean diameters in Λ_L are 2.5 times bigger than in Λ_S. Naturally, this ratio drops for all topologies when a higher percentage of segments is kept in the large vessel set. For the LS174T and GL261 data sets the difference in blood vessel diameters is not as large but this can be attributed to the fact that the diameters are less dispersed than in the SW1222 topology, see also the mean and standard deviation of the diameters in Table 6.1. Also in these cases, the mean value of the diameters in Λ_L is larger by approximately one standard deviation of the diameter of the entire vasculature (as in the SW1222 case). In summary, the proposed approach incorporates mainly the vessels with larger radii in the set I_L whereas also some segments with smaller radii are kept to preserve the main topology

	case 5 %			case 10 %			case 15 %			case 20 %		
	φ	CV_D	$CV_{\|Q\|}$	φ	CV_D	$CV_{\|Q\|}$	φ	CV_D	$CV_{\|Q\|}$	φ	CV_D	$CV_{\|Q\|}$
SW1222	0.29	0.39	2.40	0.28	0.45	2.14	0.26	0.50	1.77	0.24	0.55	1.53
LS174T	0.18	0.23	0.88	0.16	0.24	0.85	0.15	0.24	0.83	0.13	0.24	0.82
GL261	0.30	0.35	1.21	0.29	0.37	1.16	0.28	0.38	1.13	0.27	0.40	1.09

Table 6.3: Analysis of connectivity between fully-resolved and homogenized part of vasculature: φ is the fraction of nodes of larger vessels with a direct connection to smaller vessels, CV_D and $CV_{|Q|}$ are measures of the variability of the diameter and flow, respectively, in the segments connecting larger and smaller vessels (data includes the mean taken over five different sets of pressure boundary conditions on the 1D network produced by the methodology described in Section 6.3.2.1, "case X %" denotes the case where X % of the 1D blood vessels are retained in the hybrid approach). Table taken from the author's article [137].

of the networks in the hybrid model. Therefore, there is also a significant congruence of the sets of large vessels I_{L} between different pressure boundary condition cases. For instance, in the case where $10\,\%$ of the blood vessels are kept in the hybrid model, the average percentage of identical retained segments between two different pressure boundary condition cases is $45\,\%$ for the LS174T tumor, $51\,\%$ for the GL261 tumor and $78\,\%$ for the SW1222 tumor. Remark 6.3 contains a further comment on how the obtained topologies of larger vessels Λ_{L} relate to real *in-vivo* tumor imaging data.

Next, the line-based coupling approach between the large vessels Λ_{L} and the homogenized vasculature is justified by analyzing the connectivity between larger and smaller vessels for the fully-resolved topologies in Table 6.3. Here, $\varphi = n_{\mathrm{nodes},\Lambda_{\mathrm{L}}\cap\Lambda_{\mathrm{S}}}/n_{\mathrm{nodes},\Lambda_{\mathrm{L}}}$ denotes the proportion of nodes of the larger vessels Λ_{L} which have a direct connection to a node of the smaller vessels Λ_{S}. The presented data illustrates that for the GL261 and the SW1222 tumor almost every third to every fourth node of the main branches Λ_{L} is directly connected to a node of the smaller blood vessel segments Λ_{S}, i.e., at every third to fourth node a smaller vessel branches away from Λ_{L}. For the LS174T network, the connectivity is slightly smaller. Here, only $13 - 18\,\%$ of nodes in larger vessels are connected to smaller vessels. In all cases, these numbers obviously again drop when keeping a larger portion of the entire network in the set I_{L}.

In the hybrid approach, information about these smaller branching vessels is lost since they are removed from the 1D representation of the vasculature. As stated above, equal pressures between larger and smaller vessels are enforced as this equality also holds in the fully-resolved model at branching points. The high connectivity between the two network parts supports the line-based mortar penalty coupling between the resolved and homogenized part of the vasculature in which the entire network of big vessels Λ_{L} is coupled with the homogenized vasculature. Of course, the connecting nodes between larger and smaller vessels are known here as is the full topology of all networks, so the coupling between resolved and homogenized part could also be enforced in a point-based manner at these locations. However, in the more realistic case when only the architecture of larger vessels is known without the exact locations where smaller vessels branch away, this is not the case. Therefore, the line-based coupling is adopted within the hybrid model hereafter to compare the results with the fully-resolved reference solution. Note that the network tips of Λ_{L} (both in the interior of the domain and on the tumor hull) are actually also coupled

with the homogenized vasculature since the discrete constraint of a vanishing weighted pressure gap is enforced along the entire 1D discretization and, thus, also at the end nodes.

Finally, the elements connecting larger and smaller vessels are analyzed, i.e., those 1D elements of the smaller vessels where one node is part of Λ_{L} and the other part of Λ_{S}. These elements are gathered and their mean diameter and mean absolute flow value is computed. Then, the coefficient of variation of these quantities, CV_D and $CV_{|Q|}$ is calculated as the ratio of standard deviation of the diameter, respectively flow to its mean in these connectivity elements. The results are collected in Table 6.3. Obviously, the SW1222 case shows the highest variability in both flow and diameter followed by the GL261 and the LS174T case. For all cases, the variability of the flow is larger than for the diameter since the volumetric flow in a segment depends on the fourth power of the diameter due to the employed Hagen-Poiseuille relationship. These results are consistent with the topology of the entire network where the variability of the blood vessel diameter is also larger for the SW1222 tumor than the GL261 and the LS174T tumor, see Table 6.1. In Section 6.4.3 it will be shown that this higher variability makes it harder to match the flow from large into small vessels between the two models.

Remark 6.2. *The hybrid approach is also applicable to more organized, hierarchical networks as, for example, the topology used by Vidotto et al. [266]. In this publication the network was partitioned by a radius-based threshold, see Figure 1 therein. The larger vascular structures contain very short branches leaving the main vessels. At the tips of these short branches, the node-based coupling is performed. If one instead removed these very short branches and left only the major, flow-carrying vessels in Λ_{L}, a line-based coupling along these vessels could again be implemented.*

6.3.4 Determination of Representative Elementary Volume Size

The existence of a resentative elementary volume (REV) is an important concept for different homogenization procedures [15, 56]. Its definition is identical to the macroscopic length scale of TCAT introduced in Section 2.1.1 with the prerequisite that it should be big enough to smooth out fluctuations of spatial heterogeneities yet small enough to resolve the physical effects of interest. In this section, the REVs with correct size in the context of the employed model and data sets are chosen. Naturally, this involves investigating the properties of the smaller vessels Λ_{S} in the following since this is the part of the vasculature which is homogenized and treated as a porous continuum in the hybrid approach. Furthermore, five different sets of pressure boundary conditions on the 1D network are studied. This is again due to the fact that different pressure boundary conditions on the 1D network lead to different flow patterns in the vascular network and, therefore, also different sets I_{L} and I_{S} of large and small vessels (potentially with a different distribution throughout the domain) with the employed flow-based criterion.

For this purpose, the following procedure has been devised:

1. For each network topology five different cases are created with a different set of pressure boundary conditions on the 1D network for the fully-resolved model as described in Section 6.3.2.1.

2. All cases are partitioned into the distinct sets of large and small vessels as described in Section 6.3.3. Here, only the case $10\,\%$ is investigated for all different topologies but

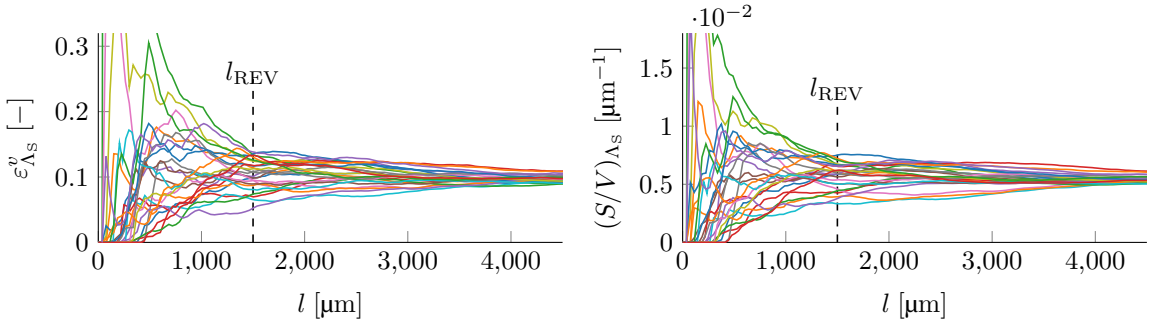

(a) SW1222

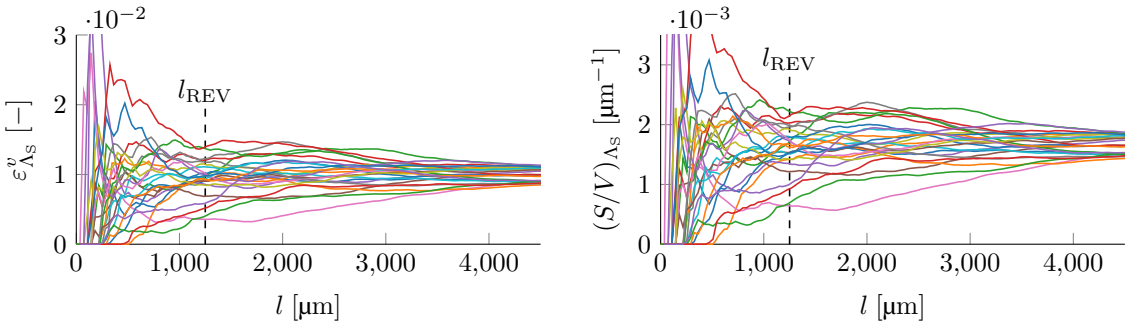

(b) LS174T

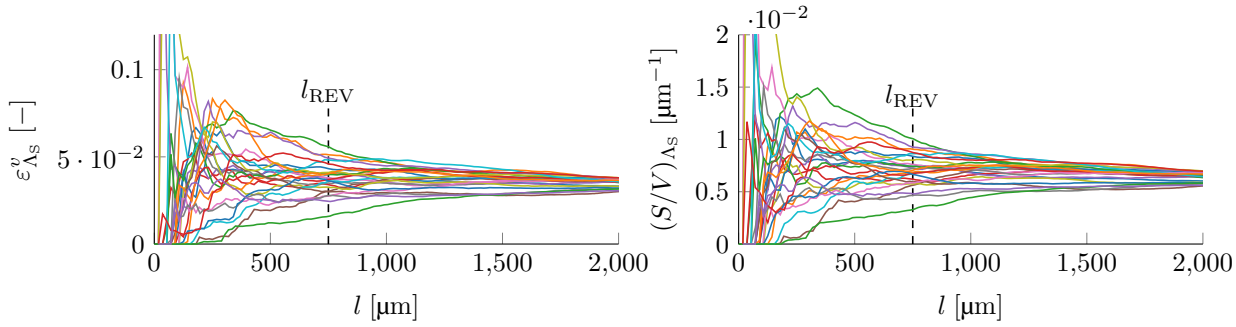

(c) GL261

Figure 6.6: Determination of representative elementary volume (REV) size – evolution of blood vessel volume fraction $\varepsilon^v_{\Lambda_S}$ and surface-to-volume ratio $(S/V)_{\Lambda_S}$ of smaller blood vessels Λ_S is shown for increasing possible REV sizes. Figure taken from the author's article [137].

equivalent results have been obtained for leaving the top 5 %, 15 % or 20 % of vessels with the largest flow in the system.

3. Random positions in the vasculature domain Ω_v in the range $[x_{min} + 0.15 \cdot l_x, x_{max} - 0.15 \cdot l_x]$, $[y_{min} + 0.15 \cdot l_y, y_{max} - 0.15 \cdot l_y]$ and $[z_{min} + 0.15 \cdot l_z, z_{max} - 0.15 \cdot l_z]$ are selected. l_i denotes the domain lengths in the respective coordinate directions and $(.)_{min}$ and $(.)_{max}$ the minimum and maximum coordinate value in each direction in Ω_v. In this way, the random positions are chosen such that they do not lie too close to the boundaries of the domain.

4. For each of the random positions within the domain, a cube with edge length $l_{\text{edge}} = 1/300 \cdot \max(l_x, \max(l_y, l_z))$ is defined. The random position is chosen as the center of that cube.

5. The size of the cubes is successively increased in all coordinate directions by l_{edge} while keeping their centers fixed. The blood vessel volume fraction $\varepsilon^v_{\Lambda_S}$ and the surface-to-volume ratio $(S/V)_{\Lambda_S}$ of smaller blood vessels Λ_S is computed for each cube at each size. If a cube protrudes from the domain during this enlargement, these quantities are calculated on the intersection of the cube with the domain Ω_v.

Per case with different boundary conditions this is performed for ten randomly generated cube centers. Figure 6.6 illustrates the results for only three REVs per boundary condition case, that is, in total 15 cases to not clutter the plots. The evolution of the blood vessel volume fraction $\varepsilon^v_{\Lambda_S}$ and of the surface-to-volume ratio $(S/V)_{\Lambda_S}$ of the smaller blood vessels Λ_S for increasing the edge length of the cubes is illustrated. Therein, the length scale is denoted as $l = \sqrt[3]{V_{\text{cube}\cap\Omega_v}}$ to account for cases when a larger cube protrudes from the domain Ω_v. All three topologies exhibit similar features: $\varepsilon^v_{\Lambda_S}$ and $(S/V)_{\Lambda_S}$ fluctuate strongly for smaller lengths. Then, most curves stabilize and remain almost stationary while increasing the size of the averaging volume. Finally, for even larger volumes the curves slowly converge to the values of these quantities across the entire domain. This behaviour can be expected in porous media [56] and the length of the REVs l_{REV} can be defined at the point where the initial oscillations of too small control volumes fade out and the values stabilize.

Splitting the domains into these REVs of equal size is not an easy task due to their irregular, elliptic shape. However, it can be achieved with the following methodology: First, a regular grid of REV centers is defined and an initial Voronoi tesselation is performed based on this grid. Due to the shape of the domain this results in too small or too large REVs. Therefore, an optimization of the Voronoi tesselation is performed with the objective function to define REVs of equal volume and equal dimensions. The resulting REVs are visualized in Figure 6.7. The mean deviation of the REVs from the previously determined volume and lengths of Figure 6.6 in all three coordinate directions is less than $5\,\%$ for the domains of all three tumor types.

Finally, these REVs are employed to study the distribution of blood vessels inside the domain. For that, the non-dimensionalized radial distance of each REV $\tilde{r}_{\text{REV}}$ is defined as the distance of the center of the REV to the center of the domain divided by the distance of the center of the domain to the tumor hull in direction of the center of the REV. Again, this analysis is performed for all three tumor types for five different sets of pressure boundary conditions on the 1D network since those influence the flow in the 1D vasculature and, consequently, also the composition of Λ_L and Λ_S as previously mentioned. The results for the volume fraction of big vessels $\varepsilon^v_{\Lambda_L}$, small vessels $\varepsilon^v_{\Lambda_S}$ and the entire vasculature ε^v_{Λ} are shown in Figure 6.8. The clearest structure is evident for the SW1222 case: towards the tumor hull, $\varepsilon^v_{\Lambda_S}$ and $\varepsilon^v_{\Lambda_L}$ and, thus, also the sum of the former two, ε^v_{Λ}, gradually increase. Close to the center of the domain, there is still a significant amount of smaller blood vessels while almost no larger blood vessels are present. This is consistent with experimental data showing higher blood vessel density and perfusion in the tumor periphery [59, 80] with only a few major vessels penetrating into the center of the tumor [109]. These trends are also present in the LS174T tumor, albeit, far less pronounced than for the SW1222 tumor. By contrast, the GL261 vascular network shows a completely different behaviour. While the vascular density of large vessels remains almost constant over the tumor

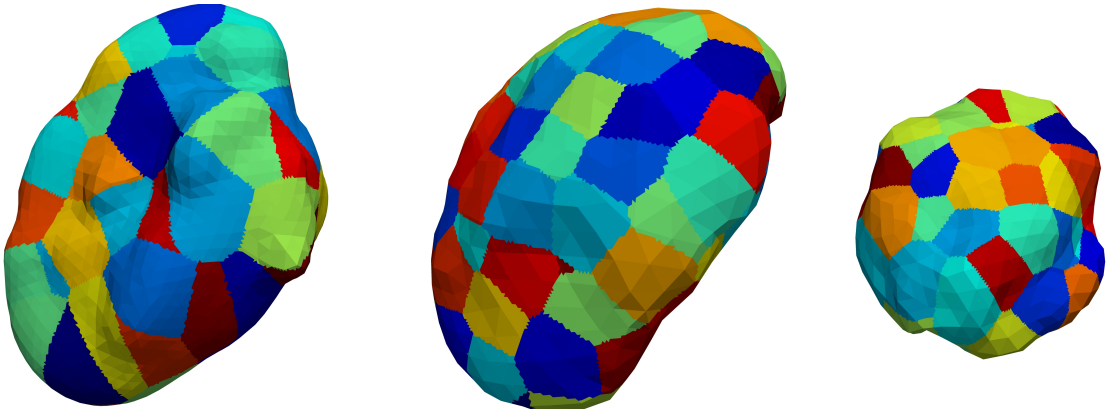

(a) SW1222, $n_{\mathrm{REV}} = 78$ (b) LS174T, $n_{\mathrm{REV}} = 114$ (c) GL261, $n_{\mathrm{REV}} = 55$

Figure 6.7: Representative elementary volumes of all three tumor domains. Figure taken from the author's article [137].

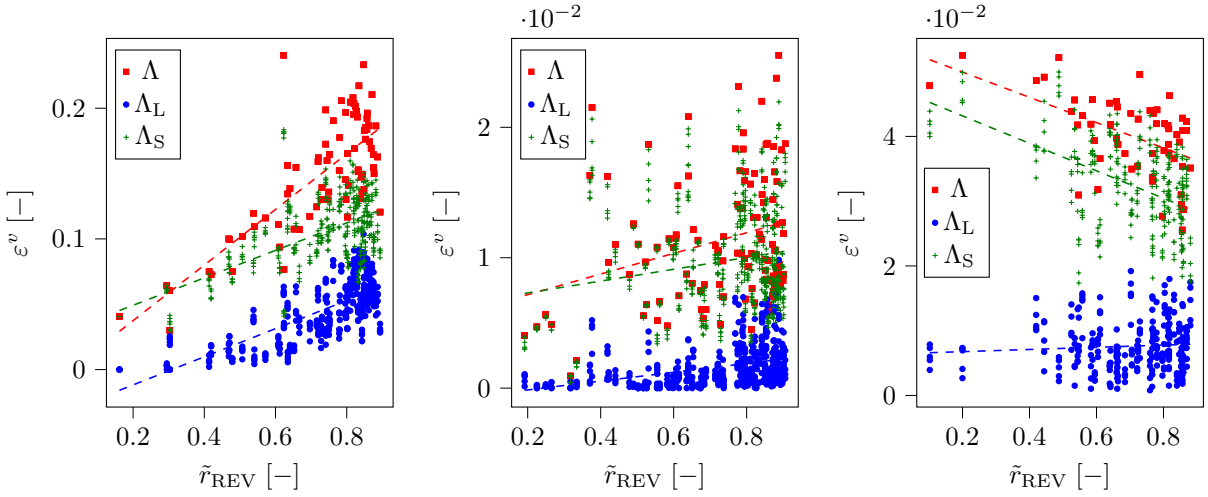

(a) SW1222 (b) LS174T (c) GL261

Figure 6.8: Dependency of volume fraction of big vessels Λ_{L}, small vessels Λ_{S} and entire vasculature Λ over non-dimensionalized radial distance from center of domain (data is taken from five different sets of 1D blood pressure boundary conditions if $10\,\%$ of 1D blood vessels are retained in hybrid model for each network structure, dashed lines indicate linear least squares fits). Figure taken from the author's article [137].

radius, the one of the smaller blood vessels Λ_{S} drops and, thus, also the overall volume fraction ε^v_{Λ}.

Remark 6.3. *The validity of the obtained topologies and distributions for Λ_{L} and Λ_{S} and the applicability of the proposed hybrid approach is supported by state-of-the art optoacoustic in-vivo imaging techniques [150]. The currently attainable spatial resolution is less than $50\,\mu\mathrm{m}$ throughout the tumor domain which is in the range of the diameter of larger vessels from Table 6.2. Furthermore, the larger vessels which are retained in the hybrid model are more concentrated at*

the tumor periphery (at least for the SW1222 and LS174T case) and are, thus, more accessible to imaging. Qualitatively, the topology of the larger vessels from Figure 6.5b is in good agreement with corresponding imaging data from tumors [150] where larger feeding vessels are visible at the tumor rim. From these experiments, one can extract a similar topology of larger vessels Λ_{L} to apply the hybrid model. Hence, it is reasonable to conclude that the employed methodology of splitting into larger and smaller vessels yields a valid scenario resembling real experimental data and can, therefore, be used to investigate the hybrid embedded/homogenized approach for solid tumor perfusion.

6.4 Numerical Experiments

This section contains several numerical experiments to evaluate the performance of the hybrid model in comparison to the fully-resolved one. First, a comparison metric is defined and the parameters of the hybrid model are inversely inferred such that the best possible correspondence between the models is achieved according to this metric. Subsequently, several other quantities are studied to compare the two models and a further improvement of the hybrid model is presented via a vascular volume fraction dependent permeability for the homogenized vessels.

The tumor hull is smoothed and triangulated using Gmsh 4.4.1 [89] and its enclosed volume is meshed with linear tetrahedral elements using Trelis 17.0 [49]. An exemplary mesh for the SW1222 topology is shown in Figure 6.3 and parameters of the 3D mesh are given in Table 6.1. As in the previous examples for 1D-3D coupling, the 3D mesh is completely independent of the discretization of the 1D networks, that is, the nodes of the two meshes do not match. Parameters for both models are listed in Table 6.4.

Remark 6.4. *In preliminary simulations, the proper range for the penalty parameter ϵ was determined. As a compromise between accuracy and a well-conditioned system matrix, the following criterion was defined:*

$$\delta = \frac{1}{n_{\mathrm{nodes},\Lambda_{\mathrm{L}}}} \sum_{i=1}^{n_{\mathrm{nodes},\Lambda_{\mathrm{L}}}} \frac{|\boldsymbol{\kappa}^{-1}[i,i]\mathbf{g}[i]|}{\mathbf{p}^{\hat{v}}[i]} < 1\,\%. \tag{6.22}$$

This rule states that the mean relative pressure error δ in terms of the length-independent nodal pressure difference vector $\boldsymbol{\kappa}^{-1}\mathbf{g}$ and the nodal pressure $\mathbf{p}^{\hat{v}}$ in the 1D network is less than $1\,\%$. The values for all cases are given in Table 6.4. As elaborated in Remark 4.6, the penalty parameter has units of a permeability ($[\mathrm{length}]^2/[\mathrm{time}\cdot\mathrm{pressure}]$) for the centerline coupling variant such that the LM field represents a 1D-3D mass transfer term, or volumetric flow per length.

Remark 6.5. *The main advantage of the hybrid model is not a reduction of computational cost compared to the full model, but the fact that it relies only on data available through non-invasive imaging. Nevertheless, a first preliminary evaluation comparing the computational costs of the two models was performed in which the hybrid model was not significantly faster than the fully-resolved one and in some cases even slower. The effort for finding 1D-3D elements interacting with each other, building the integration segments and evaluating the coupling terms along the 1D vasculature is obviously smaller for the hybrid model since less 1D vessels are present. However, this is balanced or even outweighed by its increased effort in several other aspects:*

Quantity	Symbol	Value	Unit	Ref.	Equations
Density of blood	$\rho^{\hat{v}}$, ρ^{v}	1060	$\mathrm{kg\,m^{-3}}$	[77]	(6.2),(6.8), (6.9)
Viscosity of blood	$\mu^{\hat{v}}$	[a]	$\mathrm{Pa\,s}$	[201]	(6.2),(6.8)
Density of IF and blood plasma	ρ^{l}	1000	$\mathrm{kg\,m^{-3}}$		(6.3),(6.4), (6.10),(6.11)
Hydraulic conductivity of interstitial fluid	k^{l}/μ^{l}	1.2782×10^{-1}	$\mathrm{\mu m^2\,Pa^{-1}\,s^{-1}}$	[29]	(6.4),(6.11)
Transvascular hydraulic conductivity	$L_{p,\hat{v}}$,$L_{p,v}$	2.1×10^{-5}	$\mathrm{\mu m\,Pa^{-1}\,s^{-1}}$	[13]	(6.3),(6.10)
Oncotic reflection coefficient	σ	0.82	-	[252]	(6.3),(6.10)
Oncotic pressure of blood	π^{b}	2666.4	Pa	[252]	(6.3),(6.10)
Oncotic pressure of interstitial fluid	π^{l}	1999.8	Pa	[252]	(6.3),(6.10)
Hydraulic conductivity of vasculature	k^{v}/μ^{v}	see Table 6.5	$\mathrm{\mu m^2\,Pa^{-1}\,s^{-1}}$	-	(6.10)
Surface-to-volume ratio of smaller vessels	$(S/V)_{\Lambda_\mathrm{S}}$	see Table 6.5	$\mathrm{\mu m^{-1}}$	-	(6.10)
Penalty parameter	ϵ		$\mathrm{\mu m^2\,Pa^{-1}\,s^{-1}}$	Rem. 6.4	(6.19)
SW1222: case 5 %		400			
SW1222: case 10 %, 15 %, 20 %		100			
LS174T: case 5 %		100			
LS174T: case 10 %, 15 %, 20 %		50			
GL261: case 5 %		100			
GL261: case 10 %, 15 %, 20 %		50			

[a] The value for blood viscosity is calculated separately in each 1D element using the algebraic relationship of Pries and Secomb [201] with hematocrit value fixed to 0.45.

Table 6.4: Parameters and values. Table taken from the author's article [137].

The evaluation of the 3D elements is more costly since two equations per node (in Ω_v) have to be evaluated, the system size, which is dominated by the number of 3D nodes, and, thus, the linear solver time is increased and the condition of the system is worse compared to the fully-resolved case due to the penalty approach, which in turn raises the linear solver time. However, for all studies the same 3D meshes were used for both hybrid and full model. The cost for the hybrid model could be greatly reduced by employing a coarser 3D mesh. Vidotto et al. [266] showed that this still gave acceptable results in terms of REV pressures for their approach.

6.4.1 Definition of a Metric for Comparison of the Two Models

To assess the performance of the hybrid model in predicting microvascular flow and IF pressure inside solid tumors in comparison with the fully-resolved model, a suitable discrepancy metric is a key factor in the inverse identification process. Ideally, the hybrid model should match the fully-resolved one in terms of blood and IF pressure as well as blood and IF flow to obtain an accurate representation of the perfusion through the tumor. Therefore, the employed metric is defined as a combination of these quantities. The first contribution is the correspondence of blood pressures in the large vessels Λ_L which are present both in the fully-resolved and the hybrid model. The *coefficient of determination* R^2 in terms of nodal blood pressures in the large vessels between the two models is given by

$$R^2_\mathrm{L} = 1 - \frac{\sum_{i=1}^{n_{\mathrm{nodes},\Lambda_\mathrm{L}}} \left(\mathbf{p}^{\hat{v}}\left[i\right]\big|_{\mathrm{full}} - \mathbf{p}^{\hat{v}}\left[i\right]\big|_{\mathrm{hyb}} \right)^2}{\sum_{i=1}^{n_{\mathrm{nodes},\Lambda_\mathrm{L}}} \left(\mathbf{p}^{\hat{v}}\left[i\right]\big|_{\mathrm{full}} - \mu_{I_\mathrm{L}}\left(\mathbf{p}^{\hat{v}}\big|_{\mathrm{full}}\right)\right)^2}, \tag{6.23}$$

where $\mu_{I_\mathrm{L}}\left(\mathbf{p}^{\hat{v}}\big|_{\text{full}}\right)$ is the mean blood pressure in the large vessels of the fully-resolved model. A value of $R^2 = 1$ would mean a perfect correspondence of both models while smaller values suggest larger deviations. A negative R^2 indicates that the hybrid model performs worse than simply taking the mean value of the fully-resolved model. The second contribution to the metric is the correspondence of blood pressures in the small vessels Λ_S between the fully-resolved and the hybrid model, which may be calculated as

$$R^2_\mathrm{S} = 1 - \frac{\sum_{i=1}^{n_{\text{nodes},\Lambda_\mathrm{S}}}\left(\mathbf{p}^{\hat{v}}\left[i\right]\big|_{\text{full}} - \mathbf{p}^{v}\left(\mathbf{X}\left[i\right]\right)\big|_{\text{hyb}}\right)^2}{\sum_{i=1}^{n_{\text{nodes},\Lambda_\mathrm{S}}}\left(\mathbf{p}^{\hat{v}}\left[i\right]\big|_{\text{full}} - \mu_{I_\mathrm{S}}\left(\mathbf{p}^{\hat{v}}\big|_{\text{full}}\right)\right)^2}. \tag{6.24}$$

Since the smaller vessels Λ_S are not retained in the hybrid model, nodal blood pressures in the smaller vessels of the fully-resolved model are compared with the homogenized blood pressure field $\mathbf{p}^v$ of the hybrid model evaluated at the nodal positions $\mathbf{X}\left[i\right]$ of the smaller vessels. Again, this is formulated in terms of a coefficient of determination, now involving all nodes in the small vessels and $\mu_{I_\mathrm{S}}\left(\mathbf{p}^{\hat{v}}\big|_{\text{full}}\right)$ is the mean blood pressure in the small vessels of the fully-resolved model.

Equivalently, the coefficient of determination of the IF pressure is given by

$$R^2_\mathrm{IF} = 1 - \frac{\sum_{i=1}^{n_{\text{nodes},\Omega}}\left(\mathbf{p}^{l}\left[i\right]\big|_{\text{full}} - \mathbf{p}^{l}\left[i\right]\big|_{\text{hyb}}\right)^2}{\sum_{i=1}^{n_{\text{nodes},\Omega}}\left(\mathbf{p}^{l}\left[i\right]\big|_{\text{full}} - \mu\left(\mathbf{p}^{l}\big|_{\text{full}}\right)\right)^2} \tag{6.25}$$

with the mean IF pressure $\mu\left(\mathbf{p}^{l}\big|_{\text{full}}\right)$ of the full model in the tissue domain Ω. Instead of the point-wise comparison of pressures in (6.24) and (6.25), one could also compare mean REV pressures of the two models. This will additionally be calculated and mean (blood and IF) pressures inside the REVs will be compared in Section 6.4.3. With the previous three equations, the metrics for blood and IF pressure have been defined. Also the flow in the larger vessels Λ_L is covered since larger vessels present in both models have the same diameter, length and blood viscosity. Therefore, if the nodal pressures match, also the flow between the nodes, i.e., inside the elements is identical. The same applies for flow in the IF if the same 3D mesh and hydraulic conductivity k^l/μ^l is employed in both models which will be assumed hereafter. What is still missing, is a metric for comparison of blood flow inside the smaller blood vessels Λ_S which are homogenized in the hybrid model. The definition of this measure follows as

$$R^2_{\text{flow},\Lambda_\mathrm{S}} = 1 - \frac{\sum_{i=1}^{n_\mathrm{REV}}\sum_{j=1}^{3}\left(Q^{\hat{v}}_j\big|_{\Lambda_\mathrm{S},\text{full}} - Q^{v}_j\big|_{\Lambda_\mathrm{S},\text{hyb}}\right)^2}{\sum_{i=1}^{n_\mathrm{REV}}\sum_{j=1}^{3}\left(Q^{\hat{v}}_j\big|_{\Lambda_\mathrm{S},\text{full}} - \mu\left(Q^{\hat{v}}\big|_{\Lambda_\mathrm{S},\text{full}}\right)\right)^2}, \tag{6.26}$$

i.e., for each of the n_REV REVs, the volumetric flow Q_j of the fully-resolved and the hybrid model in all three coordinate directions is compared via the coefficient of determination of flow in the smaller vessels $R^2_{\text{flow},\Lambda_\mathrm{S}}$.

Next, the calculation of flows in the REVs in both models is detailed. In the center of each REV a square $\square_j$ with dimensions $l_\mathrm{REV} \times l_\mathrm{REV}$ is defined such that its normal $\boldsymbol{n}_j$ is aligned with coordinate direction j. The volumetric flow in the homogenized part of the vasculature in

coordinate direction j is then given by

$$Q_j^v\big|_{\Lambda_\mathrm{S},\mathrm{hyb}} = \int_{\square_j} -\frac{k^v}{\mu^v}\boldsymbol{n}_j \cdot \boldsymbol{\nabla} p^v \,\mathrm{dA} \tag{6.27}$$

as the surface integral of the flux through the square. For the fully-resolved model, it is defined as

$$Q_j^{\hat{v}}\big|_{\Lambda_\mathrm{S},\mathrm{full}} = \sum_{\square_j \cap \Lambda_\mathrm{S}} -\frac{\pi R^4}{8\mu^{\hat{v}}}\frac{\partial p^{\hat{v}}}{\partial s} \cdot \mathrm{sgn}\left(\boldsymbol{t} \cdot \boldsymbol{n}_j\right), \tag{6.28}$$

which is the sum of the volumetric flow of all segments which are part of the smaller vessels and cut by the square $\square_j$. Therein, $\boldsymbol{t}$ is the tangential vector of a segment pointing from its first to its second node and $\mathrm{sgn}\left(\bullet\right)$ denotes the sign function.

Finally, the total coefficient of determination between the two models is defined as the sum of the contributions from blood pressure in large vessels (6.23), blood pressure in small vessels (6.24), IF pressure (6.25) and flow in small vessels (6.26) as

$$R^2_\mathrm{tot} = \frac{1}{4}\left(R^2_\mathrm{L} + R^2_\mathrm{S} + R^2_\mathrm{IF} + R^2_{\mathrm{flow},\Lambda_\mathrm{S}}\right). \tag{6.29}$$

This metric, where all four contributions are weighted equally, is employed to study the accuracy of the hybrid model w.r.t. the full model and to find the optimal parameters of the hybrid model.

6.4.2 Optimization of the Parameters of the Hybrid Model

Compared to the fully-resolved model, the hybrid one has two additional parameters, which are the hydraulic conductivity of the homogenized vessels k^v/μ^v in (6.9) governing blood flow and the surface-to-volume ratio $(S/V)_{\Lambda_\mathrm{S}}$ accounting for transvascular flow from the homogenized vessels into the IF in (6.10). The goal of this section is to determine these parameters such that the agreement in terms of blood flow and blood and IF pressures of the hybrid model with the fully-resolved model is maximized. For that, the total coefficient of variation (6.29) between the two models deduced in the previous section is employed and the following optimization problem is formulated in terms of the parameters of the hybrid model:

$$\underset{k^v/\mu^v,\,(S/V)_{\Lambda_\mathrm{S}}}{\mathrm{argmax}} \quad R^2_\mathrm{tot}. \tag{6.30}$$

The goal is to find the parameters of the hybrid model, for which the correspondence of the two models is optimized. With these optimal parameters the model discrepancy of the hybrid model w.r.t. the fully-resolved one can then be evaluated. For the optimization procedure, a parallelized version of the least-squares method of the SciPy package (version 1.5.2) [228] has been interfaced to the software framework QUEENS [24]. Internally, SciPy employs the Levenberg-Marquardt algorithm to solve the nonlinear least-squares problem (6.30). Derivatives of the metric (6.29) w.r.t. the parameters are approximated using forward finite differences. This implies that the hybrid model has to be solved three times per iteration step. In preliminary simulations, it was confirmed that different initial conditions from a sensible parameter range converged to the same optimum.

Since the full topology of the vasculature is available, one could also obtain these parameters by a suitable homogenization procedure for the permeability as previously done for other hybrid models [242, 266]. Here, this approach was not pursued for the following reasons: First, the chaotic structure of the blood vessel network implying also a very chaotic blood flow pattern typical for the solid tumors would make this very challenging. Second, the aim is to create a best-case scenario by fitting the parameters of the hybrid model such that possible errors introduced by a homogenization scheme are minimal.

The general algorithm can be described as follows:

1. Obtain a set of boundary conditions for the full model as described in Section 6.3.2.1 and solve the full model to generate a reference solution.

2. Extract the topology of larger vessels for the hybrid model from the full model, conf. Section 6.3.3, and apply boundary conditions on the hybrid model, conf. Section 6.3.2.2.

3. Find the optimal parameters of the hybrid model by maximizing the total coefficient of variation (6.30). During the optimization procedure repeated evaluations of the hybrid model with different parameters are required.

Representative results of the optimization scheme are depicted in Figure 6.9 for all four contributions to the total coefficient of determination. Very good agreement between the two models in terms of nodal pressures in the larger vessels $\mathbf{p}^{\hat{v}}$ can be observed in Figure 6.9a. This can be expected because the same boundary conditions on the large vessels are applied in both cases. Thus, large and small pressure values show very good agreement, further away from these boundary conditions in the medium pressure range, deviations become larger. The clusters with the largest errors are separate branches which are not directly connected to nodes of the 1D network carrying boundary conditions. The correspondence for the nodal IF pressures $\mathbf{p}^{l}$ in Figure 6.9c is also very good. For low IF pressures this is again due to the zero pressure boundary condition assigned on $\partial\Omega$ for both cases, but also for higher IF pressures inside the tumor, which is the actual domain of interest, the pressure differences are very small. In this case, the maximum absolute error is $237.1\,\mathrm{Pa}$ corresponding to a maximum relative error of $8.4\,\%$. The pressure in the smaller vessels, respectively the homogenized vasculature in the hybrid model, exhibits larger errors, see Figure 6.9b. Overall, the agreement is still reasonable. The error is largest for branches ending in tips with boundary conditions on the 1D vasculature either inside the domain or on the tumor hull. For instance, this is the case for the larger errors around $\mathbf{p}^{\hat{v}}\big|_{\mathrm{full}} \approx 3300\,\mathrm{Pa}$. The boundary conditions on these tips inside the domain are not retained in the hybrid model and for the tips on the tumor hull, they are smeared over several 3D nodes as described in Section 6.3.2.2. Hence, while the error in the medium pressure range is distributed symmetrically, larger deviations at both ends of the pressure spectrum towards the smeared values are present. This error due to point-wise non-matching boundary conditions can also not be improved by optimization of the parameters. However, in Section 6.4.3, it will be shown that averaged REV pressures of both models are in very good accordance. One can argue that this is a more interpretable and fairer comparison metric as the hybrid model cannot be expected to exactly match the pressure distribution of the fully-resolved one (in particular on the boundary) since the information about the exact topology of the smaller vessels is not represented. Finally, the results for the flow in the smaller vessels are shown in Figure 6.9d. Here, the poorest agreement of the two models is present. Especially larger flows are not met properly.

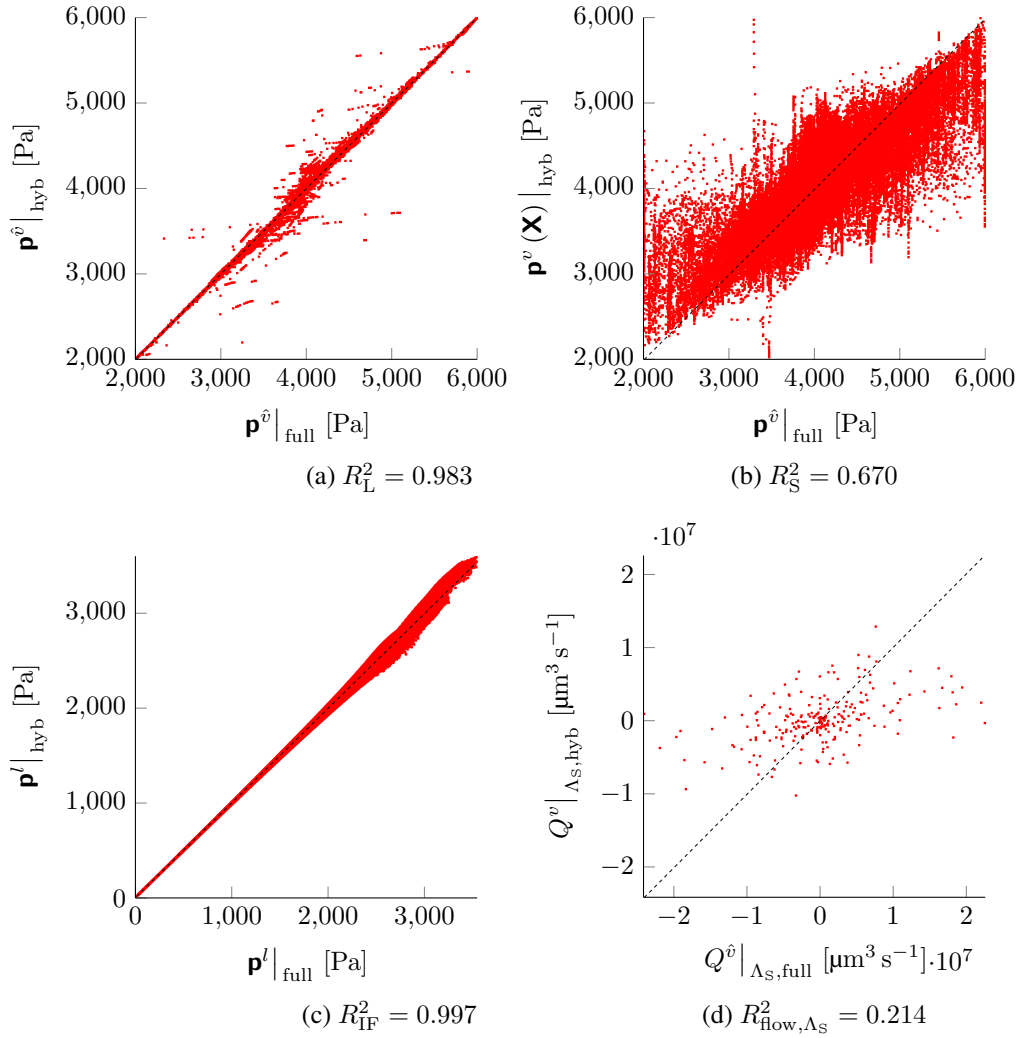

(a) $R^2_{\text{L}} = 0.983$ (b) $R^2_{\text{S}} = 0.670$

(c) $R^2_{\text{IF}} = 0.997$ (d) $R^2_{\text{flow},\Lambda_S} = 0.214$

Figure 6.9: Exemplary comparison of hybrid model (with optimized parameters) with fully-resolved model for one specific network topology (SW1222, 10 % of 1D blood vessels have been retained in hybrid model). In each subfigure, solution of hybrid model is plotted over solution of fully-resolved model and the dashed line indicates perfect agreement between the models with 1:1-correspondence. Comparison of blood pressure in large vessels is depicted in subfigure a), blood pressure in small vessels in b), IF pressure in c) and flow in small vessels in d). Coefficient of determination for agreement between both variants is given for each quantity and overall coefficient of determination calculated according to (6.29) is $R^2_{\text{tot}} = 0.716$ for this case. Figure taken from the author's article [137].

Network	Case	k^v/μ^v [µm^2]	$(S/V)_{\Lambda_S}$ [µm^{-1}]	$E_{S/V}$ [%]	R^2_L	R^2_S	R^2_{IF}	R^2_{flow,Λ_S}	R^2_{tot}
SW1222	5 %	16.060 ± 2.840	$(6.423 \pm 0.101) \times 10^{-3}$	2.17	0.944	0.488	0.994	0.163	0.647
	10 %	3.846 ± 0.506	$(5.722 \pm 0.069) \times 10^{-3}$	1.93	0.988	0.654	0.998	0.176	0.704
	15 %	1.612 ± 0.247	$(5.077 \pm 0.051) \times 10^{-3}$	2.66	0.993	0.739	0.999	0.262	0.748
	20 %	0.655 ± 0.122	$(4.532 \pm 0.048) \times 10^{-3}$	3.84	0.989	0.792	0.999	0.193	0.743
LS174T	5 %	1.799 ± 0.105	$(1.721 \pm 0.073) \times 10^{-3}$	3.21	0.905	0.643	0.990	0.282	0.705
	10 %	1.117 ± 0.096	$(1.581 \pm 0.038) \times 10^{-3}$	3.18	0.916	0.683	0.991	0.260	0.713
	15 %	0.745 ± 0.032	$(1.478 \pm 0.020) \times 10^{-3}$	2.70	0.930	0.695	0.992	0.244	0.715
	20 %	0.522 ± 0.064	$(1.382 \pm 0.021) \times 10^{-3}$	2.30	0.944	0.718	0.993	0.207	0.715
GL261	5 %	1.754 ± 0.288	$(6.184 \pm 0.099) \times 10^{-3}$	3.35	0.917	0.195	0.997	0.199	0.577
	10 %	0.802 ± 0.093	$(5.688 \pm 0.097) \times 10^{-3}$	3.63	0.927	0.233	0.996	0.107	0.566
	15 %	0.479 ± 0.073	$(5.200 \pm 0.076) \times 10^{-3}$	4.12	0.941	0.295	0.996	0.113	0.586
	20 %	0.321 ± 0.061	$(4.756 \pm 0.048) \times 10^{-3}$	4.21	0.950	0.346	0.996	0.134	0.607

Table 6.5: Results of the optimization procedure for hydraulic conductivity and surface-to-volume ratio of homogenized vasculature in the hybrid model. Relative error w.r.t. calculated surface-to-volume ratio and R^2-values for agreement between both variants in terms of blood pressure in large vessels, blood pressure in small vessels, IF pressure and flow in small vessels is additionally provided. Overall coefficient of determination R^2_{tot} between fully-resolved and hybrid model is calculated according to (6.29). (All data includes the mean taken over five different sets of pressure boundary conditions on the 1D network produced by the methodology described in Section 6.3.2.1, "case X %" denotes the case where X % of the 1D blood vessels are retained in the hybrid approach). Table taken from the author's article [137].

Further results for all cases are collected in Table 6.5. For each tumor network, five different sets of pressure boundary conditions on the 1D network are generated from which different flow patterns and, therefore, also different sets of larger and smaller blood vessels emerge as discussed in Section 6.3.3. Then, different cases, where $5 - 20\,\%$ of the larger vessels are kept in the hybrid model, are investigated. Five sets of pressure boundary conditions on the 1D network were enough to study the hybrid model since randomly picking only four out of the five boundary condition cases changed the mean result by at most $8\,\%$. Moreover, taking the mean parameter values of a case X % over all different boundary condition cases instead of the optimal values for each specific case only changed the total coefficient of determination by less than $2\,\%$. Furthermore, the result of the optimization procedure for $(S/V)_{\Lambda_S}$ is compared with the calculated surface-to-volume ratio of the smaller vessels for each case. The relative error $E_{S/V}$ is smaller than $5\,\%$ for all cases validating that the optimization procedure converges to a physically reasonable result. The permeability is largest for the SW1222 topology which can be expected considering the much denser network of this case. For all tumors, it decreases if a larger proportion of the 1D vessels is kept in the model, which is also sensible since the smaller the proportion of homogenized vessels, the less permeable these vessels.

As already described above, all cases exhibit a very good correspondence in terms of blood pressures in larger vessels and IF pressures, proven by the values for R^2_L and R^2_{IF} in Table 6.5. If the fidelity of the hybrid model is increased by resolving a larger proportion of the network structure, the agreement between the two models grows likewise. This is also the case for the coefficient of determination of blood pressure in smaller vessels R^2_S. Here, the SW1222 and the LS174T case exhibit comparable accuracy whereas the GL261 case experiences a larger

Network	Case	$\overline{E^v_{\text{abs}}}$ [Pa]	$\overline{E^v_{\text{rel}}}$ [%]	$\overline{E^l_{\text{abs}}}$ [Pa]	$\overline{E^l_{\text{rel}}}$ [%]	$R^2_{\text{flow},\Lambda_{\text{L}}\to\Lambda_{\text{S}}}$	$R^2_{\text{flow},\Lambda}$
SW1222	5 %	90.2	2.25	49.3	1.66	0.192	0.992
	10 %	57.2	1.43	32.2	1.08	0.091	0.999
	15 %	44.1	1.10	24.9	0.83	0.142	1.000
	20 %	42.1	1.05	21.5	0.72	0.100	1.000
LS174T	5 %	113.7	2.88	73.0	3.83	0.640	0.813
	10 %	99.4	2.53	68.3	3.58	0.567	0.892
	15 %	97.6	2.48	63.0	3.30	0.513	0.931
	20 %	91.4	2.33	59.2	3.10	0.444	0.956
GL261	5 %	104.2	2.64	41.6	2.16	0.472	0.962
	10 %	99.5	2.52	44.2	2.29	0.489	0.984
	15 %	87.8	2.22	44.9	2.33	0.435	0.993
	20 %	79.7	2.02	45.0	2.33	0.407	0.996

Table 6.6: Additional error measures for the agreement of both models. Shown are the absolute and relative error of the hybrid approach in terms of mean REV blood pressure in smaller vessels and mean REV interstitial fluid pressure and the R^2-values for agreement between both variants in terms of flow from large to small vessels and flow in the entire vasculature. (All data includes the mean taken over five different sets of pressure boundary conditions on the 1D network produced by the methodology described in Section 6.3.2.1, "case X %" denotes the case where X % of the 1D blood vessels are retained in the hybrid approach). Table taken from the author's article [137].

discrepancy. This can be attributed to the fact that this topology has the largest number of tips at the tumor hull and also the largest number of dead ends in relation to its size, see Table 6.1. Hence, the pressure error is largest due to non-matching boundary conditions between fully-resolved and hybrid model as mentioned above. However, in Section 6.4.3 it will be shown that in terms of REV blood pressures its conformity with the hybrid model is as good as the other cases. The difference in flow in the small vessels is the largest source of error in all cases. Also taking more 1D vessels into account for the hybrid model does not necessarily improve the behaviour. This may be due to the chaotic flow patterns in the smaller vessels and to the fact that the permeability tensor is defined as isotropic and constant over the entire domain Ω_v. Apparently, this is insufficient to resolve the flow in the homogenized vasculature in comparison to the full model. By giving a higher weight to the coefficient of determination of flow in the smaller vessels $R^2_{\text{flow},\Lambda_{\text{S}}}$ in the definition of the total coefficient of determination (6.29) no significant improvements could be achieved. However, the agreement in terms of flow in the entire (resolved and homogenized) vasculature, which will be investigated in the next section, is much better.

6.4.3 Additional Comparisons of the Results of Both Models

Subsequently, the agreement of the hybrid model with the optimized parameters from the previous section is studied in terms of several other quantities. For that, the mean REV IF pressure in the j-th REV is defined as

$$\overline{p^l}(j) = \frac{1}{V_{\text{REV}_j}} \int_{\text{REV}_j} p^l \, dV. \tag{6.31}$$

This is employed to study the absolute and relative mean IF pressure error between the two models in each REV as

$$E^l_{\text{abs}}(j) = \text{abs}\left(\overline{p^l}(j)\big|_{\text{full}} - \overline{p^l}(j)\big|_{\text{hyb}}\right) \quad \text{and} \quad E^l_{\text{rel}}(j) = \frac{\text{abs}\left(\overline{p^l}(j)\big|_{\text{full}} - \overline{p^l}(j)\big|_{\text{hyb}}\right)}{\overline{p^l}(j)\big|_{\text{full}}}. \tag{6.32}$$

Equivalently, the mean blood pressure in the homogenized vasculature of the hybrid model in the j-th REV is given by

$$\overline{p^v}(j)\big|_{\text{hyb}} = \frac{1}{V_{\text{REV}_j}} \int_{\text{REV}_j} p^v \, dV \tag{6.33}$$

and by

$$\overline{p^v}(j)\big|_{\text{full}} = \frac{1}{n_{\text{nodes},\Lambda_S \cap \text{REV}_j}} \sum_{i=1}^{n_{\text{nodes},\Lambda_S \cap \text{REV}_j}} \mathbf{p}^{\hat{v}}[i] \tag{6.34}$$

for the smaller vessels of the fully-resolved model. The latter is simply the mean blood pressure of all $n_{\text{nodes},\Lambda_S \cap \text{REV}_j}$ nodes of the smaller blood vessels which lie inside the j-th REV. This allows the definition of the absolute and relative mean blood pressure error (in the smaller vessels) between the two models in each REV as

$$E^v_{\text{abs}}(j) = \text{abs}\left(\overline{p^v}(j)\big|_{\text{full}} - \overline{p^v}(j)\big|_{\text{hyb}}\right) \quad \text{and} \quad E^v_{\text{rel}}(j) = \frac{\text{abs}\left(\overline{p^v}(j)\big|_{\text{full}} - \overline{p^v}(j)\big|_{\text{hyb}}\right)}{\overline{p^v}(j)\big|_{\text{full}}}. \tag{6.35}$$

Furthermore, the mean value of these error measures over all n_{REV} REVs is denoted by $\overline{(\bullet)}$. Note also that both the mean REV blood and IF pressure vary considerably between different REVs. The pressure difference between single REVs varies in a range of $800 - 1200\,\text{Pa}$ for the IF and a range of $800 - 2000\,\text{Pa}$ for blood. The data of this analysis is collected in Table 6.6. Overall, a remarkable agreement of the mean REV pressures for both blood and IF can be observed in all cases. As in Table 6.5, the SW1222 tumor has the best agreement, but also the GL261 case which previously showed the biggest nodal blood pressure errors in the homogenized vessels is very accurate in terms of mean REV blood pressure. As described above, the error is located mainly on the tips of the smaller vessels, of which the GL261 has the most compared to its network size. Nevertheless, the average blood pressure in the REVs is still matched very well for this and all other cases even though locally the pressure error is larger. These small-scale spatial fluctuations of blood pressures cannot be represented correctly in the homogenized vessels of the hybrid model while macroscopically the average REV pressures show good agreement. Anticipating a validation with experimental data, it is anyhow not possible to perform a point-wise comparison of (blood and IF) pressures such that the average REV pressure is the more relevant and meaningful metric.

Additionally, the volumetric flow between large and small vessels is investigated and the results of both models are compared. In the hybrid model, the flow between large and small vessels is given by the LM field $\lambda = \overset{\hat{v}\to v}{M}$ interpreted as a mass transfer term, or volumetric flow per length, as detailed in Section 6.2.3. Note that this can represent both a flow from large 1D vessels into the homogenized vasculature if locally the pressure in the resolved vasculature is bigger than the homogenized pressure or, vice versa, a flow from the homogenized vasculature

into the larger vessels if the homogenized pressure is bigger than the blood pressure in the 1D vasculature. Consequently, for each REV the flow between the two compartments is given by the integral of the LM field along the part of the larger vessels $\Lambda_\mathrm{L} \cap \mathrm{REV}_j$ inside the specific REV j, or

$$\overset{\hat{v}\to v}{M}(j)\big|_\mathrm{hyb} = \int_{\Lambda_\mathrm{L}\cap\mathrm{REV}_j} \lambda \, ds. \tag{6.36}$$

In the full model, the mass transfer between large and small vessels can directly be evaluated inside the connecting elements of both sets, which are those elements of the smaller vessels where one node is part of Λ_L and the other part of Λ_S. Assuming that the first node is part of the larger vessels and the second one part of the smaller vessels, the flow between large and small vessels in the j-th REV is given by

$$\overset{\hat{v}\to v}{M}(j)\big|_\mathrm{full} = \sum_{i=1}^{n_{\mathrm{ele},\Lambda_\mathrm{L}\to\Lambda_\mathrm{S}\cap\mathrm{REV}_j}} -\frac{\pi R^4}{8\mu^{\hat{v}}}\frac{\partial p^{\hat{v}}}{\partial s} \tag{6.37}$$

as the sum of the volumetric flows in the elements connecting large and small vessels which lie inside the specific REV j. The number of these elements is denoted by $n_{\mathrm{ele},\Lambda_\mathrm{L}\to\Lambda_\mathrm{S}\cap\mathrm{REV}_j}$ in the previous equation. To compare the mass transfer between large and small vessels in both models, a coefficient of determination is again defined as

$$R^2_{\mathrm{flow},\Lambda_\mathrm{L}\to\Lambda_\mathrm{S}} = 1 - \frac{\sum_{j=1}^{n_\mathrm{REV}} \left(\overset{\hat{v}\to v}{M}(j)\big|_\mathrm{full} - \overset{\hat{v}\to v}{M}(j)\big|_\mathrm{hyb} \right)^2}{\sum_{j=1}^{n_\mathrm{REV}} \left(\overset{\hat{v}\to v}{M}(j)\big|_\mathrm{full} - \mu\left(\overset{\hat{v}\to v}{M}(j)\big|_\mathrm{full} \right) \right)^2}, \tag{6.38}$$

with the respective mass transfer terms for the hybrid and the full model for each REV. Once more, $\mu(\bullet)$ denotes the mean of the mass transfer between large and small vessels of the full model over all n_REV REVs.

The reference solution of the fully-resolved model for this volumetric flow per REV varies considerably between the different REVs and both positive values, representing an overall outflow from the larger vessels into the smaller vessels in a specific REV, and negative values, representing an overall inflow into the larger vessels from the smaller vessels in a specific REV, are present. This indicates that in- or outflow from larger to smaller vessels is indeed a meaningful quantity describing the spatially varying flow patterns inside the vascular network. To reproduce this behaviour in the hybrid model variant, a good agreement with the reference solution is desirable. The results for the coefficient of determination $R^2_{\mathrm{flow},\Lambda_\mathrm{L}\to\Lambda_\mathrm{S}}$ are again assembled in Table 6.6. The LS174T case shows the best agreement with the fully-resolved model while the SW1222 case delivers the worst results. This can be attributed to the much higher dispersion of the diameter and, thus, also the flow in the connectivity elements, which have already been studied by the coefficient of variability in Table 6.3. The LS174T case, which has the least dispersed distribution of both values, performs best in matching the flow between larger and smaller vessels in the hybrid model. There is a small decline of the agreement for higher percentages of retained vessels in all cases. However, the flow between large and small vessels is not included in the parameter optimization procedure. Hence, the better performance in terms of the other quantities could be at the expense of this metric.

Finally, the correspondence between the two models in terms of blood flow in the entire vasculature Λ is studied. Previously, in Table 6.5 only flow in the smaller vessels Λ_S, respectively, the homogenized vasculature was investigated. For the full model, the total flow in Λ in each REV in coordinate direction j is calculated as in (6.28), but now both large and small vessels are taken into account. For the hybrid model, the total flow can be obtained as the sum of the flow in the homogenized vessels as given by (6.27) and the flow in the larger, resolved vessels, that is, equation (6.28) evaluated for the larger vessels of the hybrid model. The two quantities are compared in Table 6.6 defining a coefficient of determination for flow in the entire vasculature $R^2_{\text{flow},\Lambda}$ as in (6.26). Evidently, the agreement between the two models is very good and much better than the previously reported agreement of flow in the smaller vessels $R^2_{\text{flow},\Lambda_S}$. This is due to the fact that, as expected, flow is dominated by the larger vessels. The values calculated for flow in the entire vasculature are one to two orders of magnitude larger than those in the small vessels depending on the investigated case. As it is possible to match the pressure in the large vessels very well and, thus, also the flow therein, very good accordance can be achieved for the total flow in both small and big vessels. As flow in the big vessels is decisive for the overall perfusion of the domain and could also be more easily acquired with experiments for further validation this is an encouraging result for the applicability of the hybrid approach. Nevertheless, an enhancement of the correspondence of the hybrid model also in terms of flow in the smaller vessels is demonstrated in the following section.

6.5 Improvements for the Hybrid Model

In this section, several possible improvements for the hybrid model are discussed and one of them is implemented and tested. The most straightforward one would be to define the permeability of the homogenized vessels not as a constant over the entire domain Ω_v but per REV. Instead of an isotropic permeability tensor, one could easily integrate anisotropic effects based on the blood vessel structure inside each REV. Both was done in the hybrid model of Vidotto et al. [266], where a diagonal permeability tensor with different permeabilities in all three coordinate directions was employed. This could potentially augment the agreement in terms of mass fluxes in the homogenized vasculature, which is the main source of error in the hybrid model. However, this was not integrated into the optimization procedure since this could result in overfitting of the chaotic flow in the tumor such that every single boundary condition case would be met very well but with largely different results for the permeability tensors between the cases with distinct flow patterns. With a single scalar permeability the results for the permeability between different boundary condition cases did not fluctuate greatly. Moreover, in a real-world case where only the architecture of the larger vessels is known, it seems unrealistic to deduce the entire permeability field from the limited amount of information.

Instead the model was enhanced by taking information of volume fractions of the smaller vessels into account. The rationale behind this approach is that regions with a higher or smaller microvascular density of small vessels could still be identified whereas the complete structure of the smaller vessels cannot be obtained non-invasively. This information could then be employed to enrich the hybrid model. The overall trend observed in Table 6.5 is that the higher the volume fraction of the homogenized vessels, the larger their permeability. It also reasonable to assume that areas with a higher vascular volume fraction are more permeable to blood flow. Therefore,

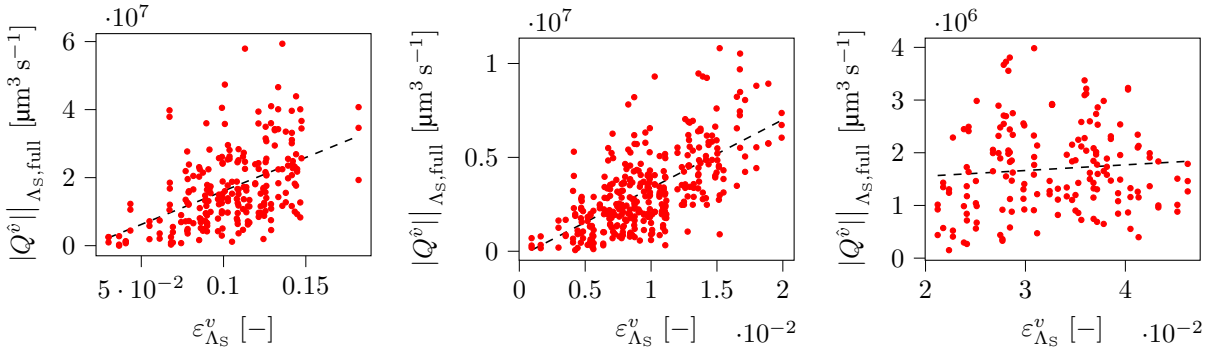

(a) SW1222, $R^2 = 0.50$ (b) LS174T, $R^2 = 0.66$ (c) GL261, $R^2 = 0.08$

Figure 6.10: Dependency of absolute flow in small vessels Λ_S of the full model on volume fraction of small vessels in REVs for one representative case per tumor topology where $10\,\%$ of 1D blood vessels have been retained in hybrid model (dashed lines indicate linear least squares fits with corresponding R^2-values). Figure taken from the author's article [137].

the relationship of the volume fraction of smaller vessels $\varepsilon^v_{\Lambda_S}$ in each REV on the perfusion of the smaller blood vessels in the full model was investigated. Results are shown in Figure 6.10. Here, the absolute volumetric flow in each coordinate direction (calculated as in (6.28) but not taking the flow direction into account) is plotted over the volume fraction of the smaller vessels $\varepsilon^v_{\Lambda_S}$. The clearest picture emerges for the LS174T topology with a good correlation of flow in smaller vessels with their volume fraction. A similar, yet less distinctive trend is present for the SW1222 case whereas no relationship can be observed for the GL261 tumor.

Therefore, inside each REV j the isotropic permeability tensor was defined as

$$\frac{k^v}{\mu^v}(j) \cdot \boldsymbol{I} = \alpha \cdot \varepsilon^v_{\Lambda_S}(j) \cdot \boldsymbol{I}, \tag{6.39}$$

that is, as a simple linear dependency of the permeability in the j-th REV on the volume fraction of smaller vessels in the j-th REV with proportionality constant α. A nonlinear Kozeny-Karman law was also tested, but slightly better results were obtained with the linear fit. Thus, only this linear dependency will be studied hereafter. Next, the optimization of the nonlinear least-squares problem (6.30) is performed for the proportionality constant α. Results are shown in Table 6.7 for the case $10\,\%$, which can be compared with the cases with constant permeability over the entire domain from Table 6.5. A slightly better agreement in terms of flow in the smaller vessels $R^2_{\text{flow},\Lambda_S}$ is obtained and, thus, also for the total coefficient of determination R^2_{tot} for the SW1222 and GL261 case. Compared to that, the correspondence of flow in the smaller vessels is markedly better than the constant permeability case for the LS174T topology. This is coherent with Figure 6.10 where the latter network showed the most evident correlation of blood flow on volume fraction. Thus, one could expect that no significant improvement was possible for the GL261 case where volume fraction and flow seem to be decoupled. However, also for the SW1222 topology, which showed at least a moderate dependency of blood flow on volume fraction, the agreement cannot be increased significantly. Therefore, at least for one of the studied

Network	α [µm^2]	R^2_{L}	R^2_{S}	R^2_{IF}	$R^2_{\mathrm{flow},\Lambda_{\mathrm{S}}}$	R^2_{tot}
SW1222	37.0 ± 5.9	0.988	0.653	0.998	0.189	0.707
LS174T	129.7 ± 10.6	0.928	0.691	0.991	0.362	0.743
GL261	26.1 ± 3.5	0.929	0.245	0.996	0.117	0.572

Table 6.7: Results of the optimization procedure for non-constant permeability depending on volume fraction of smaller vessels. $10\,\%$ of 1D blood vessels have been retained in hybrid model for each tumor topology. Shown are the proportionality constant α relating permeability and blood vessel volume fraction of smaller vessels inside each REV according to (6.39). R^2-values for agreement between both variants in terms of blood pressure in large vessels, blood pressure in small vessels, IF pressure and flow in small vessels is additionally provided. Overall coefficient of determination R^2_{tot} between fully-resolved and hybrid model is calculated according to (6.29). (All data includes mean taken over five different sets of pressure boundary conditions on the 1D network per case). Table taken from the author's article [137].

cases it is beneficial to include blood vessel volume fraction information into the hybrid model while it is not detrimental for the other two.

It also is conceivable that at least preferential directions of smaller vessels can be detected non-invasively even though their complete structure cannot be resolved. A further enhancement of the model could be achieved when taking this information about the anisotropy of smaller vessels into account. However, it is important to emphasize that the whole study is based solely on numerical results. Experimental findings indicate no dependency between blood vessel diameter and flow in tumors [60, 61, 143] and a high vascular density does not automatically imply efficient perfusion, nutrient supply and drug delivery for solid tumors [116]. These properties could make it impossible to deduce permeabilities of blood vessels inside tumors from macroscopic quantities such as blood vessel volume fractions or preferential directions. By contrast, non-invasive measurements of perfusion [59, 255] could prove helpful to enhance the hybrid model.

Similarly, improvements are possible for flow from the larger into the smaller vessels. Equal pressures in resolved and homogenized vasculature were assumed and, thereby, infinite (or at least a very large) permeability governing the flow between the two compartments such that a constraint of equal pressures holds along the resolved 1D vasculature. This has the major advantage that the coupling between resolved and homogenized vasculature is essentially parameter-free. Only the penalty parameter has to be chosen large enough such that a sufficient accuracy in the pressure constraint is achieved as described in Remark 6.4. The GL261 and LS174T case had a less dispersed distribution of the radius in connecting elements and, thus, of the permeability between larger and smaller vessels. For these topologies, the approach could estimate the mass transfer between larger 1D vessels and smaller homogenized vessels more accurately. The SW1222 case had a much higher variability of radius and flow between Λ_{L} and Λ_{S}. In this case, it could be advantageous to employ finite permeabilities to model the mass transfer and assign higher permeabilities to REVs or regions along the larger vessels where many branches go away from the main vessels. However, this would require additional parameterization of the model as well as additional data on regions where a lot of flow from larger into smaller vessels can be expected.

In addition, only very simple algorithms to optimize the parameters of the hybrid model were employed. A much more powerful framework for coarse-graining physical models has been developed by Grigo and Koutsourelakis [98] and demonstrated for flow through porous media. This could also be applied in the present case to infer the optimal parameters of the hybrid model per REV. However, this would require much more microstructural features, such as tortuosity, blood vessel distances or radius data on the smaller homogenized blood vessels to calibrate the hybrid model. Again, it is questionable if this data can be acquired non-invasively and if these parameters are determining blood flow through tumors.

6.6 Summary of the Study and Outlook

In this chapter, a hybrid embedded/homogenized model for computational modeling of solid tumor perfusion was investigated. Its guiding principle is that the complete morphology of vascular networks including blood vessel diameters and topology cannot be acquired with currently available *in-vivo* imaging techniques. Thus, fully-resolved discrete models relying on this data cannot be applied in "real world" scenarios. If, however, the structure of larger vessels constituting the main branches of the vasculature is available, the hybrid representation of the vasculature, where only these larger branches are completely resolved, is a sensible alternative. The coupling between the resolved and homogenized part of the vasculature is realized via a line-based pressure constraint along the 1D larger vessels and enforced by a mortar-type formulation with penalty regularization. This also has the advantage that compared to previous hybrid models no additional parameter – apart from the penalty parameter which has to be chosen large enough – is required to couple the two distinct representations of the vasculature.

The results of the hybrid model were compared with reference solutions generated by a fully-resolved 1D-3D model. For that, three different network topologies extracted from three different tumor types grown in mice were employed. These topologies consist of up to $420\,000$ vessel segments and have dimensions of up to $6\,\mathrm{mm} \times 8\,\mathrm{mm} \times 11\,\mathrm{mm}$. To date, this is the largest and most challenging test case for a hybrid model, especially considering the abnormal and tortuous structure of the networks typical for the vasculature inside tumors. The hybrid model was generated from the fully-resolved model, representative elementary volumes were defined and suitable boundary conditions assigned. The artificially created topologies of larger vessels are representative of real *in-vivo* imaging data sets of larger vessels inside tumors such that it is possible to draw meaningful conclusions for more realistic scenarios where the full topology is not available and a hybrid approach is the only option.

For comparison of the results of the two models, several rigorous metrics were defined involving the blood pressure in both resolved and homogenized vasculature, the pressure in the interstitial fluid and blood flow in the homogenized vasculature. These metrics were then employed to obtain the optimal parameters for the hybrid model and to study its accuracy w.r.t. the fully-resolved one. Very good agreement in terms of blood pressure in the larger vessels and IF pressure was demonstrated. Larger deviations are present for blood pressure and flow in the homogenized vasculature. However, these limitations can be expected since the information on the smaller vessels is not retained in the hybrid model. Overall, the best correspondence was achieved for the SW1222 case which also had the clearest vascular structure and distinction between larger and smaller vessels. All topologies showed a very good agreement in terms of

REV IF pressure and REV blood pressure in smaller vessels with mean deviations in a range of $20 - 70\,\mathrm{Pa}$ and $40 - 110\,\mathrm{Pa}$ respectively $0.7 - 3.8\,\%$ and $1.1 - 2.9\,\%$. It is sufficient to resolve $5 - 10\,\%$ of all blood vessels segments by keeping them in the hybrid model since there is only a marginal improvement of the agreement with the fully-resolved model in terms of all investigated metrics when retaining a higher percentage $(15 - 20\,\%)$ of blood vessels. Concerning the flow between smaller and larger vessels, the error was mainly caused by the large variability of diameter and flow in the connectivity elements between large and small vessels for the SW1222 case. Possibly, this error could be reduced by allowing a varying permeability for coupling the two compartments. By including information about the blood vessel volume fraction of smaller blood vessels into the definition of their permeability tensor a better agreement with flow therein could be achieved for the LS174T case. Nevertheless, the abnormal vascular structure and blood flow patterns of tumor vasculature could impede this approach.

Several other potential improvements were discussed and remain subject to future work. Furthermore, studies of drug delivery or nutrient transport lie at hand, especially since the framework is already capable of including species transport in all model compartments as demonstrated in the previous chapters. Such investigations could ultimately enhance our understanding of the limitations of current drug delivery strategies and aid in devising more targeted therapies.

The next step towards a more realistic or even clinical usage of hybrid computational models for tissue perfusion is to devise a strategy which combines data which is available non-invasively [150]. Faced with such a scenario, where a hybrid model is the only applicable option since the entire network topology is not known, the methods and metrics developed here could be applied in the following way:

1. Gather all physiological data, which can be accessed via *in-vivo* measurements for the specific case. For instance, this could be tissue perfusion, hypoxic areas, REV or point-wise measurements of pressure or flow, volume fractions of homogenized blood vessels or their preferential direction and the transport of tracer molecules through the domain.

2. Define the computational domain of interest as the embedded larger vessels and a surrounding domain of homogenized vasculature following the extent of the tumor. If available, include the information about volume fractions and preferential directions of smaller blood vessels in the definition of the permeability tensor.

3. Formulate an optimization problem similar to (6.30) to match the available information about transport, e.g., REV or point-wise flow and pressure data. However, not only the parameters of the homogenized vasculature would be part of the optimization as in this contribution but also the large majority of the (homogenized or resolved) pressure boundary conditions, which are additionally unknown. Note however, that far less boundary conditions compared to a fully-resolved setting need to be applied.

4. Employ the obtained flow state for *in-silico* studies of drug delivery or the optimization of treatment strategies.

7 Summary and Outlook

7.1 Summary

This thesis introduces a comprehensive computational framework for continuum-based modeling of (a-)vascular tumor growth. A number of highly relevant (bio-)physical phenomena are included and studied such as ECM deformation by the growing tumor mass, oxygen consumption, hypoxia, necrosis, TAF production, fibronectin uptake, chemo- and haptotaxis-driven angiogenesis, blood vessel collapse and regression, elevated IF pressure in the tumor core as a result of the combination of increased leakage from blood vessels and inhibited drainage by lymphatic vessels, mass transport of nutrients or drugs (both in vasculature and IF) and nanoparticle-mediated hyperthermia.

The model is based on a continuum description of solid deformation, fluid flow and transport processes in multiphase porous media. More specifically, it builds on TCAT to obtain a consistent macroscale formulation. Based on previous work [224, 225, 229–233, 235], the governing equations on the macroscale were introduced in **Chapter 2**. They are the building blocks for the multiphase tumor growth model, namely, the balance of momentum of the solid phase, the balance of mass of the solid phase, of the fluid phases and of species in both solid phase and fluid phases, and the energy balance. The latter one is, however, only needed if hyperthermia treatment is simulated. All equations are formulated in a general ALE setting allowing large deformations of the computational domain including the embedded vascular network.

These equations were then used to build the different model variants in **Chapter 3**. The avascular model corresponds to the original work of [224, 225, 229–233, 235] re-formulated to a consistent ALE description. Subsequently, three different vascular variants were developed, characterized by a homogenized, a discrete and a hybrid representation of the vascular network, respectively. In the homogenized description, it is incorporated as an additional porous network with blood flow and species transport such that a double-porosity formulation emerges. In the discrete formulation, it is embedded as a 1D inclusion into the surrounding tissue domain. The balance of mass of blood and species transport are solved inside the 1D domain and coupled with the encompassing IF with 1D-3D (fluid and species) mass transfer terms. Two coupling concepts for evaluating these terms are employed: a centerline-based and a surface-based variant with line respectively surface source terms in the mass balances of the 3D domain. The line-based method was shown to be problematic if the diameter of the 1D inclusion becomes smaller than the element size in the 3D domain due to the involved singularity of the line source, see Appendix A.1. Nevertheless, it can still be applied to the majority of practical problems where this is not the case. The third variant employs a hybrid embedded/homogenized representation of the vasculature. Its guiding principle is to resolve only the larger vessels by embedding them as 1D inclusions and to homogenize the smaller ones. Coupling of the two representations is achieved via constraints of matching blood pressure and matching species mass fractions be-

tween the resolved and the homogenized portion of the vasculature. Such an approach can be very advantageous as it relies only on *in-vivo* imaging data, that is, the structure and morphology of the larger blood vessels.

The computational solution procedure for the entire model was presented in **Chapter 4**. Its governing equations were discretized in time using the one-step-θ-scheme and in space using finite elements. A special focus was put on the interactions of the embedded 1D vasculature with the surrounding tissue domain which are the transvascular exchange terms, the constraint of matching blood pressure or species mass fraction in the 1D and the homogenized representation of the vasculature, and blood vessel diameter adaptation and collapse. A 1D segment-based integration scheme was developed for the centerline-coupled variant and a 2D element-based integration scheme for the surface-coupled variant. Based on mesh tying approaches, two different penalty-based constraint enforcement strategies, a mortar penalty and Gauss-point-to-segment scheme, were proposed to couple the homogenized and the resolved representation of the vasculature in the hybrid variant. The latter one may suffer from overconstrainment as demonstrated in Appendix A.2. Special cases of collapsed 1D elements or free-hanging network sub-parts occurring during blood vessel collapse and how to treat them from a modeling and implementation perspective were illustrated. After time and space discretization, a coupled problem of five nonlinear residuals (for the most general case) emerges. It may be grouped into three distinct fields, namely, ECM deformation, (1D and 3D porous) flow and (1D and 3D) species transport. The residuals are consistently linearized for a Newton-Raphson solution procedure with the exception of some terms of minor importance. The coupling between the distinct fields may either be resolved by a fully-monolithic, a hybrid monolithic-partitioned or two slightly different partitioned solution procedures. Sophisticated block preconditioners are available in the framework to solve the resulting linear system of equations, which has a 5×5 block pattern for the most general fully-monolithic case, in combination with iterative solvers.

The flexibility and applicability of the developed computational framework was demonstrated by various numerical examples in **Chapter 5**.

First, the four different algorithms for solving the nonlinear three-field problem were investigated using a representative numerical benchmark example. For standard parameters, the fully-monolithic approach was faster than all other variants with a speed-up of 8.4 compared to the nested-partitioned, 4.6 compared to the sequential-partitioned and 1.5 compared to the monolithic-partitioned algorithm. Its superiority was further demonstrated over a wide range of parameters. The strong coupling between fluid phases and ECM deformation limits the applicability of partitioned schemes. Among the two investigated schemes, the sequential-partitioned algorithm should be the method of choice as a smaller number of total nonlinear solver calls is required. Only if the entire solution time is dominated by solving species transport, the nested-partitioned scheme may be reasonable. Finally, for an undeformable ECM, a corresponding monolithic (fluid-species) solution scheme is still more efficient. A partitioned one can be more competitive though.

Subsequently, numerical examples of increasing complexity were presented. The interplay between tumor growth and angiogenesis was investigated using the variant with homogenized vasculature. It was demonstrated how low oxygen levels lead to TAF production and how the resulting chemotaxis-driven angiogenesis enables fast tumor progression. Thereafter, the influence of haptotaxis and blood vessel remodeling was incorporated leading to a better, respectively, worse vascularization, which, in turn, influences tumor growth. A second numerical example was

devised to study nanoparticle-based drug delivery and hyperthermia treatment. First, vascular tumor growth was simulated to obtain a physiologically reasonable transport phenotype for solid vascular tumors with elevated IF pressure and decreased blood perfusion in the tumor center and a steep pressure drop across the tumor boundary. Nanoparticles of various sizes were employed for an *in-silico* study of transport through the tumor micro-environment. The EPR effect was observed as they accumulated mainly in the tumor region, however, the active pressure gradient led to a concentration at the tumor boundary and only a slow penetration into its interior. Smaller molecules with higher diffusivities were also cleared more rapidly such that the larger molecules with weights of $10\,\mathrm{kDa}$ and $70\,\mathrm{kDa}$ had the highest drug delivery efficiency. This insight is also supported by corresponding experimental data [67]. The result of the nanoparticle transport study was then further employed to demonstrate the model's capabilities to study hyperthermia treatment. Temperature ranges corresponding to mild hyperthermia and thermal ablation were reached depending on the specific absorption rate of the nanoparticles. Next, the model with discrete representation of the vasculature was used to study tumor growth inside a 2D and a 3D vascular network. A co-opting growth pattern was present in both examples. Cuffs of viable tumor cells developed along the blood vessels where oxygen concentration was highest. In the 2D example, the developed methodology for blood vessel collapse and regression was additionally studied which resulted in a vascularization pattern frequently observed during vascular tumor growth: only some larger internal vessels penetrated into the tumor core whereas smaller vessels collapsed and regressed. Finally, the hybrid variant was used to illustrate the classical model of an angiogenic switch. Angiogenesis occurred laterally from pre-existing blood vessels which were coupled with blood flow and species transport in the neovasculature by the mortar-type method with penalty regularization. It was demonstrated how angiogenesis deregulates mass transport in the tumor microenvironment in favor of rapid tumor growth.

A validation of the vascular growth model with experimental data was beyond the scope of this thesis. However, the resulting IF pressure ranges and profiles, oxygen, necrotic cell and nanoparticle distributions, typically observed vascularizations, the time scales of angiogenesis and tumor growth patterns (angiogenic switch and co-option) could be reproduced when employing sensible parameter values. Thus, the general applicability of the developed group of models for simulating vascular tumor growth was proven. The next steps towards a more detailed validation with experimental or clinical data will be outlined below.

A standalone and major contribution of this thesis is the hybrid embedded/homogenized representation of the vasculature. It may not only be employed for vascular tumor growth but also for perfusion through solid tumors as demonstrated in **Chapter 6**. Therein, its results were compared with reference solutions of a fully-resolved discrete approach for three data sets of large vascular networks inside solid tumors. As stated before, its big advantage is that it requires only non-invasively available data. A detailed summary of the conducted study and an outlook into future work can be found in Section 6.6.

7.2 Outlook

In the following paragraphs, several possible extensions and a road map for validation of the model, in particular with respect to the involved uncertainties and currently available *in-vivo* data will be presented.

Exploiting the Potential of the Coupled Framework via Further Extensions One of the unique features of the presented framework is the full coupling between all model components and its flexibility for extensions. Hence, it is particularly well suited to incorporate additional phenomena involving the interaction of different (bio-)physical fields or processes.

The interplay between cancer progression and the ECM has recently gained a lot of interest from the biophysical research community as outlined in Chapter 1. Nevertheless, its causes and effects are not well-understood. Simulations are needed to complement experimental findings. The model can easily be enhanced by ECM remodeling, stiffening and its interaction with tumor growth. For example, the degradation of the ECM by matrix metalloproteinases can be integrated, see the single cell model of [271, 272] for details. In a similar fashion, ECM deposition, which was already partly addressed by Santagiuliana et al. [224], may be studied. Further effects of matrix stiffening, increased cross-linking and remodeling by the interaction with the growing tumor leading to a more malignant phenotype [47, 81, 144, 191] can be captured by suitable constitutive laws for the ECM, for which only simple hyperelastic behaviour was assumed throughout this thesis. Different ECM components such as collagen can be included as species in the ECM to obtain its composition by the interaction of dissolution, deposition and cross-linking. Material laws depending on the ECM composition can be formulated. An additional implication of ECM deposition and remodeling is drug resistance induced by a denser ECM, which can also be considered. An improvement in modeling the mechanical interaction with the surrounding tissue can be achieved by more realistic boundary conditions for the solid phase displacement, which for the numerical examples presented here was either fixed or left free. The influence of the surrounding tissue can be incorporated by a spring-type boundary condition.

Supplemental theoretical derivations from TCAT [170] can improve the model's handling of interfaces and, especially, cell-cell and cell-matrix interactions.

An additional straightforward extension is anti-angiogenic therapy. The original intention of this type of treatment was to reduce tumors' access to nutrients, thereby, starving them to death [75]. However, this potential has not yet been realized due to insufficient efficacy and development of resistances [37, 132]. A more recent finding is that anti-angiogenic therapy may also lead to vascular normalization [37, 116–118], that is, a transformation of tumor blood vessels into a more structurally and functionally normal vasculature. This is accompanied by better perfusion and a reduction of IF pressure and may be a promising strategy to increase the efficiency of drug delivery. Conceptually, this can be included in the model as follows: anti-angiogenic agents are an additional species, which is transported by the vasculature and the IF just as other drugs. In the homogenized variant, their effect on tumor vasculature can be incorporated by a reduction of the vascular volume fraction and decreased leakage into the IF via a smaller hydraulic conductivity. In the discrete variant, a regression of redundant blood vessels and a stabilization of larger vessels leading to more efficient blood flow and decreased leakage are conceivable. The results of such numerical studies on anti-angiogenic therapy can then be employed to examine if the access to nutrients may indeed be diminished leading to tumor regression or rather to more aggressive tumor growth fueled by hypoxia. The impact of vascular normalization on the efficiency of a subsequent therapy with a conventional or nanoparticle-based drug after barriers such as increased interstitial fluid pressure have been removed is worth studying as well.

Ancillary effects of hyperthermia treatment such as increased perfusion and oxygenation, making tumors more accessible to other therapies like radio- or chemotherapy [43, 259], can

easily be integrated into the coupled framework and its interaction with each other can be explored. Similarly, the release of nanoparticle-bound drugs triggered by external energy sources and the combined effect of hyperthermia and chemotherapy may be of interest.

Furthermore, guidelines can be developed for the design of more potent delivery systems, e.g., size-altering nanoparticles achieving optimal *in-vivo* performance: these are larger nanoparticles with longer blood half-life which disassemble into smaller particles with improved penetration through tumor tissue [142, 149]. This can be taken into account by several nanoparticle species of different sizes, diffusivities and vascular permeabilities with interrelating mass transfer terms such that smaller particles are generated by the break-up of larger ones.

So far, the cytoxicity of drugs has not been yet been studied in detail. A natural extension is to include their effect as a killing term acting on tumor cells or by decelerating tumor growth [50].

Another novel therapeutic strategy using nanoparticles is magnetic drug targeting [2, 3, 119]. Via the application of an external magnetic field, magnetic nanoparticles decorated with anti-cancer drugs can be guided to the tumor site after intra-arterial injection. Thereafter, the therapeutic desorbs from its magnetic carrier. Compared to traditional small drugs or passive targeting with the EPR effect, this enables a higher drug accumulation inside the tumor with minimal systemic side effects. The effect of the external magnetic field can be included as a flux term in the species mass balance equation on the macroscale. The interaction with blood flow, IF flow and diffusion and the desorption of the cytotoxic drug can be simulated to guide drug design. Moreover, drug delivery can be improved by *in-silico* studies on the optimal magnetic field depending on the extent of the tumor, the position of the magnets and their strength.

Sensitivity Analysis and Model Calibration Mirroring the numerous influences on *in-vivo* cancer progression, the different model types contain a large number of biological or physical parameters as specified in Appendix C. While some of them can be considered fixed, such as the density of water, others may be subject to uncertainties. This may be either because they cannot be measured with sufficient accuracy in experiments or because they vary between different tumors, patients or even intra-tumorally due to the intrinsic heterogeneity of cancer. Hence, it is indispensible to perform a global *sensitivity analysis* on the model to quantify and rank the impact of the input parameters' uncertainty which is propagated to the model output [222, 223]. Thereby, the most influential parameters and their interaction effects may be elucidated. Thus, the understanding of the model can be enhanced, it can be simplified by fixing non-influential parameters and further calibration can be eased by focusing on the most important parameters. Ideally, this should go hand in hand with experimental validation of the model to set the focus on those aspects and parameters of the numerical model which can actually also be influenced by experiments. An efficient strategy to perform sensitivity analysis if many parameters are involved is to first use a simple screening method, e.g., the *elementary effects* method by Morris [175] and Campolongo et al. [35]. Then, more insightful *variance-based* methods can be applied on the subset of influential parameters [222, 223]. Using this methodology, first studies on the sensitivity of the avascular model were conducted in the Master's thesis of Rodenberg [219]. Further research should be concerned with the vascular variants, where even more parameters are present.

After identifying the most influential parameters, the model has to be calibrated, that is, its parameters have to be identified in order for the model output to match corresponding experi-

ments. This is a classical example of an *inverse problem* [122, 254], for which suitable methods are outlined in this paragraph. In the next one, the focus lies on the required experimental data. *Bayesian* inference provides a unifying framework for model *calibration*, *validation* and *uncertainty quantification*. Thereby, the mathematically ill-posed parameter identification problem is reformulated as a statistical inference task for the model input parameters. This results in a posterior distribution for the latter rather than an inexpressive point estimate as delivered by classical deterministic treatments of the identification process, e.g., in form of a least-squares optimization problem. The accuracy and robustness of the framework for uncertainty propagation is crucial considering the inherently stochastic nature of cancer. First efforts to combine cancer modeling with a Bayesian methodology have been made by [102, 121, 152, 153, 185] but most of the work has been theoretical without a critical validation of the models due to the lack of well-suited experimental or clinical data. The software QUEENS [24], which was already applied in Chapter 6, provides a computational framework for uncertainty quantification, Bayesian optimization and inverse problems and will be used for the calibration and validation of the tumor growth model in future work.

The probabilistic methods mentioned above can require thousands of forward evaluations of the tumor growth model which might become prohibitively expensive or even unfeasible for large problems. To reduce the computational cost, multi-fidelity approaches have recently become popular. Their goal is to harness information from computationally cheap, low-fidelity approximations of a more complex model [23]. One such approach is the Bayesian multi-fidelity Monte Carlo method [21, 22, 133], whose general idea is to perform most of the sampling on the cheap, low-fidelity approximation with only a few evaluations of the high-fidelity model. The only demand on the low-fidelity model is that it exhibits a statistical dependency with the output of the high-fidelity model. To fully exploit its advantages, it is important that the computational cost of running the low-fidelity approximation is much smaller than the one of the high-fidelity model. Apart from classical multi-fidelity scenarios such as a coarser mesh [22], lower order polynomial degrees in the FE discretization or a lower floating point precision for the low-fidelity model [182], several multi-fidelity scenarios are conceivable for the developed group of tumor growth models. For instance, deformability can be neglected as a more efficient approximation of the computationally expensive ALE formulation on a moving mesh. Similarly, the homogenized variant may serve as a low-fidelity model version of the discrete or the hybrid variant. For instance, the radially symmetric example for vascular tumor growth employed in Section 5.3, whose run-time is several minutes, can be interpreted as a cheap, low-fidelity approximation of the 3D model with discrete representation of the vasculature from Section 5.4 with a computational run-time of several hours. This can enable efficient uncertainty quantification, sensitivity analysis and calibration of the much more complex discrete model variant.

Towards a Validation using a Multi-Modal Approach A myriad of mathematical and computational approaches has been proposed for modeling cancer. However, validation with clinically relevant or, at least, experimental data is still pending. This is due to the fact that a proper validation would require data at a spatial resolution which is not yet possible with state-of-the-art imaging techniques, especially not *in-vivo* and at multiple time points [294]. The present group of tumor growth models has a huge and unique potential to include clinically relevant patient-specific data as it strives after a mechanistic description of cancer with a clear descrip-

tion of biologically and physically relevant processes. Artificial components such as a generic nutrient species are not necessary. Ideally, it would require the spatio-temporal distribution of tumor cells, host cells, necrotic cells, vascular volume fraction, IF pressure, oxygen and other relevant species such as drugs or TAFs and the ECM displacement field in the domain of interest. This kind of high-resolution data which is required for physics-based tumor growth models is currently not available even though a huge amount of data has been collected for cancer [218].

The alternative, which is proposed here instead, is a multi-modal validation, i.e., an approach to combine available experimental or imaging data from different sources. Such data can for example come from elastography [162], point-wise measurements of tissue deformation or stress [236], the visualization of transport through tumor tissue at the currently possible spatial resolution [150], the vascularization pattern in the domain of interest [236, 252] and imaging of the oxygen distribution [150] with corresponding hypoxic and necrotic zones. A multi-physics approach such as the present tumor growth model combining deformation, fluid flow and species transport seems to be ideally suited to handle such scenarios where data from single sources is incomplete or not accessible, especially at the resolution required to parametrize a computational model. However, via the combination of multiple sources of data, a much clearer picture emerges. For instance, IF pressure cannot be measured over large domains but only at specific points. Combining these measurements with imaging data on the vascular volume fraction, flow in the larger blood vessels and/or the distribution of an injected drug which will not reach areas of higher IF pressure can provide a suitable data base to investigate and validate a transport model through tumor tissue as applied in Chapter 6. A similar scenario can be to obtain the solid stress field indirectly by its induced compression of blood vessels and the concurrent reduction of their diameter [236] to validate the solid phase material and the stress generated by the growing tumor. Obviously, the validation has to be performed and accompanied by the methods outlined in the previous paragraph to quantify the associated uncertainty.

Finally, further advances in biomedical imaging will contribute to a higher quality of the data needed for validation. An emerging field is *theranostics*, that is, combining therapy with diagnostics, for example via nanoparticles which can simultaneously be used to image the extent of a tumor and to deliver drugs [91].

Major contributions to the mechanistic modeling of tumor growth have been made in this thesis. The ultimate goal of patient-specific predictions of cancer progression being one day as common and reliable as weather forecasts are nowadays, may seem like an almost impossible endeavour. Nevertheless, the tremendous challenges are outweighed by the huge potential of predictive cancer models and science has proven over centuries that, in the long term, it is capable of previously unimaginable achievements.

A Additional Numerical Examples

A.1 Comparison of Different 1D-3D Coupling Variants and Convergence Tests

In this section, a comparison of the two different coupling variants employed in this thesis, namely, centerline coupling and lateral surface coupling, is performed. Both approaches are also classified w.r.t. previous work on such problems of mixed dimensionality. For that, a model problem whose governing equations are

$$-\frac{\pi R^4}{8\mu_{\hat{v}}}\frac{\partial^2 p^{\hat{v}}}{\partial s^2} = -\overset{\hat{v}\to l}{M} \qquad \text{on } \Lambda_0, \tag{A.1}$$

corresponding to blood flow and

$$-\Delta p^l = \delta_{\Lambda_0/\partial\mathcal{D}_0}\overset{\hat{v}\to l}{M} \qquad \text{in } \Omega_0, \tag{A.2}$$

corresponding to flow in the surrounding tissue domain, i.e., in the IF. A simple mass transfer term

$$\overset{\hat{v}\to l}{M} = \kappa\left(p^{\hat{v}} - p^l\right) \tag{A.3}$$

depending on the pressure difference between embedded blood vessels and IF is employed. Thus, for lateral surface coupling the terms

$$\left(\delta p^{\hat{v}}, \kappa\left(p^{\hat{v}}(s) - p^l\left(\boldsymbol{x}(s,\gamma)\right)\right)\right)_{\partial\mathcal{D}_0} \quad \text{and} \quad -\left(\delta p^l, \kappa\left(p^{\hat{v}}(s) - p^l\left(\boldsymbol{x}(s,\gamma)\right)\right)\right)_{\partial\mathcal{D}_0} \tag{A.4}$$

appear in the corresponding weak forms. For centerline coupling, they simplify to

$$\left(\delta p^{\hat{v}}, \pi D_0 \cdot \kappa\left(p^{\hat{v}}(s) - p^l\left(\boldsymbol{x}(s)\right)\right)\right)_{\Lambda_0} \quad \text{and} \quad -\left(\delta p^l, \pi D_0 \cdot \kappa\left(p^{\hat{v}}(s) - p^l\left(\boldsymbol{x}(s)\right)\right)\right)_{\Lambda_0}. \tag{A.5}$$

The employed mass transfer term allows a comparison with previously developed 1D-3D coupling formulations. Often subtle but important differences between the various formulations are present which will be discussed hereafter. A more extensive overview is also given in the thesis of Koch [125, Chapter 6]. There, two criteria are proposed to categorize the different approaches, namely, (1) how the source term of the blood vessels is distributed in the domain (line, surface or volume source) and (2) the type of evaluation and/or reconstruction of variables of the porous domain problem to evaluate the source term.

In the centerline variant, a line source term is employed and the variables of the porous domain are evaluated along the centerline of the inclusion. As previously discussed, this is problematic since the employed line source leads to a singularity of the solution along the centerline of the inclusion. Hence, the pressure (or mass fraction) at the centerline $p^l\left(\boldsymbol{x}(s)\right)$ is not defined

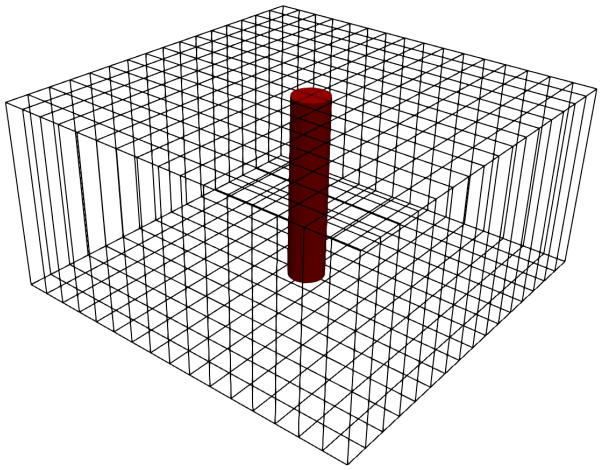

Figure A.1: Domain employed for convergence tests – diameter of inclusion is 0.2 and exemplary mesh with mesh size $h = 0.125$ and 16×16 elements is shown.

and can, strictly speaking, not be employed. Nevertheless, in a discretized setting where the mesh size is sufficiently larger than the diameter of the inclusion, it is still a valid alternative and corresponds to the lumped approach of D'Angelo [52]. To circumvent this problem, an alternative formulation was proposed in the foundational works of [51–53]. The contributions to the employed weak form read as

$$\left(\delta p^{\hat{v}}, \pi D_0 \cdot \kappa \left(p^{\hat{v}}(s) - \overline{p^l}(s)\right)\right)_{\Lambda_0} \quad \text{and} \quad -\left(\delta p^l, \pi D_0 \cdot \kappa \left(p^{\hat{v}}(s) - \overline{p^l}(s)\right)\right)_{\Lambda_0} \tag{A.6}$$

where $\overline{p^l}$ denotes the average pressure along the perimeter of the inclusion calculated as

$$\overline{p^l}(s) = \frac{1}{\pi D_0(s)} \int_0^{\pi D_0(s)} p^l(\boldsymbol{x}(s,\gamma)) \, \mathrm{d}\gamma. \tag{A.7}$$

Thus, the mass transfer is evaluated along the centerline and represents a line source in the porous domain but the average value of the porous medium domain is taken to reconstruct the pressure in the mass transfer term. This leads to a well-posed system for which convergence in weighted or local norms can be shown [53, 129].

The surface-coupled variant introduces a surface source into the governing equations of the 3D domain and the variables of the porous medium domain are evaluated directly at the lateral surface of the embedded network. In the original work discussing this approach [130], a slightly different version was derived by splitting the values at the lateral surface in the average along the perimeter (A.7) plus small fluctuations. This results in the following contributions:

$$\left(\delta p^{\hat{v}}, \pi D_0 \cdot \kappa \left(p^{\hat{v}}(s) - \overline{p^l}(s)\right)\right)_{\Lambda_0} \quad \text{and} \quad -\left(\delta \overline{p^l}, \pi D_0 \cdot \kappa \left(p^{\hat{v}}(s) - \overline{p^l}(s)\right)\right)_{\Lambda_0}. \tag{A.8}$$

Compared to (A.6), the perimeter-average is now also performed for the test functions. Note that both these variants also include an integral along the perimeter of the inclusion as the average (A.7) has to be numerically evaluated. However, the version (A.8) has two distinct disadvantages. First, the numerical evaluation is quite complex. At a specific position s along the centerline, all GPs defined on the lateral surface for evaluating the product of averaged test functions

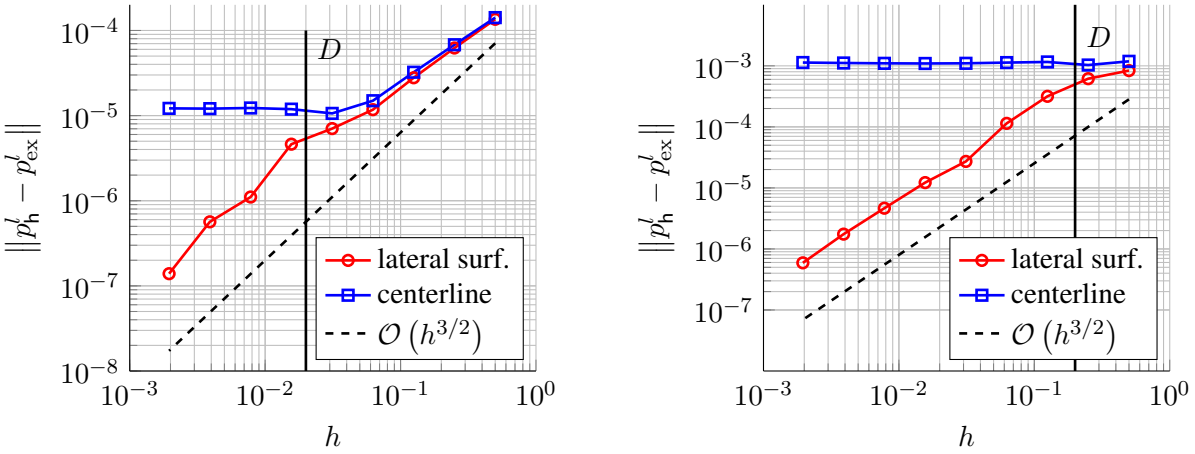

(a) $D = 0.02$ (b) $D = 0.2$

Figure A.2: Convergence of different 1D-3D coupling variants

for the second term in (A.8) interact with each other. This implies that a local assembly of one pair of a 1D element and a 3D element is not possible. Second, and related to the first issue, as the GPs interact with each other, also different DOFs of distinct elements all along the perimeter contribute entries in the coupling matrices which leads to much denser patterns. Thus, the lateral surface coupling variant (A.4), which was also employed in combination with a finite volume discretization in [131], is preferable. Finally, volume source terms with smoothed approximations of the Dirac delta distribution via kernel functions have been introduced by [125–127] but are not further studied here.

In the following, the convergence behaviour of the two applied approaches in this thesis is illustrated with the model problem (A.1)-(A.3). For that, an example originally presented by Köppl et al. [130] is repeated. Here, it is adapted to a 3D domain, where a single blood vessel is embedded into a cuboid of dimensions $2 \times 2 \times 1$. The domain is depicted in Figure A.1. The blood vessel lies along the z-axis at the origin of the domain in the middle of the block. The pressure value is fixed to $p^{\hat{v}} = 1$ along the entire line which is discretized with a single 1D element. The exact analytical solution for this quasi 2D example is given by

$$p_{\mathrm{ex}}^l(\boldsymbol{x}) = \begin{cases} \frac{\kappa}{1+\kappa} \cdot \left(1 - R \cdot \ln\left(\frac{r(\boldsymbol{x})}{R}\right)\right), & r(\boldsymbol{x}) > R \\ \frac{\kappa}{1+\kappa}, & r(\boldsymbol{x}) \leq R \end{cases} \tag{A.9}$$

with

$$r(\boldsymbol{x}) = \sqrt{x \cdot x + y \cdot y}. \tag{A.10}$$

The IF pressure values at the outer surfaces of the block are fixed by a Dirichlet condition to the appropriate values of (A.9). The sole parameter of the problem is set to $\kappa = 0.1$.

The L^2-error of the numerical solution of the IF pressure p_{h}^l is evaluated as

$$\left\|p_{\mathsf{h}}^l - p_{\mathrm{ex}}^l\right\| = \sqrt{\int_\Omega \left(p_{\mathsf{h}}^l - p_{\mathrm{ex}}^l\right) \cdot \left(p_{\mathsf{h}}^l - p_{\mathrm{ex}}^l\right) \, \mathrm{d}V} \tag{A.11}$$

and its convergence for refining the mesh of the 3D domain for inclusions with two different diameters, namely 0.2 and 0.02, is studied in Figure A.2. For lateral surface coupling, the error converges with a rate of $h^{3/2}$ as predicted and shown by Köppl et al. [130]. Better convergence cannot be expected as the pressure solution (A.9) exhibits a kink at the lateral surface of the inclusion. Nevertheless, this could be remedied with a graded or δ-resolving mesh at the interface of the embedded tube [130] to obtain second order convergence in the L^2-norm. However, as this contradicts the major benefit of independent 1D and 3D meshes, this approach is not further followed. As previously studied by D'Angelo [52], the centerline coupling variant converges only if the diameter is smaller than the mesh size. Then, its results are almost equivalent to the surface-coupled variant. For smaller mesh sizes, convergence cannot be achieved due to the involved singularity. This has recently also been investigated in the analogous solid mechanics problem of embedding thin 1D structures, i.e., beams, into 3D solid volumes with similar results [246]. However, for practical problems of the tumor growth model, also smaller mesh sizes than the diameter of the vascular networks seem to provide acceptable results. For instance, in [136] the centerline variant was employed using a mesh size of $h = 0.01\,\mathrm{mm}$ and the diameter of the network was $D = 0.015\,28\,\mathrm{mm}$. Macroscopically, no difference in the results was observed when re-calculating the example with the surface-coupled variant in Section 5.4.

A.2 Comparison of GPTS and MP Constraint Enforcement

A validation and comparison of the GPTS and MP constraint enforcement strategies is performed in this section, which is taken from the author's article [136]. For that, the model has been simplified by neglecting any deformability and solving only the equations

$$-\frac{\pi R^4}{8\mu_{\hat{v}}}\frac{\partial^2 p^{\hat{v}}}{\partial S^2} = 0 \qquad \text{on } \Lambda_0, \tag{A.12}$$

which is a simplified version of blood flow in the 1D reference domain (3.79) without mass transfer into the IF, and

$$-\boldsymbol{\nabla}_0 \cdot \left(\frac{k^v}{\mu_v}\boldsymbol{\nabla}_0 p^v\right) = 0 \qquad \text{in } \Omega_0, \tag{A.13}$$

which is a simplified version of blood flow in the 3D reference domain (3.47) with constant vascular volume fraction and without mass transfer to another phase, together with the constraint

$$g = p^{\hat{v}}(s,t) - p^v(\boldsymbol{x}(s),t) = 0 \qquad \text{on } \Lambda_0 \tag{A.14}$$

i.e., the line-based constraint equation (3.110) for pressures. Figure A.3 depicts the computational domain which is used to solve these equations. A straight blood vessel with radius $R = 0.005$ is embedded into a porous block with dimensions $1 \times 1 \times 1$. Its endpoints are $[-0.5, -0.35, -0.35]$ and $[0.5, -0.35, -0.35]$ and the origin of the domain lies in the middle of the block. The permeability is set to $k^v = 1 \cdot 10^{-7}$ and the viscosities are $\mu_v = \mu_{\hat{v}} = 1.0$. A Neumann boundary condition is applied on the lower left end of the vessel in Figure A.3 and on the upper right end the pressure is set to zero. The 3D block only carries no-flux boundary conditions. It is discretized with a regular grid of $10 \times 10 \times 10$ trilinear elements while the 1D

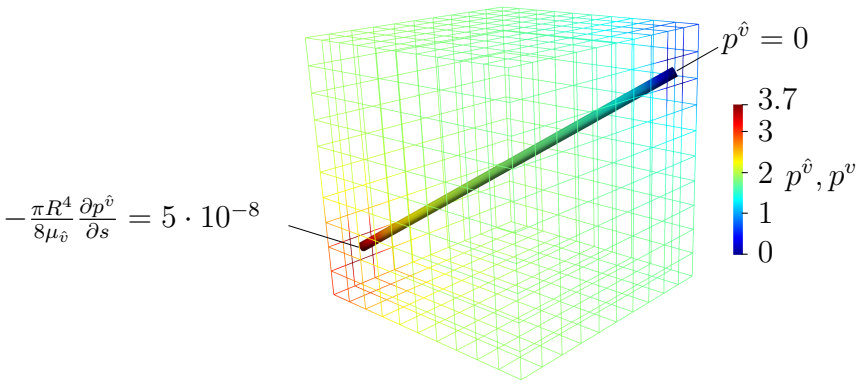

Figure A.3: Computational domain and pressure solution of porous block with straight inclusion. MP approach with $\epsilon_{\text{MP}} = 10^{-1}$ is applied to couple pressures on both sides (radius of 1D elements not to scale). Figure taken from the author's article [136].

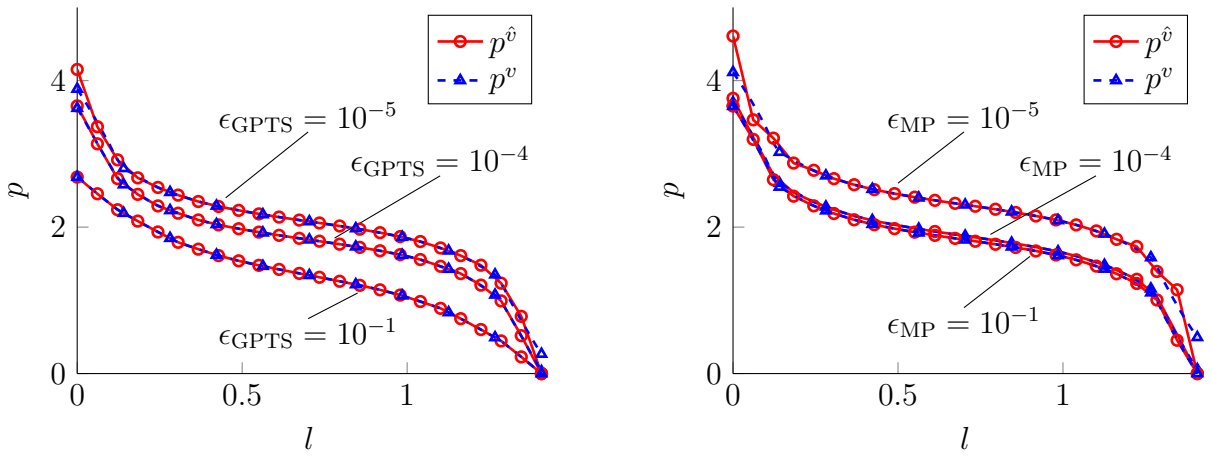

(a) Gauss-point-to-segment

(b) Mortar penalty

Figure A.4: Comparison of coupling approaches with different penalty parameters (red circles denote 1D nodal values). Figure taken from the author's article [136].

domain is discretized with 23 equally spaced linear elements such that the two discretizations are non-conforming. As the element size in the 3D domain is larger by a factor of 10 than the diameter of the inclusion, the centerline variant is employed.

Figure A.3 illustrates the pressure distribution in both domains. For a more detailed investigation, the pressures on the 1D domain $p^{\hat{v}}$ and in the 3D domain p^{v} along the inclusion Λ_0^{h} are plotted in Figure A.4. The chosen penalty parameters are at least two orders larger than the characteristic order of magnitude defined by the permeability k^{v}, which leads to good fulfillment of the constraint for all depicted values. The advantage of the MP formulation compared to the GPTS approach becomes evident from these plots. For very large values of the penalty parameter the latter formulation becomes overconstrained due to a lack of inf-sup stability. When increasing the penalty parameter it converges towards a collocation method where the discrete

constraint has to be fulfilled at every Gauss point. In this case the number of discrete constraints is too high for the number of discrete degrees of freedom [226]. No convergence towards a physically reasonable result can be expected for $\epsilon_{\mathrm{GPTS}} \to \infty$ due to the overconstraint. Indeed, if the penalty parameter is chosen even higher than the values shown in Figure A.4a a linear pressure drop from inflow to outflow emerges since this is the only solution which satisfies the constraint (A.14) at every Gauss point.

By contrast, the MP method converges to the solution of the Lagrange multiplier method. No visible difference in the result is present for penalty parameters larger than $\epsilon_{\mathrm{MP}} = 0.1$ (not shown here). Still, in the range of moderate penalty parameters both methods perform with similar accuracy such that the GPTS approach seems applicable especially when a very high accuracy for fulfilling the constraints (3.110) for species and pressures is not needed. Indeed, from an implementational point of view, the GPTS approach can also be integrated more easily since the additional terms can be evaluated on element level together with the other transvascular mass exchange terms. By contrast, the penalized Lagrange multiplier method requires a global assembly of the mortar matrices and only then the Lagrange multipliers can be eliminated. Nevertheless, the MP method has been applied in all other examples of this thesis due to its theoretical advantages outlined in this section. Further studies in the related context of beam-to-solid mesh tying can be found in [134, 246].

A.3 Validation of Large Deformations of Embedded Vasculature

In this section, the spatial integration for large deformations of the embedded vasculature domain is presented in more detail. An additional numerical example is used to prove its correct implementation. A general scenario with large deformations is sketched in Figure A.5. The undeformed configuration is given in Figure A.5a. Then, the lower right node is moved to the right as illustrated in Figure A.5b. Under the assumptions made in Section 3.4.1, the embedded vasculature completely follows the resulting deformation inside the second element while its remaining part in the first and third element remains fixed. Thus, the 1D domain changes its length. Concurrently, the mapping between the element parameter space and the physical space changes. In other words, the mapping and the partitioning of integration segments depend on the deformation of the underlying 2D/3D mesh. In the illustrated example, the middle segment is enlarged at the expense of the two other segments. Recall that the linearization of these terms w.r.t. the solid phase displacement is not calculated in the framework since the respective terms have been set to zero in (4.136) and (4.138).

To validate the implementation, a small academic example is studied. It involves the domain depicted in Figure A.6a, which is a block of dimensions $8 \times 2 \times 2$ meshed with $24 \times 6 \times 6$ trilinear elements. The centerline of the block is congruent with the x-axis. Inside the block, four separate blood vessels with a diameter of 0.2 are embedded along the x-axis starting at $[0, \pm 0.5, \pm 0.5]$. Each segment is discretized with eight linear elements. The block is then deformed according to

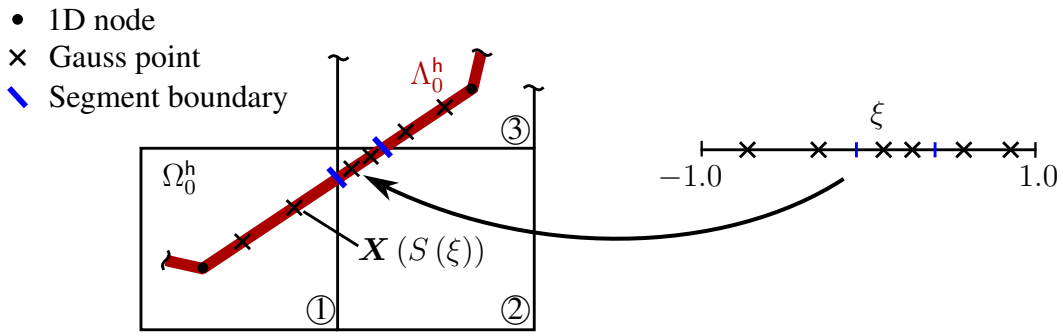

(a) Undeformed configuration

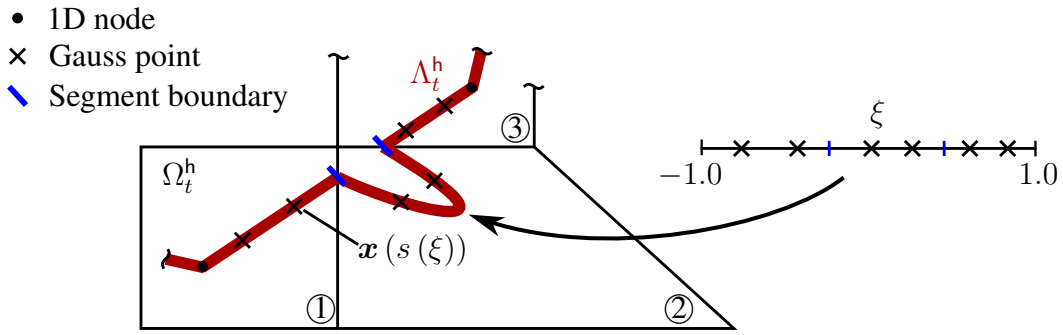

(b) Deformed configuration

Figure A.5: Sketch of large deformations of embedded vasculature domain including one-dimensional segment-based integration for centerline coupling (in 2D)

the deformation map

$$\boldsymbol{x}(\boldsymbol{X},t) = \begin{bmatrix} x \\ y \\ z \end{bmatrix} = \begin{bmatrix} X \\ \cos(\pi/4 \cdot X) \cdot Y - \sin(\pi/4 \cdot X) \cdot Z \\ \sin(\pi/4 \cdot X) \cdot Y + \cos(\pi/4 \cdot X) \cdot Z \end{bmatrix} \tag{A.15}$$

resulting in the twisted shape depicted in Figure A.6b. Evidently, the embedded blood vessels completely follow the deformation of the surrounding domain. They form a spiral such that each point on their centerline follows the respective point in the 3D domain.

Using the 1D-3D coupling variant, the example is set up such that the equation

$$-\frac{\partial^2 p^{\hat{v}}}{\partial s^2} + p^{\hat{v}} = 0 \tag{A.16}$$

is solved on each of the four initially straight segments of the embedded deformed domain with the aforementioned 1D discretization. On the tips at the left hand side of the domain the pressure is set to one, at the right hand side to zero.

Note that the arc-length in deformed configuration for all embedded vessels (with coordinates $[X, \pm 0.5, \pm 0.5]$) may be calculated as

$$s(S) = \sqrt{1 + 0.5 \cdot (\pi/4)^2)} \cdot S \approx 1.14386 \cdot S \tag{A.17}$$

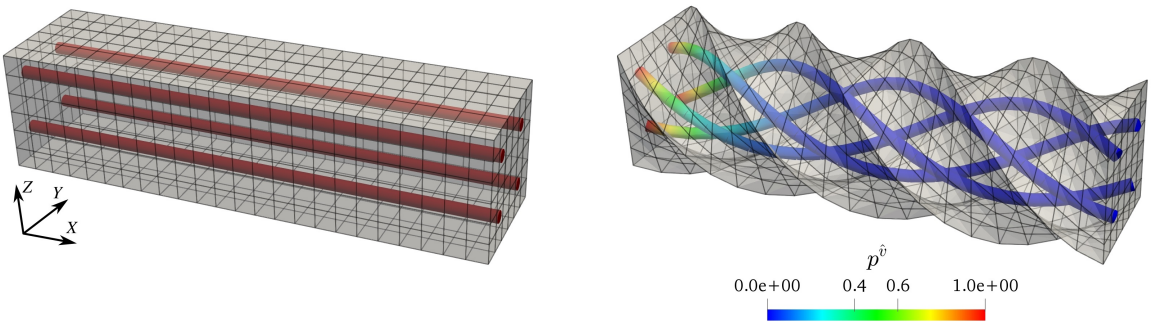

(a) Undeformed configuration (b) Deformed configuration

Figure A.6: Large twist of embedded 1D domain

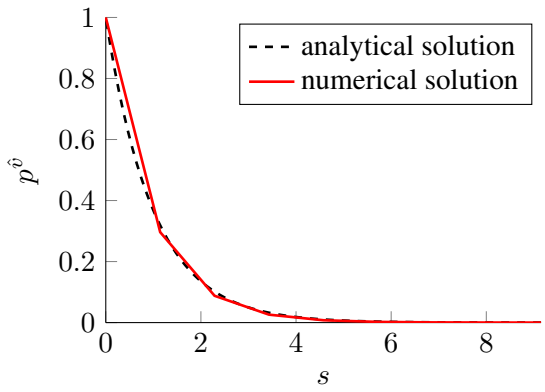

Figure A.7: Comparison between analytical and numerical solution for large twist example

for this example from the deformation gradient $\boldsymbol{F}$ of the twisting motion (A.15) and the initial unit tangential vector of the embedded blood vessels $\boldsymbol{t}_0 = [1, 0, 0]$ according to (3.71). Thus, the initial vasculature domain of each vessel Λ_0 with $S \in [0, 8]$ is stretched to become the deformed vasculature domain Λ_t with $s \in [0, 8 \cdot \sqrt{1 + 0.5 \cdot (\pi/4)^2})]$.

The 1D elements are now not straight any more but curved following the deformation of the domain. However, the pressure between the nodes is still linearly interpolated with linear shape functions. This is illustrated in Figure A.7 where the analytical solution of equation (A.16) on one branch with the corresponding boundary conditions is compared to the numerical solution obtained with eight linear elements. Obviously, the numerical solution matches the analytical one very well. With further refinement, convergence towards the analytical solution is obtained. While such a deformation seems unlikely in any biological scenario, this example demonstrates the general applicability of the large deformation approach for the embedded vasculature.

B Mass Transfer Relationships of the Tumor Growth Model

In this appendix, the arithmetic expressions for the mass transfer relationships for phases and species in the tumor growth model are summarized. The ones for the avascular compartment are taken from the earlier papers of Schrefler and co-workers [225, 230, 232, 233] while the ones including homogenized and discrete representation of the vasculature were added in Kremheller et al. [135, 136]. The following sections are based on the two aforementioned publications by the author. The terms employed for nanoparticle extravasation and drainage are given directly in Section 5.3.

B.1 Phase Mass Transfer Relationships

Tumor Growth Based on Sciumè et al. [230], growth of the tumor phase is described by

$$\overset{l\to t}{M}_{\text{growth}} = \left(\gamma^{t}_{\text{growth}} \left\langle \frac{\omega^{n\bar{l}} - \omega^{n\bar{l}}_{\text{crit}}}{\omega^{n\bar{l}}_{\text{env}} - \omega^{n\bar{l}}_{\text{crit}}} \right\rangle_{+} \right) \left(1 - \omega^{N\bar{t}}\right) \varepsilon S^{t}, \tag{B.1}$$

where $\langle \bullet \rangle_{+}$ denote the Macaulay brackets which return the value of their argument if the argument is positive and zero otherwise. The previous equation describes the consumption of nutrients and water from the IF during tumor cell growth with coefficient $\gamma^{t}_{\text{growth}}$. The multiplication with the mass (or volume) fraction of LTCs $\left(1 - \omega^{N\bar{t}}\right) \varepsilon S^{t}$ indicates that only LTCs are able to grow whereas NTCs are inert. In that formulation, tumor growth is regulated by the local mass fraction of oxygen $\omega^{n\bar{l}}$. If it is smaller than a constant critical mass fraction $\omega^{n\bar{l}}_{\text{crit}}$, one assumes that tumor growth is inhibited. This is reflected by the Macaulay brackets which return zero in this case. The model parameter $\omega^{n\bar{l}}_{\text{env}}$ denotes the oxygen mass fraction in healthy tissue. Thus, depending on the locally available oxygen the Macaulay brackets vary between zero for $\omega^{n\bar{l}} \leq \omega^{n\bar{l}}_{\text{crit}}$ and one for $\omega^{n\bar{l}} = \omega^{n\bar{l}}_{\text{env}}$. An additional term inhibiting TC growth above a certain critical tumor cell pressure was incorporated in [230] but is not considered throughout this thesis.

Leakage from Homogenized Vasculature into Interstitial Fluid Transcapillary leakage of fluid from the HV into the IF is modeled with the Starling equation, which describes fluid flow across a semi-permeable membrane, as

$$\overset{v\to l}{M}_{\text{leak}} = \rho^{l} \cdot \left(L_p \frac{S}{V} \right)_{v} \cdot \left(p^{\text{eff}} - p^{l} \right) \cdot \varepsilon^{v}, \tag{B.2}$$

with hydraulic conductivity L_p and surface-to-volume ratio S/V for transcapillary flow [115, 287]. If the effective pressure

$$p^{\text{eff}} = p^v - \omega_{\text{osm}} \left(\pi^{\text{blood}} - \pi^l \right) \tag{B.3}$$

is higher than the IF pressure p^l, a net outflow from the vessels into the interstitial fluid, i.e., leakage from the vasculature into the IF, occurs. Thus, the pressure difference between blood and IF drives the flow across the semipermeable capillary blood vessel wall together with the osmotic (or oncotic) pressure difference $\omega_{\text{osm}} \left(\pi^{\text{blood}} - \pi^l \right)$. To a certain extent, the latter term balances the fluid leakage from the vasculature into the IF as fluid is also pulled inward from IF to vasculature due to differences in plasma protein concentrations. Furthermore, in (B.2) it has been assumed that the leakage is proportional to the vascular volume fraction ε^v.

Drainage of Fluid via the Lymphatic System The lymphatic system is not considered as a distinct phase including flow. However, it is assumed that it is present throughout the domain such that a continuous drainage of excessive fluid and waste products from the IF into the lymphatic system occurs. For that, the relationship

$$\overset{l \to ly}{M}_{\text{drain}} = \rho^l \cdot \left(L_p \frac{S}{V} \right)_{ly} \cdot \left\langle p^l - p^{ly} \right\rangle_+ \cdot \left\langle 1 - \frac{p^t}{p^t_{\text{coll},ly}} \right\rangle_+ , \tag{B.4}$$

which is an adaptation of the lymphatic drainage term used by Wu et al. [287], is applied. Again, a Starling equation is defined for the outflow of fluid into the lymph system. Additionally, the tumor pressure-induced collapse of the lymph vessels, which is a major factor contributing to interstitial hypertension as discussed in the main part of this thesis, is considered by the last factor of (B.4). Until the collapsing pressure $p^t_{\text{coll},ly}$ the drainage capacity of the lymph system decreases linearly. Above this pressure, it is assumed that the lymph vessels have collapsed and no uptake of fluid is possible anymore. It is further postulated that the lymphatic pressure is small compared to the other pressures of the multiphase system, that is, $p^{ly} \approx 0$. Again, Macaulay brackets are employed such that only flow from IF into lymph system occurs and not vice versa.

B.2 Species Mass Transfer Relationships and Intra-Phase Reaction Terms

Necrosis NTCs are present as a species of the tumor cells. Hence, necrosis is modeled as an intra-phase reaction term of the TC phase, which, following Sciumè et al. [230, 232, 233], reads as

$$\varepsilon^t r^{Nt} = \gamma^t_{\text{necrosis}} \left\langle \frac{\omega^{n\bar{l}}_{\text{crit}} - \omega^{n\bar{l}}}{\omega^{n\bar{l}}_{\text{env}} - \omega^{n\bar{l}}_{\text{crit}}} \right\rangle_+ \left(1 - \omega^{N\bar{t}}. \right) \varepsilon S^t . \tag{B.5}$$

This equation is closely related to the term for tumor growth (B.1). The rate of cell death is regulated via the coefficient $\gamma^t_{\text{necrosis}}$ and proportional to the mass fraction of LTCs. In turn, the local oxygen mass fraction $\omega^{n\bar{l}}$ influences necrosis. Note that the numerator inside the Macaulay brackets is switched w.r.t. (B.1) such that necrotic cells emerge only if the oxygen mass fraction is below the critical mass fraction $\omega^{n\bar{l}}_{\text{crit}}$. Also here, necrosis due to excessive tumor stresses is neglected.

Consumption of Oxygen Both HCs and LTCs consume oxygen. The oxygen uptake of LTCs is modeled via the mass transfer relation for oxygen

$$\overset{nl\to t}{M}_{\text{cons}} = \overset{nl\to nt}{M} = \left(\gamma^{nt}_{\text{growth}} \left\langle \frac{\omega^{n\,\bar{l}} - \omega^{n\,\bar{l}}_{\text{crit}}}{\omega^{n\,\bar{l}}_{\text{env}} - \omega^{n\,\bar{l}}_{\text{crit}}} \right\rangle_{+} + \gamma^{nt}_{0} \sin\left(\frac{\pi}{2} \frac{\omega^{n\,\bar{l}}}{\omega^{n\,\bar{l}}_{\text{env}}} \right) \right) \left(1 - \omega^{N\,\bar{t}} \right) \varepsilon S^{t}. \tag{B.6}$$

Two contributions are incorporated: the first term accounts for the consumption of oxygen during growth with coefficient $\gamma^{nt}_{\text{growth}}$. Hence, it is zero if the oxygen level drops below the critical oxygen threshold. The second term represents the normal metabolism of LTCs with parameter γ^{nt}_{0}. Since the oxygen mass fraction always varies between 0 and $\omega^{n\,\bar{l}}_{\text{env}}$, the sine function varies between 0 and 1. As it is assumed that NTCs do not consume any oxygen, the entire term is once more scaled with the LTC mass fraction. Note that the two parameters were previously denoted as $\gamma^{nl}_{\text{growth}}$ and γ^{nl}_{0}, respectively [230, 232, 233].

The oxygen consumption by host cells is defined as

$$\overset{nl\to h}{M}_{\text{cons}} = \overset{nl\to nh}{M} = \gamma^{nh}_{0} \cdot \sin\left(\frac{\pi}{2} \frac{\omega^{n\,\bar{l}}}{\omega^{n\,\bar{l}}_{\text{env}}} \right) \cdot \varepsilon S^{h} \tag{B.7}$$

equivalently to the second term for the normal metabolism of LTCs in (B.6) with HC oxygen consumption coefficient γ^{nh}_{0}.

Transcapillary Oxygen Exchange between Interstitial Fluid and Homogenized Vasculature Throughout this thesis, the primary variable for oxygen is its mass fraction (either in the IF or the homogenized vasculature). However, oxygen concentration per unit volume of plasma or tissue $C^{n\overline{\alpha}}\,[\mathrm{mlO_2/ml}]$ or oxygen partial pressures $P^{\alpha}_{\text{oxy}}\,[\mathrm{mmHg}]$ are commonly used for oxygen transport models [92, 237, 241, 250, 279]. Hence, oxygen mass fractions have to be converted to oxygen partial pressures first in order to re-use the mass transfer relations which are normally applied. The mass fraction of oxygen in the IF in terms of oxygen partial pressure in the IF P^{l}_{oxy} is given by Henry's law as

$$\omega^{n\,\bar{l}}\left(P^{l}_{\text{oxy}}\right) = \frac{\rho^{n}}{\rho^{l}} \cdot C^{n\bar{l}} = \frac{\rho^{n}}{\rho^{l}} \cdot \alpha_{l} P^{l}_{\text{oxy}}, \tag{B.8}$$

where α_l is the solubility of oxygen in the IF and ρ^n and ρ^l are the respective densities of oxygen and the IF. Oxygen transport in blood follows a more complex mechanism [279] since it can be either dissolved in the blood plasma or bound to hemoglobin. Hence, the mass fraction of oxygen in blood may be written as

$$\omega^{n\,\overline{v}}\left(P^{v}_{\text{oxy}}\right) = \frac{\rho^{n}}{\rho^{v}} \cdot C^{n\overline{v}} = \frac{\rho^{n}}{\rho^{v}} \cdot \left(\alpha_{v,\text{eff}} P^{v}_{\text{oxy}} + H_{D} \cdot C^{n\overline{v}}_{0} \cdot S\left(P^{v}_{\text{oxy}}\right)\right). \tag{B.9}$$

As in (B.8) the first term represents the dissolved oxygen with effective solubility $\alpha_{v,\text{eff}}$ while the second one stands for the oxygen bound to hemoglobin (whose contribution to the total amount of oxygen is actually much larger). So, the mass fraction $\omega^{n\,\overline{v}}$ accounts for the total mass fraction of oxygen which is dissolved in plasma and bound to hemoglobin. Furthermore, H_D is the

discharge hematocrit, that is, the volume flux of red blood cells divided by the total blood volume flux [240] and $C_0^{n\bar{v}}$ the concentration of oxygen at maximum saturation. Constant discharge hematocrit is assumed in the HV, see Table C.6. For the binding of oxygen to hemoglobin the Hill equation

$$S\left(P_{\mathrm{oxy}}^{v}\right) = \frac{\left(P_{\mathrm{oxy}}^{v}\right)^{n}}{\left(P_{\mathrm{oxy}}^{v}\right)^{n} + \left(P_{\mathrm{oxy},50}^{v}\right)^{n}} \tag{B.10}$$

is typically applied. Here, the Hill exponent n and the partial pressure $P_{\mathrm{oxy},50}^{v}$ at 50% oxygen saturation have been introduced. As stated above, mass fractions of oxygen are the primary variable of the oxygen transport model so, actually, the inverses of (B.8) and (B.9) are required to get the oxygen partial pressure at a specific mass fraction. For oxygen in the IF (B.8) this is trivial, however, the relation for oxygen in blood (B.9) is inverted numerically in the computational framework via a local Newton algorithm. Then, for transvascular oxygen exchange from the vasculature into the IF, the relationship

$$\overset{nv\to nl}{M}_{\mathrm{tv}} = \gamma_{\mathrm{tv}} \cdot \rho^{n} \cdot \left(\frac{S}{V}\right)_{v} \cdot \left\langle P_{\mathrm{oxy}}^{v} - P_{\mathrm{oxy}}^{l} \right\rangle_{+} \cdot \varepsilon^{v} \tag{B.11}$$

in terms of partial pressures of oxygen is employed. Basically, the parameter γ_{tv} models the radial transport resistance of oxygen. Here, it represents the homogenized resistance of the corresponding discrete 1D-3D mass transfer term introduced in Section B.4. Further details are given there. In addition, it is presumed that oxygen mass exchange is proportional to the vascular volume fraction ε^{v} and surface-to-volume ratio $(S/V)_{v}$. Macaulay brackets are employed to allow only oxygen transfer from the homogenized vasculature into the IF and not vice versa.

Simplified Model for Transcapillary Oxygen Exchange between Interstitial Fluid and Homogenized Vasculature A simplified model for oxygen exchange was employed in [135] and is also used in Section 5.2. The corresponding species mass transfer term of oxygen from the homogenized vasculature into the IF reads as

$$\overset{nv\to nl}{M}_{\mathrm{tv,s}} = \omega^{n\bar{v}} \overset{v\to l}{M}_{\mathrm{leak}} + \rho_{l} \left(\frac{S}{V}\frac{D_{tc}}{t}\right)_{v} \cdot \left\langle \omega^{n\bar{v}} - \omega^{n\bar{l}} \right\rangle_{+} \cdot \varepsilon^{v}. \tag{B.12}$$

Herein, the first summand denotes the flux of oxygen dissolved in the plasma with mass fraction $\omega^{n\bar{v}}$ due to transcapillary leakage $\overset{v\to l}{M}_{\mathrm{leak}}$ over the blood vessel wall given by (B.2). The second term is employed for the transcapillary diffusion with diffusion coefficient D_{tc} and blood vessel wall thickness t. Again, this term is proportional to the volume fraction of the homogenized vasculature.

Production of Tumor Angiogenic Factors Once LTCs become hypoxic, they start producing TAFs which is incorporated by the term

$$\overset{TAFt\to TAFl}{M}_{\mathrm{prod}} \approx \varepsilon^{t} r^{TAFt} = \left(1 - \omega^{N\bar{t}}\right) \varepsilon S^{t} \cdot \gamma_{\mathrm{prod}}^{\mathrm{TAF}} \cdot H\left(\omega_{\mathrm{hyp}}^{n\bar{l}} - \omega^{n\bar{l}}\right) \cdot \left[\frac{1}{2} + \frac{1}{2}\cos\left(\pi \frac{\omega^{n\bar{l}}}{\omega_{\mathrm{hyp}}^{n\bar{l}}}\right)\right]. \tag{B.13}$$

Here, it was assumed that all the TAFs produced by LTCs with an intra-phase production term $\varepsilon^t r^{TAFt}$ equivalent to [225] are immediately transferred into the interstitial fluid. By employing the Heaviside function $H(\bullet)$, it is ensured that TAFs are produced by the living tumor cells at a rate of $\gamma_{\text{prod}}^{\text{TAF}}$ only if the nutrient mass fraction falls below an oxygen threshold $\omega_{\text{hyp}}^{n\bar{l}}$, which is termed hypoxic limit. Thus, the term in square brackets involving the cosine function scaled with the Heaviside function varies between one for $\omega^{n\bar{l}} = 0$ and zero for $\omega^{n\bar{l}} \geq \omega_{\text{hyp}}^{n\bar{l}}$. In summary, also the production of TAFs by LTCs depends on the local oxygen mass fraction in the IF.

Uptake of Fibronectin Following Anderson [6], the uptake and binding of fibronectin by endothelial cells is modeled as a sink term, that is, in the TCAT formalism as an intra-phase reaction term

$$-\overset{Fs\to Fv}{M}_{\text{up}} \approx -\varepsilon^s r^{is} = -\zeta_{\text{up}} \varepsilon^v \omega^{F\bar{s}} \tag{B.14}$$

which is proportional to a model constant ζ_{up}, the HV volume fraction ε^v and the fibronectin mass fraction $\omega^{F\bar{s}}$. This formulation was also used by Wirthl [281]. Strictly speaking, a more consistent form would be an inter-phase exchange term from ECM to endothelial cells but since they are not explicitly modeled and since mass transfer to and from the ECM has been assumed as zero, here, an intra-phase reaction term is employed. In addition, no production term by endothelial cells as in the original formulation of [6] is comprised in the current formulation. However, one could also think of the term $\varepsilon^s r^{is}$ as the net difference between fibronectin production and consumption which is assumed to be always negative.

Extravasation of nanoparticles The extravasation of nanoparticles from homogenized vasculature into the IF is described by (5.4) which is a simplified version of (5.3) combining both the interendothelial and the transendothelial pathway into a single term with apparent vascular permeability $P_{v,\text{app}}$.

Lymphatic drainage of nanoparticles Lymphatic drainage of nanoparticles from the IF into the lymph vessels is described by (5.5).

B.3 1D-3D Fluid Mass Transfer Relationships

Leakage from Embedded Vasculature into Interstitial Fluid As for the leakage of fluid from homogenized vasculature into IF given by (B.2), the Starling equation is applied. The corresponding term for lateral surface coupling reads as

$$\overset{\hat{v}\to l}{M}_{\text{leak}} = \int_0^{\pi D_t(s)} \rho^l \cdot L_{p,\hat{v}} \cdot \left(p^{\hat{v}}(s) - p^l(\boldsymbol{x}(s,\gamma)) - \omega_{\text{osm}}\left(\pi^{\text{blood}} - \pi^l\right)\right) \mathrm{d}\gamma \tag{B.15}$$

and for centerline coupling as

$$\overset{\hat{v}\to l}{M}_{\text{leak}} \approx \pi D_t \cdot \rho^l \cdot L_{p,\hat{v}} \cdot \left(p^{\hat{v}}(s) - p^l(\boldsymbol{x}(s)) - \omega_{\text{osm}}\left(\pi^{\text{blood}} - \pi^l\right)\right). \tag{B.16}$$

Therein, $L_{p,\hat{v}}$ is again the hydraulic conductivity and $\omega_{\text{osm}}\left(\pi^{\text{blood}} - \pi^{l}\right)$ the osmotic pressure difference. This 1D-3D mass transfer term scaled with the respective Dirac measure also appears in the mass balance of the IF as

$$\delta_{\partial\mathcal{D}_t} \cdot \overset{\hat{v}\to l}{M}_{\text{leak}} = \delta_{\partial\mathcal{D}_t} \cdot \rho^{l} \cdot L_{p,\hat{v}} \cdot \left(p^{\hat{v}}(s) - p^{l}(\boldsymbol{x}(s,\gamma)) - \omega_{\text{osm}}\left(\pi^{\text{blood}} - \pi^{l}\right)\right) \tag{B.17}$$

$$\approx \delta_{\Lambda_t} \cdot \pi D_t(s) \cdot \rho^{l} \cdot L_{p,\hat{v}} \cdot \left(p^{\hat{v}}(s) - p^{l}(\boldsymbol{x}(s)) - \omega_{\text{osm}}\left(\pi^{\text{blood}} - \pi^{l}\right)\right) \tag{B.18}$$

for the lateral surface coupling variant, respectively, the centerline coupling variant.

B.4 1D-3D Species Mass Transfer Relationships

Transcapillary Oxygen Exchange between Interstitial Fluid and Embedded Vasculature For transvascular oxygen exchange from the embedded 1D vasculature into the IF, the relation

$$\overset{n\hat{v}\to nl}{M}_{\text{tv}} = \int_0^{\pi D_t(s)} \hat{\gamma}_{\text{tv}}(R) \cdot \rho^{n} \cdot \left(P^{\hat{v}}_{\text{oxy}}(s) - P^{l}_{\text{oxy}}(\boldsymbol{x}(s,\gamma))\right) \mathrm{d}\gamma \tag{B.19}$$

$$\approx \pi D_t \cdot \hat{\gamma}_{\text{tv}}(R) \cdot \rho^{n} \cdot \left(P^{\hat{v}}_{\text{oxy}}(s) - P^{l}_{\text{oxy}}(\boldsymbol{x}(s))\right) \tag{B.20}$$

is employed for the two different coupling types. Hence, oxygen exchange depends on the difference in partial pressures of oxygen between embedded 1D blood vessels $P^{\hat{v}}_{\text{oxy}}$ and surrounding IF P^{l}_{oxy}. The oxygen partial pressures again have to be calculated with the inverse relationships of (B.8) and (B.9) depending on the respective mass fractions $\omega^{n\,\bar{l}}$ and $\omega^{n\,\hat{v}}$. This formulation has been proposed by Welter et al. [279] based on earlier works of Hellums et al. [104]. Basically, the parameter $\hat{\gamma}_{\text{tv}}(R)$ models the radial transport resistance of oxygen. Such a radial resistance [104] has also been employed elsewhere [237, 241, 250]. Here, a phenomenological fit for varying radii is re-used [279, Appendix S1] reading as

$$\hat{\gamma}_{\text{tv}}(R) = \frac{D_p \alpha_p}{2R} \cdot Nu(R) = \frac{D_p \alpha_p}{2R} \cdot p_2 \left(1 - \exp\left(-\frac{R}{p_1}\right)\right) \tag{B.21}$$

with parameters $\alpha_p = 3.1 \times 10^{-5}\,\text{mmHg}^{-1}$, $D_p = 2.75 \times 10^{-3}\,\text{mm}^2\,\text{s}^{-1}$, $p_1 = 8\,\mu\text{m}$ and $p_2 = 4.7$. Thus, oxygen passes the blood vessel wall and goes into the IF with the following source term

$$\delta_{\partial\mathcal{D}_t} \cdot \overset{n\hat{v}\to nl}{M}_{\text{tv}} = \delta_{\partial\mathcal{D}_t} \cdot \hat{\gamma}_{\text{tv}}(R) \cdot \rho^{n} \cdot \left(P^{\hat{v}}_{\text{oxy}}(s) - P^{l}_{\text{oxy}}(\boldsymbol{x}(s,\gamma))\right) \tag{B.22}$$

$$\approx \delta_{\Lambda_t} \cdot \pi D_t(s) \cdot \hat{\gamma}_{\text{tv}}(R) \cdot \rho^{n} \cdot \left(P^{\hat{v}}_{\text{oxy}}(s) - P^{l}_{\text{oxy}}(\boldsymbol{x}(s))\right) \tag{B.23}$$

scaled with the corresponding Dirac measure depending on which 1D-3D coupling variant is used.

C Employed Parameters

C.1 Parameters for the Extracellular Matrix

Quantity	Symbol	Value	Unit	Source	Equations
Intrinsic permeability of the ECM	k	1.0×10^{-15}[a]	m^2	[211]	(3.41)
Density	ρ^s	1000	$\mathrm{kg\,m^{-3}}$	[232]	(3.41)
Poisson's ratio	ν^s	0.4	–	[232]	(2.41)
Young's modulus	E^s	800[b]	Pa	[135]	(2.41)

[a] The baseline value for the performance comparison of Section 5.1 is set to $k = 1.8 \times 10^{-15}\,\mathrm{m}^2$ [233, Table 3].
[b] The baseline value for the performance comparison of Section 5.1 is set to $E^s = 400\,\mathrm{Pa}$.

Table C.1: Parameters for the ECM

C.2 Parameters for Tumor Cells, Host Cells and Interstitial Fluid

Quantity	Symbol	Value	Unit	Source	Equations
Density of TC, HC and IF	ρ^l, ρ^h, ρ^t	1000	$\mathrm{kg\,m^{-3}}$	[232]	(3.20),(3.21)
HC-IF interfacial tension	σ_{hl}	72	$\mathrm{mN/m}$	[232]	(3.36)
TC-HC interfacial tension	σ_{th}	36	$\mathrm{mN/m}$	[232]	(3.36)
Coefficient a in saturation-pressure relationship	a	590	Pa	[232]	(3.35),(3.36)
Coefficient b in saturation-pressure relationship	b	1	–	[232]	(3.35),(3.36)
Dynamic viscosity of IF	μ_l	0.001[a]	$\mathrm{Pa\,s}$		(3.20),(3.21)
Dynamic viscosity of HC and TC	μ_h, μ_t	20	$\mathrm{Pa\,s}$	[233]	(3.20),(3.21)
Relative permeability law exponent for IF	A_l	4	–	[232]	(3.41)
Relative permeability law exponent for HCs and TCs	A_h, A_t	2	–	[232]	(3.41)
Growth coefficient of tumor cells	$\gamma^t_{\mathrm{growth}}$	4×10^{-2}	$\mathrm{kg\,m^{-3}\,s^{-1}}$	[233]	(B.1)

[a] Since the IF consists primarily of water, the value for the viscosity of water has been employed. In the examples of Section 5.1 and 5.2, a value of $\mu_l = 0.01\mathrm{Pa\,s}$ is used as in [233, Table 3].

Table C.2: Parameters for TCs, HCs and IF

C.3 Parameters for the Homogenized Vasculature

Quantity	Symbol	Value	Unit	Source	Equations
Density of blood	ρ^v	1060	$\mathrm{kg\,m^{-3}}$	[77]	(3.47)
Viscosity of blood	μ^v	0.004	$\mathrm{Pa\,s}$	[38]	(3.47)
Diffusion coefficient of HV	D^v	$5 \cdot 10^{-15}$[a]	$\mathrm{m^2\,s^{-1}}$	[6]	(3.51)
Chemotactic coefficient	χ_0	7.5×10^{-3}[b]	$\mathrm{m^2\,s^{-1}}$		(3.67)
Haptotactic coefficient	Θ	1×10^{-2}[c]	$\mathrm{m^2\,s^{-1}}$		(3.51)
Constant for receptor-kinetic law	$\omega_{\chi_0/2}^{TAF\,\bar{l}}$	1×10^{-10}	–	[6]	(3.67)
(Isotropic) permeability of the HV	k^v	1×10^{-17}[d]	$\mathrm{m^2}$		(3.47)
Osmotic pressure difference	$\omega_{\mathrm{osm}}\left(\pi^v - \pi^l\right)$	1333	Pa	[287]	(B.3)
Transvascular hydraulic conductivity	$L_{p,v}$	2.1×10^{-11}[e],[i]	$\mathrm{m\,Pa^{-1}\,s^{-1}}$	[13]	(B.2)
Surface-to-volume ratio of HV	$(S/V)_v$	2×10^4	$\mathrm{m^{-1}}$	[13]	(B.2),(B.11)
Hydraulic conductivity and surface-to-volume ratio for lymphatic drainage	$\left(L_p \frac{S}{V}\right)_{ly}$	1.04×10^{-6}[f],[i]	$\mathrm{Pa^{-1}\,s^{-1}}$	[14]	(B.4)
Threshold for lymphatic vessel collapse	$p^t_{\mathrm{coll},ly}$	500[g],[i]	Pa	[135]	(B.4)
Threshold for blood vessel collapse	$p^t_{\mathrm{coll},v}$	600[h],[i]	Pa		(3.68)
Rate of blood vessel collapse	γ^v_{coll}	1×10^{-6}[h]	$\mathrm{s^{-1}}$		(3.68)

[a] Half the value of Anderson [6].

[b] This value has been estimated to obtain plausible results from the investigation of different chemotactic coefficients in Section 5.2.1 respectively in [135].

[c] Anderson [6] assumed that the haptotactic coefficient has the same order of magnitude as the chemotactic coefficient. Therefore, it was set to the same value as the chemotactic coefficient χ_0 from case 2 in Table 5.1.

[d] Estimated as two orders of magnitudes smaller than the permeability of the ECM from Table C.1 due to the high irregularity and tortuosity of tumor vasculature. In Section 5.3, a value of $k^v = 1 \times 10^{-15}\,\mathrm{m^2}$ is employed as the homogenized vasculature here corresponds to healthy pre-existing vasculature which is not as irregular and tortuous as the neovasculature.

[e] The value for tumor vasculature of Baxter and Jain [13] is used.

[f] In the examples of Section 5.2, a slightly higher value of $\left(L_p \frac{S}{V}\right)_{ly} = 2 \times 10^{-5}\,\mathrm{Pa^{-1}\,s^{-1}}$ is employed. It corresponds to the value used in Kremheller et al. [135], where the hydraulic conductivity of the lymphatic system was estimated to be two orders of magnitude higher than the one of the neovasculature. This ensures a correct behaviour of a functioning lymph system which drains the liquid leaking from the irregular neovasculature.

[g] Was estimated such that a tumor cell saturation of $S^t \approx 0.3$ completely inhibits lymphatic drainage.

[h] See Remarks in Section 5.2.3.

[i] Slightly different values were used for the NP transport study in Section 5.3, see page 143.

Table C.3: Parameters for blood flow, angiogenesis and transcapillary and lymphatic exchange

C.4 Parameters for Species Transport

Quantity	Symbol	Value	Unit	Source	Equations
Diffusion coefficient of NTCs in TC	D^{Nt}	0[a]	$\mathrm{m^2\,s^{-1}}$	[230]	(3.43)
Necrosis coefficient	$\gamma^t_{\mathrm{necrosis}}$	1×10^{-2}	$\mathrm{kg\,m^{-3}\,s^{-1}}$	[233]	(B.5)

[a] NTCs are modeled as inert, thus, their diffusion coefficient is equal to zero.

Table C.4: Parameters for NTCs

Quantity	Symbol	Value	Unit	Source	Equations
Diffusion coefficient of oxygen in IF	D_0^{nl}	3.2×10^{-9}	$\mathrm{m^2\,s^{-1}}$	[232]	(3.43)
Nonlinear diffusion law coefficient in IF	δ	2	–	[232]	(3.43)
Normal mass fraction of oxygen in IF	$\omega_{\mathrm{env}}^{n\bar{l}}$	4.2×10^{-6}[a]	–	[233]	(B.1),(B.6),(B.7)
Critical mass fraction of oxygen	$\omega_{\mathrm{crit}}^{n\bar{l}}$	1.0×10^{-6}	–	[233]	(B.1),(B.6)
Limit mass fraction in IF for hypoxia	$\omega_{\mathrm{hyp}}^{n\bar{l}}$	4.0×10^{-6}	–	[225]	(B.13)
Density of oxygen	ρ^n	1.429	$\mathrm{kg\,m^{-3}}$	known	(B.8),(B.9),(B.11) (B.19)-(B.23)
Consumption due to growth	$\gamma_{\mathrm{growth}}^{nt}$	2.4×10^{-4}	$\mathrm{kg\,m^{-3}\,s^{-1}}$	[232]	(B.6)
Consumption due to metabolism of TCs	γ_0^{nt}	6×10^{-4}	$\mathrm{kg\,m^{-3}\,s^{-1}}$	[232]	(B.7)
Consumption due to metabolism of HCs	γ_0^{nh}	2×10^{-4}[b]	$\mathrm{kg\,m^{-3}\,s^{-1}}$		(B.7)
Solubility of oxygen in the IF	α_l	3×10^{-5}	$\mathrm{mmHg^{-1}}$	[196]	(B.8)

[a] This value can be obtained from Henry's law for the oxygen mass fraction in the IF (B.8) with a partial pressure of oxygen of $P_{\mathrm{oxy}}^l = 97.8\,\mathrm{mmHg}$ (almost fully oxygen-saturated) together with the densities of oxygen, IF and the solubility of oxygen in the IF.

[b] This value has been estimated based on the rate of consumption by TCs of the earlier contributions on the model. It was assumed that HCs consume only one third of the oxygen needed by TCs.

Table C.5: Parameters for oxygen in the IF, consumption by cells, hypoxia and necrosis

Quantity	Symbol	Value	Unit	Source	Equations
Effective solubility of oxygen in blood	$\alpha_{v,\mathrm{eff}}$	3.1×10^{-5}	$\mathrm{mmHg^{-1}}$	[279]	(B.9)
Discharge hematocrit	H_D	0.45	–	[279]	(B.9)
Oxygen concentration at max. saturation	$C_0^{n\bar{v}}$	0.5	–	[279]	(B.9)
Hill exponent	n	2.7	–	[92]	(B.10)
Partial pressure at 50% oxygen saturation	$P_{\mathrm{oxy},50}^v$	37	mmHg	[92]	(B.10)
Transvascular oxygen exchange coefficient	γ_{tv}	1.429×10^{-8}[a]	$\mathrm{m\,mmHg^{-1}\,s^{-1}}$	[279]	(B.11)
Diffusion coefficient of oxygen in blood	$D^{n\hat{v}}$, D_0^{nv}	2.775×10^{-11}[b]	$\mathrm{m^2\,s^{-1}}$		(3.63),(3.84)

[a] Since the smaller vessels are regarded in a homogenized way, it was assumed that the average radius of the blood vessels in the homogenized vasculature is $0.01\,\mathrm{mm}$. The value for γ_{tv} was then calculated with the fit employed by Welter et al. [279, Appendix S1].

[b] This value is a simple approximation. It has been obtained from the value of oxygen diffusion in blood plasma of $D_p = 2.75 \times 10^{-9}\,\mathrm{m^2\,s^{-1}}$ [279]. In the present model the mass fractions $\omega^{n\,\bar{v}}$ respectively $\omega^{n\,\hat{v}}$ represent both the oxygen dissolved in plasma and bound to hemoglobin. At an oxygen partial pressure of $P_{\mathrm{oxy}}^v = P_{\mathrm{oxy},50}^v = 37\,\mathrm{mmHg}$ the ratio of the mass fraction of dissolved oxygen to the mass fraction of the total oxygen present is approximately 0.01. Hence, the value for D_p [279] was scaled by this factor to only include diffusion of the oxygen dissolved in the plasma and not the one bound to hemoglobin. Therefore, the oxygen transport model is similar to the one of Beard and Bassingthwaighte [16] and Fang et al. [71].

Table C.6: Parameters for oxygen in the vasculature and transvascular exchange

Quantity	Symbol	Value	Unit	Source	Equations
Diffusion coefficient of TAF in IF	D^{TAFl}	2.9×10^{-11}[a]	$\mathrm{m^2\,s^{-1}}$	[6]	(3.43)
Coefficient δ for nonlinear diffusion law in IF	δ	0	–		(3.43)
Production rate of TAF under hypoxia	$\gamma_{\mathrm{prod}}^{\mathrm{TAF}}$	1×10^{-10}[a]	$\mathrm{kg\,m^{-3}\,s^{-1}}$		(B.13)

[a] Throughout Section 5.2, values of $D^{TAFl} = 3.5 \times 10^{-4}$ and $\gamma_{\mathrm{prod}}^{\mathrm{TAF}} = 1 \times 10^{-3}$ are used. The former is the non-dimensional value employed by Anderson [6], which was also used in [135] and [225]. The production rate of TAF under hypoxia $\gamma_{\mathrm{prod}}^{\mathrm{TAF}}$ is scaled accordingly such that the ratio of diffusion and production remains almost equal.

Table C.7: Parameters for TAF

Quantity	Symbol	Value	Unit	Source	Equations
Diffusion coefficient of fibronectin in ECM	D^{Fs}	0[a]	$\mathrm{m^2\,s^{-1}}$	[6]	(3.43)
Uptake rate of fibronectin	ζ_{up}	1.1×10^{-4}[b]	$\mathrm{kg\,m^{-3}\,s^{-1}}$		(B.14)

[a] Fibronectin is bound to the ECM and does not diffuse [6].
[b] Estimated.

Table C.8: Parameters for Fibronectin

Quantity	Symbol	Value	Unit	Source	Equations
Diffusion coefficient of nanoparticles in IF	D_0^{NPl}	[a]	$\mathrm{m^2\,s^{-1}}$	[45]	(3.43)
Coefficient δ for nonlinear diffusion law in IF	δ	0	–		(3.43)
Apparent vascular permeability of nanoparticles	$P_{v,\mathrm{app}}$	[a]	$\mathrm{m\,s^{-1}}$	[67]	(5.4)
Diffusive drainage of nanoparticles	$\left(P\frac{S}{V}\right)_{ly}$	1×10^{-2}[b]	$\mathrm{s^{-1}}$		(5.5)

[a] Depends on weight of particles, see Table 5.2.
[b] Estimated.

Table C.9: Parameters for nanoparticle transport

C.5 Parameters for the Embedded Vasculature

Quantity	Symbol	Value	Unit	Source	Equations
Density of blood	$\rho^{\hat{v}}$	1060	$\mathrm{kg\,m^{-3}}$	[77]	(3.79)
Viscosity of blood	$\mu^{\hat{v}}$	0.004[a]	$\mathrm{Pa\,s}$	[38]	(3.79)
Osmotic pressure difference	$\omega_{\mathrm{osm}}\left(\pi^v - \pi^l\right)$	1333	Pa	[287]	(B.15)-(B.18)
Transvascular hydraulic conductivity	$L_{p,\hat{v}}$	2.7×10^{-12}[b]	$\mathrm{m\,Pa^{-1}\,s^{-1}}$	[13]	(B.2)

[a] This constant value is employed for all numerical examples of Chapter 5. In Chapter 6 an empirical blood viscosity law [201] is used.
[b] The value for normal vasculature of Baxter and Jain [13] is used.

Table C.10: Parameters for the embedded vasculature

C.6 Parameters for Hyperthermia Treatment

Quantity	Symbol	Value	Unit	Source	Equations
Specific absorption rate	SAR	$0.5 \times 10^7 - 3 \times 10^7$	$\mathrm{W\,kg^{-1}}$	[41], Rem. 5.1	(5.9)
Blood temperature	T_{bl}	310.15	K	known	(5.10)
Heat exchange coefficent	β_T	20	$\mathrm{W\,m^{-2}\,K^{-1}}$	[178]	(5.10)
Heat capacities	c_p^{α}[a]	3470	$\mathrm{J\,kg^{-1}\,K^{-1}}$	[41]	(2.47)
(Isotropic) conductivities	κ^{α}[a]	0.51	$\mathrm{W\,m^{-1}\,K^{-1}}$	[41]	(2.48)

[a] It is assumed that all present phases have the same heat capacity and isotropic conductivity such that the overall heat capacity and conductivity of the domain corresponds to the one given for tissue by [41].

Table C.11: Parameters for hyperthermia treatment

C.7 Parameters for the Blood Vessel Diameter Adaption and Collapse Model

Quantity	Symbol	Value	Unit	Source	Equations
Collapse factor	f_{coll}	0.8	–		(3.101)
Maximum saturation	S^t_{max}	0.8	–		(3.102)
Minimum saturation	S^t_{min}	0.2	–		(3.102)
Maximum diameter	D_{max}	20	µm		(3.102)
Minimum diameter	D_{min}	3.2	µm		(3.102)
Collapse threshold	$D_{\mathrm{coll-thresh}}$	0.1	µm		(3.103)

Table C.12: Parameters for the blood vessel diameter adaption and collapse model (estimated for the numerical example of Section 5.5)

Bibliography

[1] T. Alarcón, H. Byrne, and P. Maini. A cellular automaton model for tumour growth in inhomogeneous environment. *Journal of Theoretical Biology*, 225(2):257–274, 2003. DOI: 10.1016/S0022-5193(03)00244-3.

[2] C. Alexiou, W. Arnold, R. J. Klein, F. G. Parak, P. Hulin, C. Bergemann, W. Erhardt, S. Wagenpfeil, and A. S. Lübbe. Locoregional cancer treatment with magnetic drug targeting. *Cancer research*, 60(23):6641–8, 2000.

[3] C. Alexiou, R. Jurgons, R. Schmid, A. Hilpert, C. Bergemann, F. Parak, and H. Iro. In vitro and in vivo investigations of targeted chemotherapy with magnetic nanoparticles. *Journal of Magnetism and Magnetic Materials*, 293(1):389–393, 2005. DOI: 10.1016/j.jmmm.2005.02.036.

[4] K. Alitalo and P. Carmeliet. Molecular mechanisms of lymphangiogenesis in health and disease. *Cancer Cell*, 1(3):219–227, 2002. DOI: 10.1016/S1535-6108(02)00051-X.

[5] P. M. Altrock, L. L. Liu, and F. Michor. The mathematics of cancer: integrating quantitative models. *Nature Reviews Cancer*, 15(12):730–745, 2015. DOI: 10.1038/nrc4029.

[6] A. Anderson. Continuous and Discrete Mathematical Models of Tumor-induced Angiogenesis. *Bulletin of Mathematical Biology*, 60(5):857–899, 1998. DOI: 10.1006/bulm.1998.0042.

[7] A. Andreozzi, L. Brunese, M. Iasiello, C. Tucci, and G. P. Vanoli. Modeling Heat Transfer in Tumors: A Review of Thermal Therapies. *Annals of Biomedical Engineering*, 47(3): 676–693, 2019. DOI: 10.1007/s10439-018-02177-x.

[8] BACI. A Comprehensive Multi-Physics Simulation Framework. https://baci.pages.gitlab.lrz.de/website/, 2021. Accessed: 2021-03-22.

[9] S. Badia and R. Codina. Stabilized continuous and discontinuous Galerkin techniques for Darcy flow. *Computer Methods in Applied Mechanics and Engineering*, 199(25-28): 1654–1667, 2010. DOI: 10.1016/j.cma.2010.01.015.

[10] N. Baeyens, C. Bandyopadhyay, B. G. Coon, S. Yun, and M. A. Schwartz. Endothelial fluid shear stress sensing in vascular health and disease. *Journal of Clinical Investigation*, 126(3):821–828, 2016. DOI: 10.1172/JCI83083.

[11] F. R. Balkwill, M. Capasso, and T. Hagemann. The tumor microenvironment at a glance. *Journal of Cell Science*, 125(23):5591–5596, 2012. DOI: 10.1242/jcs.116392.

[12] P. Baluk, H. Hashizume, and D. M. McDonald. Cellular abnormalities of blood vessels as targets in cancer. *Current Opinion in Genetics & Development*, 15(1):102–111, 2005. DOI: 10.1016/j.gde.2004.12.005.

[13] L. T. Baxter and R. K. Jain. Transport of fluid and macromolecules in tumors. I. Role of interstitial pressure and convection. *Microvascular Research*, 37(1):77–104, 1989. DOI: 10.1016/0026-2862(89)90074-5.

[14] L. T. Baxter and R. K. Jain. Transport of fluid and macromolecules in tumors. II. Role of heterogeneous perfusion and lymphatics. *Microvascular Research*, 40(2):246–263, 1990. DOI: 10.1016/0026-2862(90)90023-K.

[15] J. Bear and Y. Bachmat. *Introduction to Modeling of Transport Phenomena in Porous Media*. Springer Netherlands, Dordrecht, 1990. DOI: 10.1007/978-94-009-1926-6.

[16] D. A. Beard and J. B. Bassingthwaighte. Modeling Advection and Diffusion of Oxygen in Complex Vascular Networks. *Annals of Biomedical Engineering*, 29(4):298–310, 2001. DOI: 10.1114/1.1359450.

[17] F. B. Belgacem. The Mortar finite element method with Lagrange multipliers. *Numerische Mathematik*, 84(2):173–197, 1999. DOI: 10.1007/s002110050468.

[18] T. Belytschko, W. Liu, B. Moran, and K. Elkhodary. *Nonlinear Finite Elements for Continua and Structures*. Wiley, 2013.

[19] G. Bergers and L. E. Benjamin. Tumorigenesis and the angiogenic switch. *Nature Reviews Cancer*, 3(6):401–410, 2003. DOI: 10.1038/nrc1093.

[20] M. O. Bernabeu, J. Köry, J. A. Grogan, B. Markelc, A. Beardo, M. D'Avezac, R. Enjalbert, J. Kaeppler, N. Daly, J. Hetherington, T. Krüger, P. K. Maini, J. M. Pitt-Francis, R. J. Muschel, T. Alarcón, and H. M. Byrne. Abnormal morphology biases hematocrit distribution in tumor vasculature and contributes to heterogeneity in tissue oxygenation. *Proceedings of the National Academy of Sciences*, 117(45):27811–27819, 2020. DOI: 10.1073/pnas.2007770117.

[21] J. Biehler. *Efficient uncertainty quantification for large-scale biomechanical models using a bayesian multi-fidelity approach*. PhD thesis, Technische Universität München, 2016. https://mediatum.ub.tum.de/?id=1294756.

[22] J. Biehler, M. W. Gee, and W. A. Wall. Towards efficient uncertainty quantification in complex and large-scale biomechanical problems based on a Bayesian multi-fidelity scheme. *Biomechanics and Modeling in Mechanobiology*, 14(3):489–513, 2015. DOI: 10.1007/s10237-014-0618-0.

[23] J. Biehler, M. Mäck, J. Nitzler, M. Hanss, P. Koutsourelakis, and W. A. Wall. Multifidelity approaches for uncertainty quantification. *GAMM-Mitteilungen*, 42(2):e201900008, 2019. DOI: 10.1002/gamm.201900008.

[24] J. Biehler, J. Nitzler, S. Brandstaeter, W. A. Wall, and V. Gravemeier. *QUEENS – A Software Platform for Uncertainty Quantification, Physics-Informed Machine Learning, Bayesian Optimization, Inverse Problems and Simulation Analytics: User Guide*. AdCo Engineering^{GW}, 2021.

[25] C. R. Birdwell, A. R. Brasier, and L. A. Taylor. Two-dimensional peptide mapping of fibronectins from bovine aortic endothelial cells and bovine plasma. *Biochemical and Biophysical Research Communications*, 97(2):574–581, 1980. DOI: 10.1016/0006-291X(80)90302-2.

[26] A. W. Bishop and L. Bjerrum. *The principle of effective stress*. Norges Geotekniske Inst., Oslo, 1960.

[27] E. Blanco, H. Shen, and M. Ferrari. Principles of nanoparticle design for overcoming biological barriers to drug delivery. *Nature biotechnology*, 33(9):941–51, 2015. DOI: 10.1038/nbt.3330.

[28] J. Bonet and R. D. Wood. *Nonlinear continuum mechanics for finite element analysis*. Cambridge University Press, 1997.

[29] Y. Boucher, C. Brekken, P. A. Netti, L. T. Baxter, and R. K. Jain. Intratumoral infusion of fluid: estimation of hydraulic conductivity and implications for the delivery of therapeutic agents. *British Journal of Cancer*, 78(11):1442–1448, 1998. DOI: 10.1038/bjc.1998.705.

[30] Y. Boucher, L. T. Baxter, and R. K. Jain. Interstitial pressure gradients in tissue-isolated and subcutaneous tumors: implications for therapy. *Cancer research*, 50(15):4478–84, 1990.

[31] F. Brezzi and M. Fortin. *Mixed and Hybrid Finite Element Methods*, volume 15 of *Springer Series in Computational Mathematics*. Springer New York, NY, 1991. DOI: 10.1007/978-1-4612-3172-1.

[32] A. K. Bui. Investigations of the influence of anisotropy on (a-)vascular tumor growth with a computational model. Term paper, Technische Universität München, 2019.

[33] R. A. Burrell, N. McGranahan, J. Bartek, and C. Swanton. The causes and consequences of genetic heterogeneity in cancer evolution. *Nature*, 501(7467):338–345, 2013. DOI: 10.1038/nature12625.

[34] Y. Cai, J. Wu, Z. Li, and Q. Long. Mathematical Modelling of a Brain Tumour Initiation and Early Development: A Coupled Model of Glioblastoma Growth, Pre-Existing Vessel Co-Option, Angiogenesis and Blood Perfusion. *PLOS ONE*, 11(3):e0150296, 2016. DOI: 10.1371/journal.pone.0150296.

[35] F. Campolongo, J. Cariboni, and A. Saltelli. An effective screening design for sensitivity analysis of large models. *Environmental Modelling and Software*, 22(10):1509–1518, 2007. DOI: 10.1016/j.envsoft.2006.10.004.

[36] P. Carmeliet and R. K. Jain. Angiogenesis in cancer and other diseases. *Nature*, 407 (6801):249–257, 2000. DOI: 10.1038/35025220.

[37] P. Carmeliet and R. K. Jain. Principles and mechanisms of vessel normalization for cancer and other angiogenic diseases. *Nature Reviews Drug Discovery*, 10(6):417–427, 2011. DOI: 10.1038/nrd3455.

[38] L. Cattaneo and P. Zunino. A computational model of drug delivery through microcirculation to compare different tumor treatments. *International Journal for Numerical Methods in Biomedical Engineering*, 30(11):1347–1371, 2014. DOI: 10.1002/cnm.2661.

[39] L. Cattaneo and P. Zunino. Computational models for fluid exchange between microcirculation and tissue interstitium. *Networks & Heterogeneous Media*, 9(1):135–159, 2014. DOI: 10.3934/nhm.2014.9.135.

[40] D. Cerroni, F. Laurino, and P. Zunino. Mathematical analysis, finite element approximation and numerical solvers for the interaction of 3D reservoirs with 1D wells. *GEM - International Journal on Geomathematics*, 10(1):4, 2019. DOI: 10.1007/s13137-019-0115-9.

[41] A. Cervadoro, C. Giverso, R. Pande, S. Sarangi, L. Preziosi, J. Wosik, A. Brazdeikis, and P. Decuzzi. Design Maps for the Hyperthermic Treatment of Tumors with Superparamagnetic Nanoparticles. *PLoS ONE*, 8(2):e57332, 2013. DOI: 10.1371/journal.pone.0057332.

[42] M. A. J. Chaplain, S. R. McDougall, and A. R. A. Anderson. Mathematical modeling of tumor-induced angiogenesis. *Annual Review of Biomedical Engineering*, 8(1):233–257, 2006. DOI: 10.1146/annurev.bioeng.8.061505.095807.

[43] D. K. Chatterjee, P. Diagaradjane, and S. Krishnan. Nanoparticle-mediated hyperthermia in cancer therapy. *Therapeutic Delivery*, 2(8):1001–1014, 2011. DOI: 10.4155/tde.11.72.

[44] J. J. Choi, S. Wang, Y.-S. Tung, B. Morrison, and E. E. Konofagou. Molecules of Various Pharmacologically-Relevant Sizes Can Cross the Ultrasound-Induced Blood-Brain Barrier Opening in vivo. *Ultrasound in Medicine & Biology*, 36(1):58–67, 2010. DOI: 10.1016/j.ultrasmedbio.2009.08.006.

[45] C.-Y. Chou, C.-K. Huang, K.-W. Lu, T.-L. Horng, and W.-L. Lin. Investigation of the Spatiotemporal Responses of Nanoparticles in Tumor Tissues with a Small-Scale Mathematical Model. *PLoS ONE*, 8(4):e59135, 2013. DOI: 10.1371/journal.pone.0059135.

[46] O. Coussy. *Poromechanics*. John Wiley & Sons, Ltd, Chichester, UK, 2003. DOI: 10.1002/0470092718.

[47] T. R. Cox and J. T. Erler. Remodeling and homeostasis of the extracellular matrix: implications for fibrotic diseases and cancer. *Disease Models & Mechanisms*, 4(2):165–178, 2011. DOI: 10.1242/dmm.004077.

[48] V. Cristini and J. Lowengrub. *Multiscale Modeling of Cancer*. Cambridge University Press, Cambridge, 2010. DOI: 10.1017/CBO9780511781452.

[49] Csimsoft. Trelis (Version 17.0) [Computer software]. American Fork, UT: csimsoft. Retrieved from http://csimsoft.com, 2020.

[50] L. T. Curtis, M. Wu, J. Lowengrub, P. Decuzzi, and H. B. Frieboes. Computational Modeling of Tumor Response to Drug Release from Vasculature-Bound Nanoparticles. *PLOS ONE*, 10(12):e0144888, 2015. DOI: 10.1371/journal.pone.0144888.

[51] C. D'Angelo and A. Quarteroni. On the coupling of 1D and 3D diffusion equations: Application to tissue perfusion problems. *Mathematical Models and Methods in Applied Sciences*, 18(08):1481–1504, 2008. DOI: 10.1142/S0218202508003108.

[52] C. D'Angelo. *Multiscale modelling of metabolism and transport phenomena in living tissues*. PhD thesis, École polytechnique fédérale de Lausanne, 2007. http://infoscience.epfl.ch/record/103742/files/EPFL_TH3803.pdf.

[53] C. D'Angelo. Finite Element Approximation of Elliptic Problems with Dirac Measure Terms in Weighted Spaces: Applications to One- and Three-dimensional Coupled Problems. *SIAM Journal on Numerical Analysis*, 50(1):194–215, 2012. DOI: 10.1137/100813853.

[54] C. Danowski, V. Gravemeier, L. Yoshihara, and W. A. Wall. A monolithic computational approach to thermo-structure interaction. *International Journal for Numerical Methods in Engineering*, 95(13):1053–1078, 2013. DOI: 10.1002/nme.4530.

[55] M. K. Das, P. P. Mukherjee, and K. Muralidhar. *Modeling Transport Phenomena in Porous Media with Applications*. Mechanical Engineering Series. Springer International Publishing, Cham, 2018. DOI: 10.1007/978-3-319-69866-3.

[56] Y. Davit, C. G. Bell, H. M. Byrne, L. A. Chapman, L. S. Kimpton, G. E. Lang, K. H. Leonard, J. M. Oliver, N. C. Pearson, R. J. Shipley, S. L. Waters, J. P. Whiteley, B. D. Wood, and M. Quintard. Homogenization via formal multiscale asymptotics and volume averaging: How do the two techniques compare? *Advances in Water Resources*, 62:178–206, 2013. DOI: 10.1016/j.advwatres.2013.09.006.

[57] T. S. Deisboeck and G. Stamatakos. *Multiscale Cancer Modeling*. Chapman & Hall/CRC Mathematical and Computational Biology. CRC Press, 2010.

[58] T. S. Deisboeck, Z. Wang, P. Macklin, and V. Cristini. Multiscale Cancer Modeling. *Annual Review of Biomedical Engineering*, 13(1):127–155, 2011. DOI: 10.1146/annurev-bioeng-071910-124729.

[59] A. D'Esposito, P. W. Sweeney, M. Ali, M. Saleh, R. Ramasawmy, T. A. Roberts, G. Agliardi, A. Desjardins, M. F. Lythgoe, R. B. Pedley, R. Shipley, and S. Walker-Samuel. Computational fluid dynamics with imaging of cleared tissue and of in vivo perfusion predicts drug uptake and treatment responses in tumours. *Nature Biomedical Engineering*, 2(10):773–787, 2018. DOI: 10.1038/s41551-018-0306-y.

[60] M. W. Dewhirst and T. W. Secomb. Transport of drugs from blood vessels to tumour tissue. *Nature Reviews Cancer*, 17(12):738–750, 2017. DOI: 10.1038/nrc.2017.93.

[61] M. W. Dewhirst, C. Tso, R. Oliver, C. S. Gustafson, T. W. Secomb, and J. F. Gross. Morphologic and hemodynamic comparison of tumor and healing normal tissue microvasculature. *International Journal of Radiation Oncology*Biology*Physics*, 17(1):91–99, 1989. DOI: 10.1016/0360-3016(89)90375-1.

[62] S. Dimmeler and A. M. Zeiher. Endothelial Cell Apoptosis in Angiogenesis and Vessel Regression. *Circulation Research*, 87(6):434–439, 2000. DOI: 10.1161/01.RES.87.6.434.

[63] P. Dogra, J. D. Butner, Y.-l. Chuang, S. Caserta, S. Goel, C. J. Brinker, V. Cristini, and Z. Wang. Mathematical modeling in cancer nanomedicine: a review. *Biomedical Microdevices*, 21(2):40, 2019. DOI: 10.1007/s10544-019-0380-2.

[64] B. Döme, S. Paku, B. Somlai, and J. Tímár. Vascularization of cutaneous melanoma involves vessel co-option and has clinical significance. *The Journal of Pathology*, 197(3): 355–362, 2002. DOI: 10.1002/path.1124.

[65] B. Döme, M. J. C. Hendrix, S. Paku, J. Tóvári, and J. Tímár. Alternative vascularization mechanisms in cancer: Pathology and therapeutic implications. *The American journal of pathology*, 170(1):1–15, 2007. DOI: 10.2353/ajpath.2007.060302.

[66] J. Donea, A. Huerta, J. Ponthot, and A. Rodriguez-Ferran. Arbitrary Lagrangian-Eulerian Methods. In E. Stein, R. Borst, and T. J. R. Hughes, editors, *Encyclopedia of Computational Mechanics*, chapter 14. John Wiley & Sons, Ltd, Chichester, UK, 2004. DOI: 10.1002/0470091355.ecm009.

[67] M. R. Dreher, W. Liu, C. R. Michelich, M. W. Dewhirst, F. Yuan, and A. Chilkoti. Tumor Vascular Permeability, Accumulation, and Penetration of Macromolecular Drug Carriers. *JNCI: Journal of the National Cancer Institute*, 98(5):335–344, 2006. DOI: 10.1093/jnci/djj070.

[68] A. C. Dudley. Tumor Endothelial Cells. *Cold Spring Harbor Perspectives in Medicine*, 2 (3):a006536–a006536, 2012. DOI: 10.1101/cshperspect.a006536.

[69] P. Ehrlich. Aus Theorie und Praxis der Chemotherapie. *Folia Serologica*, 7:698–714, 1911.

[70] R. Erber, U. Eichelsbacher, V. Powajbo, T. Korn, V. Djonov, J. Lin, H.-P. Hammes, R. Grobholz, A. Ullrich, and P. Vajkoczy. EphB4 controls blood vascular morphogenesis during postnatal angiogenesis. *The EMBO Journal*, 25(3):628–641, 2006. DOI: 10.1038/sj.emboj.7600949.

[71] Q. Fang, S. Sakadžić, L. Ruvinskaya, A. Devor, A. M. Dale, and D. A. Boas. Oxygen advection and diffusion in a three-dimensional vascular anatomical network. *Optics Express*, 16(22):17530, 2008. DOI: 10.1364/OE.16.017530.

[72] R. Fang, M. Kronbichler, M. Wurzer, and W. A. Wall. Parallel, physics-oriented, monolithic solvers for three-dimensional, coupled finite element models of lithium-ion cells. *Computer Methods in Applied Mechanics and Engineering*, 350:803–835, 2019. DOI: 10.1016/j.cma.2019.03.017.

[73] P. Farah, A. Popp, and W. A. Wall. Segment-based vs. element-based integration for mortar methods in computational contact mechanics. *Computational Mechanics*, 55(1): 209–228, 2015. DOI: 10.1007/s00466-014-1093-2.

[74] M. Ferrari. Frontiers in cancer nanomedicine: directing mass transport through biological barriers. *Trends in Biotechnology*, 28(4):181–188, 2010. DOI: 10.1016/j.tibtech.2009.12.007.

[75] J. Folkman. Tumor Angiogenesis: Therapeutic Implications. *New England Journal of Medicine*, 285(21):1182–1186, 1971. DOI: 10.1056/NEJM197111182852108.

[76] J. Folkman. What Is the Evidence That Tumors Are Angiogenesis Dependent? *JNCI: Journal of the National Cancer Institute*, 82(1):4–7, 1990. DOI: 10.1093/jnci/82.1.4.

[77] A. Formaggia, A. Quarteroni, and A. Veneziana. *Cardiovascular Mathematics*. Springer Milan, Milano, 2009. DOI: 10.1007/978-88-470-1152-6.

[78] C. Förster. *Robust methods for fluid-structure interaction with stabilised finite elements*. PhD thesis, Universität Stuttgart, 2007. http://elib.uni-stuttgart.de/handle/11682/287.

[79] C. Förster, W. A. Wall, and E. Ramm. On the geometric conservation law in transient flow calculations on deforming domains. *International Journal for Numerical Methods in Fluids*, 50(12):1369–1379, 2006. DOI: 10.1002/fld.1093.

[80] J. Forster, W. Harriss-Phillips, M. Douglass, and E. Bezak. A review of the development of tumor vasculature and its effects on the tumor microenvironment. *Hypoxia*, Volume 5: 21–32, 2017. DOI: 10.2147/HP.S133231.

[81] C. Frantz, K. M. Stewart, and V. M. Weaver. The extracellular matrix at a glance. *Journal of Cell Science*, 123(24):4195–4200, 2010. DOI: 10.1242/jcs.023820.

[82] T. Fredrich, M. Welter, and H. Rieger. Tumorcode: A framework to simulate vascularized tumors. *European Physical Journal E*, 41(4), 2018. DOI: 10.1140/epje/i2018-11659-x.

[83] H. B. Frieboes, F. Jin, Y.-L. Chuang, S. M. Wise, J. S. Lowengrub, and V. Cristini. Three-dimensional multispecies nonlinear tumor growth–II: Tumor invasion and angiogenesis. *Journal of Theoretical Biology*, 264(4):1254–1278, 2010. DOI: 10.1016/j.jtbi.2010.02.036.

[84] H. B. Frieboes, M. Wu, J. Lowengrub, P. Decuzzi, and V. Cristini. A Computational Model for Predicting Nanoparticle Accumulation in Tumor Vasculature. *PLoS ONE*, 8 (2):e56876, 2013. DOI: 10.1371/journal.pone.0056876.

[85] B. C. Fry, J. Lee, N. P. Smith, and T. W. Secomb. Estimation of Blood Flow Rates in Large Microvascular Networks. *Microcirculation*, 19(6):530–538, 2012. DOI: 10.1111/j.1549-8719.2012.00184.x.

[86] W. G. Gray and B. A. Schrefler. Analysis of the solid phase stress tensor in multiphase porous media. *International Journal for Numerical and Analytical Methods in Geomechanics*, 31(4):541–581, 2007. DOI: 10.1002/nag.541.

[87] T. C. Gasser, R. W. Ogden, and G. A. Holzapfel. Hyperelastic modelling of arterial layers with distributed collagen fibre orientations. *Journal of The Royal Society Interface*, 3(6): 15–35, 2006. DOI: 10.1098/rsif.2005.0073.

[88] M. W. Gee, U. Küttler, and W. A. Wall. Truly monolithic algebraic multigrid for fluid-structure interaction. *International Journal for Numerical Methods in Engineering*, 85(8): 987–1016, 2011. DOI: 10.1002/nme.3001.

[89] C. Geuzaine and J.-F. Remacle. Gmsh: A 3-d finite element mesh generator with built-in pre- and post-processing facilities. *International Journal for Numerical Methods in Engineering*, 79(11):1309–1331, 2009. DOI: 10.1002/nme.2579.

[90] J. L. Gevertz, G. T. Gillies, and S. Torquato. Simulating tumor growth in confined heterogeneous environments. *Physical Biology*, 5(3):036010, 2008. DOI: 10.1088/1478-3975/5/3/036010.

[91] O. L. Gobbo, K. Sjaastad, M. W. Radomski, Y. Volkov, and A. Prina-Mello. Magnetic Nanoparticles in Cancer Theranostics. *Theranostics*, 5(11):1249–1263, 2015. DOI: 10.7150/thno.11544.

[92] D. Goldman. Theoretical models of microvascular oxygen transport to tissue. *Microcirculation*, 15(8):795–811, 2008. DOI: 10.1080/10739680801938289.

[93] W. G. Gray and C. T. Miller. Thermodynamically constrained averaging theory approach for modeling flow and transport phenomena in porous medium systems: 1. Motivation and overview. *Advances in Water Resources*, 28(2):161–180, 2005. DOI: 10.1016/j.advwatres.2004.09.005.

[94] W. G. Gray and C. T. Miller. Thermodynamically constrained averaging theory approach for modeling flow and transport phenomena in porous medium systems: 5. Single-fluid-phase transport. *Advances in Water Resources*, 32(5):681–711, 2009. DOI: 10.1016/j.advwatres.2008.10.013.

[95] W. G. Gray and C. T. Miller. *Introduction to the Thermodynamically Constrained Averaging Theory for Porous Medium Systems*. Advances in Geophysical and Environmental Mechanics and Mathematics. Springer International Publishing, Cham, 2014. DOI: 10.1007/978-3-319-04010-3.

[96] W. G. Gray, B. A. Schrefler, and F. Pesavento. The solid phase stress tensor in porous media mechanics and the Hill-Mandel condition. *Journal of the Mechanics and Physics of Solids*, 57(3):539–554, 2009. DOI: 10.1016/j.jmps.2008.11.005.

[97] W. G. Gray, C. T. Miller, and B. A. Schrefler. Averaging theory for description of environmental problems: What have we learned? *Advances in Water Resources*, 51:123–138, 2013. DOI: 10.1016/j.advwatres.2011.12.005.

[98] C. Grigo and P.-S. Koutsourelakis. A physics-aware, probabilistic machine learning framework for coarse-graining high-dimensional systems in the Small Data regime. *Journal of Computational Physics*, 397:108842, 2019. DOI: 10.1016/j.jcp.2019.05.053.

[99] D. Hanahan and R. A. Weinberg. The Hallmarks of Cancer. *Cell*, 100(1):57–70, 2000. DOI: 10.1016/S0092-8674(00)81683-9.

[100] D. Hanahan and R. A. Weinberg. Hallmarks of Cancer: The Next Generation. *Cell*, 144 (5):646–674, 2011. DOI: 10.1016/j.cell.2011.02.013.

[101] A. Hawkins-Daarud, K. G. van der Zee, and J. Tinsley Oden. Numerical simulation of a thermodynamically consistent four-species tumor growth model. *International Journal for Numerical Methods in Biomedical Engineering*, 28(1):3–24, 2012. DOI: 10.1002/cnm.1467.

[102] A. Hawkins-Daarud, S. Prudhomme, K. G. van der Zee, and J. T. Oden. Bayesian calibration, validation, and uncertainty quantification of diffuse interface models of tumor growth. *Journal of Mathematical Biology*, 67(6-7):1457–1485, 2013. DOI: 10.1007/s00285-012-0595-9.

[103] C.-H. Heldin, K. Rubin, K. Pietras, and A. Östman. High interstitial fluid pressure – an obstacle in cancer therapy. *Nature Reviews Cancer*, 4(10):806–813, 2004. DOI: 10.1038/nrc1456.

[104] J. D. Hellums, P. K. Nair, N. S. Huang, and N. Ohshima. Simulation of intraluminal gas transport processes in the microcirculation. *Annals of Biomedical Engineering*, 24(1): 1–24, 1995. DOI: 10.1007/BF02770991.

[105] M. A. Heroux, R. A. Bartlett, V. E. Howle, R. J. Hoekstra, J. J. Hu, T. G. Kolda, R. B. Lehoucq, K. R. Long, R. P. Pawlowski, E. T. Phipps, A. G. Salinger, H. K. Thornquist, R. S. Tuminaro, J. M. Willenbring, A. Williams, and K. S. Stanley. An overview of the Trilinos project. *ACM Transactions on Mathematical Software*, 31(3):397–423, 2005. DOI: 10.1145/1089014.1089021.

[106] R. Hesketh. *Introduction to Cancer Biology*. Cambridge University Press, Cambridge, 2012. DOI: DOI: 10.1017/CBO9781139012904.

[107] C. S. Hogea, B. T. Murray, and J. A. Sethian. Simulating complex tumor dynamics from avascular to vascular growth using a general level-set method. *Journal of Mathematical Biology*, 53(1):86–134, 2006. DOI: 10.1007/s00285-006-0378-2.

[108] J. Holash. Vessel Cooption, Regression, and Growth in Tumors Mediated by Angiopoietins and VEGF. *Science*, 284(5422):1994–1998, 1999. DOI: 10.1126/science.284.5422.1994.

[109] J. Holash, S. J. Wiegand, and G. D. Yancopoulos. New model of tumor angiogenesis: dynamic balance between vessel regression and growth mediated by angiopoietins and VEGF. *Oncogene*, 18(38):5356–5362, 1999. DOI: 10.1038/sj.onc.1203035.

[110] G. A. Holzapfel. *Nonlinear solid mechanics: a continuum approach for engineering*. Wiley, 2000.

[111] R. O. Hynes. *Fibronectins*. Springer Series in Molecular Biology. Springer New York, NY, 1990. DOI: 10.1007/978-1-4612-3264-3.

[112] A. K. Iyer, G. Khaled, J. Fang, and H. Maeda. Exploiting the enhanced permeability and retention effect for tumor targeting. *Drug Discovery Today*, 11(17-18):812–818, 2006. DOI: 10.1016/j.drudis.2006.07.005.

[113] R. K. Jain. Transport of molecules across tumor vasculature. *Cancer and metastasis review*, 6(4):559–593, 1987. DOI: 10.1007/BF00047468.

[114] R. K. Jain. Barriers to Drug Delivery in Solid Tumors. *Scientific American*, 271(1):58–65, 1994. DOI: 10.1038/scientificamerican0794-58.

[115] R. K. Jain. Delivery of Molecular and Cellular Medicine to Solid Tumors. *Microcirculation*, 4(1):1–23, 1997. DOI: 10.3109/10739689709148314.

[116] R. K. Jain. Normalization of Tumor Vasculature: An Emerging Concept in Antiangiogenic Therapy. *Science*, 307(5706):58–62, 2005. DOI: 10.1126/science.1104819.

[117] R. K. Jain and T. Stylianopoulos. Delivering nanomedicine to solid tumors. *Nature Reviews Clinical Oncology*, 7(11):653–664, 2010. DOI: 10.1038/nrclinonc.2010.139.

[118] R. K. Jain, R. T. Tong, and L. L. Munn. Effect of Vascular Normalization by Antiangiogenic Therapy on Interstitial Hypertension, Peritumor Edema, and Lymphatic Metastasis: Insights from a Mathematical Model. *Cancer Research*, 67(6):2729–2735, 2007. DOI: 10.1158/0008-5472.CAN-06-4102.

[119] C. Janko, T. Ratschker, K. Nguyen, L. Zschiesche, R. Tietze, S. Lyer, and C. Alexiou. Functionalized Superparamagnetic Iron Oxide Nanoparticles (SPIONs) as Platform for the Targeted Multimodal Tumor Therapy. *Frontiers in Oncology*, 9(FEB):1–9, 2019. DOI: 10.3389/fonc.2019.00059.

[120] C. D. Kaddi, J. H. Phan, and M. D. Wang. Computational nanomedicine: modeling of nanoparticle-mediated hyperthermal cancer therapy. *Nanomedicine*, 8(8):1323–1333, 2013. DOI: 10.2217/nnm.13.117.

[121] C. Kahle, K. Lam, J. Latz, and E. Ullmann. Bayesian Parameter Identification in Cahn–Hilliard Models for Biological Growth. *SIAM/ASA Journal on Uncertainty Quantification*, 7(2):526–552, 2019. DOI: 10.1137/18M1210034.

[122] J. P. Kaipio and E. Somersalo. *Statistical and Computational Inverse Problems*, volume 160 of *Applied Mathematical Sciences*. Springer-Verlag, New York, 2005. DOI: 10.1007/b138659.

[123] P. Kaur, M. L. Aliru, A. S. Chadha, A. Asea, and S. Krishnan. Hyperthermia using nanoparticles – Promises and pitfalls. *International Journal of Hyperthermia*, 32(1):76–88, 2016. DOI: 10.3109/02656736.2015.1120889.

[124] Y. Kim, M. A. Stolarska, and H. G. Othmer. A hybrid model for tumor spheroid growth in vitro I: Theoretical development and early results. *Mathematical Models and Methods in Applied Sciences*, 17(supp01):1773–1798, 2007. DOI: 10.1142/S0218202507002479.

[125] T. Koch. *Mixed-dimension models for flow and transport processes in porous media with embedded tubular network systems*. PhD thesis, University of Stuttgart, 2020. http://elib.uni-stuttgart.de/handle/11682/10992.

[126] T. Koch, R. Helmig, and M. Schneider. A new and consistent well model for one-phase flow in anisotropic porous media using a distributed source model. *Journal of Computational Physics*, 410:109369, 2020. DOI: 10.1016/j.jcp.2020.109369.

[127] T. Koch, M. Schneider, R. Helmig, and P. Jenny. Modeling tissue perfusion in terms of 1d-3d embedded mixed-dimension coupled problems with distributed sources. *Journal of Computational Physics*, 410:109370, 2020. DOI: 10.1016/j.jcp.2020.109370.

[128] M. Kojic, M. Milosevic, V. Simic, E. Koay, J. Fleming, S. Nizzero, N. Kojic, A. Ziemys, and M. Ferrari. A composite smeared finite element for mass transport in capillary systems and biological tissue. *Computer Methods in Applied Mechanics and Engineering*, 324(Supplement C):413–437, 2017. DOI: 10.1016/j.cma.2017.06.019.

[129] T. Köppl and B. Wohlmuth. Optimal A Priori Error Estimates for an Elliptic Problem with Dirac Right-Hand Side. *SIAM Journal on Numerical Analysis*, 52(4):1753–1769, 2014. DOI: 10.1137/130927619.

[130] T. Köppl, E. Vidotto, B. Wohlmuth, and P. Zunino. Mathematical modeling, analysis and numerical approximation of second-order elliptic problems with inclusions. *Mathematical Models and Methods in Applied Sciences*, 28(05):953–978, 2018. DOI: 10.1142/S0218202518500252.

[131] T. Köppl, E. Vidotto, and B. Wohlmuth. A 3D-1D coupled blood flow and oxygen transport model to generate microvascular networks. *International Journal for Numerical Methods in Biomedical Engineering*, 36(10):e3386, 2020. DOI: 10.1002/cnm.3386.

[132] C. Korn and H. G. Augustin. Mechanisms of Vessel Pruning and Regression. *Developmental Cell*, 34(1):5–17, 2015. DOI: 10.1016/j.devcel.2015.06.004.

[133] P.-S. Koutsourelakis. Accurate Uncertainty Quantification Using Inaccurate Computational Models. *SIAM Journal on Scientific Computing*, 31(5):3274–3300, 2009. DOI: 10.1137/080733565.

[134] J. Kremheller. Bottom-Up Finite Element Modeling of Endovascular Stent Grafts. Master's thesis, Technische Universität München, 2016.

[135] J. Kremheller, A.-T. Vuong, L. Yoshihara, W. A. Wall, and B. A. Schrefler. A monolithic multiphase porous medium framework for (a-)vascular tumor growth. *Computer Methods in Applied Mechanics and Engineering*, 340:657–683, 2018. DOI: 10.1016/j.cma.2018.06.009.

[136] J. Kremheller, A.-T. Vuong, B. A. Schrefler, and W. A. Wall. An approach for vascular tumor growth based on a hybrid embedded/homogenized treatment of the vasculature within a multiphase porous medium model. *International Journal for Numerical Methods in Biomedical Engineering*, 35(11):e3253, 2019. DOI: 10.1002/cnm.3253.

[137] J. Kremheller, S. Brandstaeter, B. A. Schrefler, and W. A. Wall. Validation and parameter optimization of a hybrid embedded/homogenized solid tumor perfusion model. *International Journal for Numerical Methods in Biomedical Engineering*, 37(8):e3508, 2021. DOI: 10.1002/cnm.3508.

[138] U. Küttler. *Effiziente Lösungsverfahren für Fluid-Struktur-Interaktions-Probleme*. PhD thesis, Technische Universität München, 2009. http://mediatum.ub.tum.de/?id=820910.

[139] U. Küttler, M. Gee, C. Förster, A. Comerford, and W. A. Wall. Coupling strategies for biomedical fluid-structure interaction problems. *International Journal for Numerical Methods in Biomedical Engineering*, 26(3-4):305–321, 2010. DOI: 10.1002/cnm.1281.

[140] U. Küttler and W. A. Wall. Fixed-point fluid-structure interaction solvers with dynamic relaxation. *Computational Mechanics*, 43(1):61–72, 2008. DOI: 10.1007/s00466-008-0255-5.

[141] L. Lamalice, F. Le Boeuf, and J. Huot. Endothelial Cell Migration During Angiogenesis. *Circulation Research*, 100(6):782–794, 2007. DOI: 10.1161/01.RES.0000259593.07661.1e.

[142] L. A. Lane. Physics in nanomedicine: Phenomena governing the in vivo performance of nanoparticles. *Applied Physics Reviews*, 7(1):011316, 2020. DOI: 10.1063/1.5052455.

[143] M. Leunig, F. Yuan, M. D. Menger, Y. Boucher, A. E. Goetz, K. Messmer, and R. K. Jain. Angiogenesis, Microvascular Architecture, Microhemodynamics, and Interstitial Fluid Pressure during Early Growth of Human Adenocarcinoma LS174T in SCID Mice. *Cancer Research*, 52(23):6553 – 6560, 1992.

[144] K. R. Levental, H. Yu, L. Kass, J. N. Lakins, M. Egeblad, J. T. Erler, S. F. T. Fong, K. Csiszar, A. Giaccia, W. Weninger, M. Yamauchi, D. L. Gasser, and V. M. Weaver. Matrix crosslinking forces tumor progression by enhancing integrin signaling. *Cell*, 139 (5):891–906, 2009. DOI: 10.1016/j.cell.2009.10.027.

[145] J. R. Levick and C. C. Michel. Microvascular fluid exchange and the revised Starling principle. *Cardiovascular Research*, 87(2):198–210, 2010. DOI: 10.1093/cvr/cvq062.

[146] R. W. Lewis and B. A. Schrefler. *The Finite Element Method in the Deformation and Consolidation of Porous Media*. Chichester: Wiley, 1998.

[147] R. W. Lewis and B. A. Schrefler. A finite element simulation of the subsidence of gas reservoirs undergoing a water drive. In R. Gallagher, D. Norrie, J. Oden, and O. Zienkiewicz, editors, *Finite Elements in Fluids*, pages 177–197. Wiley, Chichester, 1982.

[148] R. W. Lewis and Y. Sukirman. Finite element modelling of three-phase flow in deforming saturated oil reservoirs. *International Journal for Numerical and Analytical Methods in Geomechanics*, 17(8):577–598, 1993. DOI: 10.1002/nag.1610170804.

[149] J.-X. Li, Q.-Y. Huang, J.-Y. Zhang, and J.-Z. Du. Engineering nanoparticles to tackle tumor barriers. *Journal of Materials Chemistry B*, 8(31):6686–6696, 2020. DOI: 10.1039/D0TB00967A.

[150] J. Li, A. Chekkoury, J. Prakash, S. Glasl, P. Vetschera, B. Koberstein-Schwarz, I. Olefir, V. Gujrati, M. Omar, and V. Ntziachristos. Spatial heterogeneity of oxygenation and haemodynamics in breast cancer resolved in vivo by conical multispectral optoacoustic mesoscopy. *Light: Science & Applications*, 9(1):57, 2020. DOI: 10.1038/s41377-020-0295-y.

[151] E. A. B. F. Lima, J. T. Oden, and R. C. Almeida. A hybrid ten-species phase-field model of tumor growth. *Mathematical Models and Methods in Applied Sciences*, 24(13):2569–2599, 2014. DOI: 10.1142/s0218202514500304.

[152] E. A. B. F. Lima, N. Ghousifam, A. Ozkan, J. T. Oden, A. Shahmoradi, M. N. Rylander, B. Wohlmuth, and T. E. Yankeelov. Calibration of Multi-Parameter Models of Avascular Tumor Growth Using Time Resolved Microscopy Data. *Scientific Reports*, 8(1):14558, 2018. DOI: 10.1038/s41598-018-32347-9.

[153] E. A. Lima, J. T. Oden, B. Wohlmuth, A. Shahmoradi, D. A. Hormuth, T. E. Yankeelov, L. Scarabosio, and T. Horger. Selection and validation of predictive models of radiation effects on tumor growth based on noninvasive imaging data. *Computer Methods in Applied Mechanics and Engineering*, 327:277–305, 2017. DOI: 10.1016/j.cma.2017.08.009.

[154] E. A. Logsdon, S. D. Finley, A. S. Popel, and F. M. Gabhann. A systems biology view of blood vessel growth and remodelling. *Journal of Cellular and Molecular Medicine*, 18 (8):1491–1508, 2014. DOI: 10.1111/jcmm.12164.

[155] G. Lorenzo. *Tissue-scale, patient-specific modeling and simulation of prostate cancer growth*. PhD thesis, University of A Coruña, 2018. http://hdl.handle.net/2183/20826.

[156] G. Lorenzo, M. A. Scott, K. Tew, T. J. R. Hughes, Y. J. Zhang, L. Liu, G. Vilanova, and H. Gomez. Tissue-scale, personalized modeling and simulation of prostate cancer growth. *Proceedings of the National Academy of Sciences*, 113(48):E7663–E7671, 2016. DOI: 10.1073/pnas.1615791113.

[157] J. S. Lowengrub, H. B. Frieboes, F. Jin, Y.-L. Chuang, X. Li, P. Macklin, S. M. Wise, and V. Cristini. Nonlinear modelling of cancer: bridging the gap between cells and tumours. *Nonlinearity*, 23(1):R1–R91, 2010. DOI: 10.1088/0951-7715/23/1/R01.

[158] P. Macklin, S. McDougall, A. R. A. Anderson, M. A. J. Chaplain, V. Cristini, and J. Lowengrub. Multiscale modelling and nonlinear simulation of vascular tumour growth. *Journal of Mathematical Biology*, 58(4-5):765–798, 2009. DOI: 10.1007/s00285-008-0216-9.

[159] S. Maman and I. P. Witz. A history of exploring cancer in context. *Nature Reviews Cancer*, 18(6):359–376, 2018. DOI: 10.1038/s41568-018-0006-7.

[160] N. V. Mantzaris, S. Webb, and H. G. Othmer. Mathematical modeling of tumor-induced angiogenesis. *Journal of Mathematical Biology*, 49(2):111–187, 2004. DOI: 10.1007/s00285-003-0262-2.

[161] M. Marchand, C. Monnot, L. Muller, and S. Germain. Extracellular matrix scaffolding in angiogenesis and capillary homeostasis. *Seminars in Cell & Developmental Biology*, 2018. DOI: 10.1016/J.SEMCDB.2018.08.007.

[162] Y. K. Mariappan, K. J. Glaser, and R. L. Ehman. Magnetic resonance elastography: A review. *Clinical Anatomy*, 23(5):497–511, 2010. DOI: 10.1002/ca.21006.

[163] J. E. Marsden and T. J. R. Hughes. *Mathematical foundations of elasticity*. Dover, 1994.

[164] P. Mascheroni and B. A. Schrefler. In Silico Models for Nanomedicine: Recent Developments. *Current Medicinal Chemistry*, 25(34):4192–4207, 2018. DOI: 10.2174/0929867324666170417120725.

[165] MathWorks Inc. Documentation of matlab's `alphaShape` function. https://de.mathworks.com/help/matlab/ref/alphashape.html, 2018. Accessed: 2021-03-22.

[166] Y. Matsumura and H. Maeda. A new concept for macromolecular therapeutics in cancer chemotherapy: mechanism of tumoritropic accumulation of proteins and the antitumor agent Smancs. *Cancer research*, 46(12 Part 1):6387–6392, 1986.

[167] J. Metzcar, Y. Wang, R. Heiland, and P. Macklin. A Review of Cell-Based Computational Modeling in Cancer Biology. *JCO Clinical Cancer Informatics*, 3:1–13, 2019. DOI: 10.1200/CCI.18.00069.

[168] F. Michor, J. Liphardt, M. Ferrari, and J. Widom. What does physics have to do with cancer? *Nature Reviews Cancer*, 11(9):657–670, 2011. DOI: 10.1038/nrc3092.

[169] C. T. Miller, F. J. Valdés-Parada, and B. D. Wood. A Pedagogical Approach to the Thermodynamically Constrained Averaging Theory. *Transport in Porous Media*, 119(3):585–609, 2017. DOI: 10.1007/s11242-017-0900-6.

[170] C. T. Miller, W. G. Gray, and B. A. Schrefler. A continuum mechanical framework for modeling tumor growth and treatment in two- and three-phase systems. *Archive of Applied Mechanics*, 2021. DOI: 10.1007/s00419-021-01891-8.

[171] M. J. Mitchell, R. K. Jain, and R. Langer. Engineering and physical sciences in oncology: challenges and opportunities. *Nature Reviews Cancer*, 17(11):659–675, 2017. DOI: 10.1038/nrc.2017.83.

[172] S. M. Moghimi and D. Simberg. Nanoparticle transport pathways into tumors. *Journal of Nanoparticle Research*, 20(6):169, 2018. DOI: 10.1007/s11051-018-4273-8.

[173] J. Moreira and A. Deutsch. Cellular automaton models of tumor development: A critical review. *Advances in Complex Systems*, 05(02n03):247–267, 2002. DOI: 10.1142/S0219525902000572.

[174] S. Morikawa, P. Baluk, T. Kaidoh, A. Haskell, R. K. Jain, and D. M. McDonald. Abnormalities in Pericytes on Blood Vessels and Endothelial Sprouts in Tumors. *The American Journal of Pathology*, 160(3):985–1000, 2002. DOI: 10.1016/S0002-9440(10)64920-6.

[175] M. D. Morris. Factorial Sampling Plans for Preliminary Computational Experiments. *Technometrics*, 33(2):161–174, 1991. DOI: 10.2307/1269043.

[176] W. Mueller-Klieser. Three-dimensional cell cultures: from molecular mechanisms to clinical applications. *American Journal of Physiology-Cell Physiology*, 273(4):C1109–C1123, 1997. DOI: 10.1152/ajpcell.1997.273.4.C1109.

[177] M. Nabil, P. Decuzzi, and P. Zunino. Modelling mass and heat transfer in nano-based cancer hyperthermia. *Royal Society Open Science*, 2(10):150447, 2015. DOI: 10.1098/rsos.150447.

[178] M. Nabil and P. Zunino. A computational study of cancer hyperthermia based on vascular magnetic nanoconstructs. *Royal Society Open Science*, 3(9):160287, 2016. DOI: 10.1098/rsos.160287.

[179] A. Nakayama and F. Kuwahara. A general bioheat transfer model based on the theory of porous media. *International Journal of Heat and Mass Transfer*, 51(11-12):3190–3199, 2008. DOI: 10.1016/j.ijheatmasstransfer.2007.05.030.

[180] H. T. Nia, L. L. Munn, and R. K. Jain. Physical traits of cancer. *Science*, 370(6516): eaaz0868, 2020. DOI: 10.1126/science.aaz0868.

[181] N. Nishida, H. Yano, T. Nishida, T. Kamura, and M. Kojiro. Angiogenesis in cancer. *Vascular Health and Risk Management*, 2(3):213–219, 2006. DOI: 10.2147/vhrm.2006.2.3.213.

[182] J. Nitzler, J. Biehler, N. Fehn, P.-S. Koutsourelakis, and W. A. Wall. A Generalized Probabilistic Learning Approach for Multi-Fidelity Uncertainty Propagation in Complex Physical Simulations. http://arxiv.org/abs/2001.02892, 2020.

[183] S. Nizzero, A. Ziemys, and M. Ferrari. Transport Barriers and Oncophysics in Cancer Treatment. *Trends in Cancer*, 4(4):277–280, 2018. DOI: 10.1016/j.trecan.2018.02.008.

[184] J. T. Oden, A. Hawkins, and S. Prudhomme. General diffuse-interface theories and an approach to predictive tumor growth modeling. *Mathematical Models and Methods in Applied Sciences*, 20(03):477–517, 2010. DOI: 10.1142/S0218202510004313.

[185] J. T. Oden, E. A. B. F. Lima, R. C. Almeida, Y. Feng, M. N. Rylander, D. Fuentes, D. Faghihi, M. M. Rahman, M. DeWitt, M. Gadde, and J. C. Zhou. Toward Predictive Multiscale Modeling of Vascular Tumor Growth. *Archives of Computational Methods in Engineering*, 23(4):735–779, 2016. DOI: 10.1007/s11831-015-9156-x.

[186] R. W. Ogden. *Non-linear elastic deformations*. Dover Publications, 1997.

[187] T. P. Padera, B. R. Stoll, J. B. Tooredman, D. Capen, E. di Tomaso, and R. K. Jain. Cancer cells compress intratumour vessels. *Nature*, 427(6976):695–695, 2004. DOI: 10.1038/427695a.

[188] R. Pankov. Fibronectin at a glance. *Journal of Cell Science*, 115(20):3861–3863, 2002. DOI: 10.1242/jcs.00059.

[189] J. C. Parker and R. J. Lenhard. A model for hysteretic constitutive relations governing multiphase flow: 1. Saturation-pressure relations. *Water Resources Research*, 23(12): 2187–2196, 1987. DOI: 10.1029/WR023i012p02187.

[190] J. Parker and R. Lenhard. Determining three-phase permeability-saturation-pressure relations from two-phase system measurements. *Journal of Petroleum Science and Engineering*, 4(1):57–65, 1990. DOI: 10.1016/0920-4105(90)90046-6.

[191] M. J. Paszek, N. Zahir, K. R. Johnson, J. N. Lakins, G. I. Rozenberg, A. Gefen, C. A. Reinhart-King, S. S. Margulies, M. Dembo, D. Boettiger, D. A. Hammer, and V. M. Weaver. Tensional homeostasis and the malignant phenotype. *Cancer Cell*, 8(3):241–254, 2005. DOI: 10.1016/j.ccr.2005.08.010.

[192] J. Peiró and A. Veneziani. Reduced models of the cardiovascular system. In L. Formaggia, A. Quarteroni, and A. Veneziani, editors, *Cardiovascular Mathematics*, pages 347–394. Springer Milan, Milano, 2009. DOI: 10.1007/978-88-470-1152-6_10.

[193] H. H. Pennes. Analysis of Tissue and Arterial Blood Temperatures in the Resting Human Forearm. *Journal of Applied Physiology*, 1(2):93–122, 1948. DOI: 10.1152/jappl.1948.1.2.93.

[194] F. Pesavento, B. A. Schrefler, and G. Sciumè. Multiphase Flow in Deforming Porous Media: A Review. *Archives of Computational Methods in Engineering*, 24(2):423–448, 2017. DOI: 10.1007/s11831-016-9171-6.

[195] K. Plöckl. Modeling of Blood Vessel Compression in a Computational Tumor Growth Model. Master's thesis, Technische Universität München, 2020.

[196] A. S. Popel. Theory of oxygen transport to tissue. *Critical reviews in biomedical engineering*, 17(3):257–321, 1989.

[197] A. Popp. *Mortar methods for computational contact mechanics and general interface problems*. PhD thesis, Technische Universität München, 2012. https://mediatum.ub.tum.de/node?id=1109994.

[198] A. Popp, M. W. Gee, and W. A. Wall. A finite deformation mortar contact formulation using a primal-dual active set strategy. *International Journal for Numerical Methods in Engineering*, 79(11):1354–1391, 2009. DOI: doi:10.1002/nme.2614.

[199] A. Popp, M. Gitterle, M. W. Gee, and W. A. Wall. A dual mortar approach for 3D finite deformation contact with consistent linearization. *International Journal for Numerical Methods in Engineering*, 83(11):1428–1465, 2010. DOI: 10.1002/nme.2866.

[200] L. Preziosi and A. Tosin. Multiphase modelling of tumour growth and extracellular matrix interaction: mathematical tools and applications. *Journal of Mathematical Biology*, 58(4-5):625–656, 2009. DOI: 10.1007/s00285-008-0218-7.

[201] A. R. Pries and T. W. Secomb. Microvascular blood viscosity in vivo and the endothelial surface layer. *American Journal of Physiology-Heart and Circulatory Physiology*, 289 (6):H2657–H2664, 2005. DOI: 10.1152/ajpheart.00297.2005.

[202] A. R. Pries, T. W. Secomb, P. Gaehtgens, and J. F. Gross. Blood flow in microvascular networks. Experiments and simulation. *Circulation Research*, 67(4):826–834, 1990. DOI: 10.1161/01.RES.67.4.826.

[203] A. R. Pries, D. Neuhaus, and P. Gaehtgens. Blood viscosity in tube flow: dependence on diameter and hematocrit. *American Journal of Physiology-Heart and Circulatory Physiology*, 263(6):H1770–H1778, 1992. DOI: 10.1152/ajpheart.1992.263.6.H1770.

[204] A. R. Pries, T. W. Secomb, and P. Gaehtgens. Structural adaptation and stability of microvascular networks: theory and simulations. *American Journal of Physiology-Heart and Circulatory Physiology*, 275(2):H349–H360, 1998. DOI: 10.1152/ajpheart.1998.275.2.H349.

[205] A. R. Pries and T. W. Secomb. Making Microvascular Networks Work: Angiogenesis, Remodeling, and Pruning. *Physiology*, 29(6):446–455, 2014. DOI: 10.1152/physiol.00012.2014.

[206] A. R. Pries, A. J. M. Cornelissen, A. A. Sloot, M. Hinkeldey, M. R. Dreher, M. Höpfner, M. W. Dewhirst, and T. W. Secomb. Structural Adaptation and Heterogeneity of Normal and Tumor Microvascular Networks. *PLoS Computational Biology*, 5(5):e1000394, 2009. DOI: 10.1371/journal.pcbi.1000394.

[207] A. J. Primeau, A. Rendon, D. Hedley, L. Lilge, and I. F. Tannock. The distribution of the anticancer drug doxorubicin in relation to blood vessels in solid tumors. *Clinical Cancer Research*, 11(24):8782–8788, 2005. DOI: 10.1158/1078-0432.CCR-05-1664.

[208] P. P. Provenzano, K. W. Eliceiri, J. M. Campbell, D. R. Inman, J. G. White, and P. J. Keely. Collagen reorganization at the tumor-stromal interface facilitates local invasion. *BMC medicine*, 4(1):38, 2006. DOI: 10.1186/1741-7015-4-38.

[209] P. P. Provenzano, D. R. Inman, K. W. Eliceiri, S. M. Trier, and P. J. Keely. Contact guidance mediated three-dimensional cell migration is regulated by Rho/ROCK-dependent matrix reorganization. *Biophysical journal*, 95(11):5374–5384, 2008. DOI: 10.1529/biophysj.108.133116.

[210] A. Quarteroni, R. Sacco, and F. Saleri. *Numerical Mathematics*, volume 37 of *Texts in Applied Mathematics*. Springer New York, New York, NY, 2007. DOI: 10.1007/b98885.

[211] S. Ramanujan, A. Pluen, T. D. McKee, E. B. Brown, Y. Boucher, and R. K. Jain. Diffusion and Convection in Collagen Gels: Implications for Transport in the Tumor Interstitium. *Biophysical Journal*, 83(3):1650–1660, 2002. DOI: 10.1016/S0006-3495(02)73933-7.

[212] A. D. Rauch, A.-T. Vuong, L. Yoshihara, and W. A. Wall. A coupled approach for fluid saturated poroelastic media and immersed solids for modeling cell-tissue interactions. *International Journal for Numerical Methods in Biomedical Engineering*, 34(11):e3139, 2018. DOI: 10.1002/cnm.3139.

[213] P. A. Raviart and J. M. Thomas. A mixed finite element method for 2-nd order elliptic problems. In I. Galligani and E. Magenes, editors, *Mathematical Aspects of Finite Element Methods*, pages 292–315. Springer Berlin Heidelberg, Berlin, Heidelberg, 1977. DOI: 10.1007/BFb0064470.

[214] J. M. Rhodes and M. Simons. The extracellular matrix and blood vessel formation: not just a scaffold. *Journal of Cellular and Molecular Medicine*, 11(2):176–205, 2007. DOI: 10.1111/j.1582-4934.2007.00031.x.

[215] K. M. Riching, B. L. Cox, M. R. Salick, C. Pehlke, A. S. Riching, S. M. Ponik, B. R. Bass, W. C. Crone, Y. Jiang, A. M. Weaver, K. W. Eliceiri, and P. J. Keely. 3D collagen alignment limits protrusions to enhance breast cancer cell persistence. *Biophysical journal*, 107(11):2546–2558, 2014. DOI: 10.1016/j.bpj.2014.10.035.

[216] H. Rieger and M. Welter. Integrative models of vascular remodeling during tumor growth. *Wiley Interdisciplinary Reviews: Systems Biology and Medicine*, 7(3):113–129, 2015. DOI: 10.1002/wsbm.1295.

[217] H. Rieger, T. Fredrich, and M. Welter. Physics of the tumor vasculature: Theory and experiment. *The European Physical Journal Plus*, 131(2):31, 2016. DOI: 10.1140/epjp/i2016-16031-9.

[218] R. C. Rockne, A. Hawkins-Daarud, K. R. Swanson, J. P. Sluka, J. A. Glazier, P. Macklin, D. A. Hormuth, A. M. Jarrett, E. A. B. F. Lima, J. Tinsley Oden, G. Biros, T. E. Yankeelov, K. Curtius, I. Al Bakir, D. Wodarz, N. Komarova, L. Aparicio, M. Bordyuh, R. Rabadan, S. D. Finley, H. Enderling, J. Caudell, E. G. Moros, A. R. A. Anderson, R. A. Gatenby, A. Kaznatcheev, P. Jeavons, N. Krishnan, J. Pelesko, R. R. Wadhwa, N. Yoon, D. Nichol, A. Marusyk, M. Hinczewski, and J. G. Scott. The 2019 mathematical oncology roadmap. *Physical Biology*, 16(4):41005, 2019. DOI: 10.1088/1478-3975/ab1a09.

[219] C. Rodenberg. Global Sensitivity Analysis of a Multiphase Model for Avascular Tumor Growth. Master's thesis, Technische Universität München, 2020.

[220] C. Roma-Rodrigues, R. Mendes, P. Baptista, and A. Fernandes. Targeting Tumor Microenvironment for Cancer Therapy. *International Journal of Molecular Sciences*, 20(4): 840, 2019. DOI: 10.3390/ijms20040840.

[221] T. Roose, S. J. Chapman, and P. K. Maini. Mathematical Models of Avascular Tumor Growth. *SIAM Review*, 49(2):179–208, 2007. DOI: 10.1137/S0036144504446291.

[222] A. Saltelli, S. Tarantola, F. Campolongo, and M. Ratto. *Sensitivity Analysis in Practice*. John Wiley & Sons, Ltd, Chichester, UK, 2002. DOI: 10.1002/0470870958.

[223] A. Saltelli, M. Ratto, T. Andres, F. Campolongo, J. Cariboni, D. Gatelli, M. Saisana, and S. Tarantola. *Global Sensitivity Analysis. The Primer*. John Wiley & Sons, Ltd, Chichester, UK, 2007. DOI: 10.1002/9780470725184.

[224] R. Santagiuliana, C. Stigliano, P. Mascheroni, M. Ferrari, P. Decuzzi, and B. A. Schrefler. The role of cell lysis and matrix deposition in tumor growth modeling. *Advanced Modeling and Simulation in Engineering Sciences*, 2(1):19, 2015. DOI: 10.1186/s40323-015-0040-x.

[225] R. Santagiuliana, M. Ferrari, and B. Schrefler. Simulation of angiogenesis in a multiphase tumor growth model. *Computer Methods in Applied Mechanics and Engineering*, 304: 197–216, 2016. DOI: 10.1016/j.cma.2016.02.022.

[226] R. A. Sauer and L. De Lorenzis. An unbiased computational contact formulation for 3D friction. *International Journal for Numerical Methods in Engineering*, 101(4):251–280, 2015. DOI: 10.1002/nme.4794.

[227] M. Scianna, C. G. Bell, and L. Preziosi. A review of mathematical models for the formation of vascular networks. *Journal of Theoretical Biology*, 333:174–209, 2013. DOI: 10.1016/j.jtbi.2013.04.037.

[228] SciPy. Documentation of scipy.optimize.least_squares (version 1.5.2). https://docs.scipy.org/doc/scipy-1.5.2/reference/generated/scipy.optimize.least_squares.html, 2020. Accessed: 2021-03-22.

[229] G. Sciumè, W. G. Gray, M. Ferrari, P. Decuzzi, and B. A. Schrefler. On Computational Modeling in Tumor Growth. *Archives of Computational Methods in Engineering*, 20(4): 327–352, 2013. DOI: 10.1007/s11831-013-9090-8.

[230] G. Sciumè, S. Shelton, W. G. Gray, C. T. Miller, F. Hussain, M. Ferrari, P. Decuzzi, and B. A. Schrefler. A multiphase model for three-dimensional tumor growth. *New Journal of Physics*, 15, 2013. DOI: 10.1088/1367-2630/15/1/015005.

[231] G. Sciumè, D. P. Boso, W. G. Gray, C. Cobelli, and B. A. Schrefler. A two-phase model of plantar tissue: a step toward prediction of diabetic foot ulceration. *International Journal for Numerical Methods in Biomedical Engineering*, 30(11):1153–1169, 2014. DOI: 10.1002/cnm.2650.

[232] G. Sciumè, W. G. Gray, F. Hussain, M. Ferrari, P. Decuzzi, and B. A. Schrefler. Three phase flow dynamics in tumor growth. *Computational Mechanics*, 53(3):465–484, 2014. DOI: 10.1007/s00466-013-0956-2.

[233] G. Sciumè, R. Santagiuliana, M. Ferrari, P. Decuzzi, and B. A. Schrefler. A tumor growth model with deformable ECM. *Physical Biology*, 11(6), 2014. DOI: 10.1088/1478-3975/11/6/065004.

[234] G. Sciumè. Mechanistic modeling of vascular tumor growth: An extension of Biot's theory to hierarchical bi-compartment porous medium system. *Acta Mechanica*, 232:1445–1478, 2021. DOI: 10.1101/2020.06.29.176982.

[235] G. Sciumè, M. Ferrari, and B. A. Schrefler. Saturation-pressure relationships for two- and three-phase flow analogies for soft matter. *Mechanics Research Communications*, 62: 132–137, 2014. DOI: 10.1016/j.mechrescom.2014.10.001.

[236] G. Seano, H. T. Nia, K. E. Emblem, M. Datta, J. Ren, S. Krishnan, J. Kloepper, M. C. Pinho, W. W. Ho, M. Ghosh, V. Askoxylakis, G. B. Ferraro, L. Riedemann, E. R. Gerstner, T. T. Batchelor, P. Y. Wen, N. U. Lin, A. J. Grodzinsky, D. Fukumura, P. Huang, J. W. Baish, T. P. Padera, L. L. Munn, and R. K. Jain. Solid stress in brain tumours causes neuronal loss and neurological dysfunction and can be reversed by lithium. *Nature Biomedical Engineering*, 2019. DOI: 10.1038/s41551-018-0334-7.

[237] T. W. Secomb and R. Hsu. Simulation of O2 transport in skeletal muscle: diffusive exchange between arterioles and capillaries. *American Journal of Physiology-Heart and Circulatory Physiology*, 267(3):H1214–H1221, 1994. DOI: 10.1152/ajpheart.1994.267.3.H1214.

[238] T. W. Secomb, R. Hsu, R. D. Braun, J. R. Ross, J. F. Gross, and M. W. Dewhirst. Theoretical Simulation of Oxygen Transport to Tumors by Three-Dimensional Networks of Microvessels. In A. G. Hudetz and D. F. Bruley, editors, *Oxygen Transport to Tissue XX*, pages 629–634. Springer US, Boston, MA, 1998. DOI: 10.1007/978-1-4615-4863-8_74.

[239] T. W. Secomb. Three-dimensional network data: Rat tumor (1998). https://physiology.arizona.edu/people/secomb/network/rattum98, 1998. Accessed: 2021-03-22.

[240] T. W. Secomb. Blood Flow in the Microcirculation. *Annual Review of Fluid Mechanics*, 49(1):443–461, 2017. DOI: 10.1146/annurev-fluid-010816-060302.

[241] T. W. Secomb, R. Hsu, E. Y. H. Park, and M. W. Dewhirst. Green's Function Methods for Analysis of Oxygen Delivery to Tissue by Microvascular Networks. *Annals of Biomedical Engineering*, 32(11):1519–1529, 2004. DOI: 10.1114/B:ABME.0000049036.08817.44.

[242] R. J. Shipley, A. F. Smith, P. W. Sweeney, A. R. Pries, and T. W. Secomb. A hybrid discrete-continuum approach for modelling microcirculatory blood flow. *Mathematical Medicine and Biology: A Journal of the IMA*, 2019. DOI: 10.1093/imammb/dqz006.

[243] J. T. Smith, J. K. Tomfohr, M. C. Wells, T. P. Beebe, T. B. Kepler, and W. M. Reichert. Measurement of Cell Migration on Surface-Bound Fibronectin Gradients. *Langmuir*, 20 (19):8279–8286, 2004. DOI: 10.1021/la0489763.

[244] J. T. Smith, J. T. Elkin, and W. M. Reichert. Directed cell migration on fibronectin gradients: Effect of gradient slope. *Experimental Cell Research*, 312(13):2424–2432, 2006. DOI: 10.1016/j.yexcr.2006.04.005.

[245] S. Soleimani, M. Shamsi, M. A. Ghazani, H. P. Modarres, K. P. Valente, M. Saghafian, M. M. Ashani, M. Akbari, and A. Sanati-Nezhad. Translational models of tumor angiogenesis: A nexus of in silico and in vitro models. *Biotechnology Advances*, 36(4): 880–893, 2018. DOI: 10.1016/j.biotechadv.2018.01.013.

[246] I. Steinbrecher, M. Mayr, M. J. Grill, J. Kremheller, C. Meier, and A. Popp. A mortar-type finite element approach for embedding 1D beams into 3D solid volumes. *Computational Mechanics*, 66(6):1377–1398, 2020. DOI: 10.1007/s00466-020-01907-0.

[247] M. A. Stolarska, Y. Kim, and H. G. Othmer. Multi-scale models of cell and tissue dynamics. *Philosophical Transactions of the Royal Society A: Mathematical, Physical and Engineering Sciences*, 367(1902):3525–3553, 2009. DOI: 10.1098/rsta.2009.0095.

[248] T. Stylianopoulos, B. Diop-Frimpong, L. L. Munn, and R. K. Jain. Diffusion Anisotropy in Collagen Gels and Tumors: The Effect of Fiber Network Orientation. *Biophysical Journal*, 99(10):3119–3128, 2010. DOI: 10.1016/j.bpj.2010.08.065.

[249] T. Stylianopoulos, J. D. Martin, V. P. Chauhan, S. R. Jain, B. Diop-Frimpong, N. Bardeesy, B. L. Smith, C. R. Ferrone, F. J. Hornicek, Y. Boucher, L. L. Munn, and R. K. Jain. Causes, consequences, and remedies for growth-induced solid stress in murine and human tumors. *Proceedings of the National Academy of Sciences of the United States of America*, 109 (38):15101–15108, 2012. DOI: 10.1073/pnas.1213353109.

[250] P. W. Sweeney, S. Walker-Samuel, and R. J. Shipley. Insights into cerebral haemodynamics and oxygenation utilising in vivo mural cell imaging and mathematical modelling. *Scientific Reports*, 8(1):1373, 2018. DOI: 10.1038/s41598-017-19086-z.

[251] P. W. Sweeney, S. Walker-Samuel, and R. J. Shipley. Vascular and interstitial flow solver for discrete microvascular networks. 2018. DOI: 10.5281/ZENODO.1414160.

[252] P. W. Sweeney, A. D'Esposito, S. Walker-Samuel, and R. J. Shipley. Modelling the transport of fluid through heterogeneous, whole tumours in silico. *PLOS Computational Biology*, 15(6):e1006751, 2019. DOI: 10.1371/journal.pcbi.1006751.

[253] A. Szabó and R. M. H. Merks. Cellular Potts Modeling of Tumor Growth, Tumor Invasion, and Tumor Evolution. *Frontiers in Oncology*, 3:87, 2013. DOI: 10.3389/fonc.2013.00087.

[254] A. Tarantola. *Inverse Problem Theory and Methods for Model Parameter Estimation*, volume xii. Society for Industrial and Applied Mathematics, 2005. DOI: 10.1137/1.9780898717921.

[255] D. L. Thomas, M. F. Lythgoe, G. S. Pell, F. Calamante, and R. J. Ordidge. The measurement of diffusion and perfusion in biological systems using magnetic resonance imaging. *Physics in Medicine and Biology*, 45(8):R97–R138, 2000. DOI: 10.1088/0031-9155/45/8/201.

[256] R. G. Thorne and C. Nicholson. In vivo diffusion analysis with quantum dots and dextrans predicts the width of brain extracellular space. *Proceedings of the National Academy of Sciences*, 103(14):5567–5572, 2006. DOI: 10.1073/pnas.0509425103.

[257] A. Tosin and L. Preziosi. Multiphase modeling of tumor growth with matrix remodeling and fibrosis. *Mathematical and Computer Modelling*, 52(7-8):969–976, 2010. DOI: 10.1016/j.mcm.2010.01.015.

[258] E. Turska and B. Schrefler. On convergence conditions of partitioned solution procedures for consolidation problems. *Computer Methods in Applied Mechanics and Engineering*, 106(1-2):51–63, 1993. DOI: 10.1016/0045-7825(93)90184-Y.

[259] J. van der Zee. Heating the patient: a promising approach? *Annals of Oncology*, 13(8): 1173–1184, 2002. DOI: 10.1093/annonc/mdf280.

[260] M. T. van Genuchten. A Closed-form Equation for Predicting the Hydraulic Conductivity of Unsaturated Soils. *Soil Science Society of America Journal*, 44(5):892–898, 1980. DOI: 10.2136/sssaj1980.03615995004400050002x.

[261] V. Vavourakis, P. A. Wijeratne, R. Shipley, M. Loizidou, T. Stylianopoulos, and D. J. Hawkes. A Validated Multiscale In-Silico Model for Mechano-sensitive Tumour Angiogenesis and Growth. *PLOS Computational Biology*, 13(1):e1005259, 2017. DOI: 10.1371/journal.pcbi.1005259.

[262] V. Vavourakis, T. Stylianopoulos, and P. A. Wijeratne. In-silico dynamic analysis of cytotoxic drug administration to solid tumours: Effect of binding affinity and vessel permeability. *PLOS Computational Biology*, 14(10):e1006460, 2018. DOI: 10.1371/JOURNAL.PCBI.1006460.

[263] F. Verdugo and W. A. Wall. Unified computational framework for the efficient solution of n-field coupled problems with monolithic schemes. *Computer Methods in Applied Mechanics and Engineering*, 310:335–366, 2016. DOI: 10.1016/j.cma.2016.07.016.

[264] F. Verdugo, C. J. Roth, L. Yoshihara, and W. A. Wall. Efficient solvers for coupled models in respiratory mechanics. *International Journal for Numerical Methods in Biomedical Engineering*, 33(2):e02795, 2017. DOI: 10.1002/cnm.2795.

[265] A. Verruijt. *Computational Geomechanics*, volume 7 of *Theory and Applications of Transport in Porous Media*. Springer Netherlands, Dordrecht, 1995. DOI: 10.1007/978-94-017-1112-8.

[266] E. Vidotto, T. Koch, T. Köppl, R. Helmig, and B. Wohlmuth. Hybrid Models for Simulating Blood Flow in Microvascular Networks. *Multiscale Modeling & Simulation*, 17(3): 1076–1102, 2019. DOI: 10.1137/18M1228712.

[267] G. Vilanova, I. Colominas, and H. Gomez. Computational Modeling of Tumor-Induced Angiogenesis. *Archives of Computational Methods in Engineering*, 24(4):1071–1102, 2017. DOI: 10.1007/s11831-016-9199-7.

[268] G. Vilanova, I. Colominas, and H. Gomez. A mathematical model of tumour angiogenesis: growth, regression and regrowth. *Journal of The Royal Society Interface*, 14(126): 20160918, 2017. DOI: 10.1098/rsif.2016.0918.

[269] A.-T. Vuong, L. Yoshihara, and W. Wall. A general approach for modeling interacting flow through porous media under finite deformations. *Computer Methods in Applied Mechanics and Engineering*, 283(Supplement C):1240–1259, 2015. DOI: 10.1016/j.cma.2014.08.018.

[270] A.-T. Vuong, C. Ager, and W. Wall. Two finite element approaches for Darcy and Darcy-Brinkman flow through deformable porous media–Mixed method vs. NURBS based (isogeometric) continuity. *Computer Methods in Applied Mechanics and Engineering*, 305 (Supplement C):634–657, 2016. DOI: 10.1016/j.cma.2016.03.005.

[271] A.-T. Vuong, A. D. Rauch, and W. A. Wall. A biochemo-mechano coupled, computational model combining membrane transport and pericellular proteolysis in tissue mechanics. *Proceedings of the Royal Society A: Mathematical, Physical and Engineering Sciences*, 473(2199):20160812, 2017. DOI: 10.1098/rspa.2016.0812.

[272] A.-T. Vuong. *A Computational Approach to Coupled Poroelastic Media Problems*. PhD thesis, Technische Universität München, 2016. http://mediatum.ub.tum.de/?id=1341399.

[273] S. Walker-Samuel. Mesentery Network. https://github.com/CABI-SWS/reanimate/blob/reanimate/data/Mesentery/Flow2AmiraPressure.am, 2021. Accessed: 2021-03-22.

[274] R. A. Weinberg. *The Biology of Cancer*. W.W. Norton, 2013.

[275] S. M. Weis and D. A. Cheresh. Tumor angiogenesis: molecular pathways and therapeutic targets. *Nature Medicine*, 17(11):1359–1370, 2011. DOI: 10.1038/nm.2537.

[276] M. Welter and H. Rieger. Physical determinants of vascular network remodeling during tumor growth. *The European Physical Journal E*, 33(2):149–163, 2010. DOI: 10.1140/epje/i2010-10611-6.

[277] M. Welter and H. Rieger. Interstitial Fluid Flow and Drug Delivery in Vascularized Tumors: A Computational Model. *PLoS ONE*, 8(8):e70395, 2013. DOI: 10.1371/journal.pone.0070395.

[278] M. Welter and H. Rieger. Computer Simulations of the Tumor Vasculature: Applications to Interstitial Fluid Flow, Drug Delivery, and Oxygen Supply. In *Systems Biology of Tumor Microenvironment: Quantitative Modeling and Simulations*, pages 31–72. Springer International Publishing, Cham, 2016. DOI: 10.1007/978-3-319-42023-3_3.

[279] M. Welter, T. Fredrich, H. Rinneberg, and H. Rieger. Computational Model for Tumor Oxygenation Applied to Clinical Data on Breast Tumor Hemoglobin Concentrations Suggests Vascular Dilatation and Compression. *PLOS ONE*, 11(8):e0161267, 2016. DOI: 10.1371/journal.pone.0161267.

[280] S. Wilhelm, A. J. Tavares, Q. Dai, S. Ohta, J. Audet, H. F. Dvorak, and W. C. W. Chan. Analysis of nanoparticle delivery to tumours. *Nature Reviews Materials*, 1(5):16014, 2016. DOI: 10.1038/natrevmats.2016.14.

[281] B. Wirthl. Modelling of drug delivery and hyperthermia treatment in a multiphase tumour growth model. Master's thesis, Technische Universität München, 2018.

[282] B. Wirthl, J. Kremheller, B. A. Schrefler, and W. A. Wall. Extension of a multiphase tumour growth model to study nanoparticle delivery to solid tumours. *PLOS ONE*, 15(2): e0228443, 2020. DOI: 10.1371/journal.pone.0228443.

[283] S. Wise, J. Lowengrub, H. Frieboes, and V. Cristini. Three-dimensional multispecies nonlinear tumor growth–I: Model and numerical method. *Journal of Theoretical Biology*, 253(3):524–543, 2008. DOI: 10.1016/j.jtbi.2008.03.027.

[284] B. I. Wohlmuth. A Mortar Finite Element Method Using Dual Spaces for the Lagrange Multiplier. *SIAM Journal on Numerical Analysis*, 38(3):989–1012, 2000. DOI: 10.1137/S0036142999350929.

[285] World Health Organization. Cancer. https://www.who.int/health-topics/cancer, 2021. Accessed: 2021-03-22.

[286] P. Wriggers. *Nonlinear Finite Element Methods*. Springer Berlin Heidelberg, Berlin, Heidelberg, 2008. DOI: 10.1007/978-3-540-71001-1.

[287] M. Wu, H. B. Frieboes, S. R. McDougall, M. A. Chaplain, V. Cristini, and J. Lowengrub. The effect of interstitial pressure on tumor growth: Coupling with the blood and lymphatic vascular systems. *Journal of Theoretical Biology*, 320(Supplement C):131–151, 2013. DOI: 10.1016/j.jtbi.2012.11.031.

[288] M. Wu, H. B. Frieboes, M. A. Chaplain, S. R. McDougall, V. Cristini, and J. S. Lowengrub. The effect of interstitial pressure on therapeutic agent transport: Coupling with the tumor blood and lymphatic vascular systems. *Journal of Theoretical Biology*, 355: 194–207, 2014. DOI: 10.1016/j.jtbi.2014.04.012.

[289] J. Xu, G. Vilanova, and H. Gomez. A Mathematical Model Coupling Tumor Growth and Angiogenesis. *PLOS ONE*, 11(2):e0149422, 2016. DOI: 10.1371/journal.pone.0149422.

[290] J. Xu, G. Vilanova, and H. Gomez. Phase-field model of vascular tumor growth: Three-dimensional geometry of the vascular network and integration with imaging data. *Computer Methods in Applied Mechanics and Engineering*, 359:112648, 2020. DOI: 10.1016/j.cma.2019.112648.

[291] G. D. Yancopoulos, S. Davis, N. W. Gale, J. S. Rudge, S. J. Wiegand, and J. Holash. Vascular-specific growth factors and blood vessel formation. *Nature*, 407(6801):242–248, 2000. DOI: 10.1038/35025215.

[292] B. Yang, T. A. Laursen, and X. Meng. Two dimensional mortar contact methods for large deformation frictional sliding. *International Journal for Numerical Methods in Engineering*, 62(9):1183–1225, 2005. DOI: 10.1002/nme.1222.

[293] T. E. Yankeelov. What if we had a mathematical equation for cancer? https://thehill.com/opinion/healthcare/463656-what-if-we-had-a-mathematical-equation-for-cancer, 2019. Accessed: 2021-03-22.

[294] T. E. Yankeelov, N. Atuegwu, D. Hormuth, J. A. Weis, S. L. Barnes, M. I. Miga, E. C. Rericha, and V. Quaranta. Clinically Relevant Modeling of Tumor Growth and Treatment Response. *Science Translational Medicine*, 5(187):187ps9–187ps9, 2013. DOI: 10.1126/scitranslmed.3005686.

[295] T. E. Yankeelov, V. Quaranta, K. J. Evans, and E. C. Rericha. Toward a Science of Tumor Forecasting for Clinical Oncology. *Cancer Research*, 75(6):918–923, 2015. DOI: 10.1158/0008-5472.CAN-14-2233.

[296] Q. Yu and I. Stamenkovic. Angiopoietin-2 Is Implicated in the Regulation of Tumor Angiogenesis. *The American Journal of Pathology*, 158(2):563–570, 2001. DOI: 10.1016/S0002-9440(10)63998-3.

[297] Y.-R. Zhang, R. Lin, H.-J. Li, W.-l. He, J.-Z. Du, and J. Wang. Strategies to improve tumor penetration of nanomedicines through nanoparticle design. *Wiley Interdisciplinary Reviews: Nanomedicine and Nanobiotechnology*, 11(1):e1519, 2019. DOI: 10.1002/wnan.1519.

[298] X. Zheng, S. M. Wise, and V. Cristini. Nonlinear simulation of tumor necrosis, neovascularization and tissue invasion via an adaptive finite-element/level-set method. *Bulletin of Mathematical Biology*, 67(2):211, 2005. DOI: 10.1016/j.bulm.2004.08.001.

[299] A. Ziemys, K. Yokoi, M. Kai, Y. Liu, M. Kojic, V. Simic, M. Milosevic, A. Holder, and M. Ferrari. Progression-dependent transport heterogeneity of breast cancer liver metastases as a factor in therapeutic resistance. *Journal of Controlled Release*, 291:99–105, 2018. DOI: 10.1016/j.jconrel.2018.10.014.

[300] O. C. Zienkiewicz and R. L. Taylor. *The Finite Element Method for Solid and Structural Mechanics*. Elsevier, 2014. DOI: 10.1016/C2009-0-26332-X.

[301] O. C. Zienkiewicz, R. L. Taylor, and J. Z. Zhu. *The Finite Element Method: its Basis and Fundamentals*. Elsevier, 2013. DOI: 10.1016/C2009-0-24909-9.

[302] O. C. Zienkiewicz, R. L. Taylor, and P. Nithiarasu. *The Finite Element Method for Fluid Dynamics*. Elsevier, 2014. DOI: 10.1016/C2009-0-26328-8.

Verzeichnis der betreuten Studienarbeiten

Im Rahmen dieser Dissertation entstanden am Lehrstuhl für Numerische Mechanik (LNM) in den Jahren von 2017 bis 2021 unter wesentlicher wissenschaftlicher, fachlicher und inhaltlicher Anleitung des Autors die im Folgenden aufgeführten studentischen Arbeiten. Der Autor dankt allen Studierenden für ihr Engagement bei der Unterstützung dieser wissenschaftlichen Arbeit.

Studierende/r	**Studienarbeit**
Barbara Wirthl	*Modelling of drug delivery and hyperthermia treatment in a multiphase tumour growth model*, Masterarbeit, 2018, eingeflossen in Kapitel 2.3.3 und Kapitel 5.3
An Khang Bui	*Investigations of the influence of anisotropy on (a-)vascular tumor growth with a computational model*, Semesterarbeit, 2019, eingeflossen in Bemerkung 3.6 und Bemerkung 3.9
Antonia Seibold	*Output Monitoring Routines for Parameter Studies in a Finite Element Tumour Growth Model*, Bachelorarbeit, 2019
Catrin Rodenberg	*Global Sensitivity Analysis of a Multiphase Model for Avascular Tumor Growth*, Masterarbeit (Physik), 2020
Katharina Plöckl	*Modeling of Blood Vessel Compression in a Computational Tumor Growth Model*, Masterarbeit, 2020, eingeflossen in Kapitel 3.4.5, Kapitel 4.3.3.3 und Kapitel 5.5